Creep Mechanisms in High-Temperature In-Situ Composites

by

Dr. Bernard P. Bewlay
Dr. Melvin R. Jackson
Prof. Clyde L. Briant

AFOSR FINAL REPORT

This research was sponsored by the Air Force Office of Scientific Research,
Directorate of Aerospace and Materials Science
Under Contract FQ8671-96005872306/AS

The views and conclusions contained in this document are those of the authors and should not be interpreted as necessarily representing the official policies or endorsement, either expressed or implied, of the Air Force Office of Scientific Research or the U.S. Government

August 1999



BROWN UNIVERSITY



GE Corporate Research & Development

DISTRIBUTION STATEMENT A
Approved for Public Release
Distribution Unlimited

399

REPORT DOCUMENTATION PAGE

AFRL-SR-BL-TR-99-

0232

Public reporting burden for this collection of information is estimated to average 1 hour per response, including t
gathering and maintaining the data needed, and completing and reviewing the collection of information. Send cc
collection of information, including suggestions for reducing this burden, to Washington Headquarters Services, Directorate for Information Operations
Davis Highway, Suite 1204, Arlington, VA 22202-4302, and to the Office of Management and Budget, Paperwork Reduction Project (0704-0188) Washington, DC 20503

1. AGENCY USE ONLY (Leave Blank)	2. REPORT DATE	3. REPORT TYPE AND DATES COVERED
	August 31, 1999	Final Report; June 1996 –August 1999

4. TITLE AND SUBTITLE
Creep Mechanisms in High-Temperature In-Situ Composites

3. FUNDING NUMBERS
FQ8671-96005872306/AS

F49620-96-C-0022

6. AUTHORS
Dr. Bernard P. Bewlay, Dr. Melvin R. Jackson, Prof. Clyde L. Briant

7. PERFORMING ORGANIZATION NAME(S) AND ADDRESS(ES)
GE Corporate Research and Development, Schenectady, NY 12301

8. PERFORMING ORGANIZATION REPORT NUMBER
99SRD007

9. SPONSORING / MONITORING AGENCY NAME(S) AND ADDRESS(ES)
Air Force Office of Scientific Research, Directorate of Aerospace and Materials Science
801 North Randolph Street, Mail Room 732
Arlington,. VA 22203-1977

10. SPONSORING / MONITORING AGENCY REPORT NUMBER

11. SUPPLEMENTARY NOTES

12a. DISTRIBUTION / AVAILABILITY STATEMENT
Approved for public release; distribution is unlimited

12b. DISTRIBUTION CODE
FQ8671-96005872306/AS

13. ABSTRACT (Maximum 200 words)

The present work describes a three-year investigation of creep and toughening mechanisms in high-strength, directionally solidified Nb-silicide based in-situ composites. These composites consist of a Nb-based silicide toughened with a Nb-based solid solution. These composites have melting temperatures in excess of 1700°C and densities less than 8 g/cc.

The motivation for this study was to derive an understanding of a class of materials that possess a long-term high-temperature capability in excess of current nickel-based superalloys. These studies have shown that room temperature fracture toughness can be increased to above 20 MPa$\sqrt{m}$ in a range of complex silicide-based composites with creep rupture behaviors superior to that of nickel-based superalloys. The chemistries of the constituent phases, their volume fractions and their morphologies are critical features that control the balance of high- and low-temperature properties in this family of composites.

During this program a thorough investigation of the dominant creep and toughening mechanisms that can be enhanced by independent modifications of the microstructure and properties of the metal and silicide phases has been completed. This investigation has examined the effect of volume fraction of silicide and strength of the metallic phase on the creep performance and fracture toughness of the composites. In-situ composite alloying concepts have been developed to provide a scheme for optimizing creep performance through control of the constituent phases. A series of phase equilibria studies have also been completed. These include liquid-solid and solid-state phase equilibria in the following systems: Nb-Ti-Si, Hf-Si, Nb-Hf-Si, and Hf-Ti-Si. These investigations have been published in the open literature during the present contract.

14. SUBJECT TERMS	15. NUMBER OF PAGES
	16. PRICE CODE

17. SECURITY CLASSIFICATION OF REPORT	18. SECURITY CLASSIFICATION OF THIS PAGE	19. SECURITY CLASSIFICATION OF ABSTRACT	20. LIMITATION OF ABSTRACT
unclassified	unclassified	unclassified	UL

NSN 7540-01-280-5500

Standard Form 298 (Rev. 2-89)
Prescribed by ANSI Std. Z39-19
298-102

DTIC QUALITY INSPECTED 4

19990928 307

Creep Mechanisms in High-Temperature In-Situ Composites

Annual Report: August 1999

Creep Mechanisms in High-Temperature In-Situ Composites: Report for Period 9-1-98 to 8-31-99

(Contract Number: FQ8671-96005872306/AS)

Research Contributors

Dr. Bernard P. Bewlay, GE-CRD, Staff Metallurgist
Dr. Melvin R. Jackson, GE-CRD, Staff Metallurgist
Dr. John A. Sutliff, GE-CRD, Staff Materials Scientist
Prof. Clyde L. Briant, Brown University, Professor
Mr. Scott D. Sitzman, GE-CRD, Materials Scientist

Summary

This report describes the activities of the third year of our studies on creep and toughening mechanisms in high-strength, directionally solidified Nb-silicide based in-situ composites. The motivation for this study was to derive an understanding of a class of materials that possess a long-term high-temperature capability in excess of current nickel-based superalloys. During this program a thorough investigation of the creep and toughening mechanisms that can be enhanced by modification of the microstructure and properties of the metal and silicide phases of the composite has been completed. Detailed consideration of the mechanisms that control high-temperature creep deformation of the individual phases at temperatures above 1000 °C is required in order to exploit the full potential of these in-situ composites.

This investigation has examined the effect of volume fraction of silicide and strength of the metallic phase on the creep performance and fracture toughness of the composites. These studies have shown that room temperature fracture toughness can be increased to above 20 MPa$\sqrt{m}$ in a range of complex silicide-based composites with creep rupture behaviors superior to that of nickel-based superalloys. In-situ composite alloying concepts have been developed to provide a scheme for optimizing creep performance through identification of the critical Nb, Hf and Ti concentrations in the parent alloy. A series of phase equilibria studies have also been completed. These include liquid-solid and solid-state phase equilibria in the Nb-Hf-Si and Hf-Ti-Si systems. This report will describe first, recent studies on composite toughening mechanisms, second, the progress on creep studies, and, third, the progress on phase equilibria investigations.

1.0. Objectives

The objective of this research was to investigate high-temperature creep and low-temperature toughening mechanisms in high-strength directionally solidified (DS) niobium silicide in-situ compos-

ites. The composites that were investigated consist of Nb-based silicides toughened by a Nb-based solid solution. A broad range of effects has been studied. These include deformation of the metallic phase, plastic deformation and damage of the silicide, the role of the volume fraction of silicide, and the creep performance of the silicide. The effects of Hf, Ti, Mo, Cr and Al additions on the high- and low-temperature properties of these composites have been examined. In addition, phase stability in composites generated from Nb-Ti-Si, Nb-Hf-Si, and Nb-Hf-Ti-Si alloys has been investigated.

2.0 Approach

For the investigation of creep mechanisms and toughening mechanisms a broad range of effects has been examined. These include the strength of the metallic phase, the type of silicide (Nb_5Si_3-tI32, Nb_3Si-tP32, $Nb(Hf,Ti)_5Si_3$-hP16), the role of the volume fraction of silicide, the effect of increasing the creep strength of the silicide, and the role of texture of the individual phases. The approach for investigation of creep mechanisms has focused on compression creep tests at temperatures from 1000 °C to 1200 °C with selected tensile creep tests on those composites that show promising properties. We have used directional solidification for composite fabrication because it provides highly controlled and reproducible in-situ composite microstructures.

The effects of silicide precipitates in the metallic toughening phase, and metal precipitates in the silicide, have received significant attention during the course of the present study. These can have critical effects on both the low- and high-temperature mechanical properties. In addition, phase equilibria in ternary systems, such as Nb-Ti-Si, Nb-Hf-Si, Nb-Hf-Ti-Si, and Hf-Ti-Si, have been defined.

3.0 Progress and Status of Effort

The work of the third year of this contract falls into the following categories: evaluation of composite fracture toughness, studies of creep mechanisms, and determination of phase stability in high-temperature in-situ composites. The base Nb-silicide in-situ composite alloy composition that has shown strong promise is Nb-8Hf-25Ti-2Al-2Cr-16Si (MASC) [1-4]. In order to understand the effects of phase composition, volume fraction and phase morphology on composite properties, a series of toughness and creep studies were performed on composites generated from ternary Nb-Hf-Si and quaternary Nb-Hf-Ti-Si alloys [4,5].

3.1 Fracture Toughness Measurements

The Effect of the Volume Fraction of (Nb) on Fracture Toughness

The composite from the base Nb-8Hf-25Ti-2Al-2Cr-16Si composition possessed a complex microstructure and in order to examine the effect of the volume fraction of (Nb) on room temperature fracture toughness a series of studies based on the Nb-8Hf-25Ti-16Si quaternary alloy were performed. This composite consisted of (Nb) and $(Nb)_3Si$. In order to explore the effect of volume fraction of silicide, the Si concentration was adjusted from 12% to 22% (substituting for Nb). It was also recognised that adjusting the Si and Nb alone leads to changes in the compositions of the (Nb) and the $(Nb)_3Si$. Thus, an additional series of composites was generated where the Hf and Ti compositions were adjusted along with the Si concentration in an effort to keep the (Nb) and $(Nb)_3Si$ compositions constant. The microstructures of these composites are described subsequently in the section on creep mechanisms.

Room temperature fracture toughness measurements are shown in Table 1 and Figure 1 below for a range of in-situ composites generated from quaternary Nb-Hf-Ti-Si alloys. The toughness levels

Table 1. Room temperature fracture toughness of a range of in-situ composites generated from quaternary Nb-Hf-Ti-Si alloys.

Composition	**Fracture Toughness** ($\mathbf{MPa\sqrt{m}}$)	**Volume Fraction of (Nb)**
Nb-8Hf-25Ti-12Si	13.3	
Nb-8Hf-25Ti-14Si	10.9	
Nb-8Hf-25Ti-16Si	16.6	0.40
Nb-8Hf-25Ti-18Si	11.0	0.29
Nb-8Hf-25Ti-20Si	12.5	
Nb-8Hf-25Ti-22Si	11.5	0.26
Nb-18.2Si	6.5	0.35
Nb-6Hf-19Ti-12Si	12.5	
Nb-7Hf-22Ti-14Si	11.7	0.47
Nb-7Hf-10Ti-16Si	11.7	
Nb-7.5Hf-21Ti-16Si	12.2	
Nb-10Hf-21Ti-16Si	11.9	
Nb-12.5Hf-21Ti-16Si	12.1	
Nb-21Ti-16Si	11.6	
Nb-33Ti-16Si	11.1	

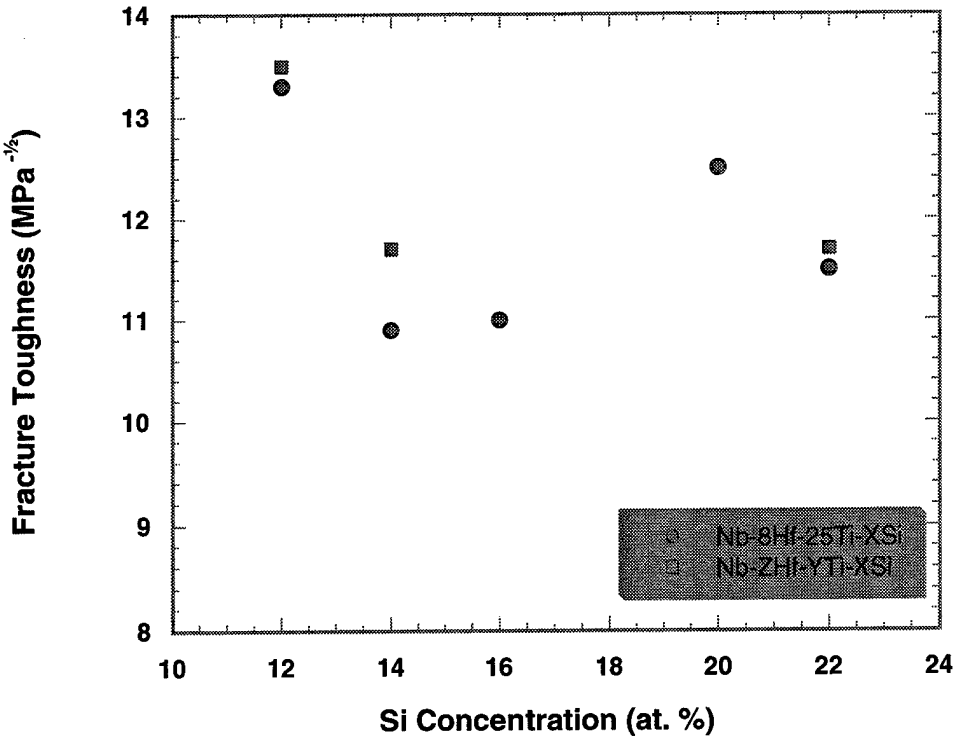


Figure 1. Graph of the room temperature fracture toughness as a function of Si concentration for a range of quaternary Nb-Hf-Ti-Si alloys.

are substantially higher than those of binary alloys of the same Si concentration and volume fraction of (Nb). The toughness level is higher at low Si concentrations (higher volume fraction of (Nb)) than at high Si concentration, but there is less sensitivity of the room temperature fracture toughness to Si concentration in quaternary alloys than in binary alloys. In addition, there is no minimum in the room temperature fracture toughness at the 18%Si concentration as has been observed in the case of the binary Nb-Si alloys.

The above data also indicate that the room temperature fracture toughness was relatively insensitive to Hf: Ti composition ratios in the range 0.2-0.6. However, Ti additions appear to have a stronger effect on toughness than Hf additions. The room temperature fracture toughness of composites with 33Ti were generally higher than those at 21Ti.

Fracture Toughness in Complex Alloy Composites

Table 2 shows a range of alloys derived from the base MASC composition [1, 2] (last row of the table below). The effects of Ti concentation, Hf concentration and Si concentration on room temperature fracture toughness were examined in these complex systems.

Table 2 : Room temperature fracture toughness of Nb-16Si composites modified with Hf, Ti, Cr and Al.

Composition	**Fracture Toughness** (MPa)
Nb-20Ti-8Hf-2Al-2Cr-16Si	21.0
Nb-30Ti-8Hf-2Al-2Cr-16Si	19.3
Nb-24.6Ti-11Hf-2Al-2Cr-16Si	21.8
Nb-23.6Ti-14Hf-2Al-2Cr-16Si	18.2
Nb- 25Ti-8Hf-2Al-2Cr-18Si	20.0
Nb-26.5Ti-8Hf-2Al-10Cr-16Si	18.7
Nb-24.7Ti-8.2Hf-2.0Cr-1.9Al-16.0Si	23.3

For Ti concentrations in the range 20-30%, there is little effect on toughness. In addition, the Si concentration of the MASC can be increased to 18% without compromising composite toughness. It can also be seen from the above data that increasing the Hf from 8 to 14%, or increasing the Cr concentration up to 10% leads to a reduction in toughness. Nevertheless, toughness levels of this range of composites are promising. Higher Cr levels improve high temperature oxidation resistance. At high Cr concentrations Laves phases can also be generated in the composites. However, in the above systems no Laves phases were observed.

3.2 Creep Mechanisms

The present section describes studies of the creep behavior of Nb-silicide composites. The effects of Hf, Ti and Mo additions to a range of composites have been examined, and their effect on secondary creep rate has been measured. The role of texture in these composites has also been measured using electron back scattering pattern analysis (EBSP). The effect of the hP16 type silicide, which can be stabilized at high Hf and Ti concentrations, has also been examined. Finally, the effect of volume fraction of Nb_3Si on creep properties has been examined in detail.

Nb-Ti-Hf-Si In-Situ Composites

The effect of Hf and Ti concentrations on creep performance of Nb silicide-based composites has been investigated for a range of quaternary Nb-Hf-Ti-Si silicide composites, as well as higher-order alloys [1,2,6]. The effect of increasing Hf and Ti concentrations is shown in Figure 2 and Table 3 for a series of quaternary DS Nb-Hf-Ti-Si alloys at a temperature of 1200°C and at stress levels in the range 140-280 MPa. Data for the Nb-7.5Hf-16Si ternary alloy are also included. Hf concentrations in the range 7.5-12.5 and Ti concentrations in the range 21-33 were examined, providing

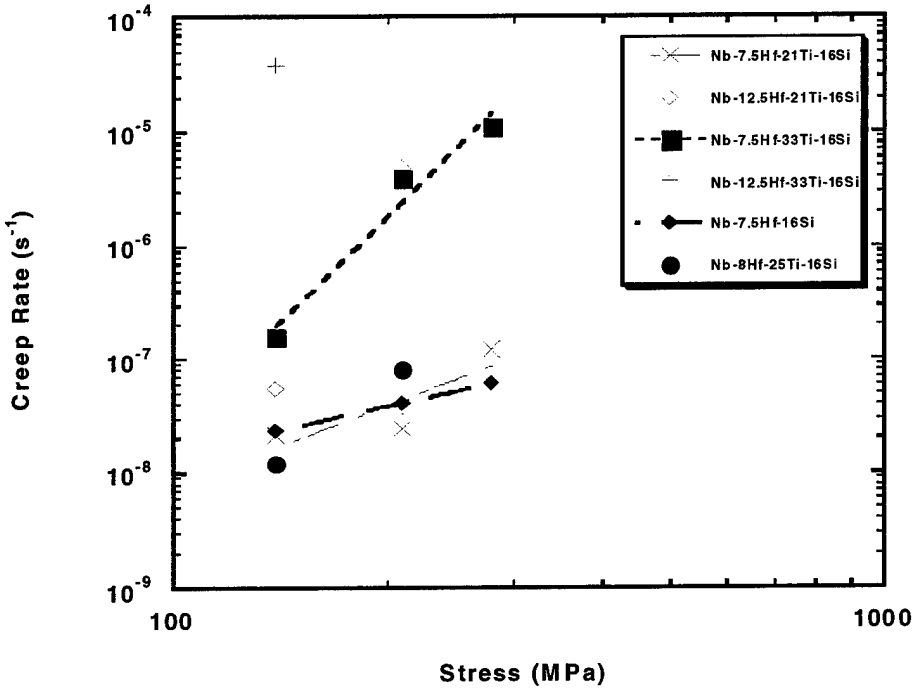


Figure 2. Graph of secondary creep rates at 1200 °C for a range of quaternary Nb-Hf-Ti-Si alloys.

Table 3. Secondary creep rates at 1200 °C for a range of Nb-Hf-Ti-Si alloys.

Composition	**140 MPa Creep Rate (s^{-1})**	**210 MPa Creep Rate (s^{-1})**	**280 MPa Creep Rate (s^{-1})**
Nb-7.5Hf-16Si	2.3×10^{-8}	4.0×10^{-8}	4.8×10^{-8}
Nb-7.5Hf-21Ti-16Si	2.1×10^{-8}	3.2×10^{-8}	1.2×10^{-7}
Nb-7.5Hf-33Ti-16Si	1.6×10^{-7}	3.9×10^{-6}	1.1×10^{-5}
Nb-12.5Hf-21Ti-16Si	5.5×10^{-8}	4.8×10^{-6}	--
Nb-12.5Hf-33Ti-16Si	3.8×10^{-5}	--	--
Nb-16Si	1.5×10^{-8}	4.9×10^{-8}	--

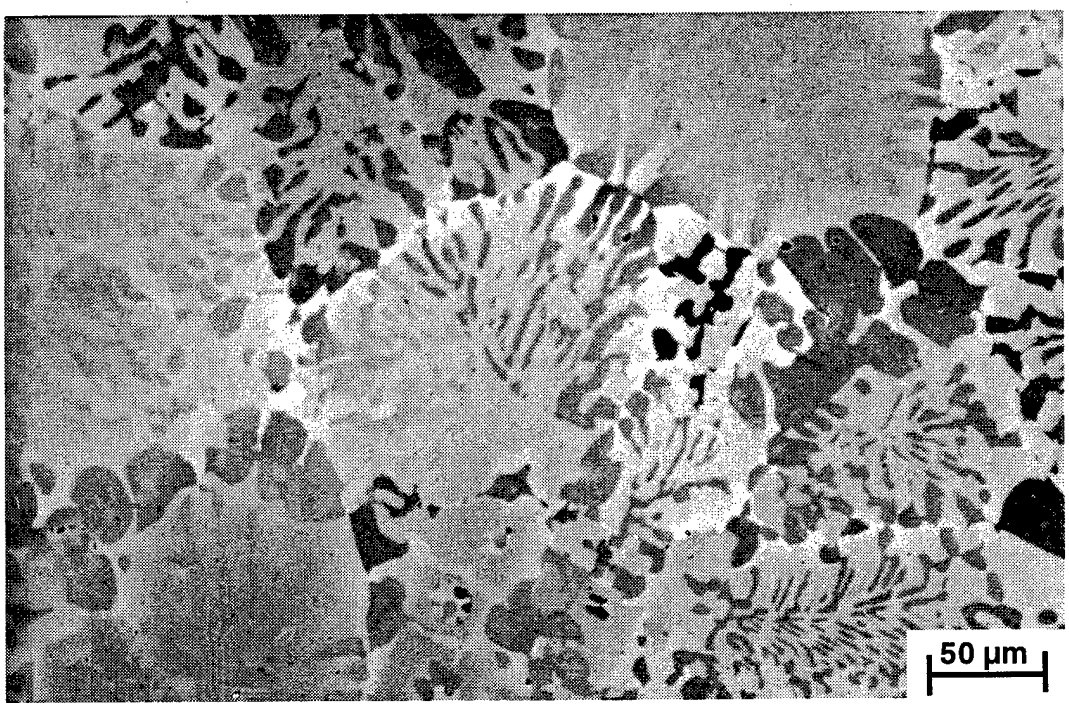


Figure 3. Typical microstructure (BSE image) of the transverse section of a DS composite generated from a quaternary Nb-16Ti-8Hf-16Si alloy at a growth rate of 5 mm/min. The (Nb) is the dark phase and the M_3Si is the light phase.

Ti:Hf ratios in the range 1.7 to 4.4. The microstructures of these composites are similar to that shown in Figure 3. At Hf concentrations up to 8%, and Ti concentrations up to 25%, the secondary creep rates are similar to those of the binary Nb-16Si. However, if the Hf concentration, the Ti concentration, or the Hf+Ti concentration are increased above 8% Hf and 25% Ti, then the secondary creep rates are increased.

These data suggest that for optimum creep performance the Ti:Hf ratio should be maintained at a level less than 3 and the Ti concentration should be kept below 21%. There are several mechanisms that contribute to this behavior. At Nb:(Ti+Hf) ratios below a limit of ~1.5, the hP16 Ti_5Si_3 type silicide is stabilized in preference to the tI32 Nb_5Si_3 type or Nb_3Si type silicides. The creep performance of Ti_5Si_3 is inferior to Nb_5Si_3 and Nb_3Si. This will be discussed in more detail subsequently. The Nb_5Si_3 has a higher melting temperature than either the Ti_5Si_3 or the Hf_5Si_3, and this probably contributes to the improved creep resistance in addition to the more complex crystal structures.

Mo-Modified Composites

It was considered that Mo can increase the strength of the metallic phase and Mo can also reduce creep deformation in Nb_5Si_3. A range of Mo-modified composites was therefore investigated. Secondary creep rates are shown in Table 4 and Figure 4 for a temperature of 1200°C for the Nb-8Hf-25Ti-16Si alloy, as well as alloys containing 3% and 9% Mo (substituting Mo for Nb). Com-

Table 4. Secondary creep rates at 1200 °C for a range of Nb-Hf-Ti-Si alloys modified with Mo.

Composition	70 MPa Creep Rate (s^{-1})	140 MPa Creep Rate (s^{-1})	210 MPa Creep Rate (s^{-1})	280 MPa Creep Rate (s^{-1})
Nb-7.5Hf-16Si	--	$2.3x10^{-8}$	$4.0x10^{-8}$	$4.8x10^{-8}$
Nb-8Hf-25Ti-16Si	$6.3x10^{-9}$	$1.2x10^{-8}$	$8.0x10^{-8}$	Failed
Nb-3Mo-8Hf-21Ti -16Si	$1.4x10^{-8}$	$2.5x10^{-8}$	$6.4x10^{-8}$	Failed
Nb-9Mo-8Hf-21Ti -16Si	$2.6x10^{-8}$	$2.2x10^{-7}$	$4.5x10^{-6}$	Failed
Nb-8Hf-25Ti-2Al-2Cr-16Si	$9.1x10^{-8}$	Failed	--	--
Nb-16Si	$1.7x10^{-9}$	$1.5x10^{-8}$	$4.9x10^{-8}$	--

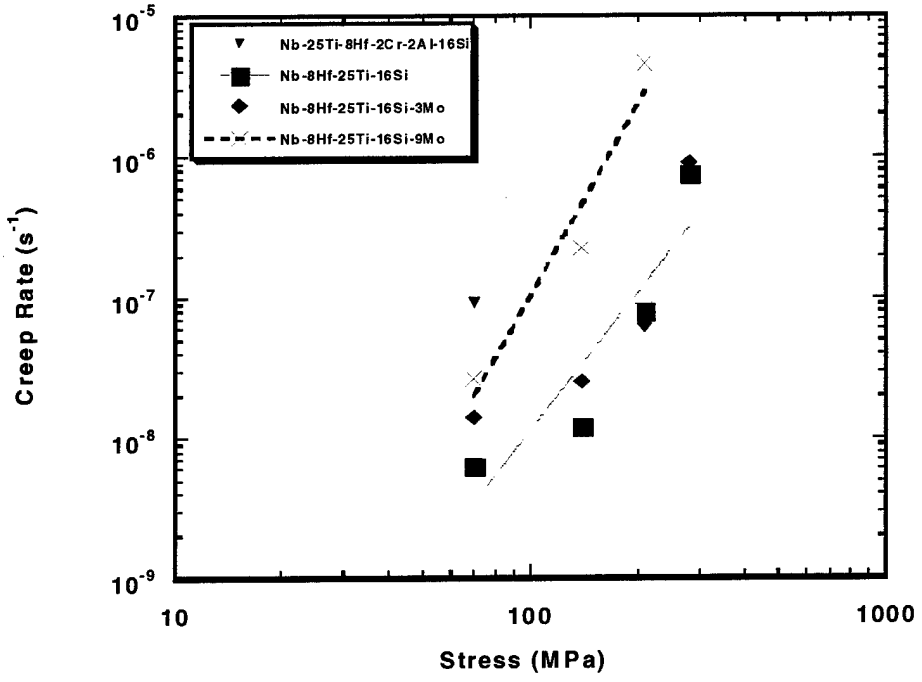


Figure 4. Graph of secondary creep rates at 1200 °C for a range of Nb-Hf-Ti-Si alloys modified with Mo.

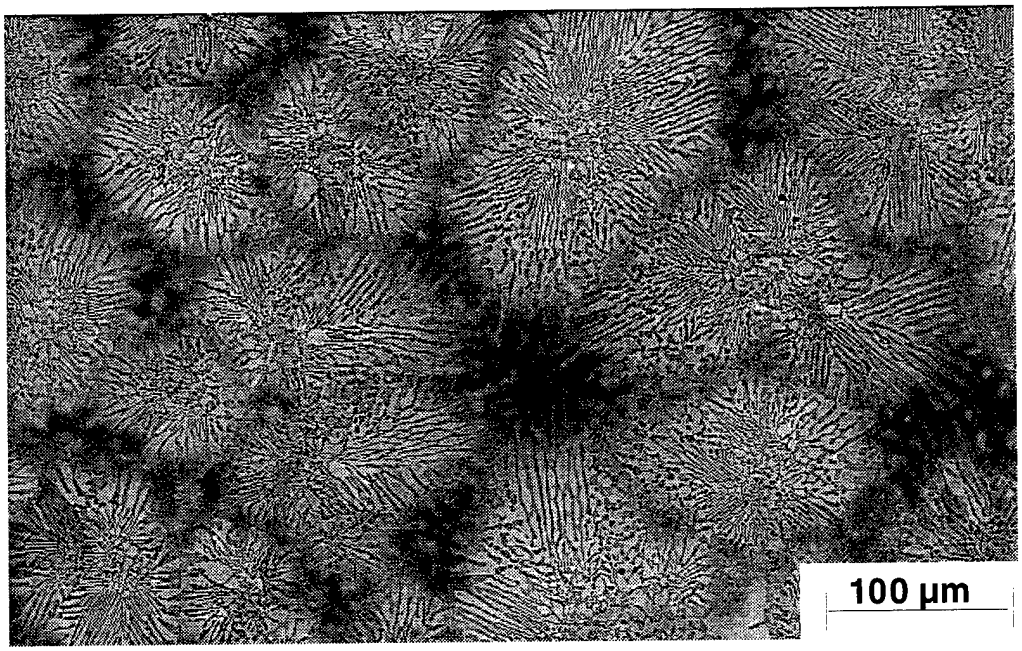


Figure 5. Typical microstructure (BSE image) of the transverse section of a DS composite generated from a Nb-9Mo-22Ti-8Hf-16Si alloy at a growth rate of 5 mm/min. The composite consists of eutectic cells of (Nb) (light phase) and hP16 M_5Si_3(dark phase).

parison of the creep rates of the Mo-modified alloys with those of the base Nb-8Hf-25Ti-16Si composite indicates that at any given set of creep conditions the creep rate increases with increasing Mo concentration from 0 to 3 to 9%, with a larger increase from 3 to 9%. These trends were observed at both 1100 °C and 1200 °C.

It can be seen that the performance of the Nb-7.5Hf-16Si and the Nb-8Hf-25Ti-16Si is similar to that of the Nb-16Si, but at Mo concentrations greater than 3 the creep rates are increased. The microstructure of the composite generated from a Nb-9Mo-22Ti-8Hf-16Si alloy is shown in Figure 5. This composite consisted of eutectic cells of M_5Si_3 with (Nb). The M_5Si_3 possessed the hP16 structure rather than the previously reported Nb_5Si_3 tI32 [1,5]. The hP16 structure was stabilized by the high Ti and Hf additions. The scale of the microstructure shown in Figure 5 is significantly finer than that in Figure 3. The reason for the poor creep performance of the composite with 9% Mo relates to the presence of the hP16 type silicide and the scale of the structure, as will be discussed in the following section. At the lower Mo concentration, it appears that strengthening the metallic phase by Mo additions can add little to the composite creep performance.

In comparison with the Nb-8Hf-25Ti-2Cr-2Al-16Si, the Mo additions have a less detrimental effect on the creep rate than the Cr and Al additions, as shown in Figure 6. However, unlike the Mo additions, the Cr and Al additions are required for oxidation resistance (they also appear to provide some toughening). It appears therefore that there is no net benefit associated with substitution of Mo for Nb.

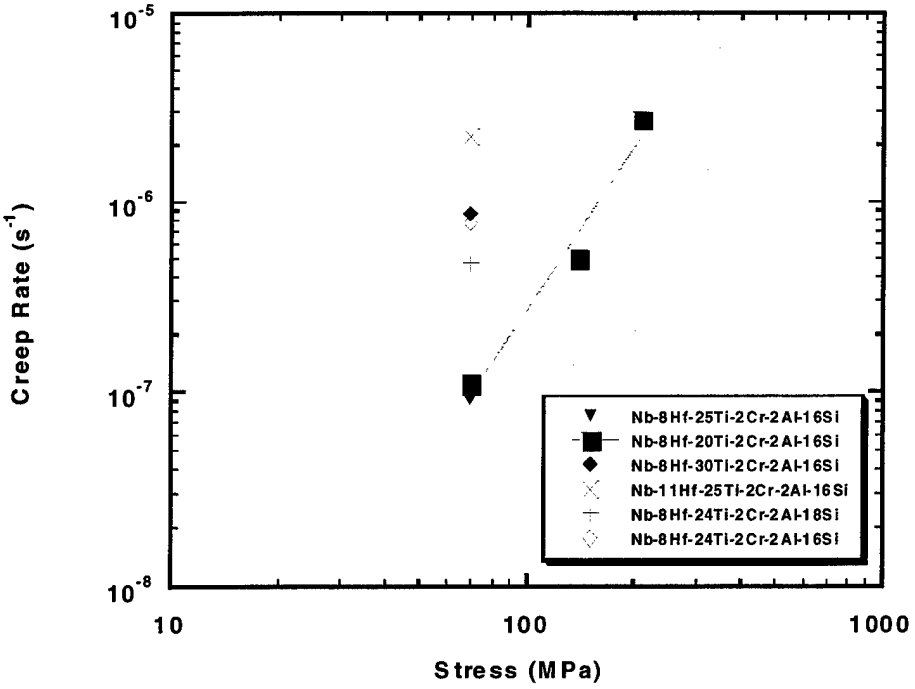


Figure 6. Graph of secondary creep rates at 1200 °C for a range of Nb-Hf-Ti-Si-Cr-Al alloys.

Role of the hP16 Silicide

In Nb-silicide composites Hf and Ti additions have been found to enhance the balance of oxidation performance, fracture toughness, and high-temperature strength. In order to define the maximum allowable Hf and Ti concentrations and their effect on stabilization of the hP16 silicide, we first considered the creep rates of Nb_3Si-Nb composites derived from binary Nb-16Si, ternary Nb-7.5Hf-16Si, and quaternary Nb-7.5Hf-21Ti-16Si. The secondary creep rates at 1200 °C and at stresses up to 210 MPa are all similar. The data in Table 5 suggest that above specific Ti and Hf concentrations the creep rates exceed the creep rate goal of 3 x $10^{-8}s^{-1}$ [1,4]. The Nb:(Hf+Ti) concentration ratios are also shown in Table 5. Although these higher Hf and Ti concentrations may be desirable for oxidation resistance, they are deleterious to creep performance. It appears that at Nb:(Hf+Ti) ratios less than ~1.5 (in atom per cent) the creep performance is degraded beyond acceptable levels for application stresses of 140 MPa and above, as shown in Figure 7.

In the compositions that possess Nb:(Hf+Ti) concentration ratios less than 1.5, the hP16 phase is stabilized. Typically, the quaternary alloy composites with Nb:(Hf+Ti) concentration ratios greater than 1.5 possess only (Nb) and Nb_3Si phases, and they have creep performance similar to that of the binary Nb-16Si. At ratios lower than 1.5, the creep performance becomes catastrophic. While the importance of this ratio has been recognized phenomenologically in quaternary systems, the basis for it needs to be understood in greater detail. The validity of this ratio also needs to be examined in higher order systems where a range of properties are being optimized.

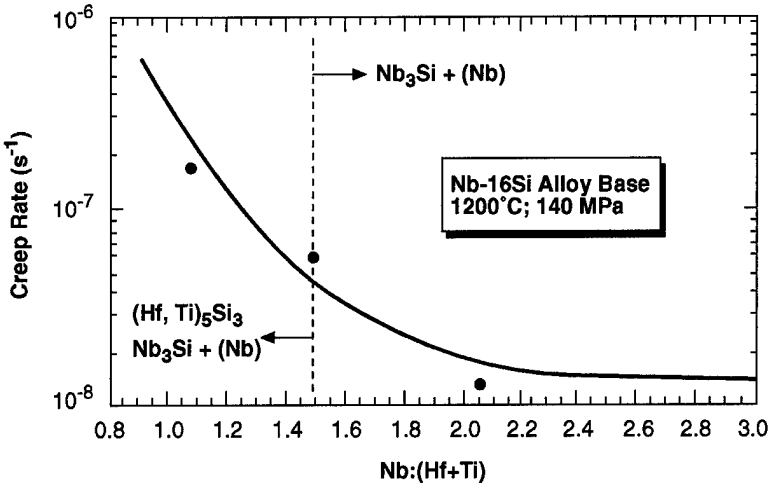


Figure 7. Composite secondary creep rate at 1200 °C and 140 MPa as a function of the Nb:(Hf+Ti) bulk concentration ratio in the alloy from which the composite was directionally solidified.

Table 5. Secondary creep rates at 1200 °C for a range of Nb-silicide in-situ composites, together with constituent phases, and Nb:(Hf+Ti) ratios.

Composition	Constituent Phases	Nb:(Hf+Ti) Ratio	70 MPa Creep Rate (s^{-1})	140 MPa Creep Rate (s^{-1})	210 MPa Creep Rate (s^{-1})
Nb-16Si	(Nb), Nb_3Si	—	$1.7x10^{-9}$	$1.5x10^{-8}$	$4.9x10^{-8}$
Nb-7.5Hf-16Si	(Nb), Nb_3Si	10.2	—	$2.3x10^{-8}$	$4.0x10^{-8}$
Nb-7.5Hf-21Ti-16Si	(Nb), Nb_3Si	1.95	—	$2.1x10^{-8}$	$3.2x10^{-8}$
Nb-12.5Hf-21Ti-16Si	(Nb), Nb_3Si, $(Ti,Hf)_5Si_3$	1.51	—	$5.5x10^{-8}$	$4.8x10^{-6}$
Nb-12.5Hf-33Ti-16Si	(Nb), Nb_3Si, $(Ti,Hf)_5Si_3$	0.85	—	$3.8x10^{-5}$	Failed
Nb-8Hf-25Ti-16Si	(Nb), Nb_3Si	1.56	$6.3x10^{-9}$	$1.2x10^{-8}$	$8.0x10^{-8}$
Nb-3Mo-8Hf-25Ti -16Si	(Nb), Nb_3Si	1.46	$1.4x10^{-8}$	$2.5x10^{-8}$	$6.4x10^{-8}$
Nb-9Mo-8Hf-25Ti -16Si	(Nb), $(Ti,Hf)_5Si_3$	1.27	$2.6x10^{-8}$	$2.2x10^{-7}$	$4.5x10^{-6}$
Nb-8Hf-25Ti-2Al-2Cr-16Si	(Nb), Nb_3Si, $(Ti,Hf)_5Si3$	1.42	$9.1x10^{-8}$	Failed	—

The deformation behavior of the phases within these composites has been examined microstructurally. The microstructure of the transverse and longitudinal sections of the Nb-12.5Hf-33Ti-16Si sample that was subjected to 50% creep deformation at 1200 °C is shown in Figures 8 and 9. The deformation behaviors of the Nb_3Si, (Nb) and $(Ti,Hf)_5Si_3$ are shown in Figure 9. The left-hand side figures show the microstructure, EBSP orientation images, and pole figures for all phases in the as-DS composite. The right-hand side figures show the same in the as-deformed composite. The (Nb) and the $(Ti,Hf)_5Si_3$ experienced substantial deformation and recrystallization. These phases essentially



Figure 8. Typical microstructure of the transverse section of DS Nb-12.5Hf-33Ti-16Si. The volume fraction of large-scale (Nb) was 0.40 and the volume fraction of faceted $(Nb)_3Si$ was 0.39. There was interdendritic $(Hf,Ti)_5Si_3$ eutectic.

provided little creep resistance at 1200 °C and stresses greater than 140 MPa. The composite creep resistance is provided essentially by the Nb_3Si and the deformation that it has experienced is described by the orientation imaging micrograph and the pole figure. The rotation that the (001) Nb_3Si poles have experienced is clearly described.

These data strongly suggest that the removal of the $(Ti,Hf)_5Si_3$ type silicide may lead to enhanced creep performance, but this may not be the only explanation. For example, if we examine deformation of the individual phases within the Nb-12.5Hf-33Ti-16Si composite in Figure 9, we see that both the Nb_3Si and the $(Ti,Hf)_5Si_3$ type phases have experienced substantial deformation. Clearly, at these high Ti and Hf concentrations, the Nb_3Si has experienced substantial plastic deformation. However, in alloys with lower Ti and Hf concentrations, the Nb_3Si does not experience plastic deformation, even at temperatures up to 1100 °C. Thus, the silicide chemistry can also have a significant effect on the deformation behavior of these composites.

The importance of the Nb:(Hf+Ti) ratio is also demonstrated in quaternary Nb-Hf-Ti-Si modified with Mo, also shown in Table 5. The data indicate that, at any given set of creep conditions, the creep rate increases with increasing Mo concentration from 0 to 3 to 9%. The composite with 9% Mo possesses a structure of fine-scale two-phase eutectic cells of (Nb), and hP16 $(Ti,Hf)_5Si_3$ type phases, as shown in Figure 5, whereas the Mo-modified composite with 3% Mo possesses large-scale (Nb) and Nb_3Si. The dramatic change in the creep behavior at a Mo concentration of 9% is associated with the introduction of the hP16 silicide phase. The (Nb)-hP16 $(Ti,Hf)_5Si_3$ composite

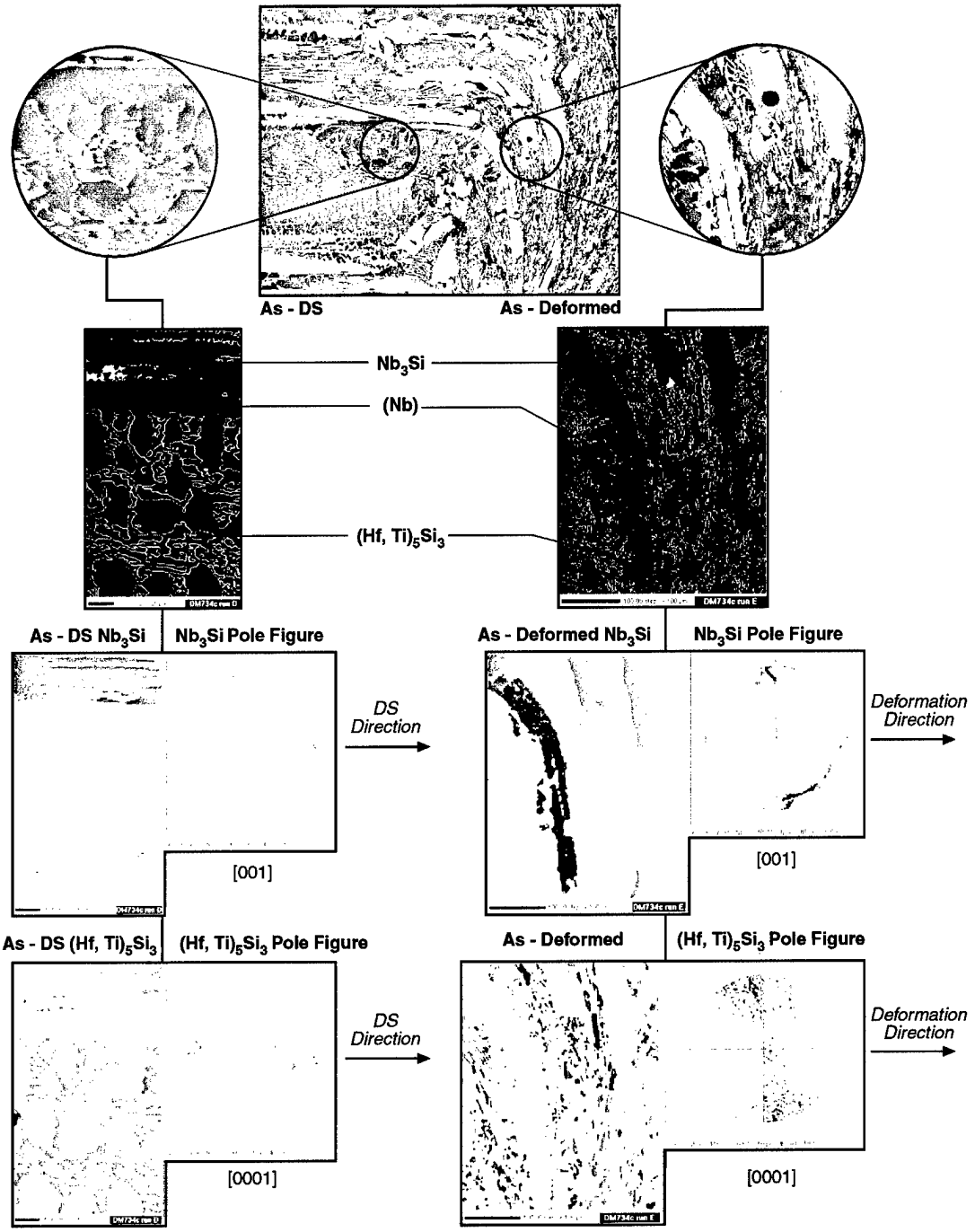


Figure 9. Microstructures of the longitudinal section of a Nb-12.5Hf-33Ti-16Si composite before and after creep deformation at 1200 °C. The left hand side figures show the microstructure and EBSP orientation images of a region that was as-directionally solidified. The [001] Nb_3Si and the [0001] $(Hf,Ti)_5Si_3$ were parallel to the growth direction. The right hand side figures show the microstructure and EBSP orientation images of a deformed region. The [001] Nb_3Si and the [0001] $(Hf,Ti)_5Si_3$ have rotated such that they are almost perpendicular to the deformation direction.

has very poor creep performance. Similar behavior can also be seen in Table 5 for the six-element alloy Nb-8Hf-25Ti-2Al-2Cr-16Si, which has a ratio less than 1.5 (1.42). In this case, the creep rate at 1200 °C and stresses >70 MPa were high and led to premature failure.

The Effect of the Volume Fraction of Tetragonal Silicide

The composite from the base Nb-8Hf-25Ti-2Al-2Cr-16Si composition possessed a complex microstructure. In order to examine the effect of the volume fraction of silicide on both room temperature fracture toughness and high-temperature creep performance, a series of studies based on the Nb-8Hf-25Ti-16Si quaternary alloy were conducted. This composite consisted of (Nb) and $(Nb)_3Si$. In order to explore the effect of volume fraction of silicide, the Si concentration was adjusted from 12% to 22% (substituting for Nb). However, it was recognized that adjusting the Si and Nb alone would lead to changes in the compositions of the (Nb) and the $(Nb)_3Si$. Thus, an additional series of composites was generated where the Hf and Ti compositions were adjusted along with the Si concentration in an effort to keep the (Nb) and $(Nb)_3Si$ compositions constant.

The typical microstructure of hypoeutectic quaternary Nb-Hf-Ti-Si alloys is shown in the micrograph of the Nb-8Hf-25Ti-16Si in Figure 10. The microstructure is two-phase with large-scale (Nb) and large-scale $(Nb)_3Si$ type dendrites. Figure 10 reveals the cellular nature of the microstructure. The light phase is (Nb) and the grey phase is $(Nb)_3Si$. The dark intercellular regions possess a higher Ti concentration and they therefore provide less BSE signal. The toughness of the Nb-8Hf-25Ti-16Si was measured as 16.1 MPa$\sqrt{m}$. The toughness of the Nb-8Hf-25Ti-12Si was measured as 13.3 MPa$\sqrt{m}$.

The microstructure of the transverse section of a Nb-8Hf-25Ti-18Si alloy is shown in Figure 11. It consists of a double dendrite type structure of $(Nb)_3Si$ and (Nb). The light grey faceted phase was $(Nb)_3Si$ and the (Nb) was generally dark, although Hf segregation in the interdendritic regions led to significant variation in the BSE signal provided by the (Nb). The (Nb) is the toughening phase and it typically possessed a scale of ~30 μm; this is substantially larger than has been observed in the binary eutectic Nb-18.2Si where the (Nb) had a scale of ~2 μm. The toughness was measured as 11.0 MPa$\sqrt{m}$. The volume fraction of (Nb) was 0.29; the volume fraction of $(Nb)_3Si$ was 0.71.

The microstructure of the transverse section of the Nb-8Hf-25Ti-22Si alloy is shown in Figure 12. The microstructure consists of primary $(Nb)_5Si_3$ type dendrites (tP32 structure type) with peritectic $(Nb)_3Si$, and a small volume fraction of interdenditic (Nb). The phases were identified using EBSP and EMPA. The toughness of this composite was 11.5 MPa$\sqrt{m}$. The creep rate is shown as a function of stress in Figure 13. The volume fraction of (Nb) was 0.26, the volume fraction of $(Nb)_5Si_3$ was 0.09 and the $(Nb)_3Si$ 0.65.

The microstructure of a composite based on the Nb-8Hf-25Ti-18Si, but with the Hf concentration increased to 12.5 and the Ti concentration increased to 33, is shown in Figure 8. It is distinguished

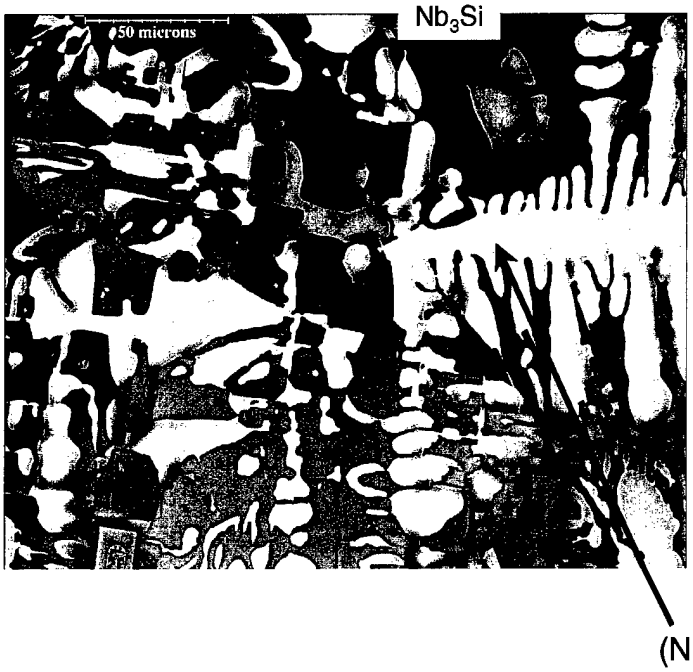


Figure 10. Typical microstructure of the transverse section of DS Nb-8Hf-25Ti-16Si. The light phase is (Nb) and the grey phase $(Nb)_3Si$. The Nb_3Si volume fraction was 0.60.

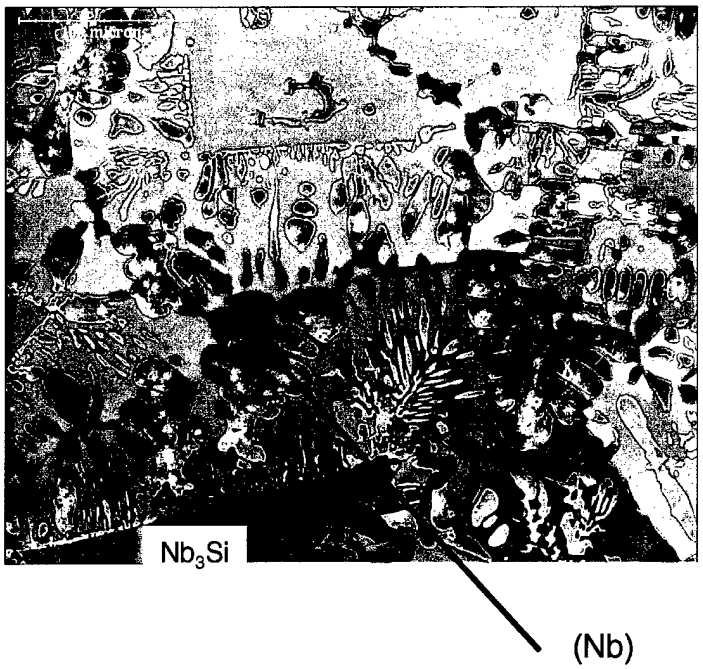


Figure 11. Typical microstructure of the transverse section of DS Nb-8Hf-25Ti-18Si. The grey faceted phase is Nb_3Si with a volume fraction of 0.71.

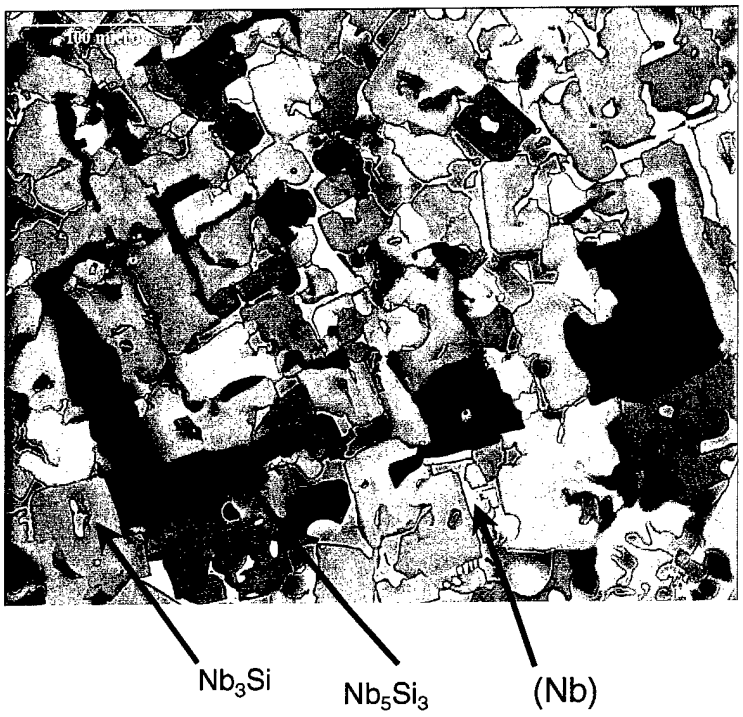


Figure 12. Typical microstructure of the transverse section of DS Nb-8Hf-25Ti-22Si. The black faceted phase is $(Nb)_5Si_3$ and the grey phase is $(Nb)_3Si$ (volume fraction 0.65), and the bright phase is (Nb) (volume fraction 0.26).

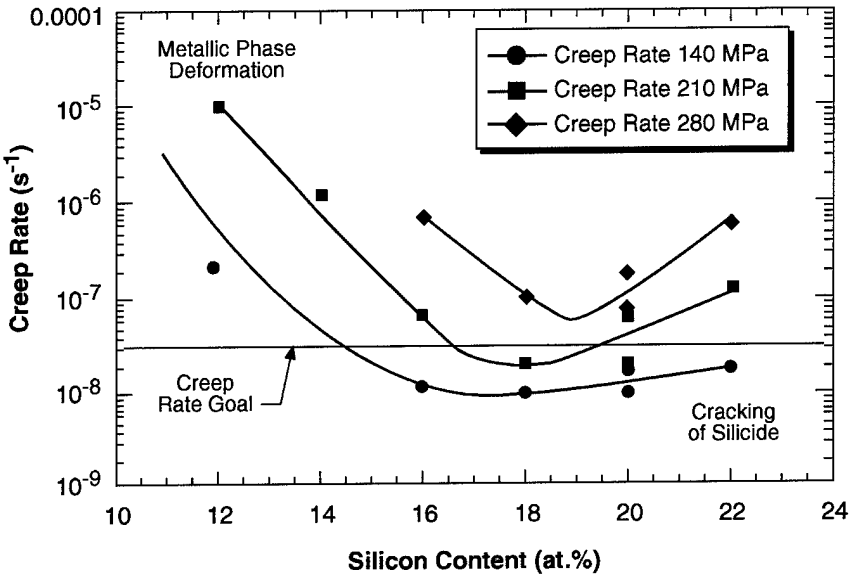


Figure 13. The effect of volume fraction of metal and silicide on secondary creep rate for stresses of 140-280 MPa at a temperature of 1200 °C. At low Si concentrations, deformation is controlled by creep of the (Nb) and at high Si concentrations, composite deformation is controlled by cracking of the silicide.

from the previous composites in that it possesses the $Hf(Ti)_5Si_3$ hP16 type silicide. The microstructure in Figure 8 shows large-scale (Nb), large-scale $(Nb)_3Si$, and an intercellular fine-scale eutectic of (Nb) and $(Hf,Ti)_5Si_3$. The fine-scale eutectic (Nb) is dark and the $(Hf,Ti)_5Si_3$ is light.

The effect of the volume fraction of silicide on composite creep behavior is shown in Figure 13. This figure shows the effect of stress on secondary creep rate for quaternary alloy composites with Si concentrations from 12 to 22%. This Si concentration range provides volume fractions of the metallic phase from ~0.70 to 0.25, respectively. Increasing the Si concentration from 12% leads to a minimum in the creep rate at ~18% Si. At Si concentrations lower than 12%, the composite creep performance is dominated by the creep behavior of the metallic phase and is therefore relatively poor, as indicated in Figure 14. Figure 15(a) shows ductile tearing of the (Nb). The secondary creep rates at 1100 °C of three monolithic solid solutions are shown in Figure 14. Data are shown for the Nb solid solution of a binary Nb- Nb_3Si composite, a ternary composite modified with Ti, and the solid solution of the MASC. At 1200 °C creep rates higher than $10^{-6}s^{-1}$ were observed for these alloys. The data at 1100 °C indicate that the Nb-1Si has the best creep performance. The creep performance is degraded by Ti additions. The creep behavior of the solid solution from the MASC possesses a lower Ti concentration (27% vs 46%) and at any stress level it has lower creep rates than the ternary alloy, but higher creep rates than the binary alloy.

Damage of the silicide can also contribute to creep strain. At Si concentrations greater than 20%, the composite creep performance is dominated by damage of the silicide [6]. Examples of damage as a result of creep deformation are shown in the three composites in Figure 15. Figures 15(b) and (c) show cracking of the Nb_3Si. Extensive cracking perpendicular to the compression axis was observed. The cracks were essentially contained within the silicide. The 18% Si composition experienced minimal creep deformation, tearing of the metallic phase and cracking of the silicide.

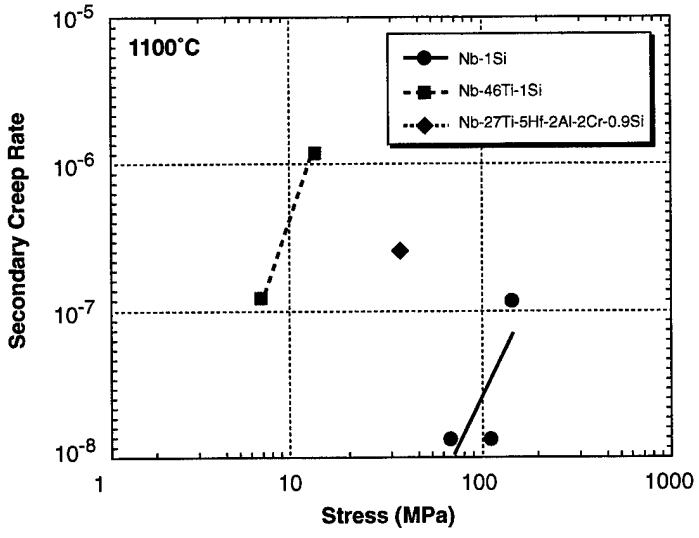
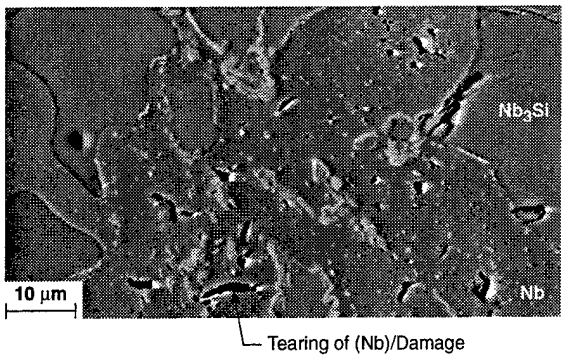
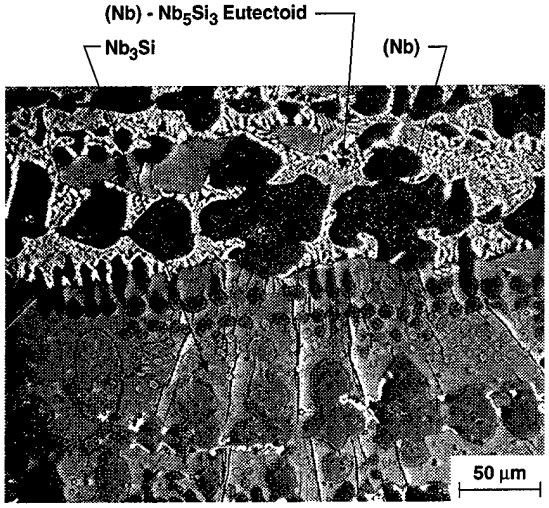


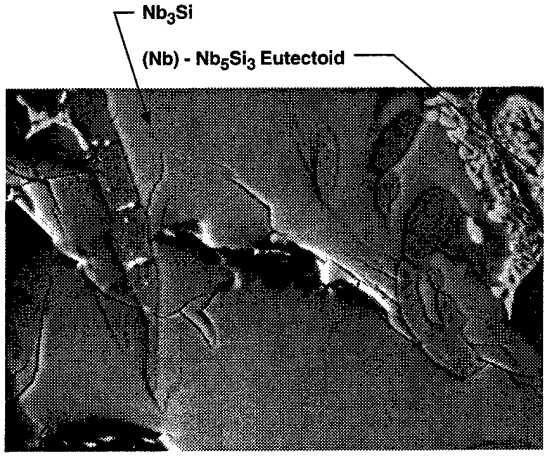
Figure 14. Creep behavior at 1100 °C of single-phase Nb alloys modified with Si, Hf, Al, Cr, and Ti.



(a)



(b)



(c)

Figure 15. Micrographs of DS Nb_3Si-(Nb) composites after creep testing showing damage in (a) the (Nb); (b) the Nb_3Si at low magnification; (c) the Nb_3Si at high magnification.

Although the role of the hP16 silicide is important, the architecture of the composite may also control the composite creep rate. It is considered necessary for the silicide phase to be the continuous phase in order to support stresses of >100 MPa at low secondary creep rates (~$10^{-8}s^{-1}$) at high temperatures (>1200 °C) [6]. The creep performance of the metallic phase is substantially inferior to that of the silicide at temperatures above 1100 °C, as shown in Figure 14, and this renders the composite creep performance heavily dependent on that of the silicide.

If the silicide is not continuous at the onset of creep, it is possible that, as a result of compression deformation during primary creep, the silicide phase becomes continuous. In this case, the initial continuity of the silicide may not have a significant effect on the secondary creep rate, but it will have a substantial effect on the primary creep strain. However, the tensile behavior could be significantly different if the silicide is not continuous at the onset of creep.

In addition to plastic deformation and damage of the silicide, it can be see in Figure 15(c) that there is a small volume fraction of (Nb)-Nb_5Si_3 eutectoid. The eutectoid transformation occurred during creep testing at temperatures as low as 1100 °C. This result is surprising, given that on heat treatment without stress at temperatures up to 1500 °C, the Nb_3Si that contains Ti and Hf does not transform even after several hundred hours. However, the application of stress appears to accelerate the eutectoid transformation. The contribution of the eutectoid transformation during creep testing to secondary creep rate requires further investigation.

The creep exponents for the Nb-7.5Hf-16Si and the Nb-8Hf-25Ti-16Si were ~1 and ~2 respectively. At higher Hf and/or Ti concentrations, the exponents were increased substantially. The change in slope suggests a change in creep mechanism. For the Nb-3Mo-8Hf-25Ti-16Si, the creep exponent was ~1; but at 9Mo, the exponent was ~5. These data suggest that at higher alloying levels, the creep rate is controlled less by the behavior of the monolithic silicide for which the creep exponent is ~1. The stress sensitivity of the creep rate is also strongly dependent on the Nb:(Hf+Ti) ratio.

The present tensile creep rupture behavior and its stress sensitivity at temperatures below 1100 °C [2,6] is due, in part, to damage of the silicide, the type of silicide (Nb_5Si_3, Nb_3Si,$(Ti,Hf)_5Si_3$), debonding of the metallic phase from the silicide, the high creep rates of the metallic phase, and the high stress sensitivity of the creep rate of the metallic phase.

Summary

The addition of Ti, Hf and Mo can have a substantial effect on composite secondary creep rates. The threshold Hf, Ti and Mo concentrations above which the creep performance degenerates beyond that of the Nb-16Si composite has been defined, together with the appropriate stress levels for possible component operations. The goal for creep performance for application of these materials is 1% in 100 hours at >1200 °C at stresses up to 200 MPa. If there is minimal primary creep this corresponds to a secondary creep rate of $3x10^{-8}s^{-1}$. The data indicate that the creep performance of the Nb-8Hf-25Ti-16Si is compatible with the creep goals at temperatures up to 1200 °C.

The effect of volume fraction of silicide on composite secondary creep rate has been examined by adjusting the alloy composition. At 1200 °C and over the stress range 70-280 MPa it was observed that increasing the Si concentration from 12% to 22% leads to a minimum in the creep rate at ~18% Si (71% Nb_3Si). Independent creep testing of monolithic (Nb) solid solutions indicates that the (Nb) provides little creep strength at 1200 °C.

At high Ti concentrations it is possible to stabilize the $(Hf,Ti)_5Si_3$ hP16 silicide in preference to the tetragonal Nb silicides. It was found that composites with the hP16 silicide possessed inferior creep performance to those strengthened by the tP32 and tI32 silicides. For hypoeutectic Nb-Si alloys, the critical ratio above which the Nb:(Hf+Ti) concentration ratio has to be maintained to prevent hP16 phase stabilization and retain creep performance is considered to be ~1.5.

There are two areas for further improvement of the creep performance of these materials. The first is to improve the creep rupture performance to a level greater than that of CMSX-10, and the second is to reduce the stress sensitivity of the creep rupture performance. It is also necessary to understand the stress sensitivity of the creep rupture behavior of these RMICs in order to improve their performance above that of Ni-based superalloys across a wide range of stress and temperature.

3.3 Phase Stability Investigations

Several investigations of phase stability have been completed in the third year of the present contract. These include determination of solid-state phase equilibria in Nb-Ti-Si alloys, description of the Nb-Hf-Si solid-state phase equilibria, and definition of the Hf-Ti-Si liquidus surface. Significant effort has been placed on defining phase stability in the Nb-Ti-Si, Nb-Hf-Si, and Nb-Hf-Ti-Si systems, because Ti and Hf additions to Nb-Si based composites have been shown to provide improvements in fracture toughness, tensile strength, creep performance, and oxidation behavior [1,5,7,9]. Phase stability information is a critical requirement for definition of both the manufacture of these high-temperature in-situ composite systems and their stability during service.

All of these investigations have been published in the open literature with the exception of the most recent data on the Hf-Ti-Si system.

Hf-Ti-Si Ternary Phase Stability

Hf is an important alloying addition to in-situ composites based on Nb-Si alloys because it improves oxidation resistance and strength. However, there is little previous knowledge of phase equilibria in the Hf-Ti-Si system. Several options were considered for the liquidus surface of the Hf-Ti-Si system. Of these options, Figure 15 represents the proposed liquidus projection that is the most consistent with the data that have been obtained.

At the metal-rich end of the Hf-Ti-Si ternary phase diagram there is a eutectic trough between the two binary eutectics [9]. However, because of the different binary eutectic reactions, L —> Hf(Si) + Hf_2Si (1820°C) and the L —> Ti_5Si_3 + Ti(Si) (1330°C), there is a change in the nature of the liquidus surface, and the eutectic groove, with decreasing Hf and increasing Ti concentration. There is a ~500°C difference in temperatures of the two binary eutectics [9] and the slope of this trough is therefore quite steep. The loci of the L + Hf_5Si_3 —>Hf_2Si peritectic ridge, p_1, the L —> β(Hf,Ti,Si)-$Hf(Ti)_2Si$ eutectic groove, e_1, the L —> $(Hf,Ti)_5Si_3$ + β(Hf,Ti,Si) eutectic groove, e_2, and the location of the transition reaction that occurs are complex, and particular emphasis has been placed on these features in the present study.

In Figure 16, the peritectic ridge, p_1, intersects the eutectic groove, e_1, to generate the transition reaction, U_1. The alloy compositions that were investigated are shown as the solid points on the liquidus surface projection in Figure 16.

$$U_1 \qquad L + (Hf,Ti)_5Si_3 \rightarrow \beta(Hf,Ti,Si) + Hf(Ti)_2Si$$

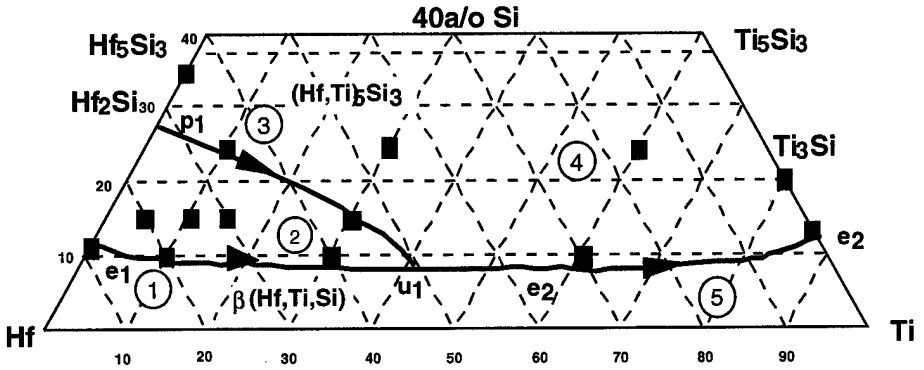


Figure 16. Schematic diagram showing the proposed projection of the Hf-Ti-Si liquidus surface. The projection shows the peritectic ridge, p_1, the eutectic valleys, e_1, and e_2, and the invariant reaction, U_1. The actual compositions investigated are also shown.

Results and Discussion

Microstructural and microchemical evidence for the solidification paths is presented first for the Hf-rich alloys, second for the Hf_2Si-rich compositions, third for the Hf_5Si_3-rich alloys, fourth for the Ti_5Si_3-rich compositions, and finally for Ti-rich compositions.

Hf-Rich Compositions: GROUP 1

This regime contained primary β(Hf,Ti,Si) dendrites with an interdendritic eutectic of β(Nb,Hf,Si) and $Hf(Ti)_2Si$. Ternary Hf-Ti-Si alloys with Ti concentrations of 5-30 and Si concentrations of 5-10 were examined.

The typical microstructure of the transverse section is shown in Figure 17 for the Hf-10Ti-5Si composition. The microstructure consisted of primary β(Hf,Ti,Si) dendrites, which are the light grey phase in the BSE micrograph, together with an interdendritic β(Hf,Ti,Si)- $Hf(Ti)_2Si$ eutectic. On post-solidification cooling both the primary and eutectic β(Hf,Ti,Si) transformed to α(Hf,Ti,Si). After transformation, it is difficult to distinguish the primary and eutectic β(Hf,Ti,Si).

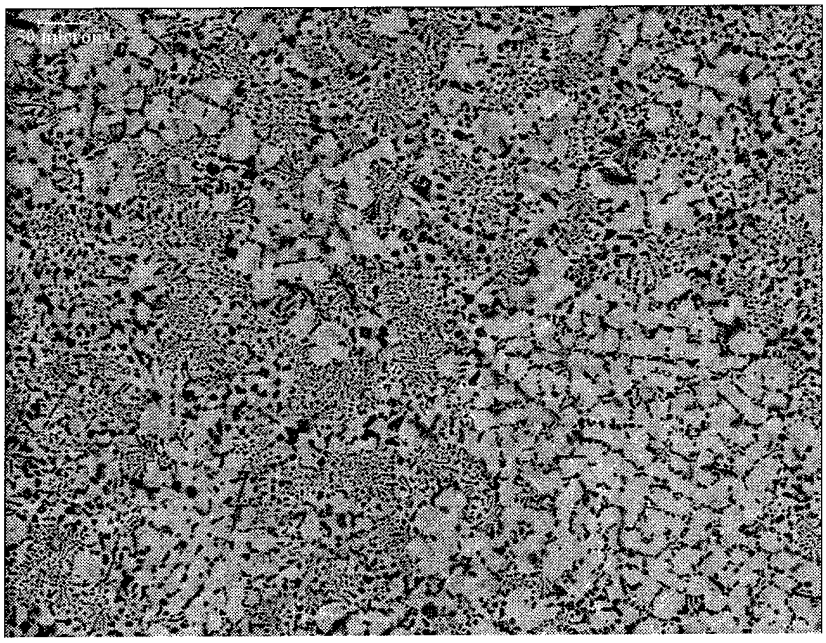


Figure 17. Typical microstructure (BSE image) of the transverse section of a DS Hf-10Ti-5Si alloy. There are light β(Hf,Si) dendrites with interdendritic eutectic cells of $Hf(Ti)_2Si$ (dark grey) and transformed β(Hf,Ti,Si).

$Hf(Ti)_2Si$ -Rich Compositions: GROUP 2

This regime is on the Si-rich side of the eutectic, e_1, and it contains primary $Hf(Ti)_2Si$ dendrites, and the β(Hf,Ti,Si)-$Hf(Ti)_2Si$ eutectic. Four ternary compositions were examined from this regime, Hf-10Ti-16Si, Hf-30Ti-10Si, Hf-30Ti-16Si, Hf-10Ti-25Si.

The microstructure of the Hf-10Ti-16Si alloy is shown in Figure 18. It consists of a small volume fraction of primary $Hf(Ti)_2Si$ dendrites with an interdendritic eutectic of fine-scale (5-10μm) $Hf(Ti)_2Si$ in a β(Hf,Ti,Si) matrix. The β(Hf,Ti,Si) transformed to α(Hf,Ti,Si) and β (Hf,Ti,Si) on post-solidification cooling; there was strong contrast between the α(Hf,Ti,Si) and β(Hf,Ti,Si). The light phase is α(Hf,Ti,Si) and the dark phase is β(Hf,Ti,Si). These data indicate that the transition reaction occurs at Ti concentrations greater than 10%.

The microstructure of the Hf-30Ti-10Si alloy is shown in Figure 19. It consists of a very small volume fraction of primary $Hf(Ti)_2Si$ dendrites with an interdendritic eutectic of $Hf(Ti)_2Si$ in a β(Hf,Ti,Si) matrix. The β(Hf,Ti,Si) had transformed to α(Hf,Ti,Si) and β (Hf,Ti,Si) on post-solidification cooling. These data indicate that the Hf-30Ti-10Si is very close to the eutectic valley, and that the transition reaction occurs at Ti concentrations greater than 30%. At the higher Ti concentration the $Hf(Ti)_2Si$ appears to be brighter than the matrix, whereas at 10Ti the $Hf(Ti)_2Si$ appeared darker. There was no β(Hf,Ti,Si)-$Hf(Ti)_5Si_3$ eutectic, which suggests that the liquid composition did not reach the composition of the transition reaction, U_1.

The microstructure of the Hf-30Ti-16Si alloy is shown in Figure 20. It consists of primary $Hf(Ti)_2Si$ dendrites with an interdendritic eutectic of $Hf(Ti)_2Si$ in a β(Hf,Ti,Si) matrix. There was a larger volume fraction of $Hf(Ti)_2Si$ than in the Hf-30Ti-10Si alloy. All the large scale silicide phase was $Hf(Ti)_2Si$, no $Hf(Ti)_5Si_3$ was observed. There was some crystallographic contrast from different $Hf(Ti)_2Si$ grains. Large-scale β(Hf,Ti,Si) dendrites were also observed and appeared to grow cooperatively with the $Hf(Ti)_2Si$.

The β(Hf,Ti,Si)-$Hf(Ti)_2Si$ in the Hf-30Ti-16Si alloy has a slightly different morphology from the eutectic in alloys of lower Ti concentrations. There is a larger volume fraction of $Hf(Ti)_2Si$ and the silicide has a higher degree of continuity. This suggests that at higher Ti concentrations the eutectic trough has moved to higher Si concentrations, or there may be a change in the positions of the β(Hf,Ti,Si) and $Hf(Ti)_2Si$ solvii.

$(Hf,Ti)_5Si_3$ -Rich Compositions: GROUP 3

This regime contained primary $(Hf,Ti)_5Si_3$ dendrites, peritectic $Hf(Ti)_2Si$, and β(Hf,Ti,Si)-$Hf(Ti)_2Si$ eutectic. Two ternary compositions were examined from this regime: Hf-20Ti-25Si and Hf-30Ti-25Si.

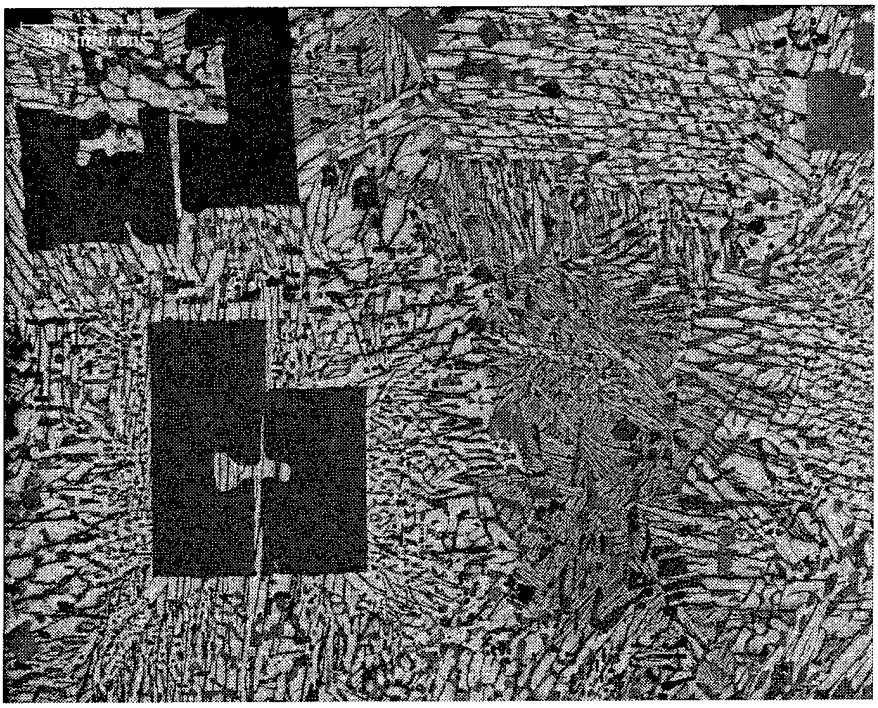


Figure 18. Typical microstructure (BSE image) of the transverse section of a DS Hf-10Ti-16Si alloy. There are dark $Hf(Ti)_2Si$ dendrites with an interdendritic eutectic cells of $Hf(Ti)_2Si$ (dark grey) and transformed β(Hf,Ti,Si).

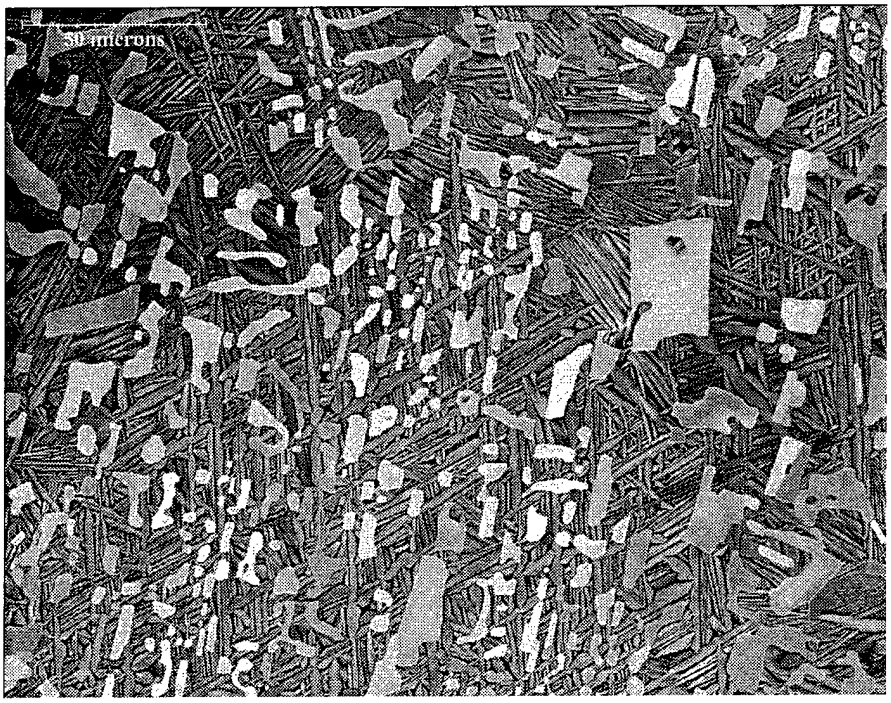


Figure 19. Typical microstructure (BSE image) of the transverse section of a DS Hf-30Ti-10Si alloy. There is a small volume fraction of $Hf(Ti)_2Si$ dendrites with interdendritic eutectic cells of $Hf(Ti)_2Si$ (light grey) and transformed β(Hf,Ti,Si).



Figure 20. Typical microstructure (BSE image) of the transverse section of a DS Hf-30Ti-16Si alloy. There is a large volume fraction of faceted $Hf(Ti)_2Si$ dendrites (light phase) with interdendritic eutectic cells of $Hf(Ti)_2Si$ and transformed β(Hf,Ti,Si).

The microstructure of the Hf-30Ti-25Si contained a small volume fraction of primary $Hf(Ti)_5Si_3$ dendrites, peritectic $Hf(Ti)_2Si$ and interdendritic β(Hf,Ti,Si)-$Hf(Ti)_2Si$ eutectic. This suggests that the Hf-30Ti-25Si composition is close to the L+ $(Hf,Ti)_5Si_3 \rightarrow Hf(Ti)_2Si$ peritectic ridge, and that the peritectic ridge is close to the eutectic valley. No β(Hf,Ti,Si)- $Hf(Ti)_5Si_3$ eutectic was observed.

$(Hf,Ti)_5Si_3$ -Rich Compositions: GROUP 4

This regime contained primary $(Hf,Ti)_5Si_3$ dendrites, with interdendritic β(Hf,Ti,Si)- $(Hf,Ti)_5Si_3$ eutectic. Two ternary compositions were examined from this regime: Hf-60Hf-25Si and Hf-60Ti-10Si.

The microstructure of the Nb-60Hf-25Si is shown in Figure 21. It possessed hP16 $(Hf,Ti)_5Si_3$ silicide and an interdendritic eutectic of β(Hf,Ti,Si) and $(Hf,Ti)_5Si_3$. The eutectic $(Hf,Ti)_5Si_3$ exists as hexagonal rods and ribbons in a β(Hf,Ti,Si) matrix. The β(Hf,Ti,Si) transformed on post-solidification cooling. The eutectic is similar to the βTi(Si)-Ti_5Si_3 binary eutectic. This microstructure suggests that the liquid composition shifted to the eutectic trough without experiencing the transition reaction involving $Hf(Ti)_2Si$.

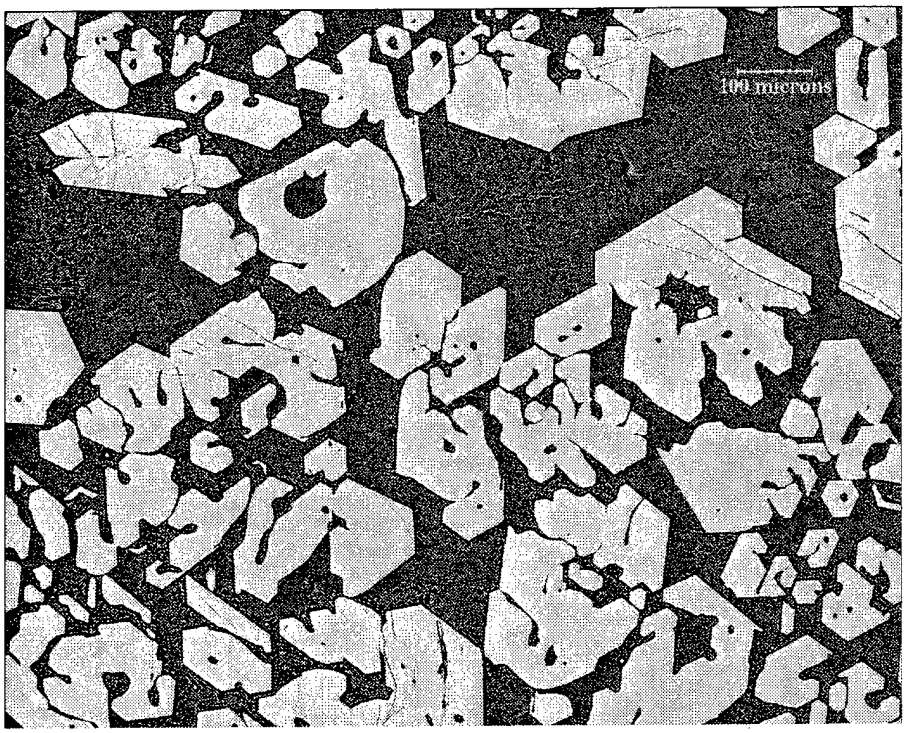


Figure 21. Typical microstructure (BSE image) of the transverse section of a DS Hf-60Ti-25Si alloy. The Hf-60Ti-25Si contained a large volume fraction of primary $Hf(Ti)_5Si_3$ dendrites and interdendritic β(Hf,Ti,Si)- $Hf(Ti)_5Si_3$ eutectic.

The morphology of the eutectic observed in this composition is entirely different from that observed in compositions with lower Ti concentrations where the β(Hf,Ti,Si)-$Hf(Ti)_2Si$ eutectic was observed. The faceted hexagonal $(Hf,Ti)_5Si_3$ rods have a different morphology to the $Hf(Ti)_2Si$ rods. There is also a higher volume fraction of β(Hf,Ti,Si) in the eutectic in these alloys than in the case of the binary βTi(Si)-Ti_5Si_3 eutectic. This may be because the eutectic valley moves to Si concentrations leaner than 13.5% Si as Ti is replaced with Hf.

Hf-Rich Hf-Ti-Si Compositions : GROUP 5

This group consists of Ti-rich compositions from the metal-rich side of the eutectic valley, e_2. The alloys contained primary β(Hf,Ti,Si) dendrites, and β(Hf,Ti,Si)-$(Hf,Ti)_5Si_3$ eutectic. Both the dendritic and eutectic β(Hf,Ti,Si) experienced the β–α allotropic phase transformation on post solidification cooling. This group is distinguished from Group 1 by the presence of the β(Hf,Ti,Si)-$Hf(Ti)_5Si_3$ interdendritic eutectic; alloys from Group 1 possess the β(Hf,Ti,Si)-$Hf(Ti)_2Si$ eutectic.

Summary

Microstructural, microchemical and crystallographic (XRD and EBSP) evidence indicates that the liquidus surface of the Hf-Ti-Si ternary phase diagram possesses the following reactions:

$$L + (Hf,Ti)_5Si_3 \longrightarrow Hf(Ti)_2Si \text{ peritectic}$$
$$L \longrightarrow \beta(Hf,Ti,Si) + Hf(Ti)_2Si \text{ eutectic}$$
$$L \longrightarrow (Hf,Ti)_5Si_3 + \beta(Hf,Ti,Si) \text{ eutectic}$$

These reactions give rise to the following transition reaction:

$$L + (Hf,Ti)_5Si_3 \longrightarrow \beta(Hf,Ti,Si) + Hf(Ti)_2Si$$

This transition reaction occurs at a composition of approximately Hf-40Ti-9Si, and at a temperature of ~1500°C.

4.0 References

[1] B.P. Bewlay, M.R. Jackson, and P.R. Subramanian, "Processing of High-Temperature Refractory Metal Silicide In-Situ Composites," Journal of Metals, April 1999 Vol 51(4), pp. 32-36.

[2] B.P. Bewlay, M.R. Jackson and H.A. Lipsitt, *Metall. and Mater. Trans.*, 1996, Vol 279, pp. 3801-3808.

[3] M.G. Mendiratta, J.J. Lewandowski and D.M. Dimiduk, *Metall. Trans. 22A* (1991), pp. 1573-1581.

[4] M.R. Jackson, B.P. Bewlay, R.G. Rowe, D.W. Skelly, and H.A. Lipsitt, J. of Metals 48 (1), (1996), pp. 38-44.

[5] P.R. Subramanian, M.G. Mendiratta and D.M. Dimiduk, *Mat. Res. Soc. Symp. Proc.*, 322 (1994), pp. 491-502.

[6] P.R. Subramanian, T.A. Parthasarathy, and M.G. Mendiratta, Scritpa Met. and Mater., Vol. 32(8), pp. 39-54.

[7] B.P. Bewlay, M.R. Jackson and H.A. Lipsitt, *Journal of Phase Equilibria*, Vol 18(3), 1997, pp. 264-278.

[8] A. Gokhale and R. Abbaschian, Bulletin of Alloy Phase Diagrams, 10, Vol. 4, pp. 390-393, 1989.

[9] B.P. Bewlay, R.R. Bishop and M.R. Jackson, Z. Metallkunde, June 1999, Vol 90(60), pp. 413-422.

5.0 Collaborations

Throughout the present program there have been numerous interactions with scientists at universities and the AF laboratories. These have included staff at Case Western Reserve University, Ohio State University, Brown University, and UES. These interactions have involved regular discussions of composite models, data, and exchange of samples. The results of the collaborations have been presented at international conferences and published in the open literature throughout this program.

6.0 Publications

The following articles have been published in refereed journals and conference proceedings during the last year of research in the area of the present contract.

1. B.P. Bewlay, R.R. Bishop and M.R. Jackson, "The Nb-Hf-Si Ternary Phase Diagram : Liquid-Solid Phase Equilibria In Nb and Hf Rich Alloys", Z. Metallkunde, June 1999, Vol 90(60), pp. 413-422.

2. B.P. Bewlay, M.R. Jackson, and P.R. Subramanian, "Processing of High-Temperature Refractory Metal Silicide In-Situ Composites", Journal of Metals, April 1999 Vol 51(4), pp. 32-36.

3. J-C. Zhao, B.P. Bewlay, M.R. Jackson and Q. Chen, "Hf-Si Phase Diagram Determination and Thermodynamic Modeling", accepted for the Journal of Phase Equilibria, June 1999.

4. B.P. Bewlay, P. Whiting, A.W. Davis and C.L. Briant, "Creep Mechanisms in Niobium-Silicide Based In-Situ Composites," M.R.S. Proceedings on High Temperature Ordered Intermetallic Alloys VIII, 1999, pp. KK6.11.1- KK6.11.5.

5 R.J. Grylls, B.P. Bewlay, H.L. Fraser and H.A. Lipsitt, "On the Formation of Silicide Precipitates in Nb-Si-Based Composites," M.R.S. Proceedings on High Temperature Ordered Intermetallic Alloys VIII, 1999, pp. KK5.27.1- KK5.27.5.

6 B.P. Bewlay, M.R. Jackson and J-C. Zhao, "Determination of the Effect of Hf Additions on Phase Stability in Nb-Silicide Based In-Situ Composites", M.R.S. Proceedings on High Temperature Ordered Intermetallic Alloys VIII, 1999, pp. KK6.8.1- KK6.8.6.

7. S.D. Sitzman and B.P. Bewlay, "Creep Deformation Microstructures in Nb-Hf-Ti-Si In-Situ Composites,", Microscopy and Microanalysis, 1999, Vol. 5, Supplement 2, pp. 258-259.

8. B.P. Bewlay, M.R. Jackson and J.A. Sutliff, "Creep Mechanisms in High-Temperature In-Situ Composites", Proceedings of the U.S.-Japan Workshop on Very High Temperature Structural Materials, 1999, pp. 17-24.

9. M.R. Jackson, B.P. Bewlay and R.R. Corderman, "Nb-Silicide In-Situ Composites: Oxidation Behavior", Proceedings of the U.S.-Japan Workshop on Very High Temperature Structural Materials, 1999, pp. 49-53.

10. R.J. Grylls, B.P. Bewlay, H.L. Fraser and H.A. Lipsitt, "Characterization of Silicide Precipitates in Nb-Si and Nb-Ti-Si Alloys", accepted for publication in the Philosophical Magazine, August 1999.

11. B.P. Bewlay, R.R. Bishop and M.R. Jackson, "The Nb-Ti-Si Ternary Phase Diagram : Determination of Solid-State Phase Equlibria in Nb and Ti Rich Alloys", Journal of Phase Equilibria, Vol 19(6), 1998, pp. 577-586.

12. B.P. Bewlay, J.A. Sutliff, and R.R. Bishop, "Evidence For the Existence of Hf_5Si_3", Journal of Phase Equilibria, Vol 20(2), 1999, pp 109-112.

13. B.P. Bewlay and M.R. Jackson "High-Temperature Directionally Solidified In-Situ Composites : Processing and Properties", to be published in "Comprehensive Composite Materials", A Kelly and C. Zweben (eds.) "Volume 3 - Metal Matrix Composites", T.W.Clyne (ed.), Elsevier (2000).

14. B.P. Bewlay, M.R. Jackson and M.F.X. Gigliotti "Single Crystals and Directionally Solidified In-Situ Composites for High-Temperature Applications" , to be published in Intermetallic Compounds-Principles and Practice, John Wiley, 2000.

15. J.-C. Zhao, B.P. Bewlay, and M.R. Jackson, "Determination of the Nb-Hf-Si Phase Diagram at 1500°C", manuscript in preparation.

7.0 Presentations

The following presentations have been given during the last year of the contract. Both invited and contributed papers are shown.

1. B.P. Bewlay and M.R. Jackson , "A Review of Niobium Silicide-Based In-Situ Composites", presented at the 1999 TMS Annual Meeting Symposium on "Structural Silicides", San Diego 1999. (Invited).

2 B.P. Bewlay, M.R. Jackson and J.A. Sutliff, "Creep Mechanisms in High-Temperature In-Situ Composites", U.S.-Japan Workshop on Very High Temperature Structural Materials, December 1999. (Invited).

3. B.P. Bewlay and M.R. Jackson, "Directionally Solidified Niobium Silicide In-Situ Composites: Processing and Properties", Brown University, January 1998. (Invited).

4. B.P. Bewlay, P.Whiting and C.L. Briant, "Creep Mechanisms in Niobium-Silicide Based In-Situ Composites", presented at the M.R.S. Symposium on High Temperature Ordered Intermetallic Alloys VIII, Boston, December 1998.

5. R.J. Grylls, B.P. Bewlay, H.L. Fraser and H.A. Lipsitt, "On the Formation of Silicide Precipitates in Nb-Si-Based Composites", presented at the M.R.S. Symposium on High Temperature Ordered Intermetallic Alloys VIII, Boston, December 1998.

6. J-C. Zhao, B.P. Bewlay, and M.R. Jackson, "Determination of the Effect of Hf Additions on Phase Stability in Nb-Silicide Based In-Situ Composites", presented at the M.R.S. Symposium on High Temperature Ordered Intermetallic Alloys VIII, Boston, December 1998.

7. B.P. Bewlay, R. J. Grylls and H.L. Fraser, "Formation of Silicide Precipitates in Nb-Si-Based In-Situ Composites", presented at the 1999 TMS Annual Meeting Symposium on "Structural Silicides", San Diego 1999.

8. B.P. Bewlay, R. J. Grylls and H.L. Fraser, "Observations of the Fracture Behavior of Nb-Si In-Situ Composites Using Cross-Sectional Electron Microscopy", presented at the 1999 TMS Annual Meeting Symposium on "Structural Silicides", San Diego 1999.

9. P.W. Whiting, B.P. Bewlay and C.L. Briant , "Creep Mechanisms in Niobium-Silicide Based In-Situ Composites", presented at the 1999 TMS Annual Meeting Symposium on "Structural Silicides", San Diego 1999.

8.0 Technology Transfers and Transitions

The Nb-base silicide based composites that have been investigated in this program are targeted for aircraft engine applications. Both civilian and military applications are under consideration. The near-term application is for the Integrated High Performance Turbine Engine Technology (IHPTET) joint services (Air Force, Navy, Army, and NASA) program. The team of GE Aircraft Engines and Allison Advanced Development Company has selected these Nb-base silicide composites for the proposed full demonstration of IHPTET Phase III goals as the primary material for the high pressure turbine (HPT) blades, and as the back-up material for HPT vanes. Toughness and creep properties demonstrated in the current program, as well as other efforts in oxidation and fatigue of these

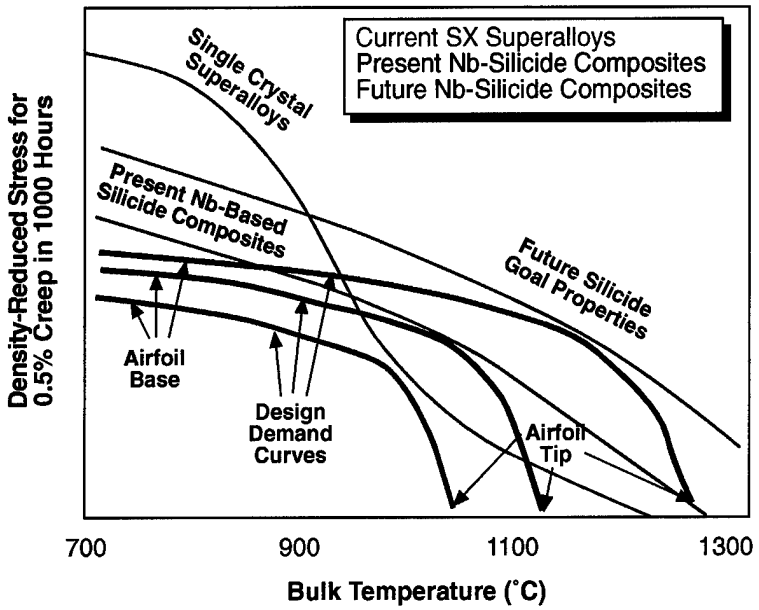


Figure 22. The density-reduced stress for 0.5% creep in 1000 hours as a function of temperature for a Nb silicide-based composite and a single-crystal superalloy. Also shown are design demand curves for current turbine blades, as well as airfoil designs using a Nb silicide-based composite with present creep rupture properties. Required goal properties are also shown against future airfoil requirements.

materials, have resulted in their selection for IHPTET demonstration. These composites are also under consideration for turbine applications in the advanced versions of the GE90.

In order to explain the technological potential for this class of composites, let us consider Figure 22, which shows the density-reduced stress for 0.5% creep in 1000 hours as a function of temperature for a Nb silicide-based composite and a single-crystal superalloy. Also shown in Figure 22 are design demand curves for current turbine blades, as well as airfoil designs using a Nb silicide-based composite with present creep rupture properties [1,2]. Outlined on these design demand curves are the high-temperature/low-stress regions of the turbine blade tip and the low-temperature/ high-stress regions of the airfoil base. The design is limited by the proximity of the design demand curve to the material property curve: ~1000 °C for the superalloy; and ~1200 °C for future Nb silicide-based composites. This figure illustrates that the capability of present Nb silicide-based composites is greater than that of Ni-based superalloys at temperatures above 1000 °C. At temperatures below 1000 °C, further strengthening of the Nb silicide composites is required to provide the same safety margin as for Nb-based superalloys with present turbine blade designs.

Primary Contact:

Bernard P. Bewlay
GE Corporate Research and Development
PO Box 8
Schenectady, NY12301
Tel: 518 387 6121

The Nb-Hf-Si Ternary Phase Diagram: Liquid-Solid Phase Equilibria in Nb and Hf Rich Alloys

B.P. Bewlay, R.R. Bishop and M.R. Jackson

Z. Metallkunde, June 1999

Bernard P. Bewlay, Rachel R. Bishop and Melvin R. Jackson*

General Electric Company, Corporate Research and Development, Schenectady, NY, U.S.A.; *Northwestern University, Evanston, IL, U.S.A.

The Nb–Hf–Si Ternary Phase Diagram: Liquid-Solid Phase Equilibria in Nb- and Hf-rich Alloys

Liquid-solid phase equilibria in ternary Nb–Hf–Si alloys have been investigated using scanning electron microscopy, X-ray diffraction, and electron beam microprobe analysis. A range of alloys was directionally solidified using cold crucible Czochralski crystal growth and six phases were identified: $Nb(Hf)_5Si_3$, $Hf(Nb)_5Si_3$, $Nb(Hf)_3Si$, $Hf(Nb)_2Si$, β(Nb, Hf, Si), and α(Nb, Hf, Si). A range of compositions was investigated for Si concentrations up to 35.0 %. Microstructural and microchemical evidences provided a clear definition of the Nb–Hf–Si liquidus surface and indicate that the metal-rich end of the ternary phase diagram possesses three transition reactions:

$$L + Nb(Hf)_5Si_3 \rightarrow Nb(Hf)_3Si + \beta(Nb, Hf, Si)$$

$$L + Hf(Nb)_5Si_3 \rightarrow Hf(Nb)_2Si + Nb(Hf)_5Si_3$$

$$L + Nb(Hf)_5Si_3 \rightarrow Hf(Nb)_2Si + \beta(Nb, Hf, Si)$$

The first of these transition reactions occurs at a composition of approximately Nb-21Hf-16Si, and at a temperature of ~ 1850 °C. The second of these transition reactions occurs at a composition of approximately Nb-27Hf-22Si, and a temperature of ~ 2040 °C. The third transition reaction occurs at a composition of approximately Nb-26Hf-14Si, and a temperature of ~ 1840 °C.

1 Introduction

Directionally solidified in-situ composites based on niobium and niobium-based silicides are presently under investigation as high-temperature structural materials. There has been extensive work on composites generated from binary Nb–Si alloys [1 to 4], as well as those with additions such as Ti, Hf, Cr and Al. Hf is an important alloying addition because it has been shown to improve oxidation resistance and strength [1, 2]. However, there is little previous knowledge of phase equilibria in the Nb–Hf–Si system. Many of these Nb-silicide based composites are generated by liquid-solid processing techniques [1, 2]. Thus, knowledge of the Nb–Hf–Si liquidus surface is required in order to predict the phase content and volume fractions of phases in these in-situ composites. The present paper provides a description of the liquidus surface of the metal-rich end of the Nb–Hf–Si phase diagram.

There has been extensive previous work on the binary Nb–Si system [4], and only limited work on the Hf–Si binary system [4 to 6]. However, there has been almost no previous work on the Nb–Hf–Si ternary system. An isometric projection of the metal-rich end of the proposed Nb–Hf–Si phase diagram is shown in Fig. 1. Several options were considered for the projection of the liquidus surface, as shown in Fig. 2. The bases for these options will be described in the following section. Of these options, Fig. 2c represents the proposed liquidus projection that is the most consistent with the data that will be described in the present paper.

Six phases are considered in the present description of the liquidus surface: a Nb–Hf–Si solid solution (the bcc solid solution is given the prefix β, and the hcp solid solution is given the prefix α), Nb_3Si, Nb_5Si_3, Hf_5Si_3 and Hf_2Si. In the present paper, the Nb_5Si_3 with Hf in solid solution is referred to as $Nb(Hf)_5Si_3$, the Hf_5Si_3 with Nb in solid solution is referred to as $Hf(Nb)_5Si_3$, the Hf_2Si with Nb in solid solution is referred to as $Hf(Nb)_2Si$, and the Nb_3Si with Hf in solid solution is referred to as $Nb(Hf)_3Si$. The Hf–Si solid solution in the binary alloys is referred to as Hf(Si). The Nb_5Si_3 and Hf_5Si_3 have *tI*32 and *hP*16 crystal structures, respectively. The Hf_2Si has the *tI*12 crystal structure, and the Nb_3Si has the *tP*32. Thus, none of these silicides are isomorphous.

Some of the difficulties associated with the definition of the Nb–Hf–Si system lie in an incomplete knowledge of the binary Hf–Si system [4 to 6]. Karpinsky and Evseyev [7] identified Hf_5Si_3, Hf_3Si_2, Hf_5Si_4, HfSi and $HfSi_2$. Kieffer and Benesovsky [8] provided a more complete review of crystallography of high temperature silicides. They ex-

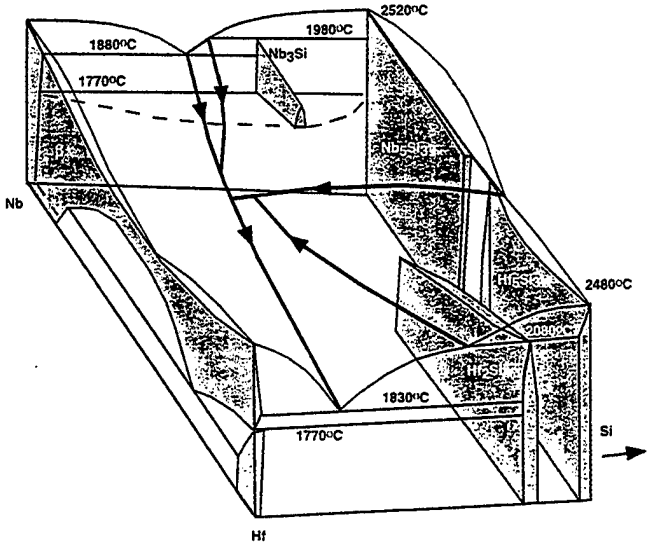
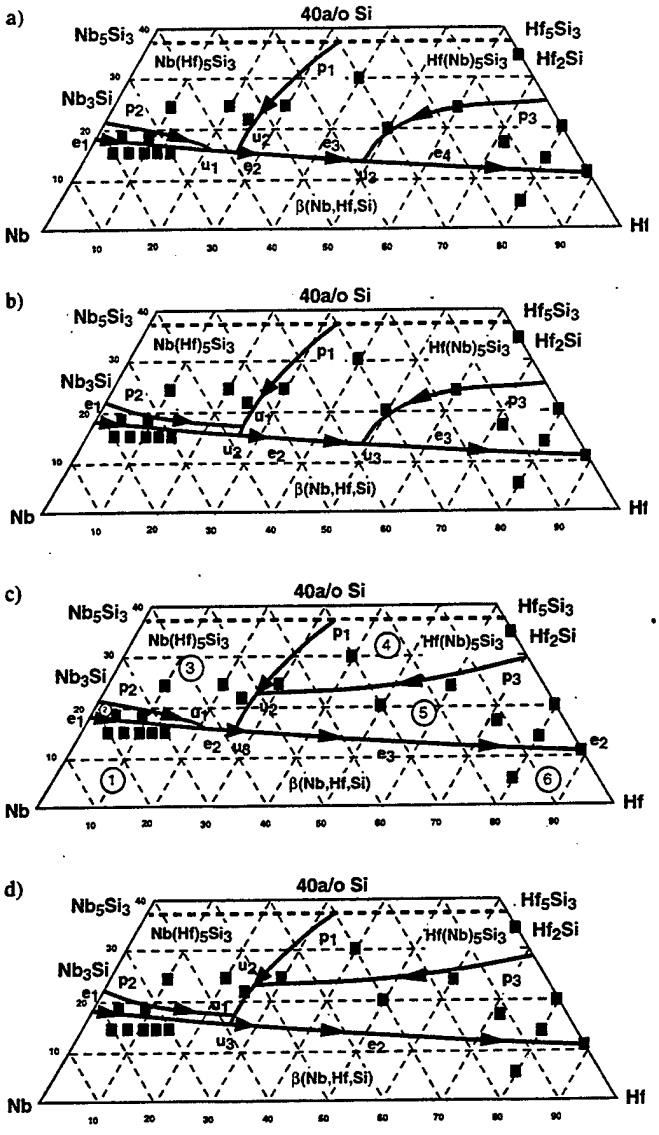


Fig. 1. Isometric projection of the proposed Nb–Hf–Si ternary phase diagram for compositions between 0 and 37.5%Si. The eutectoid reaction reported by Brukl [6] has been omitted.



Figs 2a to d. Schematic diagrams showing the projection of the liquidus surface for option 1, (a), option 2, (b), option 3, (c), and option 4, (d). Each projection shows the peritectic ridges, p_1, p_2, p_3, the eutectic valleys, e_1, e_2, e_3, and the invariant reactions, U_1, U_2, U_3. The actual compositions investigated are also shown.

pressed some uncertainty regarding the existence of the Hf_5Si_3 and claimed that it was only stable in the presence of oxygen, nitrogen or carbon. The data reported in the present study using high purity elements indicate that Hf_5Si_3 is stable even at very low interstitial levels [9]. Thus, in the present description of the liquidus surface, only Hf_5Si_3 and Hf_2Si binary silicides are considered.

2 Background on Nb–Hf–Si Phase Equilibria

The binary Nb–Si phase diagram contains a eutectic of the form $L \rightarrow Nb_3Si + (Nb)$ at 1880 °C and a peritectic of the form $L + Nb_5Si_3 \rightarrow Nb_3Si$ at 1980 °C [4]. The eutectic occurs at a composition of Nb-18.2%Si (all compositions are given in atom percent throughout the present paper). The microstructures of the directionally solidified (DS) binary alloys have been described previously [2]. The metal-rich end of the binary Hf–Si phase diagram [4, 5] has a eutectic of the form $L \rightarrow (Hf) + Hf_2Si$ at 1830 °C, and a peritectic of the form $L + Hf_5Si_3 \rightarrow Hf_2Si$ at 2080 °C. The eutectic composition is reported to be Hf-12%Si [4], although data that will be described in the present paper indicate that the eutectic reaction occurs at a composition closer to Hf-11%Si. The eutectic microstructure consists of Hf_2Si rods and ribbons in a βHf matrix [9]. Thus, at the metal-rich end of the Nb–Hf–Si ternary phase diagram there is a eutectic trough between the two binary eutectics, as shown in Fig. 1. However, there is only a 50 °C difference in temperatures of these two binary eutectics, and the slope of this trough is therefore very shallow.

The details of the Nb–Hf–Si liquidus surface are now described, and in the following Sect. 4 the substantiating data are presented. Although a eutectic groove extends between the two binary eutectics, because of the different binary eutectic reactions there is a change in the nature of the liquidus surface, and the eutectic groove, with decreasing Nb and increasing Hf concentration. The loci of the peritectic ridge from the $L + Nb_5Si_3 \rightarrow Nb_3Si$ peritectic, p_2, the $L + Hf_5Si_3 \rightarrow Hf_2Si$ peritectic ridge, p_3, the Hf-Hf_2Si eutectic groove, e_3, and the locations of the three transition reactions [10] that occur are complex, and particular emphasis is placed on these features in the present section. For the purpose of the present discussion, a peritectic, p_1, $L + Nb(Hf)_5Si_3 \rightarrow Hf(Nb)_5Si_3$ is assumed between $Nb(Hf)_5Si_3$ and $Hf(Nb)_5Si_3$. However, either a eutectic or a peritectic reaction between $Nb(Hf)_5Si_3$ and $Hf(Nb)_5Si_3$ provide a groove, or ridge, that falls towards the valley between the binary eutectics, as shown in Fig. 1.

Four options for the ternary liquidus surface are shown in Figs 2a to d, and are described below. The alloy compositions that were investigated are shown as the solid points on the liquidus surface projections in Fig. 2. Many other independent options of the liquidus surface were considered, but the data indicate that the option shown in Fig. 2c is the most likely.

Option 1 :

The three peritectic ridges, p_1, p_2, and p_3, intersect the groove between the two binary eutectics at different Hf compositions providing the following invariant reactions:

$$U_1 \quad L + Nb(Hf)_5Si_3 \rightarrow Nb(Hf)_3Si + \beta(Nb, Hf, Si)$$

$$U_2 \quad L + Nb(Hf)_5Si_3 \rightarrow \beta(Nb, Hf, Si) + Hf(Nb)_5Si_3$$

$$U_3 \quad L + Hf(Nb)_5Si_3 \rightarrow \beta(Nb, Hf, Si) + Hf(Nb)_2Si$$

The individual eutectic reactions that ensue at higher Hf concentrations than the invariant reactions are designated e_2, e_3, and e_4.

Option 2 :

The peritectic ridges, p_1 and p_2, intersect to generate U_1 and the resulting ridge intersects the eutectic groove, e_1, to generate U_2 and the following eutectic groove, e_2. The peritectic ridge, p_3, intersects the eutectic groove, e_2, to generate U_3.

$$U_1 \quad L + Nb(Hf)_5Si_3 \rightarrow Nb(Hf)_3Si + Hf(Nb)_5Si_3$$

$$U_2 \quad L + Nb(Hf)_3Si \rightarrow \beta(Nb, Hf, Si) + Hf(Nb)_5Si_3$$

$$U_3 \quad L + Hf(Nb)_5Si_3 \rightarrow \beta(Nb, Hf, Si) + Hf(Nb)_2Si$$

Table 1. Compositions and constituent phases of the range of alloys that were investigated.

Group	Composition	Melting Temperature (°C)	Constituent Phases	XRD results
1	Nb-5%Hf-16%Si	1960	Primary β(Nb, Hf, Si) dendrites with interdendritic cellular eutectic. **Solidification path:** L → β(Nb, Hf, Si) → $Nb(Hf)_3Si$-β(Nb, Hf, Si) eutectic.	–
1	Nb-7.5%Hf-16%Si	1950	**Solidification path:** L → β(Nb, Hf, Si) → $Nb(Hf)_3Si$-β(Nb, Hf, Si) eutectic.	–
1	Nb-10%Hf-16%Si	1930	**Solidification path:** L → β(Nb, Hf, Si) → $Nb(Hf)_3Si$-β(Nb, Hf, Si) eutectic.	–
1	Nb-12.5%Hf-16%Si	1895	**Solidification path:** L → β(Nb, Hf, Si) → $Nb(Hf)_3Si$-β(Nb, Hf, Si) eutectic.	–
1	Nb-15%Hf-16%Si	1880	**Solidification path:** L → β(Nb, Hf, Si) → $Nb(Hf)_3Si$-β(Nb, Hf, Si) eutectic.	–
2	Nb-5%Hf-19%Si	1920	Primary $Nb(Hf)_3Si$ with cellular eutectic of $Nb(Hf)_3Si$ and β(Nb, Hf, Si). **Solidification path:** L → $Nb(Hf)_3Si$ → $Nb(Hf)_3Si$-β(Nb, Hf, Si) eutectic.	Nb_3Si and Nb
2	Nb-10%Hf-18.5%Si	1900	**Solidification path:** L → $Nb(Hf)_3Si$ → $Nb(Hf)_3Si$-β(Nb, Hf, Si) eutectic.	-
3	Nb-10%Hf-25%Si	> 2200	Primary $Nb(Hf)_5Si_3$, peritectic $Nb(Hf)_3Si$ with eutectic between β(Nb, Hf, Si) and $Nb(Hf)_3Si$. **Solidification path:** L → $Nb(Hf)_5Si_3$ → peritectic $Nb(Hf)_3Si$ → $Nb(Hf)_3Si$ + β(Nb, Hf, Si).	Nb, Nb_3Si, and Nb_5Si_3
3	Nb-25%Hf-22%Si	1960	Primary $Nb(Hf)_5Si_3$ with eutectic between $Nb(Hf)_5Si_3$ and β(Nb, Hf, Si). **Solidification path:** L → $Nb(Hf)_5Si_3$ → $Nb(Hf)_5Si_3$ + β(Nb, Hf, Si).	–
3	Nb-20%Hf-25%Si	1966	Primary $Nb(Hf)_5Si_3$ with eutectic between $Nb(Hf)_5Si_3$ and β(Nb, Hf, Si). **Solidification path:** L → $Nb(Hf)_5Si_3$ → $Nb(Hf)_5Si_3$ + β(Nb, Hf, Si).	–
4	Nb-30%Hf-25%Si	–	Primary $Hf(Nb)_5Si_3$, with peritectic $Hf(Nb)_2Si$, and $Hf(Nb)_2Si$-β(Nb, Hf, Si) eutectic cells. **Solidification path:** → $Hf(Nb)_5Si_3$ → $Hf(Nb)_2Si$ → β(Nb, Hf, Si) + $Hf(Nb)_2Si$	–
4	Nb-40%Hf-30%Si	> 2200	Primary $Hf(Nb)_5Si_3$, with peritectic $Hf(Nb)_2Si$, and $Hf(Nb)_2Si$-β(Nb, Hf, Si) eutectic cells. **Solidification path:** L → $Hf(Nb)_5Si_3$ → $Hf(Nb)_2Si$ → β(Nb, Hf, Si) + $Hf(Nb)_2Si$	–
4	Hf-35%Si	> 2200	Primary Hf_5Si_3, with peritectic Hf_2Si, with eutectic between Hf_2Si and metal. **Solidification path:** L → Hf_5Si_3 → peritectic Hf_2Si → Hf_2Si and βHf(Si)	Hf_2Si and Hf_5Si_3
5	Nb-60%Hf-25%Si	2085	Primary $Hf(Nb)_2Si$ with rod-like eutectic between $Hf(Nb)_2Si$ and β(Nb, Hf, Si). **Solidification path:** L → $Hf(Nb)_2Si$ → β(Nb, Hf, Si) + $Hf(Nb)_2Si$	Hf_2Si, αHf, and βHf
5	Nb-73%Hf-17%Si	1870	Primary $Hf(Nb)_2Si$, $Hf(Nb)_2Si$-β(Nb, Hf, Si) eutectic; β(Nb, Hf, Si) transformed into α(Nb, Hf, Si). **Solidification path:** L → $Hf(Nb)_2Si$ → β(Nb, Hf, Si) + $Hf(Nb)_2Si$ eutectic.	αHf, βHf, and Hf_2Si
5	Nb-80%Hf-14%Si	1845	Primary $Hf(Nb)_2Si$, $Hf(Nb)_2Si$-β(Nb, Hf, Si) eutectic; β(Nb, Hf, Si) transformed into α(Nb, Hf, Si). **Solidification path:** L → $Hf(Nb)_2Si$ → β(Nb, Hf, Si) + $Hf(Nb)_2Si$ eutectic.	αHf, βHf, and Hf_2Si
5	Nb-50%Hf-20%Si	2010	Primary $Hf(Nb)_2Si$ with $Hf(Nb)_2Si$-β(Nb, Hf, Si) eutectic. **Solidification path:** L → $Hf(Nb)_2Si$ → β(Nb, Hf, Si) + $Hf(Nb)_2Si$	–
5	Hf-12%Si	1830	Small volume fraction Hf_2Si, eutectic between Hf_2Si and β(Hf, Si). **Solidification path:** L → Hf_2Si → βHf(Si) + Hf_2Si eutectic	Hf_2Si and αHf
5	Hf-20%Si	1865	Primary Hf_2Si, with eutectic between Hf_2Si and β(Hf, Si). **Solidification path:** L → Hf_2Si → β Hf(Si) + Hf_2Si eutectic	–
6	Nb-80%Hf-5%Si	1910	Primary β(Nb, Hf, Si) dendrites with $Hf(Nb)_2Si$-β(Nb, Hf, Si) eutectic. The β(Nb, Hf, Si) transformed to α(Nb, Hf, Si) on post-solidification cooling. **Solidification path:** L — β(Nb, Hf, Si) — β(Nb, Hf, Si) + $Hf(Nb)_2Si$	βHf and αHf

The eutectic groove, e_2, follows from U_2, and e_3 follows from U_3.

Option 3 :

The peritectic ridge, p_2, intersects the eutectic groove, e_1, to generate U_1. The peritectic ridges, p_1 and p_3, intersect to generate U_2, and the subsequent ridge intersects the eutectic groove, e_1, to generate U_3. The data that will be discussed subsequently indicate that this is the correct version of the liquidus surface.

$$U_1 \quad L + Nb(Hf)_5Si_3 \rightarrow Nb(Hf)_3Si + \beta(Nb, Hf, Si)$$

$$U_2 \quad L + Hf(Nb)_5Si_3 \rightarrow Nb(Hf)_5Si_3 + Hf(Nb)_2Si$$

$$U_3 \quad L + Nb(Hf)_5Si_3 \rightarrow \beta(Nb, Hf, Si) + Hf(Nb)_2Si$$

Option 4 :

The three peritectic ridges, p_1, p_2, and p_3, intersect to generate U_1 and U_2 at Si concentrations higher than the eutectic groove, e_1, and the subsequent ridge intersects the eutectic groove, e_1, to generate U_3.

$$U_1 \quad L + Hf(Nb)_5Si_3 \rightarrow Nb(Hf)_5Si_3 + Hf(Nb)_2Si$$

$$U_2 \quad L + Nb(Hf)_5Si_3 \rightarrow Nb(Hf)_3Si + Hf(Nb)_2Si$$

$$U_3 \quad L + Nb(Hf)_3Si \rightarrow \beta(Nb, Hf, Si) + Hf(Nb)_2Si$$

There are four other possible options in addition to the four described so far, with the second transition reaction being a ternary eutectic [10]. However, there was no evidence for the formation of a ternary eutectic in any of the alloys that were examined. There are no previously reported data on the compositions or temperatures at which the above transition reactions occur. The aim of the present paper is to describe the data that substantiate the proposed liquidus surface.

3 Experimental

The samples for this study were directionally solidified using cold crucible directional solidification [2, 3] after triple melting the starting charges from high purity elements (> 99.99 %). The directional solidification procedure has been described in more detail previously [3]. Typically at least two samples were generated for each composition. Several compositions were prepared by cold crucible induction levitation melting followed by solidification in the cold crucible. The alloy melt temperatures were measured using a two-wavelength optical pyrometer. The pyrometer was calibrated against both the melting temperature of 99.9 % pure Ti (1670 °C) and the temperature of the Hf–Hf_2Si eutectic (1830 °C) [4]. Errors in temperature measurements were estimated as < 20 °C. These temperatures are reported in Table 1; several compositions possessed melting temperatures higher than the maximum temperature capability of the pyrometer (2200 °C), and these are marked accordingly. Liquidus and solidus temperatures were not measured because they were too high for conventional differential thermal analysis.

Table 1 shows the range of compositions that was investigated, where the listed compositions are those of the starting charges. Mass losses were measured after preparation of each sample and they were found to be less that 0.1 wt.%. The interstitial levels of the Hf that was used were: 20, 780 and 27 weight ppm of C, O and N respectively. The interstitial levels of the C, H, N, and O in Nb that was used were 230, 23, 9 and 250 weight ppm, respectively.

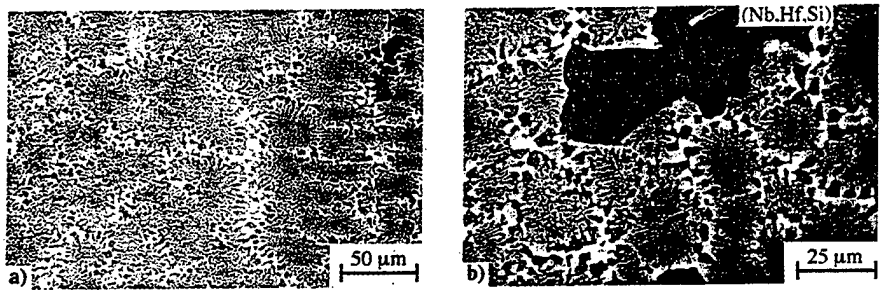
All of the samples were examined using scanning electron microscopy (back scatter electron (BSE) imaging) and energy dispersive spectrometry (EDS). Electron beam microprobe analysis (EMPA) was also performed on selected samples. Transmission electron microscopy (TEM), X-ray diffraction (XRD), and automated electron back scattering pattern analysis in the SEM (EBSP), were also performed on selected samples. These analyses allowed determination of the chemistry and crystal structure of the individual phases.

EMPA was employed using a 15 kV, 20 nA, ~ 1 µm diameter beam to determine phase chemistries. High purity Nb, Hf, and Si were used as standards and conventional matrix corrections (Z, A, and F) were used to calculate the wt.% compositions from measured X-ray intensities. The Hf-rich silicides were identified using both EMPA and XRD data. Analysis of microprobe data was complicated due to absorption of the Si signal by Hf, and as a result large ZAF corrections were required; the ZAF models that have been developed previously were not accurate when absorption was so strong, and no independent monolithic standards were available for the silicide. However, the Hf_2Si in the binary Hf-20Si alloy was identified using XRD, and used as a standard for identification of the Hf_5Si_3 in the binary, and all the Hf-based silicides in the ternary alloys. The limit of detection of Si and Hf was 0.04 wt.% and the limit of detection of Nb was 0.13 wt.%. Errors in Hf and Si measurement were ~ 1.0 % relative, and in the Nb measurement the error was ~ 2 % relative.

4 Results and Discussion

4.1 Microstructures of Nb–Hf–Si Alloys

Microstructural evidence for the solidification paths will be discussed first for the Nb-rich alloys, second for the Nb_3Si-rich alloys, third for the Nb_5Si_3-rich alloys, fourth for the



Figs 3a and b. Typical microstructure (BSE image) of the transverse section of a DS Nb-15Hf-16Si alloy at (a) low and (b) high magnifications. There are large-scale dark β(Nb, Hf, Si) dendrites with interdendritic cells of $Nb(Hf)_3Si$ (light grey) and β(Nb, Hf, Si) (dark grey).

Hf_5Si_3-rich compositions, fifth for the Hf_2Si-rich compositions, and finally for Hf-rich compositions. These categories are listed as 1–6 in Table 1 and in the following sections. The phases that were identified in the DS alloys of Groups 1–6 are summarized in Table 1. There was no evidence of a ternary eutectic in any of the alloys examined.

4.2 Nb-rich Compositions: Group 1

This regime contained primary β(Nb, Hf, Si) dendrites with $Nb(Hf)_3Si$-β(Nb, Hf, Si) eutectic. Ternary Nb–Hf–Si alloys with Hf concentrations of 5–15 and Si concentrations of 16 were all on the metal-rich side of the $Nb(Hf)_3Si$-β(Nb, Hf, Si) eutectic valley.

Typical microstructures of the transverse section are shown in Fig. 3 for the Nb-15Hf-16Si composition. The microstructure consisted of a small volume fraction of primary β(Nb, Hf, Si) dendrites (the darker phase in these BSE micrographs), together with an interdendritic $Nb(Hf)_3Si$-β(Nb, Hf, Si) cellular eutectic. The Nb-15Hf-16Si composition also appeared to contain a small volume fraction of intercellular eutectic of $Nb(Hf)_5Si_3$ and β(Nb, Hf, Si), which suggests that the liquid composition of the Nb-15Hf-16Si passed through the invariant reaction U_1. The strong BSE contrast towards the boundaries of the eutectic cells was consistent with Hf segregation in these regions.

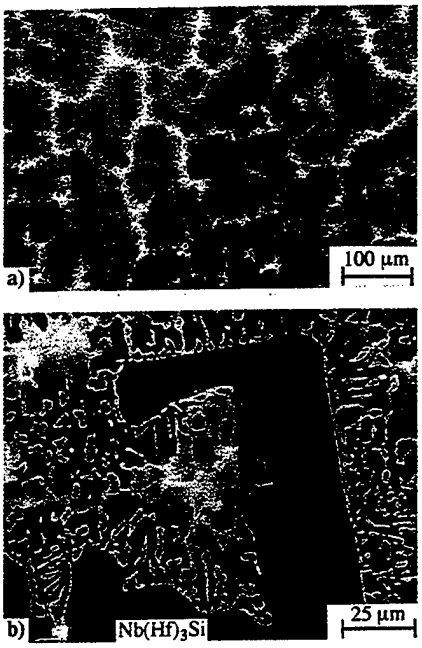
Phase compositions for the Nb-12.5Hf-16Si are shown in Table 2. The primary β(Nb, Hf, Si) dendrites had an average composition of Nb-8.1Hf-1.8Si, and the eutectic β(Nb, Hf, Si) of the $Nb(Hf)_3Si$-β(Nb, Hf, Si) eutectic was Nb-12.3Hf-1.9Si. The eutectic $Nb(Hf)_3Si$ composition was Nb-11.8Hf-26.5Si and the eutectic $Nb(Hf)_5Si_3$ composition was Nb-22.2Hf-37.6Si.

The Nb-5Hf-16Si also contained primary β(Nb, Hf, Si) dendrites with inter-dendritic regions of $Nb(Hf)_3Si$ and fine-scale β(Nb, Hf, Si). However, no $Nb(Hf)_5Si_3$ was observed in this microstructure, which suggested that the composition of the final inter-dendritic liquid remained in the $Nb(Hf)_3Si$-β(Nb, Hf, Si) eutectic groove, and it never reached the that invariant reaction U_1. The melt temperature data suggest the temperature of the eutectic trough, e_1, decreases from 1880 °C to 1830 °C with increasing Hf concentration.

4.3 $Nb(Hf)_3Si$ -rich Compositions: Group 2

This regime contained primary $Nb(Hf)_3Si$ dendrites with $Nb(Hf)_3Si$-β(Nb, Hf, Si) eutectic. Two compositions were examined from this region, Nb-5Hf-19Si and Nb-10Hf-18.5Si.

Microstructures of the transverse section of the DS Nb-5Hf-19Si composition are shown in Fig. 4. The primary solidification phase was faceted dendrites of $Nb(Hf)_3Si$ (dark grey). The interdendritic eutectic consisted of $Nb(Hf)_3Si$-β(Nb, Hf, Si) eutectic cells, and there was heavy segregation of Hf to the cell boundaries, as shown in the transverse section in Fig. 4a. The matrix of the eutectic was $Nb(Hf)_3Si$, as was the case in the binary Nb-Nb_3Si eutectic [2]. EMPA indicates that the bright regions at the intercellular boundaries were Hf-rich. This composition was Si-rich of the eutectic valley, but Si-lean of the $L + Nb(Hf)_5Si_3 \rightarrow Nb(Hf)_3Si$ peritectic ridge, p_2.



Figs 4a and b. Typical microstructure (BSE images) of the transverse section of a DS Nb-5Hf-19Si alloy at (a) low and (b) high magnifications. The faceted grey dendrites are $Nb(Hf)_3Si$; they are surrounded by eutectic cells of β(Nb, Hf, Si) (light phase) and $Nb(Hf)_3Si$ (grey phase).

The Nb-10Hf-18.5Si was also from this same region, but it was closer to the eutectic valley. This composition possessed a smaller volume fraction of primary $Nb(Hf)_3Si$ dendrites and a larger volume fraction of eutectic. However, there was no evidence for the first transition reaction, U_1, in either of these compositions, which is consistent with the relatively low Hf concentration in relation to the composition at U_1.

In the binary Nb-Nb_3Si eutectic, the eutectic composition and the liquid composition of the $L + Nb_5Si_3 \rightarrow Nb_3Si$ peritectic, p_2, are very close to each other (18.2 vs 19.5 Si). The situation is similar in the Nb–Hf–Si ternary phase diagram. This means it is difficult to define the region between the peritectic ridge and the eutectic groove. It appears that these two lines are within several per cent Si of each other. Compositions as high as 19Si experienced the peritectic reaction, and compositions as low as 16Si did not experience this reaction (i.e. they were hypoeutectic). This describes the narrow nature of the composition range between the $Nb(Hf)_3Si$-β(Nb, Hf, Si) eutectic groove, e_1, and the $L + Nb(Hf)_5Si_3 \rightarrow Nb(Hf)_3Si$ peritectic, p_2.

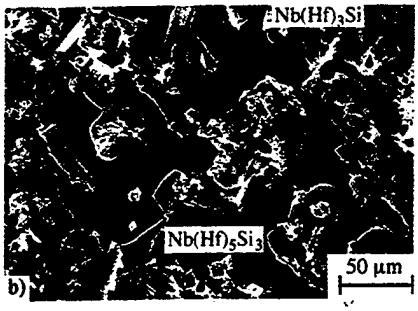
4.4 $Nb(Hf)_5Si_3$-rich Compositions: Group 3

This regime contained primary $Nb(Hf)_5Si_3$ dendrites, peritectic $Nb(Hf)_3Si$, and $Nb(Hf)_3Si$-β(Nb, Hf, Si) eutectic.

Table 2. EMPA data of the phases within the Nb-12.5Hf-16Si alloy.

Phase	Hf	Nb	Si
Primary β(Nb, Hf, Si)	8.1	90.1	1.8
Eutectic I: β(Nb, Hf, Si)	7.8	90.3	1.9
Eutectic I: $Nb(Hf)_3Si$	11.8	61.7	26.5
Eutectic II: β(Nb, Hf, Si)	12.3	85.8	1.9
Eutectic II: $Nb(Hf)_5Si_3$	22.2	40.2	37.6





Figs 5a and b. Typical microstructures (BSE images) of (a) the longitudinal and (b) the transverse section of a DS Nb-10Hf-25Si alloy. The large black phase is $Nb(Hf)_5Si_3$, the large dark grey phase is $Nb(Hf)_3Si$, and the light grey phase is β(Nb, Hf, Si).

Three compositions were examined from this regime, Nb-10Hf-25Si, Nb-20Hf-25Si, Nb-25Hf-22Si.

Typical microstructures (BSE images) of the (a) longitudinal and (b) transverse sections of the DS Nb-10Hf-25Si alloy are shown in Fig. 5. As shown in the transverse section, the large black phase was $Nb(Hf)_5Si_3$, and it was surrounded by dark grey peritectic $Nb(Hf)_3Si$. This composition experienced the peritectic reaction, $L + Nb(Hf)_5Si_3 \rightarrow Nb(Hf)_3Si$. The peritectic and dendritic $Nb(Hf)_3Si$ appeared to have grown in a coupled manner with the β(Nb, Hf, Si) dendrites (light phase). Hf partitioning between the $Nb(Hf)_3Si$ and β(Nb, Hf, Si) was such that there was little contrast between these two phases. The $Nb(Hf)_3Si$ also contained some brighter regions that were probably Hf-rich. There was a high degree of consistency between the compositions of the β(Nb, Hf, Si) and the $Nb(Hf)_3Si$ of the eutectics in both the hypo- and the hypereutectic alloys.

The compositions of the phases that were observed are shown in Table 3. The primary $Nb(Hf)_5Si_3$ had a composition of Nb-10.6Hf-36.5Si, and the peritectic $Nb(Hf)_3Si$ had a composition of Nb-9.3Hf-24.0Si. The eutectic $Nb(Hf)_3Si$ possessed more Hf than the peritectic, the typical composition being Nb-12.0Hf-24.3Si, although in some of the brighter regions of Fig. 5 the Hf concentration was even higher than 12.0. The composition of the β(Nb, Hf, Si) was Nb-8.2Hf-1.5Si; the Si concentration was typically slightly lower in the Nb-rich β(Nb, Hf, Si) than in the Hf-rich β(Nb, Hf, Si).

Table 3. EMPA data of the phases within the Nb-10Hf-25Si alloy.

Phase	Hf	Nb	Si
Primary $Nb(Hf)_5Si_3$	10.6	52.9	36.5
Peritectic $Nb(Hf)_3Si$	9.3	66.7	24.0
Eutectic β(Nb, Hf, Si)	8.2	90.3	1.5
Eutectic $Nb(Hf)_3Si$	12.0	63.7	24.3

Table 4. EMPA data of the phases within the Nb-25Hf-22Si alloy.

Phase	Hf	Nb	Si
Primary $Nb(Hf)_5Si_3$	27.6	35.9	36.5
Eutectic $Nb(Hf)_5Si_3$	29.9	33.5	36.6
Eutectic β(Nb, Hf, Si)	21.0	77.9	1.1

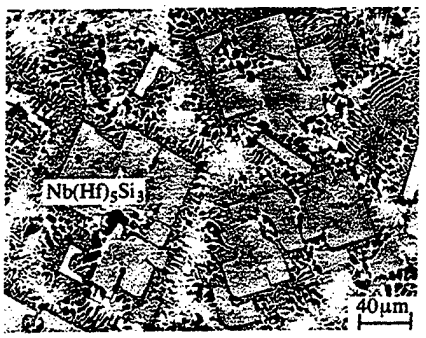


Fig. 6. Typical microstructure (BSE image) of the DS Nb-25Hf-22Si alloy. The large primary dendrites are $Nb(Hf)_5Si_3$ (grey), and the eutectic consists of β(Nb, Hf, Si) and $Nb(Hf)_5Si_3$. The β(Nb, Hf, Si) is the dark grey phase.

The microstructure of the Nb-25Hf-22Si alloy is shown in Fig. 6. The microstructure consisted of large grey faceted dendrites (40–60 µm) with an interdendritic eutectic of $Nb(Hf)_5Si_3$ and β(Nb, Hf, Si). The β(Nb, Hf, Si) was dark grey/black and the $Nb(Hf)_5Si_3$ was light grey/white. The β(Nb, Hf, Si) was the discontinuous phase in the $Nb(Hf)_5Si_3$ matrix. The eutectic β(Nb, Hf, Si) was darker than the primary $Nb(Hf)_5Si_3$ dendrites; the composition of the primary $Nb(Hf)_5Si_3$ was Nb-27.6Hf-36.5Si. The composition of the eutectic β(Nb, Hf, Si) was Nb-21.0Hf-1.1Si, and the eutectic $Nb(Hf)_5Si_3$ was Nb-29.9Hf-36.6Si; these data suggest that the high Hf concentration of the eutectic $Nb(Hf)_5Si_3$ was the reason for it appearing brighter than the eutectic β(Nb, Hf, Si). The eutectic $Nb(Hf)_5Si_3$ provided slightly lighter contrast than the primary $Nb(Hf)_5Si_3$ because of the higher Hf concentration. The phase compositions are included in Table 4. EBSP was performed and the phases were identified as β(Nb, Hf, Si) and a tetragonal phase, but because of the large concentrations of Nb and Hf in the silicide it was difficult to distinguish the Nb_5Si_3 and Hf_2Si type silicides. Therefore, the EMPA data were used to identify the silicide as $Nb(Hf)_5Si_3$.

Thus, the Hf concentration of the Nb-25Hf-22Si was sufficiently Hf-rich that on solidification the composition of the liquid moved directly into the eutectic valley, e_2, and it missed the peritectic ridge, p_2, as well as e_1 and U_1. There was little evidence that the liquid composition proceeded down the eutectic trough, e_2, as far as U_3. In principle this is possible, but only a small number of EMPA measurements detected the presence of β(Nb, Hf, Si)-$Hf(Nb)_2Si$ eutectic, and they were therefore not included in Table 4.

4.5 $Hf(Nb)_5Si_3$-Rich Compositions: Group 4

This regime contained primary $Hf(Nb)_5Si_3$ dendrites, peritectic $Hf(Nb)_2Si$, and β(Nb, Hf, Si)-$Hf(Nb)_2Si$ eutectic. Two ternary compositions were examined from this re-

gime, Nb-30Hf-25Si and Nb-40Hf-30Si. The binary Hf-35Si alloy was also examined.

The microstructure of the binary Hf-35Si is shown in Fig. 7. It consisted of a small volume fraction of Hf_5Si_3 surrounded by Hf_2Si peritectic with a small volume fraction of the Hf(Si)-Hf_2Si interdendritic eutectic. The individual phases were identified using EBSP [9]. The Hf_2Si is the black phase and the Hf(Si) is the light phase. The Hf_5Si_3 was also black and it was difficult to identify because there was little contrast with the peritectic Hf_2Si. The Hf_5Si_3 possessed a high density of cracks which did not propagate in to the Hf_2Si. Only Hf_5Si_3 and Hf_2Si were detected. No Hf_3Si_2 or Hf_5Si_4 phases were detected. The presence of Hf_5Si_3 and Hf_2Si silicides was confirmed using XRD, EMPA and EBSP data. This is evidence for the peritectic and the eutectic reactions. The melting temperature was greater than 2200 °C.

The microstructure of the Nb-30Hf-25Si is shown in Figs 8a and b. It possessed a small volume fraction of primary $Hf(Nb)_5Si_3$ (large-scale light grey phase), which was surrounded by peritectic $Hf(Nb)_2Si$, which are the faceted grey dendrites in the transverse section of Fig. 8a. There was an interdendritic eutectic of $Hf(Nb)_2Si$ (light grey phase) and β(Nb, Hf, Si) (dark phase). The $Hf(Nb)_5Si_3$ was difficult to identify within the cores of the $Hf(Nb)_2Si$ dendrites, but it was identified using both EMPA and EBSP (hP16 crystal structure). The $Hf(Nb)_5Si_3$ also possessed many regular cracks, as shown in the micrograph of Fig. 8b. The individual phases were also identified using extensive analysis with EBSP.

Both phases of the eutectic appeared to be continuous and they had similar volume fractions. The eutectic β(Nb, Hf, Si) was bcc at this Nb concentration. Although the eutectic had a slightly different morphology to the Hf(Si)-Hf_2Si binary eutectic, the EMPA data indicated that the silicide was Hf_2Si type. The melting temperature of the Nb-30Hf-25Si was 2115 °C.

There was a large volume fraction of β(Nb, Hf, Si)-$Hf(Nb)_2Si$ eutectic, and small volume fractions of peritectic $Hf(Nb)_2Si$ and primary $Hf(Nb)_5Si_3$ dendrites. This suggests that the Nb-30Hf-25Si composition is close to the $L + Hf(Nb)_5Si_3 \rightarrow Hf(Nb)_2Si$ peritectic ridge, and that the peritectic ridge is close to the eutectic valley. This observation also suggests that the peritectic ridge, p_3, is closer to the eutectic valley, e_3, at these Hf concentrations than in the binary Hf–Si system.

The primary $Hf(Nb)_5Si_3$ had a composition of Nb-33.2Hf-37.5Si, as shown in Table 5. The peritectic $Hf(Nb)_2Si$ had a composition of Nb-33.8Hf-33.2Si, and

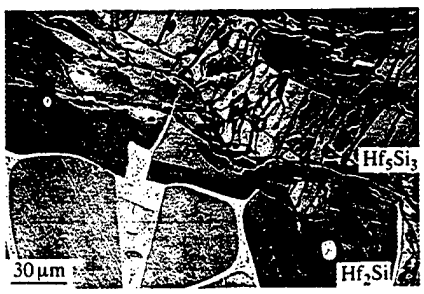
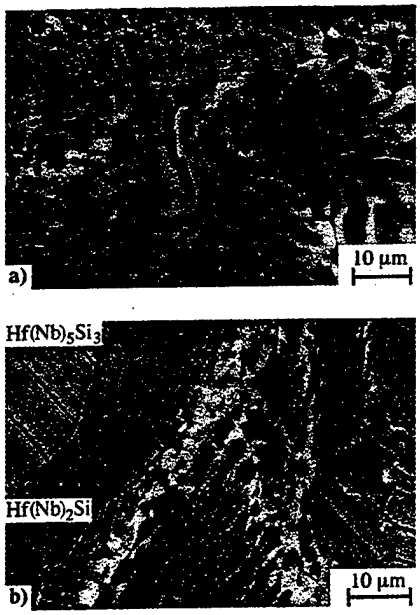


Fig. 7. Typical microstructure (BSE image) of the induction melted Hf-35Si alloy. The black phase is Hf_5Si_3 and the white phase is αHf(Si). The black peritectic phase is Hf_2Si.



Figs 8a and b. Typical microstructure (BSE image) of (a) the transverse, and (b) the longitudinal section of the Nb-30Hf-25Si alloy. The large primary dendrites are $Hf(Nb)_5Si_3$ (dark grey), and there is peritectic $Hf(Nb)_2Si$ (light grey). The $Hf(Nb)_5Si_3$ possessed many cracks.

the eutectic $Hf(Nb)_2Si$ had a composition of Nb-43.0Hf-32.3Si. Both the $Hf(Nb)_5Si_3$ and the $Hf(Nb)_2Si$ show extensive solubility for Nb. The eutectic β(Nb, Hf, Si) had a composition of Nb-22.7Hf-1.4Si. The eutectic $Hf(Nb)_2Si$ possessed a higher Hf concentration than the peritectic $Hf(Nb)_2Si$. EMPA was performed on samples from both the DS rods and the induction cast ingots. The compositions of the peritectic $Hf(Nb)_2Si$ were similar in the alloys prepared by the two separate techniques. However, a slightly larger volume fraction of $Hf(Nb)_5Si_3$ was observed in the induction cast ingots. There was a gradation in the eutectic β(Nb, Hf, Si) composition away from the peritectic $Hf(Nb)_2Si$ because during solidification the liquid composition moved toward the Hf-rich corner of the phase diagram.

The microstructure of the Nb-40Hf-30Si was similar to that of the Nb-30Hf-25Si, except that it contained a larger volume fraction of primary $Hf(Nb)_5Si_3$ and a smaller volume fraction of eutectic. This observation is consistent with it being further from the peritectic ridge.

The melting temperatures are 2520 °C for binary Nb_5Si_3 and 2480 °C for binary Hf_5Si_3 [4 to 6]. Thus, at compositions greater than ~ 20 Si the liquidus surface is very flat. It is assumed in Figs 1 and 2 that there is a peritectic reaction between the Nb_5Si_3 and the Hf_5Si_3. On the basis of the data presented in this paper it is difficult to be more specific about the nature of the reaction between $Nb(Hf)_5Si_3$ and

Table 5. EMPA data for the primary, peritectic and eutectic phases observed in the Nb-30Hf-25Si alloy.

Phase	Hf	Nb	Si
Primary $Hf(Nb)_5Si_3$	33.2	29.2	37.5
Peritectic $Hf(Nb)_2Si$	33.8	32.9	33.2
Eutectic $Hf(Nb)_2Si$	43.0	24.7	32.3

$Hf(Nb)_5Si_3$, but the data appear to be more consistent with a peritectic than a eutectic.

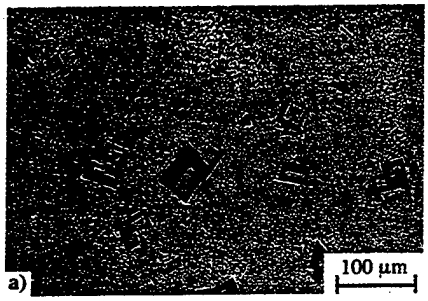
4.6 $Hf(Nb)_2Si$-rich Compositions: Group 5

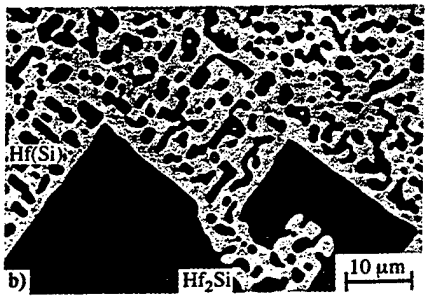
This regime contained primary $Hf(Nb)_2Si$ dendrites, and the β(Nb, Hf, Si)-$Hf(Nb)_2Si$ eutectic. Four ternary compositions were examined from this regime Nb-60Hf-25Si, Nb-50Hf-20Si, Nb-73Hf-17Si, and Nb-80Hf-14Si. In addition, two binary compositions were also examined, Hf-20Si and Hf-12Si. The microstructures of the binary alloys will be described first and then the ternary alloys will be described.

The microstructure of the Hf-12Si is shown in Fig. 9. The microstructure consisted of rods/fibres of Hf_2Si (grey phase) in a Hf(Si) matrix (white phase). There was also a small volume fraction of faceted Hf_2Si dendrites indicating that the Hf-12Si composition was slightly Si-rich of the eutectic composition. The βHf(Si) appeared to have transformed completely to αHf(Si). The Hf-Hf_2Si eutectic can be distinguished from the Nb-Nb_3Si eutectic by two characteristics. First, in the binary Hf-Hf_2Si eutectic the Hf is the matrix phase, whereas in the binary Nb_3Si-Nb the Nb_3Si is the matrix phase. Second, the morphology of the eutectic Hf_2Si is quite different to the Nb rods in the Nb_3Si–Nb eutectic. The melting temperature was consistent with that reported previously for the Hf-Hf_2Si eutectic, although the Hf-12Si composition is in fact Si-rich of the eutectic composition.

The microstructure of the Hf-20Si also contained primary faceted Hf_2Si dendrites and eutectic Hf-Hf_2Si. The volume fraction of primary dendrites was much larger than in the Hf-12Si. No Hf_5Si_3 was detected; thus the Hf-20Si composition allows the peritectic ridge to be placed in the Hf–Si binary at a composition greater than 20Si.

The microstructure of the Nb-60Hf-25Si is shown in Fig. 10. It consisted of a large volume fraction of faceted primary $Hf(Nb)_2Si$ dendrites (grey phase), with an interdendritic eutectic of β(Nb, Hf, Si) and $Hf(Nb)_2Si$. The eutectic consisted of rods/ribbons of $Hf(Nb)_2Si$ in a β(Nb, Hf, Si) matrix (light phase). The eutectic β(Nb, Hf, Si) showed no apparent solid-state transformation in the as-solidified sample.





Figs 9a and b. Typical microstructure (BSE image) of the transverse section of a DS Hf-12Si alloy. There are faceted grey Hf_2Si dendrites, with an interdendritic eutectic of Hf_2Si and Hf(Si). (a) Overview, (b) detail.

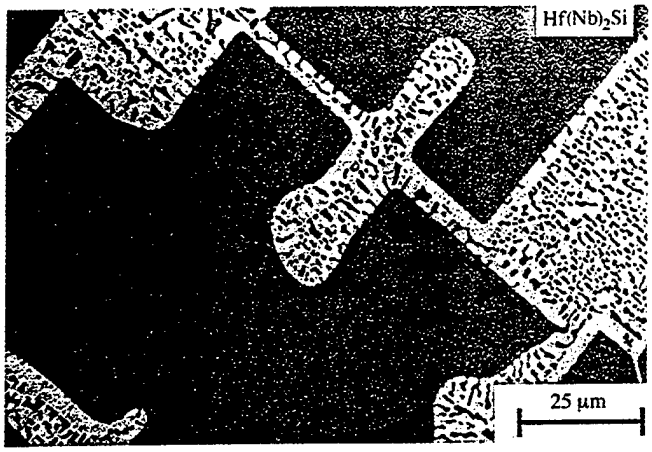


Fig. 10. Typical microstructure (BSE image) of the DS Nb-60Hf-25Si alloy. There are large primary faceted $Hf(Nb)_2Si$ dendrites (grey phase), and inter-dendritic β(Nb, Hf, Si)-$Hf(Nb)_2Si$ eutectic. The light phase is the β(Nb, Hf, Si) eutectic matrix.

This composition was considered to be very close to the $L + Hf(Nb)_5Si_3 \rightarrow Hf(Nb)_2Si$ peritectic ridge, p_3, because no $Hf(Nb)_5Si_3$ was identified in the microstructure and there was a relatively small volume fraction of β(Nb, Hf, Si)-$Hf(Nb)_2Si$ eutectic. At higher Nb compositions, such as Nb-30Hf-25Si, the eutectic $Hf(Nb)_2Si$ possessed a more continuous morphology, and it also occupied a larger volume fraction of the eutectic.

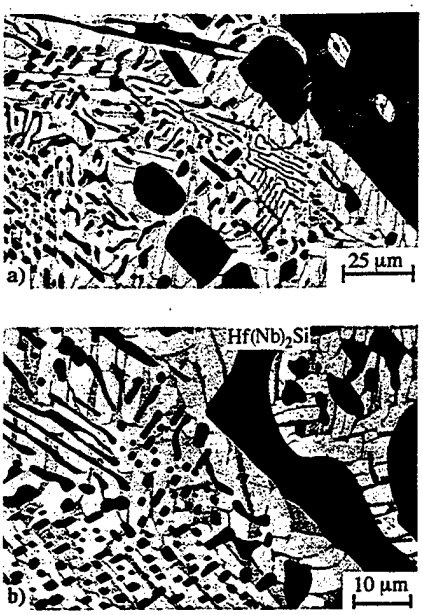
The phase compositions for the Nb-60Hf-25Si are shown in Table 6. The compositions of the primary and eutectic $Hf(Nb)_2Si$ were similar and were Nb-58.8Hf-32.5Si and Nb-58.4Hf-32.7Si, respectively. The eutectic β(Nb, Hf, Si) had a composition of Nb-68.1Hf-2.0Si. Thus, the $Hf(Nb)_2Si$ shows extensive solubility for Nb.

The microstructure of the Nb-50Hf-20Si was similar to the Nb-60Hf-25Si except that it contained a larger volume fraction of eutectic. The eutectic cells showed heavy segregation of the Hf to the cell boundaries. The eutectic grew in a cellular manner; the individual cells and the cell boundaries were well defined. The eutectic consisted of a matrix of β(Nb, Hf, Si) with rods/fibers of $Hf(Nb)_2Si$.

A typical microstructure of the Nb-80Hf-14Si alloy is shown in Fig. 11. The microstructure contained primary $Hf(Nb)_2Si$ faceted dendrites (black phase) with an interdendritic eutectic of β(Nb, Hf, Si) and fine-scale (~ 2 µm) rods of $Hf(Nb)_2Si$ (black phase). The grey β(Nb, Hf, Si) was the matrix of the eutectic. On post-solidification cooling the β(Nb, Hf, Si) transformed to α(Nb, Hf, Si) (white phase)

Table 6. EMPA data for the primary and eutectic phases observed in the Nb-60Hf-25Si alloy.

Phase	Hf	Nb	Si
Primary $Hf(Nb)_2Si$	58.8	8.7	32.5
Eutectic $Hf(Nb)_2Si$	58.4	8.9	32.7
Eutectic β(Nb, Hf, Si)	68.1	29.9	2.0



Figs 11a and b. Typical microstructures (BSE images) of the transverse section of the DS Nb-80Hf-14Si alloy, at (a) low, and (b) high magnifications. The large black faceted dendrites are $Hf(Nb)_2Si$ and there is inter-dendritic β(Nb, Hf, Si)-$Hf(Nb)_2Si$ eutectic. The β(Nb, Hf, Si) has transformed to α(Nb, Hf, Si), which is the light phase in the transformed eutectic matrix, and β(Nb, Hf, Si) which is the dark phase.

and β(Nb, Hf, Si) (grey phase). The Nb-80Hf-14Si composition is therefore on the Si-rich side of the β(Nb, Hf, Si)-$Hf(Nb)_2Si$ eutectic trough. This suggests an increase in the Si composition of the eutectic trough with increasing Nb concentration from the binary Hf-Hf_2Si eutectic. The melting temperature was 1845 °C which is consistent with the composition being from the Si-rich side of the eutectic valley.

The phase chemistries for the Nb-80Hf-14Si alloy are shown in Table 7. The primary and the eutectic $Hf(Nb)_2Si$ had similar compositions. The compositions of the α and β formed from the eutectic β(Nb, Hf, Si) are also shown in Table 7. The Si concentration of the α(Nb, Hf, Si) was higher than expected which may have been a result of errors associated with EMPA of the fine-scale transformed structure.

The microstructure of the Nb-73Hf-17Si composition was similar to that of the Nb-80Hf-14Si except that there

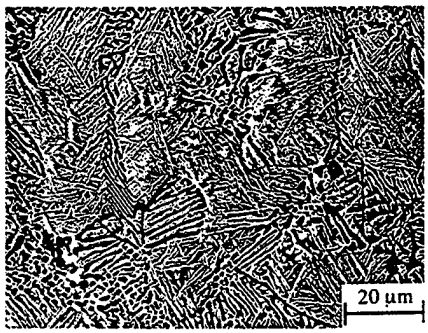


Fig. 12. Typical microstructures (BSE images) of the transverse section of a DS Nb-80Hf-5Si alloy. There are transformed primary β(Nb. Hf. Si) dendrites with an interdendritic eutectic of β(Nb. Hf. Si) and $Hf(Nb)_2Si$. Both the primary β(Nb. Hf. Si) and the eutectic β(Nb. Hf. Si) have transformed to α(Nb. Hf. Si) (white phase) and β(Nb. Hf. Si) (dark phase).

Table 7. EMPA data for the primary $Hf(Nb)_2Si$ and eutectic phases including α and β (Hf, Nb, Si) in the Nb-80Hf-14Si alloy.

Phase	Hf	Nb	Si
Primary $Hf(Nb)_2Si$	65.4	1.6	33.0
Eutectic $Hf(Nb)_2Si$	64.6	1.8	33.6
Eutectic metal			
α (Hf, Nb, Si)	94.9	2.6	2.4
β (Hf, Nb, Si)	17.2	80.7	2.1

Table 8. EMPA data for the primary $Hf(Nb)_2Si$ and eutectic phases within the Nb-73Hf-17Si alloy.

Phase	Hf	Nb	Si
Primary $Hf(Nb)_2Si$	64.5	3.4	32.1
Eutectic $Hf(Nb)_2Si$	64.2	3.7	32.1
Eutectic metal			
α (Nb, Hf, Si)	96.1	3.8	0.1
β (Hf, Nb, Si)	23.9	76.0	0.1

Table 9. EMPA data for the primary $Hf(Nb)_2Si$ and eutectic phases within the Nb-80Hf-5Si alloy.

Phase	Hf	Nb	Si
Primary β (Hf, Nb, Si) dendrite	80.0	17.6	2.4
Eutectic $Hf(Nb)_2Si$	60.7	5.4	33.9

was a larger volume fraction of primary $Hf(Nb)_2Si$ and a smaller volume fraction of eutectic. This composition was therefore considered to be further away from the eutectic trough on the Si-rich side of the eutectic valley. The β(Nb, Hf, Si) also experienced the β → α transformation on post-solidification cooling.

The phase chemistries for the Nb-73Hf-17Si alloy are shown in Table 8. The primary and eutectic $Hf(Nb)_2Si$ compositions were similar to those in the Nb-80Hf-14Si alloy, but they contained slightly more Nb and less Si. The composition of the primary $Hf(Nb)_2Si$ was Nb-64.5Hf-32.1Si and the eutectic $Hf(Nb)_2Si$ was Nb-64.2Hf-32.1Si. The compositions of the transformed metallic phases were Nb-23.9Hf-0.1Si for the β(Nb, Hf, Si), and Nb-96.1Hf-0.1Si for the α(Nb, Hf, Si). The α and β phases appear to possess less Si in the Nb-73Hf-17Si than in the Nb-80Hf-14Si. The reason is not obvious but may be due in part to EMPA difficulties.

4.7 Hf-rich Nb–Hf–Si Compositions: Group 6

This group consists of Hf-rich compositions from the metal-rich side of the eutectic valley. The alloys contained primary β(Nb, Hf, Si) dendrites, and β(Nb, Hf, Si)-$Hf(Nb)_2Si$ eutectic. However, the dendritic and eutectic β(Nb, Hf, Si) experienced the β → α allotropic phase transformation on post-solidification cooling, unlike the β(Nb. Hf, Si) in the Nb-rich compositions. This group is distinguished from Group 1 by, (a) transformation of the primary β(Nb. Hf. Si), and (b) the presence of the β(Nb. Hf. Si)-$Hf(Nb)_2Si$ interdendritic eutectic.

The microstructure of the Nb-80Hf-5Si alloy is shown in Fig. 12 and it contained β(Hf. Nb. Si) dendrites with an interdendritic β(Nb. Hf. Si)-$Hf(Nb)_2Si$ eutectic. The primary

β dendrites transformed to fine-scale laths of α and β(Hf, Nb, Si) on post-solidification cooling; the individual β sub-grains can be seen in Fig. 12. The eutectic β(Nb, Hf, Si) also transformed to α(Hf, Nb, Si) (white phase) and β(Hf, Nb, Si) (dark phase).

EMPA analysis data are shown for the primary and eutectic phases in the Nb-80Hf-5Si in Table 9. The primary β(Nb, Hf, Si) had an average composition of Nb-80.0Hf-2.4Si; the compositions of the individual laths of the transformed structure could not be resolved. The $Hf(Nb)_2Si$ had a composition of Nb-60.7Hf-33.9Si, which is a slightly higher Nb concentration than the $Hf(Nb)_2Si$ of the hypereutectic alloys.

5 Conclusions

The microstructures generated in the ternary Nb–Hf–Si alloys investigated contained a total of six phases: β(Nb, Hf, Si), α(Nb, Hf, Si), $Nb(Hf)_5Si_3$, $Nb(Hf)_3Si$, $Hf(Nb)_2Si$ and $Hf(Nb)_5Si_3$. The phases that were observed were dendritic, peritectic, or eutectic in their nature, depending on the composition and solidification path. These phases were identified using microscopy, EMPA, EBSP, and XRD.

Microstructural, microchemical and crystallographic evidences indicate that the liquidus surface of the Nb–Hf–Si ternary phase diagram possesses the following reactions:

$L + Nb(Hf)_5Si_3 \rightarrow Hf(Nb)_5Si_3$ peritectic (assumed)

$L + Nb(Hf)_5Si_3 \rightarrow Nb(Hf)_3Si$ peritectic

$L \rightarrow Nb(Hf)_3Si + \beta(Nb, Ti, Si)$ eutectic

$L \rightarrow Nb(Hf)_5Si_3 + \beta(Nb, Ti, Si)$ eutectic

$L + Hf(Nb)_5Si_3 \rightarrow Hf(Nb)_2Si$ peritectic

$L + Nb(Hf)_5Si_3 \rightarrow Hf(Nb)_2Si$ peritectic (assumed)

$L \rightarrow \beta(Nb, Hf, Si) + Hf(Nb)_2Si$ eutectic

These reactions give rise to the following three transition reactions :

$L + Nb(Hf)_5Si_3 \rightarrow Nb(Hf)_3Si + \beta(Nb, Hf, Si)$

$L + Hf(Nb)_5Si_3 \rightarrow Hf(Nb)_2Si + Nb(Hf)_5Si_3$

$L + Nb(Hf)_5Si_3 \rightarrow \beta(Nb, Hf, Si) + Hf(Nb)_2Si$

The first of these transition reactions (at higher Si concentration) occurs at a composition of approximately Nb-21Hf-16Si, and at a temperature of ~ 1850 °C. The second of these transition reactions occurs at a composition of approximately Nb-27Hf-22Si, and a temperature of ~ 2040 °C. The third transition reaction occurs at a composition of approximately Nb-26Hf-14Si, and a temperature of ~ 1840 °C. No ternary eutectic was observed in the compositions that were investigated.

The authors would like to thank D.J. Dalpe for the directional solidification. This research was partially sponsored by AFOSR under contract #F49620-96-C-0022 with Capt. C.H. Ward and Dr. S. Wu as Program Managers. The authors would also like to thank Dr. D.A. Wark of R.P.I. for the EMPA measurements. The authors are also grateful to Drs. M.G. Mendiratta and P.R. Subramanian, UES, and Dr. J-C Zhao, GE-CRD, for very helpful discussions.

Literature

1. *Subramanian, P.R.; Mendiratta, M.G.; Dimiduk, D.M.:* Mater. Res. Soc. Symp. Proc. *322* (1994) 491–502
2. *Jackson, M.R.; Bewlay, B.P.; Rowe, R.G.; Skelly, D.W.; Lipsitt, H.A.:* J. Metals *48* (1996) 38–39
3. *Bewlay, B.P.; Jackson, M.R.; Reeder, W.J.; Lipsitt, H.A.:* Mater. Res. Soc. Symp. Proc. *364* (1994) 943–948
4. *Massalski, T.B.:* Binary Alloy Phase Diagrams, ASM, Metals Park, OH (1991)
5. *Gokhale, A.B.; Abbaschian, G.J.:* Bull Alloy Phase Diagrams *10* (1989) 390–393
6. *Brukl, C.E::* Tech. Rep. AFML-TR, 65-2, Air Force Materials Lab., WPAFB, OH (1968) 72
7. *Karpinsky, O.G.; Evseyev, B.A.:* Russ. Metall. *3* (1969) 128–130
8. *Kieffer, R.; Benesovsky, F.:* Powder Metall. 1/2 (1958) 145–171
9. *Bewlay, B.P.; Bishop, R.R.; Sutliff, J.A.:* J. Phase Equilib. *20* (1998) 109–112
10. *Rhines, F.N.:* Phase Diagrams in Metallurgy – Their Development and Application, McGraw-Hill, London (1956)

(Received November 2nd, 1998)

Correspondence Addresses
B.P. Bewlay, M.R. Jackson
General Electric Company
Corporate Research and Development
Schenectady, NY 12301, USA

R.R. Bishop
Department of Materials Science and Engineering
Northwestern University
Evanston, 60208, USA

Processing of High-Temperature Refractory Metal Silicide In-Situ Composites

B.P. Bewlay, M.R. Jackson, and P.R. Subramanian

Journal of Metals, April 1999

Processing High-Temperature Refractory-Metal Silicide In-Situ Composites

B.P. Bewlay, M.R. Jackson, and P.R. Subramanian

High-temperature, refractory-metal, intermetallic, in-situ composites consist of high-strength, niobium-based silicides with a niobium-based metallic toughening phase. A variety of processing schemes have been used to generate these in-situ composites, including solidification and vapor phase processes. Secondary processing, such as forging and extrusion, has also been employed. These composites offer an excellent balance of high- and low-temperature mechanical properties with promising environmental resistance at temperatures above 1,100°C.

INTRODUCTION

The elevated-temperature capability and weight of turbine-blade materials have a substantial effect on the efficiency of current gas-turbine engines.[1,2] For further improvements in gas turbine thrust-to-weight ratio, new materials with improved high-temperature properties, such as strength, creep performance, and environmental behavior, are required.

Refractory-metal intermetallic in-situ composites (RMICs) are a class of materials that have the potential to replace nickel-based superalloys in the hottest sections of turbine engines; in this class of composites, niobium-silicide-based composites offer increased temperature capability and reduced density. These composites consist of high-strength, high-stiffness niobium silicides, such as Nb_3Si and Nb_5Si_3, toughened with a niobium solid solution [(Nb)] to generate composites with toughness levels that are sufficient for component applications.[1-7]

Nb-Si in-situ composites have an attractive balance of high- and low-temperature mechanical properties.[1,2,8,9] From model binary Nb-Si alloys, entire families of ternary, quaternary, and higher order alloys have been developed to generate in-situ composites with improved oxidation performance and mechanical behavior.[1,2,7-9] The intrinsic thermodynamic stability of RMICs is an important characteristic of these high-temperature materials.



Figure 1. Typical microstructures reported for composites generated from binary Nb-Si alloys. (a) The longitudinal section of directionally solidified Nb-14Si; the white phase is (Nb) and the light gray phase is Nb_3Si. (b) The longitudinal section of Nb-10Si extruded at 1,480°C and a 10:1 extrusion ratio; the extruded composite was heat treated at 1,500°C for 100 hours. The white phase is (Nb), and the black phase is Nb_5Si_3.

Niobium-based RMICs have much higher potential application temperatures than nickel-based superalloys, because they have higher melting temperatures (>1,700°C). The potential increased temperature capability is ~200°C for both bulk average temperature and maximum surface temperature, as compared to current single-crystal superalloys. These projected application temperatures represent a smaller fraction of the melting temperature for niobium-based RMICs than is the case for current single-crystal superalloys. Initial creep-rupture performance of niobium-based RMICs compares well to second- and third-generation single-crystal superalloys.[9] However, a 200°C improvement appears to be reasonable in terms of the potential processing and alloy development opportunities available to improve their performance.[1,2,4]

The basis for the (Nb):Nb-silicide composites is the niobium-rich side of the Nb-Si phase diagram, where there is a eutectic between Nb_3Si and (Nb)[4,10] and a eutectoid between Nb_5Si_3 and (Nb). The eutectic occurs at 1,880°C and 18.2% silicon, and the eutectoid occurs at 1,660°C.[10] (Nb)-Nb_3Si and (Nb)-Nb_5Si_3 composites have been prepared by arc melting, as well as directional solidification, of binary Nb-Si alloys.[1,5,6,9]

A typical composite from a directionally solidified Nb-14Si alloy is shown in the backscatter electron (BSE) scanning electron microscopy (SEM) image in Figure 1a. The microstructure consists of (Nb) dendrites with an interdendritic Nb_3Si-(Nb) eutectic. A typical composite from an extruded Nb-10Si alloy heat treated at 1,500°C is shown in Figure 1b; this composite consists of primary (Nb) dendrites aligned with the extrusion direction, and there is an

Authors' Note: All compositions are given in atom percent.

interdendritic eutectoid of Nb_5Si_3 and (Nb). In these high-strength in-situ composites, extrinsic toughening is provided by the (Nb); there is no intrinsic ductility of the silicide.

Analogous ternary Nb-Ti-Si alloy composites have also been investigated.[1,2] These composites typically consist of interpenetrating dendrites of (Nb) and Nb_3Si. Similar composite structures have also been directionally solidified and extruded from higher order alloys.[1-3,8,9]

Processing in-situ composites offers substantial challenges, due to the high melting temperatures and reactivity of the complex alloys that are used. It is not possible to use the melting and investment casting technologies that are employed for current nickel-based superalloys. The processing schemes that are required are considerably more complex than those employed for existing turbine and compressor airfoils.

A range of processing approaches have been used to generate RMICs, including arc casting,[1-6] directional solidification,[7,9,11-14] physical vapor deposition (PVD),[15-17] forging,[18] and extrusion.[1,3-6] Powder-metallurgy and foil-laminate processing[19,20] have also been employed. Each of these processes provides a characteristic microstructure and phase chemistry.

Solid-liquid processing of these high-temperature reactive materials is severely limited by the high melting temperatures of the alloys used and the capability of suitable mold materials. As a result, cold-crucible methods have been adopted. The most widely used methods for these RMICs include arc melting plus extrusion and directional solidification. The directional-solidification techniques that have been employed include float zone,[13,14] Bridgman, and Czochralski methods.

VACUUM-ARC MELTING

Conventional consumable and nonconsumable vacuum-arc melting techniques have been used to produce RMICs from binary Nb-Si and higher order alloys containing Hf, Mo, Ta, Ti, Cr, and Al.[1,8] Consumable arc melting has been used to produce ingots with diameters up to 75 mm and up to ~200 mm long. Alloy compositions have been selected to obtain two-phase or three-phase microstructures consisting of (Nb) in equilibrium with one or more refractory silicides. Alloys for phase-stability investigations have also been produced in the form of ~250 g cigar-shaped castings by arc melting the constituent elements in a water-cooled copper hearth using a nonconsumable tungsten electrode.

Mold condition, getter system, initial electrode fabrication, and electrode melting conditions are of great importance in preparing ingots of RMICs that possess limited ductility. Electrode fabrication is a key element of the melting technology required for the preparation of an ingot with minimal surface cracking and shrinkage porosity. Generally, electrodes of the raw material are fabricated by arc-melting the constituent elements in the form of strips, flakes, or pellets into a rod. Several such rods are assembled together to form the consumable electrode for vacuum-arc remelting. The electrode is then melted into a water-cooled copper mold.

Typically, vacuum-arc-melted ingots of these RMICs have been subjected to subsequent consolidation by hot isostatic pressing and/or hot extrusion.[5,6,8] Vacuum-arc melting has the advantage of producing ingots large enough for prototype component manufacture, and it is also compatible with well-established conventional processing techniques. However, it has the disadvantages of poor solidification control, randomly oriented composite structures, and a population of relatively large-scale defects. Large thermal gradients can also be introduced during ingot casting into water-cooled copper crucibles, and the multicomponent niobium alloy ingots can suffer macrocracking.

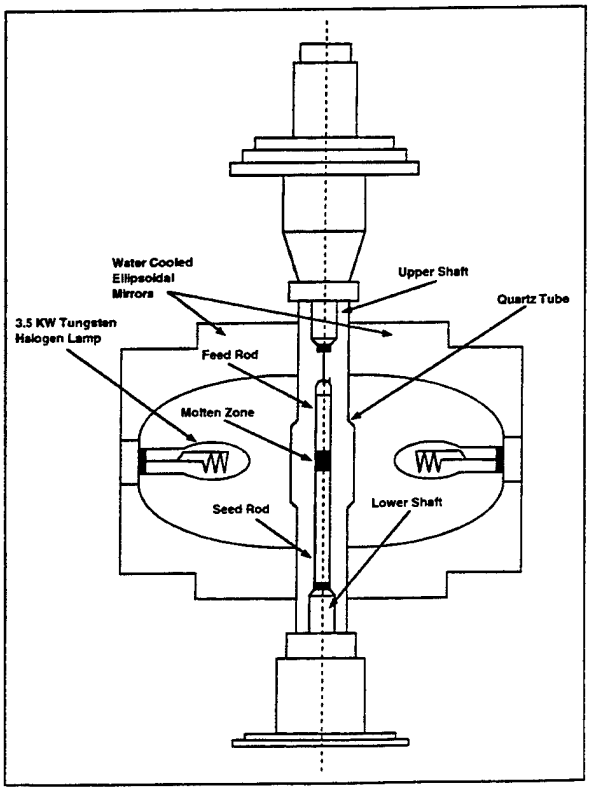
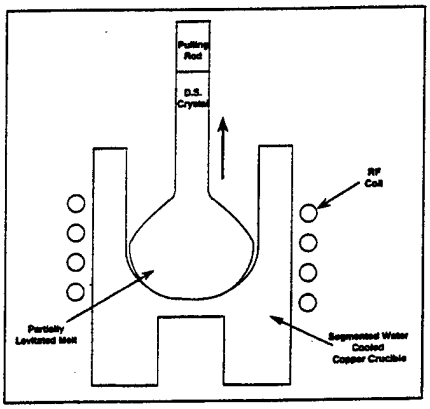
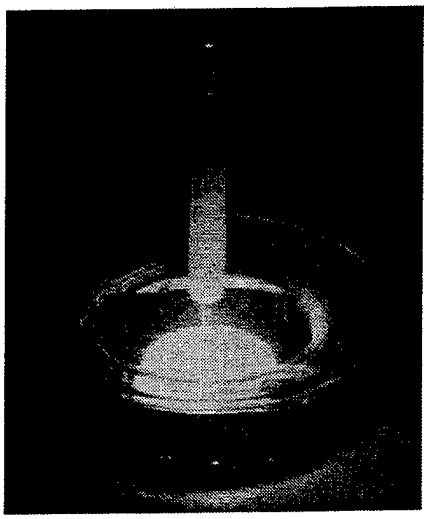


Figure 2. A schematic of OIFZ processing.[13]



a



b

Figure 3. (a) A schematic of cold-crucible Czochralski directional solidification and (b) a photograph of a directionally solidified composite on removal from the cold crucible.

DIRECTIONAL SOLIDIFICATION

Float-Zone Processing

The directional solidification of RMICs has been performed using an optical-imaging float zone (OIFZ) process developed by Pope et al.[13] and Shah et al.[14] This float-zone method is derived from the principle of zone melting, where a small volume of material in a relatively large rod-type charge is melted, and then the molten zone is translated along the rod. The molten zone is retained in position by surface tension between two colinear rods of the same alloy, and as a result, a crucible is not required to retain the melt.

The OIFZ system used by Pope et al.[13] and Kishida et al.[21] consists of two 3.5 kW tungsten halogen lamps enclosed in a double ellipsoidal, water-cooled, copper chamber (Figure 2). Pope et al.[13] reported the directional solidification of a range of RMICs and monolithic intermetallic compounds using the OIFZ technique.

In addition to the optical-imaging heat source, induction heating and electron-

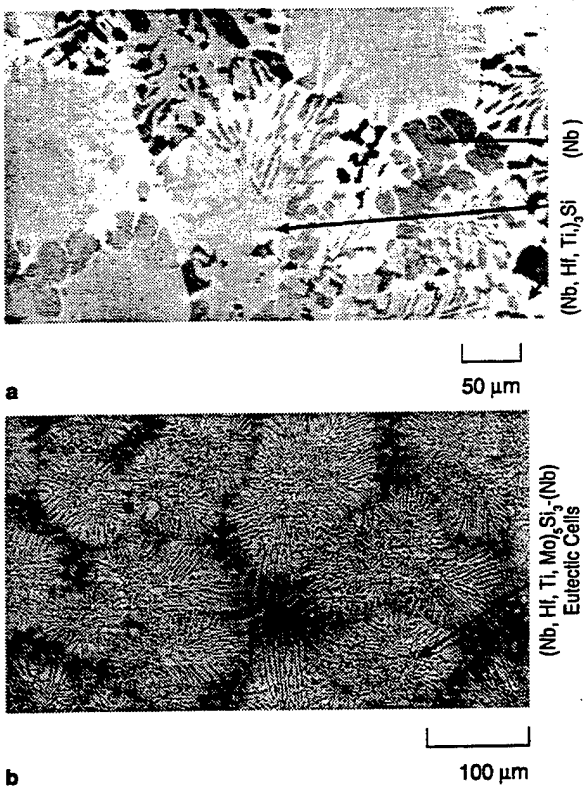


Figure 4. Typical microstructures (BSE images) of transverse sections of directionally solidified composites generated from (a) a quaternary Nb-16Ti-8Hf-16Si alloy at a growth rate of 5 mm/min. The (Nb) is the dark phase and the M_5Si_3 is the light phase. (b) A Nb-9Mo-22Ti-8Hf-16Si alloy at a growth rate of 5 mm/min. The composite consists of eutectic cells of (Nb) and hP16 M_5Si_3.

beam heating sources have been used for the directional solidification of high-temperature composite materials.[22] Electron-beam heating sources are not preferred for RMICs, because this heating method requires a high vacuum, and, hence, it is difficult to use with alloys that contain species with a high vapor pressure. Induction-heating float zone processing requires the sample to be a conductor, but it has the advantage that the electromagnetic-levitation forces may be used to contain the molten zone and, thereby, allow the growth of samples with a larger diameter.[22]

Pope et al.[13] also discussed the advantages and disadvantages of the OIFZ approach. The principal advantages of the OIFZ technique are that it is very clean and capable of working with a range of different materials. There are also several disadvantages. First, the specimen size is limited by a compromise between liquid surface tension and the hot-zone dimension (in this regard, induction heating can also offer additional flexibility). Second, the starting material must possess a high level of homogeneity. Third, evaporation of volatile species, such as chromium, and condensation on the furnace tube can lead to attenuation of the heat input from the optical source and destabilization of the directional-solidification conditions. For small-scale samples, the advantages appear to outweigh the disadvantages. However, the scale-up issues for the float-zone directional solidification of RMICs have not yet been completely defined.

Czochralski Methods

Directionally solidified ingots have been produced by using Czochralski crystal growth from an induction-levitated melt. This process is shown in Figure 3. The alloys are induction-levitation melted in a segmented, water-cooled copper crucible,[7,9,23-26] typically three times, and then a previously prepared seed of the alloy to be directionally solidified is lowered into the melt and withdrawn at a controlled rate. Growth rates in the range 0.5–15 mm/min. have been used. These growth rates are consistent with economical, low-defect, ingot manufacture. A broad range of niobium-based RMICs with melting points up to ~2,300°C[2,7,9,23] has been produced.

The Czochralski method is a flexible method that has been used for high-temperature alloys, such as Nb-Si, Cr-Si, Cr-Nb, Mo-Si, and higher order alloys derived from these binary systems. Samples up to ~15 mm diameter and more than 100 mm long have been directionally solidified by using the Czochralski approach. Typically, high-purity (>99.99%) elements have been used for preparing these composites, because great attention to the interstitial level is required.

For mechanistic studies of mechanical and oxidation behavior, directional solidification provides excellent control of the microstructure and chemistry in samples with low-defect concentration and size. Directional solidification also has great potential as a small solid airfoil manufacturing technique. The ingots can be machined by lathe turning and grinding into airfoil configurations, as is the practice for oxide-dispersion strengthened (ODS) nickel alloys. At present, there is limited experience in providing components with cooling channels using this technique.

The microstructure of a directionally solidified composite generated from a quaternary Nb-16Ti-8Hf-16Si alloy is shown in Figure 4a. The directionally solidified composite contained a Nb_3Si-type phase (tP32) together with (Nb); both phases possess hafnium and titanium in solid solution.

The microstructure of a composite generated from a Nb-9Mo-22Ti-8Hf-16Si alloy is shown in Figure 4b. This composite consisted of eutectic cells of M_5Si_3 with (Nb). The M_5Si_3 possessed the hP16 structure rather than the previously reported Nb_5Si_3 tI32;[10,27] the hP16 structure was stabilized by the high titanium and hafnium additions.

The scale of the microstructure shown in Figure 4b is significantly finer than that in Figure 4a, even though they were

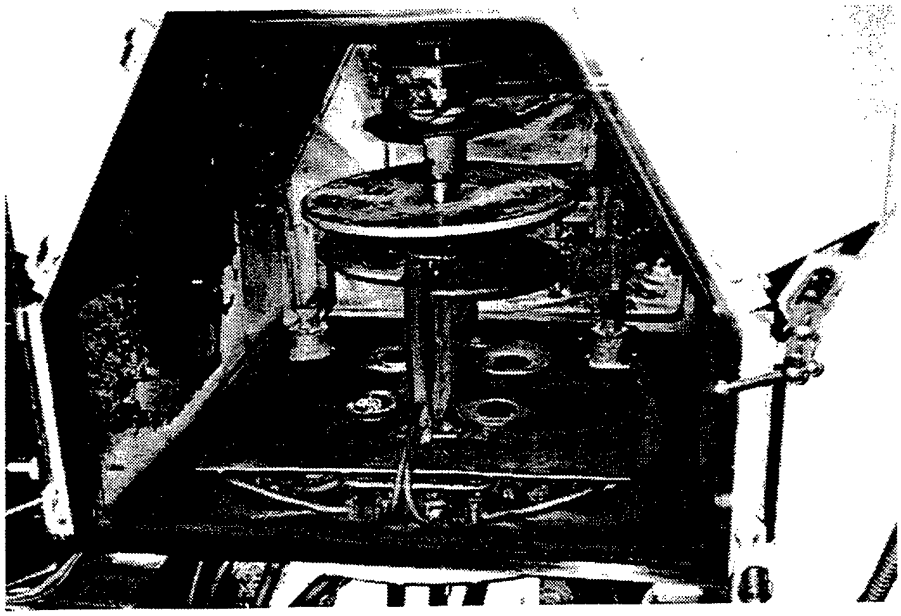


Figure 5. The EB-PVD unit used for the production of Nb-Ti-Hf-Si microlaminates. This system employs an 80 kW EB gun for the (Nb) and three 40 kW sources for the titanium, hafnium, and silicon. Each source has a diameter of 70 mm and a length of 250 mm. The substrate can accommodate disk preforms of up to 0.5 m diameter.

PROCESSING CONSIDERATIONS FOR FUTURE TURBINE ENGINE APPLICATIONS

High-pressure turbine blade temperatures have increased by 125°C in the past 30 years as a result of controlled solidification to form single-crystal nickel-based superalloy components and the use of substantial additions of Re, W, Ta, and Mo. The niobium-based RMICs[1,2,4,7] have much higher potential application temperatures, because of their dramatically increased melting temperatures. The estimated maximum temperature capability is ~200°C higher than that of current single-crystal superalloys. Designs using these RMICs will result in service at much higher bulk and surface temperatures than can be achieved with superalloys.[7]

Further evaluation of the effects of both alloying and processing modifications on the properties of these composites is necessary in order to achieve the required oxidation and creep goals. Process developments are required to enhance RMIC properties and to establish the capability to manufacture complex articles of these composites. Process developments will probably include cold-wall casting schemes and vapor-deposition approaches. Vapor deposition of RMICs offers exciting potential in terms of designing composite microstructures and complex component articles, such as hollow blades and vanes. However, a sufficient combination of chemistry and microstructure control has to be developed to provide the required balance of high- and low-temperature mechanical properties and environmental behavior. Phase-stability information is also a critical requirement for definition of both the manufacture of these high-temperature in-situ composite systems and their stability during service.

Although solid components are attractive for early engine testing of the RMICs, due to the simplicity of machining from stock to final part, applications in hollow parts will extract the greatest advantage of the RMIC high-temperature capability. The cooling techniques presently used for precision-cast nickel-based superalloy single crystals will be required for RMICs in order to achieve their potential 200°C gains. At present, there is little experience in using RMICs in conjunction with advanced airfoil cooling schemes.

Joining methods can be used to produce hollow, cooled components in order to exploit the potential of selecting the optimum processing method for different parts of the turbine component. For example, an EB-PVD airfoil wall could be joined to an extruded turbine-blade spar or root. This hybrid structure can tailor the chemistry and microstructure to optimize properties in the different regions of the component, and it can also take advantage of process economics for thin-wall versus thick-section regions of the component. The economics of the processes and the optimization of properties will decide which is ultimately the optimum method for airfoil manufacture.

Hollow RMIC airfoils will require both internal and external coatings to prevent loss of material by oxidation/corrosion and to avoid embrittlement and subsequent reduction in fracture toughness. Although coating systems have been developed that resist oxidation at temperatures as high as 1,400°C,[2] defects in the coating or foreign object damage of the coating can result in localized coating failure and rapid catastrophic attack of the underlying substrate. The addition of titanium and other elements to niobium-silicide-based RMICs can lead to acceptable rates of oxidation, so that coating failure does not result in a catastrophic attack of the substrate.

Chemical vapor deposition, PVD, thermal spray, plating, and slurry coating are all processes that may find application for forming protective coatings on RMICs. It may be possible to deposit internal coatings before joining sections of the hollow structures. For PVD-processed sections of components, an EB-PVD coating may become integral to the formation of the load-bearing structure.

directionally solidified at the same rate. The texture of all phases within the composites was examined using electron backscattering pattern (EBSP) for electron diffraction in the scanning electron microscope. EBSP data indicate that in Nb-9Mo-22Ti-8Hf-16Si, the [0001] hP16 M_5Si_3 and the [001] of the (Nb) were strongly aligned with the growth direction. In Nb-16Ti-8Hf-16Si, the [001] M_3Si was aligned with the growth direction, but the (Nb) was not strongly textured. Thus, composition has a substantial impact on both the constituent phases, the microstructural scale, and the texture of the phases in the composite.

Bridgman Methods

Bridgman methods using segmented water-cooled copper crucibles instead of ceramic crucibles have been used for the directional solidification of RMICs. This approach has effectively produced ingots with diameters up to 35 mm, although the structure is not as consistently aligned with the axis of withdrawal as in ingots produced using the Czochralski method. In the Bridgman approach, the water-cooled copper crucible is withdrawn in a controlled manner through the electromagnetic field that is used to induction-levitation melt the alloy charge in the crucible.

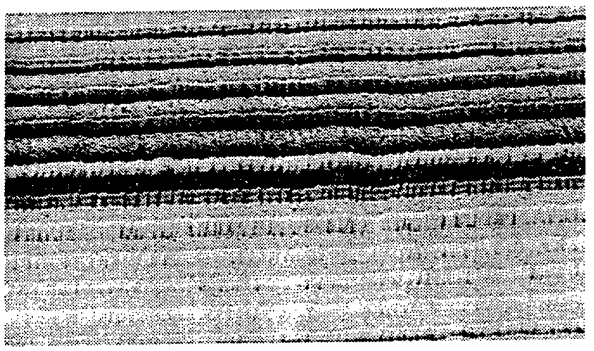
EXTRUSION

RMICs that consist of approximately equiaxed structures of (Nb) and (Nb) silicide have been evaluated in the extruded plus heat-treated conditions.[3-6,8] Extrusions have been produced by machining consumable arc-melted large castings to a diameter of ~70 mm and placing them in molybdenum cans with a wall thickness of ~6 mm. Prior to extrusion, the canned ingots were heated in an induction furnace to a temperature between 1,400°C and 1,600°C and extruded through tool-steel dies maintained at 260°C at extrusion ratios in the range of 3–10. This scheme provides a composite microstructure aligned with the extrusion direction and an acceptable process yield.

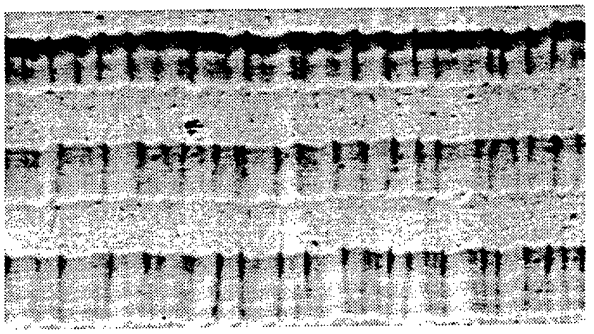
A typical microstructure is shown in Figure 1b, as described earlier. By cotrolling the silicon concentration, the volume fraction of silicide phase has been adjusted over the range of 0.25–0.45. The extrusion of bar stock for eventual machining of turbine vanes and blades is an approach similar to that used for ODS nickel superalloy airfoils, such as Inco alloys MA754 or MA6000.

There has been limited work on forging these composites. Laboratory studies have been performed to examine the constitutive properties of Nb-10Si at temperatures in the range of 1,000–1,650°C and strain rates in the range of 10^{-3}–$10^{-1}s^{-1}$.[18] However, there has been little on work to date on the net-shape forging of components.

There have been several studies of microtexture in niobium-silicide-based composites of binary and higher order alloys in the as-extruded and di-rectionally solidified conditions.[28] The texture of the phases has a significant effect on the mechanical properties of these in-situ composites. The microtexture of Nb-Si binary composites in the as-directionally solidified, directionally solidified + heat-treated, and arc-cast + extruded + heat-treated



a



b

Figure 6. The microstructure at (a) low and (b) high magnification of a 0.75 mm thick laminate produced by EBPVD of alternate 5 μm thick layers of (Nb) with a composition of Nb-35Ti-5Hf and Nb_5Si_3 with a composition of Nb-22Ti-12Hf-37Si. The difference in BSE contrast from the bottom to the top of the micro-laminate reflects a gradation in the hafnium and titanium concentrations. The laminate was produced in about nine hours.

conditions has been determined using EBSP. In the directionally solidified Nb-Si composite, the primary niobium dendrites had little texture, but in the eutectic/eutectoid (Nb), a [113] texture was observed. The [001] of the eutectoid Nb_5Si_3 was perpendicular to the growth direction of the directionally solidified composite. In the extruded Nb-10Si, a [110] Nb fiber texture was observed parallel to the extrusion direction of the single- and double-extruded composites[18], and the [001] Nb_5Si_3 was observed to be perpendicular to the extrusion direction. Thus, when optimizing properties, the role of processing on the texture of the phases must be carefully considered.

VAPOR-PHASE PROCESSING

A range of composite-phase morphologies have been produced using both magnetron and electron-beam (EB) sputter deposition of alternate layers of metal and intermetallic.[15-17] With vapor-phase processing, the laminate thickness and volume fraction of each phase can be controlled by the time of exposure to the source and/or deposition rate. The microstructure can also be graded or produced with specific architectures, again by controlling exposure time to the source. For laminates, the lamellar thickness must be small, because this controls the intrinsic defect size in the laminate and, thus, the fracture strength. Micro-laminate structures produced by PVD may allow greater volume fractions of silicide and, thereby, provide higher strength while retaining toughness.

Sputtering is a very time-intensive deposition process (~0.2 µm/min.), well-suited to the study of a specific composite-phase combination, but an impractical process for economic airfoil manufacture when wall thicknesses are greater than ~0.3 mm. However, EB evaporation is a much more economically attractive route for the production of laminated structures thicker than 0.3 mm, since rates of deposition of about 1–25 µm/min. have been achieved for nickel alloys and RMICs.[2,17] Airfoil wall deposition times of several hours make EB-PVD an economically attractive route for net-shape or near-net-shape outer walls.

Further improvement in the RMIC oxidation resistance is required, and this must be achieved without degrading other properties, such as fracture toughness, creep resistance, and fatigue response. The production of bulk materials with the required balance of properties is a substantial challenge. It is also necessary to achieve stability in thin-walled airfoils, since the turbine blade designs currently envisioned have hot-wall thicknesses of 0.3–1.0 mm. Within that dimension must fit not only the structural composite, but also an internal and an external protective coating.

Recent work at General Electric, Corporate Research and Development and the International Center for Electron Beam Technology, Kiev,[17] has been performed to develop experience with the deposition of niobium-silicide-based composites and the coatings demanded by the service conditions. The EB-PVD unit employed to produce disk-shaped Nb-Ti-Hf-Si microlaminates up to ~1 mm thick and 0.5 m diameter is shown in Figure 5. This system employs an 80 kW EB gun for the (Nb) and three 40 kW sources for the titanium, hafnium, and silicon. Figure 6 shows the microstructure of a quaternary Nb-Ti-Hf-Si microlaminate that consists of alternate 5 µm thick layers of (Nb) with a composition of Nb-35Ti-5Hf and Nb_5Si_3 with a composition of Nb-22Ti-12Hf-37Si. EB-PVD offers the potential to tailor the through-thickness chemistry, microstructure, and properties.

CONCLUSIONS

This article has described a range of processing techniques used for processing RMICs, with particular emphasis on niobium-silicide based in-situ composites. Oxidation and creep performance are the major challenges for the future use of niobium-based RMICs. Although alloying additions to niobium-based RMICs have increased oxidation resistance and creep performance substantially, considerable further improvement is needed. Material loss rates due to oxidation are comparable with the best current superalloys, but the RMICs will be expected to operate equally successfully at surface temperatures up to 1,315°C. In this arena, advanced processing techniques will be required to make key contributions through adjusting phase chemistries of the RMICs to improve both metal strength and intermetallic strength, as well as optimizing RMIC architecture.

ACKNOWLEDGEMENTS

The authors thank D.J. Dalpe, J.A. Sutliff, S. Sitzman, and E.H. Hearn for their contributions to the experimental work. This research was partially sponsored by the U.S. Air Force Office of Scientific Research under contracts F49620-96-C-0022 with Dr. C.H. Ward and Dr. S. Wu as program managers, and by WRDC under contract F33615-92-C-5977 with M.A. Stucke as program manager. The authors are also grateful to Dr. M.G. Mendiratta, Dr. D.M. Dimiduk, Dr. H.A. Lipsitt, Dr. R.J. Grylls, and Prof. C.L. Briant for very helpful discussions. P.R. Subramanian acknowledges financial support from the U.S. Air Force Research Laboratory, Materials and Manufacturing Directorate under contract F33615-96-C-5458. The authors also thank Drs. B.A. Movchan, G.S. Marinski, and O. Gavriljuk of the International Center for Electron Beam Technology, Kiev, and Dr. R. Corderman, of General Electric, Corporate Research and Development, for the EB-PVD of the microlaminates.

References

1. P.R. Subramanian, M.G. Mendiratta, and D.M. Dimiduk, *JOM*, 48 (1) (1996), pp. 33–38.
2. M.R. Jackson et al., *JOM*, 48 (1) (1996), pp. 39–45.
3. P.R. Subramanian, M.G. Mendiratta, and D.M. Dimiduk, *Mat. Res. Soc. Symp. Proc.*, 322 (Pittsburgh, PA: MRS, 1994), pp. 491–502.
4. D.M. Dimiduk, M.G. Mendiratta, and P.R. Subramanian, *Structural Intermetallics*, ed. R. Darolia et al. (Warrendale, PA: TMS, 1993), pp. 619–630.
5. M.G. Mendiratta, J.J. Lewandowski, and D.M. Dimiduk, *Metall. Trans. A*, 22A (1991), pp. 1573–1581.
6. M.G. Mendiratta and D.M. Dimiduk, *Metall. Trans. A*, 24A (1993), pp. 501–504.
7. B.P. Bewlay, J.J. Lewandowski, and M.R. Jackson, *JOM*, 49 (8) (1997), pp. 46–48.
8. P.R. Subramanian et al., *Mater. Sci. Eng.*, A239-240 (1997), pp. 1–13.
9. B.P. Bewlay, M.R. Jackson, and H.A. Lipsitt, *Metall. and Mater. Trans.*, 279 (1996), pp. 3801–3808.
10. T.B. Massalski, *Binary Alloy Phase Diagrams* (Metals Park, OH: ASM, 1991).
11. B.P. Bewlay et al., *Processing and Fabrication of Advanced Materials for High Temperature Applications III*, ed. V.A. Ravi, T.S. Srivatsan, and J.J. Moore (Warrendale, PA: TMS, 1994), pp. 547–565.
12. B.P. Bewlay et al., *Mat. Res. Soc. Symp. Proc. 364* (Pittsburgh, PA: MRS, 1995, pp. 943–948.
13. D.P. Pope et al., in Ref. 3, pp. 461–472.
14. D.M. Shah et al., *Mater. Sci. Eng.*, A192/193 (1995), pp. 658–672.
15. R.G. Rowe et al., in Ref. 3, pp. 461–472.
16. M.R. Jackson, R.G. Rowe, and D.W. Skelly, *Mat. Res. Soc. Symp. Proc. 364* (1995), pp. 1339–1344.
17. B.A. Movchan and G.S. Marinski, *Surface and Coating Technology*, 100–101 (1–3) (1998), pp. 304–310.
18. I. Weiss, M. Thirukkonda, and R. Srinivasan, *Advances in Hot Deformation Textures and Microstructures*, ed. by J.J. Jonas, T.R. Bieler, and K.J. Bowman (Warrendale, PA: TMS, 1994), pp. 559–578.
19. J. Kajuch, J. Short, and J.J. Lewandowski, *Acta Metall. Mater*, 43 (5) (1995), pp. 1955–1967.
20. J. Kajuch, J.D. Rigney, and J.J. Lewandowski, *Mater. Sci and Eng.*, A155 (1992), pp. 59–65.
21. K. Kishida et al., *Mat. Res. Soc. Symp. Proc. 460* (Pittsburgh, PA: MRS, 1997), pp. 53–63.
22. D.R. Johnson et al., *Processing and Fabrication of Advanced Materials for High Temperature Applications II*, ed. V.A. Ravi and T.S. Srivatsan (Warrendale, PA: TMS, 1993), pp. 77–90.
23. B.P. Bewlay, M.R. Jackson, and H.A. Lipsitt, *Processing and Design Issues in High Temperature Materials*, ed. N.S. Stoloff and R.H. Jones (Warrendale, PA: TMS, 1997), pp. 247–262.
24. P.G. Clites and R.A Beall, U.S. Patent 3,775,091 (1973).
25. P.G. Clites, U.S. Patent 4,058,668 (1977).
26. D.A. Hukin, U.S. Patent 3,702,368 (1972).
27. B.P. Bewlay and J.A. Sutliff, *Microscopy and Microanalysis*, vol. 4, supplement 2 (1998), pp. 278–279.
28. J.A. Sutliff and B.P. Bewlay, *Proceedings of the 53rd Annual Meeting of the Microscopy Society of America*, ed. G.W. Bailey et al. (San Francisco, CA: San Francisco Press, 1995). pp. 122–123.

B.P. Bewlay is a metallurgist with General Electric Company, Corporate Research and Development. M.R. Jackson is a metallurgist with General Electric Company, Corporate Research and Development. P.R. Subramanian is a senior scientist with the Materials and Manufacturing Directorate, Wright Patterson Air Force Base and the Materials and Process Division, Universal Energy Systems.

For more information, contact B.P. Bewlay, General Electric Company, Corporate Research and Development, Schenectady, New York 12301; (518) 387-6121; fax (518) 387-5576.

Coming in Next Month's *JOM*:
At the Smelter
- Innovations in Smelter Gas Handling
- Primary Aluminum Production

Hf-Si Phase Diagram Determination and Thermodynamic Modeling

J-C. Zhao, B.P. Bewlay, M.R. Jackson and Q. Chen

accepted for the Journal of Phase Equilibria, June 1999

Hf-Si Binary Phase Diagram Determination and Thermodynamic Modeling

J.-C. Zhao[1], B.P. Bewlay[1], M.R. Jackson[1], and Q. Chen[2]

[1] General Electric Company, Corporate Research and Development, P.O. Box 8, Schenectady, NY 12301, USA

[2] Department of Materials Science and Engineering, Royal Institute of Technology, S-10044, Stockholm, Sweden

Abstract

A new version of the Hf-Si binary phase diagram was constructed based on recent confirmation of the existence of the Hf_5Si_3 phase, and the observation of the following eutectoid reaction: $Hf_5Si_3 \leftrightarrow Hf_2Si + Hf_3Si_2$ at 1925 ± 25 °C. The peritectic reaction, $L + Hf_3Si_2 \leftrightarrow Hf_5Si_3$ at ~ 2360 ± 30 °C was proposed based on Brukl's incipient melting results. Thermodynamic modeling of the binary Hf-Si system was performed via Thermo-Calc™ using existing phase diagram data, the experimental results described in this paper, and the reported enthalpies of formation for Hf silicides. A complete thermodynamic description of the Gibbs energies of all stable phases in the binary system was developed, which was consistent with the majority of the phase diagram and thermochemistry data.

Keywords: phase diagram; Hf-Si system; thermodynamic calculation; CALPHAD, Gibbs energy; enthalpy of formation, silicides, intermetallics, eutectoid reaction.

1. Introduction

Nb silicide-based composites show high promise for application as the next generation turbine airfoil materials with significantly higher operating temperatures than current generation advanced Ni-base superalloys [89Men, 96Jac, 96Sub, 97Bew]. Hf is an important alloying element for strength, toughness and oxidation resistance of these composites [96Jac, 97Bew]. Thus, the phase stability and thermochemistry of the Hf-Si system, especially the stability of the Hf_5Si_3 phase, is of great interest to the development of the Nb silicide-based composites. This work is part of an effort [99Lia] to build a thermodynamic database for predictive modeling of phase equilibria in the complex Nb silicides system.

The Hf-Si phase diagram has been assessed by Gokhale and Abbaschian [89Gok]. It was mostly based on the experimental results of Brukl [68Bru]. Five intermetallic compounds, Hf_2Si, Hf_3Si_2, Hf_5Si_4, HfSi, and $HfSi_2$, have been included in the assessed phase diagram. The crystal structures of these silicides are listed in Table 1. A Hf_5Si_3 phase with the Mn_5Si_3 (hP16, $P6_3/mmc$) crystal structure was identified by [58Now, 69Kar]. Several investigators included this phase in their phase diagrams based on their observations [60Now, 60Vic, 71Shu]. The Hf_5Si_3 phase was originally thought to be stabilized by interstitial impurities by [68Bru, 89Gok] and was not included in the assessed phase diagram of Gokhale and Abbaschian [89Gok]. Recently, Bewlay *et al.* [99Bew] found that the Hf_5Si_3 phase existed in a Hf-35at.%Si alloy containing very low interstitial impurities (total O, N, and C concentrations less than 100 weight ppm), thus O, N or C were not required to stabilize this phase. In fact, Brukl found the Hf_5Si_3 phase, although he attributed its existence to interstitial impurities [68Bru]. However, Brukl found that the elimination of the Hf_5Si_3 phase in Hf_2Si containing alloys was not possible even by careful arc melting (to remove interstitial impurities). As an interesting comparison, Brukl also attributed the existence of a Zr_5Si_3 phase in Zr-Si alloys to interstitial impurities [68Bru], however, the phase was included in the assessed Zr-Si phase diagram of Okamoto [90Oka], and also in the thermodynamic modeling of

Gueneau *et al.* [94Gue] based on the evidence of other investigations. The Hf-Si and Zr-Si phase diagrams are similar.

In addition to the direct evidence for the existence of the Hf_5Si_3 phase [99Bew], there were also other indications that Hf_5Si_3 was a stable phase in the Hf-Si binary system. Shurin and Todorov [71Shu] found that the Hf_5Si_3 phase decomposed eutectoidally when annealed at 1500 and 1600 °C while it remained stable at 2000 °C. Brukl [68Bru] also reported that this phase started to decompose at temperatures lower than 1600 °C. All these results are consistent with the fact that Hf_5Si_3 is a stable phase in the Hf-Si binary system.

The upper stability temperature of the Hf_5Si_3 phase was estimated at 2360 ± 30 °C, based on the incipient melting and collapsing data of Brukl [68Bru]. The incipient melting and collapsing data exhibited a small plateau in the phase diagram while there was an invariant reaction, as shown in Fig. 1. It seems that there was a plateau at about 2360 ± 30 °C in the composition region close to Hf_5Si_3, thus this temperature was tentatively accepted for the peritectic reaction, $L + Hf_3Si_2 \leftrightarrow Hf_5Si_3$. The lower stability (eutectoid) temperature has been determined experimentally in the present investigation.

Table 1 Crystal structures of the Hf silicides

Phase	Prototype	Space group	Lattice parameters, nm	Reference
Hf_2Si	Al_2Cu	I4/mcm	a = 0.6553, c = 0.5186	72Hav, 91Vil
Hf_5Si_3	Mn_5Si_3	$P6_3/mcm$	a = 0.7844, c = 0.5492	69Kar, 91Vil
Hf_3Si_2	U_3Si_2	P4/mbm	a = 0.6988, c = 0.3675	69Kar, 91Vil
Hf_5Si_4	Zr_5Si_4	$P4_12_12$	a = 0.7039, c = 1.283	69Kar, 91Vil
HfSi	FeB	Pnma	a = 0.6889, b = 0.3772, c = 0.5223	69Kar, 91Vil
$HfSi_2$	$ZrSi_2$	Cmcm	a = 0.3672, b = 1.457, c = 0.3641	69Kar, 91Vil

Table 2 Invariant reactions of the Hf-Si binary system.

Reaction	Type	Temp. (exp.) °C [68Bru]	Temp. (calc.) °C	Liquid Composition (exp.) (at.% Si) [68Bru]	Liquid Composition (calc.) (at.% Si)
$L \leftrightarrow BCC\ (Hf) + Hf_2Si$	Eutectic	1831 ± 5	1828	11.5 ± 1	11.1
$BCC\ (Hf) + Hf_2Si \leftrightarrow HCP\ (Hf)$	Peritectoid	1743 (for Hf)	1743	---	---
$L + Hf_5Si_3 \leftrightarrow Hf_2Si$	Peritectic	2083 ± 12	2086	---	17.9
$L + Hf_3Si_2 \leftrightarrow Hf_5Si_3$	Peritectic	2360 ± 30*	2357	---	27.7
$Hf_5Si_3 \leftrightarrow Hf_2Si + Hf_3Si_2$	Eutectoid	1925 ± 25**	1924	---	---
$L \leftrightarrow Hf_3Si_2$	Congruent	2480 ± 20	2480	40	40
$Hf_3Si_2 + L \leftrightarrow Hf_5Si_4$	Peritectic	2320 ± 15	2313	---	54.6
$Hf_5Si_4 + L \leftrightarrow HfSi$	Peritectic	2142 ± 15	2133	---	62.8
$HfSi + L \leftrightarrow HfSi_2$	Peritectic	1543 ± 8	1546	---	80.8
$L \leftrightarrow HfSi_2 + Diamond_A4\ (Si)$	Eutectic	1330 ± 8	1325	91 ± 2	90.8

* Estimated in the present study. ** Measured in the present study

Table 3 Enthalpies of formation for the Hf silicides at 25 °C (298 K) of the Hf-Si system in kJ / (mole of atoms)

Phase	Enthalpy of Formation	Reference & Comments
Hf_2Si	-62.7	[80Sam]
	-72.0	[88Boe] - predicted*
	-63.8	This work - modeling
Hf_5Si_3	-70.2 ± 3.3	[71Gol]
	-70.2	[80Sam]
	-79.0	[88Boe] - predicted*
	-68.5	This work - modeling
Hf_3Si_2	-83.0	[88Boe] - predicted*
	-80.0 ± 4.7	[90Top] at 1473 ± 2K
	-76.8	This work - modeling
Hf_5Si_4	-75.0	This work - modeling
HfSi	-71.1 ± 4.6	[71Gol]
	-71.1	[80Sam]
	-91.0	[88Boe] - predicted*
	-70.9±2.0	[98Mes] at 1473±2K
	-73.0	This work - modeling
$HfSi_2$	-55.7 to -69.7	[57Smi] - est. from volume contraction
	-75.2	[80Sam]
	-74.0	[88Boe] - predicted*
	-69.7	This work - modeling

* Predicted using semi-empirical Miedema model [88Boe]

The remainder of the Hf-Si phase diagram used for the present thermodynamic modeling was based on Brukl [68Bru] which agreed with the assessment of Gokhale and Abbaschian [89Gok]. There were very little data on the liquidus. The invariant reactions and their temperatures are listed in Table 2.

The only available thermochemistry data for the Hf-Si binary system were the enthalpies of formation for the Hf silicides [57Smi, 71Gol, 76Bon, 80Sam, 88Boe, 90Top, 98Mes], as shown in Table 3. The data of [71Gol, 76Bon] will be discussed in more detail after the thermodynamic modeling.

The aim of this paper is to measure the eutectoid decomposition temperature of Hf_5Si_3 and to perform thermodynamic modeling of the binary system.

2. Experimental Procedures and Results

A binary Hf-35 at.%Si alloy was prepared from > 99.9% Hf (not including Zr) and 99.999% Si by induction levitation melting in a segmented water-cooled copper crucible. The alloy was triple melted. The interstitial levels of the Hf were: C < 11, O < 52 and N < 22 weight ppm, respectively. Chemical analyses were performed on the starting materials but not on the final cast alloy. However, it has been shown previously that the cold crucible melting system prevents any increase in the interstitial levels from those in the starting elements [97Hen]. There is indigenous Zr in essentially all commercially available Hf. The Zr content in the cast alloy was estimated at ~ 2 at.%. Fortunately, the Zr_5Si_3 phase has very similar stability as Hf_5Si_3 – this can be appreciated by the similarity of the Hf-Si and Zr-Si binary phase diagrams. In this connection, Zr does not significantly affect the results for the Hf-Si alloy.

The as-cast microstructure consisted of primary Hf_5Si_3, peritectic Hf_2Si, and a eutectic of Hf_2Si and a Hf-Si solid solution, (Hf). Detailed characterization of the as-cast structure was described in [99Bew]. According to the phase diagram shown in Fig. 1, the primary phase for the Hf-35at.%Si alloy should be Hf_3Si_2. However, since the cooling rate during solidification was low and the peritectic ($L + Hf_3Si_2 \leftrightarrow Hf_5Si_3$) reaction temperature was

very high (2360 ± 30 °C), it is probable that the primary Hf_3Si_2 phase transformed to Hf_3Si_2 during cooling. Thus, the observed "primary" phase in as-cast samples was Hf_5Si_3.

The as-cast samples were cut into pieces and wrapped in Nb foil (for heat treatment temperatures < 1700 °C) or Ta foils (for heat treatment temperatures > 1700 °C) and heat treated at 1500 °C (100 hrs), 1650 °C (50 hrs), 1700 °C (100 hrs), and 1800 °C (20 hrs), 1900 °C (20 hrs), and 1950 °C (5 hrs), respectively. The annealing time for each temperature was selected to minimize contamination from the furnace atmosphere.

All of the samples were examined by back scatter electron (BSE) imaging using scanning electron microscopy (SEM). Phase identification was also performed using an electron back scatter pattern (EBSP) technique for electron diffraction in SEM. This technique allowed easy selection of microstructural features using BSE imaging for rapid diffraction pattern collection and analysis. A CamScan CS44 SEM (Cam Scan Electron Optics, Ltd., Cambridge, England) was operated using a 40 kV, ~10 nA electron beam, and the sample surface normal was tilted 70 degrees away from the beam axis. A Nordiff (Jarle Hjelen Ltd., Trondheim, Norway) CCD-based EBSP detector was used. Positive phase identification was accomplished by direct comparison of the location and character of the diffraction bands in the experimental pattern with those calculated from simulated patterns generated using the possible structure types and lattice parameters.

The microstructure of the Hf-35 at.% Si annealed at 1950 °C consisted mostly of the Hf_5Si_3 and Hf_2Si, as shown in Fig. 2. In this BSE image, the Hf_5Si_3 phase is slightly darker since it has a slightly lower atomic number density than Hf_2Si. The crystal structures of these phases were identified using EBSP, as shown in Figs. 3 and 4. It is clear that the primary Hf_5Si_3 phase did not decompose at 1950 °C.

At temperatures ≤ 1900 °C, the primary Hf_5Si_3 phase underwent a eutectoid decomposition into Hf_2Si and Hf_3Si_2, as shown in Fig. 5. The two-phase region in Fig. 5 was the eutectoid decomposition product of the primary Hf_5Si_3 phase. The Hf_3Si_2 phase is

slightly darker in the BSE image since it has a lower atomic number density than Hf_2Si. Again the crystal structure of the phases was identified using EBSP. The EBSP pattern of the Hf_3Si_2 phase is shown in Fig. 6.

Based on the above data, it is clear that the eutectoid reaction, $Hf_5Si_3 \leftrightarrow Hf_2Si + Hf_3Si_2$, exists at 1925 ± 25 °C.

3. Thermodynamic Modeling Procedures and Results

Thermo-Calc [85Sun] was employed for optimizing the thermodynamic parameters and also for the calculation of the phase diagram and enthalpies. The pure elemental data for Hf and Si were taken from the SGTE (Scientific Group Thermodata Europe) database [91Din].

The solubility of Si in Hf (both the bcc and hcp phase) was estimated at < 1 at. %; similarly, the solubility of Hf in Si was also very low [68Bru]. Thus, the three solid solution phases, bcc, hcp and diamond_A4, were treated as pure substances. The Gibbs energy of the liquid phase in terms of one mole of atoms was treated as a disordered solution with a subregular solution model:

$$G_m^L = x_{Hf}\,{}^\circ G_{Hf}^L + x_{Si}\,{}^\circ G_{Si}^L + RT(x_{Hf}\,ln\,x_{Hf} + x_{Si}\,ln\,x_{Si}) + x_{Hf}x_{Si}\Sigma^n L^L(x_{Hf} - x_{Si})^n$$

Where x_i and ${}^\circ G_i^L$ are the mole fraction and the liquid phase molar Gibbs energy of element i (i = Hf, Si), R is the gas constant and T is temperature. The last term in the above equation is the excess Gibbs energy with interaction parameters expressed in Redlich-Kister polynomials [48Red]. All the Hf silicides were treated as having stoichiometric compositions and their Gibbs energies were described by:

$$G_{HfpSiq} = x_{Hf}\,{}^\circ G_{Hf}^{hcp} + x_{Si}\,{}^\circ G_{si}^{diamond} + \Delta G_f$$

where $\Delta G_f = a + bT$, is the molar Gibbs energy of formation of the compound, and a and b are constants to be generated by the optimization.

The model parameters were optimized from the experimental phase diagram information, especially the invariant reaction temperatures, as well as the enthalpies of formation data of the silicides (Table 3).

The modeled thermodynamic parameters are listed in Table 4. The calculated phase diagram is shown in Fig. 1. It can be seen from Fig. 1 and Tables 2 and 3 that the calculated phase diagram and enthalpies agree well with the majority of the experimental data. All the invariant temperatures were within the error of the experimental measurements. The enthalpies of formation of Samsonov and Vinitskii [80Sam] agree the best with our assessed values, as shown in Fig. 7 and Table 3. The enthalpies of formation predicted by Boer *et al.* [88Boe] were lower than both the experimentally determined data and our assessed values. The enthalpies of formation data of Golutvin and Maslennikova [71Gol] showed wide scatter, especially in the composition range of

Table 4 Thermodynamic parameters for the phases in the Hf-Si binary system. All values are in SI units and for one mole of atoms. The thermodynamic data for pure Hf and Si were adopted from SGTE and can be found in [91Din].

Liquid:	${}^0L^L = -177631 + 6.42546T$ ${}^1L^L = -1830$
Hf_2Si:	$G_{Hf2Si} = 0.667\ {}^\circ G_{Hf}^{hcp} + 0.333\ {}^\circ G_{Si}^{diamond} - 63785 + 1.5413T$
Hf_5Si_3:	$G_{Hf5Si3} = 0.625\ {}^\circ G_{Hf}^{hcp} + 0.375\ {}^\circ G_{Si}^{diamond} - 68537 + 0.8153T$
Hf_3Si_2:	$G_{Hf3Si2} = 0.600\ {}^\circ G_{Hf}^{hcp} + 0.400\ {}^\circ G_{Si}^{diamond} - 76772 + 2.8296T$
Hf_5Si_4:	$G_{Hf5Si4} = 0.556\ {}^\circ G_{Hf}^{hcp} + 0.444\ {}^\circ G_{Si}^{diamond} - 74987 + 2.0556T$
HfSi:	$G_{HfSi} = 0.500\ {}^\circ G_{Hf}^{hcp} + 0.500\ {}^\circ G_{Si}^{diamond} - 73013 + 1.9597T$
$HfSi_2$:	$G_{HfSi2} = 0.333\ {}^\circ G_{Hf}^{hcp} + 0.667\ {}^\circ G_{Si}^{diamond} - 69725 + 10.480T$

~40 to ~65 at.% Si. This is partly due to the fact that some alloys may have been in non-equilibrium states; for instance, their 42.4 at.% Si alloy contained three phases (Hf_3Si_2 + Hf_5Si_4 + Hf_5Si_3) whereas at equilibrium there should be Hf_3Si_2 + Hf_5Si_4 (two-phase state) according to the phase diagram. Due to the wide scatter, the enthalpy data of [71Gol] were not included in the present modeling. The temperature variation of the enthalpy of a Hf-66.7at%Si alloy with the $HfSi_2$ phase at 298K as a reference state is shown in Fig. 8. The calculated results agree well with the experimental data of Bondarenko [76Bon].

4. Conclusions

A new version of the Hf-Si binary phase diagram was constructed in which the Hf_5Si_3 phase was included as a stable phase in the binary system. A complete thermodynamic description of the Gibbs energies of all stable phases in the system was developed. This was consistent with the majority of the phase diagram and thermochemistry data. The calculated invariant reaction temperatures were within 9 °C of the experimental data of Brukl [68Bru]. The global optimization of both phase diagram and thermochemistry data have been used to check the reliability of the experimental results. The enthalpy of formation data of [76Bon, 80Sam, 90Top, 98Mes] agree well with one another and they also agree well with the optimized results. The current assessment takes into account the existence of the Hf_5Si_3 phase and the eutectoid reaction, $Hf_5Si_3 \leftrightarrow Hf_2Si + Hf_3Si_2$, at 1925 ± 25 °C.

Acknowledgments

The authors would like to thank D.J. Dalpe for melting the alloy, S.D. Sitzman and J.A. Sutliff for the EBSP. This research was partially sponsored by AFOSR under contract #F49620-96-C-0022 with Dr. Spencer Wu as Program Manager.

References

48Red O. Redlich and A. Kister, Ind. Eng. Chem., 40, 345-348 (1948).

57Smi J.F. Smith and D.M. Bailey, Acta Crystallogr., 10, 341-342 (1957).

58Now H. Nowotny, E. Laube, R. Kieffer, and F. Benesovsky, Monatsh. Chem., 89, 701-707 (1958).

60Now H. Nowotny, H. Braun, and F. Benesovsky, Radex Rundsch, 6, 367-372 (1960).

60Vic R.C. Vickery and H.M. Muir "Refractory Gd and Hf Compounds", Tech. Rep. Research Chemicals, No. RC-145, AD258218, Dept. of the Navy, Bureau of Ships, Washington, DC, 88 p. (1960).

68Bru C.E. Brukl, "Ternary Phase Equilibria in Transition Metal-B-C-Si Systems. Part I. Binary System, Vol. 13. The Zr-Si and Hf-Si Systems", Tech. Rep. AFML-TR-65-2, Air Force Materials Lab., WPAFB, OH, 72 p. (1968).

69Kar O.G. Karpinsky and B.A. Evseyev, Russ. Metall., 3, 128-130 (1969).

71Gol Yu.M. Golutvin and E.G. Maslennikova, Izv. Akad. Nauk SSSR Metall., 13 (1), 174-180 (1971).

71Shu A.K. Shurin and N. Todorov, Metallofizika, 33, 100-102 (1971).

72Hav E.E. Havinga, H. Damsma, and P. Hokkeling, J. Less-Comm. Metals, 27, 169-186 (1972).

76Bon V.P. Bondarenko, Sov. Powder Metall. Met. Ceram., 15, 938-941(1976).

80Sam G.V. Samsonov and I.M. Vinitskii, Handbook of Refractory Compounds, IFI/Plenum, New York, 1980.

85Sun B. Sundman, B. Jansson, and J.O. Anderson, CALPHAD, 9, 153-190 (1985).

88Boe F.R. de Boer, R. Boom, W.C.M. Mattens, A.R. Miedema and A.K. Niessen, Cohesion in Metals, North-Holland, Amsterdam/New York, 1988.

89Gok A.B. Gokhale and G.J. Abbaschian, Bull. Alloy Phase Diagr., 10, 390-393 (1989).

89Men M.G. Mendiratta and D.M. Dimiduk, Mat. Res. Soc. Symp. Proc., 133, 441- 446 (1989).

90Oka H. Okamoto, Bull. Alloy Phase Diagr., 11, 513-519 (1990).

90Top L. Topor and O.J. Kleppa, J. Less-Common Metals, 167, 91-99 (1990).

91Din A.T. Dinsdale, CALPHAD, 15, 317-425 (1991).

91Vil P. Villars and L.D. Calvert, Pearsons Handbook of Crystallographic Data for Intermetallic Phases, 2nd ed., Vol. 1-4, ASM International, 1991.

94Gue C. Gueneau, C. Servant, I. Ansara, and N. Dupin, CALPHAD, 18, 319-327 (1994).

96Jac M.R. Jackson, B.P. Bewlay, R.G. Rowe, D.W. Skelly, and H.A. Lipsitt, JOM, 48, 39-44 (1996).

96Sub P.R. Subramanian, M.G. Mendiratta and D.M. Dimiduk, JOM, 48, 33-38 (1996).

97Bew B.P. Bewlay, J.J. Lewandowski, and M.R. Jackson, JOM, 49, 44-45 (1997).

97Hen G.A. Henshall, M.J. Strum, B.P. Bewlay, and J.A. Sutliff, Metall. Mater. Trans., 28A, 2555-2564 (1997).

98Mes S.V. Meschel and O.J. Kleppa, J. Alloys Compounds, 280,231-239 (1998).

99Bew B.P. Bewlay, M.R. Jackson, and R.R. Bishop, J. Phase Equilibria, 20, 109-112 (1999).

99Lia H. Liang and Y.A. Chang, Intermetallics, 7, 561-570 (1999).

Figure Captions:

Fig. 1 Comparison of the calculated phase diagram with the experimental data. See Table 1 for invariant reaction temperatures and their comparison with experimental data [68Bru].

Fig. 2 BSE image of a Hf-35 at.%Si alloy heat treated at 1950 °C for 5 hrs. The darker phase is Hf_5Si_3 and lighter phase is Hf_2Si. Note that the Hf_5Si_3 phase was stable at this temperature.

Fig. 3 EBSP of Hf_5Si_3 (a), with the indexed pattern shown in (b).

Fig. 4 EBSP of Hf_2Si (a), with the indexed pattern shown in (b).

Fig. 5 BSE image of a Hf-35 at.%Si alloy heat treated at 1800 °C for 20 hrs. The large gray phase is Hf_2Si which is separated by two-phase regions of Hf_2Si (lighter) and Hf_3Si_2 (darker) phases which are products of the eutectoid decomposition of the primary Hf_5Si_3 phase.

Fig. 6 EBSP of Hf_3Si_2 (a), with the indexed pattern shown in (b).

Fig. 7 Comparison of calculated and experimental enthalpies of formation of the Hf silicides at 25 °C (298 K).

Fig. 8 Comparison of calculated and experimental H(T) - $^{\circ}H_{HfSi_2}^{298}$ for a Hf-66.7 at.%Si alloy.

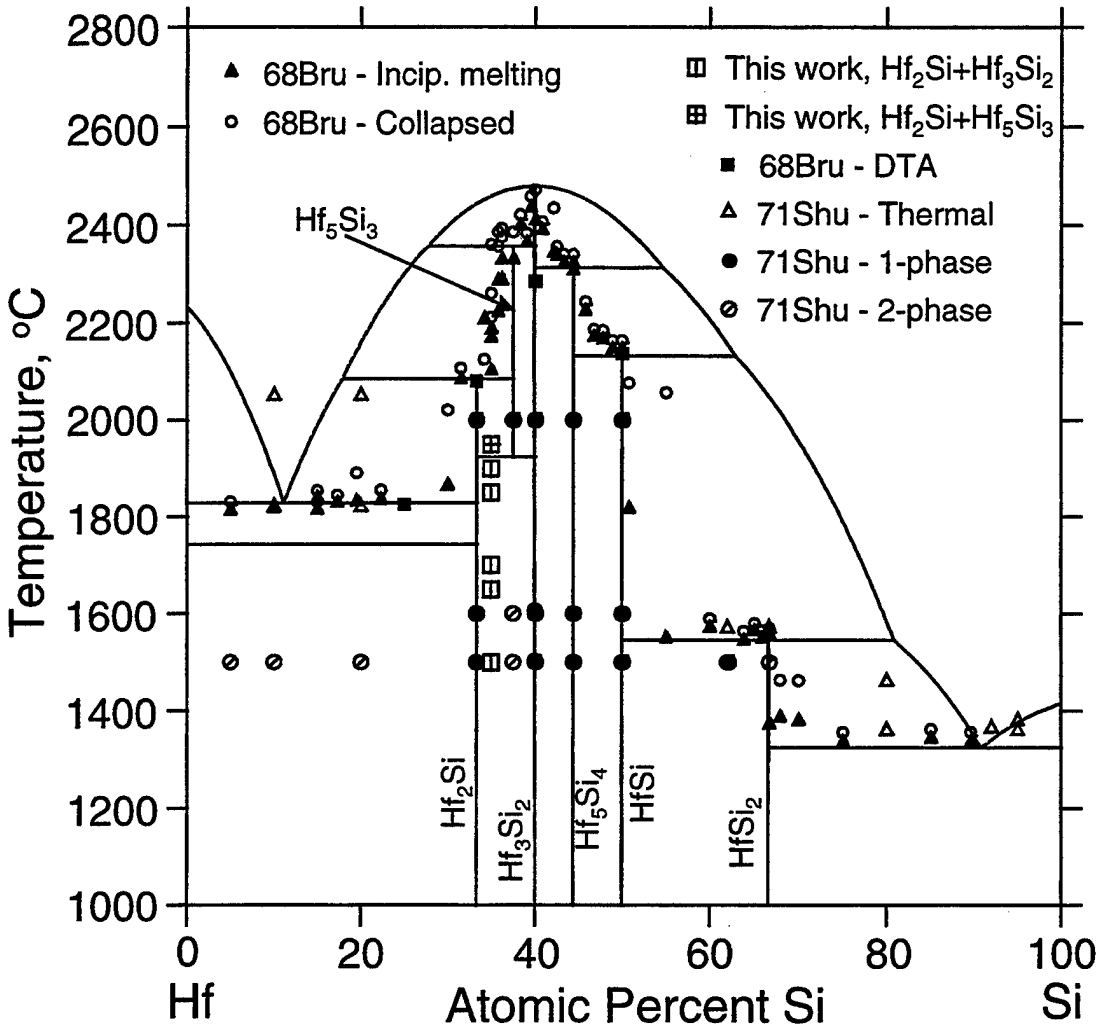


Fig. 1 Comparison of the calculated phase diagram with the experimental data. See Table 1 for invariant reaction temperatures and their comparison with experimental data [68Bru].

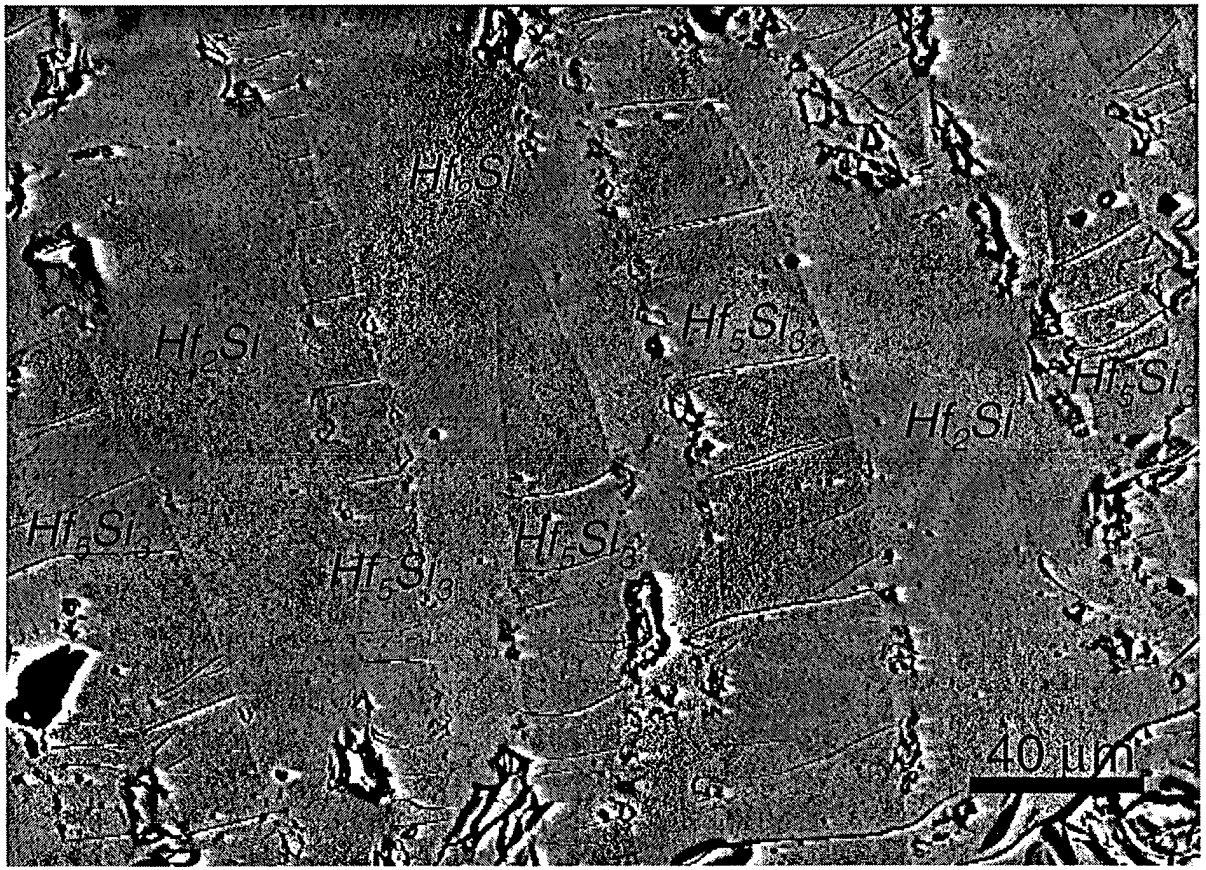


Fig. 2. BSE image of a Hf-35 at.%Si alloy heat treated at 1950 °C for 5 hrs. The darker phase is Hf_5Si_3 and lighter phase is Hf_2Si. Note that the Hf_5Si_3 phase was stable at this temperature.

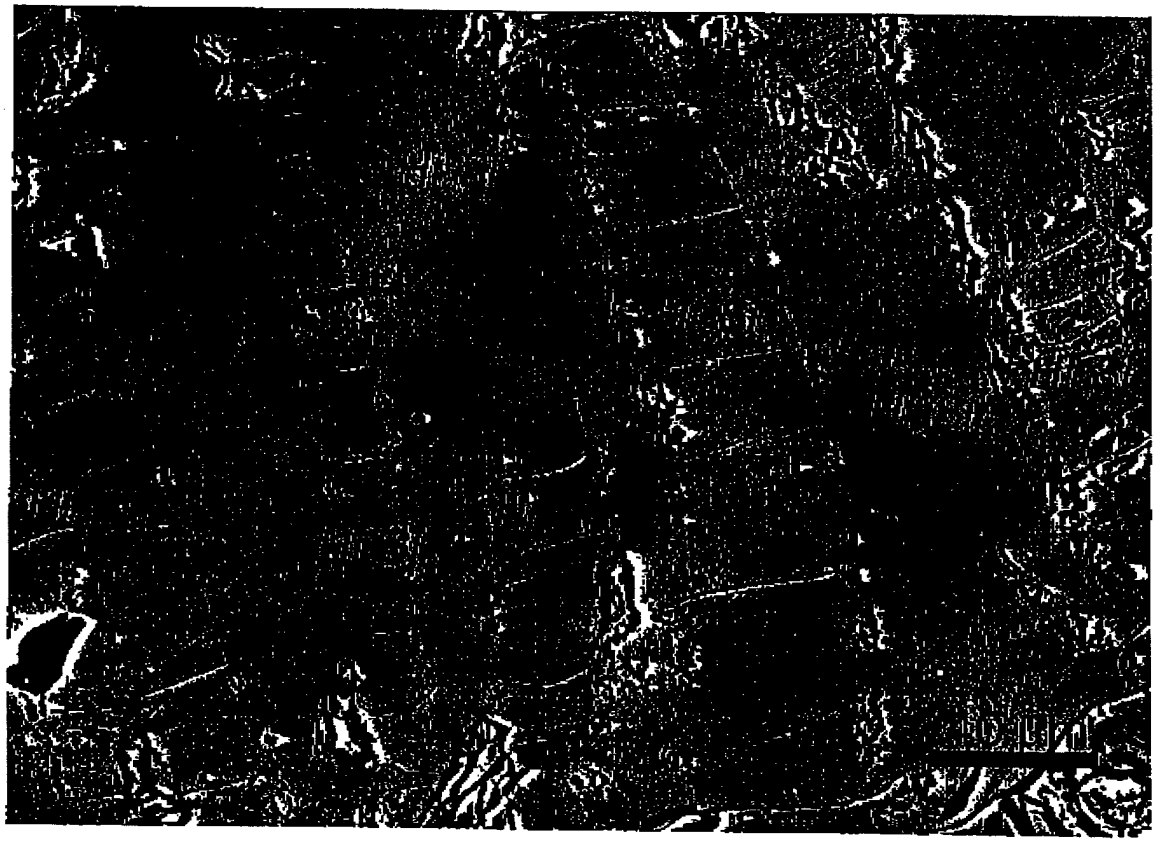


Fig. 3. BSB image of a Hf-35 at.%Si alloy heat treated at 1950 °C for 5 hrs. The darker phase is Hf_5Si_3 and lighter phase is Hf_2Si. Note that the Hf_5Si_3 phase was stable at this temperature.

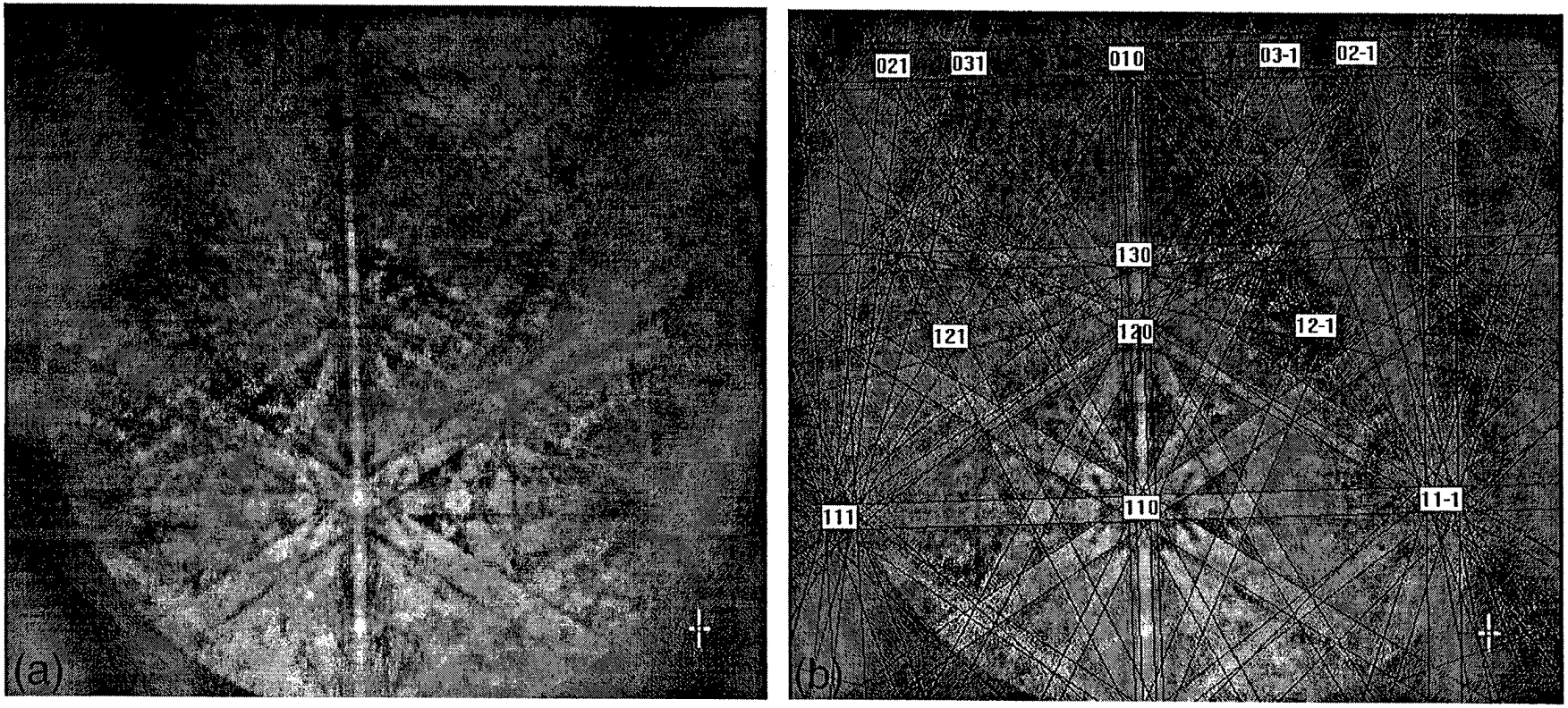


Fig. 4. EBSP of Hf_2Si (a), with the indexed pattern shown in (b).



Fig. 5. BSE image of a Hf-35 at.%Si alloy heat treated at 1800 °C for 20 hrs. The large gray phase is Hf_2Si which is separated by two-phase regions of Hf_2Si (lighter) and Hf_3Si_2 (darker) phases which are products of the eutectoid decomposition of the primary Hf_5Si_3 phase.

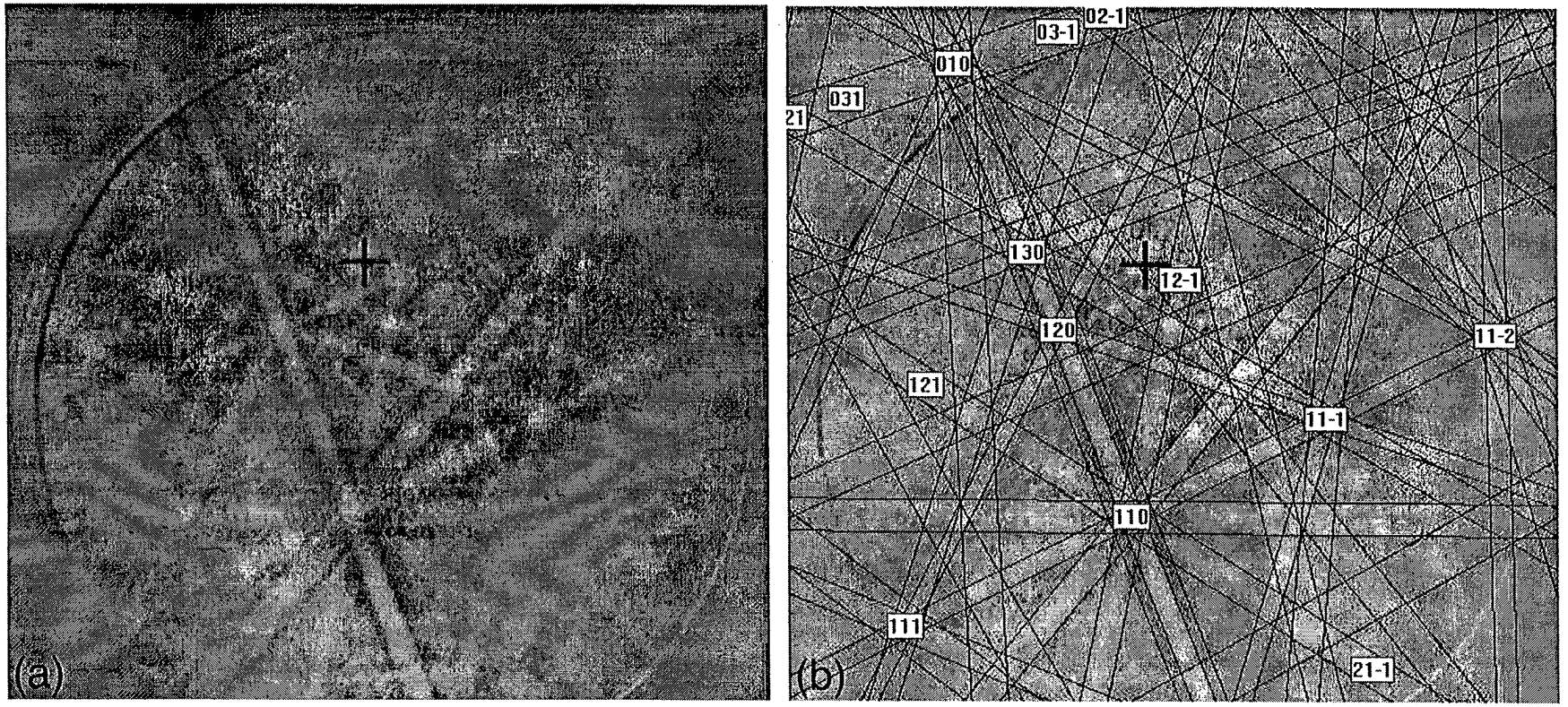


Fig. 6. EBSP of Hf_3Si_2 (a), with the indexed pattern shown in (b).

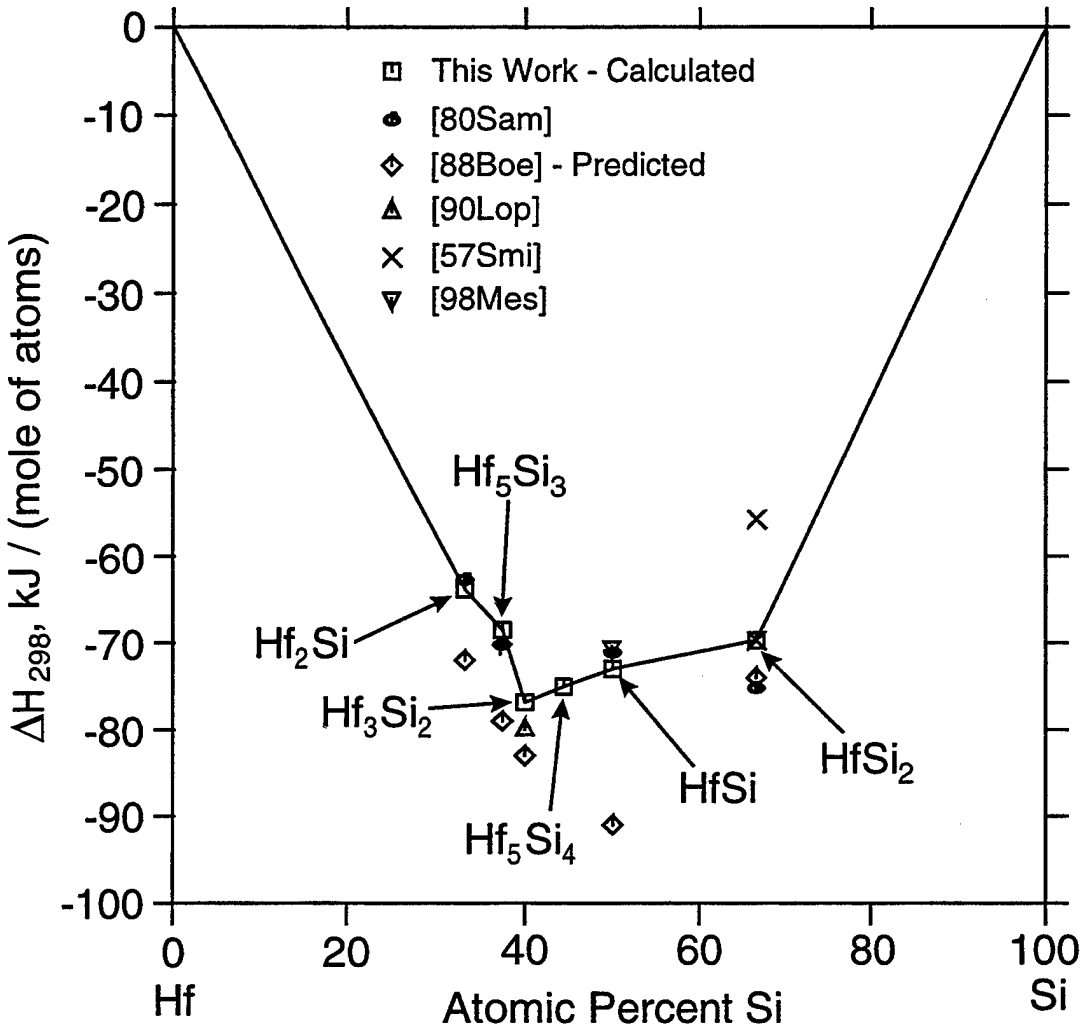


Fig. 7 Comparison of calculated and experimental enthalpies of formation of the Hf silicides at 25 °C (298 K).

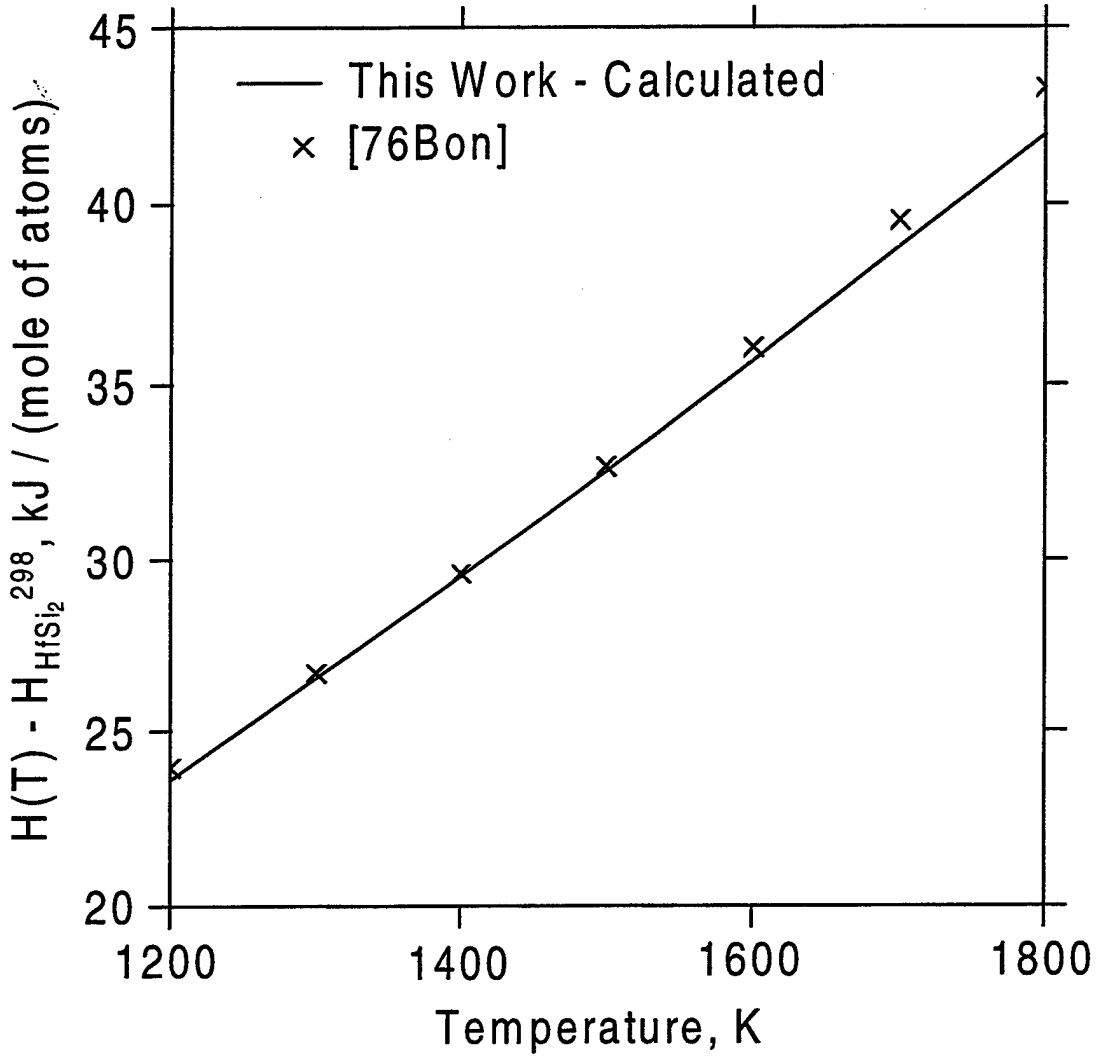


Fig. 8 Comparison of calculated and experimental H(T) - $^{\circ}H_{HfSi_2}^{298}$ for a Hf-66.7 at.%Si alloy.

Creep Mechanisms in Niobium-Silicide Based In-Situ Composites

B.P. Bewlay, P. Whiting, A.W. Davis and C.L. Briant

M.R.S. Proceedings on High Temperature Ordered Intermetallic Alloys VIII, 1999

CREEP MECHANISMS IN NIOBIUM-SILICIDE BASED IN-SITU COMPOSITES

B.P. Bewlay[1], P.W. Whiting[2], A.W. Davis[2] and C.L. Briant[2]

[1]GE Corporate Research and Development, Schenectady, NY 12301, USA.

[2]Division of Engineering, Brown University, Providence, RI 02912, USA.

ABSTRACT

This paper will discuss the relationship between microstructure and creep behavior in high-temperature niobium-silicide based in-situ composites. The creep behavior of composites generated from binary Nb-Si alloys, and higher order alloys containing Mo, Hf and Ti additions, will be described. In-situ composites were tested in compression at temperatures up to 1200°C and stress levels in the range 70 to 280MPa. It was found that the Hf concentration can be increased to 7.5 with little increase in creep rate, over that for the binary Nb_3Si-Nb composite, but at higher concentrations the creep rate is increased at stress levels higher than 210MPa. At stresses less than 210MPa the Ti concentration can be increased to 21 without a detrimental effect on creep performance, but at higher concentrations there is a substantial increase in the creep rate.

INTRODUCTION

Niobium silicide based in-situ composites are potential candidates for use as structural materials at very high temperatures [1-4]. These composites consist of Nb_5Si_3/Nb_3Si toughened with a Nb solid solution (abbreviated by (Nb) in the present paper). Previous investigations of in-situ composites generated from binary Nb-Si alloys have shown a promising combination of high-temperature strength, creep resistance, and room-temperature fracture toughness [1-3]. The present paper focuses on creep behavior, and in particular the effect of Ti, Hf, and Mo additions on the secondary creep rates of Nb_3Si-(Nb) in-situ composites. The composites described in this paper were produced by directional solidification, which gives a microstructure consisting of (Nb) dendrites together with Nb_3Si aligned with the growth direction.

The present approach for investigating creep is separated into two stages: first compression creep tests at temperatures from 1000°C to 1200°C were conducted, and second, in selected composites tensile creep tests were performed. Previous work indicated that creep deformation in Nb_5Si_3 is controlled by bulk diffusion of Nb in the Nb_5Si_3 [5]. Mo and Hf have a relatively large atomic size and it was therefore considered that they may be effective in improving the intrinsic creep performance of both the silicide and the composite. Mo and Hf additions were also considered because they increase the strength of the (Nb). Ti and Hf are added to these composites to improve room temperature fracture toughness and high-temperature oxidation performance [1, 4]. The aim of the present paper is to describe high-temperature creep in directionally solidified (DS) in-situ composites, and the effect of Ti, Hf and Mo additions on the secondary creep rate.

EXPERIMENTAL

The samples were prepared using cold crucible directional solidification [1,3] after triple melting the starting charges from high purity elements (>99.99%). Induction melting in a segmented water-cooled copper crucible was used. The directional solidification procedure has been described in more detail previously [3]. The Nb-16Si composition was used as the base

from which the higher order alloys were derived. All of the samples were examined using scanning electron microscopy and electron beam microprobe analysis (EMPA).

Compression creep tests were performed at a temperatures of 1100 and 1200°C, and at stress levels in the range 70-280 MPa. Compression creep testing was performed in a vacuum of ~$4x10^{-5}$ Torr. The cylindrical specimens were 7.6 mm in diameter and 15.3 mm in length. The samples were first machined by EDM and then centerless ground to final dimensions. In each test the sample was placed between two 18.7 mm diameter silicon nitride platens to prevent breakage of the graphite rams. Pure niobium foil was placed at the interface between the platens and the sample to prevent any contamination of the sample or reaction with the platens. In order to perform a creep experiment, a sample was placed between the platens and the furnace was first heated to the desired temperature. The sample was then loaded to the first stress level of 70MPa and held at that level for 24 hours. The strain was determined from the cross-head position during the experiment and checked against the final strain after the experiment. The creep rate was determined from the slope of the strain-time data. At the end of 24 hours the sample dimensions were determined and the load was increased to the next desired stress level. This process was continued until the test was terminated.

RESULTS AND DISCUSSION

In the present section the Nb-Ti-Hf-Si in-situ composites will be described first and the effect of Mo additions will be described second.

Nb-Ti-Hf-Si In-Situ Composites

The typical microstructure of the DS composites generated from the Nb-Ti-Hf-Si alloys is shown in Figure 1. Secondary creep rates at 1200°C are shown in Table 1 and Figure 2 for composites generated from a range of quaternary Nb-Hf-Ti-Si alloys. Data for the binary Nb-16Si and the ternary Nb-7.5Hf-16Si are also included. Hf concentrations in the range 7.5-12.5 and Ti concentrations in the range 21-33 were examined, providing Ti:Hf ratios in the range 1.7 to 4.4.

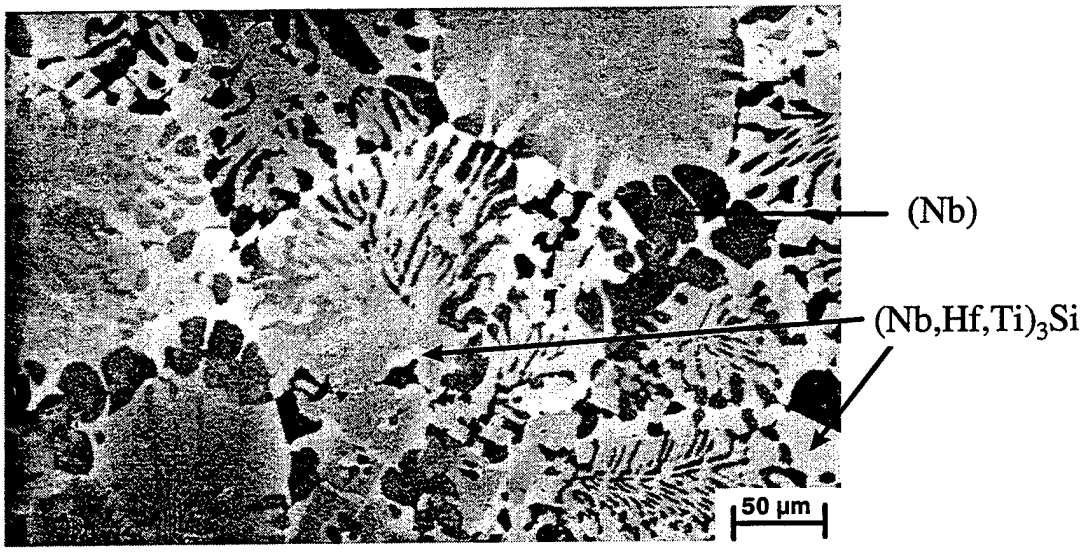


Figure 1. Typical microstructure of the transverse section of DS Nb-8Hf-16Ti-16Si. The microstructure consists of an Nb_3Si type silicide (light grey phase) toughened by (Nb) (dark grey phase).

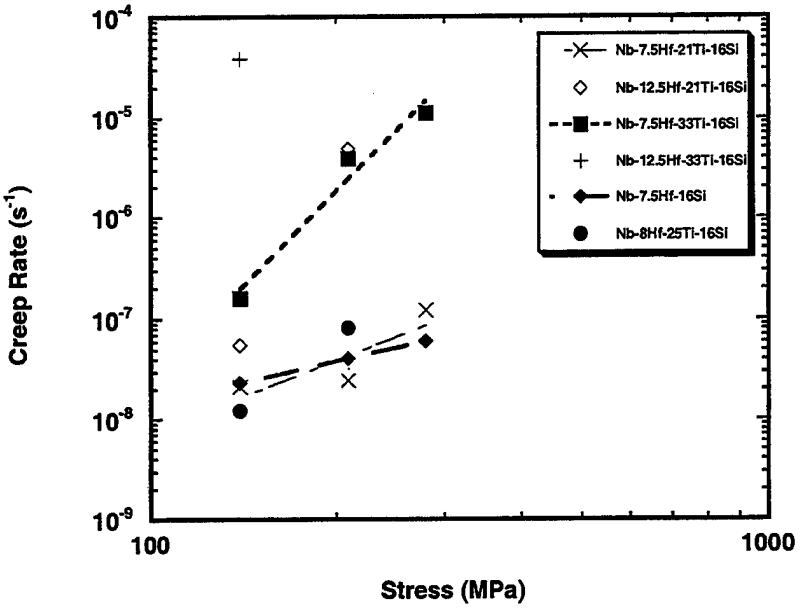


Figure 2. Secondary creep rates at 1200°C for a range of quaternary Nb-Hf-Ti-Si alloys.

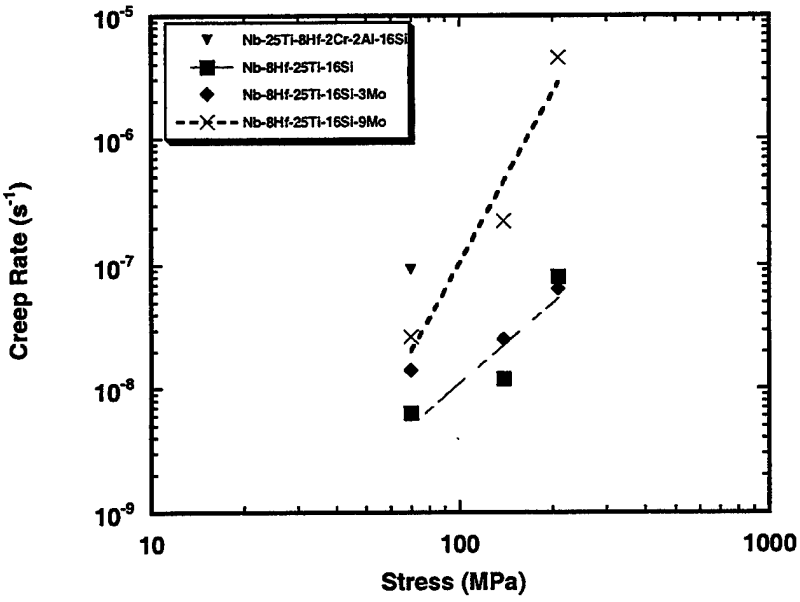


Figure 3 Secondary creep rates at 1200°C for Nb-8Hf-25Ti-16Si alloys modified with 3Mo and 9Mo.

Table 1: Secondary creep rates at 1200°C for a range of Nb-Hf-Ti-Si alloys.

Composition	**Constituent Phases**	**140 MPa Creep Rate (s^{-1})**	**210 MPa Creep Rate (s^{-1})**	**280 MPa Creep Rate (s^{-1})**
Nb-7.5Hf-16Si	(Nb), Nb_3Si	$2.3x10^{-8}$	$4.0x10^{-8}$	$4.8x10^{-8}$
Nb-7.5Hf-21Ti-16Si	(Nb), Nb_3Si	$2.1x10^{-8}$	$3.2x10^{-8}$	$1.2x10^{-7}$
Nb-7.5Hf-33Ti-16Si	(Nb), Nb_3Si, $(Ti,Hf)_5Si_3$	$1.6x10^{-7}$	$3.9x10^{-6}$	$1.1x10^{-5}$
Nb-12.5Hf-21Ti-16Si	(Nb), Nb_3Si, $(Ti,Hf)_5Si_3$	$5.5x10^{-8}$	$4.8x10^{-6}$	Failed
Nb-12.5Hf-33Ti-16Si	(Nb), Nb_3Si, $(Ti,Hf)_5Si_3$	$3.8x10^{-5}$	Failed	--

The creep data indicate that the Nb-7.5Hf-16Si and the Nb-16Si composites possessed the lowest creep rates, and that at any selected stress level and Hf concentration the creep rate increased with increasing Ti concentration. Clearly, Ti and Hf additions can have a significant effect on the creep performance. For example, at 7.5Hf increasing the Ti concentration from 21 to 33% increased the creep rate from $2.1x10^{-8}s^{-1}$ to $1.6x10^{-7}s^{-1}$ at 140MPa. At stress levels of 210MPa and below there is little difference between the secondary creep rates of the Nb-16Si, the Nb-7.5Hf-16Si and the Nb-7.5Hf-21Ti-16Si compositions. At higher stress levels the Ti additions have a detrimental effect on creep performance. Similarly, at Hf concentrations of 12.5 and stress levels of 140MPa, increasing the Ti concentration from 21 to 33% increases the creep rate from $5.5x10^{-8}s^{-1}$ to $3.8x10^{-5}s^{-1}$. At higher stress levels the effect of increasing the Ti concentration led to premature failure; under these conditions the composites could not support steady-state creep, and they proceeded rapidly from the primary to the tertiary creep regime, and failed prematurely.

At any selected stress level, increasing the Hf concentration leads to an increase in the creep rate. For example, at a stress level of 140 MPa and Ti concentration of 21%, increasing the Hf concentration from 7.5 to 12.5% increases the creep rate from $2.1x10^{-8}s^{-1}$ to $5.5x10^{-8}s^{-1}$, but there is a strong stress sensitivity of this effect, so that at 210MPa the creep rates are $3.2x10^{-8}s^{-1}$ and $4.8x10^{-6}s^{-1}$, i.e. Hf concentrations higher than 7.5% provide a strong sensitivity of the secondary creep rate to stress. However, the creep rates of the Nb-7.5Hf-21Ti-16Si are similar to those of the Nb-7.5Hf-16Si, and the stress sensitivities of the creep rates are also similar.

These creep data suggest that the Ti:Hf ratio should be maintained at a level less than 3 and the Ti concentration should be kept below 21%. The mechanisms that lead to increased creep rates at higher Ti, higher Hf, or higher (Hf+Ti) concentrations are still under investigation. One of the effects that is significant is that at high (Ti+Hf) concentrations the hP16 Ti_5Si_3 type silicide is stabilized in preference to the tI32 Nb_5Si_3 type or tP32 Nb_3Si type silicides [6, 7]. The Nb_5Si_3 has a higher melting temperature than either the Ti_5Si_3 or the Hf_5Si_3, and this probably contributes to the improved creep resistance. Thus at high (Ti+Hf) concentrations the creep performance is modified by changes in the constituent phases rather than the intrinsic performance of the silicide or the (Nb). It appears that the $(Ti,Hf)_5Si_3$ is highly detrimental to

creep performance. For example, at 280MPa failure of the composites was observed to occur by shear band formation in the large-scale $(Ti,Hf)_5Si_3$ dendrites. There is a suggestion that this behavior is controlled by the crystal structure and texture of the hP16 relative to the loading axis because the melting temperature of binary Hf_5Si_3 is close to that of Nb_5Si_3 [7].

Mo-Modified Composites

Secondary creep rates are shown in Table 2 and Figure 3 for Nb-8Hf-25Ti-16Si, as well as alloys containing 3% and 9% Mo (substituting Mo for Nb). The data for the binary Nb-16Si and the ternary Nb-7.5Hf-16Si are also included for stress levels from 70-280MPa.

Table 2: Secondary creep rates at 1200°C for Nb-8Hf-25Ti-16Si modified with Mo.

Composition	**70 MPa Creep Rate (s^{-1})**	**140 MPa Creep Rate (s^{-1})**	**210 MPa Creep Rate (s^{-1})**	**280 MPa Creep Rate (s^{-1})**
Nb-7.5Hf-16Si	--	$2.3x10^{-8}$	$4.0x10^{-8}$	$4.8x10^{-8}$
Nb-8Hf-25Ti-16Si	$6.3x10^{-9}$	$1.2x10^{-8}$	$8.0x10^{-8}$	Failed
Nb-3Mo-8Hf-25Ti -16Si	$1.4x10^{-8}$	$2.5x10^{-8}$	$6.4x10^{-8}$	Failed
Nb-9Mo-8Hf-25Ti -16Si	$2.6x10^{-8}$	$2.2x10^{-7}$	$4.5x10^{-6}$	Failed
Nb-8Hf-25Ti-2Al-2Cr-16Si	$9.1x10^{-8}$	Failed	--	--
Nb-16Si	$1.7x10^{-9}$	$1.5x10^{-8}$	$4.9x10^{-8}$	Failed

The effect of Cr and Al additions (substituting for Nb) has also been examined as shown above. Comparison of the creep rates of the Mo-modified alloys with those of the base Nb-16Si, Nb-7.5Hf-16Si and Nb-8Hf-25Ti-16Si composites indicates that at any given set of test conditions the creep rate increases with increasing Mo concentration from 0 to 3 to 9%. These trends were observed at both 1100°C and 1200°C. It appears therefore that there is no net benefit associated with substitution of Mo for Nb. However, it is not clear why the substitution of Mo for Nb leads to an increase in the creep rate. It appears that substitution of Mo for Nb leads to an increase in the volume fraction of $(Ti,Hf)_5Si_3$ and this has a detrimental effect on creep performance. In the Mo-modified composites the (Nb) and silicide compositions were Nb-17Ti-5Hf-22Mo-2Si and Nb-19Ti-13Hf-3Mo-38Si, repsectively.

The creep exponents for the Nb-7.5Hf-16Si and the Nb-8Hf-25Ti-16Si were ~1 and ~2, respectively. At higher Hf and/or Ti concentrations the exponents were increased substantially. For the Nb-3Mo-8Hf-25Ti-16Si the creep exponent was ~1, but at 9Mo the exponent was ~5. These data suggest that at higher alloying levels the creep rate is controlled less by the behavior of the monolithic silicide for which the creep exponent is ~1 [5].

CONCLUSIONS

The addition of Ti, Hf and Mo have a substantial effect on the secondary creep rates of Nb_3Si-(Nb) in-situ composites. The threshold Hf, Ti and Mo concentrations above which the creep performance degenerates beyond that of the Nb-16Si composite have been defined, together with the maximum stress levels above which secondary creep could not be maintained. The data indicate that the Hf and Mo concentrations should be maintained below 8% and 3%, respectively, for a Ti concentration 25%. The presence of the hP16 silicide in DS in-situ composites has a highly detrimental effect on the secondary creep rate.

ACKNOWLEDGMENTS

The authors would like to thank D.J. Dalpe for the directional solidification, and C. Bull for assistance with creep testing. This research was partially sponsored by AFOSR under contract #F49620-96-C-0022 with Major C.H. Ward and Dr. S. Wu as Program Managers.

REFERENCES

[1] B.P. Bewlay, M.R. Jackson and H.A. Lipsitt, *Metall. and Mater. Trans.*, 1996, Vol 279, pp. 3801-3808.

[2] M.G. Mendiratta, J.J. Lewandowski and D.M. Dimiduk, *Metall. Trans. 22A (*1991), pp. 1573-1581.

[3] M.R. Jackson, B.P. Bewlay, R.G. Rowe, D.W. Skelly, and H.A. Lipsitt, J. of Metals 48 (1), (1996), pp. 38-44.

[4] P.R. Subramanian, M.G. Mendiratta and D.M. Dimiduk, *Mat. Res. Soc. Symp. Proc.*, 322 (1994), pp. 491-502.

[5] P.R. Subramanian, T.A. Parthasarathy and M.G. Mendiratta, Scripta Met. and Mater., Vol. 32(8), pp. 39-54.

[6] B.P. Bewlay, M.R. Jackson and H.A. Lipsitt, *Journal of Phase Equilibria*, Vol 18(3), 1997, pp. 264-278.

[7] B.P. Bewlay, R.R. Bishop and M.R. Jackson, submitted to Zeitschrift für Metallkunde, 1998.

On the Formation of Silicide Precipitates in Nb-Si-Based Composites

R.J. Grylls, B.P. Bewlay, H.L. Fraser and H.A. Lipsitt

M.R.S. Proceedings on High Temperature Ordered Intermetallic Alloys VIII, 1999

ON THE FORMATION OF SILICIDE PRECIPITATES IN NIOBIUM-SILICIDE BASED COMPOSITES

B.P. Bewlay[1], R. J. Grylls[2] and H.L. Fraser[3]
[1]GE Corporate Research and Development, Niskayuna, NY 12309, USA.
[2]GE Aircraft Engines, 1 Neumann Way M85, Cincinnati, OH 45215, USA.
[3]Dept. of Materials Science and Engineering, Ohio State University, Columbus, OH 43210, USA.

ABSTRACT

Composites based on Nb-Si are attractive candidates for use as structural materials at the very high temperatures required for future aircraft engines. The composites described were produced by directional solidification, which gives a microstructure consisting of Nb dendrites with an Nb_3Si-Nb eutectic. The aim of this paper is to provide a detailed characterization of precipitates observed in the Nb dendrites in both binary and higher-order alloys. The precipitates possess the Nb_3Si stoichiometry, but not the stable Nb_3Si structure. The precipitates form a metastable orthorhombic crystal structure which is related to the Nb matrix via a simple orientation relationship.

INTRODUCTION

Previous investigations of Nb-Si in-situ composites have shown a promising combination of high-temperature strength, creep resistance, and room-temperature fracture toughness [1-3]. These composites consist of Nb_5Si_3/Nb_3Si toughened with a Nb solid solution (abbreviated here by (Nb). The (Nb) also contains a dispersion of silicide precipitates [4, 5]. The present paper describes the morphology, crystallography and chemistry of precipitates in Nb solid solutions of directionally solidified (DS) composites of binary Nb-Si and ternary Nb-Ti-Si alloys.

Mendiratta and Dimiduk [5] reported Si-rich precipitates in binary Nb-Si alloys, and they postulated that these precipitates were generated as a result of the decrease in the solubility of Si in (Nb) with decreasing temperature. The Nb-Si phase diagram [6] indicates that Nb has a maximum Si solubility of 3.5% at the eutectic temperature (1880°C) and it decreases to 0.5% at 1770°C. These data can therefore account for the precipitation that has been reported. Phase stability in the Nb-Ti-Si system has also been investigated, and two-phase composites have been reported [7, 8]. The Nb_3Si with Ti in solid solution is referred to as $(Nb,Ti)_3Si$, because Nb_3Si and Ti_3Si are isomorphous. Similarly, the Nb with Ti and Si in solid solution is referred to as (Nb,Ti).

EXPERIMENTAL

Binary Nb-Si and ternary Nb-Ti-Si alloys were prepared by induction levitation melting of elemental Nb, Ti, and Si in a segmented water-cooled copper crucible. The alloys were triple melted and then in-situ composites were generated using directional solidification [9]. Foils for Transmission Electron Microscopy (TEM) were prepared from transverse sections of the DS composites. Samples were examined using a Philips XL-30 Field Emission Gun Scanning Electron Microscope (FEGSEM), a Philips CM200 TEM, and a Philips CM300 FEGTEM.

RESULTS AND DISCUSSION

The Nb-14%Si alloy contained (Nb) dendrites and an inter-dendritic eutectic of (Nb) and Nb_3Si [3]. Nb_3Si was the continuous phase of the eutectic, and electron microdiffraction patterns showed that it possessed the stable tP32 structure (the Nb_5Si_3 and Nb_3Si have tI32 (space group I4/mcm) and tP32 (space group $P4_2/n$) crystal structures, respectively). Each (Nb) dendrite was essentially

a single crystal: no subgrains were observed. Heterogeneous precipitation of large-scale silicide precipitates was observed. A typical group of large-scale silicide precipitates within the (Nb) dendrite of the Nb-14Si composite is shown in Figure 1. EDS indicated that these silicides possessed the Nb_3Si stoichiometry. The principal axis of the large (~500nm long), central precipitate was parallel to the [100] direction of the (Nb). Secondary precipitates have grown off the large central precipitate in directions parallel to the [010] and [001] of the (Nb). Precipitate-free zones ~100nm wide were observed in the (Nb) around the silicide precipitates. In the (Nb) dendrite away from the large-scale silicide precipitates, contrast was observed from fine-scale (~50nm long) acicular silicide precipitates, as indicated in Figure 2.

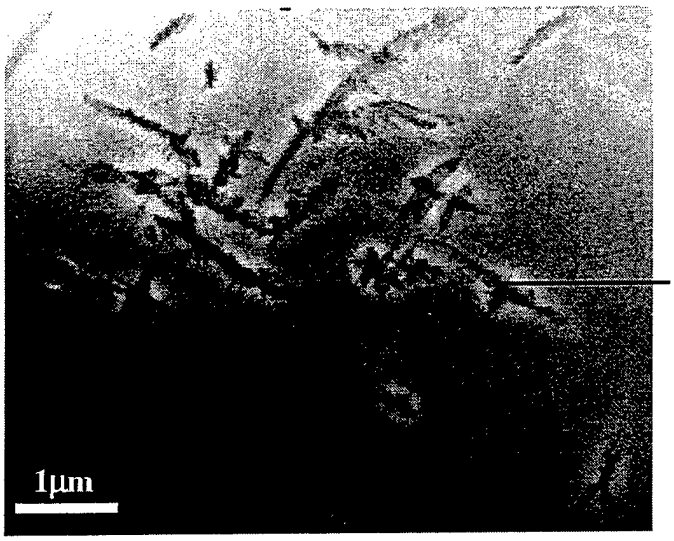


Figure 1. Many-beam bright-field TEM showing the typical precipitate groups in a (Nb) dendrite. Each group consists of many precipitates. Beam direction **B** is close to $<001>_{(Nb)}$.

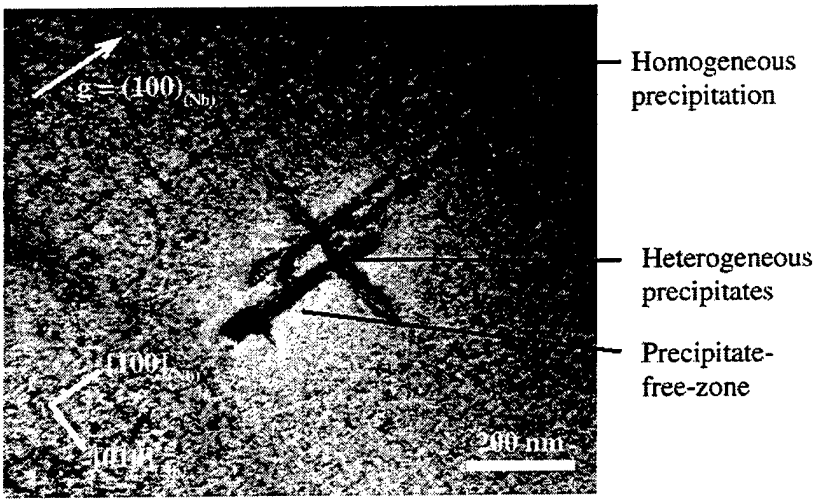


Figure 2. Two-beam bright-field TEM showing a typical group of heterogeneously-nucleated precipitates in a (Nb) dendrite. A precipitate-free zone can be seen. Outside this zone, fine-scale, homogeneously-nucleated precipitates are observed. **B** is close to $[001]_{(Nb)}$.

These precipitates are distributed homogeneously throughout the dendrite, except in the precipitate-free-zones. Precipitate-free-zones, typically 1μm wide, were also found at the boundaries of the (Nb) dendrites. No precipitates were found in the eutectic (Nb). This was expected, since the width of the eutectic (Nb) was less than the width of the precipitate-free-zones.

The silicide precipitate chemistry was determined using EDS. Several precipitate compositions were compared to the composition of the eutectic Nb_3Si using EDS measurements taken from thin regions at the edge of the foil, where any spectral interference from the (Nb) matrix was minimized. The eutectic Nb_3Si was used to determine k-factors assuming it had the exact 3:1 stoichiometry; the compositions of the precipitates were 24-27%Si, balance Nb.

Diffraction data, shown in Figure 3, indicate that these large-scale silicide precipitates possessed an orthorhombic crystal structure. Extensive tilting experiments were performed to determine the point group and lattice parameters. In the CM200 TEM it was possible to tilt 90° from one <100> pole to the next, and thereby determine that the structure was orthorhombic. Approximate precipitate lattice parameters were obtained assuming a lattice parameter for (Nb) of 3.30Å. The precipitate lattice parameters were a = 9.3Å, b = 15.9Å, and c = 3.4Å, which are ~3x, 5x, and 1x of the (Nb) lattice parameter. The point group was determined to be mmm, and it is suggested that the space group is Immm, based on the reflections observed to be absent in Figure 3.

The orientation relationship below was observed between the precipitates and the (Nb):

$$[100]_{Nb} \parallel [100]_{ppt} ; (001)_{Nb} \parallel (001)_{ppt}$$

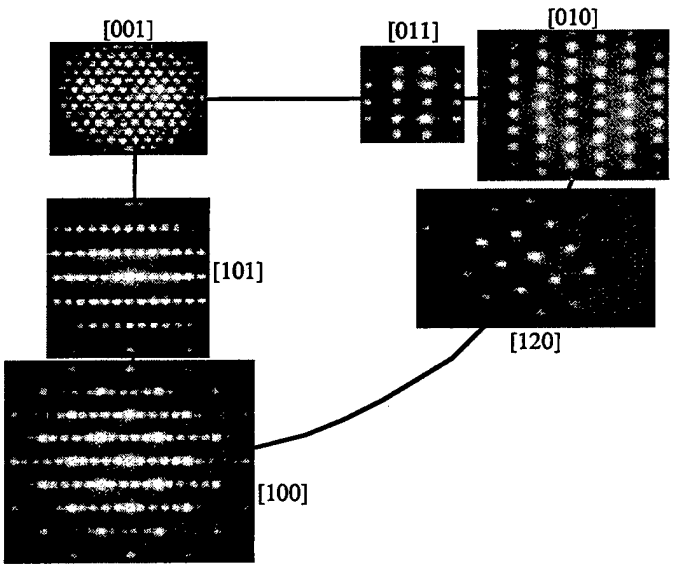


Figure 3. Microdiffraction patterns from large-scale Nb_3Si precipitates within a (Nb) dendrite. All poles and angles between poles are consistent with an orthorhombic structure, point group mmm, a = 9.3Å, b = 15.9Å, c = 3.4Å.

The homogeneously nucleated fine-scale precipitates shown in Figure 2, and shown in detail in Figure 4, were found to have the same structure as the large-scale precipitates. The precipitates were faceted, with facet faces parallel to $\{110\}_{ppt}$, as shown in Figure 4. The precipitates had an acicular morphology, with $[001]_{ppt}$ parallel to the axis of the needle.

The microstructure of the DS Nb-42.5Ti-15Si consisted of (Nb,Ti) dendrites (20-50μm), the lighter phase in Figure 5, together with large-scale (~50 μm) faceted $(Nb,Ti)_3Si$ dendrites.

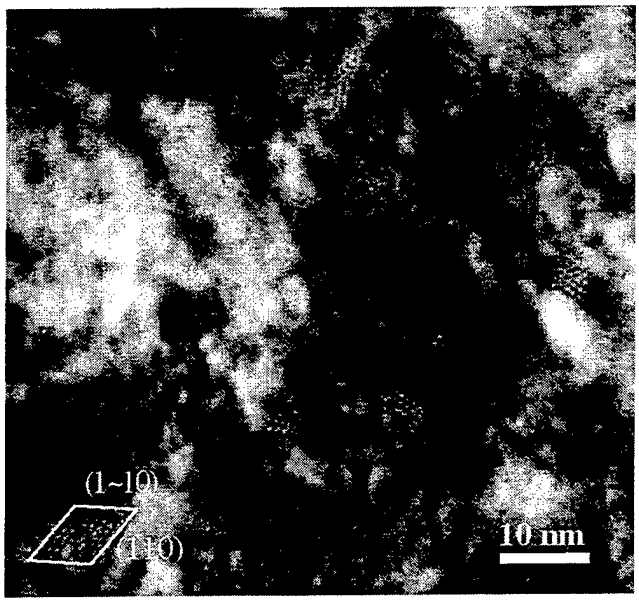


Figure 4. Many-beam bright-field TEM showing orthorhombic precipitates. The precipitates were faceted, with facet faces parallel to $\{110\}_{ppt}$. Only precipitates with [001] parallel to the beam direction are imaged. Precipitates lying in the plane of the foil are invisible. One precipitate has been outlined, and the faceted planes identified. $\underline{\mathbf{B}} = \langle 001 \rangle_{(Nb)}$.



Figure 5. BSE scanning electron micrograph showing a transverse section through the as-DS ternary composite. (Nb,Ti) is the lighter phase, and $(Nb,Ti)_3Si$ the darker phase.

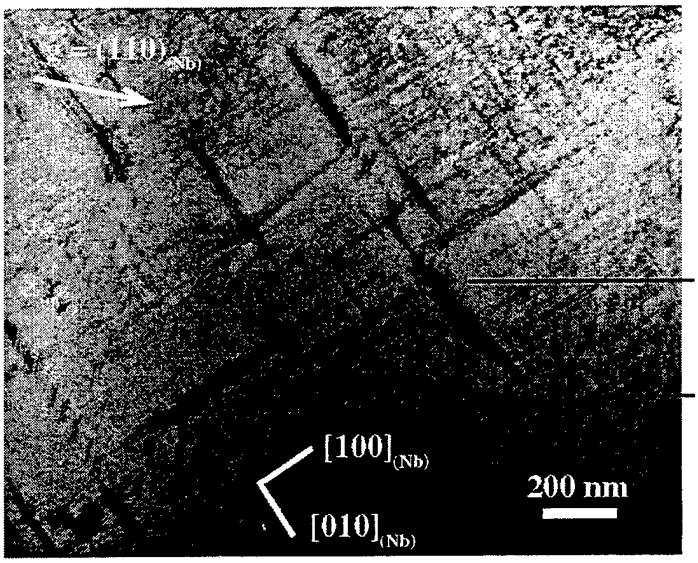


Figure 6. Two-beam bright-field TEM showing typical precipitates within a (Nb,Ti) dendrite. Precipitate-free zones can be seen around the larger precipitates. Outside this zone, fine-scale, homogeneously-nucleated acicular precipitates are observed. **B** is close to $[001]_{(Nb)}$.

A typical array of silicide precipitates within a (Nb,Ti) dendrite is shown in Figure 6. The precipitates are elongated in the $[001]_{ppt}$ direction, and all possible orientation variants with the matrix were observed. Precipitation was generally homogeneous, but there were occasional groups of heterogeneously-nucleated precipitates, as shown in Figure 6.

The silicide precipitates in the (Nb,Ti) have the same orthorhombic crystal structure and orientation relationship with the (Nb,Ti) matrix as found in the binary alloy, and similar lattice parameters. Typically, the homogeneous precipitates had a width of ~10nm (facet-to-facet) in the as-DS condition. Again, EDS identified these silicide precipitates as $(Nb,Ti)_3Si$-type rather than $Nb(Ti)_5Si_3$ type. While the details of these precipitates are reported for the (Nb,Ti) of the Nb-42.5Ti-15Si, similar precipitates have also been observed in Nb-44Ti-12Si, Nb-1Si and other Nb-Ti-Si alloys in the DS condition, as well as after a range of heat treatments.

In the (Nb,Ti) it was expected that the precipitates would be Nb_3Si type because additions of >17% Ti stabilize Nb_3Si in preference to Nb_5Si_3 [7, 8]. However, in the binary alloy Nb_3Si is unstable below 1770°C, and thus not only is the precipitate *composition* metastable with respect to Nb_5Si_3, but the *crystal structure* is also metastable with respect to the stable tP32 structure.

The orthorhombic phase is unexpected. However, considering the mismatch between precipitate and matrix, it can be seen that the interface between matrix and orthorhombic precipitate will only require one extra plane of atoms when the precipitate size reaches ~5nm. Thus the interphase interface would be expected to be coherent up to a certain precipitate size, and semi-coherent for larger sizes. Although the atomic structure of the precipitates has not been determined, diffraction evidence suggests that the orthorhombic precipitate is body-centered, and it may nucleate easily by ordering of the bcc matrix, thereby providing a low barrier to nucleation. No simple lattice match exists between the (Nb) matrix and either tP32 Nb_3Si or tI32 Nb_5Si_3. This suggests that the barrier to nucleation of orthorhombic Nb_3Si may be lower than the barrier to nucleation of either of the stable structures. It is postulated that the orthorhombic structure occurs because of close lattice matching of the precipitate and matrix, and as a result the orthorhombic precipitates are able to form at a lower undercooling than either tP32 Nb_3Si or Nb_5Si_3.

CONCLUSIONS

Precipitates were observed in (Nb) and (Nb,Ti) of the in-situ composites of both binary Nb-Si and ternary Nb-Ti-Si alloys. The precipitates possessed an ordered orthorhombic structure, with lattice parameters a = 9.3Å, b = 15.9Å, c = 3.4Å. The following precipitate-matrix orientation relationship was observed in both the Nb-Si binary and the Nb-Ti-Si ternary alloys :

$$[100]_{Nb} \parallel [100]_{ppt} ; (001)_{Nb} \parallel (001)_{ppt}$$

The precipitates exhibited a bimodal distribution, and it is suggested that the large-scale precipitates nucleate heterogeneously and finer-scale homogeneously. The $(Nb,Ti)_3Si$ precipitates were metastable with respect to the tP32 structure, and they possessed the stable stoichiometry. The Nb_3Si precipitates were metastable with respect to both the stoichiometry and crystal structure of tI32 Nb_5Si_3. Ordering to the metastable orthorhombic Nb_3Si requires a smaller nucleation barrier than to the stable tI32 Nb_5Si_3, and the close matching of the lattice plane spacing of the matrix and precipitate allows the interfacial energy to be minimized.

ACKNOWLEDGMENTS

The authors would like to thank D.J. Dalpe for the DS sample preparation and Suqin Meng for the TEM sample preparation. This research was partially sponsored by AFOSR under contract #F49620-96-C-0022 with Capt. C.H. Ward and Dr. S. Wu as Program Managers.

REFERENCES

[1] Mendiratta and D.M. Dimiduk, *Mat. Res. Soc. Symp. Proc.,* 133 (1989), pp. 441-447.

[2] Dimiduk, M.G. Mendiratta and P.R. Subramanian, in *Structural Intermetallics*, Eds. R. Darolia, J.J. Lewandowski, C.T. Liu, P.L. Martin, D.B. Miracle, and M.V. Nathal, TMS Publications, Warrendale, Pa., (1993), pp. 619-630.

[3] Jackson, B.P. Bewlay, R.G. Rowe, D.W. Skelly, and H.A. Lipsitt, *J. of Metals* 48 (1), (1996), pp. 39-45.

[4] Cockeram, H.A. Lipsitt, R. Srinivasan and I. Weiss, *Scripta Met. and Mater.,* 25 (1991), pp. 2109-2114.

[5] Mendiratta and D.M. Dimiduk, *Scripta Metall. Mater.,* 25 (1991), pp. 237-242.

[6] Massalski, *Binary Alloy Phase Diagrams,* ASM Metals Park, Ohio (1992).

[7] Subramanian, M.G. Mendiratta and D.M. Dimiduk, *Mat. Res. Soc. Symp. Proc.,* 322 (1994), pp. 491-502.

[8] Bewlay, M.R. Jackson, and H.A. Lipsitt, *J. Phase Equilibria*, 18(3) (1997), pp. 264-278.

[9] Bewlay, M.R. Jackson, W.J. Reeder, and H.A. Lipsitt *Mat. Res. Soc. Symp. Proc.,* 364 (1994), pp. 943-948.

Determination of the Effect of Hf Additions on Phase Stability in Nb-Silicide Based In-Situ Composites

B.P. Bewlay, M.R. Jackson and J-C. Zhao

M.R.S. Proceedings on High Temperature Ordered Intermetallic Alloys VIII, 1999

DETERMINATION OF THE EFFECT OF Hf ADDITIONS ON PHASE STABILITY IN Nb-SILICIDE BASED IN-SITU COMPOSITES

B.P. Bewlay, J.-C. Zhao, M.R. Jackson, and R.R. Bishop
General Electric Company, Corporate Research and Development
Schenectady, New York 12301.

ABSTRACT

In-situ composites based on Nb-Si alloys are potential candidates for application as structural materials in future aircraft engines. In order to achieve the balance of properties that is required, additional alloying species, such as Ti, Hf, Mo, Cr, Al, are employed. The present paper describes the effect of Hf additions on phase stability of Nb-Si alloys. Liquid-solid and solid-state phase equilibria have been investigated. The Nb-Hf-Si liquidus surface and the isothermal section at 1500°C will be described. A broad range of Nb and Hf compositions were investigated for Si concentrations up to 35.0%.

INTRODUCTION

Niobium silicide based in-situ composites are potential candidates for application as structural materials in advanced aircraft engines. There have been several studies of composites generated from binary Nb-Si alloys [1-4]. Hf has been used to improve oxidation resistance and strength [1, 2]. However, there is little previous knowledge of Nb-Hf-Si phase equilibria. Many of these Nb-silicide based composites are generated by liquid-solid processing techniques [1, 2]. Thus, knowledge of the Nb-Hf-Si liquidus surface is required for manufacture of these in-situ composites. The 1500°C isothermal section is required to define phase stability in service.

Figure 1(a) represents the Nb-Hf-Si liquidus surface projection, and Figure 1(b) the 1500°C isothermal section. Karpinsky and Evseyev identified five binary Hf silicides: Hf_5Si_3, Hf_3Si_2, Hf_5Si_4, HfSi and $HfSi_2$ [4-7]. In the present paper, only Hf_3Si_2, Hf_5Si_3 and Hf_2Si binary silicides are considered. In total six phases are considered in the present paper [8, 9]: a Nb-Hf-Si solid solution (the bcc is given the prefix β, and the hcp is given the prefix α), Nb_3Si, Nb_5Si_3, Hf_5Si_3 and Hf_2Si. The Nb_5Si_3 with Hf in solid solution is referred to as $Nb(Hf)_5Si_3$, the Hf_5Si_3 with Nb in solid solution, $Hf(Nb)_5Si_3$, the Hf_2Si with Nb in solid solution, $Hf(Nb)_2Si$, and the Nb_3Si with Hf in solid solution, $Nb(Hf)_3Si$. None of these silicides are isomorphous.

The binary Nb-Si phase diagram contains a eutectic, $L \rightarrow Nb_3Si + (Nb)$ at 1880°C and 18.2%Si (all compositions are given in atom percent throughout the present paper), and a peritectic $L + Nb_5Si_3 \rightarrow Nb_3Si$ at 1980°C [4]. The binary Hf-Si phase diagram [4-6] has a eutectic, $L \rightarrow (Hf) + Hf_2Si$ at 1830°C and 11.5%Si, and a peritectic, $L + Hf_5Si_3 \rightarrow Hf_2Si$ at 2080°C. Thus, at the metal-rich end of the Nb-Hf-Si phase diagram there is a eutectic trough between the two binary eutectics, as shown in Figure 1(a), but there is a change in the nature of the eutectic groove with decreasing Nb and increasing Hf concentration.

The loci of the peritectic ridge from the $L + Nb_5Si_3 \rightarrow Nb_3Si$ peritectic, p_2, the $L + Hf_5Si_3 \rightarrow Hf_2Si$ peritectic ridge, p_3, the Hf-Hf_2Si eutectic groove, e_3, and the locations of the three transition reactions, U_1, U_2, U_3, that occur are critical. The peritectic ridge, p_2, intersects the eutectic groove, e_1, to generate U_1. The peritectic ridges, p_1 and p_3, intersect to generate U_2, and the subsequent ridge intersects the eutectic groove, e_1, to generate U_3.

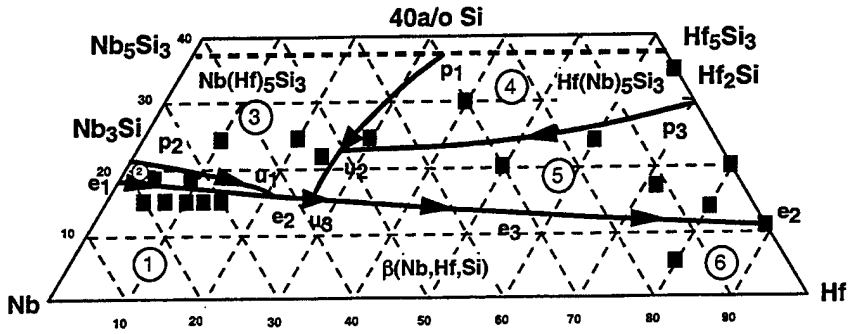


Figure 1(a). Schematic diagram showing the projection of the liquidus surface. The projection shows the peritectic ridges, p_1, p_2, p_3, the eutectic valleys, e_1, e_2, e_3, and the invariant reactions, U_1, U_2, U_3. The actual compositions investigated are also shown (in filled squares).

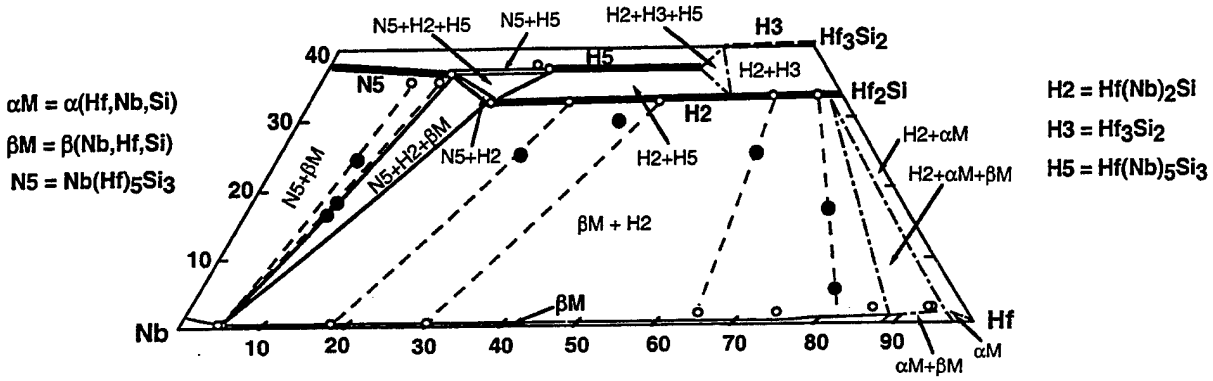


Figure 1(b). Isothermal section of the Nb-Hf-Si phase diagram at 1500°C. Bulk compositions are shown as solid bullets. EMPA measurements of phase compositions are shown as open circles.

U_1 $\quad L + Nb(Hf)_5Si_3 \rightarrow Nb(Hf)_3Si + \beta(Nb,Hf,Si)$

U_2 $\quad L + Hf(Nb)_5Si_3 \rightarrow Nb(Hf)_5Si_3 + Hf(Nb)_2Si$

U_3 $\quad L + Nb(Hf)_5Si_3 \rightarrow \beta(Nb,Hf,Si) + Hf(Nb)_2Si$

The aim of the present paper is to describe liquidus surface and the isothermal section at 1500°C of the metal-rich end of the Nb-Hf-Si phase diagram. The alloy compositions that were investigated are also shown in Figure 1.

EXPERIMENTAL

The samples were prepared using cold crucible directional solidification [2, 3] after triple melting the starting charges from high purity elements (>99.99%). The directional solidification procedure has been described in more detail previously [3]. Table 1 shows the range of compositions that was investigated. Samples for heat treatment were wrapped in niobium foil and heat treated at 1500°C for 100 hours. All of the samples were examined using scanning electron microscopy (back scatter electron (BSE) imaging) and energy dispersive spectrometry (EDS). Electron beam microprobe analysis (EMPA) [10], x-ray diffraction (XRD), and automated electron back scattering pattern analysis (EBSP) [8], were also performed on selected samples.

Table 1. Compositions and constituent phases of the range of alloys that were investigated.

Regime	Composition	Phases in As-DS Condition	Phases After 1500°C H.T.
Regime 1	Nb-15%Hf-16%Si Nb-10%Hf-16%Si	Primary β(Nb,Hf,Si) dendrites with $Nb(Hf)_3Si$-β(Nb,Hf,Si) eutectic	β(Nb,Hf,Si), $Nb(Hf)_5Si_3$, $Hf(Nb)_2Si$, and $Hf(Nb)_5Si_3$
Regime 2	Nb-5%Hf-19%Si Nb-10%Hf-18.5%Si	Primary $Nb(Hf)_3Si$ with $Nb(Hf)_3Si$-β(Nb,Hf,Si) eutectic	β(Nb,Hf,Si) and $Nb(Hf)_5Si_3$
Regime 3	Nb-10%Hf-25%Si	Primary $Nb(Hf)_5Si_3$, peritectic $Nb(Hf)_3Si$, $Nb(Hf)_3Si$-β(Nb,Hf,Si) eutectic	β(Nb,Hf,Si), $Nb(Hf)_5Si_3$, and $Hf(Nb)_5Si_3$
Regime 4	Nb-30%Hf-25%Si	Primary $Hf(Nb)_5Si_3$, peritectic $Hf(Nb)_2Si$, $Hf(Nb)_2Si$-β(Nb,Hf,Si) eutectic	$Hf(Nb)_2Si$ and β(Nb,Hf,Si)
Regime 5	Nb-60%Hf-25%Si Nb-40%Hf-30%Si	Primary $Hf(Nb)_2Si$ with $Hf(Nb)_2Si$-β(Nb,Hf,Si) eutectic	$Hf(Nb)_2Si$ and β(Nb,Hf,Si)
Regime 5	Nb-80%Hf-14%Si Nb-73%Hf-17%Si	Primary $Hf(Nb)_2Si$, $Hf(Nb)_2Si$-β(Nb,Hf,Si) eutectic; $\beta \rightarrow \beta + \alpha$	$Hf(Nb)_2Si$ and β(Nb,Hf,Si) ; $\beta \rightarrow \beta + \alpha$
Regime 6	Nb-80%Hf-5%Si	Primary β(Nb,Hf,Si) with $Hf(Nb)_2Si$-β(Nb,Hf,Si) eutectic	$Hf(Nb)_2Si$ and β(Nb,Hf,Si) ; $\beta \rightarrow \beta + \alpha$

RESULTS AND DISCUSSION

In this section liquid-solid phase equilibria will be described first, and solid-solid phase equilibria second. Table 1 summarizes the phases that were identified.

Liquidus Surface

The liquidus surface projection has been separated into 6 separate regimes. In this section each regime will be described briefly, and more detail will be provided on regimes 1 and 3.

Regime 1: Nb-Rich Compositions

This regime contained primary β(Nb,Hf,Si) dendrites with $Nb(Hf)_3Si$-β(Nb,Hf,Si) eutectic. The microstructure is shown in Figure 2 for Nb-15Hf-16Si. It consisted of a small volume fraction of β(Nb,Hf,Si) dendrites (the darker phase), together with an interdendritic $Nb(Hf)_3Si$-β(Nb,Hf,Si) eutectic. The β(Nb,Hf,Si) dendrites had an average composition of Nb-8.1Hf-1.8Si, and the eutectic β(Nb,Hf,Si) was Nb-7.8Hf-1.9Si. The $Nb(Hf)_3Si$ composition was Nb-11.8Hf-26.5Si.

Regime 2: $Nb(Hf)_3Si$ -Rich Compositions

This regime contained primary $Nb(Hf)_3Si$ dendrites with $Nb(Hf)_3Si$-β(Nb,Hf,Si) eutectic.

Regime 3: $Nb(Hf)_5Si_3$ -Rich Compositions

This regime contained primary $Nb(Hf)_5Si_3$ dendrites, peritectic $Nb(Hf)_3Si$, and $Nb(Hf)_3Si$-β(Nb,Hf,Si) eutectic. The microstructure of the DS Nb-10Hf-25Si alloy is shown in Figure 3. The large black phase was $Nb(Hf)_5Si_3$, but Hf partitioning between the $Nb(Hf)_3Si$ and β(Nb,Hf,Si) was such that there was little contrast between these two phases.

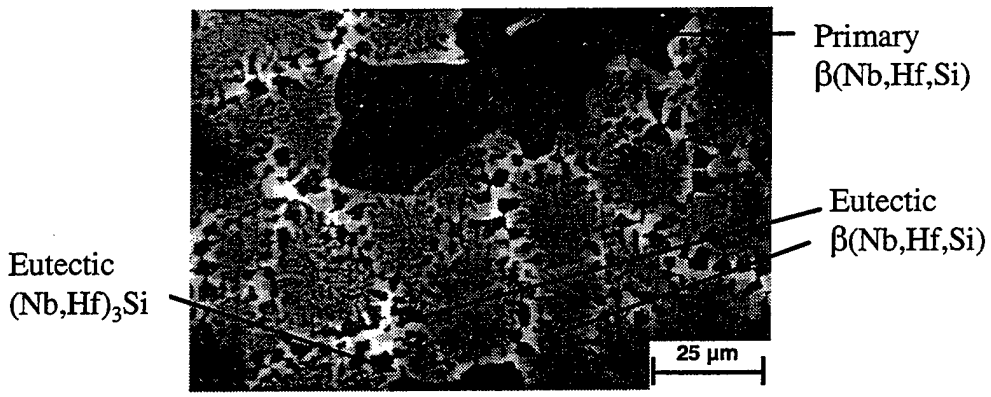


Figure 2. Typical microstructure (BSE image) of the transverse section of a DS Nb-15Hf-16Si alloy. There are large-scale β(Nb,Hf,Si) dendrites with interdendritic eutectic.

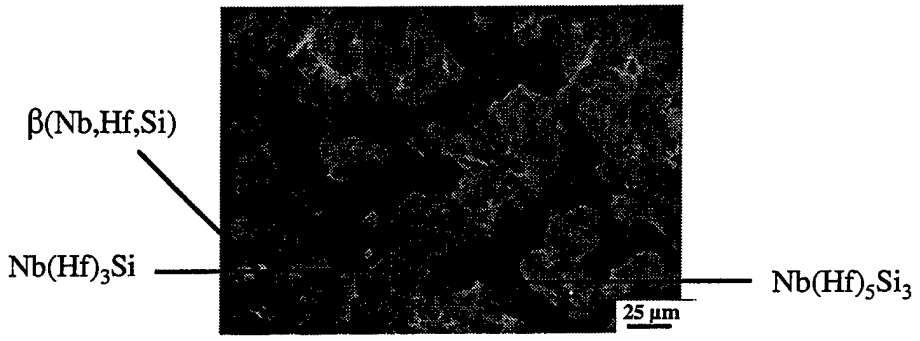


Figure 3. Typical microstructure of the transverse section of DS Nb-10Hf-25Si. The black phase is $Nb(Hf)_5Si_3$, the dark grey phase is $Nb(Hf)_3Si$, and the light grey phase is β(Nb,Hf,Si).

The primary $Nb(Hf)_5Si_3$ had a composition of Nb-10.6Hf-36.5Si, and the peritectic $Nb(Hf)_3Si$ had a composition of Nb-9.3Hf-24.0Si. The composition of the β(Nb,Hf,Si) was Nb-8.2Hf-1.5Si.

Regime 4: $Hf(Nb)_5Si_3$ -Rich Compositions

This regime contained primary $Hf(Nb)_5Si_3$ dendrites, peritectic $Hf(Nb)_2Si$, and β(Nb,Hf,Si)-$Hf(Nb)_2Si$ eutectic.

Regime 5: $Hf(Nb)_2Si$ -Rich Compositions

This regime contained primary $Hf(Nb)_2Si$ dendrites, and the β(Nb,Hf,Si)-$Hf(Nb)_2Si$ eutectic.

Regime 6: Hf-Rich Nb-Hf-Si Compositions

This regime contained primary β(Nb,Hf,Si) dendrites, and β(Nb,Hf,Si)-$Hf(Nb)_2Si$ eutectic. The dendritic and eutectic β(Nb,Hf,Si) experienced β→α allotropic phase transformation on cooling.

Isothermal Section at 1500 °C

The data from the compositions that were heat treated at 1500°C are described in this section. SEM, EMPA, and EBSP results are summarized in the isothermal section and in Table 1.

Nb-10Hf-16Si: A typical BSE micrograph is shown in Figure 4. The bright phase is $Hf(Nb)_5Si_3$, the light gray phase is $Hf(Nb)_2Si$, the darker gray phase is $Nb(Hf)_5Si_3$, and the darkest phase is

β(Nb,Hf,Si). The crystal structures of these phases were confirmed using EBSP. The eutectic $Nb(Hf)_3Si$ phase in the DS alloy (similar to Figure 2) experienced the eutectoid decomposition to β(Nb,Hf,Si) and $Nb(Hf)_5Si_3$. In addition, because of the inhomogeneous nature of the as-DS alloys, there were $Hf(Nb)_2Si$ and $Hf(Nb)_5Si_3$ phases formed in Hf rich regions. Thus, four phases were observed in the 1500°C sample, and this makes it possible to define two three-phase regions: β(Nb,Hf,Si) + $Nb(Hf)_5Si_3$ + $Hf(Nb)_2Si$ and $Nb(Hf)_5Si_3$ + $Hf(Nb)_2Si$ + $Hf(Nb)_5Si_3$.

The solubility of Hf in the $Nb(Hf)_5Si_3$ phase is ~16%. The solubility of Nb in $Hf(Nb)_5Si_3$ and $Hf(Nb)_2Si$ are ~36.4% and ~ 46 %, respectively. After 100 hrs, the alloy had still not reached full equilibrium. The $Hf(Nb)_5Si_3$ phase would have transformed to $Hf(Nb)_2Si$ (and/or $Nb(Hf)_5Si_3$) as more Nb diffused into the region (and Hf and Si diffused out) on prolonged annealing. The equilibrium microstructure is three-phase β(Nb,Hf,Si) + $Nb(Hf)_5Si_3$ + $Hf(Nb)_2Si$. The microstructure of the Nb-10Hf-18.5Si was similar to that of Nb-10Hf-16Si. Again the $Nb(Hf)_3Si$ phase experienced the eutectoid decomposition into β(Nb,Hf,Si) and $Nb(Hf)_5Si_3$.

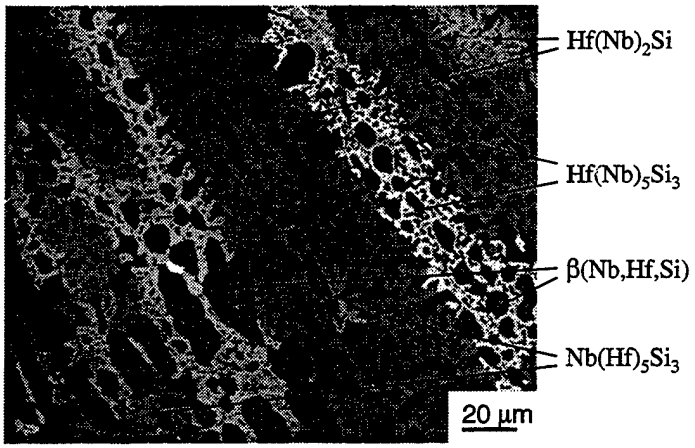


Figure 4. Typical microstructure of the DS Nb-10Hf-16Si alloy after heat treatment.

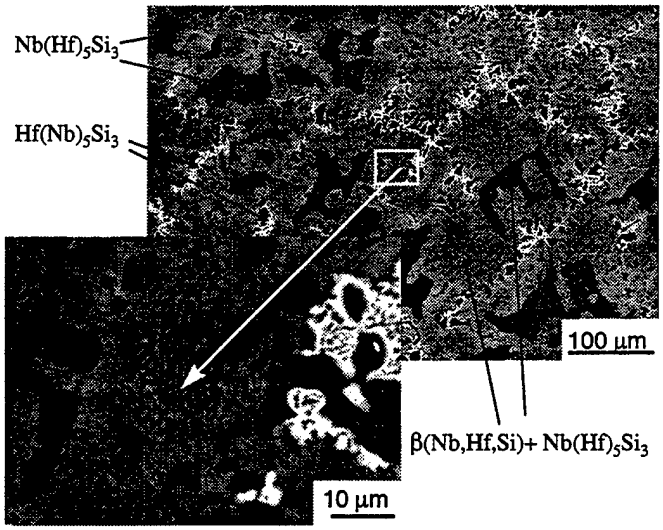


Figure 5. Typical microstructure of the DS Nb-10Hf-25Si alloy after heat treatment.

Nb-10Hf-25Si: The $Nb(Hf)_3Si$ phase in the DS alloy (Figure 3) experienced the eutectoid decomposition to β(Nb,Hf,Si) and $Nb(Hf)_5Si_3$, as shown in Figure 5. The eutectic regions in the DS alloy were richer in Hf and there was some $Hf(Nb)_5Si_3$ formed 1500°C. The alloy had not fully equilibrated after 100 hours. The equilibrium is two-phase β(Nb,Hf,Si) + $Nb(Hf)_5Si_3$.

Nb-30Hf-25Si, Nb-40Hf-30Si, and Nb-60Hf-25Si: The microstructures were predominately two-phase β(Nb,Hf,Si)+$Hf(Nb)_2Si$. The $Hf(Nb)_5Si_3$ in the DS alloy had transformed into $Hf(Nb)_2Si$.

Nb-73Hf-17Si and Nb-80Hf-5Si: The microstructures were predominately two-phase β(Nb,Hf,Si) + $Hf(Nb)_2Si$. The β(Nb,Hf,Si) transformed to β and α on cooling.

CONCLUSIONS

The microstructures generated in the Nb-Hf-Si alloys investigated contained a total of six phases: β(Nb,Hf,Si), α(Nb,Hf,Si), $Nb(Hf)_5Si_3$, $Nb(Hf)_3Si$, $Hf(Nb)_2Si$ and $Hf(Nb)_5Si_3$. The phases observed were dendritic, peritectic, or eutectic in their nature, depending on the composition and solidification path. The liquidus surface of the Nb-Hf-Si ternary phase diagram possesses three transition reactions. The first transition reaction occurs at a composition of approximately Nb-21Hf-16Si, and at a temperature of ~1850°C. The second at approximately Nb-27Hf-22Si and ~2040°C, and the third at approximately Nb-26Hf-14Si and ~1840°C.

The isothermal section of the Nb-Hf-Si system at 1500 °C has been defined. The Nb solubilities in $Hf(Nb)_5Si_3$ and $Hf(Nb)_2Si$ are 36% and 46%, respectively. The Hf solubility in $Nb(Hf)_5Si_3$ is ~16%. Two three-phase regions, β(Nb,Hf,Si) + $Nb(Hf)_5Si_3$+$Hf(Nb)_2Si$ and $Nb(Hf)_5Si_3$ + $Hf(Nb)_2Si$ + $Hf(Nb)_5Si_3$, have been defined. Two additional three-phase regions, β(Nb,Hf,Si) + α(Hf,Nb,Si) + $Hf(Nb)_2Si$ and $Hf(Nb)_2Si$ + $Hf(Nb)_5Si_3$ + $Hf(Nb)_3Si_2$, have been estimated.

ACKNOWLEDGMENTS

The authors would like to thank D.J. Dalpe for the directional solidification, and Dr. J.A. Sutliff for the EBSP. This research was partially sponsored by AFOSR under contract #F49620-96-C-0022 with Major C.H. Ward and Dr. S. Wu as Program Managers.

REFERENCES

[1] P.R. Subramanian, M.G. Mendiratta and D.M. Dimiduk, *Mat. Res. Soc. Symp. Proc.,* 322 (1994), pp. 491-502.

[2] M.R. Jackson, B.P. Bewlay, R.G. Rowe, D.W. Skelly, and H.A. Lipsitt, *J. of Metals,* Vol. 48 (1), pp. 38-39, 1996.

[3] B.P. Bewlay, M.R. Jackson, W.J. Reeder, and H.A. Lipsitt, *MRS Proceedings on High Temperature Ordered Intermetallic Alloys VI,* 364 (1994), pp. 943-948.

[4] T.B. Massalski, *Binary Alloy Phase Diagrams,* ASM Metals Park, Ohio (1991).

[5] A.B. Gokhale and G.J. Abbaschian, *Bull. of Alloy Phase Diagrams*, 10(4), pp. 390-93, 1989.

[6] C.E. Brukl, Tech. Rep. AFML-TR, 65-2, Air Force Materials Lab., WPAFB Ohio, p. 72, 1968.

[7] O.G. Karpinsky and B.A. Evseyev, *Russ. Metall.*, Vol. 3, pp. 128-130, 1969.

[8] R. Kieffer and F. Benesovsky, *Powder Metall.*, Vol. 1 / 2, pp. 145-171, 1958.

[9] B.P. Bewlay, R.R. Bishop and J.A. Sutliff, submitted to *JPE*, January 1998.

[10] B.P. Bewlay, R.R. Bishop, and M.R. Jackson, submitted *to Zeitschrift für Metallkunde*, October 1988.

Creep Deformation Microstructures in Nb-Hf-Ti-Si In-Situ Composites

S.D. Sitzman and B.P. Bewlay

Microscopy and Microanalysis, 1999

CREEP DEFORMATION MICROSTRUCTURES IN DS Nb-Hf-Ti-Si IN-SITU COMPOSITES

S.D. Sitzman and B.P. Bewlay

General Electric Corporate Research and Development, Schenectady, New York 12301

Directionally solidified (DS) in-situ composites based on (Nb) and (Nb) silicides, such as Nb_5Si_3 and Nb_3Si, are presently under investigation as high-temperature structural materials [1, 2]. Alloying additions of elements such as Hf, Ti and Mo to these silicides are also being explored. The present paper describes the microstructure of a DS Nb-silicide based composite before and after creep deformation.

Alloys were prepared from high purity elements (>99.9%) using induction levitation melting in a segmented water-cooled copper crucible. The alloys were directionally solidified using the Czochralski method [2]. Creep tests were conducted at 1200°C to 50% deformation. Characterization was performed using scanning electron microscopy, electron microprobe analysis (EMPA), and electron backscatter diffraction pattern analysis (EBSP).

The microstructure of a DS composite generated from a Nb-12.5Hf-33Ti-16Si alloy is shown in Figure 1, and exhibits three distinct structures: elongated faceted primary grains, a coarse dendritic two-phase structure, and a fine-scale eutectic. EBSP identified the faceted grains as M_3Si-type tI32 (where M denotes Nb, Hf and Ti), the coarse two phase structure as M_3Si and (Nb), and the fine-scale eutectic as M_5Si_3 (hP16 crystal strcuture) and (Nb). Automated EBSP reveals (Nb) grains that incorporate both the coarse two phase and eutectic regimes in single orientations. The M_5Si_3 does not possess a strong texture even within individual eutectic cells, whereas M_3Si grains lie in single orientations in both the coarse two-phase structure and faceted primary grains. Also observed is an M_5Si_3 <0001> and M_3Si <001> epitaxy in neighboring eutectic and coarse two phase cells.

The primary features of interest in the creep deformed DS composite are bent M_3Si grains (Figure 2a). Variations in backscatter electron intensity within the M_3Si indicate complex sub-cell structures. Quantitative characterization of the strain is achieved with EBSP. An orientation image and corresponding <001> pole figure of the deformed M_3Si grain in Figure 2a are shown in Figures 2b and 2c, respectively. Greyscale shades correlate positions and <001> poles; total <001> rotation exceeds 60 degrees within the grain.

References

1. M.R. Jackson, B.P. Bewlay, R.G. Rowe, D.W. Skelly, and H.A. Lipsitt, *JOM* 48 (1996)38-39
2. B.P. Bewlay, M.R. Jackson and H.A. Lipsitt, *Metall. and Mater. Trans.*, 279 (1996)3801-3808

Acknowlegments

This research was partially sponsored by AFOSR under contract #F49620-96-C-0022 with Capt. C.H. Ward and Dr. S. Wu as Program Managers. The authors would also like to thank Prof C.L. Briant for the creep samples.

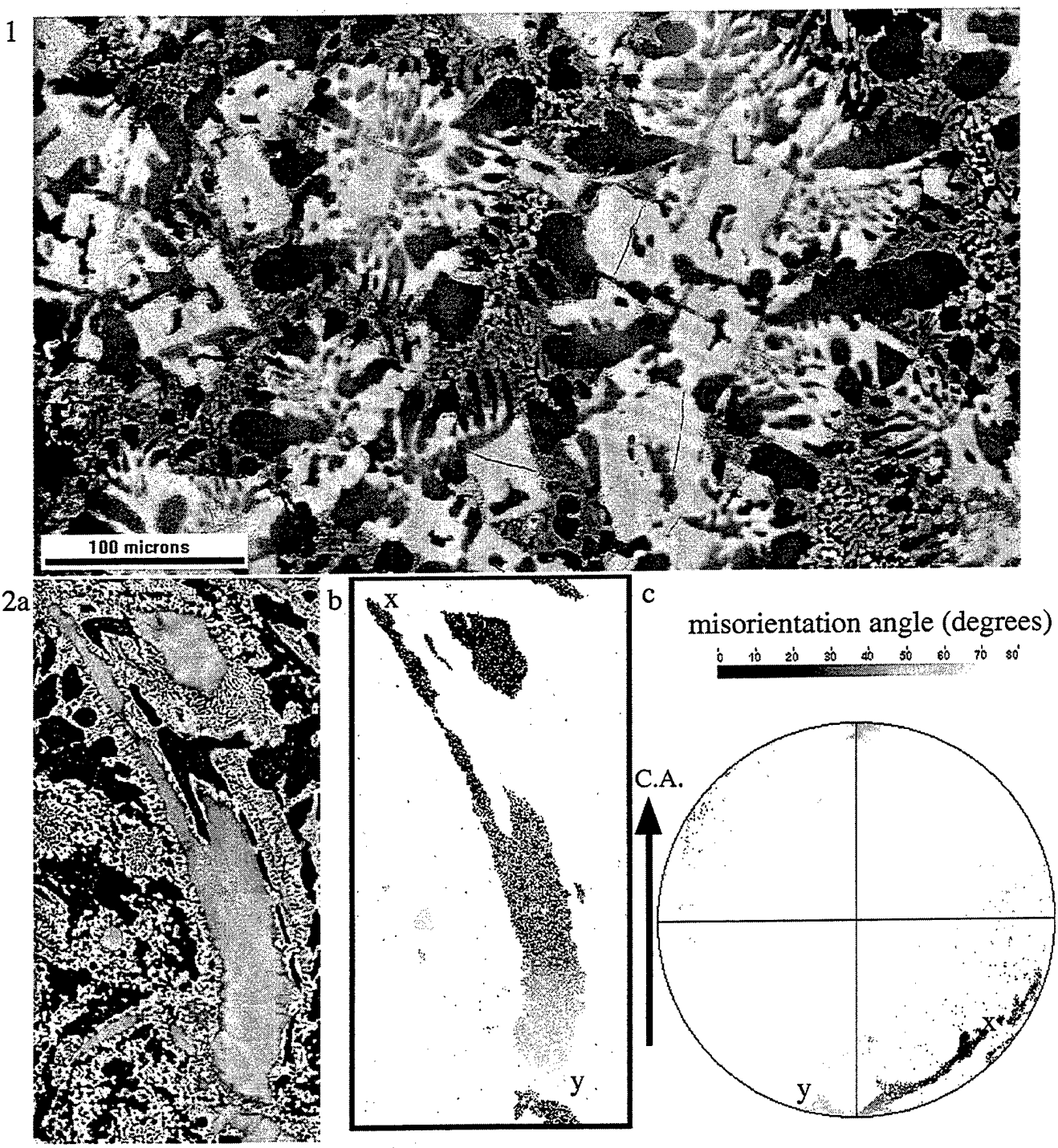


FIG. 1 Backscatter electron image of the transverse section of the Nb-12.5Hf-33Ti-16Si alloy.
FIG. 2 (a) Backscatter electron image of the longitudinal section of the Nb-12.5Hf -33Ti-16Si composite after creep deformation of 50%. Magnification as in Figure 1. (b) Orientation image of the M_3Si grain. Pixels display <001> misorientations relative to point X, in which lighter shades correspond to greater angles of misorientation. (b) <001> pole figure corresponding to the orientation image, poles for pixels X and Y in Figure 2b are indicated. Compression axis (C.A.) for all Figure 2 images indicated by the arrow.

Creep Mechanisms in High-Temperature In-Situ Composites

B.P. Bewlay, M.R. Jackson and J.A. Sutliff

Proceedings of the U.S.-Japan Workshop on Very High Temperature Structural Materials, 1999

Creep Mechanisms in High-Temperature In-Situ Composites

B.P. Bewlay[1], M.R. Jackson[1], J.A. Sutliff[1], C.L. Briant[2],
[1]GE Corporate Research and Development,
Schenectady, NY 12301, USA.
[2]Division of Engineering, Brown University,
Providence, RI 02912, USA.

1.0. Objectives and Approach

The objective of the present research is to investigate high-temperature creep and low-temperature toughening mechanisms in directionally solidified in-situ composites with melting temperatures above 1700°C. The composites under investigation consist of Nb-based silicides, such as Nb_3Si and Nb_5Si_3, that are toughened by a Nb-based solid solution [1-5]. The approach for investigation of creep mechanisms is separated into two stages : first compression creep tests are performed, and second, in those composites that show promising properties, tensile creep tests are performed.

2.0. Research Progress and Highlights

In the present section recent results of studies of fracture toughness, creep, and phase stability will be described.

2.1 Fracture Toughness Measurements

Effect of Hf:Ti Ratio on Fracture Toughness

Room temperature fracture toughness measurements are shown in Table 1 below for Hf compositions of 7.5-12.5 and Ti compositions of 21-33% (all compositions are given in atom percent throughout the present report).

Table 1 : Fracture toughness of Nb-16Si composites modified with Hf and Ti.

Composition	Fracture Toughness (MPa$\sqrt{m}$)
Nb-7.5Hf-21Ti-16Si	12.2
Nb-10Hf-21Ti-16Si	11.9
Nb-12.5Hf-21Ti-16Si	12.1
Nb-21Ti-16Si	11.6
Nb-7.5Hf-33Ti-16Si	12.6
Nb-10Hf-33Ti-16Si	13.3
Nb-12.5Hf-33Ti-16Si	14.0
Nb-33Ti-16Si	11.1

Room temperature fracture toughness was relatively insensitive to Hf: Ti composition ratios in the range 0.2-0.6. However, Ti additions appear to have a stronger effect on

toughness than Hf additions. The room temperature fracture toughness of composites with 33Ti were generally higher than those at 21Ti.

Fracture Toughness in Complex Alloy Composites

Table 2 shows a range of alloys derived from the base MASC composition [1, 2] (last row of the table below).

Table 2 : Fracture toughness of Nb-16Si composites modified with Hf, Ti, Cr and Al.

Composition	**Fracture Toughness** ($MPa\sqrt{m}$)
Nb-20Ti-8Hf-2Al-2Cr-16Si	21.0
Nb-30Ti-8Hf-2Al-2Cr-16Si	19.3
Nb-24.6Ti-11Hf-2Al-2Cr-16Si	21.8
Nb-23.6Ti-14Hf-2Al-2Cr-16Si	18.2
Nb- 25Ti-8Hf-2Al-2Cr-18Si	20.0
Nb-26.5Ti-8Hf-2Al-10Cr-16Si	18.7
Nb-24.7Ti-8.2Hf-2.0Cr-1.9Al-16.0Si	23.3

These data indicate that for Ti concentrations in the range 20-30%, there is little effect on toughness. The above data also indicate that the Si concentration of the MASC can be increased to 18% without compromising composite toughness. It can also be seen that increasing Hf from 8 to 14%, or increasing the Cr concentration up to 10% leads to a reduction in toughness. Higher Cr levels are important for oxidation resistance.

2.2 Creep Mechanisms

The effects of Ti, Hf and Mo additions on the secondary creep rate have been studied and the findings will be described in the following section.

Nb-Ti-Hf-Si In-Situ Composites

Creep tests were performed for a series of quaternary Nb-Hf-Ti-Si alloys at a temperature of 1200°C and at stress levels in the range 140-280 MPa. These data are shown in Table 3 and Figure 1. Data for the Nb-7.5Hf-16Si ternary alloy are also included. Hf concentrations in the range 7.5-12.5 and Ti concentrations in the range 21-33 were examined, providing Ti:Hf ratios in the range 1.7 to 4.4.

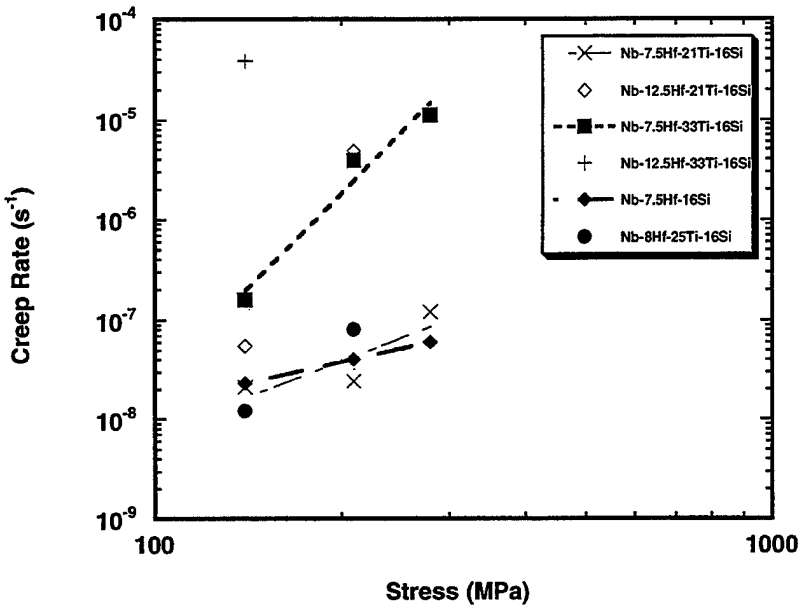


Figure 1 Secondary creep rates at 1200°C for a range of quaternary Nb-Hf-Ti-Si alloys.

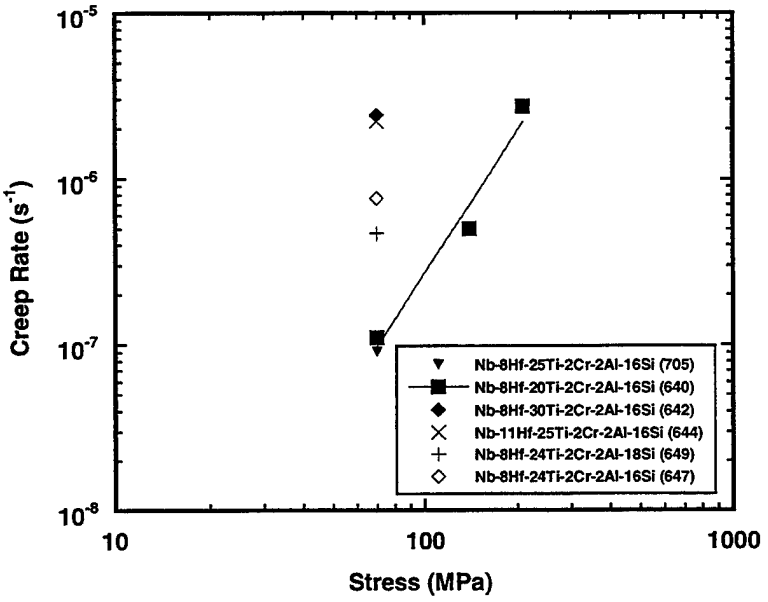


Figure 2 Secondary creep rates at 1200°C for a range of Nb-Hf-Ti-Si-Cr-Al alloys.

Table 3 : Secondary creep rates at 1200°C for a range of Nb-Hf-Ti-Si alloys.

Composition	**Constituent Phases**	**140 MPa Creep Rate (s^{-1})**	**210 MPa Creep Rate (s^{-1})**	**280 MPa Creep Rate (s^{-1})**
Nb-7.5Hf-16Si	(Nb), Nb_3Si	$2.3x10^{-8}$	$4.0x10^{-8}$	$4.8x10^{-8}$
Nb-7.5Hf-21Ti-16Si	(Nb), Nb_3Si	$2.1x10^{-8}$	$3.2x10^{-8}$	$1.2x10^{-7}$
Nb-7.5Hf-33Ti-16Si	(Nb), Nb_3Si, $(Ti,Hf)_5Si_3$	$1.6x10^{-7}$	$3.9x10^{-6}$	$1.1x10^{-5}$
Nb-12.5Hf-21Ti-16Si	(Nb), Nb_3Si, $(Ti,Hf)_5Si_3$	$5.5x10^{-8}$	$4.8x10^{-6}$	Failed
Nb-12.5Hf-33Ti-16Si	(Nb), Nb_3Si, $(Ti,Hf)_5Si_3$	$3.8x10^{-5}$	Failed	--
Nb-16Si	(Nb), Nb_3Si	$1.5x10^{-8}$	$4.9x10^{-8}$	--

The creep data indicate that the Nb-7.5Hf-16Si and the Nb-16Si composites possessed the lowest creep rates, and that at any selected stress level and Hf concentration the creep rate increased with increasing Ti concentration. Thus, Ti and Hf additions can have a significant effect on the creep performance. For example, at 7.5Hf increasing the Ti concentration from 21 to 33% increased the creep rate from $2.1x10^{-8}s^{-1}$ to $1.6x10^{-7}s^{-1}$ at 140MPa. At stress levels of 210MPa and below there is little difference between the secondary creep rates of the Nb-16Si, the Nb-7.5Hf-16Si and the Nb-7.5Hf-21Ti-16Si compositions. At higher stress levels the Ti additions have a detrimental effect on creep performance. Similarly, at Hf concentrations of 12.5 and stress levels of 140MPa, increasing the Ti concentration from 21 to 33% increases the creep rate from $5.5x10^{-8}s^{-1}$ to $3.8x10^{-5}s^{-1}$. At higher stress levels the effect of increasing the Ti concentration led to premature failure.

At any selected stress level, increasing the Hf concentration leads to an increase in the creep rate. For example, at a stress level of 140 MPa and Ti concentration of 21%, increasing the Hf concentration from 7.5 to 12.5% increases the creep rate from $2.1x10^{-8}s^{-1}$ to $5.5x10^{-8}s^{-1}$, but there is a strong stress sensitivity of this effect, so that at 210MPa the creep rates are $3.2x10^{-8}s^{-1}$ and $4.8x10^{-6}s^{-1}$, i.e. Hf concentrations higher than 7.5% provide a strong sensitivity of the secondary creep rate to stress.

These creep data suggest that the Ti:Hf ratio should be maintained at a level less than 3 and the Ti concentration should be kept below 21%. The mechanisms that lead to increased creep rates at higher Ti, higher Hf, or higher (Hf+Ti) concentrations are still under investigation. One of the effects that is significant is that at high (Ti+Hf) concentrations the hP16 Ti_5Si_3 type silicide is stabilized in preference to the tI32 Nb_5Si_3 type or tP32 Nb_3Si type silicides [6, 7]. Thus the creep performance is modified by changes in the constituent phases rather than the intrinsic performance of the silicide [6] or the (Nb). It appears that the $(Ti,Hf)_5Si_3$ is highly detrimental to creep performance. For example, at 280MPa failure of the composites was observed to occur by shear band formation in the large-scale $(Ti,Hf)_5Si_3$ dendrites. There is a suggestion that this behavior is controlled by the crystal structure and texture of the the hP16 relative to the loading axis because the melting temperature of Hf_5Si_3 is close to that of Nb_5Si_3 [7, 8].

Six Element Alloy Composites

Secondary creep rates are shown at 1200 °C and stress levels in the range 70-280 MPa in Figure 2 for a range of composites derived from Nb-Hf-Ti-Cr-Al-Si alloys. Some important trends can be seen in these data. First, the creep rate increased with increasing Ti concentration from 20 to 30%. This may have been due in part to the larger volume fraction of Hf_5Si_3 type phase in the composite, as well as the lower melting temperature of the metallic phase.

The creep data also indicate that increasing the Si concentration from 16% to 18% (substituting Si for Nb) led to a slight reduction on creep rate at 1200 °C and 70MPa from $7.6x10^{-7}s^{-1}$ to $4.7x10^{-7}s^{-1}$. Lastly, substituting Hf for Nb appears to have a detrimental effect on the secondary creep rate; increasing the Hf concentration from 8 to 11% led to a change in the creep rate from $7.6x10^{-7}s^{-1}$ to $2.2x10^{-6}s^{-1}$ at 70MPa and 1200 °C. This was probably due to the reduction in the volume fraction of Nb_5Si_3 type and the increased volume fraction of Hf_5Si_3 type silicides. These observations regarding the effects of Ti and Hf in these complex alloy composites are all consistent with those that were reported for the quaternary Nb-Hf-Ti-Si alloys.

2.3 Phase Stability Investigations

Several investigations of phase stability have been performed, including determination of solid-state phase equilibria in Nb-Ti-Si alloys, definition of silicide stability in the binary Hf-Si system, and definition of the Nb-Hf-Si liquidus surface [1, 5, 7].

Nb-Hf-Si Ternary Phase Stability

Hf is an important alloying addition to niobium silicide in-situ composites because it improves oxidation resistance and strength. Figure 3 is the Nb-Hf-Si liquidus projection.

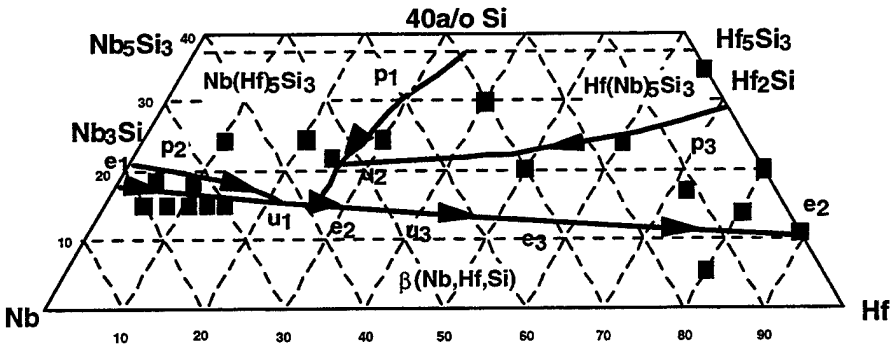


Figure 3 Diagram showing the projection of the Nb-Hf-Si liquidus surface, including the peritectic ridges, p_1, p_2, p_3, the eutectic valleys, e_1, e_2, e_3, and the invariant reactions, U_1, U_2, U_3. The compositions investigated are also shown.

At the metal-rich end of the Nb-Hf-Si ternary phase diagram there is a eutectic trough between the two binary eutectics [8]. However, because of the different binary eutectic reactions there is a change in the nature of the liquidus surface, with decreasing Nb and increasing Hf concentration. The resulting transition reactions are shown below:

U_1 $\quad L + Nb(Hf)_5Si_3 \rightarrow Nb(Hf)_3Si + \beta(Nb,Hf,Si)$

U_2 $\quad L + Hf(Nb)_5Si_3 \rightarrow Nb(Hf)_5Si_3 + Hf(Nb)_2Si$

U_3 $\quad L + Nb(Hf)_5Si_3 \rightarrow \beta(Nb,Hf,Si) + Hf(Nb)_2Si$

The first of these transition reactions occurs at a composition of Nb-21Hf-16Si, and at a temperature between ~1850°C. The second of these transition reactions occurs at a composition of Nb-27Hf-22Si, and a temperature of ~2040°C. The third transition reaction occurs at a composition of Nb-26Hf-14Si, and a temperature of ~1840°C. This work has been prepared for publication in Zeitschrift für Metallkunde. Several examples of the compositions examined are shown below.

The typical microstructure of the DS Nb-15Hf-16Si is shown in Figure 4. There is a small volume fraction of primary β(Nb,Hf,Si) dendrites, which are the dark grey phase in the BSE micrograph, together with an interdendritic $Nb(Hf)_3Si$-β(Nb,Hf,Si) cellular eutectic. The Nb-15Hf-16Si also contained a small volume fraction of intercellular eutectic of $Nb(Hf)_5Si_3$ and β(Nb,Hf,Si), which suggests that the liquid composition passed through the invariant reaction U_1.

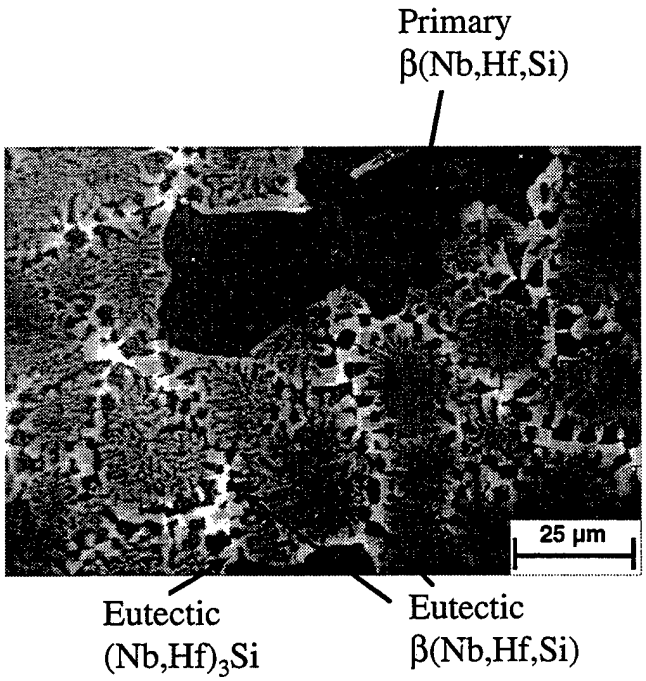


Figure 4 Typical microstructure of the transverse section of DS Nb-15Hf-16Si.

The microstructure of the transverse section of the DS Nb-10Hf-25Si alloy is shown in Figure 5. The large black phase is Nb(Hf)5Si3, and it is surrounded by dark grey peritectic Nb(Hf)3Si. This composition has experienced the peritectic reaction, L + Nb(Hf)5Si3 --> Nb(Hf)3Si. Hf partitioning between the Nb(Hf)3Si and β(Nb,Hf,Si) was such that there was little contrast between these two phases.

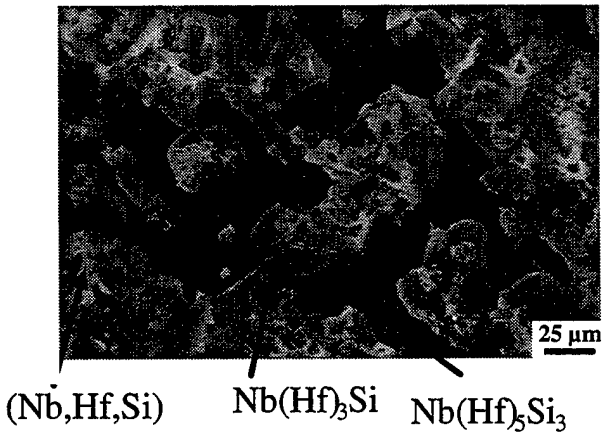


Figure 5 Typical microstructure of the transverse section of DS Nb-10Hf-25Si.

3.0 Summary

The addition of Ti, Hf and Mo have significant effects on composite room temperature fracture toughness and secondary creep rates. The threshold Hf, Ti and Mo concentrations above which the creep performance degenerates beyond that of the Nb-16Si composite have been defined, together with the appropriate stress levels for possible component operations. For example, the creep data indicate that the creep performance of the Nb-8Hf-25Ti-16Si is compatible with the creep goals at temperatures up to 1200 °C. Above these Ti and Hf compositions the creep rates are not acceptable. In addition, the initial Nb, Hf, Ti, Mo and Si composition ranges within which the room temperature fracture toughness can be maintained above 20 MPa$\sqrt{m}$ have been identified.

4.0 Acknowledgments

The authors would like to thank D.J. Dalpe for the directional solidification, and C. Bull for assistance with creep testing. This research was sponsored by AFOSR under contract #F49620-96-C-0022 with Major C.H. Ward and Dr. S. Wu as Program Managers.

5.0 References

[1] B.P. Bewlay, M.R. Jackson, W.J. Reeder, and H.A. Lipsitt, MRS Proceedings on High Temperature Ordered Intermetallic Alloys VI, 1994, Vol. 364, pp. 943-948.

[2] B.P. Bewlay, M.R. Jackson and H.A. Lipsitt, *Metall. and Mater. Trans.*, 1996, Vol 279, pp. 3801-3808.

[3] M.G. Mendiratta, J.J. Lewandowski and D.M. Dimiduk, *Metall. Trans. 22A* (1991), pp. 1573-1581.

[4] M.R. Jackson, B.P. Bewlay, R.G. Rowe, D.W. Skelly, and H.A. Lipsitt, J. of Metals 48 (1), (1996), pp. 38-44.

[5] P.R. Subramanian, M.G. Mendiratta and D.M. Dimiduk, *Mat. Res. Soc. Symp. Proc.*, 322 (1994), pp. 491-502.

[6] P.R. Subramanian, T.A. Parthasarathy, and M.G. Mendiratta, Scripta Met. and Mater., Vol. 32(8), pp. 39-54.

[7] B.P. Bewlay, M.R. Jackson and H.A. Lipsitt, *Journal of Phase Equilibria*, Vol 18(3), 1997, pp. 264-278.

[8] B.P. Bewlay, R.R. Bishop and M.R. Jackson, submitted Zeitschrift für Metallkunde, 1998.

Nb-Silicide In-Situ Composites: Oxidation Behavior

M.R. Jackson, B.P. Bewlay and R.R. Corderman

Proceedings of the U.S.-Japan Workshop on Very High Temperature Structural Materials, 1999

Nb Silicide-Based *In Situ* Composites: Oxidation Behavior

Mel Jackson, Bernard Bewlay & Reed Corderman
GE Corporate Research & Development
Schenectady, NY 12301

1.0 Objectives and Approach

Nb-based silicide composites have been identified as potential high-temperature blade alloys, based on melting range, oxidation, toughness and strength. Although oxidation behavior of these alloys was substantially better than binary Nb-Si composites, they fall far short of superalloy behavior, considering this behavior must be achieved at much higher temperatures, approaching 2400F. The objective of the present effort is to determine if the oxidation resistance of silicide systems can be improved. The approach is an iterative one, with this being the first of four iterative stages, with the goal for each stage to improve behavior over the previous iteration. Goals for the iterations, starting from current behavior as baseline, are 3X baseline, 9X, 27X, and 81X baseline.

2.0 Research Progress and Highlights

Oxidation studies of Nb-based composite alloys modified with large concentrations of Ti and lesser concentrations of Hf were reported [1] for 1000, 1200 and 1400C exposures. The alloys containing aluminides had virtually no resistance at any temperature, but those with Laves phase (Cr_2M) were reasonably resistant, and those with silicide were within a factor of five of the Laves phase (Figure 1). To try to improve the resistance of the much stronger and tougher silicide systems, we added more Cr to develop some fraction of Laves phase in the metal-silicide structures.

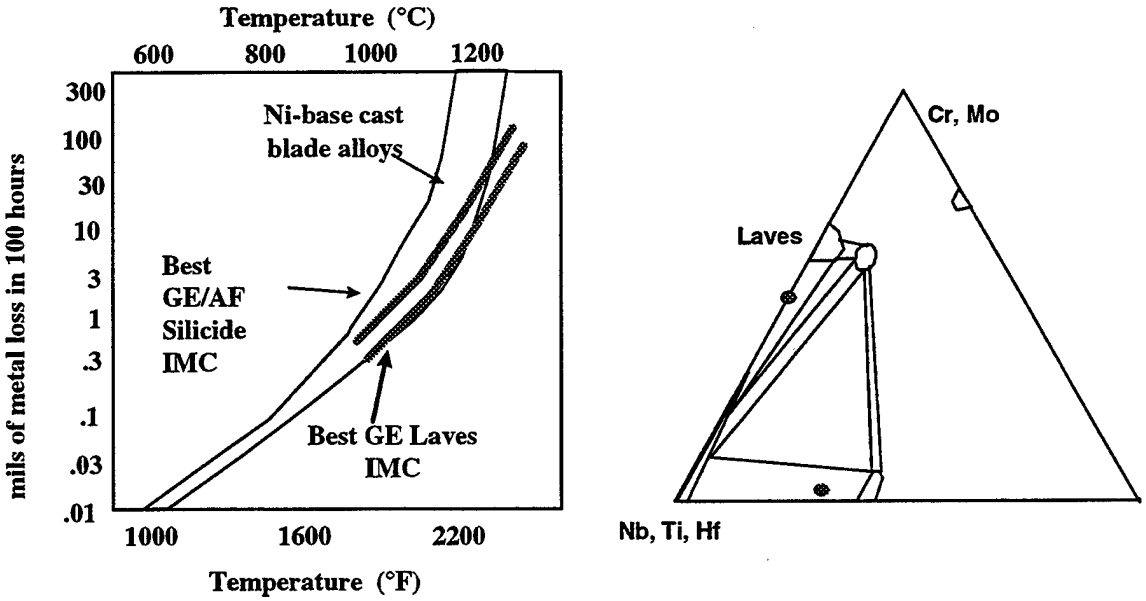


Figure 1: Earlier research showed that for Nb-based materials, the Laves composites were better in oxidation than the Silicide composites.

Oxidation testing of the Laves-containing metal-silicide alloy is shown in Figure 2 for exposures at 1204C and 1315C (2200F and 2400F), compared to a complex metal-silicide material [2]. To be useful at 1315C surface temperatures with the same robustness as superalloys at their current surface temperatures (~1150C), the oxidation behavior of the silicide alloy must be improved about 80-fold. The loss of material in 100 hours measured metallographically for the Laves-containing material was ~40 microns at 1204C and 425 microns at 1315C. These values represent improvements over the Figure 1 and 2 silicide examples of approximately 4X and 6X, at 1204 and 1315C, respectively. This is shown schematically in Figure 3. Another 16X improvement still remains.

However, the addition of Cr reduces the volume fraction of metal in the structure, and this is expected to reduce the fracture toughness of the material system. To develop a better understanding of the influence of all of the major elements, Nb, Ti, Hf, Cr, Al and Si, we developed a matrix of alloys for evaluation (a quarter factorial design of experiments). This would allow us to determine which elements and in what concentrations could be traded for Cr, without damaging oxidation behavior but retaining high fracture toughness.

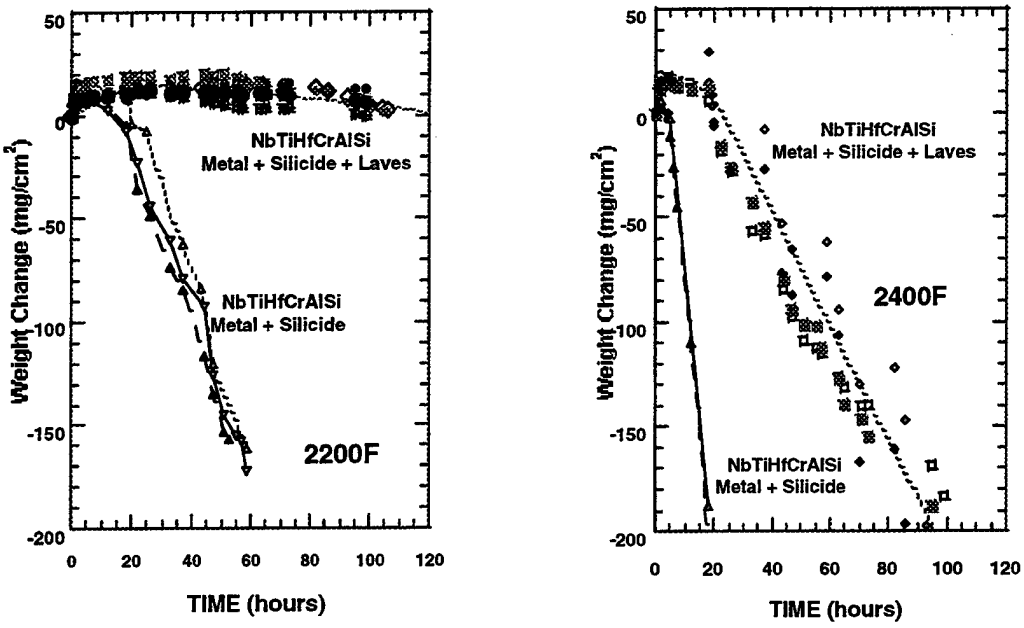


Figure 2: Comparison of 2200F and 2400F oxidation resistance of a high-Cr Nb-Ti-Hf-Cr-Al-Si composite to the baseline alloy behavior.

Figure 4 shows the results of statistical analysis of the oxidation testing at 1204C for the eight quarter-factorial DoE alloys. The largest positive effect came from increasing Si, while Cr and Ti had nearly equivalent effect, and Al had a still smaller effect. There was almost no influence of Hf on 1204C oxidation.

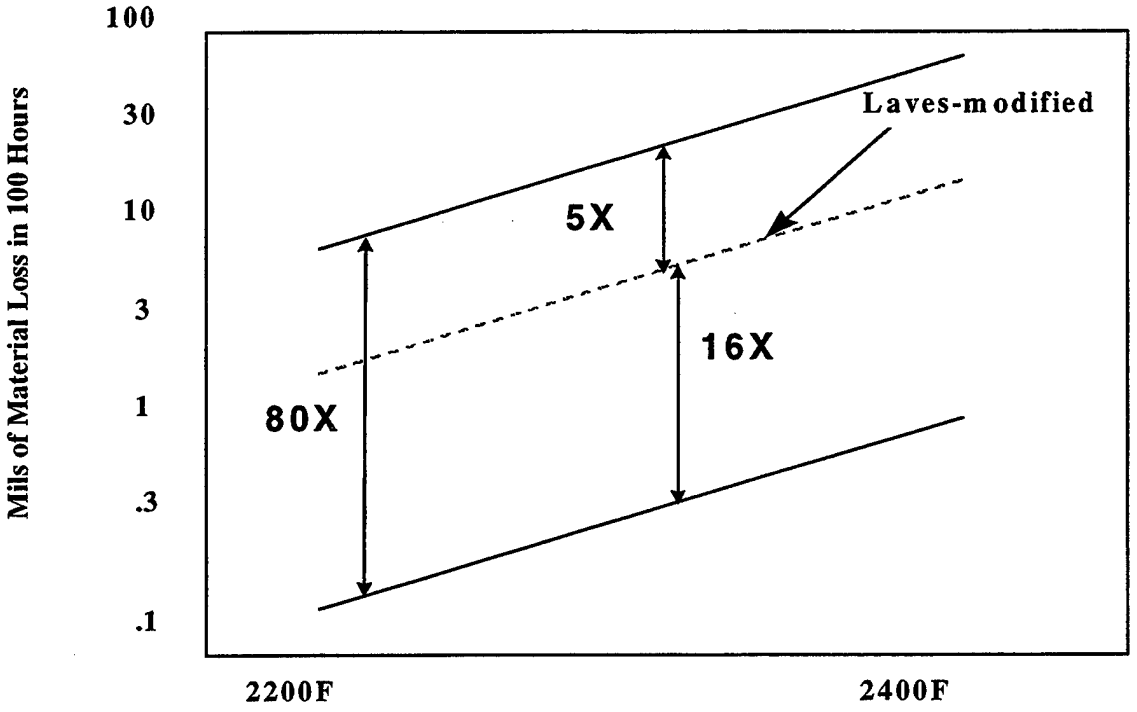
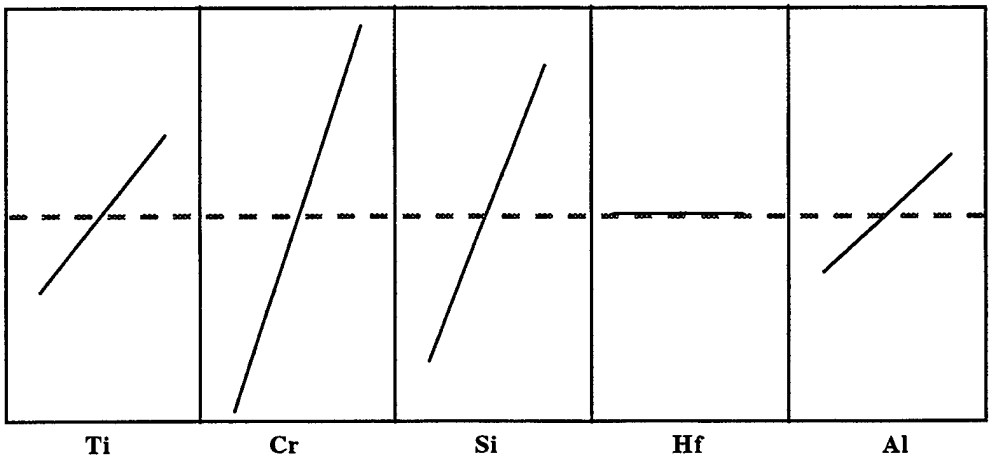


Figure 3: The improvement in oxidation behavior for the Laves-containing silicide composite leaves a further 16X improvement to be achieved.



$$\Delta wt/A]\ 1204C = f(aTi + aCr + 1.5aSi + 0.5aAl)$$

Figure 4: The relative influence of the major alloying elements on 1204C oxidation behavior. Vertical axis is weight change per unit area.

A similar analysis was conducted for oxidation at 1315C, with the functionality that described the behavior being:

$$\Delta wt/A]\ 1315C = f(\ 0.8bTi + b(Cr + Si + Al) - b/3\ Hf\ ).$$

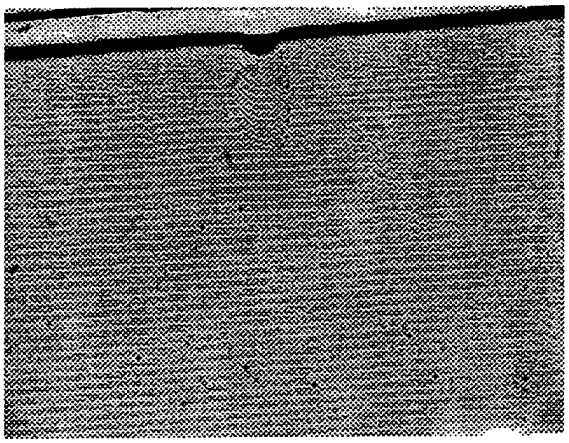
Here, Hf appeared to have a slightly negative influence on oxidation at 1315C.

The equations for 1204C and 1315C oxidation indicate that there should be compositional trades for Cr that will allow for the desired reduced oxidation degradation.

3.0 Critical Issues

Of course, as we have noted, achieving improved oxidation resistance is critical. However, this must be achieved without substantially degrading other properties, such as fracture toughness, creep resistance, and fatigue response. Producing materials with the required balance of properties remains a very difficult task. Another issue will be achieving stability in thin-walled airfoils, since the turbine blade designs currently envisioned have hot-wallthicknesses of 0.3-1.0mm. Within that thickness must fit not only the structural composite alloy, but also an internal and an external protective coating. We have been working with Movchan and Marinsky of the International Center for Electron Beam Technology (Kyiv) to begin developing some experience with deposition of such silicide composites and the coatings demanded by the service conditions. Figure 5 shows a four-element Nb-Ti-Hf-Si laminate composite fabricated at ICEBT. The possibility of tailoring the through-thickness chemistry to produce coatings, varying properties, etc., can be done directly by the EB processing.

Nb-Ti-Si-Hf Micro-laminate Made for GECRD by ICEBT



- **Graded Structures**
- **Single-Phase Surfaces (such as Laves)**
- **In situ coatings deposition**

Figure 5: An example of a Nb-Ti-Hf-Si microlaminate produced at ICEBT-Kyiv.

4.0 References

[1] M.R. Jackson, R.G. Rowe and D.W. Skelly, MRS Symp Proc 364, 1995, pp. 1339-1344.
[2] M.R. Jackson, B.P. Bewlay, R.G. Rowe, D.W. Skelly and H.A. Lipsitt, JOM 48-1, 1996, pp39-44.

Evidence For the Existence of Hf_5Si_3

B.P. Bewlay, J.A. Sutliff, and R.R. Bishop

Journal of Phase Equilibria, 1999

Evidence for the Existence of Hf_5Si_3

B.P. Bewlay, J.A. Sutliff, and R.R. Bishop

(Submitted 22 January 1998; in revised form 30 November 1998)

This article describes new evidence for the existence of Hf_5Si_3 with the Mn_5Si_3 structure type (*hP*16-*P*6$_3$/*mmc*). Binary Hf-Si alloys with Si concentrations from 11.5 to 35.0 at.% were investigated. Hf_2Si was also observed in the binary Hf-Si alloys that were investigated; this is consistent with the assessed phase diagram. The Mn_5Si_3-type structure has been observed in both binary Hf_5Si_3 and higher alloyed forms, (Hf, *X*)$_5Si_3$, where Nb and Ti were substituted for Hf. Phase identification was performed using scanning electron microscopy, electron microprobe analysis, x-ray diffraction, and automated electron backscattering pattern analysis in the scanning electron microscope. The present data indicate that high levels of O, N, or C are not required to stabilize Hf_5Si_3, and that it can exist alone as a binary compound. This result is contrary to previous reports regarding Hf_5Si_3, which claim that it only exists when stabilized by interstitials.

Introduction

Niobium silicides such as Nb_5Si_3 and Nb_3Si are presently being explored as strengthening phases in high-temperature structural materials (Ref 1, 2). Alloying additions of elements such as Hf and Ti to these silicides are also being examined in order to increase the strength and oxidation resistance. There is limited knowledge of these silicides, which is due in part to the fact that there is some degree of uncertainty in the literature relating to the binary Hf-Si phase diagram, specifically the existence of Hf_5Si_3. However, there is significant previous evidence for the existence of a second Hf-rich silicide, Hf_2Si (Ref 3). This article describes new data supporting the existence of Hf_5Si_3 and Hf_2Si in binary Hf-Si alloys. Observations of Hf_5Si_3- and Hf_2Si-type silicides in ternary directionally solidified (DS) Hf-Nb-Si alloys are also described.

The metal-rich end of the binary Hf-Si phase diagram (Ref 3) has a eutectic of the form L $\rightarrow$ (Hf) + Hf_2Si at 1830 °C, and a peritectic of the form L + Hf_5Si_3 $\rightarrow$ Hf_2Si at 2080 °C (the Hf-Si solid solution is abbreviated by (Hf) throughout this article). The eutectic composition is Hf-12%Si (all compositions are given in atomic percent throughout this article). Hf_5Si_3 has the Mn_5Si_3 structure type (*hP*16-*P*6$_3$/*mmc*) with lattice parameters of a = 0.7844 nm and c = 0.5492 nm, and Hf_2Si has the Al_2Cu structure type (*tI*12-*I*4/*mcm*) with lattice parameters of a = 0.6553 nm and c = 0.5186 nm.

The existence of Hf_5Si_3 has been previously reported by Gokhale and Abbaschian (Ref 3), but it has been considered to be stable only in the presence of O, N, or C (Ref 3, 4). Karpinsky and Evseyev (Ref 5) identified Hf_5Si_3, Hf_3Si_2, and Hf_5Si_4 in alloys prepared from 99.0% pure Hf using arc melting, and they identified Hf_5Si_3 as having the Mn_5Si_3 (*hP*16-*P*6$_3$/*mmc*)-type structure. Kieffer and Benesovsky (Ref 6) provided a more complete review of the crystallography of high-temperature Hf silicides. They expressed some uncertainty regarding the existence of the Hf_5Si_3.

B.P. Bewlay and **J.A. Sutliff,** General Electric Company, Corporate Research and Development, Schenectady, NY 12301, USA; and **R.R. Bishop,** Department of Materials Science and Engineering, Northwestern University, Evanston, IL 60208, USA.

The aim of this article is to describe new evidence for the existence of Hf_5Si_3 with the Mn_5Si_3 (*hP*16-*P*6$_3$/*mmc*) crystal structure. This structure has been observed in binary Hf_5Si_3 and higher forms, (Hf,*X*)$_5Si_3$ where Hf was substituted for Nb and Ti.

Experimental

Binary Hf-Si and ternary Nb-Hf-Si alloys were prepared from >99.9% Hf (not including Zr), >99.99% Nb, and 99.999% Si by induction levitation melting in a segmented water-cooled copper crucible. The alloys were triple melted and then directionally solidified using the Czochralski method, as has been described in more detail elsewhere (Ref 2). Binary Hf-Si alloys with Si concentrations in the range 11 to 35% were prepared. The interstitial levels of the Hf were: C < 11, O < 52, and N < 22 weight ppm, respectively. Chemical analyses were performed on the starting materials, but not on the final cast alloys. However, it has been shown previously that the cold crucible melting system prevents any increase in the interstitial levels from those levels in the starting elements (Ref 7).

All of the samples were examined using scanning electron microscopy (backscatter electron, BSE, imaging) and electron beam microprobe analysis (EMPA). X-ray diffraction (XRD) was also performed using Cu Kα radiation on powder samples that were ball milled from the original DS samples. These separate analyses allowed determination of the chemistry and crystal structure of the individual phases.

Phase identification was also performed using the automated electron backscattering pattern (EBSP) technique for electron diffraction in the scanning electron microscope. This technique allowed easy selection of microstructural features using high-resolution microscopy with rapid diffraction pattern collection and analysis. A CamScan CS44 SEM (Cam Scan Electron Optics, Ltd., Cambridge, England) was operated using a 40 kV, ~10 nA electron beam, and the sample surface normal was tilted 70° away from the beam axis. A Nordiff (Jarle Hjelen Ltd., Trondheim, Norway) CCD-based (charge coupled device) EBSP detector was used. Positive phase identification was accomplished by direct comparison of the location and character of the diffraction bands in the experimental pattern with those calculated from simulated patterns generated using the possible structure types.

Results and Discussion

The microstructure of the binary Hf-35Si is shown in the BSE image in Fig. 1. It consisted of Hf_5Si_3 surrounded by peritectic Hf_2Si, with a small volume fraction of (Hf)-Hf_2Si eutectic. In Fig. 1, the Hf_2Si is the black phase and the (Hf) is the light phase. The Hf_5Si_3 is difficult to identify in Fig. 1 because there is little contrast between the Hf_5Si_3 and the peritectic Hf_2Si. However, the Hf_5Si_3 possessed a high density of cracks that did not propagate into the Hf_2Si, and these also served to differentiate the Hf_5Si_3 from the Hf_2Si. These cracks may have arisen as a result of differential thermal contraction between the two silicides on postsolidification cooling.

The presence of both Hf_5Si_3 and Hf_2Si was confirmed using XRD and EMPA data. The EMPA data indicated that the composition of the Hf_5Si_3 was Hf-37.5Si, the peritectic Hf_2Si was Hf-33.3Si, the eutectic Hf_2Si was Hf-33.1Si, and eutectic (Hf) was Hf-2.9Si; the Si composition of the (Hf) was higher than that reported for the assessed phase diagram at the eutectic temperature (<1%).

Electron backscattering diffraction patterns are shown in Fig. 2(a) and (c) for the Hf_2Si and Hf_5Si_3, respectively, that were observed in the Hf-35Si alloy. The indexed diffraction patterns are shown in Fig. 2(b) and (d) for Hf_2Si and Hf_5Si_3. The EBSP diffraction patterns were successfully indexed using the following crystallographic data:

- αHf ($a = 0.3196$ nm, $c = 0.5058$ nm, Mg structure type, space group: $P6_3/mmc$ (Ref 8)
- Hf_2Si ($a = 0.6553$ nm, $c = 0.5186$ nm, Al_2Cu structure type, space group: $I4/mcm$ (Ref 8)
- Hf_5Si_3 ($a = 0.7844$ nm, $c = 0.5492$ nm, Mn_5Si_3 structure type, space group: $P6_3/mcm$ (Ref 5)

The following additional crystal structures were also considered (Ref 8):

- Hf_5Si_4 ($a = 0.7039$ nm, $c = 1.283$ nm, Si_4Zr_5 structure type, space group: $P4_12_12$
- Hf_3Si_2 ($a = 0.6988$ nm, $c = 0.3675$ nm, Si_2U_3 structure type, space group: $P4/mbm$
- HfSi ($a = 0.6889$ nm, $b = 0.3772$ nm, $c = 0.5223$ nm, BFe structure type, space group: $Pnma$

The symmetries and structures of the above phases were easily differentiated from each other, and indexing of the diffraction patterns obtained was found to be consistent only with αHf, Hf_2Si, and Hf_5Si_3. Of all the silicides that were considered, Hf_5Si_3 was the only silicide that provided a successful match with the EBSP pattern from the phase in Fig. 1 that was identified as Hf_5Si_3 using EMPA. These data indicate that C, N, or O levels greater than 100 ppm are not required to stabilize Hf_5Si_3, because the interstitial levels of the Hf were: C < 11, O < 52, and N < 22 weight ppm, respectively.

The XRD data for the Hf-35Si provided clear evidence for the existence of αHf and Hf_2Si. There were also x-ray lines present that were consistent with the pattern expected for Hf_5Si_3 ($hP16$-$P6_3/mcm$) using lattice parameters of 0.7890 and 0.5558 nm (Ref 9, 10). However, there was a consistent angular shift of the lines to larger angles than expected for the above lattice parameters. This observation indicates a smaller Hf_5Si_3 unit cell than that described by the above lattice parameters, which suggests that the correct lattice parameters of Hf_5Si_3 are closer to those provided by Karpinsky and Evseyev (Ref 5). No βHf was detected in the Hf-35Si.

The microstructure of the Hf-20Si was similar to that of the Hf-35Si except that no Hf_5Si_3 was detected. X-ray diffraction

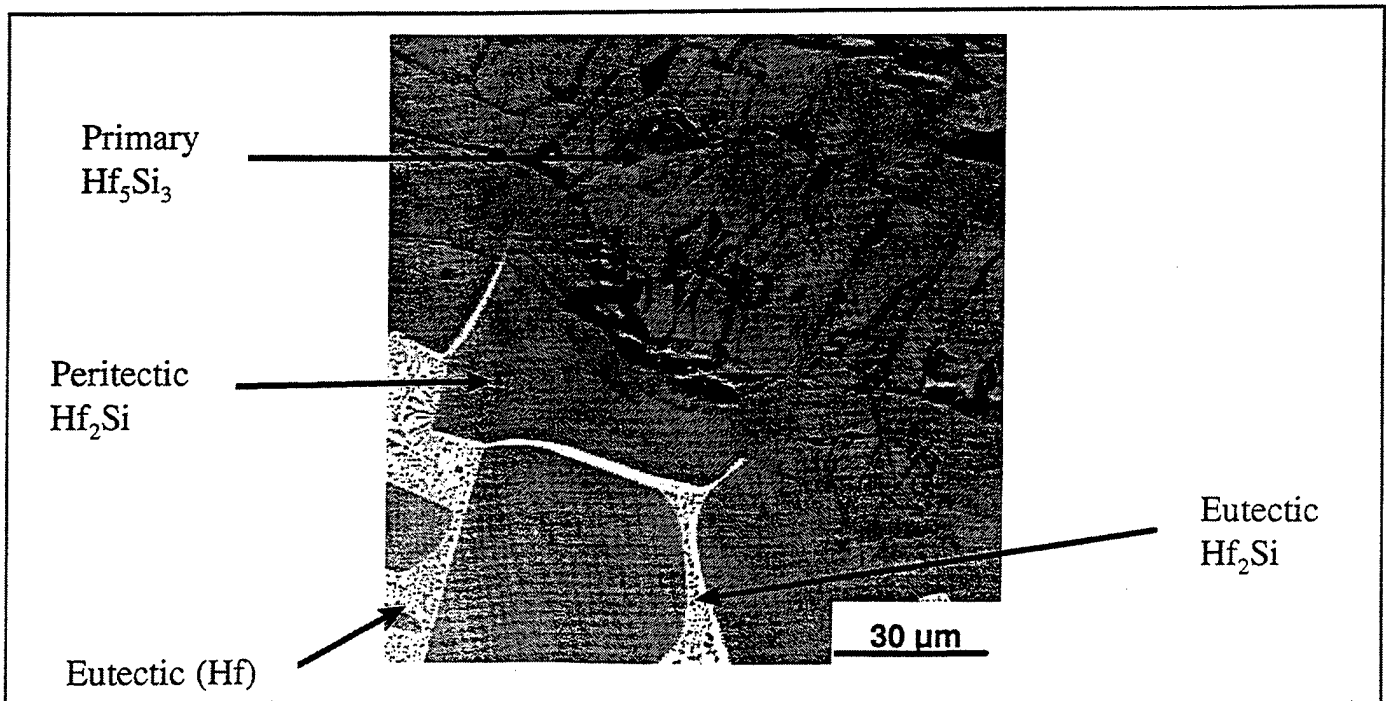


Fig. 1 Microstructure of Hf-35Si cast using cold crucible induction casting, showing primary Hf_5Si_3 (black phase with cracks), peritectic Hf_2Si (dark phase without cracks), and (Hf)-Hf_2Si eutectic. (Hf) is the light phase. Taken using BSE imaging

of the Hf-20Si did not detect any Hf_5Si_3. The Hf_2Si was also identified using transmission electron microscopy. This composition provided evidence for the peritectic and the eutectic reactions; the Hf-20Si composition allows the peritectic ridge to be placed in the Hf-Si binary.

The microstructure of the Hf-12Si eutectic composition is shown in Fig. 3(a) and (b). The microstructure consisted of rods/fibers of Hf_2Si (gray phase) in a (Hf) matrix (white phase). There was also a small volume fraction of primary faceted Hf_2Si dendrites indicating that the Hf-12Si composition was slightly Si-rich of the eutectic composition. The β(Hf) appeared to have transformed completely to α(Hf). The Hf-12Si melting temperature was 1820 °C, which was consistent with that reported previously for the Hf-Hf_2Si eutectic (Ref 3), even though the Hf-12Si was slightly Si-rich of the eutectic composition. A binary alloy of Hf-11.5Si was also directionally

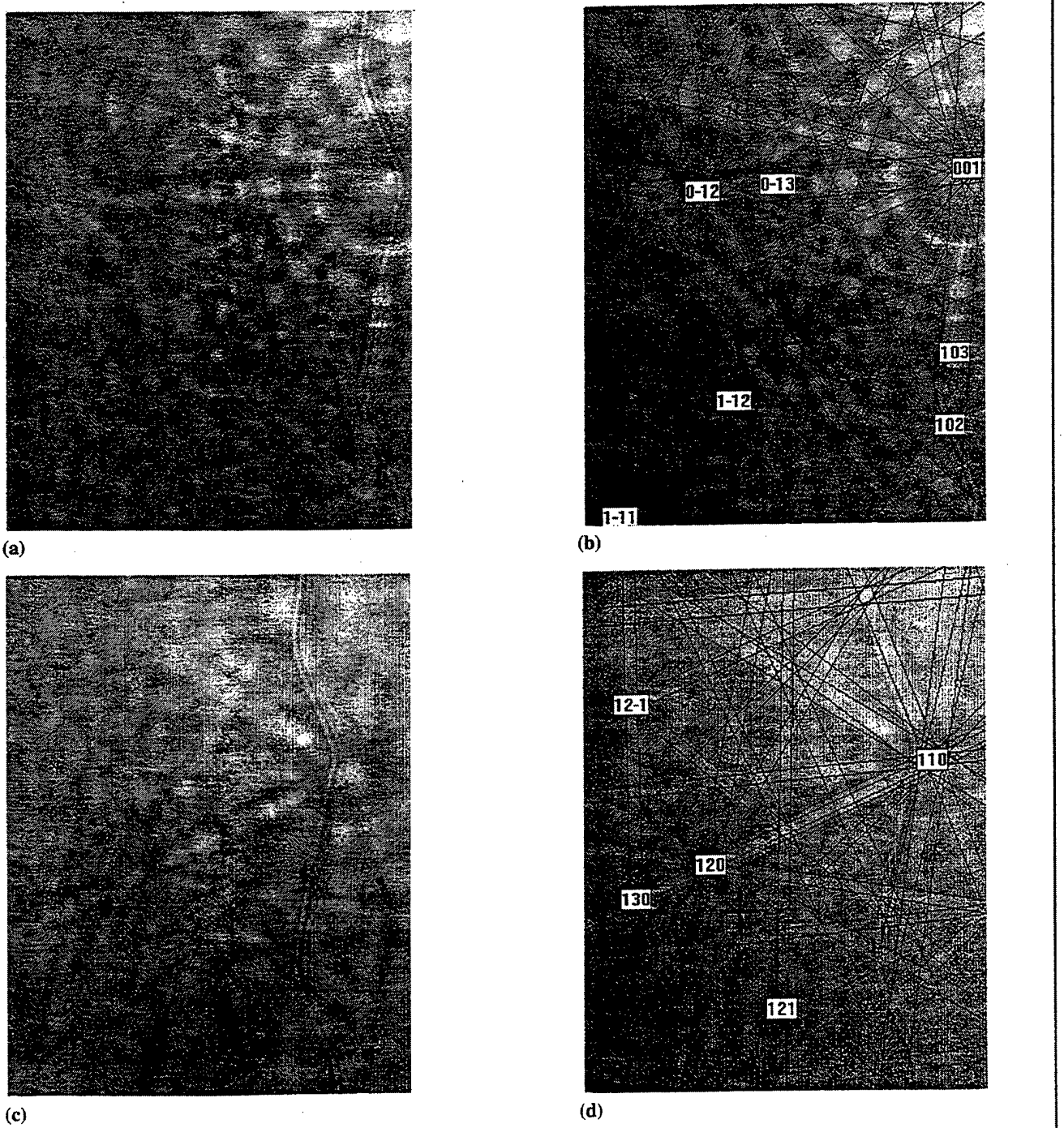


Fig. 2 EBSP diffraction patterns of (a) Hf_2Si and (c) Hf_5Si_3 in the Hf-35Si alloy. The indexed diffraction patterns are also shown for (b) Hf_2Si and (d) Hf_5Si_3.

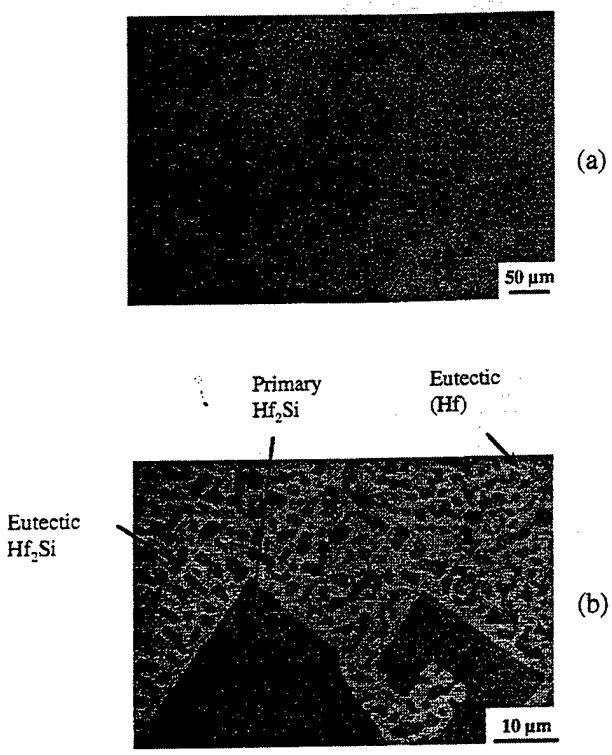


Fig. 3 Microstructure of the transverse section of DS Hf-12Si at (a) low and (b) high magnifications. These micrographs were taken using BSE imaging.

solidified and was found to contain only a very small volume fraction of primary Hf_2Si dendrites (<5%), and it was therefore considered to be much closer to the eutectic composition.

Hf_5Si_3 was also observed in Hf-Si alloys that were modified with Nb. For example, a Hf-55Nb-25Si alloy was directionally solidified, and it was found to contain primary $Hf(Nb)_5Si_3$, peritectic $Hf(Nb)_2Si$ and an interdendritic eutectic of (Hf) and $Hf(Nb)_2Si$; in this case Nb was substituted for Hf in all three phases. This microstructure was similar to that observed in the Hf-35Si. This is further evidence for the existence of Hf_5Si_3 rather than other higher-order silicides, such as Hf_3Si_2 or Hf_5Si_4.

The XRD, EMPA, and EBSP data obtained from the silicides in the binary and ternary alloys obtained in the present work provide clear evidence for the existence of Hf_5Si_3. No Hf_3Si_2 or Hf_4Si_3 phases were detected. Thus, Hf_5Si_3 is stable even at very low total interstitial concentrations (<100 ppm), contrary to previous reports (Ref 3, 4).

Conclusions

The SEM, XRD, EMPA, and EBSP data from high-purity alloys demonstrate the presence of the Mn_5Si_3 type (*hP*16-$P6_3/mmc$) Hf_5Si_3 phase in Hf-Si alloys. Hf_2Si with the Al_2Cu structure type (*tI*12-*I*4/*mcm*) was also observed. Hf_4Si_3, Hf_3Si_2, or the other silicides reported previously were not observed. These data indicate that Hf_5Si_3 is stable at total O, N, and C concentrations less than 100 ppm. This is contrary to previous reports regarding Hf_5Si_3, which claim that it only exists when stabilized by high levels of interstitials.

Evidence for the peritectic reaction $L + Hf_5Si_3 \rightarrow Hf_2Si$ has also been presented. Hf_5Si_3 and Hf_2Si were observed in both the binary Hf-Si and ternary Hf-Nb-Si alloys. The Hf-Hf_2Si eutectic reaction occurs at a similar temperature to that reported previously, but the eutectic composition is closer to Hf-11.5Si.

Acknowledgment

The authors would like to thank D.J. Dalpe for the directional solidification, S.D. Sitzman for the EBSP, and D. Marsh for the XRD. This research was partially sponsored by AFOSR under contract No. F49620-96-C-0022 with Capt. C.H. Ward as Program Manager.

References

1. M.R. Jackson, B.P. Bewlay, R.G. Rowe, D.W. Skelly, and H.A. Lipsitt, *J. Met.*, Vol 48 (No. 1), 1996, p 38-39
2. B.P. Bewlay, M.R. Jackson, W.J. Reeder, and H.A. Lipsitt, *MRS Proc. High Temperature Ordered Intermetallic Alloys VI*, Vol 364, 1994, p 943-948
3. A.B. Gokhale and G.J. Abbaschian, *Bull. Alloy Phase Diagrams*, Vol 10 (No. 4), 1989, p 390-393
4. C.E. Brukl, Tech. Rep. AFML-TR 65-2, Air Force Materials Laboratory, 1968, p 72
5. O.G. Karpinsky and B.A. Evseyev, *Russ. Metall.*, Vol 3, 1969, p 128-130
6. R. Kieffer and F. Benesovsky, *Powder Metall.*, Vol 1/2, 1958, p 145-171
7. G.A. Henshall, M.J. Strum, B.P. Bewlay, and J.A. Sutliff, *Metall. Mater. Trans.*, Vol 28A, 1997, p 2555-2564
8. P. Villars and L.D. Calvert, Ed., *Pearsons Handbook of Crystallographic Data for Intermetallic Phases*, 2nd ed., Vol 1-4, ASM International, 1991
9. H. Nowotny, E. Laube, R. Kieffer, and F. Benesovsky, *Monatsh. Chem.*, Vol 89, 1958, p 701-707
10. O. Schob, H. Nowotny, and F. Benesovsky, *Planseeber. Pulvermetall.*, Vol 10, 1962, p 65-71

Creep Mechanisms in High-Temperature In-Situ Composites

Annual Report: August 1998

Creep Mechanisms in High-Temperature In-Situ Composites : Report for Period 9-1-97 to 8-31-98

(Contract Number: FQ8671-96005872306/AS)

Research Contributors

Dr. Bernard P. Bewlay, GE-CRD, Staff Metallurgist
Dr. Melvin R. Jackson, GE-CRD, Staff Metallurgist
Dr. John A. Sutliff, GE-CRD, Staff Materials Scientist
Prof. Clyde L. Briant, Brown University, Professor

1.0. Objectives

The principal objective of the present research is to investigate high-temperature creep and low-temperature toughening mechanisms in high-strength directionally solidified (DS) in-situ composites with melting temperatures above 1700°C. The composites under investigation consist of high-strength Nb-based silicides, such as Nb_3Si and Nb_5Si_3, and are toughened by a Nb-based solid solution. In addition, phase stability in composites generated from Nb-Ti-Si and from Nb-Hf-Si alloys has been investigated.

2.0 Approach

In the investigation of creep mechanisms several effects are being examined, these include the metallic phase strength, the role of the volume fraction of intermetallic, the effect of increasing the creep performance of the intermetallic, and the effect of texture of the individual phases. The approach for investigation of creep mechanisms is separated into two stages : first compression creep tests at temperatures from 1000°C to 1200°C are performed to investigate the above effects, and second, in those composites that show promising properties, tensile creep tests are performed.

Precipitation in the metallic solid solution can have critical effects on both the low temperature mechanical properties, such as strength and toughness, as well as high temperature performance, such as creep rate and creep rupture behavior. Thus, precipitation in the metallic toughening phase has received significant attention during the course of the present study. In addition, phase equilibria in ternary systems, such as Nb-Ti-Si and Nb-Hf-Si, are being defined.

3.0 Progress and Status of Effort

The work of the second year of this contract falls into the following categories : Evaluation of composite fracture toughness, studies of creep mechanisms, investigation of silicide precipitates in Nb-Si and Nb-Ti-Si alloys (this work has been performed in close collaboration with researchers at Ohio State University), and determination of phase stability in high-temperature composites.

3.1 Fracture Toughness Measurements

Effect of Mo Additions on Fracture Toughness

Fracture toughness measurements are shown in Table 1 below for a range of alloys that contain Mo and Ti additions to a base alloy of Nb-8Hf-16Si. Ti concentrations from 8 to 25%Ti and Mo concentrations from 3 to 15% have been examined. These data suggest that there is a peak in the toughening improvement provided by the Mo additions for composites with a composition of 25Ti.

Table 1 : Room temperature fracture toughness of Mo modified composites.

Composition	**Fracture Toughness** ($MPa\sqrt{m}$)
Nb-8Hf-25Ti-16Si	16.1
Nb-3Mo-8Hf-25Ti-16Si	17.9
Nb-9Mo-8Hf-25Ti-16Si	14.0
Nb-8Ti-8Hf-16Si	12.3
Nb-9Mo-8Hf-16Si	11.9
Nb-9Mo-5Ti-8Hf-16Si	7.7
Nb-9Mo-8Ti-8Hf-16Si	8.7
Nb-9Mo-13Ti-8Hf-16Si	8.8
Nb-9Mo-16Ti-8Hf-16Si	7.4
Nb-9Mo-22Ti-8Hf-16Si	10.0
Nb-15Mo-20Ti-8Hf-16Si	11.4

When the Ti concentration is reduced below 25Ti the toughness is generally reduced with increasing Mo additions: If the Ti concentration is less than 20%, then Mo concentrations greater than 9% lead to fracture toughness values less than 10 $MPa\sqrt{m}$. However, for Mo concentrations up to 15%, fracture toughness values of >10 $MPa\sqrt{m}$ can be expected provided that the Ti concentration is greater than 20%. Thus it is important to keep the Ti:Mo ratio greater than 3 and the Mo concentration less than 9%.

Effect of Hf:Ti Ratio on Fracture Toughness

Room temperature fracture toughness measurements are shown in Table 2 below for Hf compositions of 7.5-12.5 and Ti compositions of 21-33%.

Table 2 : Room temperature fracture toughness of Nb-16Si composites modified with Hf and Ti.

Composition	**Fracture Toughness (MPa $\sqrt{m}$)**
Nb-7.5Hf-21Ti-16Si	12.2
Nb-10Hf-21Ti-16Si	11.9
Nb-12.5Hf-21Ti-16Si	12.1
Nb-21Ti-16Si	11.6
Nb-7.5Hf-33Ti-16Si	12.6
Nb-10Hf-33Ti-16Si	13.3
Nb-12.5Hf-33Ti-16Si	14.0
Nb-33Ti-16Si	11.1

Room temperature fracture toughness was relatively insensitive to Hf: Ti composition ratios in the range 0.2-0.6. However, Ti additions appear to have a stronger effect on toughness than Hf additions. The room temperature fracture toughness of composites with 33Ti were generally higher than those at 21Ti.

Fracture Toughness in Complex Alloy Composites

Table 3 shows a range of alloys derived from the base MASC composition [1, 2] (last row of the table below).

Table 3 : Room temperature fracture toughness of Nb-16Si composites modified with Hf, Ti, Cr and Al.

Composition	**Fracture Toughness (MPa $\sqrt{m}$)**
Nb-20Ti-8Hf-2Al-2Cr-16Si	21.0
Nb-30Ti-8Hf-2Al-2Cr-16Si	19.3
Nb-24.6Ti-11Hf-2Al-2Cr-16Si	21.8
Nb-23.6Ti-14Hf-2Al-2Cr-16Si	18.2
Nb- 25Ti-8Hf-2Al-2Cr-18Si	20.0
Nb-26.5Ti-8Hf-2Al-10Cr-16Si	18.7
Nb-24.7Ti-8.2Hf-2.0Cr-1.9Al-16.0Si	23.3

These data indicate that for Ti concentrations in the range 20-30%, there is little effect on toughness. The above data also indicate that the Si concentration of the MASC can be increased to 18% without compromising composite toughness. This is an important observation because the Si concentration controls the volume fraction of silicide and therefore the elevated temperature strength and creep properties.

It can also be seen from the above data that increasing the Hf from 8 to 14%, or increasing the Cr concentration up to 10% leads to a reduction in toughness. Nevertheless, toughness levels of this range of composites are promising. Higher Cr levels are important for high temperature oxidation resistance.

3.2 Creep Mechanisms

Recent work indicates that creep deformation in Nb_5Si_3 is controlled by diffusion in the Nb_5Si_3 phase [4-6]. Because elements such as, Mo and Hf have a large atomic size, they may be effective in improving the intrinsic creep performance of the silicide and therefore the composite. Mo and additions also increase the strength of the Nb solid solution. Thus, Hf and Mo additions to a range of composites have been examined and their effect on secondary creep rate has been measured. The role of texture in these composites has also been measured using electron back scattering pattern analysis (EBSP).

Nb-Ti-Hf-Si In-Situ Composites

Creep tests were performed for a series of quaternary Nb-Hf-Ti-Si alloys at a temperature of 1200°C and at stress levels in the range 138-276 MPa. These data are shown in Table 4 and Figure 1. Data for the Nb-7.5Hf-16Si ternary alloy are also included. Hf concentrations in the range 7.5-12.5 and Ti concentrations in the range 21-33 were examined, providing Ti:Hf ratios in the range 1.7 to 4.4.

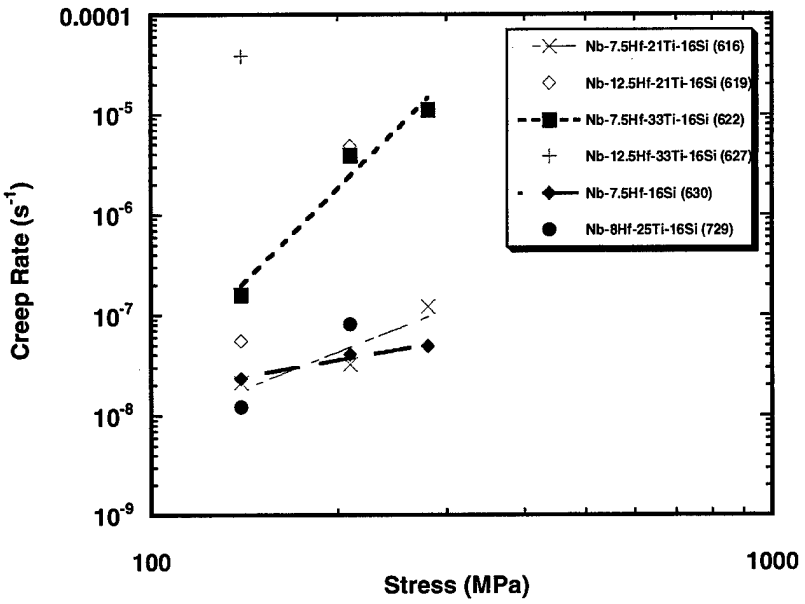


Figure 1 Graph of secondary creep rates at 1200°C for a range of quaternary Nb-Hf-Ti-Si alloys.

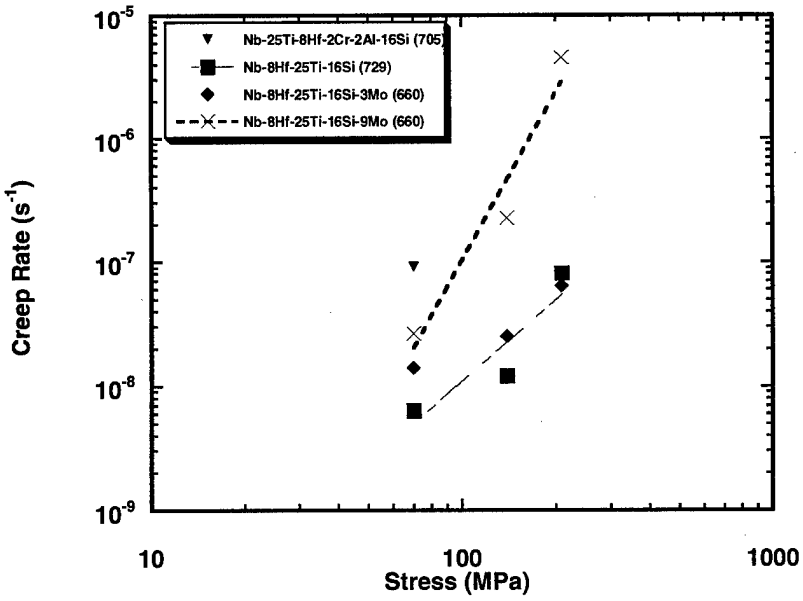


Figure 2 Graph of secondary creep rates at 1200°C for a range of Nb-Hf-Ti-Si alloys modified with Mo.

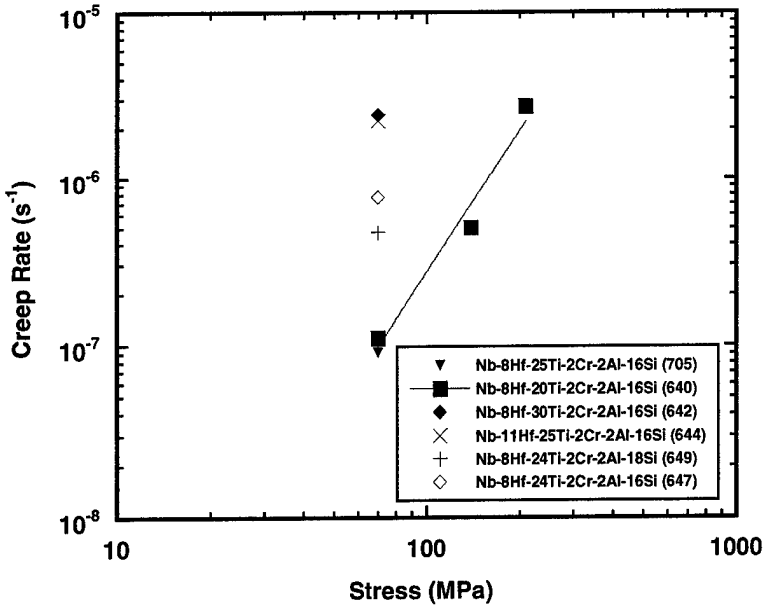


Figure 3 Graph of secondary creep rates at 1200°C for a range of Nb-Hf-Ti-Si-Cr-Al alloys.

Table 4 : Secondary creep rates at 1200°C for a range of Nb-Hf-Ti-Si alloys.

Composition	**140 MPa Creep Rate (s^{-1})**	**210 MPa Creep Rate (s^{-1})**	**280 MPa Creep Rate (s^{-1})**
Nb-7.5Hf-16Si	$2.3x10^{-8}$	$4.0x10^{-8}$	$4.8x10^{-8}$
Nb-7.5Hf-21Ti-16Si	$2.1x10^{-8}$	$3.2x10^{-8}$	$1.2x10^{-7}$
Nb-7.5Hf-33Ti-16Si	$1.6x10^{-7}$	$3.9x10^{-6}$	$1.1x10^{-5}$
Nb-12.5Hf-21Ti-16Si	$5.5x10^{-8}$	$4.8x10^{-6}$	--
Nb-12.5Hf-33Ti-16Si	$3.8x10^{-5}$	--	--
Nb-16Si	$1.5x10^{-8}$	$4.9x10^{-8}$	--

The data indicate that the Nb-7.5Hf-16Si and the Nb-16Si composites possessed the lowest creep rates and that at any selected stress level and Hf concentration the creep rate increased with increasing Ti concentration. Clearly, these alloying additions can have a

tremendous effect on the creep performance. For example, at 7.5Hf increasing the Ti concentration from 21 to 33% increased the creep rate from $2.1x10^{-8}s^{-1}$ to $1.6x10^{-7}s^{-1}$ at 140MPa. At stress levels of 210MPa and below there is little difference between the secondary creep rates of the Nb-7.5Hf-16Si and the Nb-7.5Hf-21Hf-16Si compositions. At higher stress levels there is a difference in the creep rates of these two compositions. Similarly, at Hf concentrations of 12.5 and stress levels of 140MPa, increasing the Ti concentration from 21 to 33% increases the creep rate from $5.5x10^{-8}s^{-1}$ to $3.8x10^{-5}s^{-1}$.

At any selected stress levels it also appears that increasing the Hf concentration leads to an increase in the creep rate. For example, at a stress level of 140 MPa and Ti concentration of 21%, increasing the Hf concentration from 7.5 to 12.5% increases the creep rate from $2.1x10^{-8}s^{-1}$ to $5.5x10^{-8}s^{-1}$, but there is a strong stress sensitivity of this effect, so that at 210MPa the creep rates are $3.2x10^{-8}s^{-1}$ and $4.8x10^{-6}s^{-1}$, i.e. Hf concentrations higher than 7.5% provide a strong sensitivity of the secondary creep rate to stress. However, the creep rates of the Nb-7.5Hf-21Ti-16Si are similar to those of the Nb-7.5Hf-16Si, and the stress sensitivity of the creep rates are similar for stresses in the range 140 to 280MPa.

These data suggest that for creep performance the Ti:Hf ratio should be maintained at a level less than 3 and the Ti concentration should be kept below 21%. The mechanisms that lead to increased creep rates at higher Ti or higher Hf concentrations are still under investigation. One of the effects that is significant is that at Nb : (Ti+Hf) ratios below a certain limit the hP16 Ti_5Si_3 type silicide is stabilized in preference to the tI32 Nb_5Si_3 type silicide. The Nb_5Si_3 has a higher melting temperature than either the Ti_5Si_3 or the Hf_5Si_3, and this probably contributes to the improved creep resistance. The Ti also reduces the melting temperature of the metallic toughening phase.

Mo-Modified Composites

The effect of Mo on the creep performance was investigated because it was considered that Mo can increase the strength of the metallic phase and it can also reduce creep deformation in Nb_5Si_3. Secondary creep rates are shown in Table 5 and 6 and Figure 2 for temperatures of 1100°C and 1200°C for Nb-8Hf-25Ti-16Si, as well as alloys containing 3% and 9% Mo (substituting Mo for Nb). Comparison of the creep rates of the Mo-modified alloys with those of the base Nb-8Hf-25Ti-16Si composite indicates that at any given set of creep conditions the creep rate increases with increasing Mo concentration from 0 to 3 to 9%. These trends were observed at both 1100 °C and 1200 °C.

Table 5 : Secondary creep rates at 1100°C for a range of Nb-Hf-Ti-Si alloys modified with Mo.

Composition	**70 MPa Creep Rate (s^{-1})**	**140 MPa Creep Rate (s^{-1})**	**210 MPa Creep Rate (s^{-1})**	**280 MPa Creep Rate (s^{-1})**
Nb-8Hf-25Ti-16Si	$1.6x10^{-9}$	$2.0x10^{-9}$	--	$2.9x10^{-9}$
Nb-3Mo-8Hf-21Ti -16Si	$5.2x10^{-9}$	$1.2x10^{-8}$	$1.3x10^{-8}$	$1.4x10^{-8}$
Nb-9Mo-8Hf-21Ti -16Si	--	$2.0x10^{-9}$	$1.4x10^{-8}$	$6.0x10^{-8}$
Nb-8Hf-25Ti-2Al-2Cr-16Si	$1.2x10^{-8}$	$5.0x10^{-8}$	$1.0x10^{-6}$	Fail

Table 6 : Secondary creep rates at 1200°C for a range of Nb-Hf-Ti-Si alloys modified with Mo.

Composition	**70 MPa Creep Rate (s^{-1})**	**140 MPa Creep Rate (s^{-1})**	**210 MPa Creep Rate (s^{-1})**	**280 MPa Creep Rate (s^{-1})**
Nb-7.5Hf-16Si	--	$2.3x10^{-8}$	$4.0x10^{-8}$	$4.8x10^{-8}$
Nb-8Hf-25Ti-16Si	$6.3x10^{-9}$	$1.2x10^{-8}$	$8.0x10^{-8}$	Fail
Nb-3Mo-8Hf-21Ti -16Si	$1.4x10^{-8}$	$2.5x10^{-8}$	$6.4x10^{-8}$	Fail
Nb-9Mo-8Hf-21Ti -16Si	$2.6x10^{-8}$	$2.2x10^{-7}$	$4.5x10^{-6}$	Fail
Nb-8Hf-25Ti-2Al-2Cr-16Si	$9.1x10^{-8}$	Fail	--	--
Nb-16Si	$1.7x10^{-9}$	$1.5x10^{-8}$	$4.9x10^{-8}$	--

It can be seen that the performance of the Nb-7.5Hf-16Si and the Nb-8Hf-25Ti-16Si are similar to the Nb-16Si, but at Mo concentrations greater than 3 the creep rates are increased. In comparison with the Nb-8Hf-25Ti-2Cr-2Al-16Si, the Mo additions have a less detrimental effect on the creep rate than the Cr and Al additions. However, unlike the Mo additions, the Cr and Al additions are required for oxidation resistance (they also appear to provide some toughening). It appears therefore that there is no net benefit associated with substitution of Mo for Nb. However, it is not clear why the substitution of Mo for Nb leads to an increase in the creep rate. Mo does stabilize the Nb_3Si phase in preference to Nb_5Si_3, and it may also lead to an increase in the volume fraction of the metallic phase. Both of these effects could have a detrimental effect on creep performance.

Six Element Alloy Composites

Secondary creep rates are shown at 1200 °C and stress levels in the range 70-280 MPa in Table 7 and Figure 3 for a range of composites derived from Nb-Hf-Ti-Cr-Al-Si alloys. Room temperature fracture toughness values are shown in Table 3 for these composites.

Table 7 : Secondary creep rates at 1200°C for a range of Nb-Hf-Ti-Si-Cr-Al alloys.

Composition	**70 MPa Creep Rate (s^{-1})**	**140 MPa Creep Rate (s^{-1})**	**210 MPa Creep Rate (s^{-1})**	**280 MPa Creep Rate (s^{-1})**
Nb-7.5Hf-16Si	--	$2.3x10^{-8}$	$4.0x10^{-8}$	$4.8x10^{-8}$
Nb-8Hf-20Ti-2Al-2Cr-16Si	$1.1x10^{-7}$	$5.0x10^{-7}$	$2.7x10^{-6}$	Fail
Nb-8Hf-30Ti-2Al-2Cr-16Si	$2.4x10^{-6}$	Fail	--	--
Nb-11Hf-25Ti-2Al-2Cr-16Si	$2.2x10^{-6}$	Fail	--	--
Nb-8Hf-24Ti-2Al-2Cr-16Si	$7.6x10^{-7}$	Fail	--	--
Nb-8Hf-24Ti-2Al-2Cr-16Si	$4.7x10^{-7}$	Fail	--	--
Nb-16Si	$1.7x10^{-9}$	$1.5x10^{-8}$	$4.9x10^{-8}$	--

Some important trends can be seen in these data. First, the creep rate increased with increasing Ti concentration from 20 to 30%. This may have been due in part to the larger volume fraction of Hf_5Si_3 type phase in the composite, as well as the lower melting temperature of the metallic phase.

The creep data also indicate that increasing the Si concentration from 16% to 18% (substituting Si for Nb) led to a slight reduction on creep rate at 1200 °C and 70MPa from $7.6x10^{-7}s^{-1}$ to $4.7x10^{-7}s^{-1}$. Lastly, substituting Hf for Nb appears to have a detrimental effect on the secondary creep rate; increasing the Hf concentration from 8 to 11% led to a change in the creep rate from $7.6x10^{-7}s^{-1}$ to $2.2x10^{-6}s^{-1}$ at 70MPa and 1200 °C. This was probably due to the reduction in the volume fraction of Nb_5Si_3 type and the increased volume fraction of Hf_5Si_3 type silicides. It appears that all the six element alloys have creep rates at 1200 °C that are at least an order of magnitude higher than those of the composite generated from the binary Nb-16Si alloy. Al does substitute for Si in the silicide and it may compromise the creep properties of the silicide.

At 1200°C and stress levels greater than 70MPa, composites from alloys with Ti concentrations greater than 20% and Hf concentrations greater than 8%, could not support a steady-state creep regime, and they proceeded directly from the primary to the tertiary creep regime, and they therefore experienced early failure. These observations regarding

the effects of Ti and Hf in these complex alloy composites are all consistent with those that were reported for the quaternary Nb-Hf-Ti-Si alloys.

Summary

The addition of Ti, Hf and Mo have a substantial effect on composite secondary creep rates. The threshold Hf, Ti and Mo concentrations above which the creep performance degenerates beyond that of the Nb-16Si composite have been defined, together with the appropriate stress levels for possible component operations. For example, the data indicate that the creep performance of the for Nb-8Hf-25Ti-16Si is compatible with the creep goals at temperatures up to 1200 °C.

3.4 Silicide Precipitates in Nb-Si and Nb-Ti-Si Alloys

The present section describes the chemistry and crystallography of precipitates that are generated in Nb solid solutions of DS composites of binary Nb-Si and ternary Nb-Ti-Si alloys.

Binary Nb_3Si Precipitates

The Nb-14%Si hypoeutectic alloy contains (Nb) dendrites and an inter-dendritic eutectic of (Nb) and Nb_3Si, as has been described previously [3-5]. The Nb dendrites are essentially single crystals: no subgrains have been observed. Heterogeneous precipitation of large-scale (~0.5μm) silicide precipitates was observed. These silicides possess the Nb_3Si stoichiometry; the precipitate composition was compared to the composition of the eutectic tetragonal tP32 Nb_3Si using EDS measurements taken from very thin regions at the edge of the foil. A typical group of large-scale silicide precipitates within the (Nb) dendrite of the Nb-14Si composite is shown in the attached paper (Figure 2). The principal axis of the large, central precipitate is parallel to the [010] in the (Nb). Secondary precipitates have grown off the large central precipitate in directions parallel to the [100] in the (Nb). Precipitate-free zones ~100nm wide were observed in the (Nb) around the silicide precipitates. In the (Nb) dendrite away from the large-scale silicide precipitates contrast was observed from finer-scale (~ 10nm) silicide precipitates.

Diffraction data show that these large-scale silicide precipitates possess an orthorhombic crystal structure. Extensive tilting experiments were performed to determine the point group and lattice parameters. The lattice parameters of the precipitate were determined to be a = 9.3Å, b = 3.4Å, c = 15.9Å, which approximately corresponds to factors of 3, 1, and 5 times that of the (Nb) lattice parameter. The point group was determined to be mmm,

and, based solely on the reflections observed to be absent in the microdiffraction patterns, it is suggested that the space group is Immm.

The following orientation relationship was observed between the precipitates and the (Nb) matrix :

$$[100]_{Nb} \,||\, [100]_{ppt} \,;\, (001)_{ppt} \,||\, (001)_{Nb}.$$

Mendiratta et al [3] have previously observed Si-rich particles in binary Nb-Si alloys, and they postulated that these precipitates were generated as a result of the decrease in the solubility of Si in (Nb) with decreasing temperature on cooling after a 1500°C heat treatment.

Ternary $(Nb,Ti)_3Si$ Precipitates

The microstructure of the DS Nb-44Ti-12Si consisted of non-faceted (Nb,Ti) dendrites (20-50μm), together with large-scale (~50 μm) faceted $(Nb,Ti)_3Si$ dendrites. A typical array of needle-shaped silicide precipitates within a (Nb,Ti) dendrite is shown in Figure 4. Precipitates can be seen in all three orthogonal directions. It can be seen that precipitation is generally homogeneous. There were also occasional groups of heterogeneously-nucleated precipitates surrounded by a precipitate-free zone.

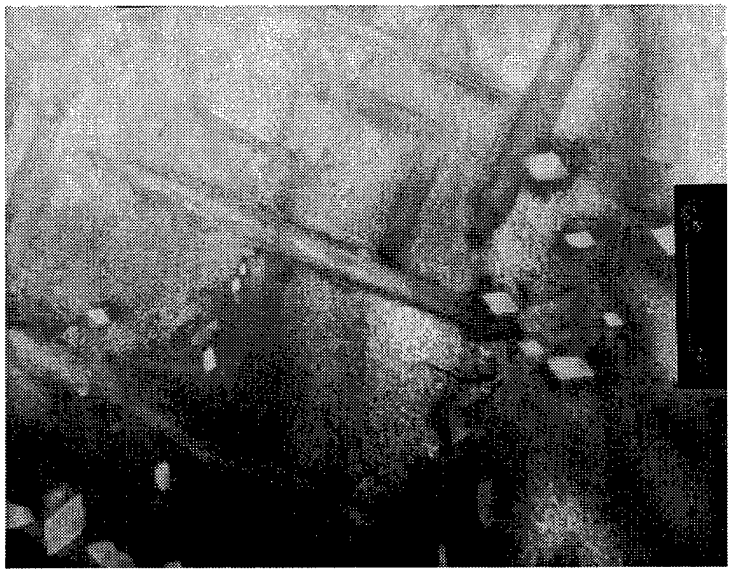


Figure 4 : Bright field transmission electron micrograph showing silicide precipitates in the (Nb,Ti,Si) of the Nb-42.5Ti-15Si composite heat treated at 1500°C for 100 hours followed by slow cooling to below 800°C.

The silicide precipitates in the (Nb,Ti) have the same orthorhombic crystal structure and orientation relationship with the (Nb,Ti) matrix as found in the binary alloy. The

precipitates are faceted, with facet faces parallel to $\{110\}_{ppt}$. Typically, the precipitates had a width of (~150nm) (facet-to-facet). Similar precipitates have also been observed in Nb-42.5Ti-15Si, Nb-1Si and other Nb-Ti-Si alloys in the DS condition, as well as after various heat treatments.

In the (Nb,Ti) it was expected that the precipitates would have the Nb_3Si type because additions of ≥17% Ti stabilize Nb_3Si in preference to Nb_5Si_3 [7]. However, in the binary alloy Nb_3Si is unstable below 1770°C. Thus, in the binary alloy, not only is the precipitate *composition* metastable with respect to Nb_5Si_3, but the *crystal structure* is also metastable with respect to the stable tP32 structure of Nb_3Si. There are two possible reasons for the occurrence of the orthorhombic Nb_3Si structure. First, the barrier for nucleation of the Nb_3Si may be lower because the Nb_3Si has a lower ordering energy than Nb_5Si_3. Second, the interfacial and strain energy terms may be lower because of close lattice matching of the precipitate and matrix. Simply from considerations of the mismatch between precipitate and matrix, it can be seen that the orthorhombic precipitates will be coherent with the matrix up to a certain size. No such simple orientation relationship exists between the (Nb) matrix and either tP32 Nb_3Si or tI32 Nb_5Si_3. This suggests that the barrier to nucleation of orthorhombic Nb_3Si may be significantly lower than the barrier to nucleation of either of the stable structures. Also, although the atomic structure of the precipitate has not been determined, the orthorhombic precipitates may be body-centered in structure, and thus may nucleate very easily by ordering of the bcc matrix, which could make the barrier to nucleation low.

Summary

Precipitates were observed in (Nb) and (Nb,Ti) of the in-situ composites of both binary Nb-Si and ternary Nb-Ti-Si alloys. The precipitates possessed an ordered orthorhombic structure, with lattice parameters of a = 9.3Å, b = 3.4Å, c = 15.9Å. The bulk Nb_3Si in the binary Nb-Si and the bulk $(Nb,Ti)_3Si$ in the Nb-Ti-Si alloys possessed the stable tP32 structure. The interfaces were semi-coherent for large precipitates and coherent for the very fine precipitates (5nm). Incoherent orthorhombic precipitates were not observed.

The $(Nb,Ti)_3Si$ precipitates are metastable with respect to the tP32 structure, but they possess the stable stoichiometry. The Nb_3Si precipitates are metastable with respect to both the stoichiometry and crystal structure of tI32 Nb_5Si_3. It is suggested that ordering to the metastable orthorhombic Nb_3Si on post-solidification cooling requires a smaller nucleation barrier than to the stable tI32 Nb_5Si_3, and the close matching of the lattice plane spacing of the matrix and precipitate allows the interfacial energy to be minimized.

3.4 Phase Stability Investigations

Several investigations of phase stability have been completed in the present contract year. These include, determination of solid-state phase equilibria in Nb-Ti-Si alloys, definition of silicide stability in the binary Hf-Si system, description of the Nb-Hf-Si liquidus surface. Significant effort has been placed on defining phase stability in the Nb-Ti-Si and Nb-Hf-Si systems, because Ti and Hf additions to Nb-Si based composites have been shown to provide improvements in fracture toughness, tensile strength, creep performance, and oxidation behavior [1, 5, 7]. Phase stability information is a critical requirement for definition of both the manufacture of these high-temperature in-situ composite systems, and their stability during service.

Nb-Hf-Si Ternary Phase Stability

Hf is an important alloying addition to in-situ composites based on Nb-Si alloys because it improves oxidation resistance and strength. However, there is little previous knowledge of phase equilibria in the Nb-Hf-Si system [8]. Knowledge of the Nb-Hf-Si liquidus surface is required in order to predict the phase content and volume fractions of phases in these in-situ composites.

Several options were considered for the liquidus surface of the Nb-Hf-Si system. Of these options, Figure 5 represents the proposed liquidus projection that is the most consistent with the data that have been obtained.

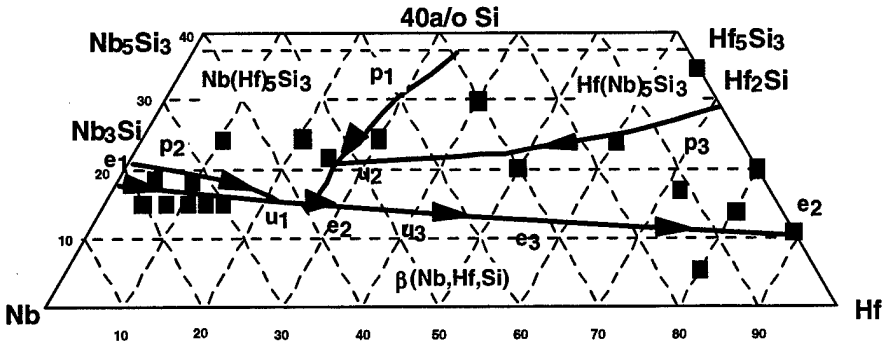


Figure 5 Schematic diagram showing the projection of the Nb-Hf-Si liquidus surface. The projection shows the peritectic ridges, p_1, p_2, p_3, the eutectic valleys, e_1, e_2, e_3, and the invariant reactions, U_1, U_2, U_3. The actual compositions investigated and are also shown.

At the metal-rich end of the Nb-Hf-Si ternary phase diagram there is a eutectic trough between the two binary eutectics [9]. However, because of the different binary eutectic reactions there is a change in the nature of the liquidus surface, and the eutectic groove,

with decreasing Nb and increasing Hf concentration. There is only a 50°C difference in temperatures of these two binary eutectics [9], and the slope of this trough is therefore very shallow. The loci of the peritectic ridge from the L+ Nb_5Si_3 --> Nb_3Si peritectic, p_2, the L + Hf_5Si_3 -->Hf_2Si peritectic ridge, p_3, the Hf-Hf_2Si eutectic groove, e_3, and the locations of the three transition reactions that occur are complex, and particular emphasis has been placed on these features in the present study. For the purpose of the present discussion, a peritectic, p_1, L + Nb(Hf)$_5Si_3$ --> Hf(Nb)$_5Si_3$ is assumed between Nb(Hf)$_5Si_3$ and Hf(Nb)$_5Si_3$. However, either a eutectic or a peritectic reaction between Nb(Hf)$_5Si_3$ and Hf(Nb)$_5Si_3$ provide a groove, or ridge, that falls towards the valley between the binary eutectics, as shown in Figure 5.

The transition reactions are shown below. In Figure 5, the peritectic ridge, p_2, intersects the eutectic groove, e_1, to generate U_1. The peritectic ridges, p_1 and p_3, intersect to generate U_2, and the subsequent ridge intersects the eutectic groove, e_1, to generate U_3. The alloy compositions that were investigated are shown as the solid points on the liquidus surface projections in Figure 5. The data that will be discussed subsequently indicate that this is the correct version of the liquidus surface.

U_1 $\quad L + Nb(Hf)_5Si_3 \rightarrow Nb(Hf)_3Si + \beta(Nb,Hf,Si)$

U_2 $\quad L + Hf(Nb)_5Si_3 \rightarrow Nb(Hf)_5Si_3 + Hf(Nb)_2Si$

U_3 $\quad L + Nb(Hf)_5Si_3 \rightarrow \beta(Nb,Hf,Si) + Hf(Nb)_2Si$

This work has been prepared for publication and will be submitted for external publication in the next month.

Results and Discussion

Microstructural and microchemical evidence for the solidification paths is presented first for the Nb-rich alloys, second for the Nb_3Si-rich alloys, third for the Nb_5Si_3-rich alloys, fourth for the Hf_5Si_3-rich compositions, fifth for the Hf_2Si-rich compositions, and finally for Hf-rich compositions.

Nb-Rich Compositions : Group 1

This regime contained primary β(Nb,Hf,Si) dendrites with Nb(Hf)$_3Si$-β(Nb,Hf,Si) eutectic. Ternary Nb-Hf-Si alloys with Hf concentrations of 5-15 and Si concentrations of 16 were examined.

The typical microstructure of the transverse section is shown in Figure 6 for the Nb-15Hf-16Si composition. The microstructure consisted of a small volume fraction of primary β(Nb,Hf,Si) dendrites, which are the dark grey phase in the BSE micrograph, together with an interdendritic Nb(Hf)$_3Si$-β(Nb,Hf,Si) cellular eutectic. The Nb-15Hf-16Si composition also appeared to contain a small volume fraction of intercellular eutectic of Nb(Hf)$_5Si_3$ and β(Nb,Hf,Si), which suggests that the liquid composition of Nb-15Hf-16Si passed through the invariant reaction U_1.

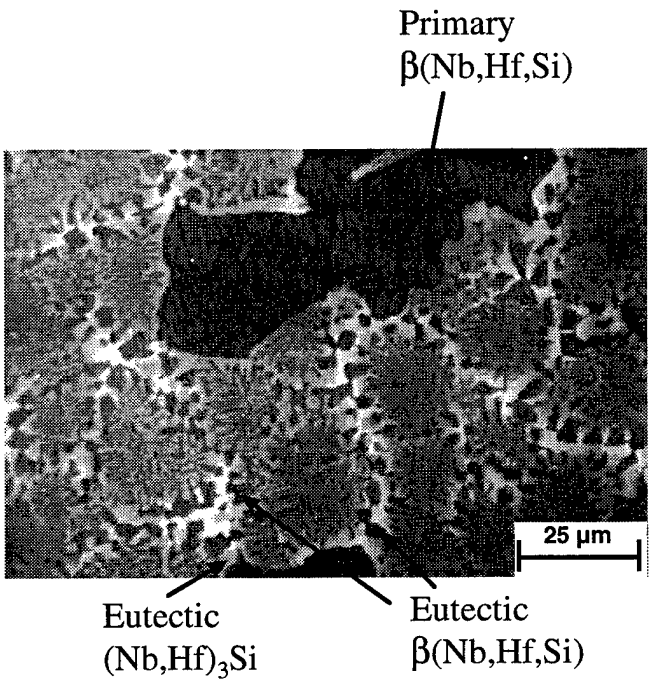


Figure 6 Typical microstructure (BSE image) of the transverse section of a DS Nb-15Hf-16Si alloy. There are large-scale dark β(Nb,Hf,Si) dendrites with interdendritic eutectic cells of Nb(Hf)3Si (light grey) and β(Nb,Hf,Si).

Nb(Hf)3Si -Rich Compositions : Group 2

This regime contained primary Nb(Hf)3Si dendrites with Nb(Hf)3Si-β(Nb,Hf,Si) eutectic. Two compositions were examined from this region, Nb-5Hf-19Si and Nb-10Hf-18.5Si. The primary solidification phase was faceted dendrites of Nb(Hf)3Si. The interdendritic eutectic consisted of Nb(Hf)3Si- β(Nb,Hf,Si) eutectic cells, and there was heavy segregation of Hf to the cell boundaries.

Nb(Hf)5Si3 -Rich Compositions : GROUP 3

This regime contained primary Nb(Hf)5Si3 dendrites, peritectic Nb(Hf)3Si, and Nb(Hf)3Si- β(Nb,Hf,Si) eutectic. Three compositions were examined from this regime Nb-10Hf-25Si, Nb-20Hf-25Si, Nb-25Hf-22Si.

The typical microstructure of the transverse section of the DS Nb-10Hf-25Si alloy is shown in Figure 7. The large black phase is Nb(Hf)5Si3, and it is surrounded by dark grey peritectic Nb(Hf)3Si. This composition has experienced the peritectic reaction, L + Nb(Hf)5Si3 --> Nb(Hf)3Si. The peritectic and dendritic Nb(Hf)3Si appears to have grown in a coupled manner with the β(Nb,Hf,Si) dendrites (light phase). Hf partitioning between the Nb(Hf)3Si and β(Nb,Hf,Si) was such that there was little contrast between

these two phases. The Nb(Hf)3Si also contained some brighter regions that were probably Hf rich.

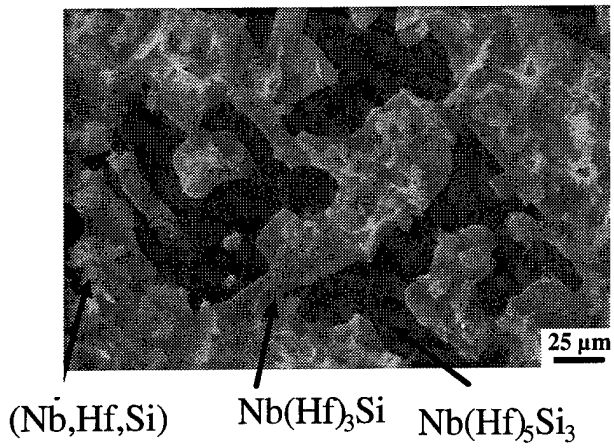


Figure 7 Typical microstructures (BSE images) of the transverse section of a DS Nb-10Hf-25Si alloy. The large black phase is Nb(Hf)5Si3, the large dark grey phase is Nb(Hf)3Si, and the light grey phase is β(Nb,Hf,Si).

The primary Nb(Hf)5Si3 had a composition of Nb-10.6Hf-36.5Si, and the peritectic Nb(Hf)3Si had a composition of Nb-9.3Hf-24.0Si. The eutectic Nb(Hf)3Si possessed more Hf than the peritectic, the typical composition being Nb-12.0Hf-24.3Si, although in some of the brighter regions of Figure 7 the Hf concentration was even higher than 12.0. The composition β(Nb,Hf,Si) was Nb-8.2Hf-1.5Si; the Si concentration was typically slightly lower in the Nb-rich β(Nb,Hf,Si) than in the Hf-rich β.

The microstructure of the Nb-25Hf-22Si alloy consisted of large grey faceted dendrites with an interdendritic eutectic of Nb(Hf)5Si3 and β(Nb,Hf,Si). The β(Nb,Hf,Si) appeared to be the discontinuous phase in the Nb(Hf)5Si3 matrix. The eutectic β(Nb,Hf,Si) was darker than the primary Nb(Hf)5Si3 dendrites; the composition of the primary Nb(Hf)5Si3 was Nb-27.6Hf-36.5Si. The composition of the eutectic β(Nb,Hf,Si) was Nb-21.0Hf-1.1Si, and the eutectic Nb(Hf)5Si3 was Nb-29.9Hf-36.6Si. Thus, the Hf concentration of the Nb-25Hf-22Si is sufficiently Hf rich that on solidification the composition of the liquid moves directly into the eutectic valley, e_2, and it misses the peritectic ridge, p_2, as well as e_1 and U_1.

$Hf(Nb)_5Si_3$ -Rich Compositions : GROUP 4

This regime contained primary $Hf(Nb)_5Si_3$ dendrites, peritectic $Hf(Nb)_2Si$, and β(Nb,Hf,Si)-$Hf(Nb)_2Si$ eutectic. Two ternary compositions were examined from this regime Nb-30Hf-25Si and Nb-40Hf-30Si. The binary Hf-35Si alloy was also examined.

The Nb-30Hf-25Si contained a large volume fraction of β(Nb,Hf,Si)-$Hf(Nb)_2Si$ eutectic, and small volume fractions of peritectic $Hf(Nb)_2Si$ and primary $Hf(Nb)_5Si_3$ dendrites. This suggests that the Nb-30Hf-25Si composition is close to the L+ $Hf(Nb)_5Si_3 \rightarrow Hf(Nb)_2Si$ peritectic ridge, and that the peritectic ridge is close to the eutectic valley.

$Hf(Nb)_2Si$ -Rich Compositions : GROUP 5

This regime contained primary $Hf(Nb)_2Si$ dendrites, and the β(Nb,Hf,Si)-$Hf(Nb)_2Si$ eutectic. Four ternary compositions were examined from this regime Nb-60Hf-25Si, Nb-50Hf-20Si, Nb-73Hf-17Si, and Nb-80Hf-14Si. In addition, two binary compositions were also examined, Hf-20Si and Hf-12Si.

The microstructure of the Nb-60Hf-25Si consisted of a large volume fraction of faceted primary $Hf(Nb)_2Si$ dendrites, with an interdendritic eutectic of β(Nb,Hf,Si) and $Hf(Nb)_2Si$. The eutectic β(Nb,Hf,Si) showed no apparent solid-state transformation in the as-solidified sample.

The microstructure of the Nb-80Hf-14Si alloy contained primary $Hf(Nb)_2Si$ faceted dendrites with an interdendritic eutectic of β(Nb,Hf,Si) and fine-scale (~2 μm) $Hf(Nb)_2Si$. On post-solidification cooling the β(Nb,Hf,Si) metal transformed to α(Nb,Hf,Si) and β (Nb,Hf,Si). The Nb-80Hf-14Si composition is on the Si-rich side of the β(Nb,Hf,Si)-$Hf(Nb)_2Si$ eutectic trough. This suggests an increase in the Si composition of the eutectic trough with increasing Nb concentration from the binary Hf-Hf_2Si eutectic.

Hf-Rich Nb-Hf-Si Compositions : Group 6

This group consists of Hf-rich compositions from the metal-rich side of the eutectic valley. The alloys contained primary β(Nb,Hf,Si) dendrites, and β(Nb,Hf,Si)-$Hf(Nb)_2Si$ eutectic. However, the dendritic and eutectic β(Nb,Hf,Si) experienced the β–α allotropic phase transformation on post solidification cooling, unlike the β(Nb,Hf,Si) in the Nb-rich compositions. This group is distinguished from Group 1 by, (a) transformation of the primary β(Nb,Hf,Si), and (b) the presence of the β(Nb,Hf,Si)-$Hf(Nb)_2Si$ interdendritic eutectic. The microstructure of the Nb-80Hf-5Si alloy is an example of an alloy from this region that was examined.

4.0 Summary

Microstructural, microchemical and crystallographic (XRD and EBSP) evidence indicate that the liquidus surface of the Nb-Hf-Si ternary phase diagram possesses the following reactions :

$L + Nb(Hf)_5Si_3 \rightarrow Hf(Nb)_5Si_3$ peritectic (assumed)

$L + Nb(Hf)_5Si_3 \rightarrow Nb(Hf)_3Si$ peritectic

$L \rightarrow Nb(Hf)_3Si + \beta(Nb,Ti,Si)$ eutectic

$L \rightarrow Nb(Hf)_5Si_3 + \beta(Nb,Ti,Si)$ eutectic

$L + Hf(Nb)_5Si_3 \rightarrow Hf(Nb)_2Si$ peritectic

$L + Nb(Hf)_5Si_3 \rightarrow Hf(Nb)_2Si$ peritectic (assumed)

$L \rightarrow \beta(Nb,Hf,Si) + Hf(Nb)_2Si$ eutectic

These reactions give rise to the following three transition reactions :

$L + Nb(Hf)_5Si_3 \rightarrow Nb(Hf)_3Si + \beta(Nb,Hf,Si)$

$L + Hf(Nb)_5Si_3 \rightarrow Hf(Nb)_2Si + Nb(Hf)_5Si_3$

$L + Nb(Hf)_5Si_3 \rightarrow \beta(Nb,Hf,Si) + Hf(Nb)_2Si$

The first of these transition reactions occurs at a composition of approximately Nb-21Hf-16Si, and at a temperature between ~1850°C. The second of these transition reactions occurs at a composition of approximately Nb-27Hf-22Si, and a temperature of ~2040°C. The third transition reaction occurs Nb-39Hf-14Si, and a temperature of ~1840°C.

References

[1] B.P. Bewlay, M.R. Jackson, W.J. Reeder, and H.A. Lipsitt, MRS Proceedings on High Temperature Ordered Intermetallic Alloys VI, 1994, Vol. 364, pp. 943-948.

[2] B.P. Bewlay, M.R. Jackson and H.A. Lipsitt, *Metall. and Mater. Trans.*, 1996, Vol 279, pp. 3801-3808.

[3] M.G. Mendiratta, J.J. Lewandowski and D.M. Dimiduk, *Metall. Trans. 22A* (1991), pp. 1573-1581.

[4] M.R. Jackson, B.P. Bewlay, R.G. Rowe, D.W. Skelly, and H.A. Lipsitt, J. of Metals 48 (1), (1996), pp. 38-44.

[5] P.R. Subramanian, M.G. Mendiratta and D.M. Dimiduk, *Mat. Res. Soc. Symp. Proc.,* 322 (1994), pp. 491-502.

[6] P.R. Subramanian, T.A. Parthasarathy, and M.G. Mendiratta, Scritpa Met. and Mater., Vol. 32(8), pp. 39-54.

[7] B.P. Bewlay, M.R. Jackson and H.A. Lipsitt, *Journal of Phase Equilibria,* Vol 18(3), 1997, pp. 264-278.

[8] A. Gokhale and R. Abbaschian, Bulletin of Alloy Phase Diagrams, 10, Vol. 4, pp. 390-393, 1989.

[9] B.P. Bewlay, R.R. Bishop and M.R. Jackson, submitted to Journal of Phase Equilibria, 1998.

4.0 Collaborations

Throughout the past year of the present program there have been numerous interactions with scientists at universities and the AF laboratories. There has been regular exchange of samples, data, and interpretations with staff at Case Western Reserve University, Ohio State University, Brown University, and UES. The results of the collaborations have been presented at international conferences and published in the open literature; this will be continued in the following year of the present contract.

5.0 Publications

The following articles have been published in refereed journals and conference proceedings during the last year of research in the area of the present contract. Reprints of these articles have been attached to the present report.

1. B.P. Bewlay, R.R. Bishop and M.R. Jackson, "The Nb-Ti-Si Ternary Phase Diagram : Determination of Solid State Phase Equlibria in Nb and Ti Rich Alloys", Journal of Phase Equilibria, Accepted for publication, April 1998.

2. B.P. Bewlay, M.R. Jackson and H.A. Lipsitt, "Directionally Solidified High-Temperature In-Situ Composites and Their Applications", Proceedings of the Fifth International Conference on Composites Engineering, pp. 59-61, 1998.

3. B.P. Bewlay, J.A. Sutliff, and R.R. Bishop, "Evidence For the Existence of Hf_5Si_3", Submitted to the Journal of Phase Equilibria, January 1998.

4. B.P. Bewlay and J.A. Sutliff, " Microstructure and Microtexture in Nb-Silicide Based Composites", Microscopy and Microanalysis, vol. 4, Supplement 2, 1998, pp. 278-279.

5. R.J. Grylls, B.P. Bewlay, H.L. Fraser and H.A. Lipsitt, "Characterisation of Silicide Precipitates in Nb-Si and Nb-Ti-Si Alloys", Submitted to the Philosophical Magazine, August 1998.

6. G. A. Henshall, M. J. Strum, B. P. Bewlay and J. A. Sutliff, "Ductile-Phase Toughening in V-V_3Si In-Situ Composites", *Metall. and Mater. Trans.*, Vol. 28A, 1997, pp. 2555-2564.

7. B.P. Bewlay, R.R. Bishop and M.R. Jackson, "The Nb-Hf-Si Ternary Phase Diagram : Liquid-Solid Phase Equilibria In Nb and Hf Rich Alloys", to be submitted to the Journal of Phase Equilibria, September 1998.

8. B.P. Bewlay and M.R. Jackson "High-Temperature Directionally Solidified In-Situ Composites : Processing and Properties", to be published in "Comprehensive Composite Materials", A Kelly and C. Zweben (eds.) "Volume 3 - Metal Matrix Composites", T.W.Clyne (ed.), Elsevier (2000).

6.0 Presentations

The following presentations have either been given during the last year of the present contract, or they are scheduled to be given during the next six months. Both invited and contributed papers are shown.

1. B.P. Bewlay and M.R. Jackson, "High-Temperature Silicide-Based In-Situ Composites", 1998 Spring Technical Symposium on High Temperature Materials: Processing Methods and Properties sponsored by the Eastern New York Chapter of ASM International and Hudson-Mohawk Chapter of TMS. (Invited).

2. B.P. Bewlay and M.R. Jackson, "Niobium Silicide-Based In-Situ Composites", Birmingham University, Interdisciplinary Research Centre for High-Temperature Structural Materials, May 1998. (Invited).

3. B.P. Bewlay, M.R. Jackson and H.A. Lipsitt, "Directionally Solidified High-Temperature In-Situ Composites and Their Applications", presented at the Fifth International Conference on Composites Engineering, Las Vegas, July 1998. (Invited).

4. B.P. Bewlay and M.R. Jackson, "Directionally Solidified Niobium Silicide In-Situ Composites: Processing and Properties", Brown University, October1998. (Invited).

5. R. J. Grylls, B.P. Bewlay, H.A. Lipsitt and H.L. Fraser, "Observations of the Fracture Processes in Nb-Si In-Situ Composite Using Cross-Sectional Electron Microscopy", to be presented at the 1998 TMS Fall symposium on, "Mechanisms and Mechanics of Composite Fracture".

6. B.P. Bewlay, P.Whiting and C.L. Briant, "Creep Mechanisms in Niobium-Silicide Based In-Situ Composites", to be presented at the MRS Symposium on High Temperature Ordered Intermetallic Alloys VIII, Boston, December 1998.

7. R.J. Grylls, B.P. Bewlay, H.L. Fraser and H.A. Lipsitt, "On the Formation of Silicide Precipitates in Nb-Si-Based Composites", to be presented at the MRS Symposium on High Temperature Ordered Intermetallic Alloys VIII, Boston, December 1998.

8. J-C. Zhao, B.P. Bewlay, and M.R. Jackson, "Determination of the Effect of Hf Additions on Phase Stability in Nb-Silicide Based In-Situ Composites", to be presented at the MRS Symposium on High Temperature Ordered Intermetallic Alloys VIII, Boston, December 1998.

9. B.P. Bewlay, R. J. Grylls and H.L. Fraser, "Formation of Silicide Precipitates in Nb-Si-Based In-Situ Composites", to be presented at the 1999 TMS Annual Meeting Symposium on "Structural Silicides", San Diego 1999.

10. B.P. Bewlay and M.R. Jackson , "A Review of Niobium Silicide-Based In-Situ Composites", to be presented at the 1999 TMS Annual Meeting Symposium on "Structural Silicides", San Diego 1999. (Invited)

11. B.P. Bewlay, R. J. Grylls and H.L. Fraser, "Observations of the Fracture Behavior of Nb-Si In-Situ Composites Using Cross-Sectional Electron Microscopy", to be presented at the 1999 TMS Annual Meeting Symposium on "Structural Silicides", San Diego 1999.

12. P.W. Whiting, B.P. Bewlay and C.L. Briant , "Creep Mechanisms in Niobium-Silicide Based In-Situ Composites", to be presented at the 1999 TMS Annual Meeting Symposium on "Structural Silicides", San Diego 1999.

7.0 Technology Transfers and Transitions

Nb-base silicide intermetallic composites that are being investigated in this program are targeted for aircraft engine applications. The near-term application is for the Integrated High Performance Turbine Engine Technology (IHPTET) joint services (Air Force, Navy, Army, and NASA) program. The team of GE Aircraft Engines and Allison Advanced

Development Company has selected these Nb-base silicide intermetallic composites for the proposed full demonstration of IHPTET Phase III goals as the primary material for the high pressure turbine (HPT) blades, and as the back-up material for HPT vanes. Toughness and creep properties demonstrated in the current program, as well as other efforts in oxidation and fatigue of these materials, have resulted in their selection for IHPTET demonstration.

Primary Contact :

Bernard P. Bewlay,
GE Corporate Research and Development
PO Box 8
Schenectady
NY12301

Tel : 518 387 6121

The Nb-Ti-Si Ternary Phase Diagram: Determination of Solid State Phase Equlibria in Nb and Ti Rich Alloys

B.P. Bewlay, R.R. Bishop and M.R. Jackson

Journal of Phase Equilibria, 1998

The Nb-Ti-Si Ternary Phase Diagram: Determination of Solid-State Phase Equilibria in Nb- and Ti-Rich Alloys

B.P. Bewlay and M.R. Jackson
General Electric Company, Corporate Research and Development
Schenectady, NY 12301
and
R.R. Bishop
Department of Materials Engineering
Northwestern University, Evanston, IL 60208

(Submitted 10 November 1997; in revised form 8 May 1998)

Ternary Nb-Ti-Si phase equilibria have been investigated for the metal-rich end of the ternary phase diagram using scanning electron microscopy, XRD, and electron beam microprobe analysis. Microstructural and microchemical observations have been used to define isothermal sections at temperatures of 1500 and 1340 °C. These temperatures delineate regimes defined by liquid-solid reactions. Additional isothermal sections were estimated at 1350, 1320, and 1150 °C using these data. A broad range of Nb and Ti compositions were investigated for Si concentrations up to 35.0%. Alloys containing up to four phases, $Nb(Ti)_5Si_3$, $Ti(Nb)_5Si_3$, $(Nb,Ti)_3Si$, and (Nb,Ti,Si) were studied. The effect of Ti on the eutectoid reaction, $(Nb,Ti)_3Si \rightarrow (Nb,Ti,Si) + Nb(Ti)_5Si_3$ was investigated, as was the effect of Nb on the peritectoid reaction, $Ti(Nb)_5Si_3 + (Nb,Ti,Si) \rightarrow (Nb,Ti)_3Si$.

1. Introduction

Composites based on refractory metals and refractory metal silicides, such as Nb-Nb_3Si in situ composites, are presently under investigation for high-temperature applications because of their high melting temperatures (>1600 °C) and high-temperature strength retention. Ternary Nb-Ti-Si alloys have been used to generate in situ composites that have displayed an attractive combination of low-temperature and high-temperature mechanical properties, together with promising environmental resistance (Ref 1-3). Phase stability of these composites upon high-temperature exposure (>1300 °C) during service is a critical property. Thus, ternary Nb-Ti-Si phase equilibria at temperatures greater than 1300 °C have been examined and are described in this article.

There has been limited previous work on Nb-Ti-Si ternary phase equilibria (Ref 1, 2, 4). A space diagram of the metal-rich region (up to 37.5% Si—all compositions are given in atomic percent) of the proposed Nb-Ti-Si phase diagram is shown in Fig. 1 (Ref 4). Five phases are considered in the present paper: a (Nb,Ti,Si) solid-solution, Nb_3Si, Nb_5Si_3, Ti_5Si_3, and Ti_3Si. Nb_5Si_3 and Ti_5Si_3 are not isomorphous and have *I*32 and *hP*16 crystal structures, respectively (Ref 5).

In this article, the Nb_5Si_3 with Ti in solid solution is referred to as $Nb(Ti)_5Si_3$, and the Ti_5Si_3 with Nb in solid solution is referred to as $Ti(Nb)_5Si_3$. The Nb_3Si with Ti in solid solution is referred to as $(Nb,Ti)_3Si$, because Nb_3Si and Ti_3Si are isomorphous. Similarly, Nb with Ti and Si in the bcc solid solution is referred to as (Nb,Ti,Si). The compositions of all the phases possess a wide range of Nb:Ti ratios; the order of the elements in the phase description (i.e., Nb, Ti) should not be taken to reflect the relative concentrations of these elements in the respective phases. The individual phases can be clearly distinguished in the composite microstructures by their morphology, scale, and contrast using backscatter electron imaging (BSE) in the scanning electron microscope (SEM).

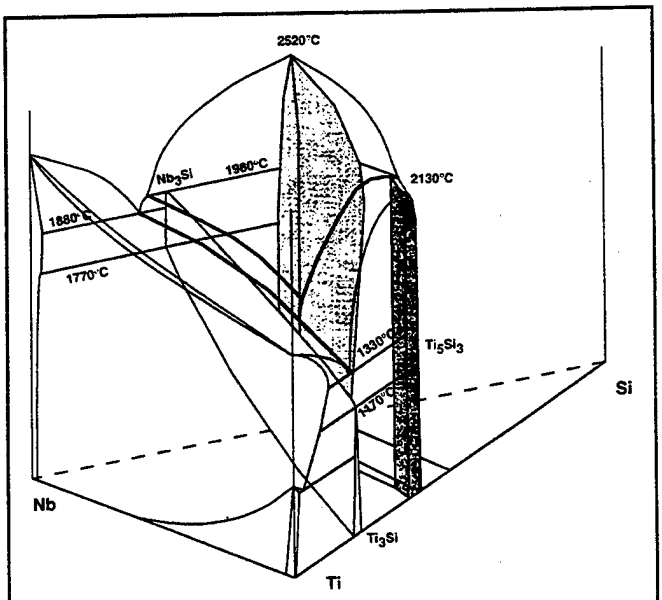


Fig. 1 Proposed Nb-Ti-Si ternary phase diagram for compositions between 0 and 37.5% Si.

2. Background on Nb-Ti-Si Phase Equilibria

The liquid-solid phase equilibria in the Nb-Ti-Si system have been described in detail in Ref 4. There are several reactions in the binary Nb-Si and Ti-Si systems that are relevant to the metal-rich end of the ternary system. First, there is the L → Ti_5Si_3 + (Ti) binary eutectic at 1330 °C (Ref 5). Second, the binary Nb-Si phase diagram (Ref 5) possesses a eutectic of the form L → Nb_3Si + (Nb) at 1880 °C, and also a peritectic of the form L + Nb_5Si_3 → Nb_3Si at 1980 °C. Ti_3Si forms by a peritectoid reaction between Ti_5Si_3 and Ti at a temperature of 1170 °C. It is assumed that the Nb and Ti form a continuous bcc solid solution (Ref 5). Although Ti_3Si and Nb_3Si are isomorphous, Nb_3Si is only stable over the temperature range 1980 to 1770 °C, and Ti_3Si is only stable below 1170 °C. The partial Scheil reaction scheme for the Si-lean region of the Nb-Ti-Si ternary has been described previously (Ref 4).

In the ternary phase diagram, a eutectic groove extends between the two binary eutectics, but due to the different binary eutectic reactions there is a change in the nature of the liquidus surface, and the eutectic groove, with decreasing Nb and increasing Ti concentration. This leads to two transition reactions (Ref 6) as shown in Fig. 2 at temperatures of 1650 and 1350 °C (Ref 4), and these have a strong influence on the nature of the isothermal sections at temperatures between 1650 and 1320 °C.

Isothermal sections at temperatures of 1500, 1350, 1340, 1320, and 1150 °C are shown in Fig. 3. The temperature of 1500 °C was selected because it describes the phase equilibria between the two transition reactions (Ref 4), and it is representative of all isothermal sections between temperatures of 1650 and 1350 °C. The isothermal section at 1350 °C represents phase equilibria at the second transition reaction (Ref 4). The isothermal section at 1340 °C was selected because it represents phase equilibria between the second transition reaction and the L → Ti_5Si_3 + (Ti) binary eutectic that occurs at 1330 °C (Ref 4, 5). The positions of the two- and three-phase fields at this temperature are similar to those at the second transition reaction temperature. The isothermal section at 1320 °C is shown because it is below the L → Ti_5Si_3 + (Ti) binary eutectic, but it is above the binary (Ti) + Ti_5Si_3 → Ti_3Si peritectoid temperature (Ref 5). It is the first isothermal section on descending temperature that does not possess a liquid region. The isothermal section at 1150 °C was selected because it is below the binary (Ti) + Ti_5Si_3 → Ti_3Si peritectoid. This last isothermal section represents the phase equilibria between this temperature and room temperature. The allotropic phase transformation in Ti-rich solid solutions is not described. The bulk compositions that were investigated are shown by solid circles in Fig. 3. Based on thermodynamic descriptions of the Nb-Si, Ti-Si and Nb-Ti binary systems, Liang and Chang (Ref 7) calculated the Nb-Ti-Si phase diagram recently.

This article describes the data that were obtained and how the isothermal sections for temperatures from 1500 to 1150 °C were constructed. In all the isothermal sections $(Nb,Ti)_3Si$ is shown as a line compound. This may not be accurate, but the data that were obtained were insufficient to provide a more complete definition of the $(Nb,Ti)_3Si$ homogeneity range.

3. Experimental

Samples for phase equilibrium studies were directionally solidified (DS) by cold crucible directional solidification (Ref 2) after triple melting the starting charges from high-purity elements (>99.99%). The directional solidification procedure that was used has been described in Ref 2. Samples for heat treatment at 1340 and 1500 °C were wrapped in Nb foil and heat treated for at least 100 h. All samples were examined with SEM (BSE) and energy dispersive spectrometry (EDS). In the case of selected alloys, electron beam microprobe analysis (EMPA) and XRD were also performed in order to determine the chemistry and crystal structure of the individual phases. The compositions that were investigated are listed in Table 1. Only compositions with Si concentrations less than 37.5% were considered in the present study. The sum of the concentrations of the interstitials of the starting elements (C, N, O, H) was less than 80 ppm.

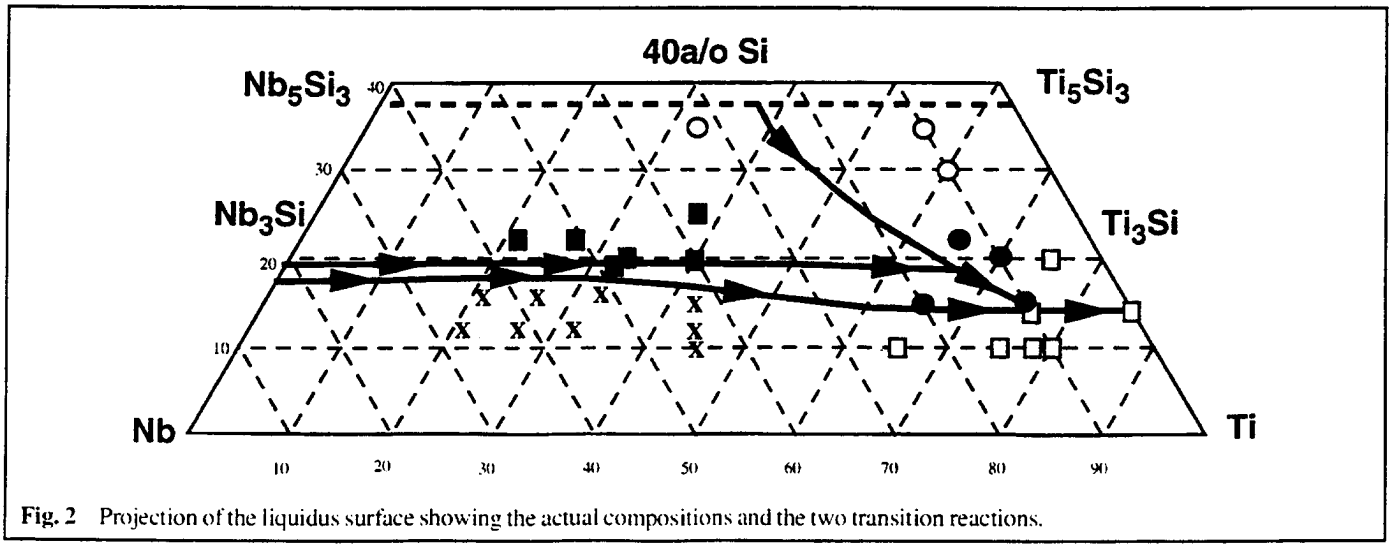


Fig. 2 Projection of the liquidus surface showing the actual compositions and the two transition reactions.

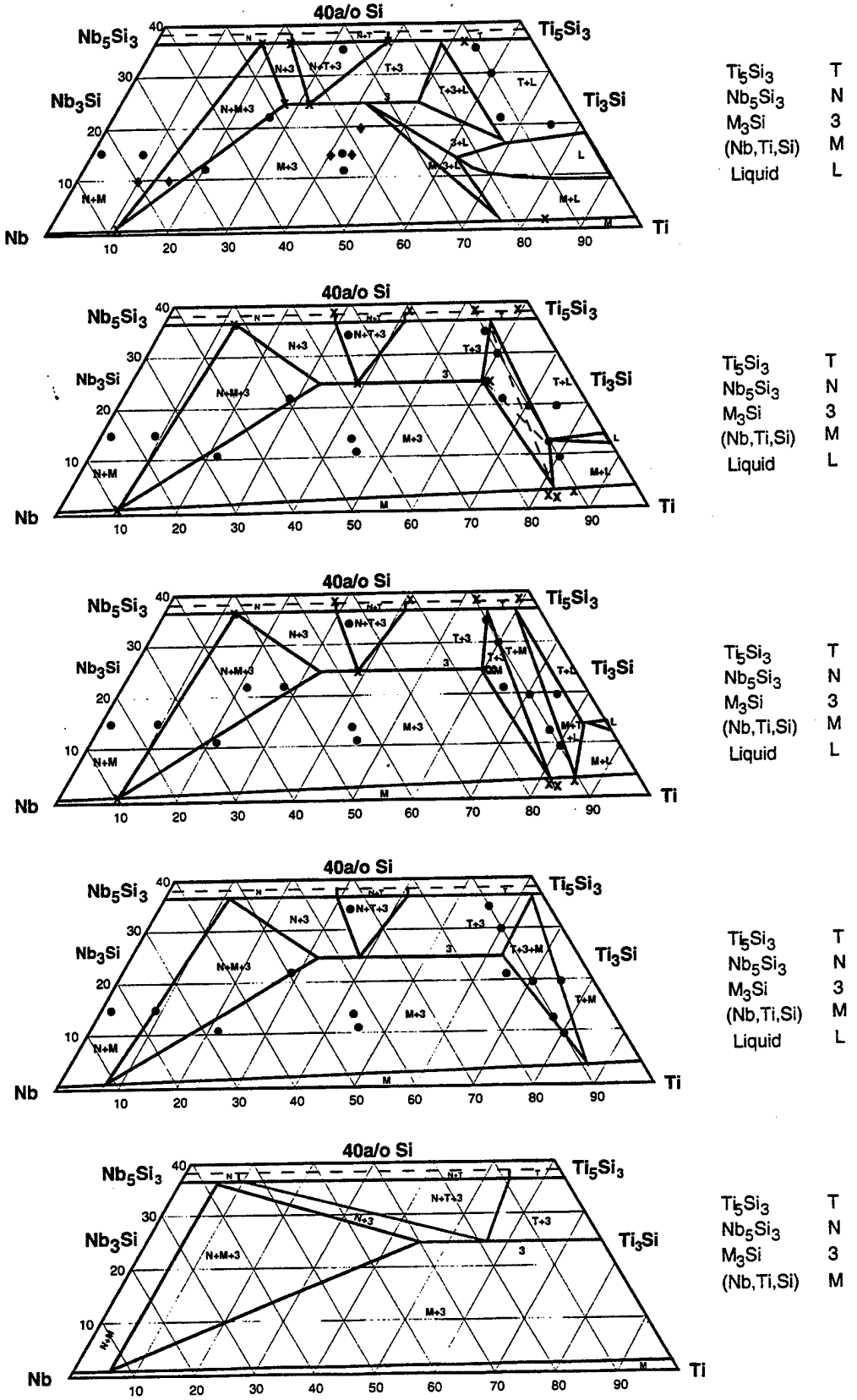


Fig. 3 Isothermal sections of the Nb-Ti-Si phase diagram at temperatures of **(a)** 1500 °C, **(b)** 1350 °C, **(c)** 1340 °C, **(d)** 1320 °C, and **(e)** 1150 °C. The compositions that were heat treated are included as solid circles. Electron beam microprobe analysis measurements of phase compositions are shown as Xs. Literature data are also included as diamonds (Ref 1). The isothermal section at 1350 °C was derived from phase composition measurements at 1340 °C.

Electron beam microprobe analysis was employed using a 15 kV, 20nA, ~1 μm diam beam. High-purity Nb, Ti, and Si were used as standards and conventional matrix corrections (*Z*, *A*, and *F*) were used to calculate the weight percent compositions from measured x-ray intensities. The compositions of each phase were measured with a minimum of 7 points. The limit of detection for all elements was 0.5% wt.% relative. Errors in the measurements were ~1.0% relative.

4. Results and Discussion

4.1 Microstructures of Ternary Alloys

Microstructural evidence for the isothermal sections at 1500 and 1340 °C are discussed by phase field proceeding from the Nb-rich side to the Ti-rich side of the phase diagram. The microstructures of the samples subjected to the 1500 °C heat treatment are presented first and the 1340 °C treatment second.

4.2 1500 °C: (Nb,Ti,Si)-$Nb(Ti)_5Si_3$ Two-Phase Field

A low-magnification micrograph of the Nb-3Ti-16Si is shown in Fig. 4(a), and it shows islands of eutectoid within th interdendritic eutectic. The initial DS structure consisted o (Nb,Ti,Si) dendrites and interdendritic eutectic of (Nb,Ti,Si) and $(Nb,Ti)_3Si$. The heat treated microstructure consists of pri mary Nb-rich dendrites, interdendritic eutectic of (Nb,Ti,Si and $(Nb,Ti)_3Si$, and interdendritic eutectoid of (Nb,Ti,Si) ano $Nb(Ti)_5Si_3$. Figure 4(b) shows a higher-magnification micrograph of where the eutectoid transformation was observed The eutectoid decomposition of $(Nb,Ti)_3Si$ had not proceedec to completion. The assumption is that the transformation will proceed to completion with more time, and this new equilibrium microstructure is one of (Nb,Ti,Si) and $Nb(Ti)_5Si_3$ and that at these Ti concentrations $(Nb,Ti)_3Si$ was not stabilized.

4.3 1500 °C: (Nb,Ti,Si)-$(Nb,Ti)_3Si$-$Nb(Ti)_5Si_3$ Three-Phase Field

The Nb-27Ti-22Si was the only composition that was examined from this region, and it is very close to the $(Nb,Ti)_3Si$

Table 1 Alloy Compositions and Phase Contents for Alloys Heat Treated at 1500 and 1340 °C

Phase chemistries for the individual phases are also shown.

Composition	Heat treated at 1500 °C	Heat treated at 1340 °C
Nb-3Ti-16Si	Two phase: (Nb,Ti,Si) dendrites with interdendritic eutectic and eutectoid $Nb(Ti)_5Si_3$	Two phase: (Nb,Ti,Si) + $Nb(Ti)_5Si_3$
Nb-9Ti-16Si	Two phase: (Nb,Ti,Si) dendrites with (Nb,Ti,Si)-$(Nb,Ti)_3Si$ eutectic. Partial transformation of $(Nb,Ti)_3Si$ into (Nb,Ti,Si) + $Nb(Ti)_5Si_3$	Two phase: (Nb,Ti,Si) + $Nb(Ti)_5Si_3$ $Nb(Ti)_5Si_3$: Nb-12.8Ti-36.5Si (Nb,Ti,Si): Nb-9.6Ti-0.5Si
Nb-21Ti-12Si	Two phase: (Nb,Ti,Si) + $(Nb,Ti)_3Si$	Two phase: (Nb,Ti,Si) + $(Nb,Ti)_3Si$
Nb-44Ti-12Si	Two phase: (Nb,Ti,Si) + $(Nb,Ti)_3Si$	Two phase: (Nb,Ti,Si) + $(Nb,Ti)_3Si$
Nb-42.5Ti-15Si	Two phase: (Nb,Ti,Si) and $(Nb,Ti)_3Si$. Large volume fraction (Nb,Ti,Si), no evidence of solidification structure	Two phase: (Nb,Ti,Si) + $(Nb,Ti)_3Si$
Nb-27Ti-22Si	Three phase: mainly $(Nb,Ti)_3Si$, small volume fractions of (Nb,Ti,Si), and $Nb(Ti)_5Si_3$ $Nb(Ti)_5Si_3$: Nb-18.9Ti-35.9Si $(Nb,Ti)_3Si$: Nb-25.6Ti-23.7Si (Nb,Ti,Si): Nb-11.0Ti-0.7Si	Two phase: (Nb,Ti,Si) + $(Nb,Ti)_3Si$
Nb-21Ti-22Si	...	Three phase: $(Nb,Ti)_3Si$, (Nb,Ti,Si), and $Nb(Ti)_5Si_3$
Nb-32.5Ti-35Si	Three phase: $Nb(Ti)_5Si_3$ + $Ti(Nb)_5Si_3$ + $(Nb,Ti)_3Si$ $Nb(Ti)_5Si_3$: Nb-23.8Ti-35.8Si $(Nb,Ti)_3Si$: Nb-32.1Ti-23.6Si $Ti(Nb)_5Si_3$: Nb-38.5Ti-35.9Si	Three phase: $Nb(Ti)_5Si_3$ + $Ti(Nb)_5Si_3$ + $(Nb,Ti)_3Si$ $Nb(Ti)_5Si_3$: Nb-28.1Ti-38.3Si $(Nb,Ti)_3Si$: Nb-38.6Ti-25.8Si $Ti(Nb)_5Si_3$: Nb-40.9Ti-38.2Si
Nb-55Ti-35Si	Two phase: L + $Ti(Nb)_5Si_3$. Small volume fraction of liquid. (Nb,Ti,Si) also observed from solidified liquid (Nb,Ti,Si): Nb-80.5Ti-1.2Si $Ti(Nb)_5Si_3$: Nb-52.9Ti-35.9Si	Three phase: $Ti(Nb)_5Si_3$ + $(Nb,Ti)_3Si$ + (Nb,Ti,Si) $Ti(Nb)_5Si_3$: Nb-51.4Ti-38.4Si $(Nb,Ti)_3Si$: Nb-61.8Ti-25.7Si (Nb,Ti,Si): Nb-84.1Ti-2.0Si
Nb-60Ti-30Si	Two phase: L + $Ti(Nb)_5Si_3$. Sample showed evidence of melting	Three phase: $Ti(Nb)_5Si_3$ + $(Nb,Ti)_3Si$ + (Nb,Ti,Si)
Nb-65Ti-22Si	Evidence of melting	Three phase: (Nb,Ti,Si) + $(Nb,Ti)_3Si$ + $Ti(Nb)_5Si_3$ $Ti(Nb)_5Si_3$: Nb-55.5Ti-38.2Si $(Nb,Ti)_3Si$: Nb-61.0Ti-25.7Si (Nb,Ti,Si): Nb-82.5Ti-3.0Si
Nb-76.5Ti-13.5Si	...	Two phase: (Nb,Ti,Si) + $Ti(Nb)_5Si_3$
Nb-80Ti-10Si	...	Two phase: (Nb,Ti,Si) + $Ti(Nb)_5Si_3$
Nb-70Ti-20Si	...	Two phase: (Nb,Ti,Si) + $Ti(Nb)_5Si_3$
Nb-75Ti-20Si	Two phase: L + $Ti(Nb)_5Si_3$	Three phase: liquid (small volume fraction) + (Nb,Ti,Si) + $Ti(Nb)_5Si_3$ $Ti(Nb)_5Si_3$: Nb-58.9Ti-38.2Si (Nb,Ti,Si): Nb-89.6Ti-4.1Si

corner of the three-phase triangle shown in Fig. 3(a). There were three phases shown in the microstructure in Fig. 5. First, there was a small volume fraction of (Nb,Ti,Si), the lightest phase in the BSE images, second, there were faceted gray $(Nb,Ti)_3Si$ dendrites; and third, there was a small volume fraction of a dark phase $Nb(Ti)_5Si_3$. There was no evidence of the prior solidification structure.

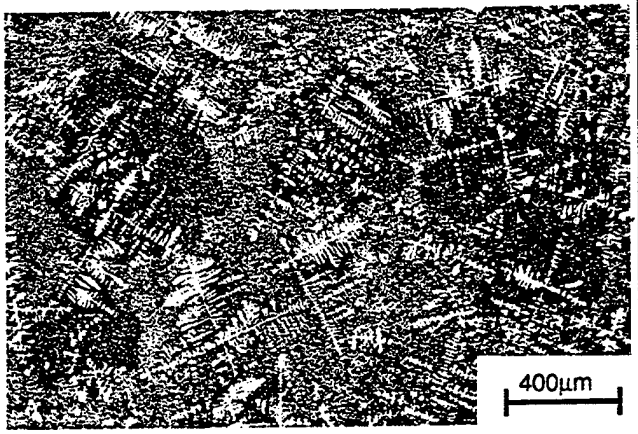
The chemistry of these phases was measured using EMPA, as shown in Table 1. The three corners of this triangle were established using the EMPA data, and are shown by Xs in Fig. 3(a). The compositions of the three phases observed were Nb-11Ti-0.7Si for the (Nb,Ti,Si), Nb-26Ti-24Si for the $(Nb,Ti)_3Si$, and Nb-19Ti-36Si for the $Nb(Ti)_5Si_3$. The Si concentrations of the silicides were slightly lean of the stoichiometric compositions.

The Nb-15Ti-10Si composition reported by Subramanian et al. (Ref 1) possessed (Nb,Ti,Si) and $(Nb,Ti)_3Si$, and the phase field was drawn considering these data. The data presented here are almost consistent with the Nb-15Ti-10Si data of Subramanian et al. (Ref 1) but not the Nb-10Ti-10Si data because they reported that the latter contained (Nb,Ti,Si), $(Nb,Ti)_3Si$, and $Nb(Ti)_5Si_3$ and the Nb-10Ti-10Si is outside the three-phase triangle shown in Fig. 3(a). The data of Subramanian et al. are shown by the solid diamonds in Fig. 3(a).

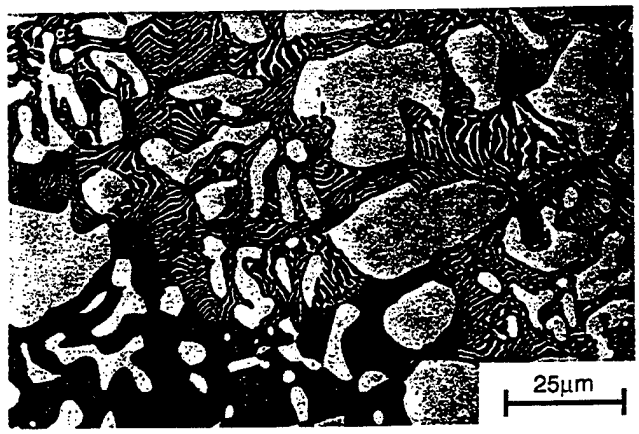
4.4 1500 °C: (Nb,Ti,Si)-$(Nb,Ti)_3Si$ Two-Phase Field

Three compositions were examined from the two-phase (Nb,Ti,Si)-$(Nb,Ti)_3Si$ field, Nb-21Ti-12Si, Nb-44Ti-12Si, and Nb-42.5Ti-15Si. A typical microstructure is shown in Fig. 6 for the Nb-21Ti-12Si composition. The microstructure consisted of (Nb,Ti,Si) in an $(Nb,Ti)_3Si$ matrix. The microstructure shows both coarsening and homogenization of the microstructure as a result of the heat treatment.

A composition examined in this regime with a higher Nb concentration was Nb-44Ti-12Si. The microstructure is shown in Fig. 7(a) and (b) and was similar to that shown in Fig. 6 with the exception of three features: first, there was a larger volume fraction of (Nb,Ti,Si) dendrites; second, $(Nb,Ti)_3Si$ precipitates were observed in the metallic phase; and, third there were (Nb,Ti,Si) precipitates in the $(Nb,Ti)_3Si$; these precipitates have been examined in more detail (Ref 8). The silicide pre-



a)



b)

Fig. 4 Typical microstructures (BSE images) of the transverse sections of a DS Nb-3Ti-16Si alloy heat treated at 1500 °C for 100 h. The large white dendrites are (Nb,Ti,Si), the faceted gray phase is $(Nb,Ti)_3Si$. The fine black phase is eutectoid $Nb(Ti)_5Si_3$, and the fine-scale white phase is eutectoid (Nb,Ti,Si).

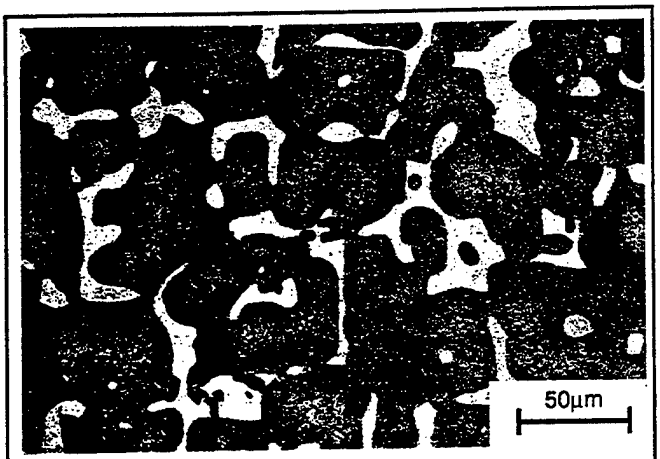


Fig. 5 Typical microstructures (BSE images) of the Nb-27Ti-22Si alloy heat treated at 1500 °C for 100 h. Phase contrast is as for Fig. 4.

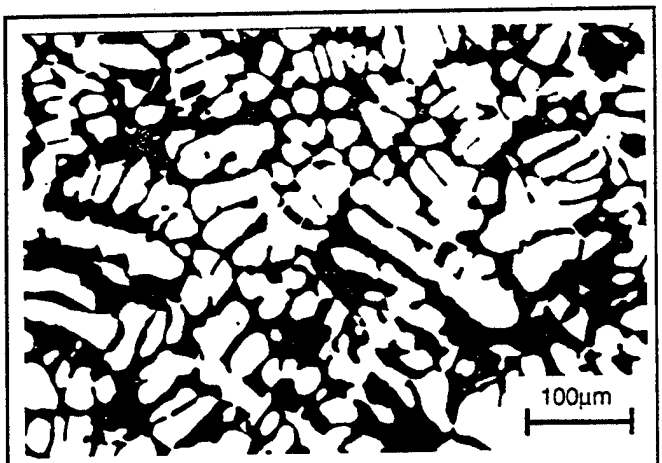


Fig. 6 Typical microstructure (BSE image) of the transverse section of a DS Nb-21Ti-12Si alloy heat treated at 1500 °C for 100 h.

cipitates are shown more clearly at higher magnification in Fig. 7(b). These data are consistent with that reported by Subramanian et al. (Ref 1).

4.5 1500 °C: $Nb(Ti)_5Si_3$-$(Nb,Ti)_3Si$-$Ti(Nb)_5Si_3$ Three-Phase Field

The microstructure of the Nb-32.5Ti-35Si composition is shown in Fig. 8(a) and (b). The microstructure consisted of large, blocky $Nb(Ti)_5Si_3$ (dark gray), together with $(Nb,Ti)_3Si$ (light gray) and $Ti(Nb)_5Si_3$. The gradation from dark to light gray towards the edges of the $Nb(Ti)_5Si_3$ is due to Ti enrichment at the edges. $Ti(Nb)_5Si_3$ was generated from $Nb(Ti)_5Si_3$ with diffusion of the Nb into the $(Nb,Ti)_3Si$. The as-solidified sample contained primary $Nb(Ti)_5Si_3$ and a small volume fraction of $(Nb,Ti)_3Si$, but not $Ti(Nb)_5Si_3$. Upon heat treatment at 1500 °C, the $Nb(Ti)_5Si_3$ decomposed to $Ti(Nb)_5Si_3$ and $(Nb,Ti)_3Si$, together with the necessary phase volume fraction and chemistry adjustments. Some TiO_2 was also observed in the microstructure as a fine-scale black phase; this probably occurred as a result of trace oxygen contamination from the furnace, or the initial charges.

Phase chemistries of the $Nb(Ti)_5Si_3$, $(Nb,Ti)_3Si$, and $Ti(Nb)_5Si_3$ were measured using EMPA and are shown in Table 1. The corners of the triangle were positioned using these data. The Si concentrations of all the silicides were slightly substoichiometric.

4.6 1500 °C: $Ti(Nb)_5Si_3$-$(Nb,Ti)_3Si$ Two-Phase Field

This phase field was not examined specifically, but is defined implicitly by the adjacent phase fields.

4.7 1500 °C: L + $Ti(Nb)_5Si_3$-$(Nb,Ti)_3Si$ Three-Phase Field

No compositions were examined from this phase field or the L + $(Nb,Ti)_3Si$ + (Nb,Ti,Si) phase field. The phase fields shown in Fig. 3(a) are therefore estimates. It is difficult to obtain reliable data from these regions because of the steep nature of the liquidus surface, and the difficulties that liquid in the microstructure generates on postheat treatment cooling.

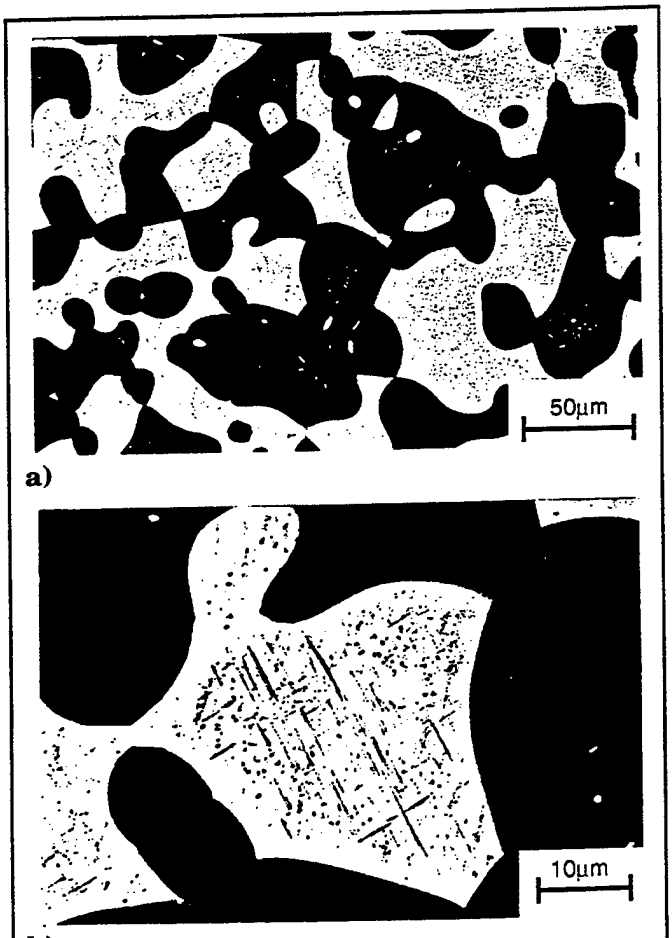


Fig. 7 Typical microstructure (BSE image) of the transverse section of a DS Nb-44Ti-12Si alloy heat treated at 1500 °C for 100 h shown at **(a)** low and **(b)** high magnifications. The large white dendrites are (Nb.Ti.Si), and the interdendritic gray phase is $(Nb.Ti)_3Si$.

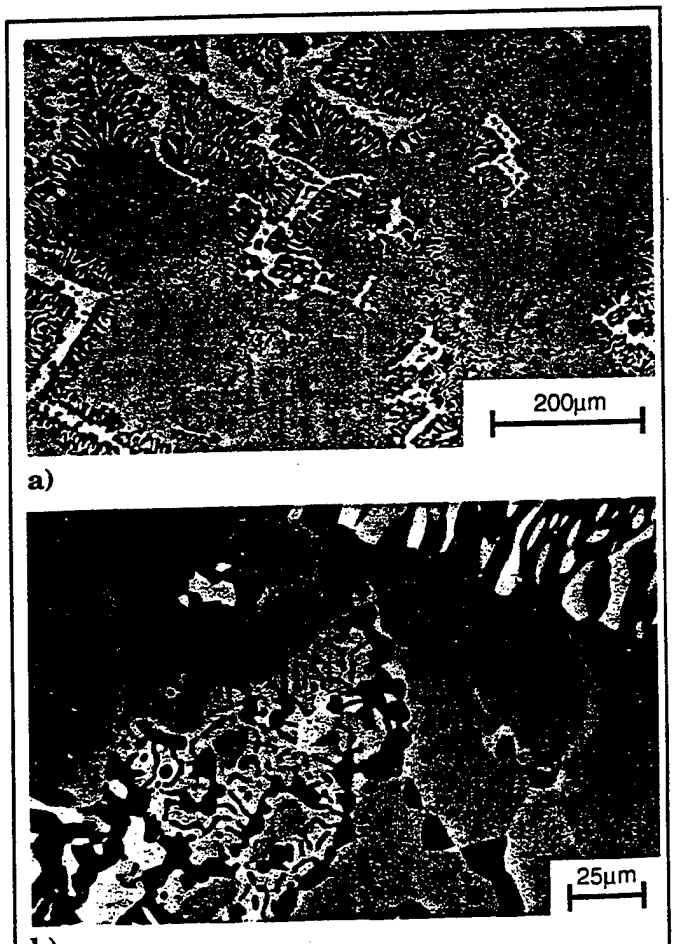


Fig. 8 Typical microstructure (BSE images) of the Nb-32.5Ti-35Si alloy shown at **(a)** low and **(b)** high magnifications. The large-scale gray phase is $Nb(Ti)_5Si_3$, the $(Nb.Ti)_3Si$ is light gray, and the $Ti(Nb)_5Si_3$ is black.

4.8 1500 °C: L + $Ti(Nb)_5Si_3$ Two-Phase Field

Four compositions were identified as being from this phase field, Nb-55Ti-35Si, Nb-60Ti-30Si, Nb-65Ti-22Si, and Nb-75Ti-20Si. The microstructure showed evidence of three phases, $Ti(Nb)_5Si_3$, (Nb,Ti,Si), and liquid. The microstructures of all these compositions were similar. A typical microstructure is that of the Nb-60Ti-30Si, as shown in Fig. 9. There was a large volume fraction of the $Ti(Nb)_5Si_3$ dendrites that originated from the original solidification structure. There was a smaller volume fraction of fine-scale eutectic $Ti(Nb)_5Si_3$ and (Nb,Ti,Si) from the solidified liquid that was retained between the dendrites. The liquid solidified as metal and eutectic on furnace cooling after the heat treatment. Fine-scale (<1 μm) precipitates were also observed within the (Nb,Ti,Si); these are shown in more detail in Fig. 10 for the Nb-65Ti-22Si alloy.

Phase chemistries of the $Ti(Nb)_5Si_3$, and (Nb,Ti,Si) in the Nb-55Ti-35Si alloy, were measured using EMPA and are shown in Table 1. The composition of the (Nb,Ti,Si) phase was Nb-80.5Ti-1.2Si. The Si solubility is higher than in the (Nb,Ti,Si) of the Nb-27Ti-22Si alloy (0.7%). The solubility limit of Nb in the $Ti(Nb)_5Si_3$ was 11%. The EMPA data points show a $Ti(Nb)_5Si_3$ point for the two-phase (Nb,Ti,Si) + L field and a (Nb,Ti,Si) point for the two-phase (Nb,Ti,Si) + L field; it was not possible to obtain a liquid composition because the furnace cooling rate was too low. The (Nb,Ti,Si) data were obtained from the eutectic that was formed on solidification after the liquid composition had shifted to the eutectic valley.

4.9 1340 °C: (Nb,Ti,Si)-$Nb(Ti)_5Si_3$ Two-Phase Field

Two compositions from this phase field were examined: Nb-3Ti-16Si and Nb-9Ti-16Si. The microstructure of the Nb-3Ti-16Si was similar to that observed at 1500 °C, as shown in Fig. 4(a). It contained large-scale primary metal dendrites, a eutectic of (Nb,Ti,Si) and $(Nb,Ti)_3Si$, and a fine-scale eutectoid of (Nb,Ti,Si) and $Nb(Ti)_5Si_3$. In the isothermal section shown in Fig. 3(c), the Nb-9Ti-16Si composition was considered to be close to the phase boundary between this two-phase field and the (Nb,Ti,Si)-$(Nb,Ti)_3Si$-$Nb(Ti)_5Si_3$ three-phase field. Although the eutectoid transformation was not complete in the Nb-3Ti-16Si, it was considered that given sufficient time, it would have proceeded to completion. A small amount of silicide precipitation was also observed in the metal dendrites.

Electron beam microprobe analysis data of the Nb-9Ti-16Si composition are shown in Table 1 for the (Nb,Ti,Si) and the $Nb(Ti)_5Si_3$; these analyses place the solvus lines and provide an estimate of the Nb-rich corners of the (Nb,Ti,Si)-$(Nb,Ti)_3Si$-$Nb(Ti)_5Si_3$ triangle. The EMPA data are shown as Xs in Fig. 3(c).

4.10 1340 °C: (Nb,Ti,Si)-$(Nb,Ti)_3Si$-$Nb(Ti)_5Si_3$ Three-Phase Field

Two compositions were examined from this phase field. Nb-21Ti-22Si and Nb-27Ti-22Si. The three-phase triangle

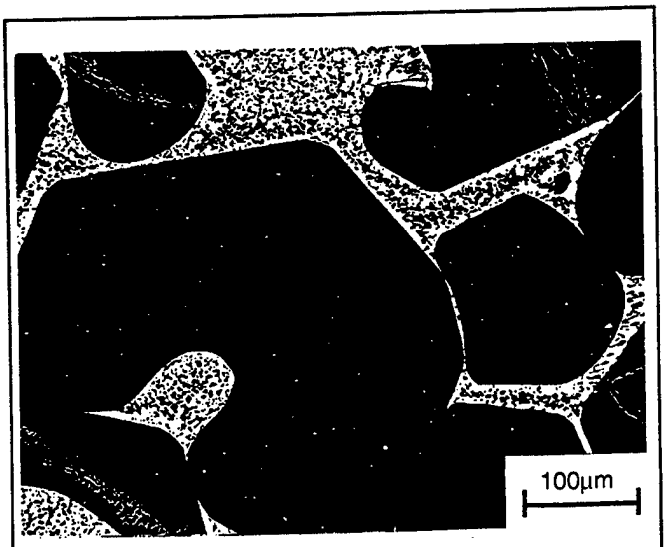


Fig. 9 Typical microstructure (BSE image) of the Nb-60Ti-30Si alloy heat treated at 1500 °C for 100 h. There are large faceted $Ti(Nb)_5Si_3$ primary dendrites, and (Nb,Ti,Si).



Fig. 10 Typical microstructure (BSE image) of the Nb-65Ti-22Si alloy heat treated at 1500 °C for 100 h.

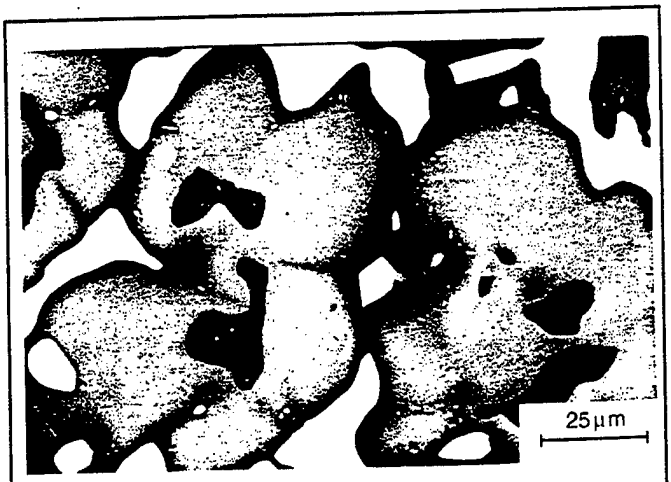


Fig. 11 Typical microstructure (BSE image) of the Nb-21Ti-22Si alloy heat treated at 1340 °C showing $Nb(Ti)_5Si_3$ (black phase), $(Nb,Ti)_3Si$ (gray phase), and (Nb,Ti,Si) (white phase).

was constructed to include both of these compositions. The three-phase triangle was also positioned using EMPA data from the Nb-21Ti-22Si. The microstructure of the Nb-21Ti-22Si composition is shown in Fig. 11. It contained $(Nb,Ti)_3Si$, (Nb,Ti,Si), and $Nb(Ti)_5Si_3$. The $Nb(Ti)_5Si_3$ was generally at the centers of the $(Nb,Ti)_3Si$ dendrites. (Nb,Ti,Si) precipitates were also observed in both silicides. $(Nb,Ti)_3Si$ precipitates were observed in the large-scale (Nb,Ti,Si). At 1500 °C the Nb-27Ti-22Si composition contained a significant volume fraction of $Nb(Ti)_5Si_3$, but at 1340 °C only a very small volume fraction of $Nb(Ti)_5Si_3$ was detected. This observation is consistent with the proximity of the composition to the phase boundary.

4.11 1340 °C: (Nb,Ti,Si)-$(Nb,Ti)_3Si$ Two-Phase Field

Three compositions were examined from this two-phase field: Nb-21Ti-12Si, Nb-44Ti-12Si, and Nb-42.5Ti-15Si. The microstructures contained large-scale metal dendrites that had coarsened substantially from the initial solidification structure. There was little evidence of any silicide precipitation within the metallic phase. The Nb-21Ti-12Si composition is important because it lies just within the two-phase field and places the phase boundary within the adjacent three-phase field. The microstructures of the samples heat treated at 1340 °C were similar to those of the same compositions that were heat treated at 1500 °C. No $Nb(Ti)_5Si_3$ was observed in any of these compositions; at these Ti concentrations, the Ti had stabilized the Nb_3Si.

4.12 1340 °C: $Nb(Ti)_5Si_3$ + $(Nb,Ti)_3Si$ Two-Phase Field

This two-phase field was outlined by the two adjacent three-phase fields which were established from the EMPA analysis data.



a)



b)

Fig. 12 Typical microstructure (BSE images) of the Nb-32.5Ti-35Si alloy heat treated at 1340 °C at (a) low and (b) high magnifications. The large-scale gray phase is $Nb(Ti)_3Si_3$, the (Nb,Ti)$_3$Si is light, and the $Ti(Nb)_5Si_3$ is black.

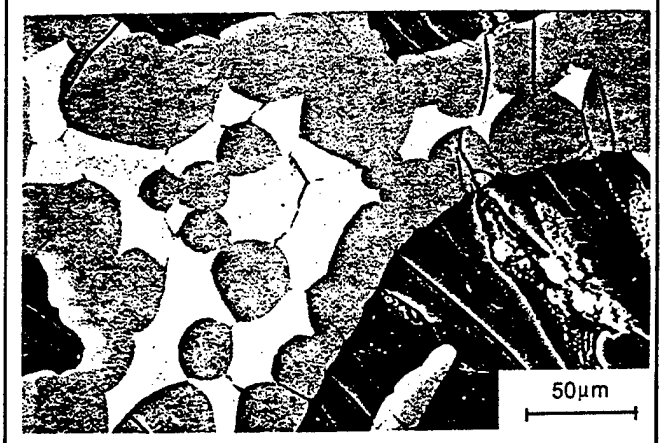


Fig. 13 Typical microstructure (BSE image) of the Nb-60Ti-30Si alloy heat treated at 1340 °C. The black phase is $Ti(Nb)_5Si_3$, the gray phase is $(Nb,Ti)_3Si$, and the white phase is (Nb,Ti,Si).



Fig. 14 Typical microstructure (BSE image) of the Nb-65Ti-22Si alloy heat treated at 1340 °C. The black phase is $Ti(Nb)_5Si_3$, the gray phase is $(Nb,Ti)_3Si$, and the white phase is (Nb,Ti,Si).

4.13 1340 °C: $Nb(Ti)_5Si_3$ + $Ti(Nb)_5Si_3$ + $(Nb,Ti)_3Si$ Three-Phase Field

Only one composition was examined from the $Nb(Ti)_5Si_3$ + $Ti(Nb)_5Si_3$ + $(Nb,Ti)_3Si$ three-phase field, Nb-32.5Ti-35Si. Typical microstructures are shown in Fig. 12 and indicate three phases. The light gray phase is $Nb(Ti)_5Si_3$, and it occupies the largest volume fraction. The black phase is $Ti(Nb)_5Si_3$, and the white phase is $(Nb,Ti)_3Si$. The $Ti(Nb)_5Si_3$ appears to be growing off the $Nb(Ti)_5Si_3$. Although the 1340 and 1500 °C samples possess the same three phases, the microstructures are different. Also the morphology of the $Ti(Nb)_5Si_3$ differs from the typical faceted morphology; this is to be expected because it has been precipitated from solid rather than liquid.

Electron beam microprobe analysis data of the $Nb(Ti)_5Si_3$, $Ti(Nb)_5Si_3$, and $(Nb,Ti)_3Si$ are shown in Table 1. They indicate that all three silicides have Si compositions close to the stoichiometric values. The corners of the three-phase triangle were positioned using the EMPA data.

4.14 1340 °C: $(Nb,Ti)_3Si$ + $Ti(Nb)_5Si_3$ Two-Phase Field

This phase field was deduced using the data from the adjacent phase fields.

4.15 1340 °C: $Ti(Nb)_5Si_3$ + $(Nb,Ti)_3Si$ + (Nb,Ti,Si) Three-Phase Field

Three compositions were examined from this phase field : Nb-60Ti-30Si, Nb-55Ti-35Si, and Nb-65Ti-22Si. The Nb-55Ti-35Si is very close to the corner of the three-phase triangle and the Nb-60Ti-30Si is very close to the boundary with the $Ti(Nb)_5Si_3$ + (Nb,Ti,Si) two-phase field. The microstructure of the Nb-60Ti-30Si is shown in Fig. 13. The $(Nb,Ti)_3Si$ appears to have grown peritectoidally from the (Nb,Ti,Si) and $Ti(Nb)_5Si_3$, although the sample may not have reached full equilibrium. In the Nb-60Ti-30Si composition, the high volume fractions of both $(Nb,Ti)_3Si$ and $Ti(Nb)_5Si_3$ are consistent with the composition being close to the silicide corners of the triangle. The Nb-55Ti-35Si composition possessed a similar microstructure to that of the Nb-60Ti-30Si except that there was a larger volume fraction of $Ti(Nb)_5Si_3$ and a much smaller volume fraction of (Nb,Ti,Si). The peritectoid transformation was probably also incomplete. It is important to note that there was no $(Nb,Ti)_3Si$ in the initial as-solidified sample. A lot of the $(Nb,Ti)_3Si$ had precipitated upon grain boundaries within the (Nb,Ti,Si) on heat treatment. The primary $Ti(Nb)_5Si_3$ from the as-solidified sample remained, but showed some evidence of peritectoid transformation. There was no evidence of any of the eutectic $Ti(Nb)_5Si_3$ of the original as-solidified sample.

The microstructure of the Nb-65Ti-22Si composition is shown in Fig. 14, and it contains $Ti(Nb)_5Si_3$, $(Nb,Ti)_3Si$, and (Nb,Ti,Si). The large-scale (~50 μm) faceted $Ti(Nb)_5Si_3$ dendrites are remnants of the original solidification structure. The large-scale $(Nb,Ti)_3Si$ possessed facets, but it did not show the same degree of faceting as the $(Nb,Ti)_3Si$ of lower Ti concentrations. The (Nb,Ti,Si) contained fine-scale αTi precipitates with a βTi matrix.

Electron beam microprobe analysis of the three phases in the Nb-55Ti-35Si alloy are shown in Table 1. Both the silicides possessed their approximate stoichiometric Si compositions. The corners of the three-phase triangle were established from the EMPA data for the Nb-55Ti-35Si and the Nb-65Ti-22Si compositions, as shown in Table 1.

4.16 1340 °C: $Ti(Nb)_5Si_3$-(Nb,Ti,Si) Two-Phase Field

Three compositions were examined from the $Ti(Nb)_5Si_3$ + (Nb,Ti,Si) two-phase field, Nb-70Ti-20Si, Nb-76.5Ti-13.5Si, and Nb-80Ti-10Si. The microstructure of the Nb-70Ti-20Si is shown in Fig. 15. The large-scale (~100 μm) $Ti(Nb)_5Si_3$ dendrites are remnants of the solidification structure. There are also finer-scale (10 to 20 μm) $Ti(Nb)_5Si_3$ faceted rods; these may have originated from the eutectic of the solidification structure that subsequently coarsened upon heat treatment. The (Nb,Ti,Si) consists of αTi and βTi; the αTi was probably formed on furnace cooling. Any liquid present would probably have solidified as fine-scale eutectic of (Nb,Ti,Si) and

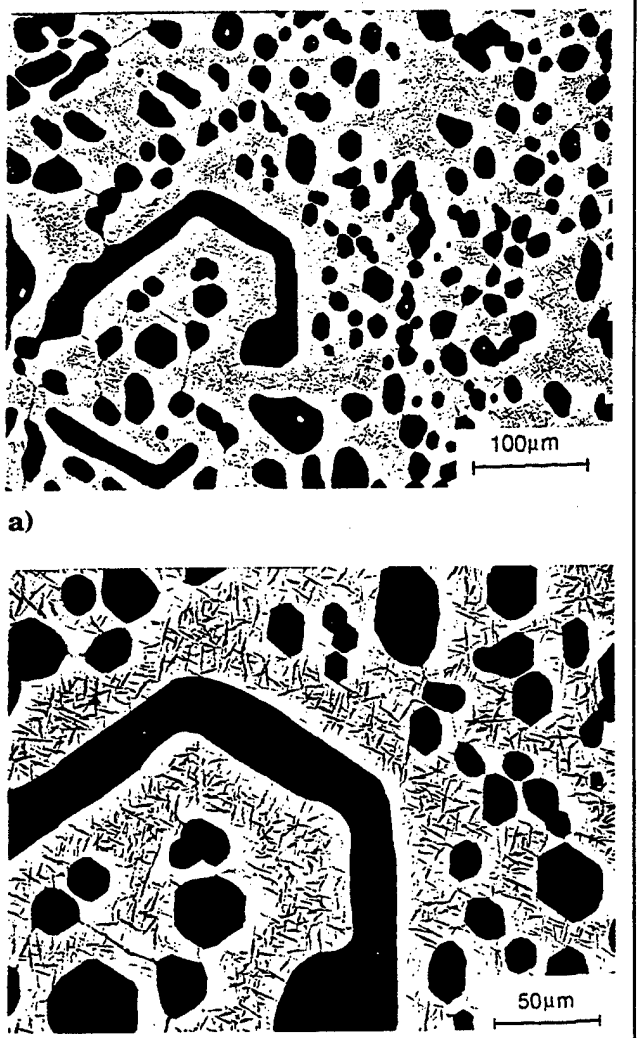


Fig. 15 Typical microstructure (BSE images) of the Nb-70Ti-20Si alloy heat treated at 1340 °C at **(a)** low and **(b)** high magnifications. The black phase is $Ti(Nb)_5Si_3$, and the white phase is (Nb,Ti,Si).

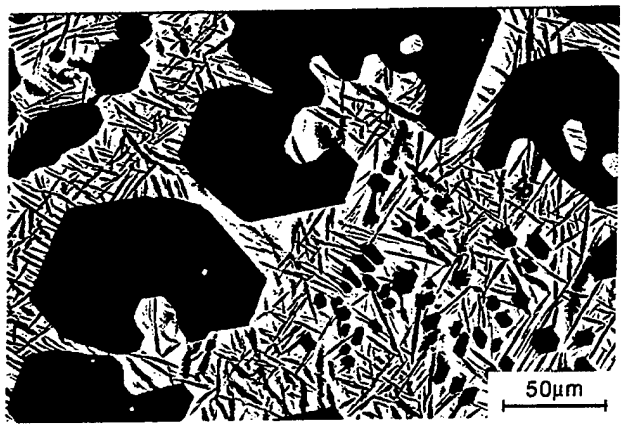


Fig. 16 Typical microstructure (BSE image) of the Nb-75Ti-20Si alloy heat treated at 1340 °C. The black phase is $Ti(Nb)_5Si_3$ and the white phase is (Nb,Ti,Si).

$Ti(Nb)_5Si_3$ rods; there was no evidence of the latter in the microstructure. There was no evidence of $(Nb,Ti)_3Si$ either as a peritectic or a peritectoid. The microstructures of the Nb-76.5Ti-13.5Si and the Nb-80Ti-10Si were similar, but they contained a larger volume fraction of (Nb,Ti,Si).

4.17 1340 °C: $Ti(Nb)_5Si_3$-(Nb,Ti,Si) + Liquid Three-Phase Field

Only one composition was examined from the $Ti(Nb)_5Si_3$ + (Nb,Ti,Si) + liquid three-phase field, namely Nb-75Ti-20Si. The microstructure of the Nb-75Ti-20Si is shown in Fig. 16, and it contained large-scale faceted $Ti(Nb)_5Si_3$ (black phase) and (Nb,Ti,Si). The metallic phase consisted of α and βTi. Electron beam microprobe analysis data from the Nb-75Ti-20Si composition are shown in Table 1. The (Nb,Ti,Si) and $Ti(Nb)_5Si_3$ corners of the triangle were positioned using this data. The liquid composition was estimated.

5. Conclusions

Nb-Ti-Si solid-state phase equilibria have been investigated at temperatures of 1500 °C and below. Microstructural analyses and EMPA data were used to establish isothermal sections at 1500 and 1340 °C. Additional isothermal sections were estimated at 1350, 1320, and 1150 °C using these data. The microstructures examined in the ternary Nb-Ti-Si alloys investigated contained four phases: (Nb,Ti,Si), $Nb(Ti)_5Si_3$, $(Nb,Ti)_3Si$, and $Ti(Nb)_5Si_3$. These phases can be clearly distinguished in the microstructures by their scale, morphology, BSE contrast, and chemistry. These present data are consistent with the following transition reaction in the solid-liquid phase equilibria at 1350 °C:

$$L + (Nb,Ti)_3Si \rightarrow (Nb,Ti,Si) + Ti(Nb)_5Si_3$$

The present data were also used to define the following eutectoid and peritectoid reactions in the Nb-Ti-Si system:

$$(Nb,Ti)_3Si \rightarrow (Nb,Ti,Si) + Nb(Ti)_5Si_3$$

$$Ti(Nb)_5Si_3 + (Nb,Ti,Si) \rightarrow (Nb,Ti)_3Si$$

Acknowledgment

The authors would like to thank D.J. Dalpe for preparation of the initial samples, M. Curran for the heat treatments, and Dr. D.A. Wark for the EMPA. This research was partially sponsored by AFOSR under contract No. F49620-96-C-0022 with Capt. C.H. Ward as program manager. The authors are also grateful to Drs. M.G. Mendiratta and P.R. Subramanian, UES, Dayton, OH, and Dr. H.A. Lipsitt for very helpful discussions.

Cited References

1. P.R. Subramanian, M.G. Mendiratta, and D.M. Dimiduk, *Mater. Res. Soc. Symp. Proc., 322*, 491-502 (1994).
2. B.P. Bewlay, M.R. Jackson, W.J. Reeder, and H.A. Lipsitt, *Mater. Res. Soc. Symp. Proc., 364*, 943-948 (1995).
3. M.R. Jackson, B.P. Bewlay, R.G. Rowe, D.W. Skelly, and H.A. Lipsitt, *J. Met., 48*(1), 33-39 (1996).
4. B.P. Bewlay, M.R. Jackson, and H.A. Lipsitt, *J. Phase Equilibria, 18*(3), 264-278 (1997).
5. T.B. Massalski, P.R. Subramanian, H. Okamoto, and L. Kacprzak, Ed., *Binary Alloy Phase Diagrams*, 2nd ed., Vol. 3, ASM International, Materials Park, OH, 3371 (1991).
6. F.N. Rhines, *Phase Diagrams in Metallurgy—Their Development and Application*, McGraw-Hill, London (1956).
7. H. Liang and Y.A. Chang, private communication (Oct 1997).
8. R. Grylls and H. Fraser, Ohio State University (Sept 1997).

Directionally Solidified High-Temperature In-Situ Composites and Their Applications

B.P. Bewlay, M.R. Jackson and H.A. Lipsitt

Directionally Solidified High-Temperature
In-Situ Composites and Their Application

Proceedings of the Fifth International Conference
on Composites Engineering, 1998

July 1998

Directionally Solidified High-Temperature In-Situ Composites and Their Applications

B.P. Bewlay, M.R. Jackson and H.A. Lipsitt,
General Electric Company,
Corporate Research and Development,
Schenectady.
New York 12301.

This paper describes processing and properties of advanced turbine blades generated from high temperature directionally solidified (DS) in-situ composites. Directional solidification is performed using cold crucible crystal growth for alloys with melting temperatures up to 2250°C. These composites consist of high-strength, Nb-based M_3Si and M_5Si_3 silicides together with a modest strength, high-toughness Nb-based metallic phase. The phases within these composites are aligned with the growth direction.

This composite approach provides advanced materials with a combination of attractive high-temperature properties and acceptable low-temperature properties. This paper describes composite microstructures, room temperature fracture toughness and elevated temperature property data. Design criteria for aircraft engine components are also described.

Figure 1 shows an advanced airfoil which consists of a Nb-silicide-based composite spar with cooling channels machined into the spar. Both the spar and skin are intermetallic matrix composite materials that are selected for an optimum combination of strength, toughness, creep and oxidation performance. The microstructure of a typical composite that is being considered for such an application is shown in Figure 2. Room temperature fracture toughness values of >20 MPa$\sqrt{m}$ have been measured in these composites. These composites have increased high-temperature strength and oxidation resistance at blade surface temperatures of 1315°C (2400F) when compared with other intermetallic-based systems; tensile strengths of >350 MPa at 1200 °C and creep rupture lives of >500 hours at 1100 °C and 100 MPa have been measured. These are typical of the characteristics that are required for the highest performance aircraft engines.

The in-situ composites that will be described in the present paper are from alloys that typically possess more than three elements. Alloys with Ti, Hf, Al and Cr additions have received particular attention recently [1-3]. Composites from alloys with more than six elements have also been described [1, 2].

The microstructure of a composite generated from a Nb-16Ti-8Hf-16Si alloy is shown in Figure 2. The composite consisted of eutectic cells that contained an M_3Si-type phase (light phase) together with a Nb-based metallic phase (dark phase). Similar composites have also been manufactured that contain M_5Si_3 silicide phases. Texture measurements obtained using electron beam scattering pattern analysis will also be described.

These materials are being used for design of high pressure turbine blades of the most advanced and highest thrust to weight ratio engines. Application of these materials in double wall airfoil cooled structures will be discussed.

Acknowlegments

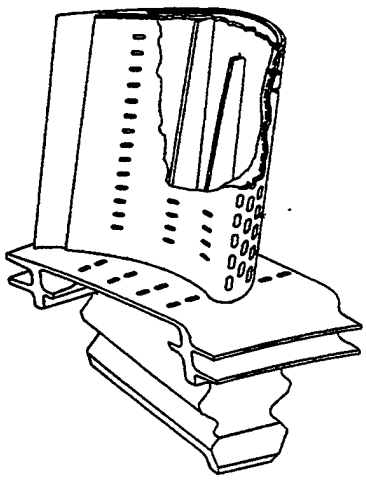
This research was partially sponsored by AFOSR under contract #F49620-96-C-0022 with Capt. C.H. Ward and Dr. S. Wu as Program Managers. The authors would also like to thank Dr. A. Chatterjee of Allison Engine Company for discussion of materials applications to new blade designs.

References

[1] M.R. Jackson, B.P. Bewlay, R.G. Rowe, D.W. Skelly, and H.A. Lipsitt, J. of Metals Vol. 48 (1), pp. 38-39, 1996.

[2] B.P. Bewlay, M.R. Jackson and H.A. Lipsitt, *Metall. and Mater. Trans.*, 1996, Vol 279, pp. 3801-3808.

[3] P.R. Subramanian, M.G. Mendiratta and D.M. Dimiduk, *Mat. Res. Soc. Symp. Proc.*, 322 (1994), pp. 491-502.



Multiple Piece Bonded Blade

Figure 1 : Multiple piece bonded turbine blade with a DS in-situ composite internally cooled spar and an intermetallic matrix composite skin.

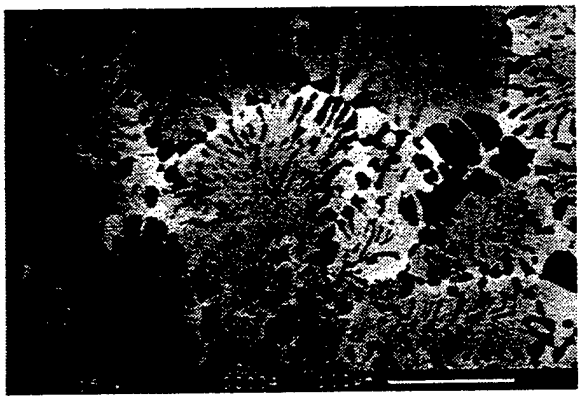


Figure 2 : Typical microstructure of the transverse section of a composite directionally solidified from an advanced Nb alloy (Nb-16Ti-8Hf-16Si). The microstructure consists of an Nb_3Si type silicide toughened by a high strength Nb solid solution.

Evidence For the Existence of Hf_5Si_3

B.P. Bewlay, J.A. Sutliff, and R.R. Bisho

Journal of Phase Equilibria, January 1999

Evidence for the Existence of Hf_5Si_3

B.P. Bewlay, J.A. Sutliff, and R.R. Bishop

(Submitted 22 January 1998; in revised form 30 November 1998)

This article describes new evidence for the existence of Hf_5Si_3 with the Mn_5Si_3 structure type (*hP*16-$P6_3/mmc$). Binary Hf-Si alloys with Si concentrations from 11.5 to 35.0 at.% were investigated. Hf_2Si was also observed in the binary Hf-Si alloys that were investigated; this is consistent with the assessed phase diagram. The Mn_5Si_3-type structure has been observed in both binary Hf_5Si_3 and higher alloyed forms, (Hf, X)$_5Si_3$, where Nb and Ti were substituted for Hf. Phase identification was performed using scanning electron microscopy, electron microprobe analysis, x-ray diffraction, and automated electron backscattering pattern analysis in the scanning electron microscope. The present data indicate that high levels of O, N, or C are not required to stabilize Hf_5Si_3, and that it can exist alone as a binary compound. This result is contrary to previous reports regarding Hf_5Si_3, which claim that it only exists when stabilized by interstitials.

Introduction

Niobium silicides such as Nb_5Si_3 and Nb_3Si are presently being explored as strengthening phases in high-temperature structural materials (Ref 1, 2). Alloying additions of elements such as Hf and Ti to these silicides are also being examined in order to increase the strength and oxidation resistance. There is limited knowledge of these silicides, which is due in part to the fact that there is some degree of uncertainty in the literature relating to the binary Hf-Si phase diagram, specifically the existence of Hf_5Si_3. However, there is significant previous evidence for the existence of a second Hf-rich silicide, Hf_2Si (Ref 3). This article describes new data supporting the existence of Hf_5Si_3 and Hf_2Si in binary Hf-Si alloys. Observations of Hf_5Si_3- and Hf_2Si-type silicides in ternary directionally solidified (DS) Hf-Nb-Si alloys are also described.

The metal-rich end of the binary Hf-Si phase diagram (Ref 3) has a eutectic of the form L $\rightarrow$ (Hf) + Hf_2Si at 1830 °C, and a peritectic of the form L + Hf_5Si_3 $\rightarrow$ Hf_2Si at 2080 °C (the Hf-Si solid solution is abbreviated by (Hf) throughout this article). The eutectic composition is Hf-12%Si (all compositions are given in atomic percent throughout this article). Hf_5Si_3 has the Mn_5Si_3 structure type (*hP*16-$P6_3/mmc$) with lattice parameters of a = 0.7844 nm and c = 0.5492 nm, and Hf_2Si has the Al_2Cu structure type (*tI*12-$I4/mcm$) with lattice parameters of a = 0.6553 nm and c = 0.5186 nm.

The existence of Hf_5Si_3 has been previously reported by Gokhale and Abbaschian (Ref 3), but it has been considered to be stable only in the presence of O, N, or C (Ref 3, 4). Karpinsky and Evseyev (Ref 5) identified Hf_5Si_3, Hf_3Si_2, and Hf_5Si_4 in alloys prepared from 99.0% pure Hf using arc melting, and they identified Hf_5Si_3 as having the Mn_5Si_3 (*hP*16-$P6_3/mmc$)-type structure. Kieffer and Benesovsky (Ref 6) provided a more complete review of the crystallography of high-temperature Hf silicides. They expressed some uncertainty regarding the existence of the Hf_5Si_3.

B.P. Bewlay and **J.A. Sutliff**, General Electric Company, Corporate Research and Development, Schenectady, NY 12301, USA; and **R.R. Bishop**, Department of Materials Science and Engineering, Northwestern University, Evanston, IL 60208, USA.

The aim of this article is to describe new evidence for the existence of Hf_5Si_3 with the Mn_5Si_3 (*hP*16-$P6_3/mmc$) crystal structure. This structure has been observed in binary Hf_5Si_3 and higher forms, (Hf,X)$_5Si_3$ where Hf was substituted for Nb and Ti.

Experimental

Binary Hf-Si and ternary Nb-Hf-Si alloys were prepared from >99.9% Hf (not including Zr), >99.99% Nb, and 99.999% Si by induction levitation melting in a segmented water-cooled copper crucible. The alloys were triple melted and then directionally solidified using the Czochralski method, as has been described in more detail elsewhere (Ref 2). Binary Hf-Si alloys with Si concentrations in the range 11 to 35% were prepared. The interstitial levels of the Hf were: C < 11, O < 52, and N < 22 weight ppm, respectively. Chemical analyses were performed on the starting materials, but not on the final cast alloys. However, it has been shown previously that the cold crucible melting system prevents any increase in the interstitial levels from those levels in the starting elements (Ref 7).

All of the samples were examined using scanning electron microscopy (backscatter electron, BSE, imaging) and electron beam microprobe analysis (EMPA). X-ray diffraction (XRD) was also performed using Cu Kα radiation on powder samples that were ball milled from the original DS samples. These separate analyses allowed determination of the chemistry and crystal structure of the individual phases.

Phase identification was also performed using the automated electron backscattering pattern (EBSP) technique for electron diffraction in the scanning electron microscope. This technique allowed easy selection of microstructural features using high-resolution microscopy with rapid diffraction pattern collection and analysis. A CamScan CS44 SEM (Cam Scan Electron Optics, Ltd., Cambridge, England) was operated using a 40 kV, ~10 nA electron beam, and the sample surface normal was tilted 70° away from the beam axis. A Nordiff (Jarle Hjelen Ltd., Trondheim, Norway) CCD-based (charge coupled device) EBSP detector was used. Positive phase identification was accomplished by direct comparison of the location and character of the diffraction bands in the experimental pattern with those calculated from simulated patterns generated using the possible structure types.

Results and Discussion

The microstructure of the binary Hf-35Si is shown in the BSE image in Fig. 1. It consisted of Hf_5Si_3 surrounded by peritectic Hf_2Si, with a small volume fraction of (Hf)-Hf_2Si eutectic. In Fig. 1, the Hf_2Si is the black phase and the (Hf) is the light phase. The Hf_5Si_3 is difficult to identify in Fig. 1 because there is little contrast between the Hf_5Si_3 and the peritectic Hf_2Si. However, the Hf_5Si_3 possessed a high density of cracks that did not propagate into the Hf_2Si, and these also served to differentiate the Hf_5Si_3 from the Hf_2Si. These cracks may have arisen as a result of differential thermal contraction between the two silicides on postsolidification cooling.

The presence of both Hf_5Si_3 and Hf_2Si was confirmed using XRD and EMPA data. The EMPA data indicated that the composition of the Hf_5Si_3 was Hf-37.5Si, the peritectic Hf_2Si was Hf-33.3Si, the eutectic Hf_2Si was Hf-33.1Si, and eutectic (Hf) was Hf-2.9Si; the Si composition of the (Hf) was higher than that reported for the assessed phase diagram at the eutectic temperature (<1%).

Electron backscattering diffraction patterns are shown in Fig. 2(a) and (c) for the Hf_2Si and Hf_5Si_3, respectively, that were observed in the Hf-35Si alloy. The indexed diffraction patterns are shown in Fig. 2(b) and (d) for Hf_2Si and Hf_5Si_3. The EBSP diffraction patterns were successfully indexed using the following crystallographic data:

- αHf ($a = 0.3196$ nm, $c = 0.5058$ nm, Mg structure type, space group: $P6_3/mmc$ (Ref 8)
- Hf_2Si ($a = 0.6553$ nm, $c = 0.5186$ nm, Al_2Cu structure type, space group: $I4/mcm$ (Ref 8)
- Hf_5Si_3 ($a = 0.7844$ nm, $c = 0.5492$ nm, Mn_5Si_3 structure type. space group: $P6_3/mcm$ (Ref 5)

The following additional crystal structures were also considered (Ref 8):

- Hf_5Si_4 ($a = 0.7039$ nm, $c = 1.283$ nm, Si_4Zr_5 structure type, space group: $P4_12_12$
- Hf_3Si_2 ($a = 0.6988$ nm, $c = 0.3675$ nm, Si_2U_3 structure type, space group: $P4/mbm$
- HfSi ($a = 0.6889$ nm, $b = 0.3772$ nm, $c = 0.5223$ nm, BFe structure type, space group: $Pnma$

The symmetries and structures of the above phases were easily differentiated from each other, and indexing of the diffraction patterns obtained was found to be consistent only with αHf, Hf_2Si, and Hf_5Si_3. Of all the silicides that were considered, Hf_5Si_3 was the only silicide that provided a successful match with the EBSP pattern from the phase in Fig. 1 that was identified as Hf_5Si_3 using EMPA. These data indicate that C, N, or O levels greater than 100 ppm are not required to stabilize Hf_5Si_3, because the interstitial levels of the Hf were: C < 11, O < 52, and N < 22 weight ppm, respectively.

The XRD data for the Hf-35Si provided clear evidence for the existence of αHf and Hf_2Si. There were also x-ray lines present that were consistent with the pattern expected for Hf_5Si_3 ($hP16$-$P6_3/mcm$) using lattice parameters of 0.7890 and 0.5558 nm (Ref 9, 10). However, there was a consistent angular shift of the lines to larger angles than expected for the above lattice parameters. This observation indicates a smaller Hf_5Si_3 unit cell than that described by the above lattice parameters, which suggests that the correct lattice parameters of Hf_5Si_3 are closer to those provided by Karpinsky and Evseyev (Ref 5). No βHf was detected in the Hf-35Si.

The microstructure of the Hf-20Si was similar to that of the Hf-35Si except that no Hf_5Si_3 was detected. X-ray diffraction

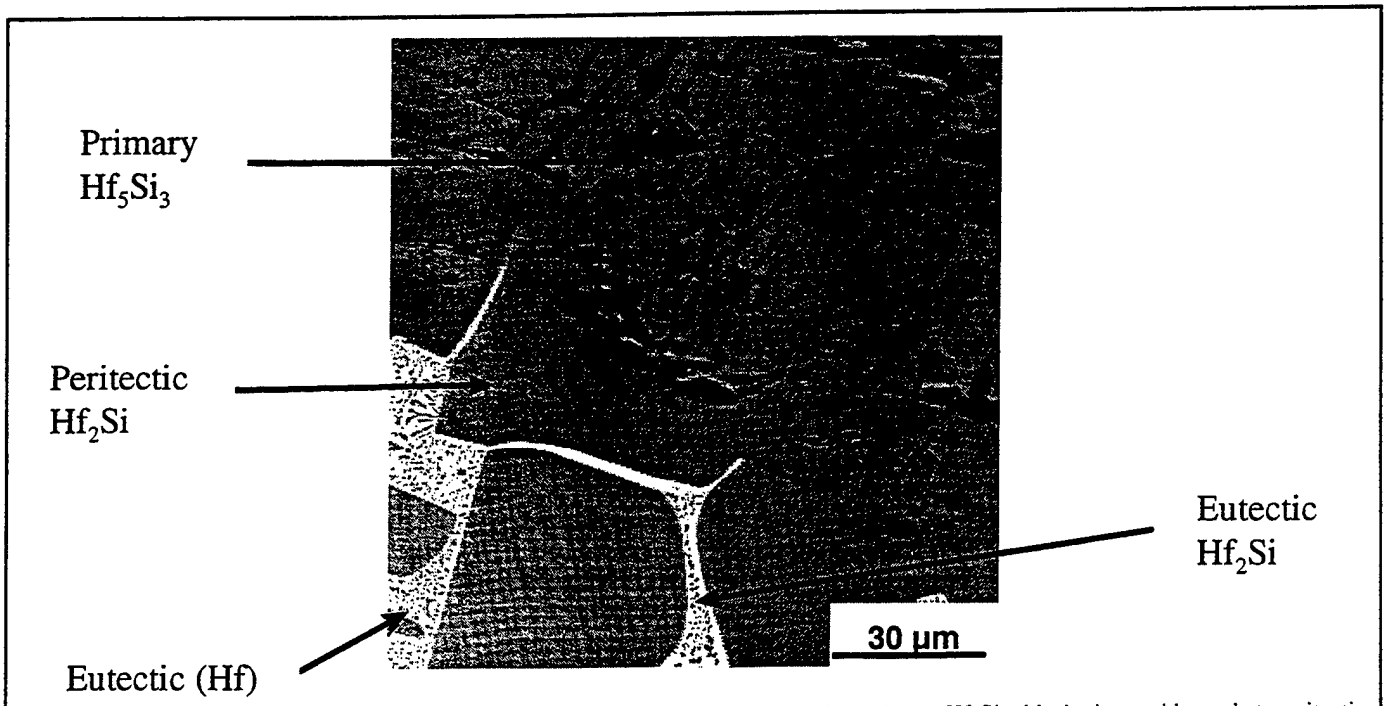
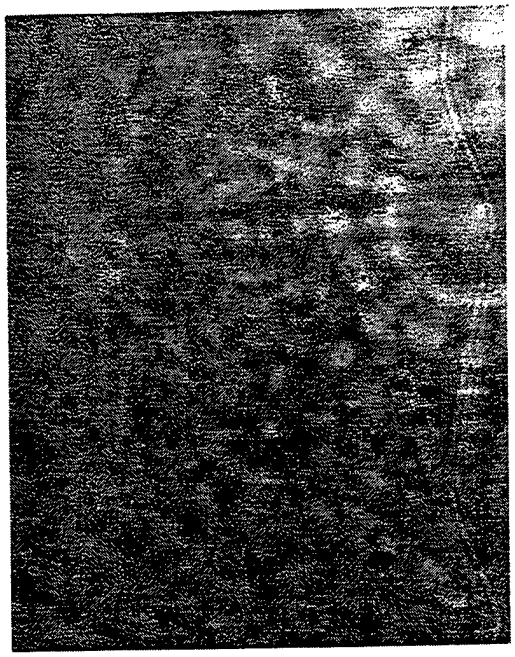


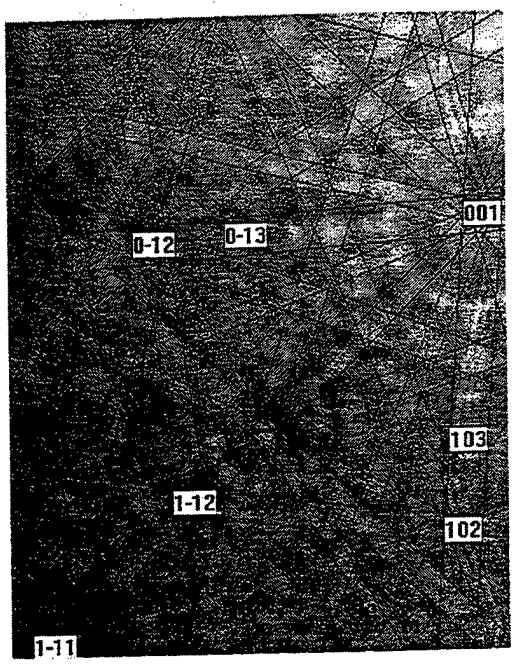
Fig. 1 Microstructure of Hf-35Si cast using cold crucible induction casting, showing primary Hf_5Si_3 (black phase with cracks), peritectic Hf_2Si (dark phase without cracks), and (Hf)-Hf_2Si eutectic. (Hf) is the light phase. Taken using BSE imaging

of the Hf-20Si did not detect any Hf_5Si_3. The Hf_2Si was also identified using transmission electron microscopy. This composition provided evidence for the peritectic and the eutectic reactions; the Hf-20Si composition allows the peritectic ridge to be placed in the Hf-Si binary.

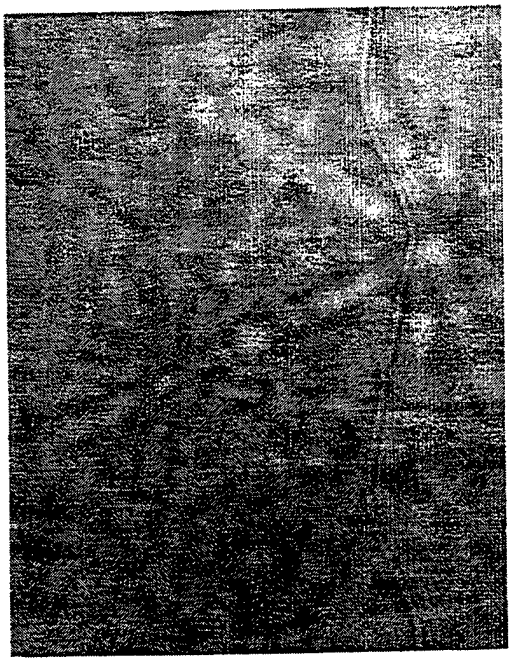
The microstructure of the Hf-12Si eutectic composition is shown in Fig. 3(a) and (b). The microstructure consisted of rods/fibers of Hf_2Si (gray phase) in a (Hf) matrix (white phase). There was also a small volume fraction of primary faceted Hf_2Si dendrites indicating that the Hf-12Si composition was slightly Si-rich of the eutectic composition. The β(Hf) appeared to have transformed completely to α(Hf). The Hf-12Si melting temperature was 1820 °C, which was consistent with that reported previously for the Hf-Hf_2Si eutectic (Ref 3), even though the Hf-12Si was slightly Si-rich of the eutectic composition. A binary alloy of Hf-11.5Si was also directionally



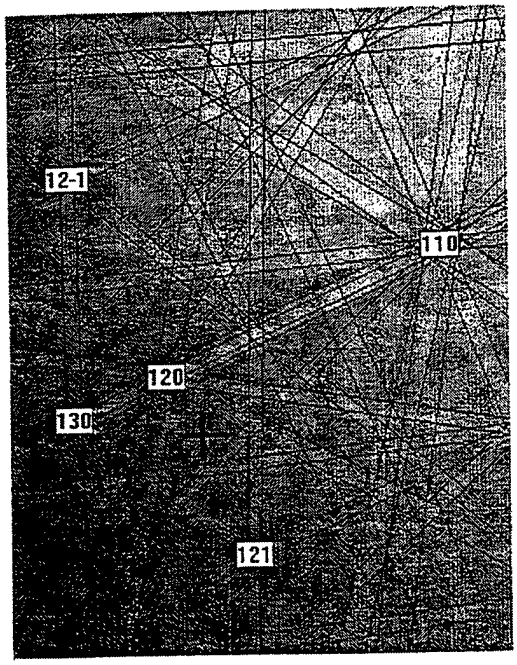
(a)



(b)



(c)



(d)

Fig. 2 EBSP diffraction patterns of (a) Hf_2Si and (c) Hf_5Si_3 in the Hf-35Si alloy. The indexed diffraction patterns are also shown for (b) Hf_2Si and (d) Hf_5Si_3.

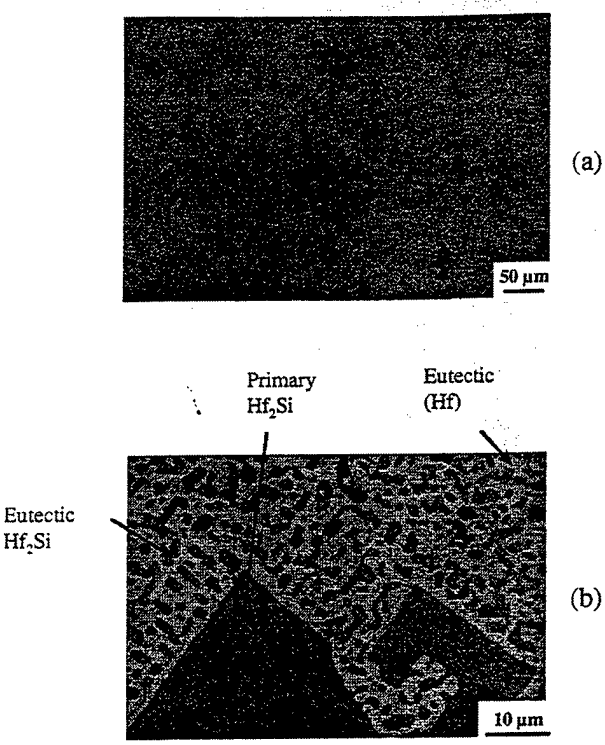


Fig. 3 Microstructure of the transverse section of DS Hf-12Si at (a) low and (b) high magnifications. These micrographs were taken using BSE imaging.

solidified and was found to contain only a very small volume fraction of primary Hf_2Si dendrites (<5%), and it was therefore considered to be much closer to the eutectic composition.

Hf_5Si_3 was also observed in Hf-Si alloys that were modified with Nb. For example, a Hf-55Nb-25Si alloy was directionally solidified, and it was found to contain primary $Hf(Nb)_5Si_3$, peritectic $Hf(Nb)_2Si$ and an interdendritic eutectic of (Hf) and $Hf(Nb)_2Si$; in this case Nb was substituted for Hf in all three phases. This microstructure was similar to that observed in the Hf-35Si. This is further evidence for the existence of Hf_5Si_3 rather than other higher-order silicides, such as Hf_3Si_2 or Hf_5Si_4.

The XRD, EMPA, and EBSP data obtained from the silicides in the binary and ternary alloys obtained in the present work provide clear evidence for the existence of Hf_5Si_3. No Hf_3Si_2 or Hf_4Si_3 phases were detected. Thus, Hf_5Si_3 is stable even at very low total interstitial concentrations (<100 ppm), contrary to previous reports (Ref 3, 4).

Conclusions

The SEM, XRD, EMPA, and EBSP data from high-purity alloys demonstrate the presence of the Mn_5Si_3 type (*hP*16-$P6_3/mmc$) Hf_5Si_3 phase in Hf-Si alloys. Hf_2Si with the Al_2Cu structure type (*tI*12-*I*4/*mcm*) was also observed. Hf_4Si_3, Hf_3Si_2, or the other silicides reported previously were not observed. These data indicate that Hf_5Si_3 is stable at total O, N, and C concentrations less than 100 ppm. This is contrary to previous reports regarding Hf_5Si_3, which claim that it only exists when stabilized by high levels of interstitials.

Evidence for the peritectic reaction $L + Hf_5Si_3 \rightarrow Hf_2Si$ has also been presented. Hf_5Si_3 and Hf_2Si were observed in both the binary Hf-Si and ternary Hf-Nb-Si alloys. The Hf-Hf_2Si eutectic reaction occurs at a similar temperature to that reported previously, but the eutectic composition is closer to Hf-11.5Si.

Acknowledgment

The authors would like to thank D.J. Dalpe for the directional solidification, S.D. Sitzman for the EBSP, and D. Marsh for the XRD. This research was partially sponsored by AFOSR under contract No. F49620-96-C-0022 with Capt. C.H. Ward as Program Manager.

References

1. M.R. Jackson, B.P. Bewlay, R.G. Rowe, D.W. Skelly, and H.A. Lipsitt, *J. Met.*, Vol 48 (No. 1), 1996, p 38-39
2. B.P. Bewlay, M.R. Jackson, W.J. Reeder, and H.A. Lipsitt, *MRS Proc. High Temperature Ordered Intermetallic Alloys VI*, Vol 364, 1994, p 943-948
3. A.B. Gokhale and G.J. Abbaschian, *Bull. Alloy Phase Diagrams*, Vol 10 (No. 4), 1989, p 390-393
4. C.E. Brukl, Tech. Rep. AFML-TR 65-2, Air Force Materials Laboratory, 1968, p 72
5. O.G. Karpinsky and B.A. Evseyev, *Russ. Metall.*, Vol 3, 1969, p 128-130
6. R. Kieffer and F. Benesovsky, *Powder Metall.*, Vol 1/2, 1958, p 145-171
7. G.A. Henshall, M.J. Strum, B.P. Bewlay, and J.A. Sutliff, *Metall. Mater. Trans.*, Vol 28A, 1997, p 2555-2564
8. P. Villars and L.D. Calvert, Ed., *Pearsons Handbook of Crystallographic Data for Intermetallic Phases*, 2nd ed., Vol 1-4, ASM International, 1991
9. H. Nowotny, E. Laube, R. Kieffer, and F. Benesovsky, *Monatsh. Chem.*, Vol 89, 1958, p 701-707
10. O. Schob, H. Nowotny, and F. Benesovsky, *Planseeber. Pulvermetall.*, Vol 10, 1962, p 65-71

Microstructure and Microtexture in Nb-Silicide Based Composites

B.P. Bewlay and J.A. Sutliff

Microscopy and Microanalysis, Vol. 4, 1998

MICROSTRUCTURE AND MICROTEXTURE IN Nb-SILICIDE BASED COMPOSITES

B.P. Bewlay and J.A. Sutliff,

General Electric - Corporate Research and Development, Schenectady. New York 12301.

Directionally solidified in-situ composites based on niobium and niobium silicides, such as Nb_5Si_3 and Nb_3Si, are presently under investigation as structural materials [1, 2]. Alloying additions of elements such as Hf, Ti and Mo to these silicides are also being explored in order to increase strength and oxidation resistance. The present paper describes the effect of Hf, Mo and Ti additions on microstructure and microtexture of high temperature silcide-based in-situ composites.

Alloys were prepared from high purity elements (>99.9%) using induction levitation melting in a segmented water-cooled copper crucible. The alloys were directionally solidified using the Czochralski method [2]. Phase identification was performed using scanning electron microscopy, electron microprobe analysis (EMPA), and automated electron back scattering pattern (EBSP) analysis. Using EBSP, positive phase identification was accomplished by direct comparison of the location and character of the diffraction bands in the experimental pattern with those calculated from simulated patterns generated using the possible structure types.

The microstructure of a composite generated from a Nb-9Mo-22Ti-8Hf-16Si alloy is shown in Figure 1. This composite consisted of eutectic cells of M_5Si_3 with a Nb-based metallic phase. The M_5Si_3 possessed the hP16-$P6_3$/mmc structure rather than the previously reported Nb_5Si_3 tI32-I4/mcm structure [3]. Possibly the hP16 structure was stabilized by the high Ti and Hf additions. EMPA analysis indicated that the approximate compositions of the phases were Nb-16Ti-4Hf-21Mo-2Si and Nb-19Ti-13Hf-2Mo-38Si. The microstructure of a composite generated from a Nb-16Ti-8Hf-16Si is shown in Figure 2. The composite consisted of eutectic cells that contained a M_3Si-type phase together with a Nb-based metallic phase. The scale of the microstructure shown in Figure 2 is significantly larger than that in Figure 1. At these lower Ti and Hf concentrations the eutectic is between the tP32 M_3Si and the Nb-based metal.

EBSP diffraction patterns are shown in Figure 3 for the hP16 M_5Si_3 (a), the Nb-based metallic phase (b), and the Nb_3Si type phase (c). Selected pole figures for the corresponding three phases are shown in Figure 4: (a) the hP16 M_5Si_3 in the Nb-9Mo-22Ti-8Hf-16Si, (b) the metallic phase in the Nb-9Mo-22Ti-8Hf-16Si, and (c) the M_3Si in the Nb-16Ti-8Hf-16Si. These data indicate that in the Nb-9Mo-22Ti-8Hf-16Si the [0001] hP16 M_5Si_3 and the [001] of the metallic phase were strongly aligned with the growth direction. In the Nb-16Ti-8Hf-16Si the [001] M_3Si was aligned with the growth direction, but the metallic phase was not strongly textured.

References

1. M.R. Jackson, B.P. Bewlay, R.G. Rowe, D.W. Skelly, and H.A. Lipsitt, *JOM* **48** (1996)38-39
2. B.P. Bewlay, M.R. Jackson and H.A. Lipsitt, *Metall. and Mater. Trans.*, **279** (1996)3801-3808
3. Pearsons Handbook of Crystallographic Data, ASM International, 1991.

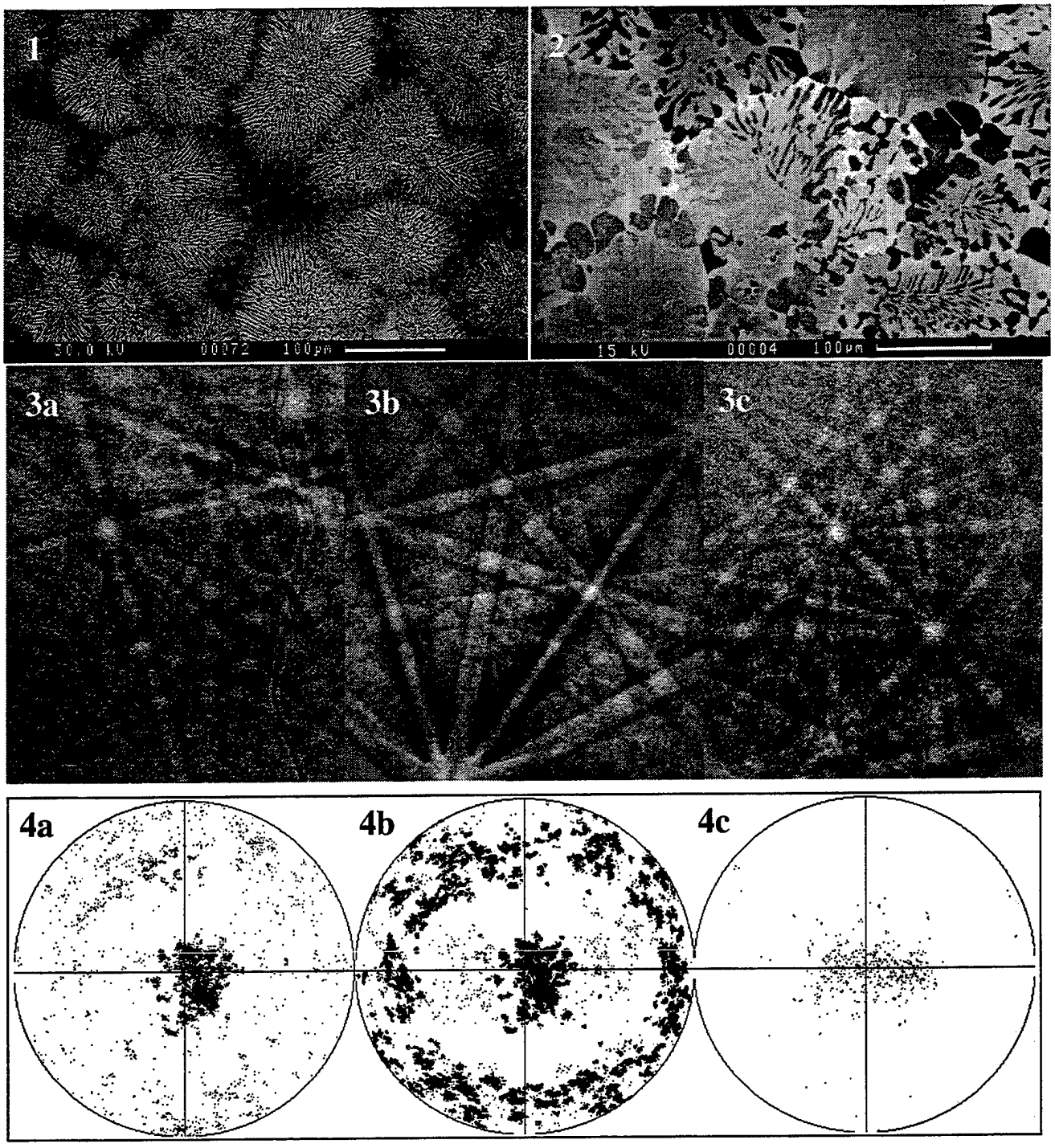


FIG. 1 Backscatter electron image (BEI) of a transverse section of the Nb-9Mo-22Ti-8Hf-16Si alloy. The composite consists of eutectic cells of a Nb solid solution (light phase) and M_5Si_3(dark phase).

FIG. 2 BEI of transverse section of the Nb-16Ti-8Hf-16Si alloy. Cells contain Nb solid solution (light) and M_3Si (dark).

FIG. 3 Diffraction patterns of (a) hP16 M_5Si_3, (b) bcc Nb-based solid solution, and (c) tP32 Nb_3Si.

FIG. 4 (a) {0001} Nb_5Si_3 pole figure and (b) {100} Nb solid solution pole figure in the Nb-9Mo-22Ti-8Hf-16Si, (c), [001] Nb_3Si pole figure in the Nb-16Ti-8Hf-16Si alloy.

Characterisation of Silicide Precipitates in Nb-Si and Nb-Ti-Si Alloys

R.J. Grylls, B.P. Bewlay, H.L. Fraser and H.A. Lipsitt

Philosophical Magazine, 1999

Characterization of silicide precipitates in Nb-Si and Nb-Ti-Si alloys

By R.J. GRYLLS[1], B.P. BEWLAY[2], H.A. LIPSITT[1] and H.L. FRASER[1]

[1]Department of Materials Science and Engineering, The Ohio State University,

Columbus, OH 43210, U.S.A.

[2]General Electric Company, Corporate Research and Development,

Schenectady, NY 12301, U.S.A.

ABSTRACT

The present paper describes the morphology, chemistry and crystallography of silicide precipitates that were observed in Nb-Si and Nb-Ti-Si solid solutions. Although the stable structure of Nb_3Si is tetragonal (tP32), within the body-centered-cubic (bcc) Nb solid solution fine-scale Nb_3Si precipitates were observed with a metastable orthorhombic crystal structure. These precipitates were observed with an acicular morphology, and with sizes ranging from 2nm to 1μm in the as-solidified condition. The orientation relationship between these precipitates and the Nb matrix is (100)//(100) [010]//[010]. It is suggested that the metastable orthorhombic structure forms due to ease of nucleation of this structure in the bcc Nb matrix. The crystallography of these precipitates is described, and these findings are compared with previous data on the Nb-Si system.

1. INTRODUCTION

Recent studies of Nb-Si in-situ composites have shown a promising combination of high-temperature strength, creep resistance and room-temperature fracture toughness (Mendiratta and Dimiduk 1989, Mendiratta *et al.* 1991, Dimiduk *et al.* 1993, Jackson *et al.* 1996, Cockeram *et al.* 1991a). These composites consist of a Nb-silicide toughened with a Nb solid solution (the Nb-Si solid solution is abbreviated by (Nb) in the present paper). The (Nb) may also contain a dispersion of silicide precipitates (Mendiratta *et al.* 1991, Cockeram *et al.* 1991b, Cockeram *et al.* 1992). The purpose of the present paper is to describe the chemistry and crystallography of precipitates that are generated in Nb solid solutions of directionally solidified (DS) composites of binary Nb-Si and ternary Nb-Ti-Si alloys.

The Nb-rich side of the Nb-Si phase diagram contains a eutectic reaction liquid $\rightarrow$ (Nb) + Nb_3Si at 1880°C and 18.2% Si (Bewlay *et al.* 1997) (compositions are given in atom percent throughout this paper), and a eutectoid reaction $Nb_3Si \rightarrow$ (Nb) + Nb_5Si_3 at 1770°C (Mendiratta and Dimiduk 1991, Massalski 1992). These eutectic and eutectoid reactions represent the basis for the in-situ composites that have been investigated previously (Mendiratta and Dimiduk 1989, Jackson *et al.* 1996). Nb_3Si forms by a peritectic reaction between liquid of composition Nb-20%Si and Nb_5Si_3. The eutectoid decomposition kinetics of Nb_3Si to (Nb) and Nb_5Si_3 are very slow (Subramanian *et al.* 1994), and in as-cast alloys with Si concentrations less than the liquid composition at the peritectic temperature, only Nb_3Si and no primary Nb_5Si_3 is observed. The Nb_5Si_3 and Nb_3Si have tI32 (space group I4/mcm) and tP32 (space group $P4_2/n$) crystal structures, respectively.

Mendiratta and Dimiduk (1989) have previously observed Si-rich particles in binary Nb-Si alloys, and they postulated that these precipitates were generated as a result of the decrease in the solubility of Si in (Nb) with decreasing temperature on cooling after a 1500°C heat treatment. Cockeram *et al.* (1991a, 1991b) also characterized silicide precipitates seen in a Nb-10Si alloy. The assessed Nb-Si phase diagram (APD) (Massalski 1992) indicates that Nb has a maximum silicon solubility of 3.5% at the eutectic temperature (1880°C) and it decreases to 0.5% at

1770°C. These data can therefore account for the precipitation that has been reported. Mendiratta and Dimiduk (1991) reported the following Si concentrations in Nb as a function of temperature: 1.31% at 1700°C, 0.61% at 1500°C and 0.60% at 1300°C. These data indicate a very sharp decrease in the Si solubility from 3.5% at 1880°C to 1.31% at 1700°C, but there is a smaller decrease from 1700°C to 1300°C. Below 1200°C the solubility of Si in Nb is < 0.1% (Massalski 1992). It should be noted that the recently-reported data regarding solubility of Si in Nb (Mendiratta and Dimiduk 1991) differs from the APD.

Cockeram *et al.* (1991b) characterized precipitates that were found in arc melted Nb-10Si. They used electron diffraction and Energy Dispersive X-ray Spectroscopy (EDS) in the Transmission Electron Microscope (TEM) to identify precipitates in primary (Nb) dendrites. They claimed that the precipitates possessed the Nb_3Si stoichiometry, and that they had the stable tP32 structure. Based on the volume fraction of Nb_3Si precipitates that they observed in the (Nb), they suggested that the maximum solubility of Si in (Nb) at the eutectic temperature was 4.4%.

Phase stability in the ternary Nb-Ti-Si system has been investigated recently and two-phase composites with a wide range of microstructures have been reported (Bewlay *et al.* 1997, Subramanian *et al.* 1994, Bewlay *et al.* 1994). For Ti concentrations up to ~50% and Si concentrations less than 16% the eutectic reaction between (Nb) and Nb_3Si still occurs. In this system the Nb_3Si with Ti in solid solution is referred to as $(Nb,Ti)_3Si$, because Nb_3Si and Ti_3Si are isomorphous. Similarly, the Nb with Ti and Si in the bcc solid solution is referred to as (Nb,Ti). The (Nb,Ti) solid solution was previously found to contain up to 1.2% Si (Bewlay *et al.* 1997). Silicide precipitates have also been observed in the metallic phase of the (Nb,Ti)-$(Nb,Ti)_3Si$ composites (Bewlay *et al.* 1998). However, there has been no previous examination of the crystallography of these precipitates or their orientation relationship with the (Nb,Ti) matrix.

The present paper describes characterization of silicide precipitates in the Nb solid solutions of composites generated from binary Nb-Si and ternary Nb-Ti-Si alloys. These findings are compared with previous data on the Nb-Si system.

2. Experimental Procedures

Binary Nb-Si and ternary Nb-Ti-Si alloys were prepared from >99.99% purity elements by induction levitation melting in a segmented water-cooled copper crucible. The alloys were triple melted and then directionally solidified using a modified Czochralski method in order to generate two-phase in-situ composites, as has been described in more detail elsewhere (Jackson *et al.* 1996, Bewlay *et al.* 1994).

TEM foils were electro-discharge-machined perpendicular to the growth direction of the DS composites. Samples were ground to 100μm thickness, mechanically dimpled to 35μm thickness, then perforated using a Gatan DuoMill ion-mill. Samples were examined using a Philips XL-30 Field Emission Gun Scanning Electron Microscope (FEGSEM), a Philips CM200 TEM and a Philips CM300 FEGTEM. Electron microdiffraction was used to determine the crystallography of the silicide precipitates and their orientation relationship with the (Nb) matrix. EDS was performed in order to determine the precipitate chemistry.

3. Results

3.1. *Binary Nb_3Si precipitates*

The Nb-14%Si hypoeutectic alloy contains (Nb) dendrites and an inter-dendritic eutectic of (Nb) and Nb_3Si, as has been described previously (Bewlay *et al.* 1993, Bewlay *et al.* 1994). Figure 1 shows the typical microstructure of the alloy, with (Nb) as the light phase, and Nb_3Si as the dark phase. Nb_3Si is continuous within the eutectic portion of the microstructure. The typical microstructure of the (Nb) of the DS composite as seen in the TEM is shown in figure 2. Each (Nb) dendrite is essentially a single crystal: no subgrains have been observed.

Heterogeneous precipitation of large-scale silicide precipitates was observed. These precipitates are indicated in figure 2, and a typical group of large-scale silicide precipitates within the (Nb) dendrite of the Nb-14Si composite is shown in more detail in figure 3. These silicides possess Nb_3Si stoichiometry, as will be shown later. The principal axis of the large (~500nm long), central precipitate is parallel to the [100] direction of the (Nb). Secondary precipitates have grown off the large central precipitate in directions parallel to the [010] and [001] of the (Nb). Precipitate-free zones ~100nm wide were observed in the (Nb) around the silicide precipitates. In the (Nb) dendrite away from the large-scale silicide precipitates contrast was observed from fine-scale (~50nm long) acicular silicide precipitates, as indicated in figure 3. These precipitates are distributed homogeneously throughout the dendrite, except in the precipitate-free-zones, where they are absent.

Precipitate-free-zones, typically 1μm wide, are also found at the boundaries of the (Nb) dendrites. Cockeram *et al.* (1991b) also reported precipitate free zones 0.6-1.3μm wide in the primary (Nb) dendrites. No precipitates are found in the eutectic (Nb). This is expected, since the width of the eutectic (Nb) ligaments is less than the width of the precipitate-free-zone seen in the (Nb) dendrite.

Electron microdiffraction patterns, shown in figure 4, indicate that the eutectic Nb_3Si possesses the stable tP32 structure. However, the silicide precipitates within the (Nb) were found to possess a different crystal structure, as will be shown.

The silicide precipitate chemistry was determined using TEM EDS, as described below. Several precipitate compositions were compared to the composition of the eutectic Nb_3Si using EDS measurements taken from very thin regions at the edge of the foil, where any spectral interference from the (Nb) matrix is minimized. Measurements were taken using the CM300 FEGTEM to make use of the fine probe size and high intensity afforded by the FEG source. Assuming that the eutectic Nb_3Si has the exact 3:1 stoichiometry, and thus using it to determine k-factors, the composition of the precipitates was determined to be in the range Nb-24%Si to Nb-

27%Si. This is sufficiently small scatter that it may be concluded that the composition of the precipitates is based on the stoichiometry Nb_3Si.

Diffraction data obtained in the present study, and shown in figure 5, show that these large-scale silicide precipitates possess an orthorhombic crystal structure. Extensive tilting experiments were performed to determine the point group and lattice parameters. The diffraction patterns in figure 5 were obtained using the high-tilt stage of the CM200 TEM, where it was possible to tilt 90° from one <100> pole to the next. Thus it was possible to determine unequivocally that the structure was orthorhombic. Approximate lattice parameters were obtained by assuming that the lattice parameter of the (Nb) matrix was 3.30Å. Thus the lattice parameters were determined to be a = 9.3Å, b = 15.9Å, c = 3.4Å, which approximately corresponds to factors of 3, 5, and 1 times that of the (Nb) lattice parameter. The point group was determined to be mmm, and, based solely on the reflections observed to be absent in the microdiffraction patterns, it is suggested that the space group is Immm.

The following orientation relationship was observed between the precipitates and the (Nb) matrix:

$$[100]_{Nb} \,||\, [100]_{ppt} \,;\, (001)_{Nb} \,||\, (001)_{ppt}.$$

The precipitates described by Cockeram *et al.* (1992) possessed a rod/plate-like morphology (0.05-0.2μm). Cockeram *et al.* (1991b) reported that the diffraction patterns from the silicide precipitates observed in that study were consistent with a tetragonal structure with lattice parameters of a = 10.224Å and c = 5.189Å.

Certain diffraction patterns obtained from the silicide precipitates in the (Nb) of the DS composites observed in the present study appear identical to those published by Cockeram *et al.* (1991b), where they are identified as originating from tetragonal Nb_3Si. Re-examination of the precipitate diffraction patterns published previously indicates that the diffraction spots in figure 3c (Cockeram *et al.* 1991b) are of approximately the correct spacing, but the angles between

reflections are inconsistent with those expected for the <311] poles* of tetragonal Nb_3Si. Essentially, the Zero-Order-Laue-Zone (ZOLZ) in figure 3c (Cockeram *et al.* 1991b) appears to show 2mm symmetry, which the <311] poles of tetragonal Nb_3Si do not possess. Furthermore, the proposed orientation relationship of $[113]_{Nb_3Si} \parallel [001]_{Nb}$; $(\sim 110)_{Nb_3Si} \parallel (100)_{Nb}$ is inconsistent with the claim that the <311] poles are parallel to $<001>_{Nb}$ directions, since the angle between [113] and [311] or [131] is ~44°, not 90°, and no <311] pole is at 90° to any <113> pole. In fact the poles shown in figures 3c and 4a (Cockeram *et al.* 1991b) correspond very well to the [010] and [100] poles shown in figure 5 of the present study. These slight inconsistencies in the analysis by Cockeram *et al.* (1991b) probably arose because the precipitates observed were small (<100nm in width) and the inter-particle spacing was small (<100nm). The diffraction patterns seen in (Cockeram *et al.* 1991b) and in the present study appear identical, and so it is concluded that the precipitates observed in the previous study of Nb-10Si were also orthorhombic.

The fine-scale precipitates, shown in detail in figure 6, were found to have the same structure as the large-scale precipitates. Figure 7 shows the three <001> poles of the orthorhombic structure taken from precipitates such as those shown in figure 6. The precipitates are faceted, with facet faces parallel to $\{110)_{ppt}$, as is shown in figure 6. Precipitates have an acicular morphology, with $[001]_{ppt}$ parallel to the axis of the needle.

3.2. *Ternary $(Nb,Ti)_3Si$ precipitates*

The microstructure of the as-DS Nb-42.5Ti-15Si consisted of non-faceted (Nb,Ti) dendrites (20-50μm), which are the lighter phase in the BSE micrograph in figure 8, together with large-scale (~50 μm) faceted $(Nb,Ti)_3Si$ dendrites. The microstructure showed good alignment of both non-faceted (Nb,Ti) dendrites and faceted $(Nb,Ti)_3Si$ dendrites with the growth direction.

---

* The mixed notation {hkl) and <uvw] is used to differentiate the first two indices from the third index, both in the case of the tetragonal structure *and* the orthorhombic structure.

A typical array of silicide precipitates within a (Nb,Ti) dendrite is shown in figure 9. The precipitates are elongated in the $[001]_{ppt}$ direction, and all possible orientational variants with the matrix are seen. Precipitation is generally homogeneous, as shown in figure 10, with groups of heterogeneously-nucleated precipitates surrounded by a precipitate-free zone, as shown in figure 9. The binary alloy discussed earlier also exhibited a bimodal precipitate distribution, although it is yet to be confirmed that the bimodal array in both alloys is formed by a similar precipitation mechanism.

The silicide precipitates in the (Nb,Ti) have the same orthorhombic crystal structure and orientation relationship with the (Nb,Ti) matrix as found in the binary alloy, and to within the limits of the TEM diffraction measurements, the same lattice parameters. The precipitates are faceted, with facet faces parallel to $\{110)_{ppt}$ as found for the binary alloy. Typically, the homogeneous precipitates had a width of ~10nm (facet-to-facet) in the as-DS condition. Again, EDS identified these silicide precipitates as $(Nb,Ti)_3Si$-type rather than $Nb(Ti)_5Si_3$ type. While the details of these precipitates are reported for the (Nb,Ti) of the Nb-42.5Ti-15Si, similar precipitates have also been observed in Nb-44Ti-12Si, Nb-1Si and other Nb-Ti-Si alloys in the DS condition, as well as after various heat treatments. Work is continuing to establish the precipitation kinetics at various temperatures, and to examine the effect of these precipitates on mechanical properties.

4. Discussion

In the (Nb,Ti) it was expected that the precipitates would be the Nb_3Si type because additions of ≥17% Ti stabilize Nb_3Si in preference to Nb_5Si_3 (Bewlay *et al.* 1997, Subramanian *et al.* 1994). However in the binary alloy Nb_3Si is unstable below 1770°C. Thus in the binary alloy not only is the precipitate *composition* metastable with respect to Nb_5Si_3, but the *crystal structure* is also metastable with respect to the stable tP32 structure of Nb_3Si.

Therefore, why is the orthorhombic phase observed in these alloys? Simply from considerations of the mismatch between precipitate and matrix, it can be seen that the interface

between matrix and orthorhombic precipitate will require one extra plane of atoms present only when the precipitate reaches ~5nm in size. Thus the interphase interface would be expected to be coherent up to a certain size of precipitate, and semi-coherent for larger sizes. Although the atomic structure of the precipitates has not been determined, diffraction evidence suggests that the orthorhombic precipitates may be body-centered in structure, and thus may nucleate easily by ordering of the bcc matrix, which could make the barrier to nucleation quite low. No simple lattice match exists between the (Nb) matrix and either tP32 Nb_3Si or tI32 Nb_5Si_3 (Cockeram *et al.* 1991a). This suggests that the barrier to nucleation of orthorhombic Nb_3Si may be significantly lower than the barrier to nucleation of either of the stable structures. Therefore it is thought that the orthorhombic structure is seen because of close lattice matching of the precipitate and matrix, and so the orthorhombic precipitates are able to form at a lower undercooling than either of the stable structures. Work is continuing to establish the heat-treatment conditions whereby the orthorhombic structure transforms to the stable phase.

The ordered orthorhombic $(Nb,Ti)_3Si$ and Nb_3Si are thus considered to be metastable precipitates that may be nucleated by ordering of Si atoms within the (Nb). In the case of $(Nb,Ti)_3Si$ the orthorhombic structure is intermediate to the stable tP32 $(Nb,Ti)_3Si$. However, Nb_3Si is intermediate to the stable tI32 Nb_5Si_3.

5. Conclusions

Precipitates were observed in (Nb) and (Nb,Ti) of the in-situ composites of both binary Nb-Si and ternary Nb-Ti-Si alloys. The precipitates possess an ordered orthorhombic structure, with lattice parameters a = 9.3Å, b = 15.9Å, c = 3.4Å. The following precipitate-matrix orientation relationships were observed in both the Nb-Si binary and the Nb-Ti-Si ternary alloys:

$$[100]_{Nb} \,||\, [100]_{ppt} \,;\, (001)_{Nb} \,||\, (001)_{ppt}$$

The precipitates exhibited a bimodal distribution, and it is suggested that the large-scale precipitates nucleate heterogeneously and finer-scale homogeneously. However, all precipitates showed the same crystal structure, orientation relationships and acicular morphology, with

$[001]_{ppt}$ being parallel to the principal axis of the precipitate. The bulk Nb_3Si in the binary Nb-Si and the bulk $(Nb,Ti)_3Si$ in the Nb-Ti-Si alloys possess the stable tP32 structure.

The $(Nb,Ti)_3Si$ precipitates are metastable with respect to the tP32 structure, but they possess the stable stoichiometry. The Nb_3Si precipitates are metastable with respect to both the stoichiometry and crystal structure of tI32 Nb_5Si_3. Ordering to the metastable orthorhombic Nb_3Si requires a smaller nucleation barrier than to the stable tI32 Nb_5Si_3 and the close matching of the lattice plane spacing of the matrix and precipitate allows the interfacial energy to be minimized.

The interphase interfaces are semi-coherent for the large-scale precipitates and are expected to be coherent for very fine precipitates (~5nm in size). Incoherent orthorhombic precipitates were not observed.

ACKNOWLEDGMENTS

The authors would like to thank D.J. Dalpe for preparation of the initial DS samples. Grateful thanks are extended to Suqin Meng for the often difficult TEM sample preparation. This research was partially sponsored by AFOSR under contract #F49620-96-C-0022 with Capt. C.H. Ward and Dr. S. Wu as Program Managers.

REFERENCES

Bewlay, B.P., Lipsitt, H.A., Reeder, W.J., Jackson, M.R., and Sutliff, J.A., 1993, *Processing and Fabrication of Advanced Materials for High Temperature Applications III*, edited by V.A. Ravi, T.S. Srivatsan, and J.J. Moore (Warrendale Pennsylvania, The Minerals Metals and Materials Society) p. 547.

Bewlay, B.P., Jackson, M.R., Reeder, W.J., and Lipsitt, H.A., 1994, *High Temperature Ordered Intermetallic Alloys VI*, Materials Research Society Symposium Proceedings, **364**, edited by J.A. Horton, I. Baker, S. Hanada, R.D. Noebe, and D.S. Schwartz (Pittsburgh, Pennsylvania: Materials Research Society) p. 943.

Bewlay, B.P., Jackson, M.R., and Lipsitt, H.A., 1997, *J. phase equil.*, **18**, 264.

Bewlay, B.P., Bishop, R.R., and Jackson, M.R., 1998, submitted to *J. phase equil.*

Cockeram, B., Lipsitt, H.A., Srinivasan, R. and Weiss, I., 1991a, *Scripta metall. mater.*, **25**, 2109.

Cockeram, B., Saqib, M., Omlor, R., Srinivasan, R., Matson, L.E. and Weiss, I., 1991b, *Scripta metall. mater.*, **25**, 393.

Cockeram, B., Lipsitt, H.A., Srinivasan, R. and Weiss, I., 1992, *Scripta metall. mater.*, **26**, 755.

Dimiduk, D.M., Mendiratta, M.G., and Subramanian, P.R., 1993, *Structural Intermetallics*, edited by R. Darolia, J.J. Lewandowski, C.T. Liu, P.L. Martin, D.B. Miracle, and M.V. Nathal (Warrendale Pennsylvania, The Minerals Metals and Materials Society) p. 619.

Jackson, M.R., Bewlay, B.P., Rowe, R.G., Skelly, D.W., and Lipsitt, H.A., 1996, *J. Metals*, **48**, 38.

Massalski, T.B., 1992, *Binary Alloy Phase Diagrams* (ASM Metals Park, Ohio), **3**, 2764.

Mendiratta, M.G., and Dimiduk, D.M., 1989, *High Temperature Ordered Intermetallic Alloys III*, Materials Research Society Symposium Proceedings, **133**, edited by C.T. Liu, A.I. Taub, N.S. Stoloff and C.C. Koch (Pittsburgh, Pennsylvania: Materials Research Society) p. 441.

Mendiratta, M.G., and Dimiduk, D.M., 1991, *Scripta metall. mater.*, **25**, 237.

Mendiratta, M.G., Lewandowski, J.J., and Dimiduk, D.M., 1991, *Metall. Trans. A*, **22**, 1573.

Subramanian, P.R., Mendiratta, M.G., and Dimiduk, D.M., 1994, *High Temperature Silicides and Refractory Alloys*, Materials Research Society Symposium Proceedings, **322**, edited by C.L. Briant, J.J. Petrovic, B.P. Bewlay, A.K. Vaseduvan and H.A. Lipsitt (Pittsburgh, Pennsylvania: Materials Research Society) p. 491.

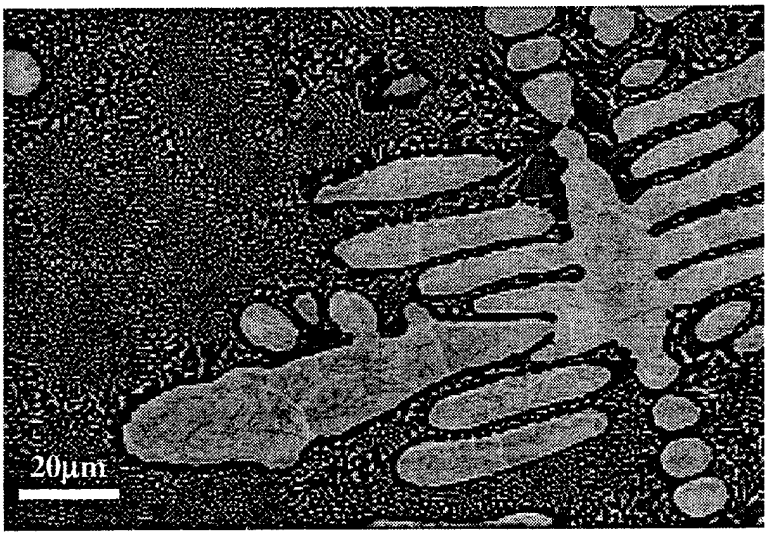


Figure 1 Backscattered Electron (BSE) scanning electron micrograph showing a transverse section through the as-DS binary composite. The (Nb) dendrite is surrounded by a eutectic mixture of Nb_3Si and (Nb). (Nb) is the lighter phase.

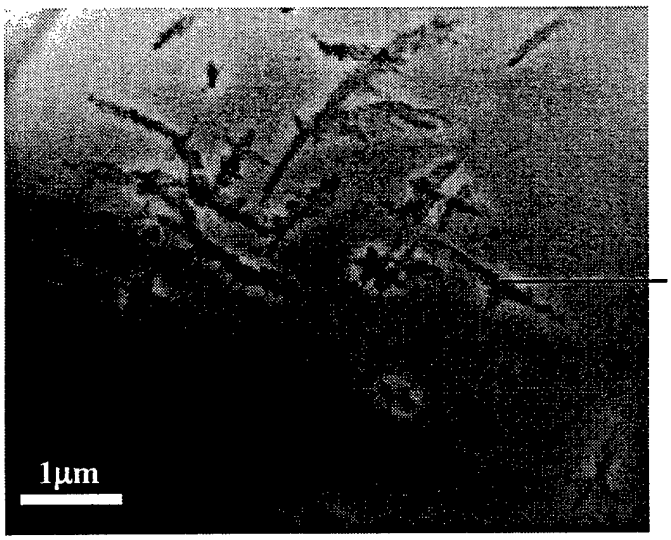


Figure 2 Many-beam bright-field transmission electron micrograph showing the typical distribution of precipitate groups within a (Nb) dendrite. Each group consists of many precipitates. Beam direction **B** is close to $<001>_{(Nb)}$.

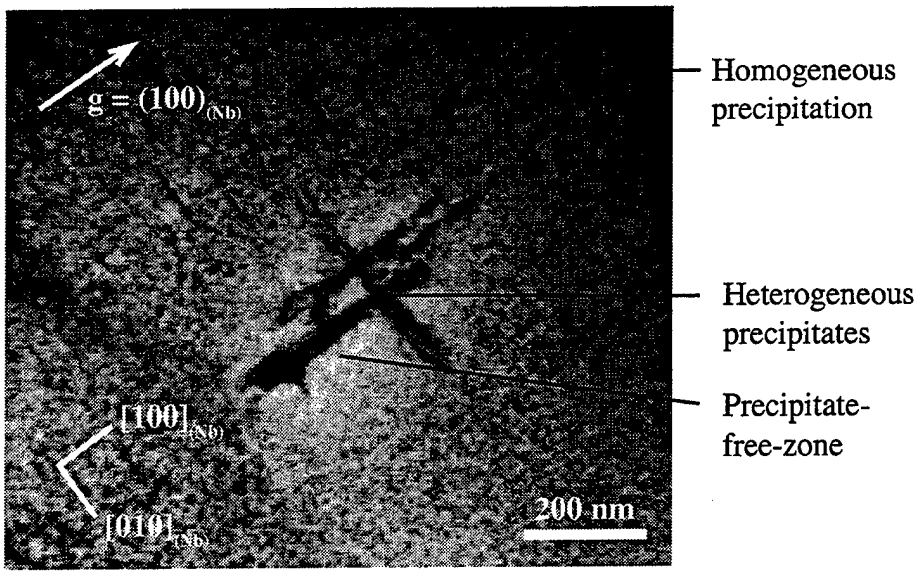


Figure 3 Two-beam bright-field transmission electron micrograph showing a typical group of heterogeneously-nucleated precipitates within a (Nb) dendrite. A precipitate-free zone can be seen around the group. Outside this zone, fine-scale, homogeneously-nucleated acicular precipitates are seen, as shown in more detail in Figure 6. **B** is close to $[001]_{(Nb)}$.

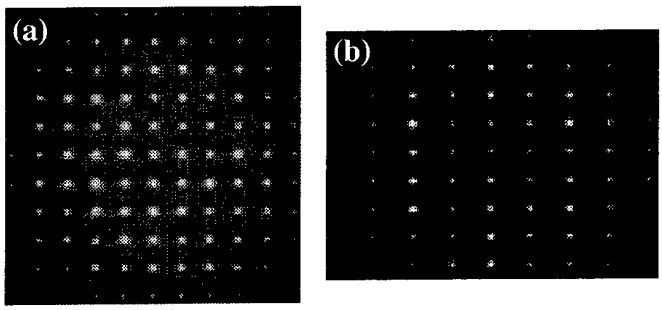


Figure 4 Microdiffraction patterns showing the (a) [001] and (b) [110] poles of the continuous Nb_3Si phase formed during eutectic solidification. All poles and angles between poles are consistent with the stable tP32 structure of Nb_3Si.

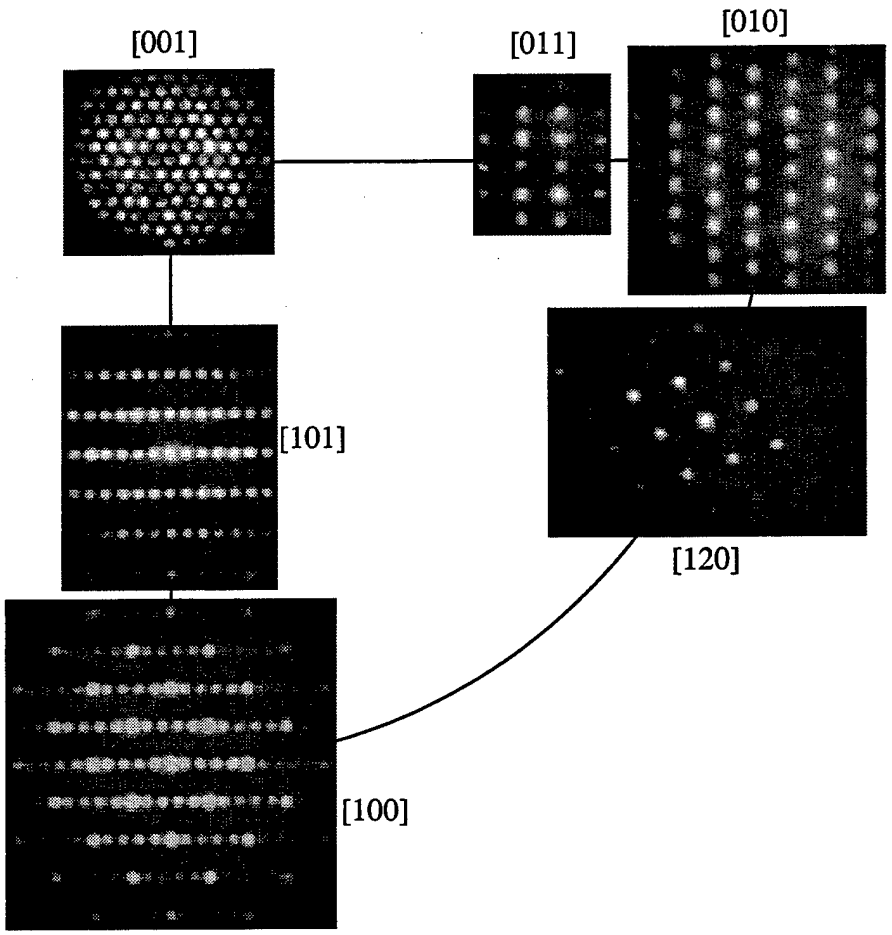


Figure 5 Microdiffraction patterns taken from large-scale Nb_3Si precipitates within a (Nb) dendrite. All poles and angles between poles are consistent with an orthorhombic structure, point group mmm, with lattice parameters a = 9.3Å, b = 15.9Å, c = 3.4Å.

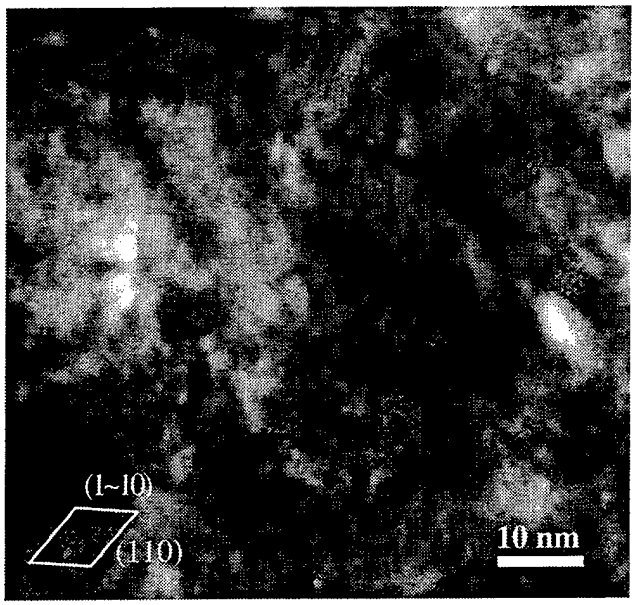


Figure 6 Many-beam bright-field transmission electron micrograph showing fine orthorhombic precipitates. The precipitates tend to be faceted, with facet faces parallel to $\{110\}_{ppt}$. Only precipitates with [001] parallel to the beam direction are imaged in this case. Precipitates lying in the plane of the foil are essentially invisible. One precipitate has been outlined, and the faceted planes identified. $\underline{\mathbf{B}} = \langle 001 \rangle_{(Nb)}$.

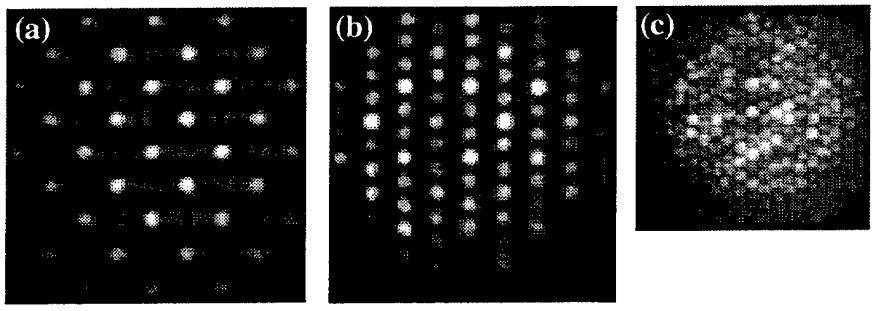


Figure 7 Microdiffraction patterns taken from the very fine Nb_3Si precipitates shown in Figure 6. The zone-axis is in each case $\langle 100 \rangle_{Nb}$, and the diffraction patterns obtained are entirely consistent with the mmm orthorhombic structure. (a) [100] (b) [010] (c) [001].



Figure 8 BSE scanning electron micrograph showing a transverse section through the as-DS ternary composite. (Nb,Ti) is the lighter phase, with $(Nb,Ti)_3Si$ the darker phase.

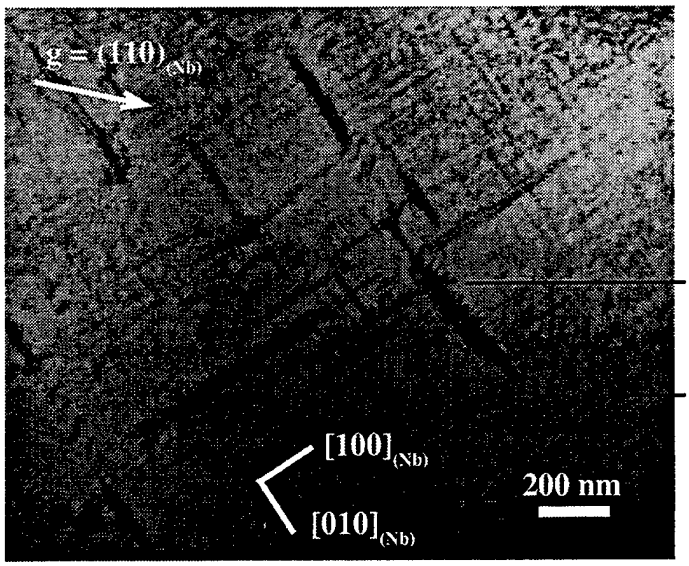


Figure 9 Two-beam bright-field transmission electron micrograph showing typical groups of precipitates within a (Nb,Ti) dendrite. Precipitate-free zones can be seen around the larger precipitates. Outside this zone, fine-scale, homogeneously-nucleated acicular precipitates are seen, as shown in Figure 10. **B** is close to $[001]_{(Nb)}$.

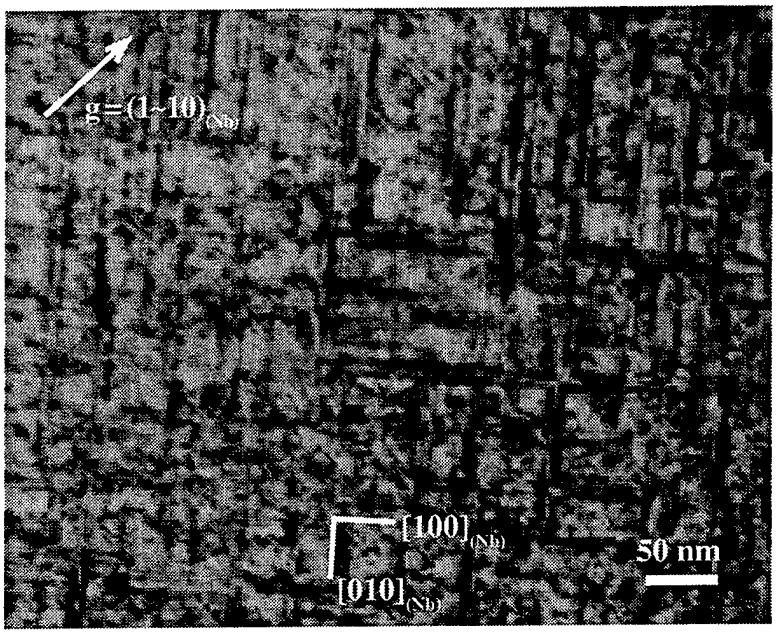


Figure 10 Two-beam bright-field transmission electron micrograph showing homogeneously-nucleated acicular precipitates within a (Nb,Ti) dendrite. **B** is close to $[001]_{(Nb)}$.

Ductile-Phase Toughening in V-V_3Si In-Situ Composites

G.A. Henshall, M.J. Strum, B.P. Bewlay, and J.A. Sutliff

Metall. and Mater. Trans. A, December 1997

Ductile-Phase Toughening in V-V_3Si *In Situ* Composites

G.A. HENSHALL, M.J. STRUM, B.P. BEWLAY, and J.A. SUTLIFF

This article describes the room-temperature fracture behavior of ductile-phase-toughened V-V_3Si *in situ* composites that were produced by arc melting (AM), cold-crucible induction melting (IM), and cold-crucible directional solidification (DS). Composites were produced containing a wide range of microstructures, interstitial impurity contents, and volume fractions of the ductile V-Si solid solution phase, denoted (V). The fracture toughness of these composites generally increases as the volume fraction of (V) increases, but is strongly influenced by the microstructure, the mechanical properties of the component phases, and the crystallographic orientation of the (V) phase with respect to the maximum principal stress direction. For eutectic composites that have a (V) volume fraction of about 50 pct, the fracture toughness increases with decreasing "effective" interstitial impurity concentration, [I] = [N] + 1.33 [O] + 9 [H]. As [I] decreases from 1400 ppm (AM) to 400 ppm (IM), the fracture toughness of the eutectic composites increases from 10 to 20 MPa $\sqrt{m}$. Further, the fracture toughness of the DS eutectic composites is greater when the crack propagation direction is perpendicular, rather than parallel, to the composite growth direction. These results are discussed in light of conventional ductile-phase bridging theories, which alone cannot fully explain the fracture toughness of V-Si *in situ* composites.

I. INTRODUCTION

STRUCTURAL applications of many monolithic intermetallic compounds are limited by their low intrinsic fracture toughness. Therefore, ductile-phase-toughened intermetallic composites have been examined widely in recent years as an approach to produce intermetallic-based composites with substantially improved fracture toughness. Such composites have been generated using both extrinsic[1–4] and *in situ*[5,6,7] methods. The *in situ* approach, in which the ductile phase dispersion is generated on solidification, is the focus of the present study because of its potential for relatively low cost production of components. Further, *in situ* composites are intrinsically thermodynamically stable.[7] However, the extent to which the microstructures can be tailored is more limited for *in situ* composites than for extrinsic ones. Solidification conditions and alloy composition are two primary variables through which *in situ* composite microstructures can be optimized.

The V-Si system was chosen as a model for studying ductile-phase-toughened *in situ* composites.[8,9] This system was chosen rather than the more technologically important and well-studied Nb-Si system, because the Nb-Si phase diagram is relatively complex, resulting in complex microstructures.[7,10] In contrast, the V-Si phase diagram[11] contains a simple eutectic between the V_3Si intermetallic and the terminal metallic solid solution, and this allows the generation of simple composite microstructures. Specifically, the eutectic reaction occurs at approximately 1870 °C and 7.6 wt pct Si (all compositions given in this article are in weight percent). At the eutectic temperature, the bcc V-Si solid solution, denoted (V), contains 4 pct Si, and the V_3Si (A15 structure), which also exists as a solid solution and is hereafter denoted (V_3Si), has a composition of 11 pct Si. The phase concentrations change as the temperature decreases from the eutectic, but below about 1400 °C, the compositions of the two solid solutions remain nearly constant at 2.7 pct Si for the (V) and 13.1 pct Si for (V_3Si). V-V_3Si composites were synthesized by (1) conventional arc melting (AM), (2) cold-crucible induction melting (IM), and (3) cold-crucible directional solidification (DS). Through the use of these different casting methods, and by varying the alloy Si concentrations, composites were produced with a wide range of microstructures, interstitial impurity concentrations, and volume fractions of the ductile (V) phase.

The fracture toughness of the V-V_3Si composites is discussed in relation to current theories of ductile-phase toughening, for which crack bridging is the most prominent assumption. The toughness enhancement provided by ductile-phase bridging has been analyzed by several investigators.[12–22] These analyses assume constrained deformation of a uniform distribution of bridging particles much larger in size than the local crack opening displacement. The particles deform and fail in a ductile manner behind the crack tip, thereby increasing the energy required to completely separate the crack surfaces. The most common expression for small, steady-state bridging zones is that of Ashby *et al.*,[12] in which the composite fracture toughness, K_c, is given by

$$K_c = K_m + E\left[CV_f \frac{\sigma_0}{E} a_0\right]^{1/2} \qquad [1]$$

which depends on K_m, the fracture toughness of the matrix, and the modulus, E, volume fraction, V_f, yield strength, σ_0, and radius, a_0, of the ductile phase. The constraint parameter, C, which is proportional to the work required to rupture the ductile phase, is given by

$$C = \frac{1}{\sigma_0 a_0} \int_0^{a^*} \sigma(u)\,du \qquad [2]$$

G.A. HENSHALL and M.J. STRUM, formerly with the Lawrence Livermore National Laboratory, Livermore, CA 94551, are with the Hewlett-Packard Company, Palo Alto, CA 94304. B.P. BEWLAY and J.A. SUTLIFF are with the General Electric Company, Schenectady, NY 12301.

Manuscript submitted September 30, 1996.

U.S. GOVERNMENT WORK
NOT PROTECTED BY U.S. COPYRIGHT

Table I. Alloy Chemical Compositions

Designation	Nominal Vol Pct (V)	Si (Wt Pct)	V (Wt Pct)	O (Ppm)	N (Ppm)	H (Ppm)	[I] (Ppm)	
AM-2	100	2.70 ± 0.05	97.2	290	370	30	1026	
IM	100	2.84 ± 0.05	97.1	250	43	19	546	hypo-
AM-1*	90	4.21 ± 0.08	95.7	470	810	9	1516	eutectic
DS	90	5.24 ± 0.10	94.7	210	40	5	364	
AM-1	70	5.42 ± 0.10	94.5	260	370	52	1184	
AM-1*	50	7.66 ± 0.15	92.2	410	870	4	1451	
AM-2	50	7.30 ± 0.15	92.6	260	280	72	1274	eutectic
DS	50	7.30 ± 0.15	92.6	130	58	22	429	
IM	50	7.25 ± 0.15	92.7	200	30	9	377	
AM-1	30	10.0 ± 0.20	89.9	240	480	20	979	hyper-
DS	15	11.5 ± 0.20	88.4	170	51	9	358	eutectic

*Degassed for 1 h at 800 °C after AM.

where σ is the nominal tensile stress in the ductile phase, u is the displacement of the ductile phase, and u^* is the displacement of the ductile phase at rupture. Experimentally determined values of C typically vary between 1.6 and 6.0,[12] depending on the extent of the interphase debonding and the material system. The value of C, and hence the composite toughness, generally increases as the debond length increases.[12–22] One aim of the present study was to evaluate the extent of ductile bridging in V-V_3Si *in situ* composites and the accuracy of Eqs. [1] and [2] in describing the fracture toughness of composites with a broad range of ductile phase volume fractions. Additional aims were to evaluate the influence of microstructure, the mechanical properties of the component phases, and the impurity elements on the fracture behavior.

II. EXPERIMENTAL PROCEDURES

The composites used in this study were prepared by arc melting,[8] induction melting, and directional solidification.[9] The first series of arc-melted alloys (AM-1) was cast using 99.8 pct pure V sheet stock that was acid cleaned in a HNO_3/HF solution. To remove interstitial hydrogen picked up during acid cleaning, some of these alloys were vacuum degassed. As shown in Table I, this procedure reduced the H content but appears to have increased the amounts of interstitial O and N. The second series of arc-melted alloys (AM-2), and all other alloys, were prepared using 99.9 pct pure V chips with low interstitial concentrations (120 ppm O, 80 ppm C, 26 ppm N, and < 3 ppm H). High-purity Si (99.999 pct) was used for all castings. Directionally solidified and induction melted composites were produced using a segmented, water-cooled copper crucible with a partially levitated melt.[23] Directional solidification was performed using the Czochralski method in which a DS seed crystal was lowered into the melt and withdrawn at 0.083 mm/s to produce an aligned composite approximately 10 mm in diameter and 75 mm in length. The IM castings were prepared in a manner similar to the DS castings, except they were allowed to resolidify within the crucible without controlled directional solidification. All of the alloys were triple melted in high-purity argon atmospheres to improve their homogeneity and to minimize interstitial contamination. The chemical compositions of the alloys, which are listed in Table I, were determined by spectrographic and LECO* inert gas fusion methods. Table I shows that the interstitial contents were sensitive to both the V melting stock (AM-1 *vs* AM-2) and the casting method. The cold-crucible methods resulted in a significant decrease in the interstitial concentrations relative to arc melting.

*LECO is a trademark of LECO Corporation, St. Joseph, MI.

Fracture toughness measurements were performed in three-point bending using single-edge-notched specimens with dimensions of approximately 3.5 × 7 × 30 mm. (Since ASTM standards[24] could not be rigorously met using these subsize specimens, the fracture toughness results are reported as K_Q instead of K_c.) The specimens were tested at a span of 28 mm and a displacement rate of 0.02 mm/s. All specimens were fabricated and notched by electrodischarge machining (EDM) with a notch opening width of 0.3 mm and a normalized crack length, a/w, of 0.45. Precracking was performed by continuously loading the EDM-notched specimen until a stable crack formed. At this point, the specimen was unloaded and the crack length was measured optically on the metallographically polished specimen surfaces that were parallel to the crack propagation direction and perpendicular to the crack plane. This method of measuring crack length was found to be quite accurate because significant crack branching or deflection was never observed. Once the initial crack length was established, which varied from specimen to specimen, the specimen was reloaded (at 0.02 mm/s) until further crack extension occurred. The specimen was then unloaded again, the new crack length was measured optically, and reloading was resumed. This sequence was followed until the specimen completely fractured apart (one to ten separate measurements). From the measured crack lengths and the maximum load measured just prior to each crack extension, the critical stress intensity could be evaluated as a function of crack length. Although this method did not provide rigorous R curves,[25] it was suitable for measuring the nature of crack growth resistance in the composites, as shown later.

The DS eutectic casting was fracture tested in two orientations: with the direction of crack propagation either perpendicular to (DS-T) or parallel with (DS-L) the composite growth direction. Because of the limited DS casting diameter, DS-L fracture toughness specimens could not be machined directly into specimens with the dimensions given

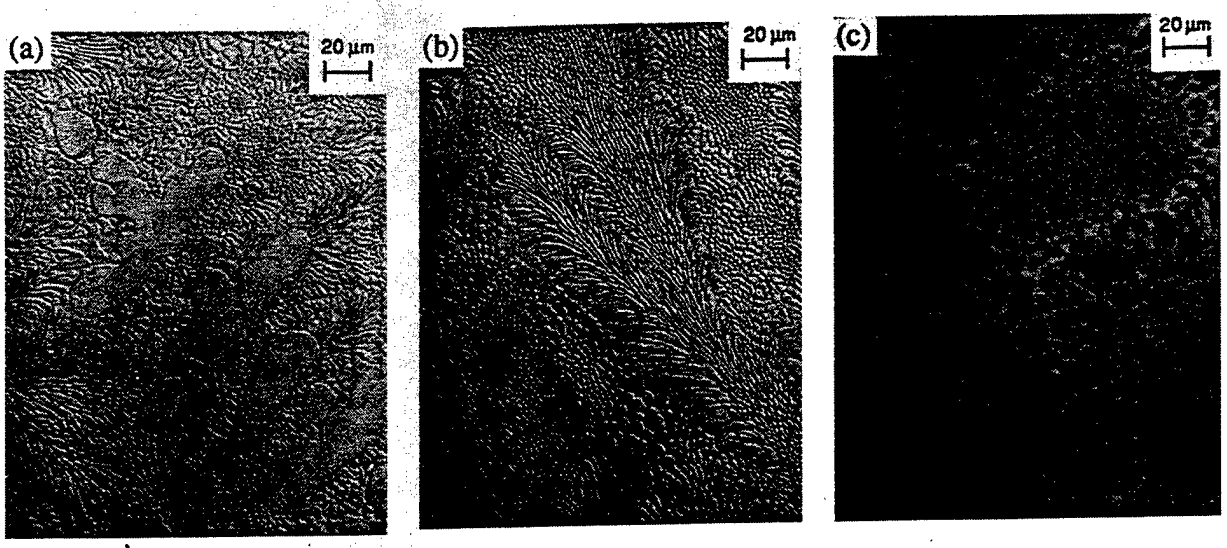


Fig. 1—Typical microstructures for the nominal eutectic arc-melted and induction-melted V-V_3Si composites: (*a*) AM-1 (V-7.66 pct Si), (*b*) AM-2 (V-7.3 pct Si), and (*c*) IM (V-7.25 pct Si).

previously. Instead, 8-mm-thick discs were cut from the cylindrical DS castings and brazed to two endpieces of eutectic material such that the growth direction in the disc was parallel to the direction of crack propagation. Vacuum brazing was performed at a peak temperature of 965 °C using a Ni-Au eutectic foil with a thickness of 0.05 mm. After brazing, the specimens were ground to the dimensions given previously and EDM notched.

Tensile testing of the bulk AM-2 V-2.7 pct Si alloy was performed to provide data on the strength and ductility of the (V) component of the composites. Testing was performed using specimens with a 7.1-mm gage length, which were fabricated by EDM. An Instron screw-driven testing machine was employed, using a constant engineering strain rate of approximately 3×10^{-4} s^{-1}. Two 5.08-mm gage length clip-on extensometers were used to measure specimen displacements, with the average value reported. From these experiments, the 0.2 pct offset yield stress, ultimate tensile or fracture stress, and failure elongation of the bulk (V) alloy were measured.

In an attempt to measure the ductile-phase extension during crack bridging, fracture profiles were prepared by electroplating 0.5 mm of Ni onto the fracture surfaces prior to sectioning and metallographic preparation. Backscattered electron imaging was used in the scanning electron microscope (SEM), and phase interference contrast in the optical microscope, for improved contrast between the (V) and (V_3Si) phases. Atomic force microscopy (AFM) was also used to measure the ductile-phase extension following fracture. The AFM was performed using a Digital Instruments Nanoscope III (Digital Instruments, Santa Barbara, CA) in the contact mode using a silicon nitride tip and a 50-μm scan size.

Determination of the crystallographic fracture planes on the surface of some failed bending specimens was performed in the SEM using a two-step process. First, the crystallographic orientations of grains on the fracture surfaces were determined using the electron backscattering pattern (EBSP) technique for electron diffraction in the SEM.[26] Second, the corresponding facet normals were determined from a pair of tilting experiments, from which two vectors in the surface facet could be determined; the facet normal then was computed by a simple vector cross-product.

III. RESULTS

A. *Microstructures*

The AM, IM, and DS casting methods and the different alloy compositions provided a range of microstructures. Beginning with the nominal eutectic alloys (7.25 to 7.66 pct Si), the microstructure consisted of almost equal volume fractions of discontinuous (V_3Si) rods in a (V) matrix. Image analysis revealed that the (V) volume fraction was 0.52 $\pm$ 0.05. The (V) and (V_3Si) compositions were measured by electron probe microanalysis to be 2.5 and 12.2 pct Si, similar to those reported in the assessed phase diagram.[11] Figures 1 and 2 show the influence of casting method on the microstructure of these eutectic composites. In the AM and IM castings, the solidification structure was cellular, with cell diameters of 75 to 100 μm and lengths of 150 to 200 μm. The individual (V_3Si) rod orientations were related within a cell but varied from cell to cell. Rod aspect ratios of up to 20:1 were present in all of the eutectics. As shown in Figure 2, the DS castings also possessed a cellular structure, but the cells were highly elongated with diameters of 100 to 200 μm and lengths of at least 1.5 to 2 mm. Within the cell cores, the (V_3Si) intermetallic rods exhibited strong alignment with the DS growth direction, but the orientation varied within the intercellular boundaries. The rod diameters were larger in the DS castings than in either the AM or IM castings. Typical rod diameters within the cell cores were between 1 and 1.5 μm in the AM and IM castings and 1.5 to 3 μm in the DS castings. In all castings, the intercellular regions had a coarse eutectic structure with (V_3Si) rods up to 4 μm in diameter; the size of the (V) regions also increased with increasing (V_3Si) rod diameter. The coarser microstructure for the DS castings may be due to the slower growth rates during DS processing compared to the other methods used in this study. Within the intercellular regions, occasional (V_3Si) dendrites were also present. Figure 1(a) shows the typical structure of these

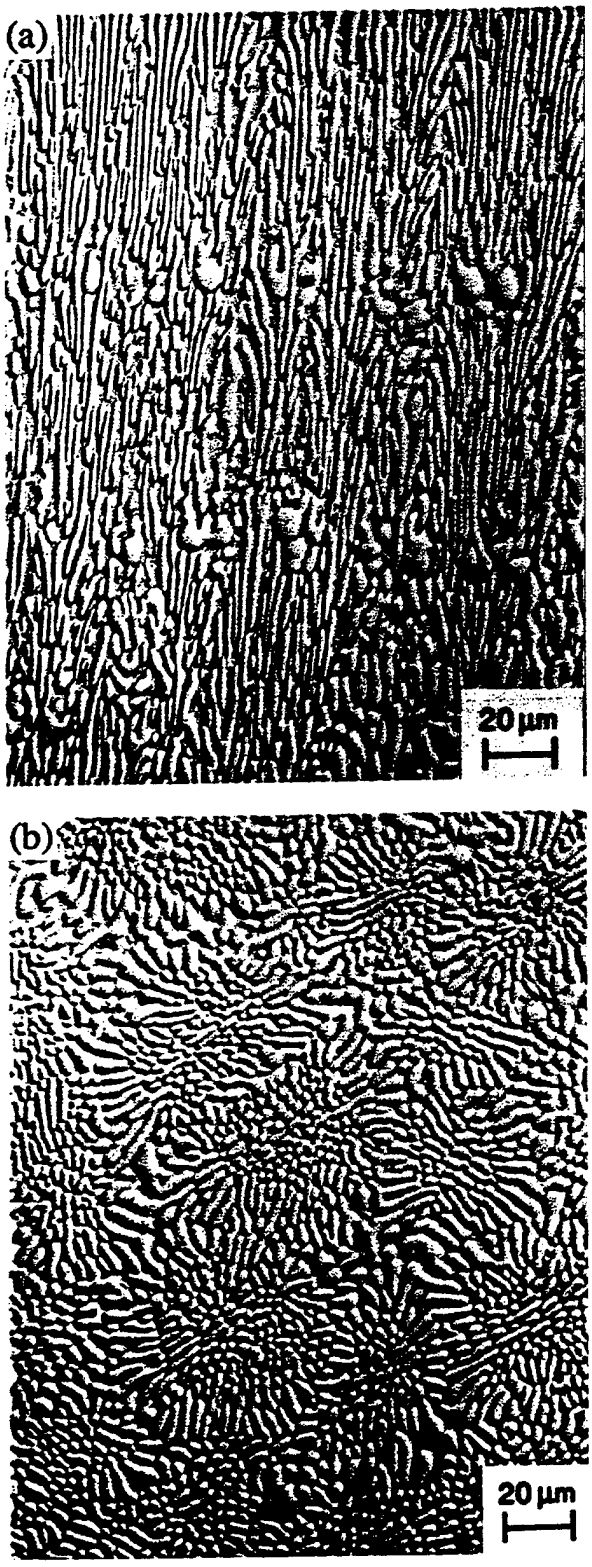


Fig. 2—Typical microstructures for the directionally solidified eutectic (V-7.3 pct Si): (*a*) longitudinal (growth) direction and (*b*) transverse direction.

infrequently observed dendrites and does not reflect their volume fraction within the microstructure. Quantitatively, the (V_3Si) dendrites accounted for less than 1 pct of the casting volume except for the AM-1 alloy (7.66 pct Si), which contained approximately 2 pct. These findings suggest an actual eutectic composition of about 7.25 pct Si (Table I), consistent with the observations of Chang *et al.*[23]

The off-eutectic compositions exhibited even greater variety in their microstructures. The lowest Si concentration hypoeutectic alloys, with 2.7 pct (AM) and 2.8 pct (IM) Si, were essentially single phase and represent the composition of the (V) phase in the composites. The V-4.2 pct Si alloy (Figure 3(a)) is close to the reported composition of maximum solubility of Si in V at the eutectic temperature.[11] This alloy contained approximately 10 vol pct (V_3Si), which was semicontinuous and was observed in the interdendritic regions. The nominal 70 pct (V) alloy, V-5.4 pct Si, consisted of primary (V) dendrites 50 to 250 μm in size, with an interdendritic eutectic of (V) and (V_3Si) (Figure 3(b)). As shown in Figure 3(c), the hypereutectic nominal 30 pct ductile phase alloy, V-10 pct Si, contained a large fraction of (V_3Si) dendrites with interdendritic eutectic. A similar microstructure, but with a greater volume fraction of (V_3Si) dendrites, was observed for the V-11.5 pct Si DS alloy. In all of the cast microstructures, including the hypereutectic alloys, the (V) was the continuous phase in the eutectic microconstituent.

B. *Composite Fracture Behavior*

The effect of the total ductile (V) phase volume fraction, V_f, on the room-temperature fracture toughness, K_Q, of V-V_3Si *in situ* composites is shown in Figure 4. The fracture toughness of the (V_3Si) was estimated from the length of cracks emanating from the corners of pyramidal microhardness indentations to be 1.3 MPa$\sqrt{m}$.[8] Clearly, the room-temperature fracture toughness of (V_3Si) can be greatly increased by *in situ* ductile-phase toughening with (V). With the exception of the anomalously low fracture toughness for the 90 pct (V) DS alloy, which will be discussed later, K_Q increases monotonically with increasing V_f. In contrast, Bewlay *et al.*[10] have shown that the fracture toughness of Nb-Si composites reaches a minimum at the eutectic composition and increases approximately linearly as the Si content either increases or decreases from the eutectic composition.

For the case of the eutectic composites, the fracture toughness is plotted as a function of normalized crack length, *a/w*, in Figure 5. The toughness values of the AM-1 and AM-2 eutectic alloys were similar, with average values of 10.4 and 10.6 MPa$\sqrt{m}$. The improvement in K_Q produced by the cleaner DS and IM casting methods is clearly shown in Figure 5. The K_Q value for the DS-T casting (tested such that the crack propagated perpendicular to the growth direction) was 18.5 MPa$\sqrt{m}$. The toughness of the DS casting decreased when tested with the crack propagating in the longitudinal (growth) direction, with K_Q = 14.4 MPa$\sqrt{m}$. The IM alloy exhibited the highest fracture toughness of all the eutectic castings: 20.4 MPa$\sqrt{m}$. Figure 5 also shows the absence of any significant changes in toughness with increasing crack extension, or "*R* curve" behavior. The data appear evenly scattered about the average K_Q, indicating the absence of significant bridging zone development with increasing crack length. Although rigorous *R*-curve measurements[25] were beyond the scope of this study, as discussed in Section II, the qualitative finding that K_Q does not significantly increase with increasing crack extension is consistent with the fracture surface characteristics that will be discussed later.

The fractographs in Figure 6 illustrate that the fracture

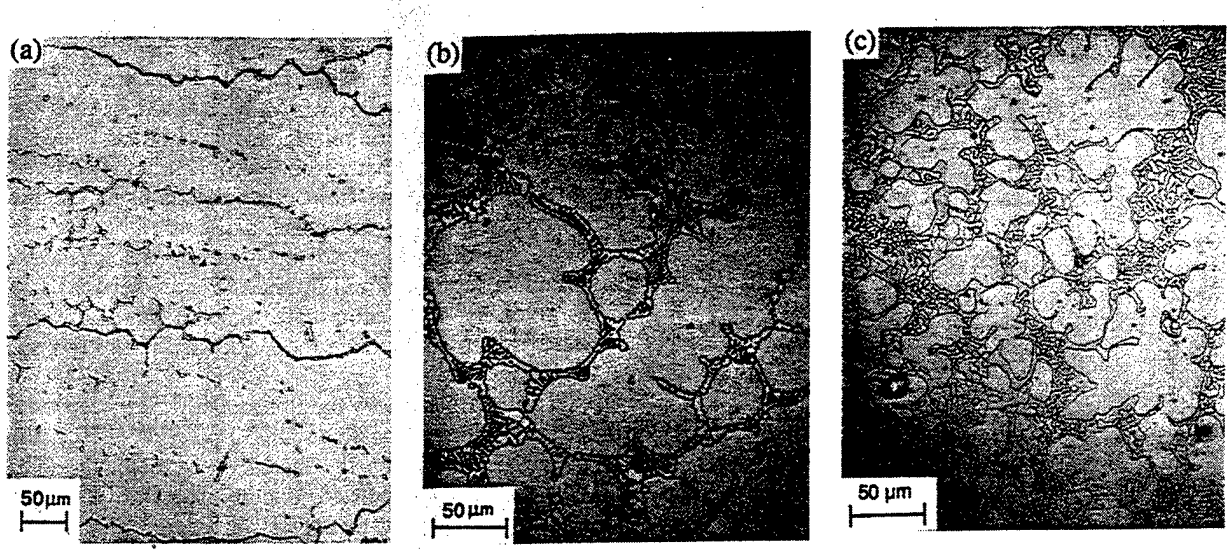


Fig. 3—As-cast microstructures for the off-eutectic AM-1 V-V_3Si composites: (*a*) V-4.2 pct Si, (*b*) V-5.4 pct Si, and (*c*) V-10.0 pct Si.

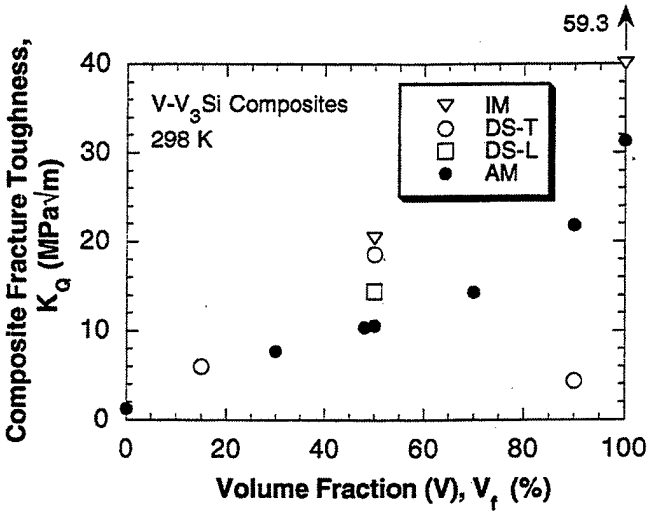


Fig. 4—The room-temperature fracture toughness, K_Q, as a function of the (V) volume fraction for arc melted, induction melted, and directionally solidified (DS-T, DS-L) *in situ* V-V_3Si composites. Each plotted point represents the average of 3 to 10 separate measurements, with a scatter of approximately ±2 MPa $\sqrt{m}$.

surfaces of all the eutectic alloys contained mixtures of two types of zones: large "cleavagelike" zones and fine "microroughened" zones. The cleavagelike zones typically consisted of a large number of nearly parallel facets, coincident with the individual (V_3Si) rods, connected by smooth or stepped regions, corresponding to the intervening (V) ligaments. (Although (V) is the continuous phase of the eutectic, during fracture, it essentially forms very short (approximately 0.5 μm) "ligaments" between the discontinuous (V_3Si) rods, which fracture ahead of the crack tip due to their much lower fracture toughness.) There was little evidence of plastic deformation of (V) ligaments in these regions, as shown in Figure 7(a) for the AM-2 eutectic casting. Conversely, the microroughened zones consisted of (V_3Si) rods containing secondary cracks and (V) ligaments displaying plastic deformation (Figure 7(b)). Behavior similar to that shown in Figure 7 was also observed in the IM and DS alloys. The size and fraction of the macroscopic cleavagelike zones were largest for the AM alloys and decreased for the DS and IM materials. It is estimated that cleavagelike zones accounted for 61 pct of the AM fracture surface area, while they made up only about 13 pct for the DS-T eutectic and 15 pct for the IM eutectic.

The lack of macroscopic (V) plasticity in the cleavagelike zones is consistent with the limited ductility measured in tensile tests of the bulk V-2.7 pct Si alloy (Figure 8). A yield strength of 430 MPa, fracture strength of 435 MPa, and maximum uniform elongation of 2.2 pct were measured in one sample, while fracture occurred prior to yielding in another. The strengthening effect of Si and the interstitial contaminants (Table I) appear to be responsible for the enhanced strength and reduced ductility of the alloy compared to pure V.[8] This is consistent with previous work on refractory metals.[5,7]

Profiles of the fracture surfaces were prepared to quantify the magnitude of the (V) plastic extensions beyond the (V_3Si) facets in the composites. Unlike the apparently large plastic extensions viewed by SEM fractography in the microroughened regions, the presence of clearly visible (V) extensions was uncommon in the fracture profiles. The maximum plastic extensions measured were 0.33 to 0.66 μm for AM-2 and 0.8 to 1.0 μm for the DS-T specimens, indicating that the deformation was localized.

IV. DISCUSSION

A. *Effect of Ductile-Phase Volume Fraction on Fracture Toughness*

The influence of the (V) volume fraction, V_f, on the composite fracture toughness is shown in Figure 4. (It is difficult to draw conclusions for the IM and DS-T composites, since only one datum point exists for each of these materials.) Although one might expect evidence for the square-root dependence of K_Q on V_f predicted by Eq. [1], this equation is not applicable to any of the V-Si composite microstructures except the eutectic, as discussed subsequently.[1,12] Therefore, factors other than those implicit in the derivation of Eq. [1] are controlling the fracture toughness in the V-V_3Si *in situ* composites.

First, for composites with either small (*e.g.*, 15 pct) or

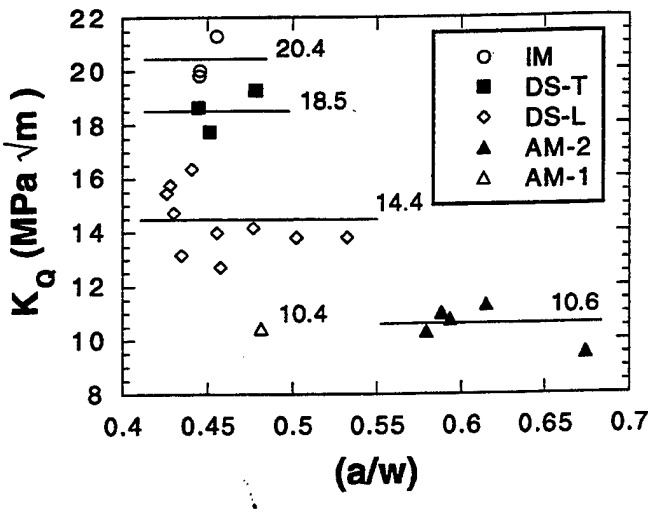


Fig. 5—The fracture toughness of the nominal eutectic composites as a function of the normalized crack length, *a/w*. Data for each type of composite are from a single specimen.

large (*e.g.*, 90 pct) V_f, the underlying assumption upon which Eq. [1] was derived, namely, bridging of a brittle crack by a series of ductile ligaments, is clearly unrealistic. This conclusion is supported by the microstructures of these composites, such as that shown in Figure 3(a) for the 90 pct V_f composite. This composite consists of large (V) dendrites with thin, semicontinuous regions of (V_3Si). Such a microstructure is not consistent with that assumed in deriving Eq. [1].[1,12]

For composites with small or large V_f, the simplest alternative to Eq. [1] is to assume that the composite K_Q is controlled by a rule of mixtures. However, the relationship between K_Q and V_f is not linear, as shown in Figure 4 for the hypoeutectic AM composites with $V_f > 50$ pct (the data are insufficient to make a similar assessment for the DS alloys or for $V_f < 50$ pct). The experimental K_Q values lie well below a linear rule-of-mixtures prediction between K_Q for the 100 pct ductile phase alloy (31.4 MPa$\sqrt{m}$) and K_Q for either the eutectic (10.5 MPa$\sqrt{m}$) or for (V_3Si) (1.3 MPa$\sqrt{m}$). Again, examination of the microstructure in Figure 3(a) for the 90 pct ductile phase composite suggests a reason why this approach is inappropriate. It appears that the interdendritic (V_3Si) provides pathways for easy fracture, thereby decreasing K_Q by an amount greater than that predicted by a rule of mixtures. This hypothesis was confirmed through analysis of the fractured bend specimens for this alloy. The fracture morphology was predominantly intergranular with grain diameters on the fracture surface between 0.4 and 2.2 mm. Examination of metallographically polished and etched fracture profiles revealed preferential cracking along the interdendritic (V_3Si).

Examination of the AM data in Figure 4 for 30 pct $\leq V_f \leq$ 70 pct shows a linear relationship between K_Q and V_f, similar to that observed for hypoeutectic Nb-Si *in situ* composites.[10] Further, the K_Q values for the eutectic composites ($V_f \cong 50$ pct) lie well below a rule-of-mixtures line connecting the fracture toughness for (V_3Si) (1.3 MPa$\sqrt{m}$) with that for the 100 pct (V) alloy of similar purity (either 31.4 or 59.3 MPa$\sqrt{m}$ for the AM or IM, respectively). If a large amount of crack bridging occurred, one would expect K_Q values for the eutectics to lie above the rule-of-mixtures line due to the additional energy absorbed during extensive plastic deformation of the (V). The fact that the (V) provides some toughening of (V_3Si), albeit less than expected even from a rule of mixtures, may be due to the limited ductile bridging that is observed (Figure 7(b)) and/or to minor contributions from other mechanisms, such as microcracking, crack deflection, and crack blunting.[10,17] Evidence for the presence of the first two mechanisms can be found in Figures 6 and 7, and evidence for crack blunting is given by observations of cracks emanating from microhardness indentations in the (V_3Si) that abruptly stop at (V) dendrites.[8]

The relatively low toughness and linear dependence of V_f on K_Q for composites with 30 pct $\leq V_f \leq$ 70 pct may be strongly affected by the fact that not all of the (V) in the composites contributes to ductile-phase bridging. A similar observation was made by Bewlay *et al.*[10] for *in situ* composites of Nb-Si. First, consider only the eutectic composites. As shown in Figures 6 and 7, the eutectic (V) exhibits plastic deformation only within some regions of the fracture surface, while cleavage occurs in the others. Unfortunately, while K_Q increased with decreasing total area fraction of cleavage as expected, it is difficult to quantify the cleavage and bridging contributions. Crack propagation is controlled by local conditions at the crack tip rather than an average behavior across the entire fracture surface. To quantify the contribution of cleavage, one would have to know the fractions of cleavage and bridging fracture along the length of the crack tip at each position for which K_Q *vs a/w* data were taken. The corresponding K_Q values then could be correlated with these fractions. Such an undertaking was not attempted in this study.

In addition to a lack of plastic deformation of the eutectic (V), significant ductility was not observed in the primary (V) dendrites of the hypoeutectic alloys. Bewlay *et al.*[10] observed similar behavior in the (Nb) dendrites of hypoeutectic Nb-Si composites. They suggested that debonding may be less extensive in the dendrites than in the high-aspect-ratio eutectic (Nb), leading to a larger degree of constraint and cleavage-type failure in the dendrites. The same may be true in the composites of the present study. In addition, the single-edge-notch fracture specimens from IM and AM castings of bulk 100 pct (V), V-2.7 pct Si, failed by cleavage,[8] as shown in Figure 9. Cleavage failure also occurred during bulk tensile testing of this alloy, as shown in Figure 8. These results are somewhat surprising given the ductility of the (V) ligaments shown in Figure 7(b). The fact that the micron-sized eutectic (V) ligaments can undergo substantial plastic stretching while the bulk (V) is brittle may be due to the short slip lengths in the eutectic microconstituent. Short slip lengths limit the intensity of internal stresses at the head of dislocation pileups, which, if large enough, could lead to crack initiation.[27,28,29] The large slip lengths in the primary (V) dendrites then may be partly responsible for their lack of ductility. It is noteworthy that a strong dependence of the cleavage fracture stress on grain size has been observed in Nb,[30] and a similar phenomenon may occur in (V). Naturally, the brittle nature of the primary (V) dendrites, whatever the cause, precludes them from contributing to a ductile crack-bridging mechanism, although they are still very tough compared to monolithic

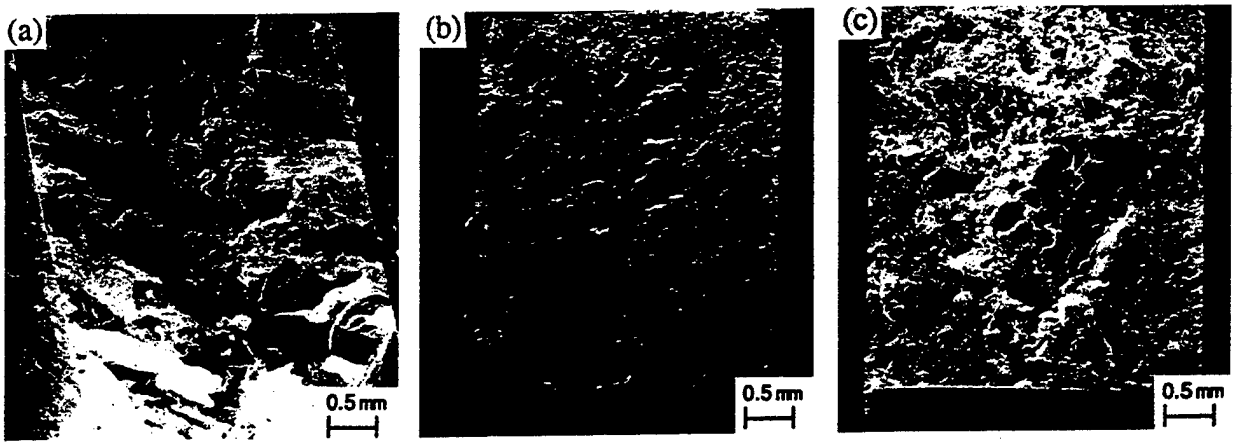


Fig. 6—Fracture surfaces of (*a*) AM-2, (*b*) DS-T, and (*c*) IM V-V_3Si eutectic composites.

V_3Si. This is similar to previous observations for Nb-Si composites.[5,7,10,30,32]

Another complication that may affect the K_Q *vs* V_f behavior of the V-Si composites is that the cleavage stress of the (V) phase is anisotropic. As shown in Figure 9, many flat facets exist on the fracture surface of the AM V-2.7 pct Si single-phase alloy. Due to the random orientation of grains, many of these facets are highly inclined to one another. The crystallographic orientations of the grains on the fracture surface were determined using EBSP, and the surface normal of each facet was determined by tilting in the SEM. As shown in Figure 10, the {001} poles of the bcc lattice correlate strongly with the facet normals. Given the precision of the SEM stage used to perform these experiments and the errors in measuring the distance of features in the tilting experiments, the facet normals have an angular error of ±5 deg.[31] The {001} poles are accurate to less than 2 pct. The data in Figure 10 show a strong correlation between the {001} poles and the facet normals (circled pairs of symbols), suggesting that the {001} planes in the (V) may be easy cleavage planes. If so, this cleavage anisotropy may explain the anomalously low K_Q of the DS 90 pct (V) alloy shown in Figure 4. If the DS process aligned the {001} planes such that they were perpendicular to the growth direction, and therefore the maximum principal stress during crack growth, then fracture could have occurred at a much lower applied stress intensity than for a specimen with randomly oriented grains.

B. *Crack Growth Resistance Behavior*

A significant increase in fracture toughness with increasing crack extension has been observed for *in situ* Nb-Si composites by Rigney and Lewandowski.[30,32] For the V-Si composites of the present study, a limited increase in K_c with increasing crack extension was observed for the AM V-5.42 pct Si hypoeutectic alloy.[8] However, the eutectic composites did not exhibit such behavior (Figure 5). The absence of *R*-curve behavior for the eutectics is consistent with the limited amount of ductile stretching observed in the (V), even within the microroughened regions, and the correspondingly small steady-state bridging zone length. Both the optical profile and AFM measurements suggest that the (V) ligaments stretched to modest lengths of approximately 0.25 to 0.3 times their diameter, although the local plasticity may be high. As stated in Section I, theories suggest that the toughness increment provided by ductile-phase bridging increases rapidly as the debond length, and thus the amount of plastic stretching, approaches the diameter of the ductile ligament.[12,13] Further, following Bao and Hui[33] and Heredia *et al.*,[17] the steady-state bridging zone length, L_{ss}, is given approximately by

$$L_{ss} = \frac{0.12\ \pi u^* E_c}{\sigma^*} \qquad [3]$$

where E_c is the composite Young's modulus, σ^* is the peak nominal tensile stress achieved in the ductile particles during fracture, and u^* is the ductile ligament failure displacement. For a debond length, h, equal to the ductile ligament radius a_0, $u^* \cong h = a_0$ and $\sigma^* \cong \sigma_0$.[17] For the V-V_3Si eutectics, this gives $u^* = 1.5$ μm and $\sigma^* = 435$ MPa (Figure 8). Using a simple rule of mixtures for the eutectics gives $E_c = 171.5$ GPa.[8] Thus, Eq. [3] predicts for the case of $h = a_0$ that $L_{ss} = 225$ μm. However, the observed ligament lengths suggest that $u^* \cong h \cong 1/3\ a_0$. In this case, the ductile ligaments are more highly constrained and σ^* is significantly larger than σ_0. Using a value of $\sigma^* = 4\sigma_0$, as suggested by Heredia *et al.*[17] and by the finite-element calculations of Henshall *et al.*,[22] and substituting these values into Eq. [3] gives $L_{ss} = 19$ μm. Such a small steady-state bridging zone is consistent with the lack of increasing crack-growth resistance with increasing crack extension shown in Figure 5.

C. *Effect of Interstitials*

While the DS eutectic casting contained a coarser microstructure than the nondirectional eutectic composites (indicative of the reduced thermal gradient and solidification rate during casting), the scale of the microstructure for both the AM and IM eutectic castings was essentially the same. Therefore, microstructural scale alone cannot account for the toughness differences between the eutectic composites. Since the detrimental effect of interstitial elements on the fracture toughness of bcc refractory metals is well known,[34] their influence on the fracture toughness of V-V_3Si composites was investigated to determine if it could account for the observed K_Q variations.

The analysis used here is based on the experimental data of Loomis and Carlson,[34] showing that the room-temperature Charpy impact toughness of pure V varies for con-

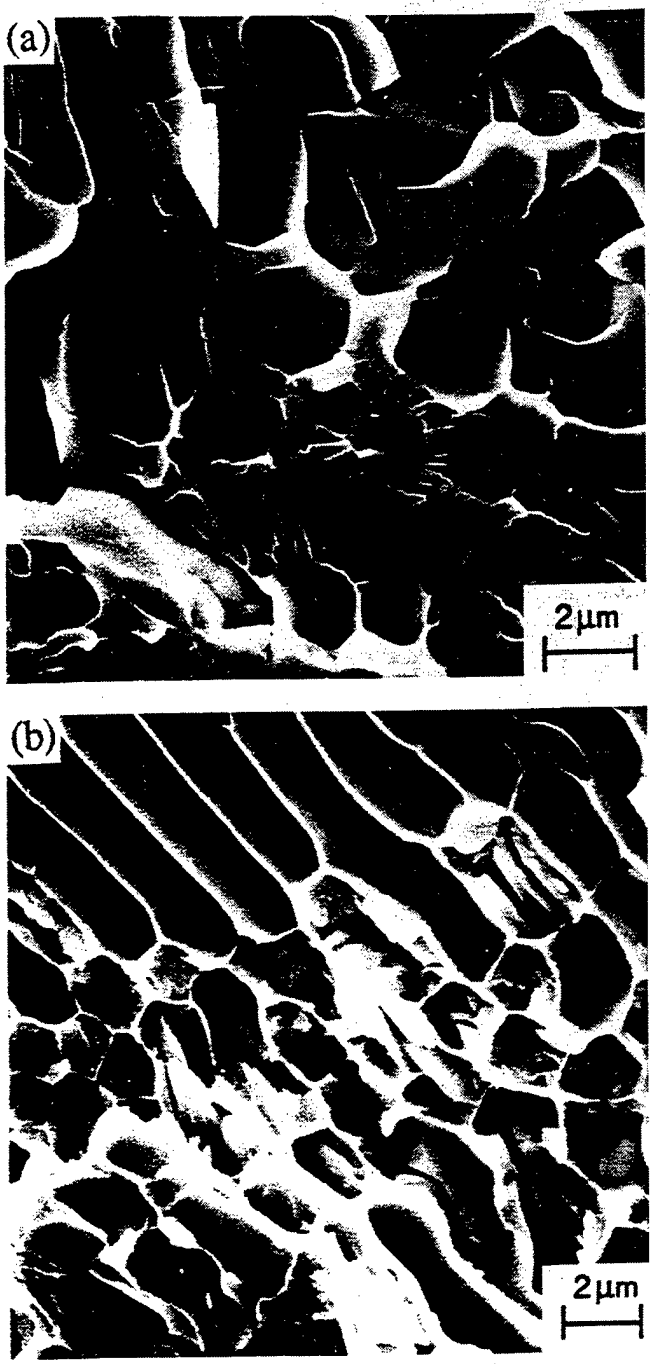


Fig. 7—SEM fractographs of the AM-2 eutectic composite showing regions of (*a*) cleavagelike and (*b*) microroughened fracture.

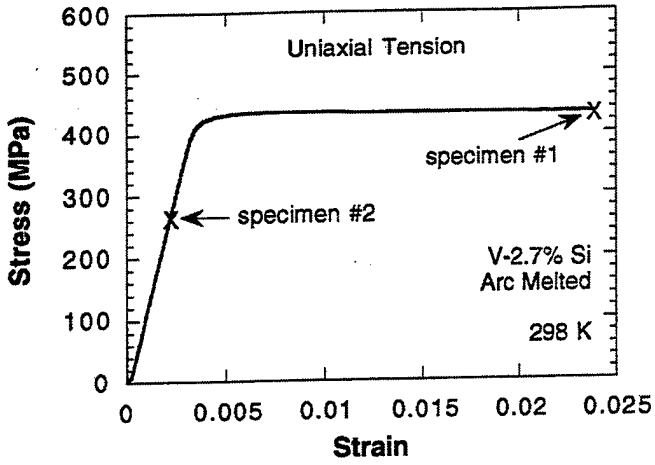


Fig. 8—The room-temperature tensile behavior of the bulk V-2.7 pct Si single-phase alloy, as measured using specimens taken from alloy AM-2. The "X" denotes the point of failure for the two specimens tested.

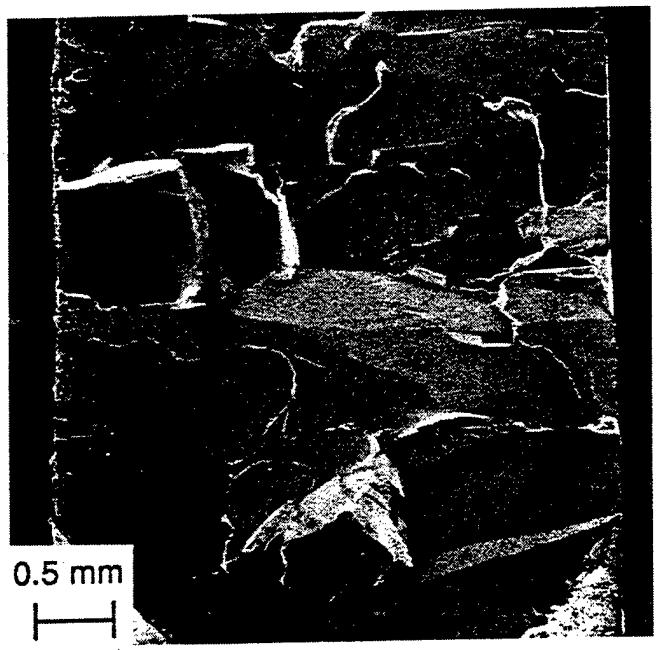


Fig. 9—The fracture surface of the V-2.7 pct Si single-phase alloy (AM-2).

centrations of N, O, and H in the ratio of 1 to 1.33 to 9. Assuming that these ratios are similar for (V), the "effective" interstitial concentration, [I] = [N] + 1.33[O] + 9[H], was calculated for each casting and is given in Table I. The validity of this assumption is supported by the data for the AM and IM 100 pct (V) alloys. The ratio of $(K_Q)^{IM}$: $(K_Q)^{AM}$ is nearly the same as the ratio of the corresponding [I] values. Therefore, K_Q for each eutectic composite is plotted as a function of [I] in Figure 11. There is good correlation between [I] and K_Q for all of the tests performed with the crack propagating through a randomly oriented microstructure, AM and IM, or transverse to the growth direction, DS-T; the influence of crack propagation parallel to the growth direction, DS-L, is discussed in Section D. Further increases in purity would be expected to improve toughness, but the data are insufficient to predict a quantitative relationship. The influence of interstitial impurities on K_Q is further emphasized by the fact that the IM and AM eutectics have the most similar microstructures, but K_Q for the IM alloy is nearly double that of the AM alloys. In addition, K_Q for the IM eutectic is essentially the same as that of the DS-T specimen, which has an interstitial content similar to the IM alloy but a significantly different microstructure. Therefore, K_Q is more sensitive to the interstitial content than to the microstructure of the eutectic composites.

D. *Effect of Crack Orientation*

The mechanism responsible for the difference in toughness for the DS-T and DS-L eutectic composites is not completely clear. This difference may result from increased

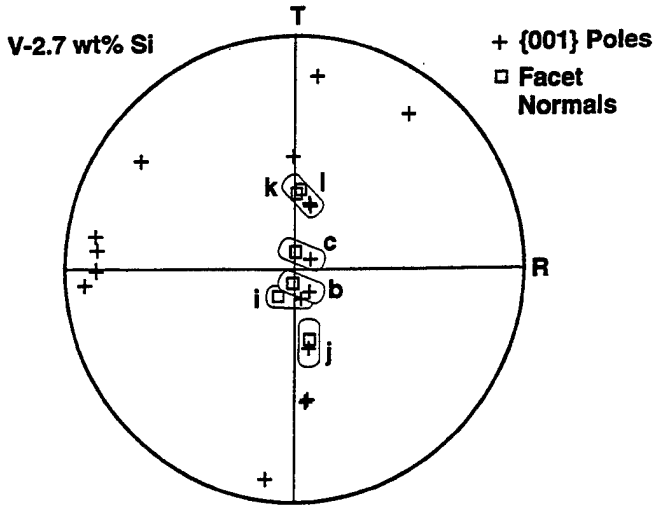


Fig. 10—Pole figure showing the {001} poles and the fracture facet normals for the 100 pct (V), 2.7 pct Si AM-2 fracture specimen shown in Fig. 9. The circled symbol pairs represent measurements from the same facet. The sample coordinate system (Fig. 9) is specified as R pointing left-to-right, T pointing bottom-to-top, and N pointing out of the specimen at zero tilt.

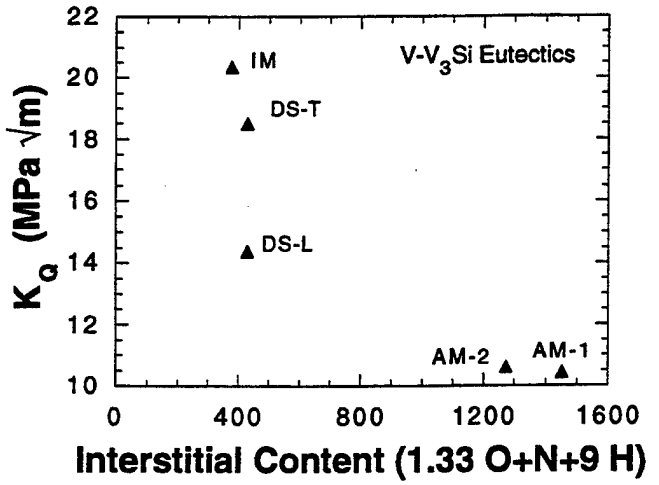


Fig. 11—The fracture toughness of the AM, IM, and DS eutectic composites as a function of the effective interstitial concentration.

constraint in the (V) for cracks propagating parallel with the (V_3Si) rods, rather than transverse to them. Although the amount of crack bridging appears to be limited (Section A), it may play a significant role in the toughening of the low impurity composites (Figures 6 and 7). If so, then the toughness should decrease with increased constraint or reduced ductile-phase stretching. The difference in crack orientation with respect to the DS growth direction may also affect the amount of crack renucleation required in the (V_3Si) phase, or the extent of crack deflection.

V. CONCLUSIONS

An investigation of the room-temperature fracture behavior of V-V_3Si *in situ* composites has led to the following conclusions.

1. The fracture toughness of (V_3Si) ($\tilde{\tilde{A}}$ 1.3 MPa$\sqrt{m}$) can be significantly improved by *in situ* ductile-phase toughening with (V). The fracture toughness of V-V_3Si composites is controlled by their microstructure and interstitial impurity content which, in turn, can be adjusted by the Si concentration and casting method. For eutectic composites, which contain nearly equal volume fractions of the continuous ductile phase and discontinuous intermetallic (V_3Si) rods, a fracture toughness of over 20 MPa$\sqrt{m}$ was measured.
2. The fracture toughness of V-V_3Si *in situ* composites generally increases with increasing volume fraction of the ductile V-Si solid solution phase, (V). The square-root dependence of fracture toughness on the volume fraction of the ductile phase predicted by theories of small-scale crack bridging is not observed in these composites, because, except for the eutectic composition, the composite microstructures are inconsistent with those assumed in developing these theories. Nor does the fracture toughness of the composites reach values as large as those expected from a rule of mixtures. Several factors contribute to this result, including the lack of a microstructure capable of supporting classical bridging phenomena for large and small volume fractions of (V), and the complex mechanical behavior of (V) depending on its purity, size, and orientation with respect to the applied principal stress.
3. The fracture toughness of V-V_3Si composites is sensitive to the method of synthesis, because this controls the interstitial impurity content and orientation of the microstructure with respect to the direction of crack propagation. For eutectic composites with a random or transverse orientation of the (V_3Si) rods with respect to the direction of crack propagation, the fracture toughness increases with decreasing effective interstitial concentration, [I] = [N] + 1.33[O] + 9[H]. The fracture toughness is predicted to increase above 20 MPa$\sqrt{m}$ for [I] < 300 ppm. A decrease in toughness of about 25 pct was observed in DS material oriented with the direction of crack propagation parallel to, rather than transverse to, the axis of the (V_3Si) rods, or growth direction.
4. The {001} planes in the (V) appear to be those of easy cleavage. Since (V) is the continuous phase in the eutectic microconstituent, the cleavage anisotropy in this phase probably has a significant influence on the fracture mode of the composites.
5. There was little evidence of ductile-phase bridging in the fractured composites, and *R*-curve behavior was not observed. These results suggest that fracture toughness models based solely on crack bridging cannot completely describe the behavior of V-V_3Si composites.

ACKNOWLEDGMENTS

The authors thank D. Hiromoto and R. Kershaw, LLNL, for their contributions to the experiments. AFM measurements by Dr. M. Balooch, LLNL, are gratefully acknowledged. Work by two of the authors (GAH and MJS) was performed under the auspices of the United States Department of Energy under Contract No. W-7405-ENG-48 at the Lawrence Livermore National Laboratory.

REFERENCES

1. L.S. Sigl, P.A. Mataga, B.J. Dalgleish, R.M. McMeeking, and A.G. Evans: *Acta Metall.*, 1988, vol. 36, pp. 945-53.

2. H.E. Dève, A.G. Evans, G.R. Odette, R. Mehrabian, M.L. Emiliani, and R.J. Hecht: *Acta Metall. Mater.*, 1990, vol. 38, pp. 1491-1502.
3. L. Xiao and R. Abbaschian: *Metall. Trans. A*, 1992, vol. 23A, pp. 2863-72.
4. W.O. Soboyejo, K.T. Venkateswara Rao, S.M.L. Sastry, and R.O. Ritchie: *Metall. Trans. A*, 1993, vol. 24A, pp. 585-600.
5. J.J. Lewandowski, D. Dimiduk, W. Kerr, and M.G. Mendiratta: *High Temperature-High Performance Composites*, Materials Research Society Symposia Proceedings, F.D. Lemkey, S.G. Fishman, A.G. Evans, and J.R. Strife, eds., Materials Research Society, Pittsburgh, PA, 1988, vol. 120, pp. 103-09.
6. D.L. Anton and D.M. Shah: *Intermetallic Matrix Composites*, Materials Research Society Symposia Proceedings, D.L. Anton, P.L. Martin, D.B. Miracle, and R. McMeeking, eds., Materials Research Society, Pittsburgh, PA, 1988, vol. 194, pp. 45-52.
7. M.G. Mendiratta, J.J. Lewandowski, and D.M. Dimiduk: *Metall. Trans. A*, 1991, vol. 22A, pp. 1573-83.
8. M.J. Strum and G.A. Henshall: *High-Temperature Ordered Intermetallic Alloys V*, Materials Research Society Symposia Proceedings, I. Baker, R. Dardia, J.D. Whittenberger, and M.H. Yoo, eds., Materials Research Society, Pittsburgh, PA, 1993, vol. 288, pp. 1093-98.
9. M.J. Strum, G.A. Henshall, B.P. Bewlay, J.A. Sutliff, and M.R. Jackson: *High Temperature Silicides and Refractory Alloys*, Materials Research Society Symposia Proceedings, C.L. Briant, J.J. Petrovic, B.P. Bewlay, A.K. Vasudevan, and H.A. Lipsitt, eds., Materials Research Society, Pittsburgh, PA, 1994, vol. 322, pp. 511-16.
10. B.P. Bewlay, H.A. Lipsitt, W.J. Reeder, M.R. Jackson, and J.A. Sutliff: in *Processing and Fabrication of Advanced Materials III*, V. Ravi, T.S. Srivatsan, and J.J. Moore, eds., TMS, Warrendale, PA, 1994, pp. 547-65.
11. *Binary Alloy Phase Diagrams*, T.B. Massalski, ed., ASM INTERNATIONAL, Metals Park, OH, 1990, vol. 3, p. 3376.
12. M.F. Ashby, F.J. Blunt, and M. Bannister: *Acta Metall.*, 1989, vol. 37, pp. 1847-57.
13. H.E. Dève and M.J. Maloney: *Acta Metall. Mater.*, 1991, vol. 39, pp. 2275-84.
14. M. Bannister and M.F. Ashby: *Acta Metall. Mater.*, 1991, vol. 39, pp. 2575-82.
15. M. Bannister, H. Shercliff, G. Bao, F. Zok, and M.F. Ashby: *Acta Metall. Mater.*, 1992, vol. 40, pp. 1531-37.
16. L. Xiao and R. Abbaschian: *Metall. Trans. A*, 1993, vol. 24A, pp. 403-15.
17. F.E. Heredia, M.Y. He, G.E. Lucas, A.G. Evans, H.E. Dève, and D. Konitzer: *Acta Metall. Mater.*, 1993, vol. 41, pp. 505-11.
18. B. Budiansky, J.C. Amazigo, and A.G. Evans: *J. Mech. Phys. Solids*, 1988, vol. 36, pp. 167-87.
19. K.S. Ravichandran: *Scripta Metall. Mater.*, 1992, vol. 26, pp. 1389-93.
20. K.S. Ravichandran: *Acta Metall. Mater.*, 1992, vol. 40, pp. 1009-22.
21. P.A. Mataga: *Acta Metall.*, 1989, vol. 37, pp. 3349-59.
22. G.A. Henshall, E. Zywicz, and M.J. Strum: in *Fatigue and Fracture of Ordered Intermetallic Materials: I*, W. Soboyejo, T.S. Srivatsan, and D.L. Davidson, eds., TMS, Warrendale, PA, 1994, pp. 39-54.
23. K.-M. Chang, B.P. Bewlay, J.A. Sutliff, and M.R. Jackson: *J. Met.*, 1992, vol. 44, pp. 59-63.
24. *Standard Test Method for Plane-Strain Fracture Toughness of Metallic Materials*, ASTM STP E399-83, ASTM, Philadelphia, PA, 1983, pp. 488-512.
25. *Standard Practice for R-Curve Determination*, ASTM STP E561-94, ASTM, Philadelphia, PA, 1996, pp. 487-99.
26. V. Randle: *Microtexture Determination and Its Applications*, Institute of Metals, London, 1992.
27. A.N. Stroh: *Adv. Phys.*, 1957, vol. 6, pp. 418-65.
28. A.H. Cottrell: *Trans. AIME*, 1958, vol. 212, pp. 192-203.
29. G.E. Dieter: *Mechanical Metallurgy*, 2nd ed., McGraw-Hill, New York, NY, 1976, pp. 262-71.
30. J.D. Rigney and J.J. Lewandowski: *Metall. Trans. Mater. A*, 1996, vol. 27A, pp. 3292-3306.
31. J.A. Sutliff, B.P. Bewlay, G.A. Henshall, and M.J. Strum: *Proc. 52nd Annual Meeting of the Microscopy Society of America*, G.W. Bailey and A.J. Garret-Reed, eds., San Francisco Press, San Francisco, CA, 1994, p. 622.
32. J.D. Rigney and J.J. Lewandowski: in *Advanced Composite Materials*, M. Sacks, ed., American Ceramics Society, Westerville, OH, 1991, pp. 519-25.
33. G. Bao and C.-Y. Hui: *Int. J. Solids Struct.*, 1990, vol. 26, pp. 631-42.
34. B.A. Loomis and O.N. Carlson: in *Reactive Metals*, W.R. Clough, ed., Interscience Publishers, New York, NY, 1958, pp. 227-43.

The Nb-Hf-Si Ternary Phase Diagram: Liquid-Solid Phase Equilibria In Nb and Hf Rich Alloys

B.P. Bewlay, R.R. Bishop and M.R. Jackson

Journal of Phase Equilibria, 1997

The Nb-Ti-Si Ternary Phase Diagram: Evaluation of Liquid-Solid Phase Equilibria in Nb- and Ti-Rich Alloys

B.P. Bewlay and M.R. Jackson
General Electric Company, Corporate Research and Development
Schenectady, New York 12301
and H.A. Lipsitt
Department of Mechanical and Materials Engineering
Wright State university, Dayton, Ohio 45435

(Submitted 25 July 1996; in revised form 27 December 1996)

Phase equilibria in ternary Nb-Ti-Si alloys have been investigated using scanning electron microscopy, XRD, and electron beam microprobe analysis. Alloys containing up to four phases, $Nb(Ti)_5Si_3$, $Ti(Nb)_5Si_3$, $(Nb,Ti)_3Si$, and (Nb,Ti,Si) were directionally solidified using cold crucible Czochralski crystal growth. A broad range of Nb and Ti compositions were investigated for Si concentrations up to 35.0%. Microstructural and microchemical evidence provided a clear definition of the Nb-Ti-Si liquidus surface and indicate that the metal-rich end of the ternary phase diagram possesses two transition reactions:

$$L + Nb(Ti)_5Si_3 \rightarrow (Nb,Ti)_3Si + Ti(Nb)_5Si_3$$
$$L + (Nb,Ti)_3Si \rightarrow (Nb,Ti,Si) + Ti(Nb)_5Si_3$$

The first of these transition reactions occurs at a composition of approximately Nb-66Ti-19Si, and probably at a temperature between 1600 and 1650 °C. The second of these transition reactions occurs at a composition of approximately Nb-76Ti-13.5Si and a temperature of approximately 1350 °C. No ternary eutectic was observed in the compositions that were investigated.

1. Introduction

Directionally solidified composites based on refractory metals and refractory-metal silicides, such as Nb-Nb_3Si composites, are presently under investigation as structural materials for high-temperature applications because of their high melting temperatures (>1600 °C) and high-temperature strength retention. In situ composites based on ternary Nb-Ti-Si alloys have displayed an attractive combination of low-temperature and high-temperature mechanical properties, together with promising environmental resistance (Ref 1, 2). The addition of Ti to Nb-Nb_3Si in situ composites of Nb-Si binary alloys has been shown to improve both toughness and oxidation resistance (Ref 1-3). Unfortunately, there is little previous knowledge of the phase equilibria that control the generation of these in situ composites. Definition of the ternary Nb-Ti-Si phase equilibria is the topic of this paper. Particular emphasis is placed on definition of the liquidus surface, because this controls the microstructure of in situ composites generated by directional solidification.

There has been limited previous work on Nb-Ti-Si ternary phase equilibria (Ref 1, 2) and almost no previous work on the liquidus surface. A space diagram of the metal-rich region (up to 37.5% Si—all compositions are given in at.%) of the proposed Nb-Ti-Si phase diagram is shown in Fig. 1. A projection of a proposed liquidus surface is shown in Fig. 2(a). The phase equilibria data substantiating these projections are described in this paper. Four phases are considered in the present section: a Nb-Ti-Si solid solution, Nb_3Si, Nb_5Si_3, and Ti_5Si_3. Nb_5Si_3 and Ti_5Si_3 are not isomorphous and have *t*I32 and *h*P16 crystal structures, respectively (Ref 4).

In this article, the Nb_5Si_3 with Ti in solid solution is referred to as $Nb(Ti)_5Si_3$, and the Ti_5Si_3 with Nb in solid solution is referred to as $Ti(Nb)_5Si_3$. The Nb_3Si with Ti in solid solution is referred to as $(Nb,Ti)_3Si$, because Nb_3Si and Ti_3Si are isomorphous. Similarly, the Nb with Ti and Si in solid solution is referred to as (Nb,Ti,Si), there being a continuous bcc solid solution between Nb and Ti at the metal-rich end of the phase diagram at elevated temperatures. The compositions of the (Nb,Ti,Si) and $(Nb,Ti)_3Si$ phases possess a wide range of Nb-to-Ti ratios; thus the order of the elements in the phase description (i.e., Nb, Ti) should not be taken to reflect the relative concentrations of these elements in the respective phases. The $Nb(Ti)_5Si_3$, $Ti(Nb)_5Si_3$, $(Nb,Ti)_3Si$, and (Nb,Ti,Si) (dendritic and eutectic) can be clearly distinguished in the directionally solidified (DS) composite microstructures by their morphology, scale, and contrast when examined using backscatter electron imaging (BSE) in the scanning electron microscope, as will be described.

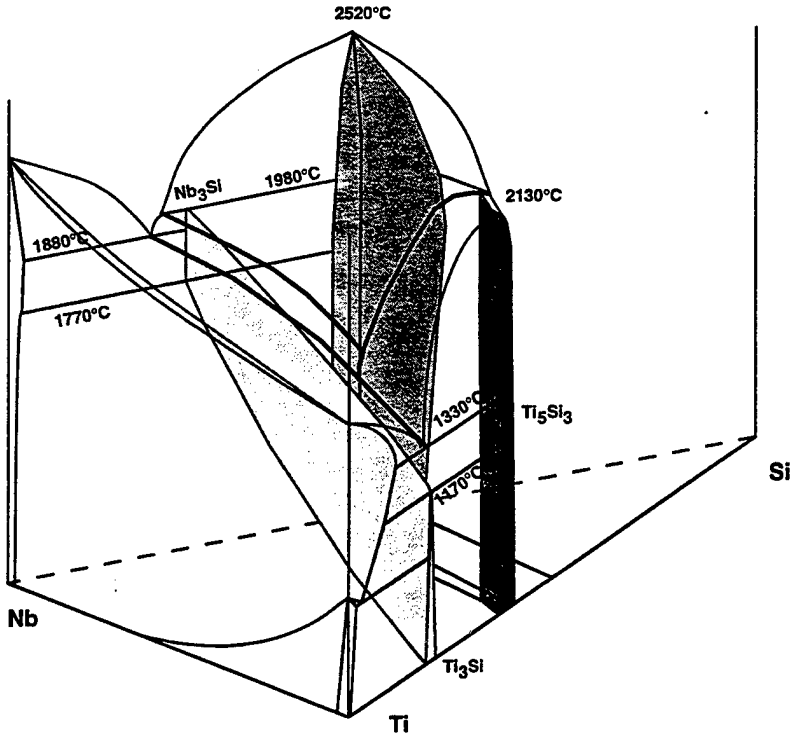


Fig. 1 Schematic of the proposed Nb-Ti-Si ternary phase diagram for compositions between 0 and 37.5% Si.

2. Background on Nb-Ti-Si Phase Equilibria

The binary Ti-Si phase diagram (Ref 4) possesses a eutectic of the form $L \rightarrow Ti_5Si_3 + (Ti)$ at 1330 °C. The binary Nb-Si phase diagram (Ref 5) has a eutectic of the form $L \rightarrow Nb_3Si + (Nb)$ at 1880 °C and a peritectic of the form $L + Nb_5Si_3 \rightarrow Nb_3Si$ at 1980 °C (Ref 2, 4, 6). In the ternary phase diagram a eutectic groove extends between the two binary eutectics, but due to the different binary eutectic reactions there is a change in the nature of the liquidus surface, and the eutectic groove, with decreasing Nb and increasing Ti concentration. The binary Nb-Si phase diagram has been studied by several researchers (Ref 2, 5, 6). The eutectic occurs at a composition of Nb-18.2Si, slightly Si-lean of the composition reported previously (Ref 4, 5). The eutectic microstructure typically consists of Nb rods and ribbons with a width of ~2 μm in a Nb_3Si matrix. Although Ti_3Si and Nb_3Si are isomorphous, Nb_3Si is only stable over the temperature range 1880 to 1770 °C, and Ti_3Si is only stable below 1170 °C. Ti_3Si forms by a peritectoid reaction between Ti_5Si_3 and Ti at temperature of 1170 °C.

The details of the Nb-Ti-Si ternary liquidus surface are now described, and in Section 4, "Results and Discussion," the substantiating data are presented. The regions close to the Nb-Si and Ti-Si binary eutectics are straightforward. The loci of the peritectic ridge from the $L + Nb_5Si_3 \rightarrow Nb_3Si$ peritectic, the Ti-Ti_5Si_3 eutectic groove, and the locations of the two transition reactions (Ref 7) that occur are more complex, and particular emphasis is placed on these features in this section. Here, a peritectic ($L + Nb(Ti)_5Si_3 \rightarrow Ti(Nb)_5Si_3$) is assumed between $Nb(Ti)_5Si_3$ and $Ti(Nb)_5Si_3$; a eutectic is also possible, but the evidence that will be discussed subsequently suggests a peritectic. However, either a eutectic or a peritectic reaction between $Nb(Ti)_5Si_3$ and $Ti(Nb)_5Si_3$ provides a groove or ridge that falls toward the valley between the binary eutectics, as shown in Fig. 1.

There are two options for the liquidus surface. In option 1, shown in Fig. 2(a), the first transition reaction (at higher Si concentration) is described by:

$$L + Nb(Ti)_5Si_3 \rightarrow (Nb,Ti)_3Si + Ti(Nb)_5Si_3$$

Thus, there is a peritectic ridge ($L + Nb(Ti)_5Si_3 \rightarrow (Nb,Ti)_3Si$) that extends from the Nb-rich side of the phase diagram and joins the peritectic ridge of the reaction between Nb_5Si_3 and Ti_5Si_3 below ~1850 °C. The second transition reaction (at lower Si concentration) in option 1 is described by:

$$L + (Nb,Ti)_3Si \rightarrow (Nb,Ti,Si) + Ti(Nb)_5Si_3$$

The above reaction occurs at the intersection between the peritectic ridge that descends from the first transition reaction and the $(Nb,Ti)_3Si$-(Nb,Ti,Si) eutectic groove, as shown in Fig. 2(a), at a temperature of ~1350 °C. The data that are discussed subsequently indicate that this is the correct version of the liquidus surface. However, the steep nature of the peritectic ridge between the two transition reactions, and the small composition interval between them, make it very difficult to determine unequivocally that option 1 is indeed correct.

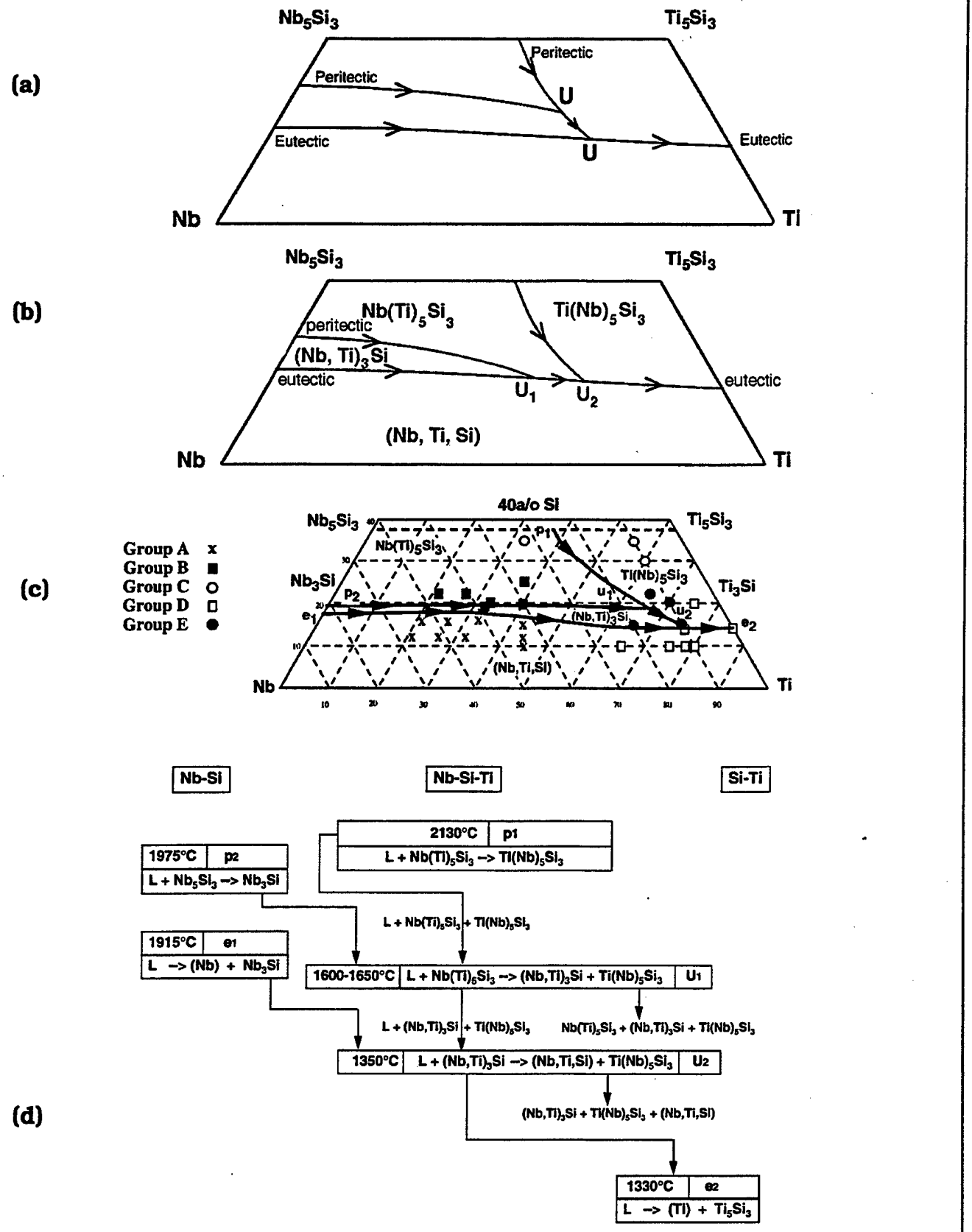


Fig. 2 (a)Schematic showing the projection of the liquidus surface for option 1. (b) Schematic diagram showing the projection of the liquidus surface for option 2. (c) Actual compositions and constituent phases shown on a projection of the liquidus surface. (d) Partial Scheil reaction scheme for the Si-lean region of the Nb-Ti-Si ternary. Eutectic and peritectic reactions are indicated by e and p, respectively. The transitions are represented by U.

Table 1 Alloy Compositions and Constituent Phases of Ternary Nb-Ti-Si Alloys

Group	Composition	Constituent phases	Melting temperature, °C
A.....	Nb-21Ti-12Si	PR (Nb,Ti,Si), EU $(Nb,Ti)_3Si$ + (Nb,Ti,Si)	1905
	Nb-21Ti-16Si	PR (Nb,Ti,Si), EU $(Nb,Ti)_3Si$ + (Nb,Ti,Si)	...
	Nb-27Ti-12Si	PR (Nb,Ti,Si), EU $(Nb,Ti)_3Si$ + (Nb,Ti,Si)	...
	Nb-27Ti-16Si	PR (Nb,Ti,Si), EU $(Nb,Ti)_3Si$ + (Nb,Ti,Si)	...
	Nb-33Ti-12Si	PR (Nb,Ti,Si), EU $(Nb,Ti)_3Si$ + (Nb,Ti,Si)	...
	Nb-33Ti-16Si	PR (Nb,Ti,Si), EU $(Nb,Ti)_3Si$ + (Nb,Ti,Si)	...
	Nb-44Ti-12Si	PR (Nb,Ti,Si), EU $(Nb,Ti)_3Si$ + (Nb,Ti,Si)	1712
	Nb-45Ti-10Si	PR (Nb,Ti,Si), EU $(Nb,Ti)_3Si$ + (Nb,Ti,Si)	1680
	Nb-42.5Ti-15Si	PR (Nb,Ti,Si), EU $(Nb,Ti)_3Si$ + (Nb,Ti,Si)	1704
B.....	Nb-21Ti-22Si	PR $Nb(Ti)_5Si_3$, PE $(Nb,Ti)_3Si$, EU $(Nb,Ti)_3Si$ + (Nb,Ti,Si)	2030
	Nb-27Ti-22Si	PR $Nb(Ti)_5Si_3$, PE $(Nb,Ti)_3Si$, EU $(Nb,Ti)_3Si$ + (Nb,Ti,Si)	2002
	Nb-33Ti-20Si	PR $Nb(Ti)_5Si_3$, PE $(Nb,Ti)_3Si$, EU $(Nb,Ti)_3Si$ + (Nb,Ti,Si)	1870
	Nb-40Ti-20Si	PR $Nb(Ti)_5Si_3$, PE $(Nb,Ti)_3Si$, EU $(Nb,Ti)_3Si$ + (Nb,Ti,Si)	1755
	Nb-32Ti-19Si	PR $Nb(Ti)_5Si_3$, PE $(Nb,Ti)_3Si$, EU $(Nb,Ti)_3Si$ + (Nb,Ti,Si)	...
	Nb-37.5Ti-25Si	PR $Nb(Ti)_5Si_3$, PE $(Nb,Ti)_3Si$, EU $(Nb,Ti)_3Si$ + (Nb,Ti,Si)	1940
	Nb-35Ti-30Si	PR $Nb(Ti)_5Si_3$, PE $(Nb,Ti)_3Si$, EU $(Nb,Ti)_3Si$ + (Nb,Ti,Si)	2050
C.....	Nb-32.5Ti-35Si	PR $Nb(Ti)_5Si_3$, interdendritic $(Nb,Ti)_3Si$, (Nb,Ti,Si)	2170
	Nb-55Ti-35Si	PR $Ti(Nb)_5Si_3$, EU (Nb,Ti,Si) + $Ti(Nb)_5Si_3$	2020
	Nb-60Ti-30Si	PR $Ti(Nb)_5Si_3$, EU (Nb,Ti,Si) + $Ti(Nb)_5Si_3$	1950
D.....	Ti-13.5Si	EU Ti + Ti_5Si_3	1328
	Nb-76.5Ti-13.5Si	EU (Nb,Ti,Si) + $Ti(Nb)_5Si_3$	1355
	Nb-75Ti-10Si	PR (Nb,Ti,Si), EU (Nb,Ti,Si) + $Ti(Nb)_5Si_3$	1550
	Nb-78Ti-10Si	PR (Nb,Ti,Si), EU (Nb,Ti,Si) + $Ti(Nb)_5Si_3$	...
	Nb-80Ti-10Si	PR (Nb,Ti,Si), EU (Nb,Ti,Si) + $Ti(Nb)_5Si_3$	1480
	Nb-75Ti-20Si	PR $Ti(Nb)_5Si_3$, EU (Nb,Ti,Si) + $Ti(Nb)_5Si_3$	1704
E.....	Nb-65Ti-15Si	PR $(Nb,Ti)_3Si$, EU $(Nb,Ti)_3Si$ + (Nb,Ti,Si)	...
	Nb-75Ti-15Si	PR $(Nb,Ti)_3Si$, EU $(Nb,Ti)_3Si$ + (Nb,Ti,Si), EU (Nb,Ti,Si) + $Ti(Nb)_5Si_3$	1458
	Nb-65Ti-22Si	PR $Ti(Nb)_5Si_3$, PE $(Nb,Ti)_3Si$, EU $(Nb,Ti)_3Si$ + (Nb,Ti,Si), EU (Nb,Ti,Si) + $Ti(Nb)_5Si_3$	1675
	Nb-70Ti-20Si	PR $Ti(Nb)_5Si_3$, PE $(Nb,Ti)_3Si$, EU $(Nb,Ti)_3Si$ + (Nb,Ti,Si), EU (Nb,Ti,Si) + $Ti(Nb)_5Si_3$	1620

PR, primary solidification phase; PE, peritectic solidification phase; EU, eutectic solidification phase

The second option for the liquidus surface is shown in Fig. 2(b) and has the following first transition reaction (at higher Nb concentration):

$$L + Nb(Ti)_5Si_3 \rightarrow (Nb,Ti)_3Si + (Nb,Ti,Si)$$

In this option the peritectic ridge that extends from the Nb-rich side of the phase diagram intersects the $(Nb,Ti)_3Si$ + (Nb,Ti,Si) eutectic groove leading to the above reaction. The groove continues to fall in temperature with increasing Ti concentration until it meets the ridge from the peritectic reaction between $Nb(Ti)_5Si_3$ and $Ti(Nb)_5Si_3$, leading to the second transition reaction (at lower Nb concentration):

$$L + Nb(Ti)_5Si_3 \rightarrow (Nb,Ti,Si) + Ti(Nb)_5Si_3$$

However, there was no evidence for this second transition reaction, as is subsequently described. This second option for the liquidus surface is therefore incorrect.

There are two other possible options in addition to the two described so far, with the second transition reaction being a class I ternary eutectic (Ref 7). However, there was no evidence for the formation of a ternary eutectic in any of the structures that were examined. There are no previous data on the compositions or temperatures at which the above transition reactions occur. The aim of this paper is to describe the results of the phase equilibrium studies. These results are summarized in Fig. 2(c) and indicate that the first of the above options is the correct version. Figure 2(d) shows a partial Scheil reaction scheme for the Si-lean region of the Nb-Ti-Si ternary.

3. Experimental

The samples for phase equilibrium studies were directionally solidified by cold crucible directional solidification (Ref 2) after triple melting the starting charges from high-purity elements (>99.99%). The directional solidification procedure used has been described previously (Ref 2). In specific cases,



(a) (b)

Fig. 3 Typical microstructures (BSE images) of the (a) longitudinal and (b) transverse sections of a DS Nb-27Ti-16Si alloy. The large white dendrites are (Nb,Ti,Si) and the faceted gray phase is $(Nb,Ti)_3Si$.

samples were also prepared by cold crucible induction levitation melting followed by solidification in the cold crucible. All samples were examined using (BSE) imaging and energy-dispersive spectrometry (EDS). In the case of selected alloys, electron beam microprobe analysis (EPMA) and XRD were also performed in order to determine the chemistry and crystal structure of the individual phases. Only compositions with Si concentrations less than 37.5% were considered in this study.

The alloy melt temperatures were measured using a two-wavelength optical pyrometer. The pyrometer was calibrated against both the melting temperature of 99.9% pure Ti (1670 °C) and the temperature of the Ti-Ti_5Si_3 eutectic (1330 °C). Errors in the temperature measurements were estimated as <20 °C. These temperatures were only approximate; liquidus and solidus temperatures were not measured because the melt temperatures were too high for conventional differential thermal analysis (DTA).

The investigated compositions are listed in Table 1. These compositions are those of the starting charges and not as analyzed after directional solidification. However, mass losses were measured for each experiment and were found to be less than 0.1 wt.%. The sum of the concentrations of the interstitials of the starting elements (C, N, O, H) was less than 80 ppm.

EPMA was employed using a 15 kV, 20 nA, ~1 μm diameter beam to determine phase chemistries. In selected cases, step scans were also performed perpendicular to the growth direction using a 2 μm step length over a total scan length of ~100 μm. High-purity Nb, Ti, and Si were used as standards and conventional matrix corrections (Z, A, and F) were used to calculate the wt.% compositions from measured x-ray intensities. The limit of detection of Si and Ti was 0.04 wt.% and the limit of detection of Nb was 0.13 wt.%. Errors in the Ti and Si measurements were ~0.8% relative, and in the Nb measurement the error was ~2% relative.

4. Results and Discussion

Microstructures of Ternary Alloys

Microstructural evidence for the solidification paths will be discussed first for the (Nb,Ti,Si)-rich alloys, second for the $Nb(Ti)_5Si_3$-rich alloys, third for the $Nb(Ti)_5Si_3$-$Ti(Nb)_5Si_3$-rich compositions, fourth for the (Nb,Ti,Si)-$Ti(Ti)_5Si_3$-rich compositions, and finally for compositions near the transition reactions. These categories are listed as A to E in Table 1 and in the following sections. The phases present in the DS alloys of groups A to E are summarized in Table 1.

4.1 Nb-Rich Nb-Ti-Si Compositions: Group A

Ternary Nb-Ti-Si alloys (group A in Table 1) with Ti concentrations of 21 to 45% and Si concentrations of 10 to 16% were all on the metal-rich side of the (Nb,Ti,Si)-$(Nb,Ti)_3Si$ eutectic valley, so that the primary solidification phase was (Nb,Ti,Si) dendrites. Typical microstructures of the longitudinal and transverse sections are shown in Fig. 3(a) and (b) for the Nb-27Ti-16Si composition. The microstructure consisted of nonfaceted (Nb,Ti,Si) dendrites, which are the lighter phase in these BSE micrographs, together with large-scale (~50 μm) faceted $(Nb,Ti)_3Si$ dendrites; the microstructure of the longitudinal section shown in Fig. 3(a) indicates reasonable alignment of both nonfaceted (Nb,Ti,Si) dendrites and faceted $(Nb,Ti)_3Si$ dendrites with the growth direction. This composition was close to the eutectic groove. The BSE contrast indicates strong Ti segregation toward the edges of the $(Nb,Ti)_3Si$ dendrites. Typically, several samples were prepared from the individual compositions and the microstructures were observed to be very consistent.

The microstructure of the transverse section of the DS Nb-21Ti-12Si composition is shown in Fig. 4. The (Nb,Ti,Si) dendrites are larger than in the case of the Nb-27Ti-16Si alloy, which may be due to the greater volume fraction of metallic

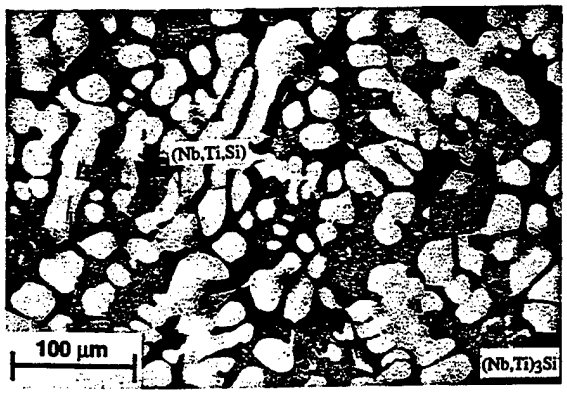


Fig. 4 Typical microstructure (BSE image) of the transverse section of a DS Nb-21Ti-12Si alloy.

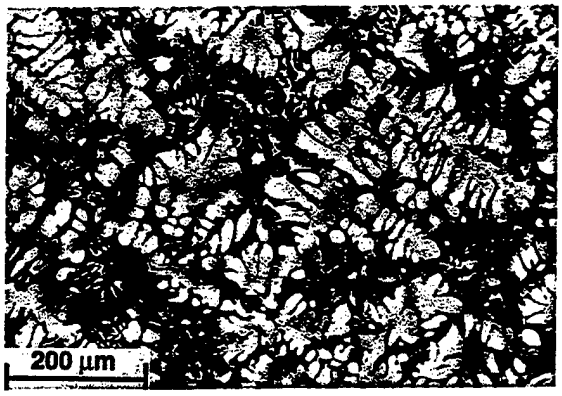


Fig. 5 Typical microstructure (BSE image) of the transverse section of a DS Nb-44Ti-12Si alloy. The large white dendrites are (Nb,Ti,Si) and the interdendritic gray phase is $(Nb,Ti)_3Si$.

phase and also the larger freezing range of this alloy (solidification begins at a higher point on the liquidus surface of the eutectic valley); this could have allowed some coarsening of the (Nb,Ti,Si) dendrites during directional solidification.

A composition examined in this regime with almost the lowest Nb concentration was Nb-44Ti-12Si. The microstructure of the transverse section of the DS composition is shown in Fig. 5. This microstructure possessed a large volume fraction of nonfaceted (Nb,Ti,Si) dendrites. The interdendritic regions contained $(Nb,Ti)_3Si$ and fine-scale (Nb,Ti,Si). No $Nb(Ti)_5Si_3$ was observed in this microstructure, which suggested that the composition of the final interdendritic liquid was in the (Nb,Ti,Si)-$(Nb,Ti)_3Si$ eutectic groove, and it never reached a transition reaction.

Table 1 indicates that the eutectic groove temperature has fallen from ~1880 °C at the Nb-Si binary eutectic to ~1700 °C at Nb-42.5Ti-15Si. There is also a larger volume fraction of metal dendrites in the Nb-21Ti-12Si alloy than the Nb-27Ti-16Si alloy. The volume fractions of metal dendrites for the Nb-27Ti-16Si and Nb-21Ti-12Si compositions were 41 and 54%, respectively. The lower volume fraction of (Nb,Ti,Si) dendrites was from the composition closer to the eutectic groove. This suggests that up to the 27Ti composition, the eutectic groove and the solvus surface are approximately parallel to the planes of constant Si composition because the $(Nb,Ti)_3Si$ probably maintains the stoichoimetric Si concentration. This is to be expected because there is only a small difference in the Si concentrations of the Nb-Nb_3Si and Ti-Ti_5Si_3 eutectics (Nb-18.2Si and Ti-13.5Si, respectively). However, the Nb-44Ti-12Si composition appears to have a larger volume fraction of metal dendrites. This could be because the eutectic groove is moving to Si-rich compositions with increasing Ti concentration, or because the solidus is moving toward the metal side of the ternary phase diagram with increasing Ti concentration. The latter seems more likely because the Ti-Ti_5Si_3 eutectic occurs at lower Si concentrations than the Nb-Nb_3Si eutectic. Thus, the locus of the eutectic groove shown in Fig. 2(c) is consistent with the microstructures for compositions as high as 16Si and as high as 44Ti.

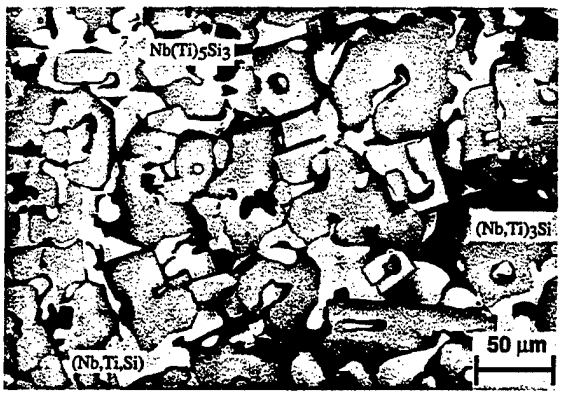
4.2 $Nb(Ti)_5Si_3$-Rich Compositions: Group B

A range of compositions was examined from the $Nb(Ti)_5Si_3$ and $(Nb,Ti)_3Si$-rich side of the eutectic valley. In the binary Nb-Nb_3Si eutectic, the eutectic composition and the liquid composition of the $L + Nb_5Si_3 \rightarrow Nb_3Si$ peritectic are very close to each other (18.2 vs. 19.5 Si). The situation is similar in the Nb-Ti-Si ternary phase diagram. Therefore, it is very hard to define the region between the peritectic ridge and the eutectic groove. Nevertheless, there is clear evidence for the existence of such a region. The purpose of this section is to describe the evidence for the range of Nb-Ti-Si compositions over which the peritectic ridge and the eutectic valley exist. It appears that these two lines are within several percent Si of each other and almost parallel to each other over a wide Ti composition range, from 0 up to ~70Ti.

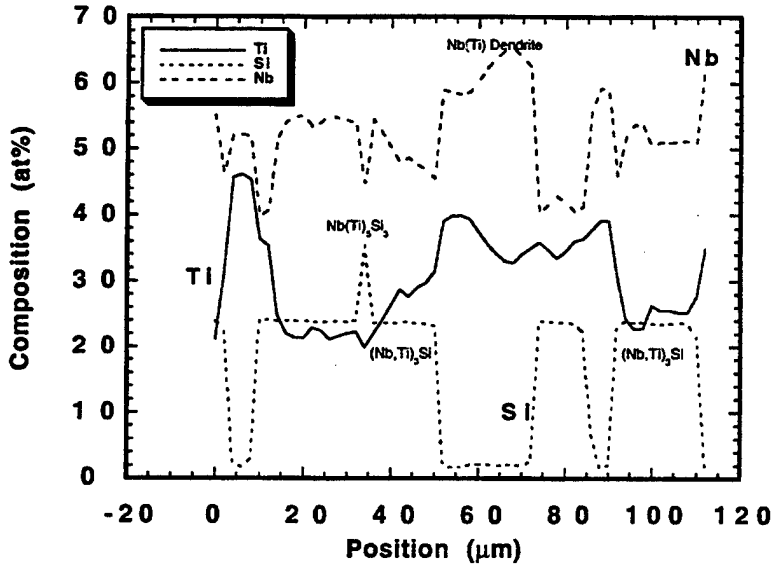
Ternary alloys with Ti concentrations of 21 to 40% and Si concentrations of 19 to 30% (group B in Table 1) were from the Si-rich side of the eutectic valley and were observed to have experienced the peritectic reaction, $L + Nb(Ti)_5Si_3 \rightarrow (Nb,Ti)_3Si$. Microstructures of longitudinal and transverse sections of the DS Nb-27Ti-22Si composition are shown in Fig. 6(a) and (b), respectively; these micrographs showed the three phases expected for the hypereutectic compositions (see also the EPMA scans in Fig. 6c). First, there were metal-rich (Nb,Ti,Si) dendrites; these were the lightest phase in the BSE images. Second, there were faceted $(Nb,Ti)_3Si$ dendrites; these were the gray phase in the BSE images. Third, there was a small volume fraction of a dark phase, primary $Nb(Ti)_5Si_3$ dendrites. The longitudinal section showed aligned (Nb,Ti,Si) and $(Nb,Ti)_3Si$ dendrites, with primary $Nb(Ti)_5Si_3$ at the cores of the $(Nb,Ti)_3Si$ dendrites. These microstructures are analogous to those that



(a)



(b)



(c)

Fig. 6 Typical microstructures (BSE images) of the **(a)** longitudinal and **(b)** transverse sections of a DS Nb-27Ti-22Si alloy. **(c)** EPMA scans perpendicular to the growth direction indicating the Nb, Ti, and Si concentration profiles perpendicular to the dendrites.

have been observed in hypereutectic binary DS Nb-Si composites (Ref 2), as shown in Fig. 7(a) and (b). The presence of these phases was confirmed using EPMA and EDS. The volume fraction of $Nb(Ti)_5Si_3$ was increased in alloys of higher Si concentrations. In addition, BSE imaging showed strong dark contrast in the interdendritic regions of the Nb-Ti-Si alloys. This could have been caused by either the presence of a silicide or segregation of either Ti or Si to the interdendritic regions. EPMA and crystallographic analyses using electron beam scattering patterns (EBSP) indicated that this contrast was caused by local Ti enrichment of $(Nb,Ti)_3Si$.

A typical EPMA scan perpendicular to the dendrites of the DS Nb-27Ti-22Si composition is shown in Fig. 6(c). The three phases were clearly different compositionally. The compositions of the three phases observed in this (Nb,Ti,Si)-$(Nb,Ti)_3Si$-$Nb(Ti)_5Si_3$ composite are shown in Table 2. For the (Nb,Ti,Si) solid solution, Nb, Ti, and Si concentrations in the range 69 to 54, 29 to 44, and 1.6 to 2.4%, respectively, were measured. A range of $(Nb,Ti)_3Si$ chemistries was measured with different Nb and Ti ratios and a narrow range of Si concentrations. The centers of the faceted $(Nb,Ti)_3Si$ dendrites were generally Nb rich, and the shaded regions at the edges of these dendrites were Ti rich. The Si concentration of the $(Nb,Ti)_3Si$ was slightly lean of the stoichiometric composition, which suggests that Ti substitutes principally for Nb and not Si. $Nb(Ti)_5Si_3$ was detected at the centers of the $(Nb,Ti)_3Si$ dendrites and not in the interdendritic regions. The Si concen-

tration of the $Nb(Ti)_5Si_3$ was also slightly lean of the stoichiometric composition.

Figures 7(a) and (b) show transverse sections of binary Nb-19Si and Nb-22Si alloys, respectively. The Nb-19Si composition contained primary Nb_3Si dendrites and an interdendritic eutectic of Nb_3Si and (Nb). The Nb-22Si contained primary Nb_5Si_3, peritectic Nb_3Si, Nb_3Si dendrites, and an interdendritic eutectic of Nb_3Si and (Nb). The morphologies of the primary solidification phases and the peritectic Nb_3Si are similar in the binary Nb-Si and ternary Nb-Ti-Si alloys.

The longitudinal sections of the ternary alloys showed microcracks perpendicular to the growth direction in the $Nb(Ti)_5Si_3$ dendrites. These cracks probably occurred upon cooling as a result of the allotropic transformation of the $Nb(Ti)_5Si_3$ phase reported previously (Ref 4). Thus, for substitution of Ti for Nb for levels of up to 27%, the $\alpha \rightarrow \beta Nb(Ti)_5Si_3$ allotropic transformation probably still occurs. These cracks are characteristic of the Nb_5Si_3 phase and help to distinguish it from other phases in the DS structure. No cracks were observed in the two-phase (Nb,Ti,Si)-$(Nb,Ti)_3Si$ composites.

The highest Ti- and Si-containing alloys investigated in group B were the Nb-40Ti-20Si and Nb-37.5Ti-25Si compositions. These both also contained primary $Nb(Ti)_5Si_3$, peritectic $(Nb,Ti)_3Si$ and interdendritic eutectic. In the Nb-37.5Ti-25Si composition there was a larger volume fraction of primary $Nb(Ti)_5Si_3$. This is evidence that the peritectic ridge extends to compositions as high as 40Ti; that is, this composition is still richer in Nb than is the composition of the transition reaction, and the peritectic ridge is very close to the 20Si composition. At 33Ti, the peritectic temperature had fallen from ~1980 °C for the binary (Ref 4) to ~1870 °C.

Compositions of 19Si and above experienced the peritectic (i.e., they were hyperperitectic) and compositions of 16Si and lower did not experience this reaction (i.e., they were hypoeutectic). This gives an indication of the narrow nature of the composition range between the (Nb,Ti,Si)-$(Nb,Ti)_3Si$ eutectic groove and the $L + Nb(Ti)_5Si_3 \rightarrow (Nb,Ti)_3Si$ peritectic.

4.3 $Nb(Ti)_5Si_3$ and $Ti(Nb)_5Si_3$-Rich Compositions: Group C

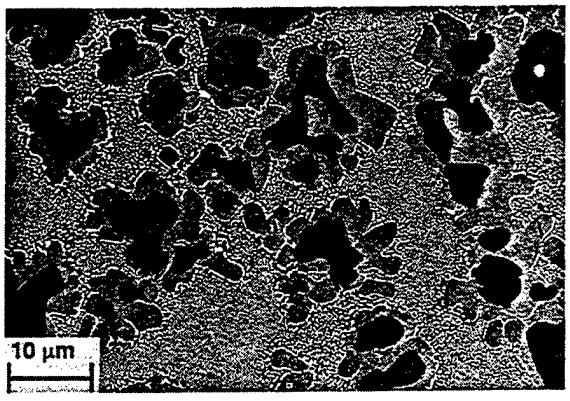
4.3.1 Nb-32.5Ti-35Si-$Nb(Ti)_5Si_3$-Rich Compositions

The microstructure of the induction cast Nb-32.5Ti-35Si composition is shown in Fig. 8. This composition (part of group C in Table 1) was investigated in an attempt to identify the nature of the reaction between $Nb(Ti)_5Si_3$ and $Ti(Nb)_5Si_3$. The composition of 35Si was selected in preference to 37.5Si so that the solidification phases formed would be metal-rich and not Si-rich. The microstructure consisted of large, gray, blocky, primary $Nb(Ti)_5Si_3$ dendrites with blocky interdendritic $(Nb,Ti)_3Si$ and a very small volume fraction (<2%) of interdendritic (Nb,Ti,Si). No primary (Nb,Ti,Si) dendrites and no $Ti(Nb)_5Si_3$ were observed. Phase chemistries of the primary $Nb(Ti)_5Si_3$, and interdendritic $(Nb,Ti)_3Si$ and (Nb,Ti,Si), were measured using EPMA and are shown in Table 3. The $Nb(Ti)_5Si_3$ occupied ~90 vol% of this composition. The $Nb(Ti)_5Si_3$ contained many cracks. The majority of the interdendritic regions consisted of $(Nb,Ti)_3Si$, but there was also a small volume fraction (<2%) of (Nb,Ti,Si), which was very difficult to distinguish from the $(Nb,Ti)_3Si$; it had similar BSE contrast, but it did not possess the distinctive faceted morphology of $(Nb,Ti)_3Si$—the morphology and the phase chemistry were the only distinguishing features. This composition is thus essentially two phase with only a very small volume fraction (<2%) of metal.

The mean composition of the core of the primary $Nb(Ti)_5Si_3$ was Nb-27.9Ti-37.9Si. The Si concentration was essentially the stoichiometric composition and the Nb-to-Ti ratio was approximately 5 to 4. The BSE images were brighter in the center, and EPMA also indicated significant coring of the $Nb(Ti)_5Si_3$ dendrites. The compositions shown in Table 3 indicate that at the edges of the $Nb(Ti)_5Si_3$ dendrites the mean



(a)



(b)

Fig. 7 Typical microstructures (BSE images) of DS (a) Nb-19Si and (b) Nb-22Si. The black phase is Nb_5Si_3, the gray phase is Nb_3Si, and the fine-scale white phase is eutectic (Nb).

composition was Nb-34.2Ti-37.2Si. Thus, there was significant Nb depletion and Ti enrichment at the edges of the dendrites; the Si concentration remained essentially at the stoichiometric composition.

The mean composition of the interdendritic $(Nb,Ti)_3Si$ was Nb-40.6Ti-25.5Si. The $(Nb,Ti)_3Si$ chemistry was similar to that observed for the edge of the $(Nb,Ti)_3Si$ phase in the Nb-27Ti-22Si alloy, but no coring of the $(Nb,Ti)_3Si$ dendrites was observed probably because of the scale and low volume fraction. The Si concentration of the $(Nb,Ti)_3Si$ was essentially the stoichiometric composition. The Nb composition of the $Nb(Ti)_5Si_3$ in the Nb-32.5Ti-35Si alloy was lower than in the same phase in the Nb-27Ti-22Si alloy. In the latter composition, EPMA of the $Nb(Ti)_5Si_3$ was difficult because of the small size and volume fraction. The solubility limit of Ti in $Nb(Ti)_5Si_3$ was ~34%. The interdendritic (Nb,Ti,Si) was probably generated because the liquid composition shifted into the $L \rightarrow (Nb,Ti)_3Si + (Nb,Ti,Si)$ eutectic groove.

Thus, the microstructure is consistent with $Nb(Ti)_5Si_3$ being the primary solidification phase with the liquid composition shifting to the $L + Nb(Ti)_5Si_3 \rightarrow (Nb,Ti)_3Si$ peritectic ridge during solidification. Coring of the Nb_5Si_3 dendrites is consistent with the liquid composition moving away from the Nb_5Si_3 composition and toward the Ti corner with the Si concentration probably remaining constant. This suggests the following reaction:

$$L + Nb(Ti)_5Si_3 \rightarrow Ti(Nb)_5Si_3$$

Although this is a consistent explanation of the microstructure, it does not prove that the reaction between $Nb(Ti)_5Si_3$ and $Ti(Nb)_5Si_3$ is a peritectic. However, if there were a eutectic reaction rather than a peritectic reaction between these two phases, it is more likely that a eutectic microstructure would have formed. The melting temperatures are 2520 °C for binary Nb_5Si_3 and 2130 °C for binary Ti_5Si_3. The melting temperature of 2170 °C for the Nb-32.5Ti-35Si is consistent with a very flat peritectic liquidus. If there were a eutectic between these two phases, a lower melting temperature would be expected, below the melting temperature of Ti_5Si_3. The groove would probably be steeper if the reaction were a eutectic, and the liquid composition would shift into the eutectic valley.



Fig. 8 Typical microstructure (BSE image) of the induction melted Nb-32.5Ti-35Si alloy. The large primary dendrites are $Nb(Ti)_5Si_3$, and there is interdendritic $(Nb,Ti)_3Si$.

4.3.2 $Ti(Nb)_5Si_3$-Rich Compositions

Nb-60Ti-30Si. The aim of examining this composition was first to try to solidify primary $Ti(Nb)_5Si_3$ dendrites in order to determine their morphology and chemistry, and second, to attempt to examine the nature of the reaction between $Nb(Ti)_5Si_3$ and $Ti(Nb)_5Si_3$. The microstructure of the Nb-60Ti-30Si composition is shown in Fig. 9. This composition was induction melted and cast in the segmented copper crucible. The microstructure consisted of large-scale (>100 µm) primary $Ti(Nb)_5Si_3$ dendrites in a (Nb,Ti,Si)-$Ti(Nb)_5Si_3$ eutectic. The microstructures of the Nb-60Ti-30Si and the Nb-75Ti-20Si compositions were similar. These compositions contained faceted hexagonal (*hP*16) dendrites, which are clearly visible in Fig. 9. The morphology and contrast are clear evidence that the silicide is $Ti(Nb)_5Si_3$ and not $Nb(Ti)_5Si_3$. Some cracks were observed in the $Ti(Nb)_5Si_3$ dendrites; this was probably due to differential thermal contraction during solidification and post solidification cooling.

Nb-55Ti-35Si. The microstructure of the Nb-55Ti-35Si alloy was similar to that of the Nb-60Ti-30Si alloy in that it contained primary $Ti(Nb)_5Si_3$ dendrites with an interdendritic eu-

Table 2 (Nb,Ti,Si), $(Nb,Ti)_3Si$, and $Nb(Ti)_5Si_3$ Phase Composition Ranges for the Nb-27Ti-22Si Composition

Alloy	Composition			Comments
	Nb	Ti	Si	
(Nb,Ti,Si)	54 to 69	29 to 44	1.6 to 2.4	...
	(61.2)	(36.7)	(2.1)	
$(Nb,Ti)_3Si$	44 to 54	22 to 29	23 to 24	Center: Nb-rich Ti-lean
	(50.6)	(25.8)	(23.6)	
	32 to 33	43 to 44	23.5 to 23.6	Edge: Ti-rich Nb-lean
	(32.8)	(43.7)	(23.5)	
$Nb(Ti)_5Si_3$	44 to 45	19 to 20	35 to 36	...
	(44.6)	(19.9)	(35.5)	

Note: Mean values of the phase chemistries are shown in parentheses.

tectic of (Nb,Ti,Si)-Ti(Nb)$_5$Si$_3$. However, the volume fraction of primary Ti(Nb)$_5$Si$_3$ was very large (>85%), and thus it was difficult to identify the faceted nature of the dendrites. At high magnifications, the typical (Nb,Ti,Si)-Ti(Nb)$_5$Si$_3$ eutectic could be observed in the interdendritic regions. This suggests that on solidification the liquid composition moved into the (Nb,Ti,Si)-Ti(Nb)$_5$Si$_3$ eutectic groove. The measured liquidus temperatures (1950 °C at 30Si and 2020 °C at 35Si) were lower than the melting temperature of binary Ti$_5$Si$_3$.

4.4 (Nb,Ti,Si)-Ti(Nb)$_5$Si$_3$-Rich Compositions: Group D

The results from the Ti-rich corner of the ternary phase diagram are now discussed in the context of the results from the following compositions:

4.4.1 Ti-13.5Si: Ti-Ti$_5$Si$_3$ Eutectic

The binary Ti-Ti$_5$Si$_3$ eutectic was examined and was confirmed as being at a composition of Ti-13.5Si. When grown at a rate of 3 mm/min, the eutectic consisted of very fine (~1 μm) faceted needles in a Ti matrix. No primary Ti or Ti$_5$Si$_3$ dendrites were observed in the microstructure, and the eutectic grew with a cellular front. The eutectic was of a similar morphology to the interdendritic eutectic shown in Fig. 9. These observations are consistent with previous reports of the binary Ti-Ti$_5$Si$_3$ eutectic (Ref 8), and Ti-Ti$_5$Si$_3$ eutectic-based composites modified with Nb and Al (Ref 9).

The Ti-Ti$_5$Si$_3$ eutectic can be distinguished from the Nb-Nb$_3$Si eutectic by two characteristics. First, in the binary Ti-Ti$_5$Si$_3$ eutectic the Ti is the matrix phase, whereas in the binary Nb-Nb$_3$Si the Nb$_3$Si is the matrix phase. Second, in the Ti-Ti$_5$Si$_3$ eutectic the Ti$_5$Si$_3$ rods are faceted, whereas in the Nb-Nb$_3$Si eutectic the Nb rods are not faceted.

4.4.2 Nb-76.5Ti-13.5Si

In an attempt to identify the locus of the groove between the (Nb,Ti,Si)-(Nb,Ti)$_3$Si and (Nb,Ti,Si)-Ti(Nb)$_5$Si$_3$ eutectics more precisely, the Nb-76.5Ti-13.5Si composition was directionally solidified. This alloy had a melting temperature of 1355 °C. The microstructure consisted of very fine faceted needles (~2 μm) of Ti(Nb)$_5$Si$_3$ in a Ti matrix, the needles being aligned with the growth direction. No primary (Nb,Ti,Si), Ti(Nb)$_5$Si$_3$, or (Nb,Ti)$_3$Si dendrites were observed; this suggests that this composition was on, or very close to, the eutectic groove. Three points on the eutectic groove can therefore be defined: Nb-18.2Si, Ti-13.5Si, and Nb-76.5Ti-13.5Si. This also indicates that the second transition reaction (at lower Si concentration) occurs at a Ti composition of less than 76.5% and a Si concentration close to 13.5 %.

4.4.3 Nb-75Ti-10Si

The microstructure of the Nb-75Ti-10Si composition is shown in Fig. 10, and it consists of primary (Nb,Ti,Si) dendrites in a (Nb,Ti,Si)-Ti(Nb)$_5$Si$_3$ eutectic. The large white dendrites are the (Nb,Ti,Si), and the fine-scale (~1 μm) black needles are the Ti(Nb)$_5$Si$_3$ of the eutectic. No (Nb,Ti)$_3$Si was observed in this composition. There was no microstructural evidence of a $\beta \leftrightarrow \alpha$ transformation in the (Nb,Ti,Si). This suggests that the β was stabilized by the Nb; the transformation kinetics may be too slow for it to occur during directional solidification. Figure 10 shows a transverse section of a sample that was grown at 5 mm/min. Compositions of Nb-80Ti-10Si and Nb-78Ti-10Si were also examined, and the microstructures observed were similar to that shown in Fig. 10. These compositions were directionally solidified in order to generate primary (Nb,Ti,Si) dendrites with interdendritic (Nb,Ti,Si)-Ti(Nb)$_5$Si$_3$ eutectic to confirm the existence of the (Nb,Ti,Si)-Ti(Nb)$_5$Si$_3$ eutectic and identify the locus of the eutectic groove. Thus, in this region the primary solidification phase was (Nb,Ti,Si) dendrites, the liquid composition moved away from the Nb-rich corner toward the eutectic groove where the (Nb,Ti,Si)-Ti(Nb)$_5$Si$_3$ eutectic was formed, and then the liquid composition moved down the eutectic groove. No ternary eutectic was observed. In some areas the (Nb,Ti,Si)-Ti(Nb)$_5$Si$_3$ looked lamellar and in others it looked like individual "sheaves" with a fine Ti(Nb)$_5$Si$_3$ rod at the center of the "sheaves." The phase contents of the Nb-75Ti-10Si, Nb-80Ti-10Si, and Nb-78Ti-10Si compositions were self-consistent.

In order to check the nature of the eutectic, the Nb-75Ti-10Si composition was grown with a Nb-27Ti-16Si seed; this seed

Table 3 Phase Chemistry Ranges for Primary Dendritic Nb(Ti)$_5$Si$_3$ and Interdendritic Phases, (Nb,Ti)$_3$Si, and (Nb,Ti,Si), in the Nb-32.5Ti-35Si Alloy, as Measured Using EPMA

Alloy	Composition			Comments
	Nb	Ti	Si	
Nb(Ti)$_5$Si$_3$	33.5 to 34.9	26.7 to 28.5	37.7 to 38.4	Primary
	(34.2)	(27.9)	(37.9)	Dendrite
				Core
Nb(Ti)$_5$Si$_3$	27.8 to 29.1	33.3 to 35.5	36.2 to 37.7	Primary
	(28.7)	(34.2)	(37.2)	Dendrite
				Edge
(Nb,Ti)$_3$Si	33.8 to 34.1	40.2 to 40.7	25.2 to 25.9	Interdendritic
	(33.9)	(40.6)	(25.5),	
(Nb,Ti,Si)	30.8 to 33.6	64.6 to 67.3	1.8 to 2.2	Metal
	(31.8)	(66.3)	(1.9),	

Note: Mean values of the phase chemistries are shown in parentheses.

possessed (Nb,Ti,Si) dendrites and $(Nb,Ti)_3Si$, as described previously. The metal dendrites grew from the Nb-75Ti-10Si melt epitaxially off the seed, but the $Ti(Nb)_5Si_3$ did not grow epitaxially. The (Nb,Ti,Si)-$Ti(Nb)_5Si_3$ eutectic also clearly possessed a different chemistry and provided a much darker BSE contrast than the $(Nb,Ti)_3Si$ (in the seed) at the seed: Nb-75Ti-10Si interface. If it were at all possible to grow $(Nb,Ti)_3Si$ from this composition, it should have nucleated and grown easily on the seed.

4.4.4 Nb-75Ti-20Si

The aim of examining this composition was to (1) try to directionally solidify primary $Ti(Nb)_5Si_3$ dendrites under controlled conditions in order to determine their morphology and chemistry, (2) attempt to examine the characteristics of the Ti-Ti_5Si_3 eutectic, and (3) examine the nature of the phase equilibria between the two transition reactions.

The microstructure of the transverse section of the DS Nb-75Ti-20Si compositions is shown in Fig. 11. It was of the hypereutectic composition giving rise to large-scale black primary $Ti(Nb)_5Si_3$ dendrites and a (Nb,Ti,Si)-$Ti(Nb)_5Si_3$ eutectic. The faceted, hexagonal $Ti(Nb)_5Si_3$ dendrites are clearly visible. The eutectic consisted of very fine (~1 μm) faceted $Ti(Nb)_5Si_3$ rods in a (Nb,Ti,Si) matrix; this can be seen more clearly in Fig. 11(b). The morphology of the eutectic did not appear to have been modified by the Nb additions. Eutectic cells are also visible in the interdendritic regions. Phase chemistries of the primary $Ti(Nb)_5Si_3$, eutectic $Ti(Nb)_5Si_3$, and eutectic (Nb,Ti,Si) in the Nb-75Ti-20Si alloy were measured using EPMA and are shown in Table 4. The chemistry of the core of the primary $Ti(Nb)_5Si_3$ dendrites was Nb-58.8Ti-37.7Si. The Si concentration was essentially the stoichiometric composition and the Ti-to-Nb ratio was ~17 to 1. The chemistry of the edge of the $Ti(Nb)_5Si_3$ dendrites was Nb-58.9Ti-37.6Si. Thus, the chemistry of the edge of the $Ti(Nb)_5Si_3$ dendrites was essentially the same as that of the center, and there was no coring of the dendrites during solidification. The composition of the eutectic $Ti(Nb)_5Si_3$ was similar to that of the primary $Ti(Nb)_5Si_3$ with the exception that there was slight (Nb) depletion (~1%) and Ti enrichment in the eutectic $Ti(Nb)_5Si_3$.

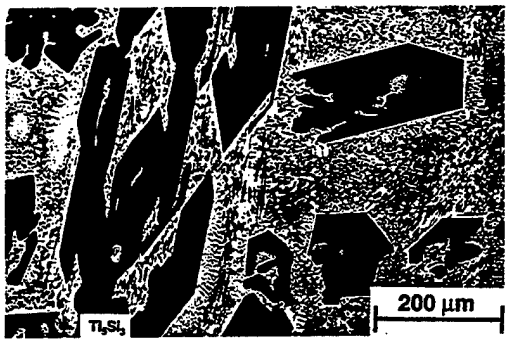


Fig. 9 Typical microstructure (BSE image) of the induction melted Nb-60Ti-30Si alloy. There are large primary faceted $Ti(Nb)_5Si_3$ dendrites and interdendritic $Ti(Nb)_5Si_3$-(Nb,Ti,Si) eutectic.

The composition of the (Nb,Ti,Si) phase was Nb-92.6Ti-0.9Si. This phase was Ti-rich with a very low Si concentration. The composition of the metallic phase was similar adjacent to the $Ti(Nb)_5Si_3$ dendrites and within the bulk of the eutectic. The Si solubility is lower than in the (Nb,Ti,Si) of the Nb-27Ti-22Si alloy (2.4%) and than in the (Nb) of the binary Nb-Si alloys; in the latter, the Si concentration was reported as 1.3% after heat treatment at 1700 °C (Ref 6). The absence of coring in the $Ti(Nb)_5Si_3$ is very different from that of the $Nb(Ti)_5Si_3$ and the $(Nb,Ti)_3Si$ dendrites, where significant enrichment of Ti was observed at the edges of the dendrites. The Nb concentration was 6.5% in the (Nb,Ti,Si) and 3.5% in the $Ti(Nb)_5Si_3$. This suggests that the solubility limit of Nb in $Ti(Nb)_5Si_3$ was lower than that of Ti in $Nb(Ti)_5Si_3$.

The solidification behavior observed for the Nb-75Ti-20Si alloy is distinct from the Nb-rich compositions of the same Si concentration where a peritectic reaction occurs. Thus, the microstructure of the Nb-75Ti-20Si indicates that the peritectic ridge had terminated at Ti compositions between 40 and 70Ti. The Nb-75Ti-20Si composition is sufficiently far away from the transition reaction that the solidification path can take the liquid composition to the (Nb,Ti,Si)-$Ti(Nb)_5Si_3$ eutectic groove, whereas in the case of the Nb-70Ti-20Si composition, discussed subsequently, the composition is close to the peritectic ridge between the two transition reactions and the microstructure is dramatically different.

There was no evidence of a ternary eutectic in any of the alloys examined. The Ti-rich compositions are also consistent with the second transition reaction (at lower Si concentration) being of the form:

$$L + (Nb,Ti)_3Si \rightarrow (Nb,Ti,Si) + Ti(Nb)_5Si_3$$

In the Nb-32.5Ti-35Si and Nb-75Ti-20Si compositions, there was no microstructural evidence of an equilibrium between $Nb(Ti)_5Si_3$ and $Ti(Nb)_5Si_3$. This suggests that the reaction between $Nb(Ti)_5Si_3$ and $Ti(Nb)_5Si_3$ is not a eutectic, but it is not conclusive evidence for a peritectic reaction.

4.5 Compositions Near Transition Reactions: Group E

4.5.1 Nb-75Ti-15Si

The microstructure of the transverse section of the DS Nb-75Ti-15Si composition (group E shown in Table 1) is shown in Fig. 12. There were three distinct features of this microstructure. First, there were large blocky gray $(Nb,Ti)_3Si$ dendrites; these generally were of the typical faceted form, and they had a width of ~30 μm. Second, the majority of the microstructure consisted of eutectic cells with distinct cell boundaries. These cells contained a two-phase microstructure of gray $(Nb,Ti)_3Si$ and white (Nb,Ti,Si). Third, at the intercellular boundaries there was a very small volume fraction of a two-phase, fine-scale, eutectic of $Ti(Nb)_5Si_3$ and (Nb,Ti,Si); this was probably generated from the final liquid to solidify. The (Nb,Ti,Si)-

$Ti(Nb)_5Si_3$ eutectic can be distinguished from the (Nb,Ti,Si)-$(Nb,Ti)_3Si$ by its morphology, scale, and contrast. In other regions where there was a larger volume fraction of (Nb,Ti,Si)-$Ti(Nb)_5Si_3$ eutectic, it possessed a lamellar morphology. No primary metal dendrites were observed.

This microstructure suggests that the Nb-75Ti-15Si composition lies between the L + $Nb(Ti)_5Si_3 \rightarrow (Nb,Ti)_3Si$ peritectic ridge and the (Nb,Ti,Si)-$(Nb,Ti)_3Si$ eutectic groove; this explains the presence of the primary $(Nb,Ti)_3Si$ dendrites. The presence of the intercellular (Nb,Ti,Si)-$Ti(Nb)_5Si_3$ eutectic is evidence for the existence of the second transition reaction:

$$L + (Nb,Ti)_3Si \rightarrow (Nb,Ti,Si) + Ti(Nb)_5Si_3$$

It also suggests that a ternary eutectic does not exist. This composition is very close to the second transition reaction and the eutectic groove, but it is from the hypereutectic side of the eutectic valley.

4.5.2 Nb-65Ti-15Si

The microstructure of the Nb-65Ti-15Si composition was similar to that of the Nb-75Ti-15Si with the exception of the following features: first, it contained a slightly larger volume fraction of primary $(Nb,Ti)_3Si$ dendrites, and second, there was no evidence of any (Nb,Ti,Si)-$Ti(Nb)_5Si_3$ eutectic. The primary $(Nb,Ti)_3Si$ dendrites were generally at the intercellular boundaries. This may have been just an artifact of the large volume fraction of cellular (Nb,Ti,Si)-$(Nb,Ti)_3Si$ eutectic. The $(Nb,Ti)_3Si$ dendrites were more evident in this alloy; the longitudinal section showed some alignment of the primary $(Nb,Ti)_3Si$ dendrites, but not the interdendritic cellular (Nb,Ti,Si)-$(Nb,Ti)_3Si$ eutectic. The eutectic grew within distinct cells that had a diameter of ~250 μm. This evidence suggests that the Nb-65Ti-15Si composition is also in the two-phase L + $(Nb,Ti)_3Si$ regime on the hypereutectic side of the eutectic valley, but the composition is very close to the eutectic groove. The implication is that this composition is further up the $(Nb,Ti)_3Si$-(Nb,Ti,Si) eutectic valley than the Nb-75Ti-15Si composition and that the composition of the residual intercellular liquid never reached the composition of the second transition reaction.

4.5.3 Nb-70Ti-20Si

The aim of examining this composition was to determine the position and nature of the peritectic (L + $Ti(Nb)_5Si_3 \rightarrow (Nb,Ti)_3Si$) ridge between the two transition reactions. A micrograph of the transverse section of the DS Nb-70Ti-20Si is shown in Fig. 13. Although there were only three phases present in this composition, five distinct morphologies were observed. First, there were hexagonal, black, faceted $Ti(Nb)_5Si_3$ dendrites. These were identified using EDS as being $Ti(Nb)_5Si_3$ rather than $Nb(Ti)_5Si_3$. The second phase was peritectic $(Nb,Ti)_3Si$, which grew in a peritectic-type manner

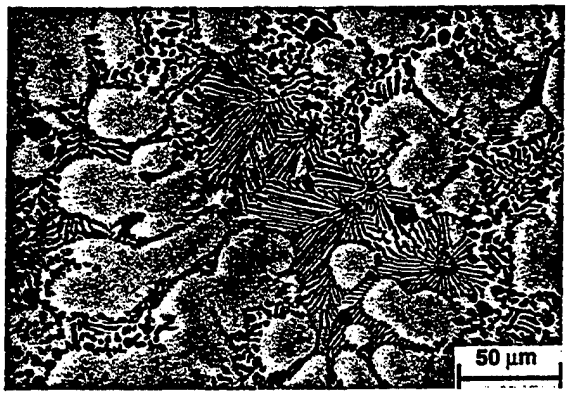
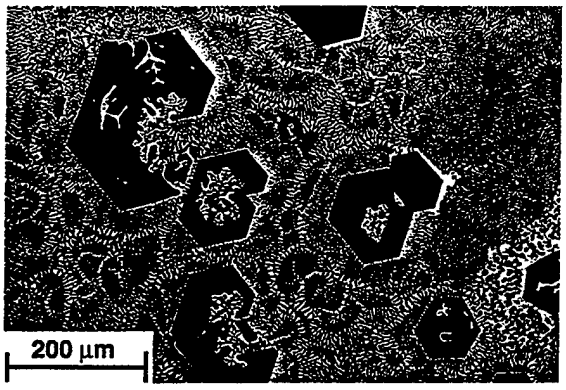
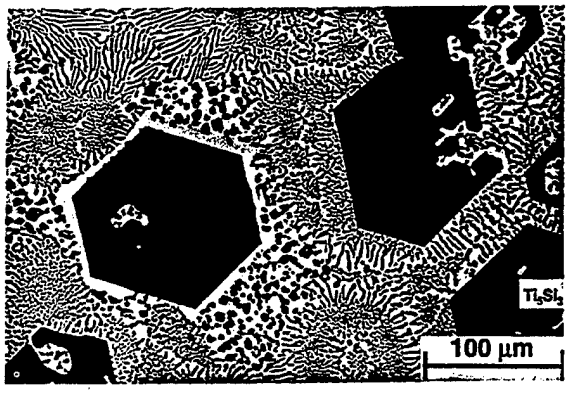


Fig. 10 Typical microstructure (BSE image) of the transverse section of a DS Nb-75Ti-10Si alloy. The large white dendrites are (Nb,Ti,Si), and there is interdendritic $Ti(Nb)_5Si_3$-(Nb,Ti,Si) eutectic.



(a)



(b)

Fig. 11 Typical microstructures (BSE images) of the transverse section of the DS Nb-75Ti-20Si alloy, at low (a) and at high (b) magnifications, showing the primary $Ti(Nb)_5Si_3$ faceted dendrites, and interdendritic eutectic (Nb,Ti,Si)-$Ti(Nb)_5Si_3$.

Table 4 Phase Chemistry Ranges for Primary Dendritic $Ti(Nb)_5Si_3$, Eutectic $Ti(Nb)_5Si_3$, and Eutectic (Nb,Ti,Si) in the Nb-75Ti-20Si Alloy, as Measured Using EPMA

Alloy	Composition			Comments
	Nb	Ti	Si	
$Ti(Nb)_5Si_3$	3.3 to 3.6	58.4 to 59.1	37.4 to 38.3	Dendrite
	(3.5)	(58.8)	(37.7)	Core
$Ti(Nb)_5Si_3$	3.3 to 3.7	58.3 to 59.4	37.1 to 38.2	Dendrite
	(3.4)	(59.0)	(37.6)	Edge
$Ti(Nb)_5Si_3$	2.5 to 2.8	59.0 to 59.9	37.6 to 38.2	Eutectic
	(2.7)	(59.4)	(37.9)	
(Nb,Ti,Si)	5.9 to 6.9	91.8 to 93.1	0.3 to 1.2	Eutectic
	(6.5)	(92.6)	(0.9)	

Note: Mean values of the phase chemistries are shown in parentheses.

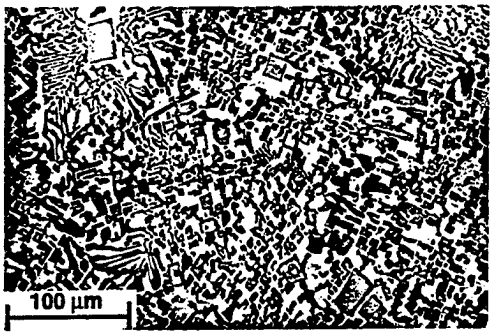


Fig. 12 Typical microstructure (BSE image) of the transverse section of a DS Nb-75Ti-15Si alloy. The gray phase is $(Nb,Ti)_3Si$ and the white phase is (Nb,Ti,Si). There is also a small volume fraction of intercellular (Nb,Ti,Si)-$Ti(Nb)_5Si_3$ eutectic.

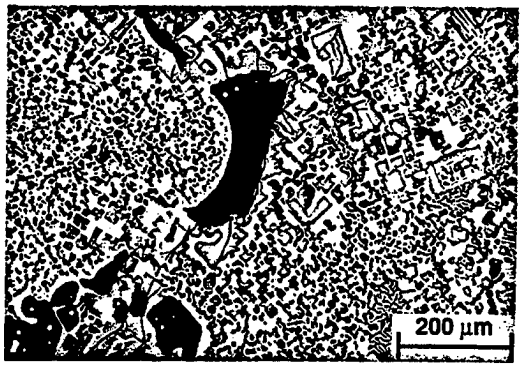


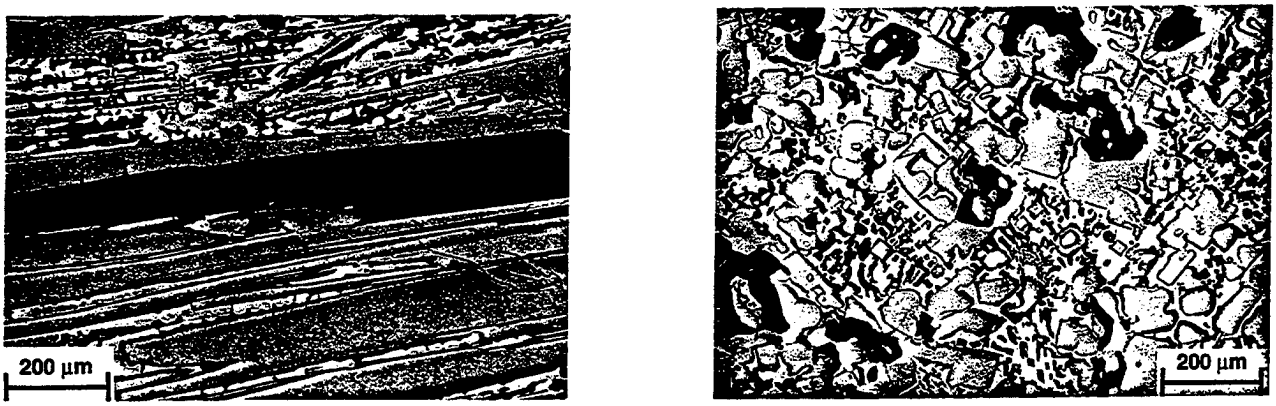
Fig. 13 Typical microstructure (BSE image) of the transverse section of a DS Nb-70Ti-20Si alloy. The black phase is $Ti(Nb)_5Si_3$, the gray phase is $(Nb,Ti)_3Si$, and the white phase is (Nb,Ti,Si).

from the $Ti(Nb)_5Si_3$ dendrites. Again, the $(Nb,Ti)_3Si$ was identified by both its faceted morphology and its chemistry. The third feature was the gray eutectic $(Nb,Ti)_3Si$ phase, which existed as eutectic-type cells together with the fourth feature, the white (Nb,Ti,Si) metallic phase. Fifth, there was a fine-scale (Nb,Ti,Si)-$Ti(Nb)_5Si_3$ eutectic within the intercellular regions generated between the $(Nb,Ti)_3Si$-(Nb,Ti,Si) eutectic cells.

Thus, the first phase to solidify was primary $Ti(Nb)_3Si_3$. This suggests that this composition is from the Ti_5Si_3-rich region, as shown in Fig. 2(c). It is also evidence for the second transition reaction. No ternary eutectic was observed in this composition. The microstructure also suggests that the Nb-70Ti-20Si composition is close to the L + $Ti(Nb)_5Si_3$ → $(Nb,Ti)_3Si$ peritectic ridge. Thus, the liquid composition shifted during solidification and met the peritectic ridge just below the first transition reaction (at higher Si concentration) and led to solidification of peritectic $(Nb,Ti)_3Si$ on the primary $Ti(Nb)_5Si_3$. However, the liquid composition only followed the peritectic ridge for a short distance, and it dropped off this ridge into the lower hypereutectic corner of the eutectic (Nb,Ti,Si)-$(Nb,Ti)_3Si$ valley. This led to solidification of cells of the latter eutectic. The liquid composition continued to move down the eutectic (Nb,Ti,Si)-$(Nb,Ti)_3Si$ valley, and it eventually reached the second transition reaction (at lower Si concentration) where the remaining liquid in the intercellular regions solidified as $Ti(Nb)_5Si_3$-(Nb,Ti,Si) eutectic. The microstructures also suggest that the reaction between $Nb(Ti)_5Si_3$ and $Ti(Nb)_5Si_3$ is not a eutectic; if it were, it seems likely that at least some $Nb(Ti)_5Si_3$ and $Ti(Nb)_5Si_3$ eutectic would have been observed between the primary $Ti(Nb)_5Si_3$ dendrites. The structure is consistent with the existence of the peritectic ridge between the two transition reactions, and it also provides evidence for the second transition reaction L + $(Nb,Ti)_3Si$ → (Nb,Ti,Si) + $Ti(Nb)_5Si_3$, but it does not provide direct evidence for the first transition reaction.

4.5.4 Nb-65Ti-22Si

This composition was from a region similar to the Nb-70Ti-20Si, but it was slightly further from the peritectic ridge and therefore possessed a higher melting temperature (1675 vs.



(a) (b)

Fig. 14 Typical microstructures (BSE images) of the **(a)** longitudinal and **(b)** transverse section of a DS Nb-65Ti-22Si alloy. The black phase is $Ti(Nb)_5Si_3$, the gray phase is $(Nb,Ti)_3Si$, and the white phase is (Nb,Ti,Si).

1620 °C); the melting temperature of the binary Ti_5Si_3 is 2130 °C. Typical microstructures of the longitudinal and transverse sections are shown in Fig. 14(a) and (b). Again, there were four distinct features of the microstructure: primary $Ti(Nb)_5Si_3$ dendrites, peritectic $(Nb,Ti)_3Si$, $(Nb,Ti)_3Si$-(Nb,Ti,Si) eutectic cells, and $Ti(Nb)_5Si_3$-(Nb,Ti,Si) eutectic. However, there was a much larger volume fraction of peritectic $(Nb,Ti)_3Si$ and a much smaller volume fraction of $Ti(Nb)_5Si_3$-(Nb,Ti,Si) eutectic in the Nb-65Ti-22Si composition than in the Nb-70Ti-20Si composition. The liquid composition probably met the L + $Ti(Nb)_5Si_3 \rightarrow (Nb,Ti)_3Si$ peritectic ridge below the first transition reaction, but closer to the first transition reaction than the Nb-70Ti-20Si composition, and it followed the peritectic ridge for a longer composition-temperature interval. In some regions, the large-scale $(Nb,Ti)_3Si$ peritectic can be seen to have consumed the primary $Ti(Nb)_5Si_3$.

The effect of growth rate on the microstructure was examined for growth rates for 0.5 to 3 mm/min to examine the effect of deviation from equilibrium on the phase content. There was essentially no effect on the phase content, although the volume fractions of the individual phases were modified. At slower growth rates there was a smaller volume fraction of (Nb,Ti,Si)-$(Nb,Ti)_3Si$ eutectic and a larger volume fraction of (Nb,Ti,Si)-$Ti(Nb)_5Si_3$ eutectic. This probably occurred because the liquid composition followed the peritectic ridge for a wider composition-temperature range than in the case of the faster growth rate.

5. Conclusions

The microstructures generated in the ternary Nb-Ti-Si alloys investigated contained four phases: (Nb,Ti,Si), $Nb(Ti)_5Si_3$, $(Nb,Ti)_3Si$, and $Ti(Nb)_5Si_3$. The phases that were observed were either dendritic, peritectic, or eutectic in nature, depending on the composition and solidification path. These phases can be clearly distinguished in the microstructures by their scale, morphology, and chemistry.

Microstructural and microchemical evidence indicate that the liquidus surface of the Nb-Ti-Si ternary phase diagram possesses the following reactions:

$$L + Nb(Ti)_5Si_3 \rightarrow Ti(Nb)_5Si_3 \text{ peritectic}$$

$$L + Nb(Ti)_5Si_3 \rightarrow (Nb,Ti)_3Si \text{ peritectic}$$

$$L \rightarrow (Nb,Ti)_3Si + (Nb,Ti,Si) \text{ eutectic}$$

$$L + Ti(Nb)_5Si_3 \rightarrow (Nb,Ti)_3Si \text{ peritectic}$$

$$L \rightarrow (Nb,Ti,Si) + Ti(Nb)_5Si_3 \text{ eutectic}$$

These reactions give rise to the following transition reactions:

$$L + Nb(Ti)_5Si_3 \rightarrow (Nb,Ti)_3Si + Ti(Nb)_5Si_3$$

$$L + (Nb,Ti)_3Si \rightarrow (Nb,Ti,Si) + Ti(Nb)_5Si_3$$

The first of these transition reactions (at higher Si concentration) occurs at a composition of approximately Nb-66Ti-19Si and at a temperature between 1600 and 1650 °C. The second of these transition reactions (at lower Si concentration) occurs at a composition of approximately Nb-76Ti-13.5Si and a temperature of ~1350 °C. No ternary eutectic was observed in the compositions that were investigated.

Acknowledgments

The authors would like to thank D.J. Dalpe for the directional solidification. This research was partially sponsored by AFOSR under contract No. F49620-93-C-0007 with Capt. C.H. Ward as Program Manager. The authors are also grateful

to Dr. M.G. Mendiratta and Dr. P.R. Subramanian, UES, Dayton, OH, for very helpful discussions.

Cited References

1. P.R. Subramanian, M.G. Mendiratta, and D.M. Dimiduk, *Mat. Res. Soc. Symp. Proc., 322,* 491-502 (1994).
2. B.P. Bewlay, M.R. Jackson, W.J. Reeder, and H.A. Lipsitt, *Mat. Res. Soc. Symp. Proc., 364,* 943-948 (1995).
3. M.R. Jackson, B.P. Bewlay, R.G. Rowe, D.W. Skelly, and H.A. Lipsitt, *JOM, 48* (1), 38-46 (1996).
4. T.B. Massalski, *Binary Alloy Phase Diagrams,* ASM International, Materials Park, OH (1990).
5. M.E. Schlesinger, H. Okamoto, A.B. Gokhale, and R. Abbaschian, *J. Phase Equilibria, 14*(4), 502 (1993).
6. M.G. Mendiratta and D.M. Dimiduk, *Scr. Metall., 25,* 237-242 (1991).
7. F.N. Rhines, *Phase Diagrams in Metallurgy—Their Development and Application,* McGraw-Hill, London (1956).
8. F.W. Crossman and A.S. Yue, *Met. Trans., 2,* 1545-1555 (1971).
9. R. Wagner, M. Es-Souni, D.Chen, B. Dogan, J. Seeger, and P.A. Beaven, *Mat. Res. Soc. Symp. Proc., 213,* 1007-1012 (1991).

Creep Mechanisms in High-Temperature In-Situ Composites

Annual Report: August 1997

Creep Mechanisms in High-Temperature In-Situ Composites

(Contract Number: FQ8671-96005872306/AS)

Research Contributors

Dr. Bernard P. Bewlay, GE-CRD, Staff Metallurgist
Dr. Melvin R. Jackson, GE-CRD, Staff Metallurgist
Prof. Harry A. Lipsitt, GE-CRD, Consultant

1.0. Objectives

The primary objective of this research is to investigate high-temperature creep and low-temperature toughening mechanisms in high-strength directionally solidified (DS) in-situ composites with melting temperatures above 1700°C. The composites under investigation consist of Nb-based silicides, such as Nb_3Si and Nb_5Si_3, and are toughened by a Nb-based solid solution. Composites have been directionally solidified from a range of complex alloys.

2.0 Approach

In order to investigate creep mechanisms in this family of composites several effects are being considered, such as the metallic phase strength, the role of the volume fraction of intermetallic, the effect of increasing the creep performance of the intermetallic, and the effect of texture of the individual phases. In addition, phase equilibria in ternary systems, such as Nb-Ti-Si and Nb-Hf-Si, are being defined.

3.0 Progress and Status of Effort

Composite Microstructures

Typical microstructures of composites produced from model Nb-Si and Nb-Ti-Si alloys have been reported previously [1]. The composites designed in the present study are from alloys that possess more than three elements and have more complex microstructures. These composites consist of high-strength, Nb-based M_3Si and $M_5(Si,Al)_3$ silicides together with a modest strength, high-toughness Nb-based metallic phase. Typical examples are shown in Figures 1 and 2 for alloys with compositions of

Nb-25Ti-8Hf-2Cr-2Al-16Si and Nb-26.5Ti-8Hf-10Cr-2Al-16Si, respectively. Electron beam microprobe analysis analyses (EPMA) of the phases within these two composites, as well as a broader family of composites, are given in Table 1. These compositions were derived from an alloy whose properties have been described in more detail elsewhere [1], and has been denoted the metal and silicide composite, or MASC. The composite shown in Figure 2 possesses an increased Cr concentration and the resulting composite contains primary metal dendrites that are rich in Cr, M_5Si_3 dendrites, and an interdendritic eutectic of the same phases with modified compositions, typically less Nb and more Ti than the primary phases; there was no M_3Si type phase detected in this composition. The Si concentrations of all the silicides are close to the stoichiometric values. The melting temperatures of the alloys that provided theses composites are also shown in Table 1.

Table 1 : EPMA data of the individual phase compositions within the range of composites.

	Melting Tmp. (°C)	**Nb**	**Ti**	**Hf**	**Cr**	**Al**	**Si**
	1720						
Nb-20Ti-8Hf-2Al-2Cr-16Si							
M		65.0	21.3	6.0	3.3	2.9	1.5
M		56.5	26.8	6.5	5.8	3.3	1.1
M3Si		47.9	17.6	10.0	0.3	0.0	24.3
M5Si3		27.8	20.5	14.4	0.5	1.4	35.4
Nb-30Ti-8Hf-2Al-2Cr-16Si	1700						
M		62.1	23.5	8.0	2.5	2.5	1.4
M3Si		47.7	16.2	11.7	0.1	0	24.3
M5Si3		26.2	19.6	17.4	0.4	1.2	35.2
Nb-23.6Ti-14Hf-2Al-2Cr-16Si	1660						
M		44.9	33.4	12.6	6.1	2.4	0.7
M3Si							
M5Si3 - primary		26.0	16.6	20.4	0.2	1.0	35.8
M5Si3 - Eutectic		22.8	18.1	21.5	0.2	1.0	36.4
Nb-26.5Ti-8Hf-10Cr-2Al-16Si	1500						
M		52.7	29.7	4.0	10.2	2.6	0.8
M - Interdendritic		47.5	34.5	4.0	10.4	2.9	0.7
M5Si3 - primary		30.1	20.1	12.5	1.0	1.0	35.3
M5Si3 - Eutectic		22.9	23.9	15.4	1.3	1.0	35.5

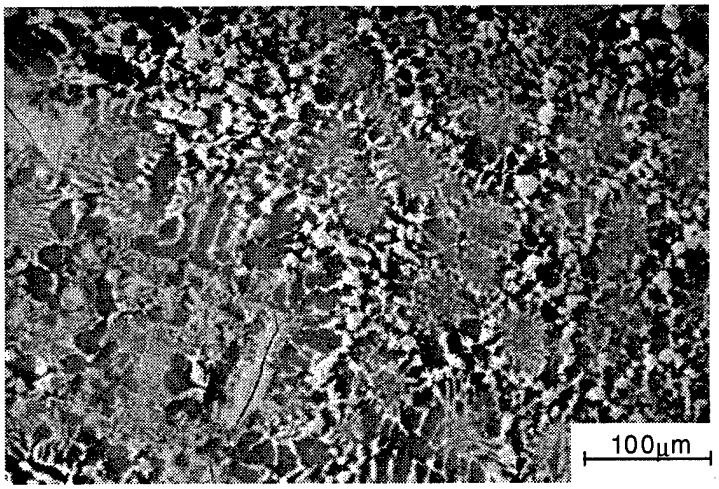


Figure 1 : Typical microstructure of the composite produced from the Nb-25Ti-8Hf-2Cr-2Al-16Si alloy.

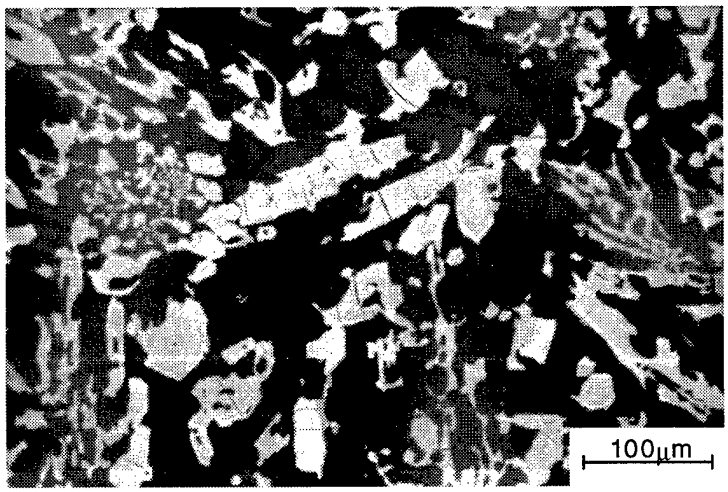


Figure 2 : Typical microstructure of the composite produced from the Nb-26.5Ti-8Hf-10Cr-2Al-16Si alloy, showing the $Nb(Hf,Ti)_5Si_3$ light phase and the (Nb,Ti,Hf,Cr,Al) dark phase.

Fracture Toughness Measurements

Effect of Mo Additions on Fracture Toughness

Alloys with Mo additions have been made in order to investigate the effect of solid solution strengthening of the metallic phase on the composite toughness and creep performance. Fracture toughness measurements are shown in the table below for a range of alloys that contain Mo additions to a base alloy of Nb-8Hf-16Si with Ti concentrations from 8 to 25%Ti and Mo concentrations from 3 to 15%. These data indicate that there is

a peak in the effect of Mo additions on the room temperature fracture toughness of these composites for a composition of 25Ti. Further examination of compositions between 3 and 8%Mo is in-process. The effect of Mo on the oxidation resistance is also being considered.

Composition	**Fracture Toughness** (MPa$\sqrt{m}$)
Nb-8Hf-25Ti-16Si	16.1
Nb-3Mo-8Hf-25Ti-16Si	17.9
Nb-9Mo-8Hf-25Ti-16Si	14.0
Nb-8Ti-8Hf-16Si	12.3
Nb-9Mo-8Hf-16Si	11.9
Nb-9Mo-8Ti-8Hf-16Si	7.6
Nb-9Mo-13Ti-8Hf-16Si	8.8
Nb-9Mo-16Ti-8Hf-16Si	7.4
Nb-15Mo-20Ti-8Hf-16Si	11.4

When the Ti concentration is reduced below 25Ti the toughness is generally reduced with increasing Mo additions: Mo concentrations greater than 9% lead to reduced fracture toughness values. Nevertheless, for Mo concentrations up to 15%, fracture toughness values of >10 MPa$\sqrt{m}$ can be expected if the Ti concentration is greater than 20%. It is also important to note that the Cr and Al in the MASC [1] make significant contributions to fracture toughness.

Effect of Hf:Ti Ratio on Fracture Toughness

The table below shows fracture toughness measurements for Hf compositions of 7.5-12.5 and Ti compositions of 21-33%.

Composition	**Fracture Toughness (MPa$\sqrt{m}$)**
Nb-7.5Hf-21Ti-16Si	12.7
Nb-10Hf-21Ti-16Si	11.9
Nb-12.5Hf-21Ti-16Si	12.8
Nb-21Ti-16Si	11.6
Nb-7.5Hf-33Ti-16Si	13.6
Nb-10Hf-33Ti-16Si	13.3
Nb-12.5Hf-33Ti-16Si	14.0
Nb-33Ti-16Si	11.1

Room temperature fracture toughness was relatively insensitive to Hf: Ti composition ratios in the range 0.2-0.6. There was essentially no effect of Hf additions in the range 7.5-12.5 for compositions of 21 or 33 Ti. Ti appears to have a stronger effect on toughness that Hf; the toughness levels at 33 Ti were higher than those at 21Ti.

Fracture Toughness in Complex Alloy Composites

The table below shows a range of alloys derived from the base MASC composition [1]. The microstructures of two of these composites are shown in Figures 1 and 2.

Composition	**Fracture Toughness** ($MPa\sqrt{m}$)
Nb-20Ti-8Hf-2Al-2Cr-16Si	22.3 MPa/m
Nb-30Ti-8Hf-2Al-2Cr-16Si	22.0
Nb-24.6Ti-11Hf-2Al-2Cr-16Si	20.5
Nb-23.6Ti-14Hf-2Al-2Cr-16Si	18.2
Nb- 25Ti-8Hf-2Al-2Cr-18Si	24.1
Nb-26.5Ti-8Hf-2Al-10Cr-16Si	18.7
Nb-24.7Ti-8.2Hf-2.0Cr-1.9Al-16.0Si	23.3

The above data indicate that the Si concentration of the MASC can be increased to 18% without compromising composite toughness. This is an important observation because the Si concentration controls the volume fraction of silicide and therefore the elevated temperature strength and creep properties.

It can also be seen from the above data that increasing the Hf from 8 to 14%, or increasing the Cr concentration up to 10% reduces the toughness. Nevertheless, toughness levels of this range of composites are promising. Higher Cr levels are being considered in order to improve oxidation resistance. These values of room temperature fracture toughness are a substantial improvement over monolithic intermetallics.

Creep Mechanisms

According to recent work by Subramanian et al [3], creep deformation in Nb_5Si_3 is controlled by diffusion in the Nb_5Si_3 phase. Because elements such as, Mo and Hf have a large atomic size, they may be effective in improving the intrinsic creep performance of the composite. Thus, Hf and Mo additions to the intermetallic have been performed and their effect on secondary creep rate and failure mechanisms is being studied.

Initial creep data are shown in Table 2 for a range of Nb-silicide based composites modified with Hf and Ti. These data show secondary creep rates, as measured using compression tests, at a temperature of 1200°C.

Table 2 : Secondary creep rates at 1200°C for a range of Nb-Hf-Ti-Si alloys.

Composition	**140 MPa Creep Rate (s^{-1})**	**210 MPa Creep Rate (s^{-1})**	**280 MPa Creep Rate (s^{-1})**
Nb-7.5Hf-16Si	$2.3x10^{-8}$	$1x10^{-8}$	$4.8x10^{-8}$
Nb-7.5Hf-16Si-21Ti	$2.1x10^{-8}$	$3.2x10^{-8}$	$1.2x10^{-7}$
Nb-7.5Hf-16Si-33Ti	$1.6x10^{-7}$	$1x10^{-5}$	$1.1x10^{-5}$
Nb-12.5Hf-16Si-21Ti	$2.4x10^{-8}$	--	--
Nb-12.5Hf-16Si-33Ti	$3.8x10^{-5}$	--	--
MASC (at 1100°C)	$1.7x10^{-7}$	--	--

These data indicate that Ti additions of 21% had little effect on the creep rate at Hf concentrations of 7.5-12.5% and stresses of up to 140 MPa. At higher stress levels the creep rate was increased with the Ti additions. Ti additions of 33% to Nb-Hf-Si ternary alloys led to increased creep rates in comparison with the base ternary alloy. The creep rate was relatively insensitive to Hf concentrations for Ti concentrations of 21% and stresses up to 140 MPa. Creep rates of less than 10^{-8} s^{-1} were measured at stresses of 70 MPa.

These compression tests at 1200 °C are being performed in order to screen composites prior to more extensive testing over a wider temperature range in both compression and tension. Further creep tests are ongoing. Creep mechanisms are also being examined using microscopy of the as-tested creep samples. The sensitivity of the creep rate/damage accumulation in the composite to the properties of the metallic phase is being examined. These will be reported in more detail separately. Thus, the degree to which the volume fraction of intermetallic can be adjusted to balance creep behavior with room temperature fracture toughness is being studied.

Phase Equilibria Studies

Significant effort has been placed on defining phase equilibria in the Nb-Ti-Si and Nb-Hf-Si systems, because Hf additions to Nb-Si based composites have been shown to provide improvements in fracture toughness, tensile strength, creep performance, and oxidation behavior. The description of the Nb-Ti-Si liquidus surface has been published recently [4]. The liquidus surface in the Nb-Hf-Si system has also been studied, although the findings have not yet been published in the open literature. The liquidus surfaces for these two systems allow an improved understanding of the solidification paths that generate the composites in the more complex alloy systems [1].

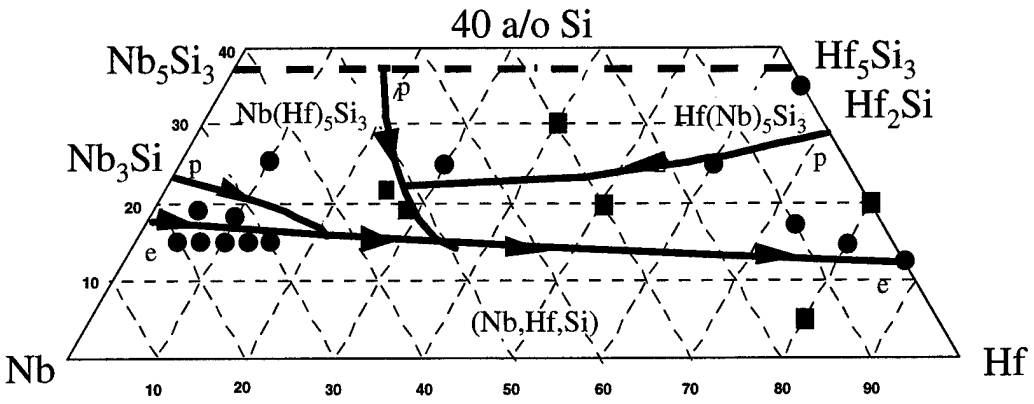


Figure 3 : Liquidus projection of the metal-rich end of the Nb-Hf-Si ternary phase diagram.

The liquidus surface of the metal-rich end of the Nb-Hf-Si phase diagram is shown in Figure 3. Four silicides were detected using EPMA and x-ray diffraction (XRD), $Nb(Hf)_5Si_3$ and $Nb(Hf)_3Si$ at the Nb-rich side of the phase diagram, together with $Hf(Nb)_5Si_3$ and $Hf(Nb)_2Si$ at the Hf-rich side of the phase diagram. The data obtained suggest three invariant reactions.

$$L + Nb(Hf)_5Si_3 \leftrightarrow Nb(Hf)_3Si + (Nb,Hf,Si) \qquad (1)$$

$$L + Nb(Hf)_5Si_3 \leftrightarrow Hf(Nb)_2Si + Hf(Nb)_5Si_3 \qquad (2)$$

$$L + Hf(Nb)_5Si_3 \leftrightarrow Hf(Nb)_2Si + (Nb,Hf,Si) \qquad (3)$$

The alloy compositions that have been investigated are shown as the solid points on the liquidus surface projection in Figure 3. Six independent options of the liquidus surface were considered, but the data indicate that the option shown in Figure 3 is the most likely. The $Hf(Nb)_5Si_3$ shows substantial solubility for Nb, with EPMA data indicating Hf:Nb concentration ratios of ~1. Further analyses of equiatomic Nb:Hf alloys is planned. A typical microstructure is shown in Figure 4 for the Nb-80Hf-14Si alloy as an example of the Hf-rich alloys that have been studied. This microstructure contains primary $Hf(Nb)_2Si$ faceted dendrites (black phase) with an interdendritic eutectic of bcc (Nb,Hf,Si) and fine-scale $Hf(Nb)_2Si$ (black phase). The bcc metal is the matrix of the eutectic (grey phase). On post-solidification cooling the bcc Hf-rich metal transforms to α Hf (white phase). The Nb-80Hf-14Si composition is on the Si-rich side of the (Nb,Hf,Si)-$Hf(Nb)_2Si$ eutectic trough.

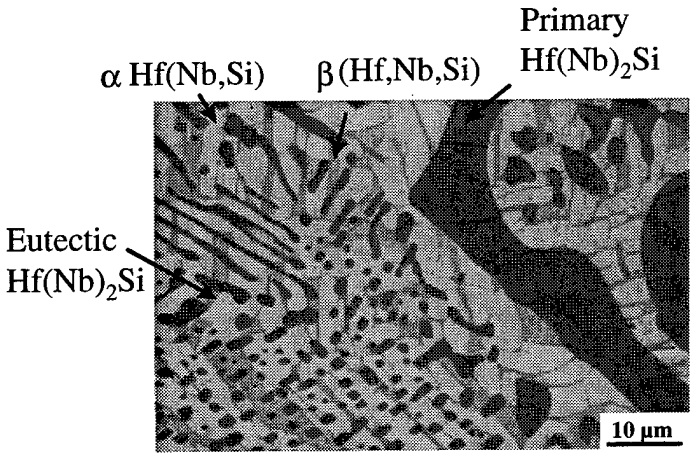


Figure 4 : Typical microstructure of the composite produced from the Nb-80Hf-14Si alloy.

The Hf-rich silicides were identified using EPMA and XRD data. Analysis of microprobe data was complicated due to absorption of the Si signal by Hf, and as a result large ZAF corrections were required; the ZAF models that have been developed previously were not accurate when absorption was so strong, and no independent monolithic standards were available for the silicide. However, the Hf_2Si in the binary Hf-20Si alloy was identified using XRD, and used as a standard for identification of the $Hf(Nb)_5Si_3$ in the binary, and all the silicides in the ternary alloys. There is significant previous evidence for the existence of the $Hf(Nb)_2Si$, but less evidence for the existence of the $Hf(Nb)_5Si_3$ [2]. However, the XRD data and microprobe data obtained from the silicides in the binary and ternary alloys obtained in the present work is quite compelling. Some of the difficulties associated with the definition of the Nb-Hf-Si system lie in an incomplete knowledge of the binary Hf-Si system [2].

References

[1] B.P. Bewlay, M.R. Jackson and H.A. Lipsitt, "The Balance of Mechanical and Environmental Properties of a Multi-Element Niobium-Niobium Silicide Based In-Situ Composite", *Metall. and Mater. Trans.*, 1996, Vol 279, pp. 3801-3808.

[2] A. Gokhale and R. Abbaschian, Bulletin of Alloy Phase Diagrams, 10, Vol. 4, pp. 390-393, 1989.

[3] P.R. Subramanian, T.A. Parthasarathy, and M.G. Mendiratta, Scritpa Met. and Mater., Vol. 32(8), pp. 39-54.

[4] B.P. Bewlay, M.R. Jackson and H.A. Lipsitt, *Journal of Phase Equilibria*, Vol 18(3), 1997, pp. 264-278.

4.0 Collaborations

Throughout the past year of the present program there have been numerous interactions with scientists at universities and AF laboratories. There has been regular exchange of samples, data, and interpretations with staff at Case Western Reserve University, Ohio State University, Brown University, and UES. Studies of the oxidation mechanisms of these composites are being conducted in collaboration with Dr R. Grylls and Prof. H. Fraser at Ohio State University. The results of the collaborations will be presented in the near future at international conferences and published in the open literature.

5.0 Publications

The following articles have been published in refereed journals and conference proceedings during the last year of research in the area of the present contract. Reprints of these articles have been attached to the present report.

1. B.P. Bewlay, M.R. Jackson and H.A. Lipsitt, "Directionally Solidified High Temperature In-Situ Composites,", in "Processing and Design Issues in High Temperature Materials", Ed N.S. Stoloff and R.H. Jones, TMS Publications, 1997, pp. 247-262.

2. B.P. Bewlay, M.R. Jackson and H.A. Lipsitt, "The Balance of Mechanical and Environmental Properties of a Multi-Element Niobium-Niobium Silicide Based In-Situ Composite", *Metall. and Mater. Trans.*, 1996, Vol 279, pp. 3801-3808.

3. B.P. Bewlay, W.J. Reeder, H.A. Lipsitt, M.R. Jackson and J.A. Sutliff, "Toughness Enhancements In Intermetallic-Based Composites : Processing and Properties", in *Processing and Fabrication of Advanced Materials for High Temperature Applications V*", Ed T.S. Srivatsan and J.J. Moore, TMS Publications, 1996, pp. 371-382.

4. B.P. Bewlay, M.R. Jackson and H.A. Lipsitt, "The Nb-Ti-Si Ternary Phase Diagram : Evaluation of Liquid-Solid Phase Equilibria in Nb and Ti-Rich Alloys", *Journal of Phase Equilibria*, Vol 18(3), 1997, pp. 264-278.

5. G. A. Henshall, M. J. Strum, B. P. Bewlay and J. A. Sutliff, "Ductile-Phase Toughening in V-V_3Si In-Situ Composites", Accepted for publication in *Metall. and Mater. Trans.*, July 1997.

6. B.P. Bewlay, M.R. Jackson and H.A. Lipsitt, "Ti-Modified Niobium-Silicide Based Directionally Solidified In-Situ Composites", MRS Proceedings on High Temperature Ordered Intermetallic Alloys VII, Vol 460, 1997, pp. 715-726.

7. B.P. Bewlay, J.J. Lewandowski amd M.R. Jackson, "Refractory Metal-Intermetallic In-Situ Composites for Aircraft Engines, *J. of Metals 49* (8), 1997, pp. 46-48.

Primary Contact :

Bernard P. Bewlay,
GE Corporate Research and Development
PO Box 8
Schenectady
NY12301

Tel : 518 387 6121

Directionally Solidified High Temperature In-Situ Composites

B.P. Bewlay, M.R. Jackson and H.A. Lipsitt

Processing and Design Issues in High Temperature Materials
TMS Publications, 1997

DIRECTIONALLY SOLIDIFIED HIGH TEMPERATURE IN-SITU COMPOSITES

B.P. Bewlay[1], M.R. Jackson[1] and H.A. Lipsitt[2]
[1]General Electric Company, Corporate Research and Development,
Schenectady, New York 12301.
[2] Department of Mechanical and Materials Engineering,
Wright State University, Dayton, Ohio 45435.

Abstract

This paper describes processing and properties of high temperature directionally solidified (DS) in-situ composites. Directional solidification is performed using cold crucible Czochralski crystal growth for alloys with melting temperatures up to 2250°C in order to generate aligned composite microstructures. This composite approach is being used to improve the low-temperature fracture toughness of intermetallic-based composites and thereby generate a material with a combination of attractive high-temperature properties and acceptable low-temperature properties. Microstructures, room temperature fracture toughness, and elevated temperature property data of DS in-situ composites generated from Nb-Si and Cr-Nb binary eutectics, and higher order systems will be presented. Fracture toughness values of >20 MPa$\sqrt{m}$ have been measured in these composites. High-temperature tensile strength and creep behavior have also been examined in selected silicide-based composites and will be described; tensile strengths of ~370 MPa at 1200 °C and creep rupture lives of >500 hours at 1100 °C and 100 MPa have been measured.

Bewlay et al

Introduction

The present paper describes the microstructures and properties which have been generated in intermetallic-matrix composites based on the Laves phase, Cr_2Nb, and niobium silicides, such as Nb_3Si and Nb_5Si_3. Particular emphasis is placed on the improvements in room temperature fracture properties and elevated temperature tensile strength (up to 1200°C), which can be effected by additions of Ti and Hf to directionally solidified (DS) in-situ composites based on Cr_2Nb and Nb_3Si. These composites are toughened by a Nb solid solution.

The Laves phase Cr_2Nb has been studied previously because it has a high melting temperature (1770°C), a lower density (7.7 g/cc) than nickel (8.9 g/cc), and promising oxidation resistance [1-7]. Although Cr_2Nb has attractive creep and tensile strengths [1, 2], it has very poor room temperature fracture toughness [4-6], a ubiquitous limitation of intermetallic-based systems. There have been previous attempts to improve the fracture toughness by generating two-phase composites with Nb and Cr [4-6], but these have met with limited success. However, composites consisting of other intermetallic materials with metallic second phases have recently been shown to possess sufficient toughness for component damage tolerance [8-11]. In this arena, Nb-Si in-situ composites, which consist of a Nb-based solid solution, (Nb), with Nb_3Si and/or Nb_5Si_3 silicides have displayed an attractive balance of high and low temperature mechanical properties [4, 6, 8-11]. From model binary Nb-Si alloys, whole families of ternary, quaternary and higher order alloys have been generated and studied [8-10]. These in-situ composite systems are beneficial because they possess long term morphological and chemical stability at elevated temperature.

In an attempt to improve the balance of high and low temperature properties of DS in-situ composites, Cr_2Nb and niobium-silicide alloys with Hf and Ti were prepared. Hf and Ti additions were considered for three reasons. First, Ti additions improve the ductility of (Nb) [12], and therefore, in a composite there is the possibility of the (Nb) providing greater composite toughness. However, Ti additions have the disadvantage of reducing the alloy melting temperature. Second, Hf is added because it is a strong solid solution strengthener for (Nb) [12, 13]. Third, Hf and Ti additions to Cr_2Nb, Nb_5Si_3, and the Nb-based solid solution improve the oxidation resistance of both phases of the composites, as reported by Subramanian, et al. [9, 10] and Jackson, et al. [13]. Cr also improves the oxidation resistance of Nb [9]. All elements partition to varying degrees between the different phases of the composites [8, 13], and this was taken into consideration in designing the alloys from which the composites were directionally solidified. By appropriate alloy selection, composites with metal volume fractions from 30-50% were designed to allow the evaluation of toughening and strengthening.

The Cr-Nb phase diagram contains two eutectics between Cr_2Nb and the constituent individual refractory metals [14, 15]. The temperature and composition of the Cr_2Nb-Nb eutectic, which contains a volume fraction of Cr_2Nb of ~70%, are 1650 ± 50°C and ~50 %Nb, respectively. All compositions in the present paper are given in atom per cent. The Cr-Hf phase diagram is analogous, there are also two eutectics, Cr_2Hf-Hf and Cr_2Hf-Cr [14]. Cr_2Ti is also a Laves phase, but it forms from a bcc Cr-Ti solid solution rather than

Bewlay et al 2 16

on solidification, as is the case for Cr_2Nb and Cr_2Hf. Thus, Cr_2Hf and Cr_2Nb can be considered to be essentially isomorphous.

Three Laves phase based alloys were investigated, in addition to the binary Cr_2Nb-Nb eutectic, in order to generate in-situ composites by directional solidification; the three quaternary alloy compositions investigated are shown in Table I. The first of the quaternary alloys was based on the Cr_2Nb-Nb eutectic [14, 16], but it was modified with Hf and Ti substituted for Nb by using a composition of Nb-16.5Ti-52.5Cr-9.5Hf. Phase compositions are shown in Table II for the metallic and Laves phases of a similar Al-containing composite heat treated at 1200°C. The Hf and Ti modified $Cr_2(Nb)$-(Nb) eutectic was designed to possess ~70% by volume of the Laves phase, which is the approximate volume fraction of the Laves phase in the Cr_2Nb-Nb eutectic [3, 4]. The additional two quaternary compositions shown in Table I contain total volume fractions of Laves phase of ~60% and ~50%. This range of compositions was selected in order to investigate the effect of volume fraction of metallic phase on room temperature fracture toughness and high temperature strength. The Hf and Ti modified Laves phase is denoted by $Cr_2(Nb)$ in the present paper because Hf and Ti generally substitute for Nb on the Nb sub-lattice (there may be some substitution on the Cr sub-lattice, but the defect level is unknown). There is some solid solubility of all alloying elements in the Nb-based metallic phase of all the composites described in the present paper, and the metallic phase is therefore described as (Nb).

Table I: Compositions of the quaternary $Cr_2(Nb)$-(Nb) composites, together with $Cr_2(Nb)$ volume fractions, melting temperatures, and tensile properties.

Composition	Liquidus Temperature (°C)	Volume Fraction of Laves Phase	Tensile Stress (MPa) Temperature : YS : UTS	Elongation (%)
Nb-50Cr	1650	0.70	Tensile bars too brittle	--
Nb-16.5Ti-52.5Cr-9.2Hf	1550	0.76	Tensile bars too brittle	--
Nb-21.2Ti-44.5Cr-8.4Hf	1563	0.60	1200°C : 132 : --	0
Nb-26Ti-36.5Cr-7.5Hf	1514	0.53	1100°C : 210 : 265 1200°C : 120 : 153	52.2% 6%

The present paper also describes an analogous in-situ composite generated from a more complex Nb-Ti-Hf-Si-Al-Cr alloy based on the Nb_3Si-(Nb) eutectic. A range of complex Nb-silicide composites have been generated from multi-element Nb-based alloys, but only one of these composites is described in the present paper. The composition of the alloy that was directionally solidified to generate this composite was Nb-24.7Ti-8.2Hf-2.0Cr-1.9Al-16.0Si. Throughout the present paper this composite will be referred to as the metal and silicide composite (MASC). This composite was derived from the binary Nb-16Si composition [4, 11].

The basis for the niobium-silicide composite is the Nb-rich side of the Nb-Si phase diagram where there is a eutectic between Nb_3Si and (Nb) [4, 14]. This eutectic occurs at 1880°C and 18.2Si. There is also a eutectoid of the form Nb_3Si-->(Nb)+Nb_5Si_3, but this has little effect on the as-DS microstructures, because of slow decomposition kinetics. A range of Nb_3Si-(Nb) composites have been directionally solidified from binary Nb-Si alloys [4]. Analogous ternary Nb-Ti-Si alloy composites have also been investigated [8-10].

The aim of the present paper is to describe the microstructure and tensile properties of Hf and Ti-modified DS $Cr_2(Nb)$-(Nb) and Nb-silicide-based in-situ composites. The microstructures of DS composites containing 50-70% by volume of the Laves phase $Cr_2(Nb)$ which was modified with Hf (7.5-9.2%) and Ti (16.5-26%) are described. Room temperature fracture toughness and tensile properties at 1100 and 1200°C are compared with those of the MASC. Stress rupture behavior of the MASC is also presented. The MASC displays a better balance of high and low temperature mechanical properties [8, 16] than do the Laves phase composites. The high temperature rupture properties are also compared with those of the most recent Ni-based superalloys.

Experimental

Directional Solidification

Alloys for directional solidification were prepared using a 50g charge of high purity (99.99%) elements. These elements were induction levitation melted in a segmented water-cooled copper crucible [17]. Each alloy was triple melted in order to ensure homogeneity prior to directional solidification. Directional solidification was performed by lowering a seed of the same alloy into the induction levitated melt and withdrawing the seed at a constant pre-selected rate in the range 0.5-5 mm/minute. This process has been described in further detail elsewhere [17]. Several samples were grown of each composition in order to generate enough bars for tensile testing. The melting temperatures of the alloys were measured using a two wavelength optical pyrometer which was calibrated against 99.9% pure Ti. Samples with a diameter of ~10 mm and a length of ~75 mm were directionally solidified using this method.

The melting and directional solidification operations were conducted sequentially in an atmosphere of ultra high purity argon. Before backfilling with argon, the chamber was evacuated to ~10^{-5} Torr. An atmosphere of ultra high purity argon was used in order to prevent contamination with interstitials. In this class of materials, the mechanical properties and phase equilibria are sensitive to interstitials, such as nitrogen, oxygen and hydrogen. Conventional microscopy and electron beam microprobe analysis were performed to characterize composite microstructures and phase chemistries.

Mechanical Properties

Fracture Toughness Measurements

Single edge notched bending specimens (SENB) were machined for room temperature fracture toughness measurements using electro-discharge machining (EDM). EDM was also used to machine a 50μm notch at the mid-point of each SENB. The samples were machined so that their longitudinal axis was parallel to the growth direction.

Bewlay et al 4 16

Fracture toughness measurements were performed using monotonic loading and four point bending. The procedures provided by the ASTM standard E-399 [18] were employed. The toughness values from the monotonic loading experiments are reported as K_Q. K_{IC} values were obtained from R-curve measurements which were performed on additional samples following the ASTM standard E-561-94 [19]. R-Curve measurements were also performed using four point bending in the displacement control mode. The crack opening displacement (COD) was monitored using a double cantilever beam type COD gage.

Tensile and Creep Rupture Testing

Tensile testing was performed in a vacuum of ~10^{-4} Torr using an initial strain rate of $8x10^{-4}s^{-1}$. The button head samples used possessed a gauge diameter of 2 mm, and a length of 10.7 mm. The samples were machined first by EDM and then by centerless grinding to the final dimensions. The tensile specimens were machined so that the growth direction was parallel to the axis of the tensile bar. There was less breakage of the MASC samples than the $Cr_2(Nb)$ based samples during centerless grinding. Creep rupture testing was performed using similar sample geometries in an argon atmosphere.

Results and Discussion

DS Composite Microstructures

$Cr_2(Nb)$-(Nb) Composites

Typical microstructures of the DS binary Cr_2Nb-Nb eutectic are shown in Figure 1. These micrographs were obtained using back scatter electron imaging (BSE); the Cr_2Nb is the dark phase and the Nb is the light phase. The microstructure consists of Nb rods and ribbons (0.5±0.1μm) in the Cr_2Nb matrix. The aspect ratio of the Nb rods was typically ~10 and there was incomplete alignment with the growth direction under these directional solidification conditions. The Cr_2Nb had the C15 structure with the [110] parallel to the growth direction [3].

Microstructures of the Nb-16.5Ti-52.5Cr-9.2Hf quaternary alloy which was based on the Cr_2Nb-Nb eutectic are shown in Figure 2. BSE imaging and energy dispersive spectrometry (EDS) indicated that the $Cr_2(Nb)$ was the light phase and the (Nb) was the dark phase. The $Cr_2(Nb)$ contained more Hf and less Ti than the darker (Nb), and as a result it provided brighter contrast than the (Nb), even though it contained more Cr and less Nb than the (Nb). It was difficult to obtain strong BSE contrast between the two phases in the quaternary alloys, because Hf is the heaviest element and it partitions to both phases in the approximate ratio of 2:1 for Laves phase to metal. In both the longitudinal and transverse sections, lighter regions were observed at the centers of the $Cr_2(Nb)$ laths. This brighter contrast was probably due to Hf enrichment and/or Ti depletion at the centers of the laths.

The transverse section of the $Cr_2(Nb)$-30%(Nb) shown in Figure 2(b) indicates that the structure consisted of coarse laths, which appeared to be arranged in grains with a width of ~300μm. The width of the (Nb) laths was ~ 20μm and the width of the $Cr_2(Nb)$ laths was ~60μm. The grains appeared to have an approximately hexagonal morphology; this type of grain morphology was not observed in the case of the binary eutectic. It is important to

Bewlay et al



(a)



(b)

Figure 1 Longitudinal (a) and transverse (b) sections of the DS Cr_2Nb-Nb eutectic grown at 1 mm/min. (BSE images).

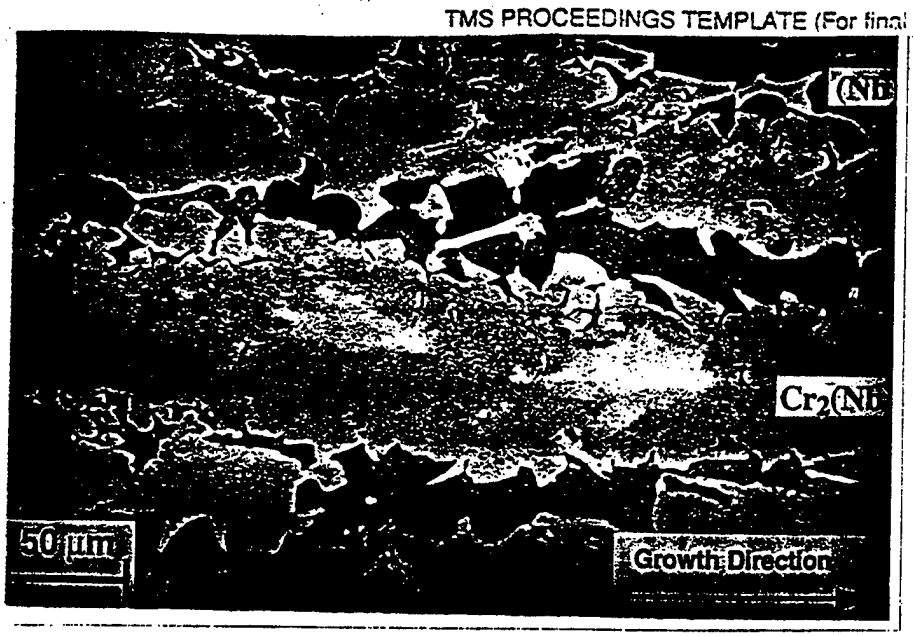
note that the microstructure had a much coarser scale than that of the binary eutectic. No primary dendrites were observed in the microstructure. In addition, the (Nb) did not exist as fibres, ribbons or lamellae, as was the case for the binary eutectic. Thus, the microstructure of the Cr_2(Nb)-(Nb) eutectic was quite different to that of the Cr_2Nb-Nb binary eutectic, even though there were similar volume fractions of metallic phase in each case. The measured volume fraction of (Nb) in the Nb-16.5Ti-52.5Cr-9.2Hf alloy was 0.24, which was smaller than that predicted. The longitudinal section in Figure 2(a) showed some alignment of the Cr_2(Nb) with the growth direction, but the (Nb) was not so well aligned and it did not possess a high degree of continuity.

Cr_2Hf is essentially isomorphous with Cr_2Nb, but it has a higher melting temperature (1825°C versus 1770°C), which is consistent with Hf enrichment being observed at the cores of the laths. The melting temperatures of the three quaternary alloys investigated are also included in Table I; these temperatures are relatively low, being in the range 1514-1563°C. X-ray diffraction data (XRD) indicated that the Cr_2(Nb) possessed the C15 crystal structure. Binary Cr_2Nb has the cubic C15 crystal structure at temperatures below 1585°C and a hexagonal C14 structure above 1585°C [4, 15]. Cr_2Hf also possesses low

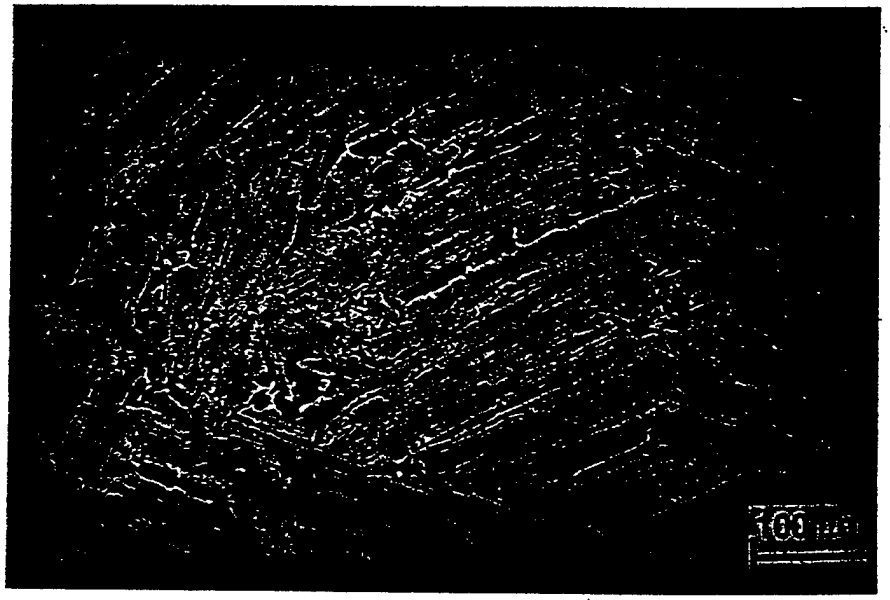
Bewlay et al

6

16



(a)



(b)

Figure 2 Typical scanning electron micrographs (BSE images) of, (a) the longitudinal, and (b) the transverse sections of DS $Cr_2(Nb)$-30%(Nb) (Nb-16.5Ti-52.5Cr-9.2Hf) composite.

temperature, C15, and high temperature, C14, crystal structures. The low temperature C15 phase is stable from room temperature to 1335°C, and the C14 phase is stable from 1335°C to the melting temperature. The XRD data indicate that the C15 $Cr_2(Nb)$ was stabilized in the quaternary alloy Laves phase composites.

The lattice parameters of the Cr_2Nb of the three quaternary compositions were measured using XRD as 0.70932(5), 0.71015(5) and 0.70964(5) nm for the Nb-26.0Ti-36.5Cr-7.5Hf, Nb-21.2Ti-44.5Cr-8.4Hf and Nb-16.5Ti-52.5Cr-9.2Hf alloys, respectively. The numbers in parentheses represent the uncertainty in the last digit. In comparison with the lattice parameters in the binary Laves phases, these lattice parameters are all similar, indicating that the phase chemistry was similar for $Cr_2(Nb)$ in the three alloys. These measurements suggest that the C15 crystal lattice is expanded as a result of the Hf additions; the lattice parameters of binary stoichiometric Cr_2Nb and Cr_2Ti are 0.6978 nm and 0.6940 nm, respectively, and the lattice parameter of binary stoichiometric Cr_2Hf is 0.7157 nm. The

Bewlay et al

lattice parameters of the binary Laves phases in the eutectics are modified according to the composition at the phase boundary [15], as is probably the case in the quaternary alloys. The lattice parameter measurements of the (Nb) were 0.32519 and 0.32490 nm for Nb-26.0Ti-36.5Cr-7.5Hf and Nb-21.2Ti-44.5Cr-8.4Hf alloys, respectively. Pure Nb has a lattice parameter of 0.33067 nm [15]. Binary alloys of Nb-Cr show lattice contraction, while Nb-Ti show no significant change, and Nb-Hf show expansion relative to the Nb lattice. These measurements indicate that there is some contraction of the Nb lattice as a result alloying with Cr and Ti, and this is greater than any expansion due to the Hf.

Electron microprobe data shown in Table II for similar arc-melted alloys containing Al, indicate that partitioning of Hf was approximately two times greater in the Laves phase than in the metal (~10% versus ~5%). The Cr concentration of the Laves phase was ~58%, while in the metal it was ~13% after heat treatment at 1200°C. Partitioning of Ti was stronger to the metal phase than to the Laves phase, and vice versa for Nb. Since the metallic phase strength and oxidation resistance is improved by Hf additions of 4-5% [12], the overall DS composite alloy chemistries were chosen in order to provide ~5%Hf in the metallic phase and ~10%Hf in the Laves phase.

Table II : Phase compositions for the metallic and Laves phases in $Cr_2(Nb)$-based composites heat treated at 1200°C for 50 hours in vacuum.

Phase	Temperature (°C)	Nb	Ti	Cr	Hf	Al
$Cr_2(Nb)$	1200°C	17.4	12.5	57.9	10.3	1.9
(Nb)	1200°C	38.9	38.7	13.0	4.6	4.8

The microstructure of the Nb-21.2Ti-44.5Cr-8.4Hf composition, which was used to generate the $Cr_2(Nb)$-40%(Nb) composite, was similar to that of the $Cr_2(Nb)$-30%(Nb) composite in both its scale and morphology, but there was a smaller volume fraction of $Cr_2(Nb)$. The microstructure of the $Cr_2(Nb)$-50%(Nb) composite (Nb-26.0Ti-36.5Cr-7.5Hf) had a similar morphology to that of the quaternary $Cr_2(Nb)$-30%(Nb) eutectic-based composition, but it had a larger volume fraction of (Nb) and as a result the (Nb) "laths" had a greater degree of continuity. The hexagonal type grains observed in the $Cr_2(Nb)$-(Nb) eutectic were not observed in the 50%(Nb) composite. This was probably a result of the lower volume fraction of $Cr_2(Nb)$, and the texture associated with it. The widths of the (Nb) and $Cr_2(Nb)$ phases were 13±4 μm and 12±4 μm, respectively. The $Cr_2(Nb)$ was finer than in the $Cr_2(Nb)$-30%(Nb) eutectic. No primary (Nb) dendrites were observed. The measured volume fraction of (Nb) in the nominal $Cr_2(Nb)$-50%(Nb) composite was 0.47, very close to that originally predicted for the selected alloy chemistry.

Niobium-Silicide Composite

A typical scanning electron micrograph (BSE imaging) of a longitudinal section of the MASC is shown in Figure 3. The composite contained both metallic and $(Nb,Hf,Ti)_3Si$ intermetallic dendrites, a small amount of an $(Nb,Hf,Ti)_5Si_3$ intermetallic, and an inter-dendritic eutectic of $(Nb,Hf,Ti)_3Si$ intermetallic and (Nb). Again, Hf partitioning leads to only small differences in the average atomic weight of the different phases, and this results in weak BSE contrast. The metallic and intermetallic dendrites of the MASC were aligned

Bewlay et al 8 16

with the growth direction. The MASC consisted of interpenetrating dendrites of the composite phases (20-40 μm). The volume fraction of the metallic phase was ~50%. The MASC is entirely analogous to hypoeutectic binary Nb-Si and ternary Nb-Ti-Si composites reported previously [4]. Typical microstructures of longitudinal and transverse sections of a Nb-33Ti-16Si ternary composite are shown in Figure 4, where the absence of Hf allows strong contrast between the phases. The $(Nb,Hf,Ti)_3Si$ dendrites shown in Figure 4 possessed the distinctive faceted morphology that has been reported previously in the binary hypereutectic binary Nb-Si alloys and the ternary Nb-Ti-Si composites [4, 10].

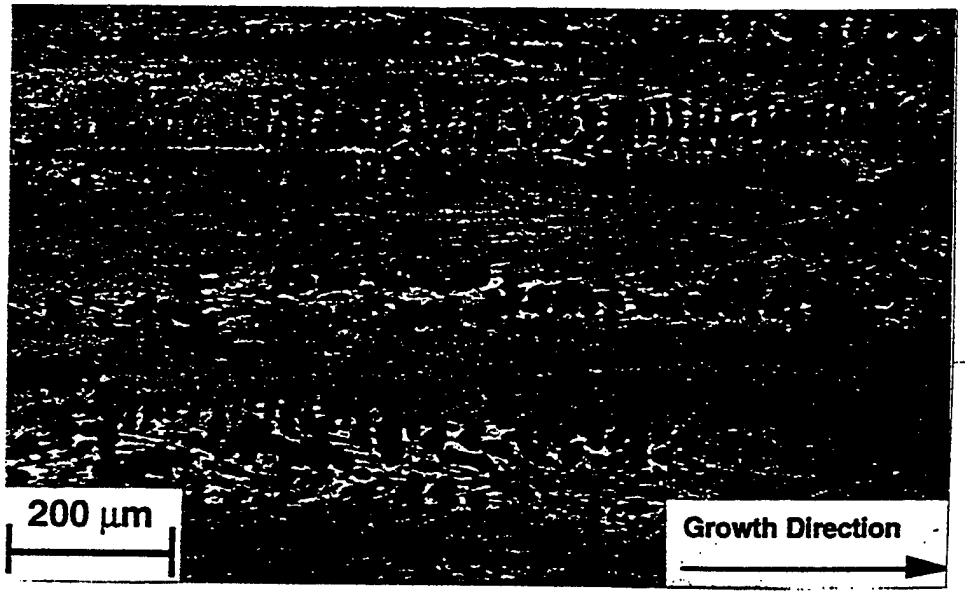


Figure 3 Micrograph (BSE image) of the longitudinal section of the DS Nb-24.7Ti-16Si-8.2Hf-2.0Cr-1.9Al composite (MASC).

The composition ranges observed in the three phases are shown in Table III. The Si concentrations of the $(Nb,Hf,Ti)_3Si$ and $(Nb,Hf,Ti)_5Si_3$ silicides were close to the stoichiometric values. Very low concentrations of Al and Cr were observed in both the $(Nb,Hf,Ti)_3Si$ and $(Nb,Hf,Ti)_5(Si,Al)_3$ silicides. There was strong Hf partitioning between the phases : 5% Hf was observed in the metallic phase, 8% Hf in $(Nb,Hf,Ti)_3Si$, and 12.5% Hf in $(Nb,Hf,Ti)_5(Si,Al)_3$; the bulk Hf composition was nominally 8.2%. The Nb:Ti:Hf ratio in the metallic phase was 12:6:1. The Nb:Ti:Hf:Si ratio in the $(Nb,Hf,Ti)_3Si$ was 6:2:1:3. In the $(Nb,Hf,Ti)_5(Si,Al)_3$ the Nb:Ti:Hf:Si ratio was 2:2:1:3. In the overall MASC chemistry, the Nb:Ti:Hf:Si ratio was approximately 6:3:1:2.

Table III : Composition ranges for the silicide and metallic phase observed in the composite which was directionally solidified from the Nb-24.7Ti-8.2Hf-2.0Cr-1.9Al-16.0Si alloy.

	Nb	Ti	Hf	Si	Al	Cr
Metallic Phase	58-61	27.2-29.4	5.0-5.3	0.9-1.3	2.5-3.0	2.8-3.9
$(Nb,Hf,Ti)_3Si$	48.3-49.0	18.2	7.8	24.7-25.4	0.1	0.13-0.16
$(Nb,Hf,Ti)_5Si_3$	25.5-27.9	22.2-23.2	12.5-12.9	35.4-37.5	1.0-1.5	0.35-0.5

Bewlay et al

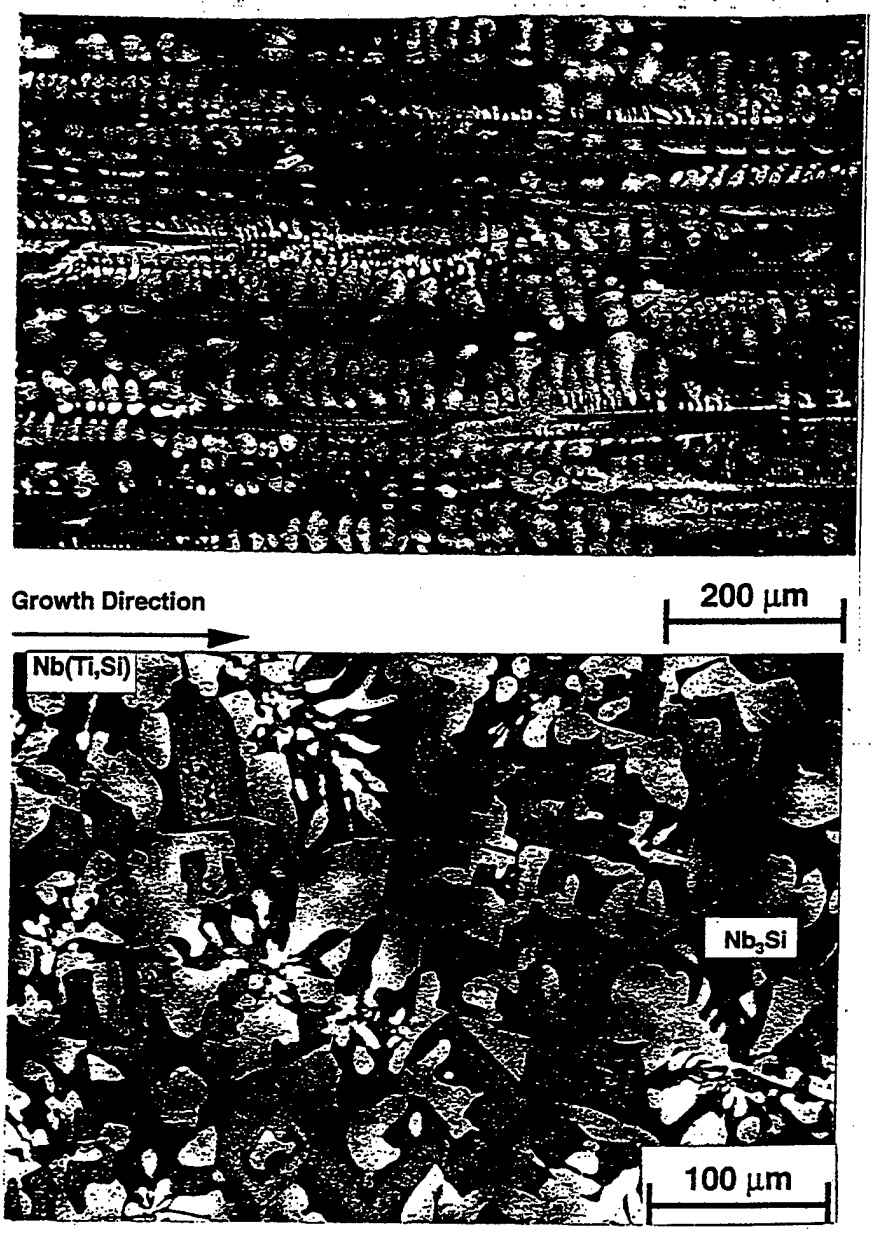


Figure 4 Scanning electron micrographs (BSE images) of (a) the longitudinal, and (b) the transverse sections of a DS Nb-33Ti-16Si composite. The structure consists of non-faceted Nb(Ti, Si) dendrites (white phase), together with large-scale (~50μm) faceted $(Nb,Ti)_3Si$ dendrites (grey phase).

Mechanical Properties

Room Temperature Fracture Toughness

Fracture toughness measurements of the composites from the quaternary alloys were not performed, but given the difficulty of preparing tensile specimens, as indicated in Table I, it can be assumed that the toughness was probably <10 MPa$\sqrt{m}$. The room temperature fracture toughness of the binary stoichiometric Laves phase, Cr_2Nb has been reported by Davidson and Chan as 1.4 MPa$\sqrt{m}$ [6], and fracture toughness values of the Cr_2Nb-Nb and Cr_2Nb-Cr binary eutectics have been reported as 3.1 MPa$\sqrt{m}$, and 3.6 MPa$\sqrt{m}$ [4] respectively.

It was not possible to grind tensile bars from the binary and quaternary eutectics, which contained a volume fraction of Laves phase of ~70%. Thus, the fracture toughness of the $Cr_2(Nb)$-(Nb) eutectic was probably similar to that of the binary eutectic, even though the

(Nb) phase width in the quaternary alloy was larger than the Nb rod width in the binary eutectic; previously it has been shown that increasing the scale of the toughening phase can lead to an increase in the toughness [4]. Given the poor machining performance of the 40% and 50% metal-containing composites, the fracture toughness values of these composites were probably <10 MPa$\sqrt{m}$, and there was little improvement at higher (Nb) volume fractions.

Room temperature fracture toughness values, K_Q, of 18.2-23.3 MPa$\sqrt{m}$ were measured from monotonic loading experiments for the MASC. R-curve measurements are shown in Figure 5, and the K_{IC} values for the MASC were 19-22 MPa$\sqrt{m}$. Higher toughness values were obtained from the MASC than were estimated for the quaternary Laves phase composites. Toughness values greater than 15 MPa$\sqrt{m}$ have also been measured in ternary Nb-Ti-Si composites [8, 9]. The form of these R-curves is similar to those reported previously in binary Nb-10Si in-situ composites, which displayed K_{IC} values of >20 MPa$\sqrt{m}$ in the extruded condition [9, 11].

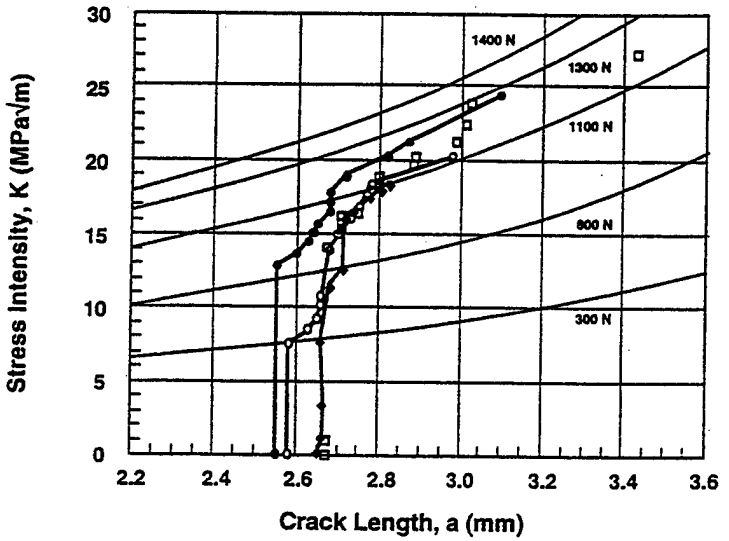


Figure 5 R-curve behavior of the DS MASC. Data points from four samples are shown.

Figure 6 shows fracture surfaces of the DS MASC. At lower magnification, the fracture surfaces were highly convoluted and suggested a high work of fracture. The (Nb) dendrites failed in a ductile manner, and were pulled out of the matrix. The fine-scale (Nb) between the silicide dendrites was also pulled to a chisel point, and microcracking of the silicide matrix was observed. All of the $(Nb,Hf,Ti)_3Si$ and $(Nb,Hf,Ti)_5Si_3$ intermetallic dendrites failed by cleavage. This suggests that the majority of the toughness was provided by the (Nb), although microcracking and interface debonding have made significant toughening contributions.

Elevated Temperature Strength

The tensile strengths of the Laves phase-based composites are shown in Table I and Figure 7. Compressive strengths at 1200°C for monolithic Cr_2Nb [2, 16] are also shown for comparison. The $Cr_2(Nb)$-40%(Nb) composite had a fracture stress of 132 MPa at 1200°C. The yield strength of the $Cr_2(Nb)$-50%(Nb) composite at 1200°C was 120 MPa. At

Bewlay et al 11 16

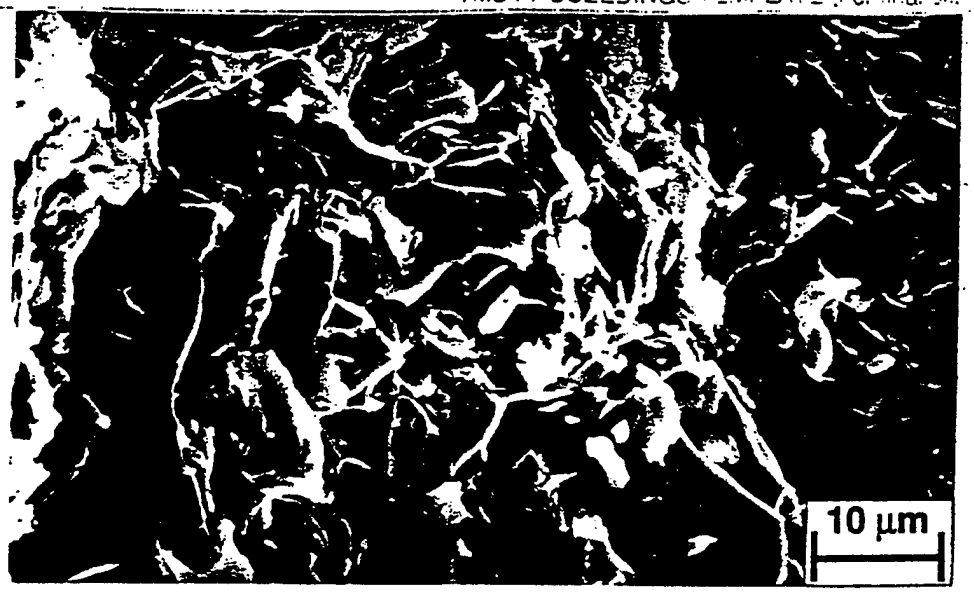


Figure 6 Fracture surface of the MASC, showing microvoid coalescence in the (Nb) and cleavage in the $(Nb,Ti)_3Si$.

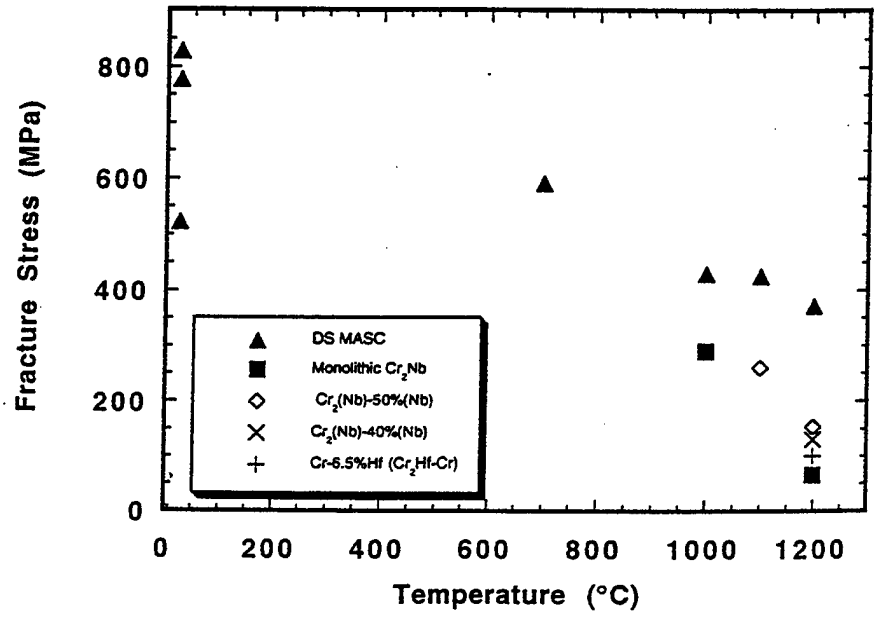


Figure 7 Tensile strengths of the MASC and the Laves phase-based composites as a function of temperature. The improvement of high temperature strength of the silicide composite over Laves phase-based composites with similar intermetallic volume fractions is apparent. Literature data for monolithic Cr_2Nb [2] and a Cr_2Hf-Cr [20] composite are included.

1200°C an ultimate tensile strength of 153 MPa and an elongation of 56% was measured for this composite. For comparison, a monolithic Nb-based alloy with a similar composition to that of the metallic phase in these composites (except for the addition of Al) had a yield strength in the range 55-70 MPa at 1200°C [12], indicating a factor of approximately two increase in the strength effected by the Laves phase. Kumar and Miracle [20] reported a compressive yield strength of two phase as-forged Cr-6.5Hf Cr_2Hf-Cr composite of ~100 MPa at 1200°C, which is less than that measured in tension for the

Bewlay et al 12 16

$Cr_2(Nb)$-(Nb) composites. This may be due in part to the lower volume fraction of Laves phase. Tensile testing of the Laves phase-based composites at room temperature was not performed because of the flaw sensitivity of these composites.

Examinination of the Laves phase composite data indicates that there are two important points. First, the $Cr_2(Nb)$-(Nb) composites which contained Hf and Ti, had higher fracture strengths at 1200°C than either the monolithic Cr $_2$Nb, or the binary Cr_2Hf-Cr composite [20]. Second, the fracture strengths of the $Cr_2(Nb)$-(Nb) with 40% and 50% (Nb) were similar. Although compressive strengths of ~600 MPa at 1200°C have been reported for Cr_2Nb-Nb by Takasugi et al [7], these strength levels have yet to be demonstrated in tension.

The yield strengths of the MASC are also shown in Figure 7. The tensile fracture stress was ~750 MPa at room temperature and the yield stress was 370 MPa at 1200°C. At 1200°C the scatter in the yield stress was ~20 MPa. However, several hundred MPa scatter was observed in the room temperature fracture stress measurements; this was probably due to the flaw sensitivity of the fracture stress at room temperature, as in the case of ceramics. At 1200°C significant plastic deformation of both the metallic and silicide phases was observed, but below 1100°C only the (Nb) exhibited plastic deformation. Monolithic alloys of similar compositions to the metallic phase of the composite have yield strengths in the range 55-70 MPa at 1200°C [12]. It can clearly be seen that at temperatures up to 1200°C, the yield strengths of the silicide-based composites were approximately twice those of the Laves phase-based composites. Thus, for a given volume fraction of intermetallic, the silicide-based composites offer a more attractive balance of room temperature fracture toughness and high temperature strength. At room temperature, the metallic phase provides the MASC with improved toughness, whereas at elevated temperatures (>1000°C) the silicide phases serve to maintain its strength. The (Nb) and $Cr_2(Nb)$ in the Laves phase composites are less effective in both of these capacities. The higher Cr concentration of the metal in equilibrium with the Laves phase, compared to the metal in equilibrium with the silicides, may lead to a smaller contribution to composite toughening in Laves phase composites.

Density-normalized bending strength-temperature data have been reported previously for Nb-42.5Ti-15Si, Nb-40Ti-15Si-5Al [9] and binary Nb-10Si composites [11]. The binary Nb-10Si composite showed bending strength levels at 1200°C of ~370MPa [11]. However, the reductions in the high temperature strength levels displayed in ternary Nb-Ti-Si and quaternary Nb-Ti-Si-Al are not experienced by the MASC. This suggests that Hf additions can have a powerful effect on the high temperature strength of the silicide and Laves phase composites, and that Hf is more effective in the former than in the latter.

Creep Rupture Behavior

Figure 8(a) compares the creep rupture behavior of the MASC with single crystal Ni-based superalloys, CMSX4 and CMSX10 [8] using a Larson-Miller plot. At 1100°C and 105 MPa the rupture life was greater than 500 hours. The density-normalized stress rupture behavior is shown in Figure 8(b) accounting for the reduced density of the composite in comparison with CMSX4 and CMSX10. Figure 8(b) illustrates that the stress rupture behavior of the MASC is similar to that of advanced single crystal Ni-based superalloys

Bewlay et al 13 16

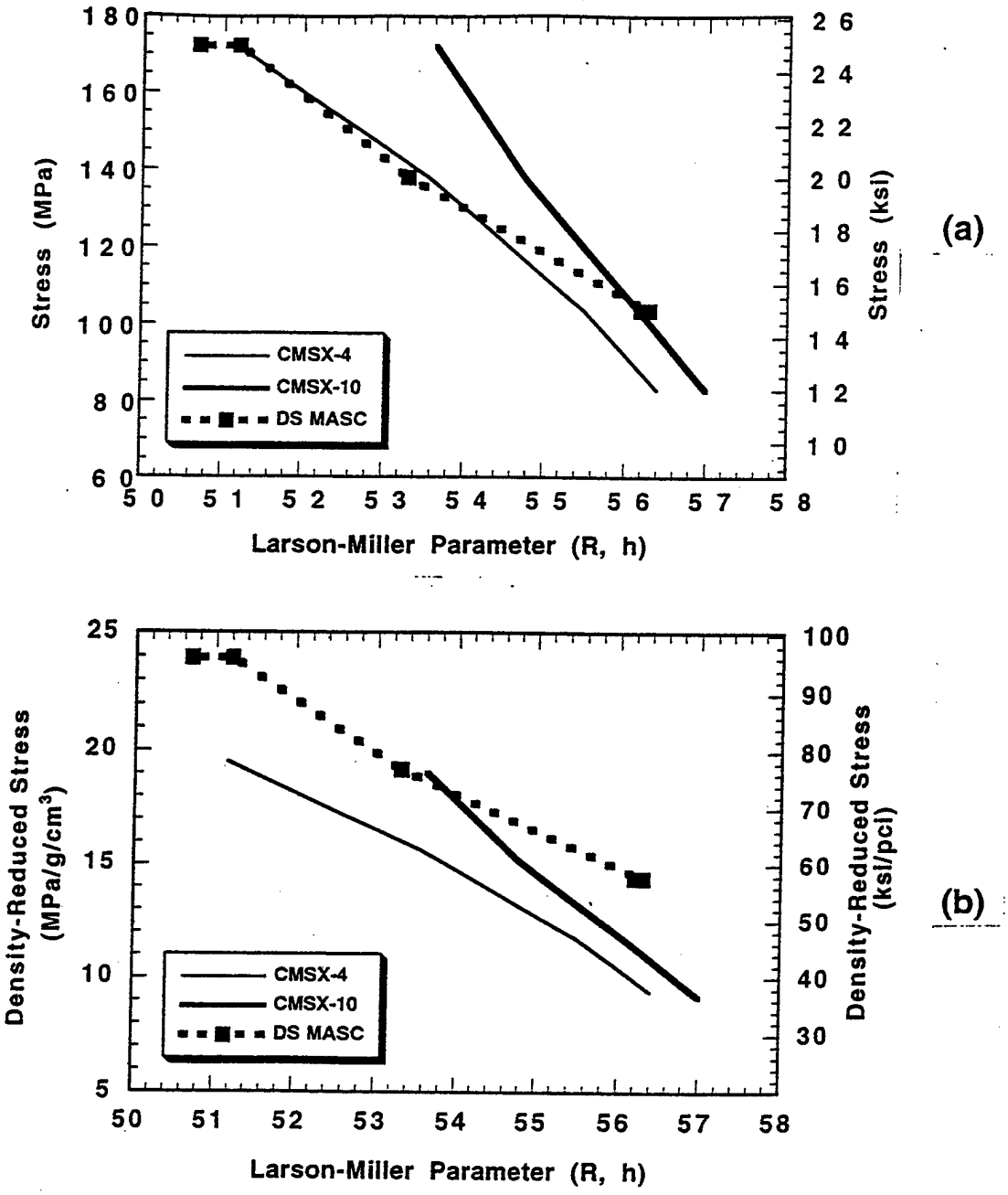


Figure 8 Stress rupture behavior of the DS MASC is compared to that of second- and third-generation single crystal Ni-based superalloys [8] in Larson-Miller plots (C=20) where the temperature-time parameter is plotted against (a) rupture stress or (b) rupture stress/material density. Stress rupture testing of MASC was performed in argon.

under similar test conditions but, after accounting for the lower density of the MASC, there is a significant improvement in the stress rupture behavior. The composite tensile creep rates have been reported separately [8], and are more than an order of magnitude lower than for commercial Nb alloys. The tensile yield strength of the best Laves phase composites at 1200°C is ~130MPa. Because the stress range that was used for creep rupture testing of the MASC was close to the yield strengths of the Laves phase composites, creep rupture testing of the latter was not performed.

Bewlay et al 14 16

Conclusions

Laves phase and niobium-silicide based composites with Hf and Ti alloying additions have been directionally solidified with intermetallic volume fractions in the range 70-50%. Complex microstructures and phase chemistries were observed in each family of composites. In the Laves phase composite, the Hf and Ti additions provided a coarser two-phase microstructure than was observed in the binary Cr_2Nb-Nb composite. However, estimates of the room temperature fracture toughness values of the quaternary Laves phase composites were low (<10 MPa$\sqrt{m}$). In the niobium silicide-based composite, the metallic phase provides more effective toughening, since toughness values of > 20 MPa$\sqrt{m}$ have been measured.

Tensile strengths for the Hf and Ti containing Cr_2(Nb)-(Nb) composites of up to 153 MPa at 1200°C were measured. However, at 1200 °C these strengths are only ~40% of that of a niobium silicide-based composite with a similar volume fraction of metallic phase. The MASC composite combines high-strength low-toughness silicides with a lower-strength high-toughness Nb-based metallic phase in order to generate a composite that has improved high temperature and low temperature mechanical properties. Room temperature fracture toughness values of >20 MPa$\sqrt{m}$ were measured with a tensile strength of 370 MPa at 1200°C. The stress rupture behavior of the MASC is similar to that of advanced single crystal Ni-based superalloys under similar test conditions and thus, due to the lower density (~25%) of the MASC, there is an increase in the density-normalized stress rupture behavior of more than one Larson-Miller parameter.

Acknowledgments

The authors would like to acknowledge W.J. Reeder for the fracture toughness measurements, C. Canestraro for the tensile testing, and L.A. Peluso for the microprobe analyses. The authors would also like to thank D.J. Dalpe for the directional solidification experiments. This research was partially funded by AFOSR under contract #F49620-93-C-0007 with Capt. C.H. Ward as Program Manager.

References

[1] D.L. Anton and D.M. Shah, Mat. Sci Eng., **A153** (1992), pp. 410-415.
[2] D.L. Anton and D.M. Shah, Mat. Res. Soc. Symp. Proc. **213** (1991), pp. 733-738.
[3] B.P. Bewlay, J.A. Sutliff, M.R. Jackson and H.A. Lipsitt, Acta Metall. Mater., **42(8)** (1994), pp. 2869-2878.
[4] B.P. Bewlay, H.A. Lipsitt, M.R. Jackson, W.J. Reeder and J.A. Sutliff, Mat. Sci. Eng., **A192/193** (1995), pp. 534-543
[5] M. Takeyama and C.T. Liu, Mat. Sci. Eng., **A132** (1991), pp. 61-66.
[6] D.L Davidson and K.S. Chan, AFOSR Final Report, April 1995.
[7] T. Takasugi, S. Hanada and K. Miyamoto, J. Mater. Res., **8 (12)** (1993), pp. 3069-3077.

Bewlay et al

[8] M.R. Jackson, B.P. Bewlay, R.G. Rowe, D.W. Skelly and H.A. Lipsitt, J. of Metals 48 (1) (1996), p. 39-44.

[9] P.R. Subramanian, M.G. Mendiratta and D.M. Dimiduk, J. of Metals 48 (1), (1996), pp. 33-38.

[10] P.R. Subramanian, M.G. Mendiratta and D.M. Dimiduk, Mat. Res. Soc. Symp. Proc. 322 (1994), pp. 491-502.

[11] M.G. Mendiratta, J.J. Lewandowski and D.M. Dimiduk, Metall. Trans. 22A (1991), pp. 1573-1581.

[12] M.R. Jackson and K.D. Jones, in Refractory Metals Extraction, Processing and Applications, Ed. K.C. Liddell, D.R. Sadoway and R.G. Bautista (TMS Publications, Warrendale, PA, 1991) pp. 310-320.

[13] M.R. Jackson, R.G. Rowe and D.W. Skelly, Annual Report, *WRDC Contract # F33615-91-C-5613*, (1994).

[14] T.B. Massalski, Binary Alloy Phase Diagrams, ASM Metals Park, Ohio (1991).

[15] D.J. Thoma and J.H. Perepezko, Mat. Sci. Eng., **A156** (1992), pp. 97-108.

[16] B.P. Bewlay and M.R. Jackson, Accepted for publication in J. Mater. Res., April 1996.

[17] K-M. Chang, B.P. Bewlay, J. A. Sutliff and M.R. Jackson, J. of Metals 44 (6), (1992), p. 59-65.

[18] "Standard Test Method for Plane-Strain Fracture Toughness of Metallic Materials", ASTM STP E-399, American Society for Testing and Materials, July 1983, pp. 488-512.

[19] "Standard Practice for R-Curve Determination," ASTM STP E 561-94, American Society for Testing and Materials, Philadelphia, 1994.

[20] K.S. Kumar and D.B. Miracle, Intermetallics **2** (1994), pp. 257-274.

Bewlay et al

16

The Balance of Mechanical and Environmental Properties of a Multi-Element Niobium-Niobium Silicide Based In-Situ Composite

B.P. Bewlay, M.R. Jackson and H.A. Lipsitt

Metall. and Mater. Trans., 1996

The Balance of Mechanical and Environmental Properties of a Multielement Niobium-Niobium Silicide-Based *In Situ* Composite

B.P. BEWLAY, M.R. JACKSON, and H.A. LIPSITT

This article describes room-temperature and high-temperature mechanical properties, as well as oxidation behavior, of a niobium-niobium silicide based *in situ* composite directionally solidified from a Nb-Ti-Hf-Cr-Al-Si alloy. Room-temperature fracture toughness, high-temperature tensile strength (up to 1200 °C), and tensile creep rupture (1100 °C) data are described. The composite shows an excellent balance of high- and low-temperature mechanical properties with promising environmental resistance at temperatures above 1000 °C. The composite microstructures and phase chemistries are also described. Samples were prepared using directional solidification in order to generate an aligned composite of a Nb-based solid solution with Nb_3Si- and Nb_5Si_3-type silicides. The high-temperature mechanical properties and oxidation behavior are also compared with the most recent Ni-based superalloys. This composite represents an excellent basis for the development of advanced Nb-based intermetallic matrix composites that offer improved properties over Ni-based superalloys at temperatures in excess of 1000 °C.

I. INTRODUCTION

The application of refractory metals in hot stages of turbine engines has been attractive for many years.[1] Developments based on Nb and Mo alloys have offered significant gains in temperature capability due to their high melting temperatures and, for the refractory metals, relatively low densities. However, oxidation resistance has remained a major barrier to their application, even in the coated condition.

Intermetallics offer great potential for high-temperature (>1000 °C) structural applications, but the intrinsic toughness of most intermetallics is too low for aircraft engine applications. However, combining intermetallic materials with metallic second phases has recently been shown to provide composites with promising toughness.[2,3] The most promising composites rely on ductile metals to provide room-temperature toughening and on intermetallics that coexist in equilibrium with those metals to provide the high-temperature strength. In this arena, Nb-Si *in situ* composites that consist of a Nb-based solid solution with Nb_3Si and/or Nb_5Si_3 silicides have been shown to have great potential because of their attractive balance of high- and low-temperature mechanical properties.[4–9] Unfortunately, the composites from binary Nb-Si alloys have very poor oxidation resistance, and, generally, elements added to these composites to improve oxidation resistance compromise high-temperature mechanical properties.[4] The present article describes an analogous *in situ* composite generated from a more complex Nb-Ti-Hf-Si-Al-Cr alloy; this composite offers an improved balance of mechanical properties and oxidation.

B.P. BEWLAY and M.R. JACKSON, Staff Metallurgists, are with the Corporate Research and Development Center, General Electric Company, Schenectady, NY 12301. H.A. LIPSITT, Professor, is with the Department of Mechanical and Materials Engineering, Wright State University, Dayton, OH 45435.

Manuscript submitted June 7, 1996.

This composite consists of high-strength, high-melting temperature Nb-based silicides together with a high melting temperature, modest strength, high-toughness Nb-based metallic phase. The composition of the alloy that was directionally solidified to generate this composite was Nb-24.7Ti-8.2Hf-2.0Cr-1.9Al-16.0Si in atomic percent (Nb-15.47Ti-19.19Hf-1.35Cr-0.68Al-5.88Si in weight percent); all compositions are given in atom percent throughout the remainder of this article. Throughout this article, this composite will be referred to as the metal and silicide composite (MASC). This composition was based on the binary Nb-16 pct Si composition;[7,10] Ti and Hf were added to improve the oxidation resistance.[11] Subramanian *et al.*[4] and Jackson *et al.*[11] reported that the oxidation resistances of both the single-phase silicide and the metallic phase were improved by partial substitution of Ti for Nb. The elements Cr and Al also improve the oxidation resistance of both the metallic and silicide phases. Titanium was also added to improve the intrinsic ductility of the metallic phase and, therefore, potentially the composite toughness. Titanium additions have the disadvantage of reducing the alloy melting temperature, and, thus, the strengths of Ti-modified single-phase alloys generally make them more suitable for sheet structures in engines rather than for airfoils.[11,12] Hafnium is added because it is also a strong solid solution strengthener of the Nb-based metallic phase.[12] All elements partition to varying degrees between the different phases of the composite,[2] and this was taken into consideration in designing the alloy from which the present composite was derived.

The aim of this article is to describe microstructures, phase chemistries, mechanical properties, and oxidation behavior of the MASC. Creep rupture properties and oxidation data are compared with those of the most recent Ni-based superalloys. The mechanical property measurements discussed include room-temperature fracture toughness, *R*-curve measurements, tensile strength from room temperature to 1200 °C, and tensile creep data at 1100 °C.

The thermal expansion and modulus of elasticity data of the composite measured at temperatures from room temperature to 1200 °C are also presented.

II. EXPERIMENTAL

A. *Directional Solidification*

Alloys from which the *in situ* composite samples were generated were prepared using high-purity (99.99 pct) elements. The alloys were induction levitation melted in a segmented water-cooled copper crucible.[10,13] The melting temperature of the alloy from which the MASC was generated was 1760 °C, as measured using a two-wavelength optical pyrometer calibrated against 99.9 pct pure Ti. Induction levitation melting and directional solidification were performed under an atmosphere of ultra-high-purity argon in order to prevent contamination with interstitials. Samples (~10 mm in diameter and ~75-mm long) were directionally solidified by the Czochralski method at constant rates of 5 mm/min. The process has been described in further detail elsewhere.[10,13] Conventional microscopy and electron beam microprobe analyses were performed to characterize phase chemistries.

B. *Mechanical Properties*

1. *Fracture toughness measurements*

Single-edge notched bending specimens (SENBs) for fracture toughness measurements were prepared by electrodischarge machining (EDM) so that their longitudinal axis was parallel to the growth direction. The SENBs were then surface ground to the finished dimensions (nominally 33 × 6 × 3 mm) to remove the EDM recast layer. The bars were notched at their midpoints using EDM with a 50-μm wire.

Fracture toughness measurements were performed using monotonic loading and four-point bending at a crosshead speed of 4.2×10^{-3} mm s^{-1}. The procedures provided by ASTM standard E-399[14] were employed; the only point of deviation from ASTM E-399 was the omission of fatigue precracking. For this reason, the toughness values for the monotonic loading experiments are reported as K_q rather than K_{IC}. The *R*-curve measurements were also performed on additional samples following the ASTM standard E-561-94.[15] The *R*-curve measurements were performed in four-point bending but with a slower crosshead speed of 2.5×10^{-4} mm/s and using displacement control. The crack opening displacement (COD) was monitored using an Instron double-cantilever beam-type COD gage. After each loading increment, the crack length on the outside of the specimen was also measured when the crack was fully arrested using an optical microscope mounted on the crosshead.

2. *Tensile and creep rupture testing*

Tensile testing was performed in a vacuum of $\sim 10^{-4}$ torr using a 2-mm-diameter gauge, 10.7-mm long uniform diameter button-head tensile specimen. An initial strain rate of 8×10^{-4} s^{-1} was used. The samples were machined by first using EDM and then centerless grinding them to final dimensions. No further surface preparation was performed. The tensile specimens were prepared so that the growth direction was parallel to the axis of the tensile bar. The improved toughness and reduced surface flaw sensitivity of the directionally solidified (DS) composite allowed centerless grinding of the tensile testing samples.

3. *Modulus and expansion measurements*

Dynamic elastic moduli were measured in air at room temperature and in an atmosphere of flowing argon at 100 °C temperature intervals up to 1200 °C. The samples were machined by first using EDM and then centerless grinding them to final dimensions. The samples were machined so that their longitudinal axes were parallel to the growth direction; the samples were nominally 2.5 mm in diameter and 25 mm in length. Sample weights and dimensions were measured, and a transducer connecting rod of a Ni-W alloy was welded to the end of the sample. Longitudinal ultrasonic waves were passed from the connecting rod along the sample axis and were reflected at the opposite end of the sample. The modulus was calculated based on the velocity of the wave through the sample.

The thermal expansion behavior of the MASC from room temperature to 1250 °C was measured in a flowing argon atmosphere using a differential dilatometer. This measurement was performed on a 25-mm-long pin with a square cross section of 2.5 mm on a side. The sample was machined by first using EDM to reach the approximate dimensions, and then surface grinding the sample to final dimensions so that the longitudinal axis of the sample was parallel to the growth direction. A standard sample of high-purity alumina was run in tandem with the MASC sample so that the axial expansion could be determined. The standard and MASC samples were heated at a rate of 10 °C/min in the dilatometer capsule, which was inserted into a furnace with $MoSi_2$ heating elements. The standard and sample lengths were measured at a sampling rate of several times per second; the length measurement and temperature were recorded whenever the sample length changed from the previous measurement. Similar data were taken during cooling, but the constant cooling rate of 10 °C/min could only be maintained to temperatures of about 800 °C, where forced cooling would have been required to maintain the cooling rate. Only data determined on heating are reported.

C. *Oxidation Testing*

Isothermal oxidation tests were performed at 1000 °C, 1200 °C, and 1400 °C in a static air $MoSi_2$ resistance-heated furnace. Periodic removal from the furnace (at 1, 2, 4, 25, 50, 100, 150, and 200 hours, or until the test was terminated due to visual observation of gross material loss) was performed to determine weight change per unit area. The samples were machined by first using EDM and then centerless grinding to final dimensions so that the longitudinal axis was parallel to the growth direction; the sample was nominally 2.5 mm in diameter and 25 mm in length. Metallography was performed at the termination of testing to determine the approximate material loss after 100 hours of exposure.

III. RESULTS AND DISCUSSION

A. *Microstructures and Phase Chemistries*

Figure 1 shows a typical scanning electron micrograph (backscatter electron (BSE) imaging) of a longitudinal sec-

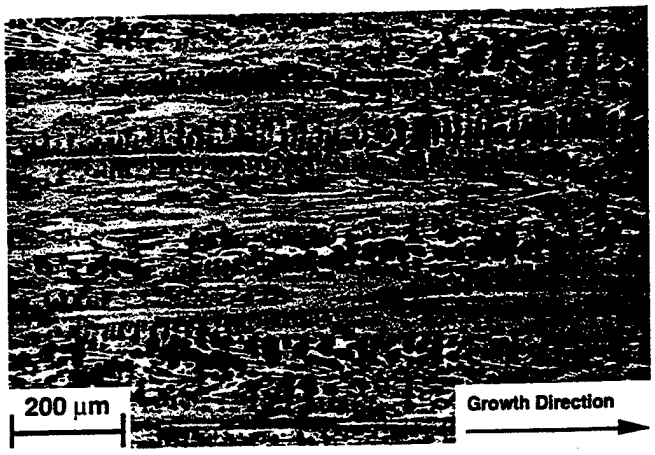
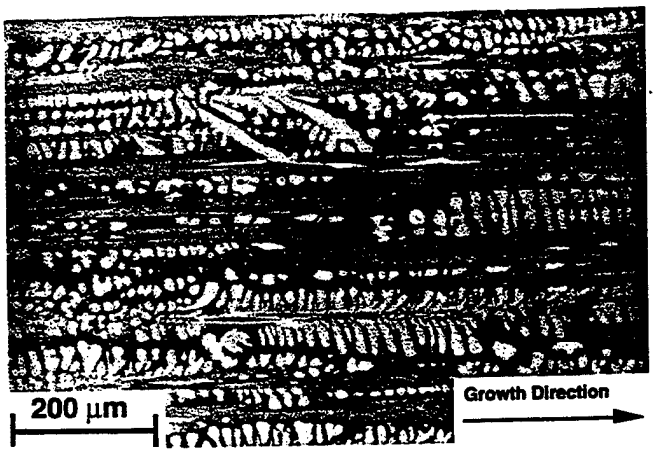
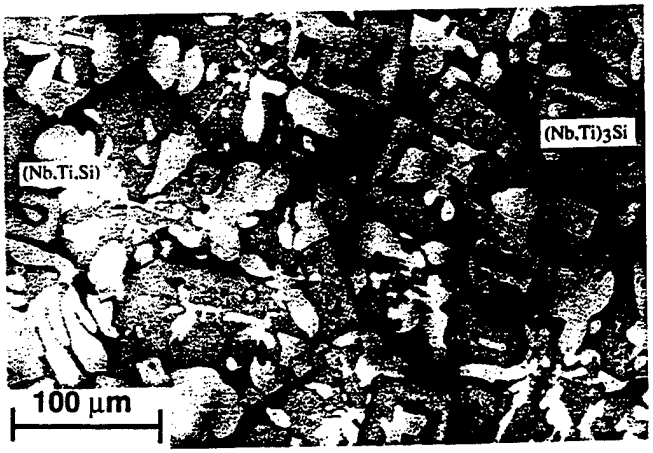


Fig. 1—Micrograph (BSE image) of the longitudinal section of the DS Nb-24.7 pct Ti-16 pct Si-8.2 pct Hf-2.0 pct Cr-1.9 pct Al composite (MASC). The composite contained both metallic and M_3Si intermetallic dendrites, aligned with the growth direction. There was also a small volume fraction of M_5Si_3 silicide.



(*a*)



(*b*)

Fig. 2—Typical scanning electron micrographs (BSE images) of (*a*) the longitudinal and (*b*) the transverse sections of a DS Nb-33Ti-16Si composite. The structure consists of nonfaceted Nb(Ti,Si) dendrites, which is the lighter phase in these BSE micrographs, together with large-scale (~50 μm) faceted $(Nb,Ti)_3Si$ dendrites.

tion of the composite microstructure. It contained both metallic and M_3Si intermetallic dendrites, a small amount of an M_5Si_3 intermetallic, and an interdendritic eutectic of M_3Si intermetallic and metal (where M represents Nb, Ti, and Hf). In this regard, it is entirely analogous to hypereutectic binary Nb-Si and ternary Nb-Ti-Si composites reported previously.[16] However, in the alloy design for the MASC, no M_5Si_3 was expected. A typical microstructure of a ternary Nb-Ti-Si alloy composite is shown in Figure 2 for clarification; it consists of interpenetrating dendrites of the composite phases with dendrite cross sections on the order of 5- to 50-μm wide. The M_3Si dendrites possessed the distinctive faceted morphology reported previously in the binary hypereutectic binary Nb-Si alloys and the ternary Nb-Ti-Si composites.[10,16] However, in the case of the MASC, Hf segregation results in only small differences in the average atomic weight of the different phases, so it is difficult to obtain strong contrast between them using BSE imaging. The metallic and intermetallic dendrites of the MASC were aligned with the growth direction. The volume fraction of the metallic phase in the MASC was 54 pct. The average dendrite size of the metallic phase, including the secondary arms, was ~24 μm.

B. *Phase Chemistries*

Electron microprobe (EMP) analysis confirmed that the composite consisted of three phases. A metallic phase containing Nb, Ti, Hf, Si, Al and Cr; an M_3Si silicide phase; and also an $M_5(Si, Al)_3$-type phase were examined. The composition ranges observed in the three phases are shown in Table I; the silicides are not line compounds. The Si concentrations of the M_3Si and M_5Si_3 silicides were close to the stoichiometric values.

Figure 3 shows a typical EMP scan perpendicular to the composite growth direction. The Ti concentration profile was approximately uniform across the dendrites perpendicular to the growth direction, but there was some reduction in the Ti concentration in the interdendritic regions. There was strong Hf partitioning from the metallic phase to the $M_5(Si, Al)_3$ and M_3Si silicides. The Hf partitioning results observed were 5 pct Hf in the metallic phase, 8 pct Hf in M_3Si, and 12.5 pct Hf in $M_5(Si, Al)_3$; the bulk Hf composition in the alloy was nominally 8.2 pct. The Nb:Ti:Hf ratio was ~12:6:1 in the metallic phase. The Nb:Ti:Hf:Si ratio in the $(Nb, Ti, Hf)_3Si$ was 6:2:1:3. In the $M_5(Si, Al)_3$, the Nb:Ti:Hf:Si ratio was 2:2:1:3. For the bulk MASC chemistry, the Nb:Ti:Hf:Si ratio was approximately 6:3:2:1. Very low concentrations of Al and Cr were observed in both the M_3Si and $M_5(Si, Al)_3$ silicides.

C. *Mechanical Properties*

1. *Fracture toughness*

Room-temperature fracture toughness values of K_q of 18.2 to 23.3 MPa $\sqrt{m}$ were measured for monotonic loading. Similar values of K_{IC} were obtained from *R*-curve measurements. These are higher levels of fracture toughness than those reported previously in DS intermetallic-based composites. The *R*-curve measurements are shown in Figure 4 together with lines of stress intensity *vs* crack length at constant load. Typically, the initiation toughness values for the MASC were 7 to 13 MPa $\sqrt{m}$, and the K_{IC} values were 19 to 22 MPa $\sqrt{m}$. The variation in stress intensity for crack initiation may have been dependent upon the position of the notch tip with respect to the intermetallic or metallic phase.

Table I. Composition Ranges for the Silicide and Metallic Phases Observed in the Composite Directionally Solidified from the Nb-24.7Ti-8.2Hf-2.0Cr-1.9Al-16.0Si Alloy (AS-DS Condition)

	Nb	Ti	Hf	Si	Al	Cr
Metal solid solution	58 to 61	27.2 to 29.4	5.0 to 5.3	0.9 to 1.3	2.5 to 3.0	2.8 to 3.9
M_3Si solid solution	48.3 to 49.0	18.2 to 18.5	7.8 to 8.0	24.7 to 25.4	0.1 to 0.2	0.13 to 0.16
M_5Si_3 solid solution	25.5 to 27.9	22.2 to 23.2	12.5 to 12.9	35.4 to 37.5	1.0 to 1.5	0.35 to 0.5

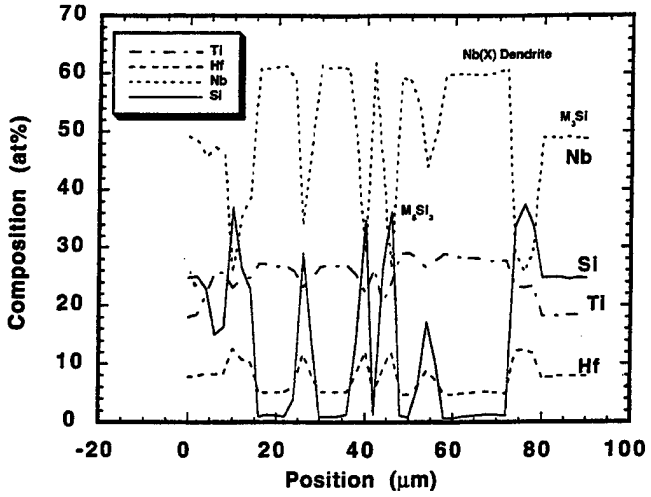


Fig. 3—Microprobe scans perpendicular to the growth direction showing the Nb, Hf, Ti, and Si concentration profiles perpendicular to the dendrites of the as-DS MASC.

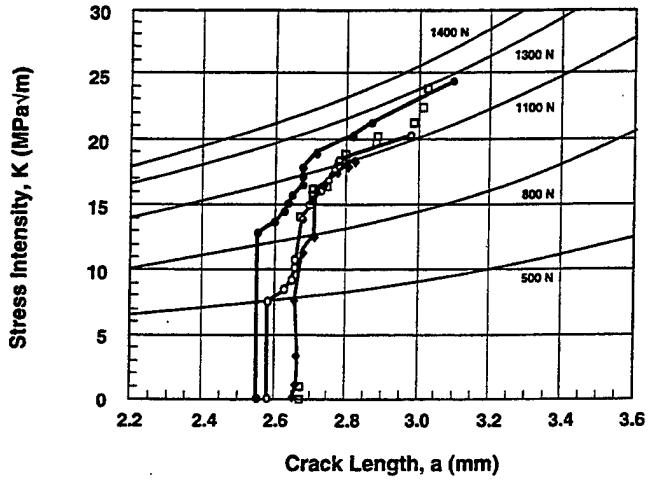
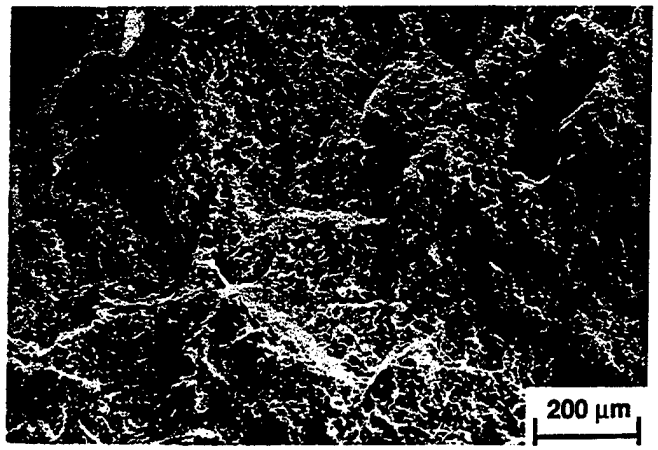
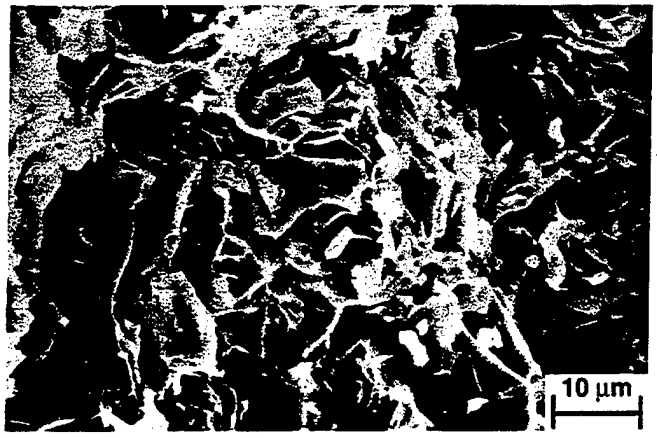


Fig. 4—*R*-curve behavior of the DS MASC. Data from four separate samples are shown. Also shown are curves of stress intensity *vs* crack length at constant load.



(*a*)



(*b*)

Fig. 5—Fracture surfaces (secondary electron images) of the DS MASC at (*a*) low and (*b*) high magnifications. The silicide matrix failed by multiple plane cleavage.

Examination of the *R*-curve data indicates that the composite exhibited *R*-curve behavior, because it displayed increasing resistance to crack growth with increasing crack length. The measured *R*-curves extend beyond the point of instability because the test was performed using displacement control rather than load control. The *R*-curve fracture toughness measurements were consistent with those from the monotonic loading experiments. These *R*-curves are similar to those reported previously in binary Nb-10 pct Si *in situ* composites that have displayed a K_{IC} of >20 MPa $\sqrt{m}$ in the single- and double-extruded conditions.[8]

Figure 5 shows fracture surfaces of the DS MASC. The fracture surfaces were similar for both monotonic loading experiments and *R*-curve measurements. The fracture surfaces were highly convoluted and consistent with a high work of fracture. The higher magnification fractograph shows that metallic dendrites failed in a ductile manner and were pulled out of the matrix. The metallic phase between the silicide dendrites was also pulled to a chisel point, and microcracking of the silicide matrix was observed. All of the M_3Si and M_5Si_3 silicide dendrites failed by cleavage. This suggests that the majority of the toughness was provided by the metallic phase, although microcracking and interface debonding may also have made significant toughening contributions.

The crack path was also examined in a partially fractured bar that was unloaded prior to unstable crack growth. Crack deflection and crack multiplication were evident. The fracture path showed distinct offsetting of the crack path and lateral crack propagation parallel to the directional solidi-

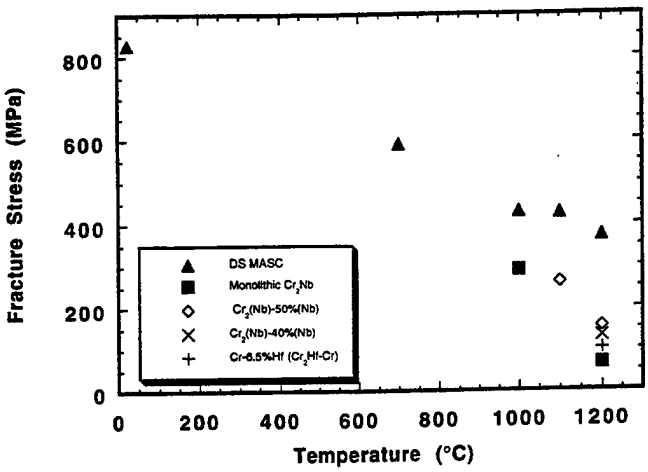


Fig. 6—Tensile strength of the DS MASC as a function of temperature, showing the improvement of high-temperature strength over Laves phase-based composites with similar intermetallic volume fractions.[2]

Table II. Tensile Strength of the MASC as a Function of Temperature

Temperature (°C)	Fracture Strength (MPa)
25	820
700	590
1000	429
1100	425
1200	370

fication direction where the crack intersected the intermetallic dendrites. Thus, the intermetallic dendrites did play an important role in toughening the composite. At higher magnifications, crack bridging and crack blunting were observed.

2. *High-temperature strength*

The composite tensile stress is shown as a function of temperature in Figure 6 and Table II. The tensile fracture stress was ~800 MPa at room temperature, and the yield stress was 370 MPa at 1200 °C. At 1200 °C, the scatter in the yield stress was ~20 MPa. However, several hundred MPa scatter was observed in the room-temperature fracture stress measurements; this was probably due to the flaw sensitivity of the fracture stress of this composite at room temperature. If the gauge sections had been polished to an improved surface finish, then the scatter in the room-temperature fracture stress measurements may have been reduced. At 1200 °C, an elongation of 19 pct was measured indicating significant plastic deformation of both the metallic and silicide phases. At room temperature, no macroscopic ductility was measured in the tensile tests, but fractographic observations indicated plastic deformation of the metallic phase. Monolithic alloys of similar compositions to the metallic phase of the composite have yield strengths of less than 55 MPa at 1200 °C.[12] Thus, the composite possesses substantially improved tensile properties. In comparison with monolithic intermetallics, the strength retention of this composite at high temperatures is very encouraging. At room temperature, the metallic phase provides the composite with improved toughness, whereas, at high temperatures (>1000 °C), the silicide phases maintain

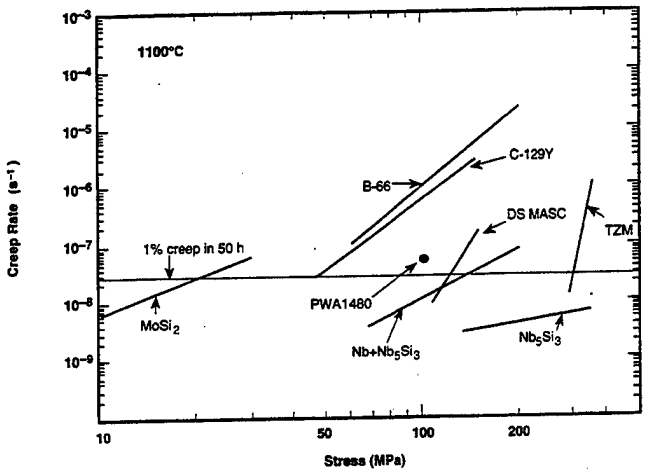


Fig. 7—Comparison of secondary tensile creep rates of the DS MASC at 1100 °C with the compressive creep behaviors of monolithic Nb_5Si_3 and Nb-Nb_5Si_3 binary composites.[17] Compressive creep behaviors of several commercial high-temperature alloys are included. The creep to 1 pct strain in 50 h is indicated by the horizontal line.

Table III. Tensile Creep Data (Rupture Life, Secondary Creep Rates, and Strain to Failure) of the MASC at 1000 °C and 1100 °C (Rupture Lives and Failure Strains, ϵ_f, Are Shown for Each Sample Tested, and Mean Secondary Creep Rates Are Shown for Two Samples)

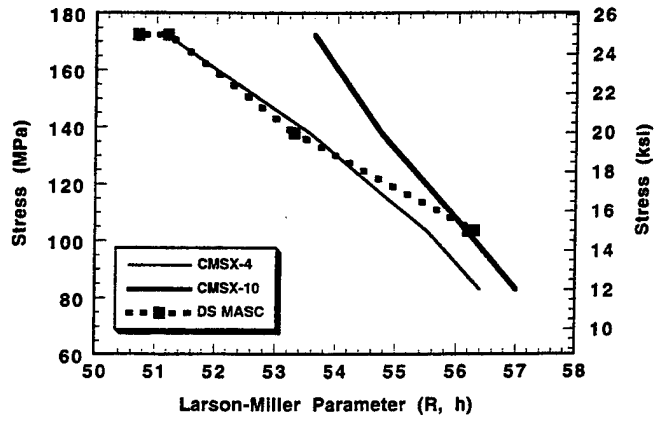
Temperature : Stress (°C) : (MPa)	Rupture Life (Hours)	Creep Rate (s^{-1})	ϵ_f (Pct)
1100 : 140	35	1.7×10^{-7}	7
1100 : 105	584, 524	9.3×10^{-9}	9.1, 11
1000 : 175	129, 212	2.9×10^{-8}	4.5, 6.0

its strength. The volume fraction of silicide in the MASC can be increased to improve the high-temperature strength and oxidation resistance, but this may compromise the attractive room-temperature toughness.

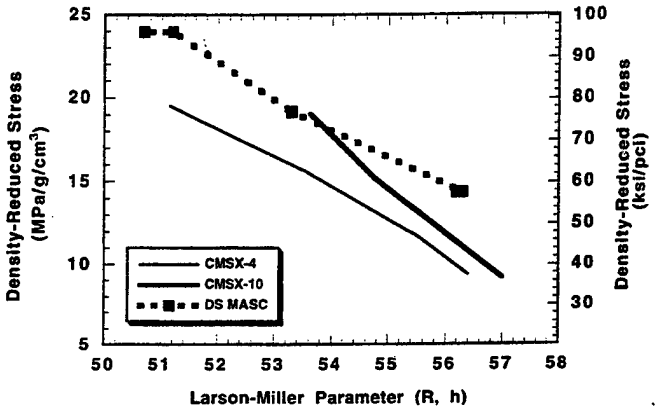
Density-normalized bending strength-temperature data have been reported previously for Nb-42.5Ti-15Si, Nb-40Ti-15Si-5Al,[4] and binary Nb-10Si composites.[6] The binary Nb-10Si composite showed bending strength levels at 1200 °C similar to the tensile strengths of the MASC (370 MPa).[6] However, the reductions in the high-temperature strength levels displayed in ternary Nb-Ti-Si and quaternary Nb-Ti-Si-Al are not experienced by the MASC. This suggests that Hf additions can have a powerful effect on both high-temperature strength and oxidation resistance. Details of the strengthening mechanism are the subject of further research.

3. *Creep rupture behavior*

Figure 7 compares the secondary tensile creep rates of the MASC with those of a range of high-temperature alloys, including PWA1480, Mo TZM, and monolithic commercial Nb-based alloys (B-66 and C129Y). Tensile creep data of the MASC are also shown in Table III. The composite creep rates are more than an order of magnitude lower than those of B-66 and C129Y. The secondary tensile creep rates at 1100 °C and 105 and 140 MPa are similar to the compressive creep rates measured in binary Nb-16 pct Si composites at 1200 °C.[3,17,18] The stress sensitivity of the creep rate of the MASC is lower than that of Mo TZM, but it is

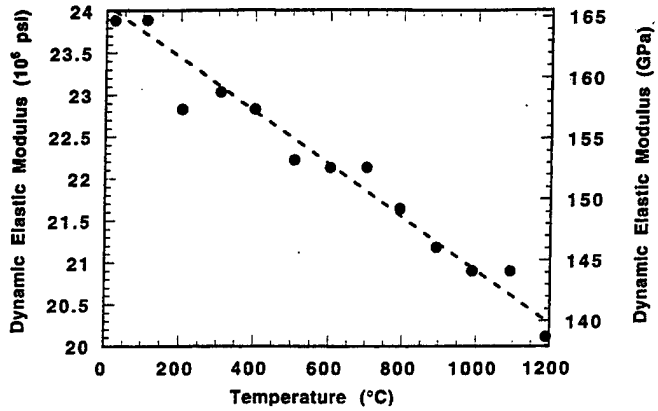


(a)

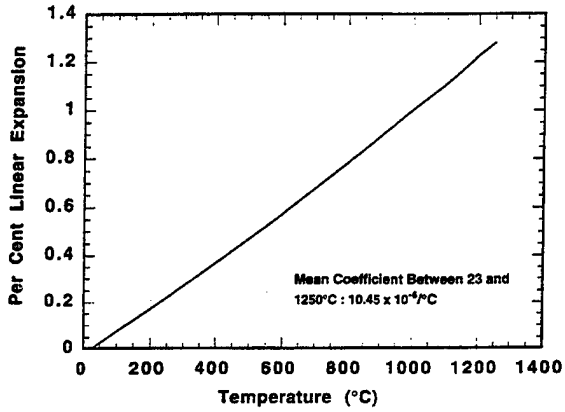


(b)

Fig. 8—Stress rupture behavior of the DS MASC is compared to that of second- and third-generation single-crystal Ni-based superalloys[4] in Larson–Miller plots ($C = 20$), where the temperature-time parameter is plotted against (*a*) the rupture stress and (*b*) the rupture stress/composite density. Stress rupture testing was performed in argon.



(a)



(b)

Fig. 9—Measurements of (*a*) elastic modulus and (*b*) thermal expansion from 23 °C to 1200 °C.

higher than that of the binary Nb-Nb_5Si_3 (as indicated by the compression data shown in Figure 7).

The creep rupture behavior of the MASC is shown in the Larson– Miller plot in Figure 8(a), and it is compared to a current generation single-crystal Ni-based superalloy, CMSX4, and an advanced-generation single-crystal Ni-based superalloy, CMSX10.[2] At 1100 °C and 105 MPa, the rupture life was greater than 500 hours. Stresses higher than 105 MPa led to shorter rupture times at either 1000 °C or 1100 °C. At low stresses, the behavior is similar to CMSX10, and at high stresses it is similar to CMSX4. The stress rupture behavior is also shown in Figure 8(b) accounting for the reduced density of the composite in comparison with CMSX4 and CMSX10. Figure 8(b) illustrates the increase in specific rupture performance that results from the substantial reduction in density of the MASC compared to the third-generation single-crystal superalloy. In summary, the stress rupture behavior of the MASC is similar to that of advanced single-crystal Ni-based superalloys under similar test conditions and, thus, after accounting for the lower density of the MASC, the creep behavior is very promising. In addition, only a small range of such composites has been evaluated to date. The rupture behavior required for future applications will be well beyond any behavior observed thus far. Current estimates are that ultimately an 80-fold increase over current rupture lives may be required for successful application of the intermetallic-based composites.[2]

4. *Physical properties*

The modulus at room temperature was 165 GPa, and it decreased approximately linearly with increasing temperature to 140 GPa at 1200 °C, as shown in Figure 9(a). In comparison, monolithic Nb_5Si_3 has been reported to have a modulus of 170 to 210 GPa at room temperature. Thus, the modulus value of 140 GPa for the composite at 1200 °C is very promising. Typical modulus values for a third-generation Ni-based superalloy at 1100 °C are 75 to 83 GPa in the ⟨001⟩ and 210 GPa in the ⟨111⟩. The specific modulus of the composite at 1200 °C is probably greater than that of Ni-based superalloys, but the anisotropy of the composite modulus needs to be investigated in further detail.

The total expansion to 1250 °C is shown in Figure 9(b). The thermal expansion of the composite is approximately linear over this temperature range with a coefficient of 10.45×10^{-6}/°C. Previously, monolithic binary Nb_5Si_3 and ternary $(Nb,Ti)_5Si_3$ silicides were reported to have expansion coefficients of $\sim 9.0 \times 10^{-6}$/°C over this temperature range.[11] Typically, the thermal expansion of a monolithic alloy of a similar composition to the metallic phase of this composite is $\sim 9.4 \times 10^{-6}$/°C.

These results suggest that the expansion mismatch between the metal and the intermetallics over this temperature range is relatively small. Thus, it is expected that the thermal ratcheting between the phases will be negligible, and

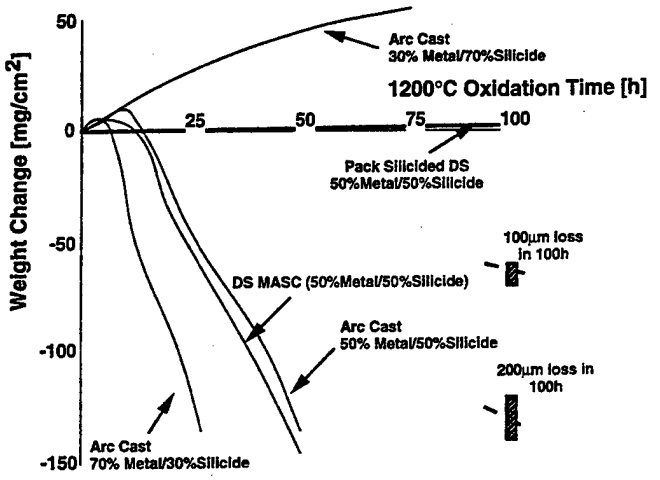


Fig. 10—Oxidation behavior of the DS MASC (50 pct metal/50 pct silicide), together with other similar silicide-based composites with volume fractions of silicide in the range 30 to 70 pct.[2]

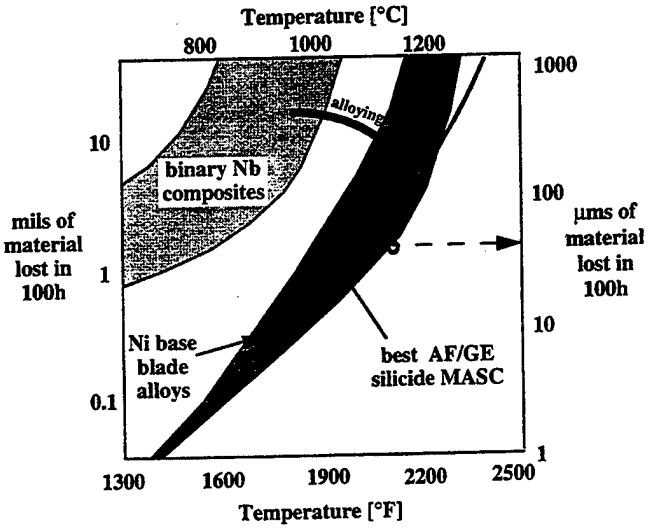


Fig. 11—Comparison of the material losses in oxidation of Nb-based Ti-modified silicides with less-oxidation-resistant Ni-based superalloys, such as IN 738.

the interface between composite phases will not suffer excess stress during thermal cycling.

C. *Oxidation Behavior*

Oxidation resistance at 1000 °C and 1200 °C has been investigated for a number of Nb-based intermetallics and refractory metal intermetallic composites.[2] The oxidation behavior of the MASC at 1200 °C is shown in Figure 10. Subramanian *et al.*[4] have reported similar oxidation performance for several ternary and quaternary silicide-based composites. The oxidation behavior of the MASC was also compared with the oxidation behavior of similar arc-cast silicides with volume fractions of metal ranging from 30 to 70 pct, as shown in Figure 10. On the basis of oxidation performance, increasing the silicide volume fraction to 70 pct is highly beneficial. Pack siliciding of the DS material also leads to a further improvement in the oxidation behavior. The oxidation data at 1200 °C show a substantial improvement over that of binary Nb-Nb_5Si_3 composites,[2] but the oxidation resistance of this composite requires further improvement. No pesting-type behavior (oxidation resistance dependent on stress and the defect content of the test sample) was observed in any of these oxidation tests. At 1400 °C and above, oxidation was catastrophic.

A comparison of oxidation performance for the DS MASC and Ni-based superalloys is shown in Figure 11. The Laves phase refractory metal *in situ* composites were slightly better than the MASC.[2] The DS MASC shows material losses at rates intermediate between the rapid losses of an older superalloy, such as IN 738, and the improved oxidation behavior of third-generation single-crystal superalloys. The horizontal dashed arrow in Figure 11 indicates the goal behavior, where component surface temperatures may be 1370 °C. This goal is derived from current superalloy capability. If superalloys can survive with surface temperatures of 1150 °C, then the rate of metal loss for the best superalloys at that temperature, ~25 μm/100 h, is a reasonable goal for the refractory metal *in situ* composites at their maximum surface temperature. Even if the goal of <25 μm loss/100 h at 1370 °C is met, the refractory metal *in situ* composites will need protective coatings, as with today's superalloys.

IV. SUMMARY

The present article describes a very high-temperature refractory metal-silicide composite system that shows improved high-temperature properties when compared with the most advanced single-crystal Ni-based alloys. This composite combines high-strength low-toughness silicides with a lower-strength, high-toughness Nb-based metallic phase in order to generate a composite that has improved high- and low-temperature mechanical properties. Room-temperature fracture toughness values of >20 MPa $\sqrt{m}$ were measured with a tensile strength of 370 MPa at 1200 °C. The stress rupture behavior of the MASC is similar to that of advanced single-crystal Ni-based superalloys under similar test conditions, and, thus, after accounting for the lower density of the MASC, there is an increase in the stress rupture behavior of more than one Larson–Miller parameter. The density is approximately 25 pct less than that of third-generation single-crystal superalloys. The composite has an elastic modulus of ~140 GPa at 1200 °C.

Both the metallic and silicide phases are designed for improved high- temperature environmental resistance; however, further improvements in the high-temperature oxidation resistance are required. The DS MASC shows material losses at rates intermediate between the rapid losses of an older superalloy, such as IN 738, and the improved oxidation behavior of third-generation single-crystal superalloys, without any pesting behavior.

ACKNOWLEDGMENTS

The authors would like to thank D.J. Dalpe for the directional solidification, C. Canestraro for the tensile testing, W.J. Reeder for the fracture toughness measurements, and L.A. Peluso for the microprobe analyses. This research was partially sponsored by AFOSR under Contract No. F49620-93-C-0007 with Captain C.H. Ward as Program Manager. The authors are also grateful to Drs. M.G. Mendiratta and P.R. Subramanian, UES (Dayton, OH), and Dr. D.M. Dim-

iduk (AFWL) for providing the compression creep data, as well as very helpful discussions.

REFERENCES

1. R.W. Buckman, Jr.: in *Alloying*, J.L. Walter, M.R. Jackson, and C.T. Sims, eds., ASM INTERNATIONAL, Metals Park, OH, 1988, pp. 419-45.
2. M.R. Jackson, B.P. Bewlay, R.G. Rowe, D.W. Skelly, and H.A. Lipsitt: *J. of Met.*, 1996, vol. 48 (1), pp. 39-46.
3. P.R. Subramanian, M.G. Mendiratta, and D.M. Dimiduk: *J. Met.* 1996, vol. 48 (1), pp. 33-38.
4. P.R. Subramanian, M.G. Mendiratta, and D.M. Dimiduk: *Mater. Res. Soc. Symp. Proc.*, 1994, vol. 322, pp. 491-502.
5. D.M. Dimiduk, M.G. Mendiratta, and P.R. Subramanian: in *Structural Intermetallics*, R. Darolia, J.J. Lewandowski, C.T. Liu, P.L. Martin, D.B. Miracle, and M.V. Nathal eds., TMS, Warrendale, PA, 1993, pp. 619-30.
6. M.G. Mendiratta, J.J. Lewandowski, and D.M. Dimiduk: *Metall. Trans. A*, 1991, vol. 22A, pp. 1573-81.
7. M.G. Mendiratta and D.M. Dimiduk: *Metall. Trans. A*, 1993, vol. 24A, pp. 501-04.
8. J.D. Rigney, P.R. Singh, and J.J. Lewandowski: *Mater. Res. Soc. Symp. Proc.*, 1994, vol. 322, pp. 502-09.
9. I. Weiss, M. Thirukkonda, and R. Srinivasan: *Mater. Res. Soc. Symp. Proc.*, 1994, vol. 322, pp. 377-86.
10. B.P. Bewlay, H.A. Lipsitt, W.J. Reeder, M.R. Jackson, and J.A. Sutliff: in *Processing and Fabrication of Advanced Materials for High Temperature Applications III*, V.A. Ravi, T.S. Srivatsan, and J.J. Moore, eds. TMS Warrendale, PA, 1993, pp. 547-65.
11. M.R. Jackson, R.G. Rowe, and D.W. Skelly: GE-CRD. WRDC Contract No. F33615-91-C-5613, Annual Report, 1994.
12. M.R. Jackson and K.D. Jones: in *Refractory Metals Extraction, Processing and Applications*, K.C. Liddell, D.R. Sadoway, and R.G. Bautista, eds., TMS, Warrendale, PA, 1991, pp. 310-20.
13. K.-M. Chang, B.P. Bewlay, J.A. Sutliff, and M.R. Jackson: *J. Met.*, 1992, vol. 44 (6), p. 59.
14. *Standard Test Method for Plane-Strain Fracture Toughness of Metallic Materials*, ASTM STP E-399, ASTM, Philadelphia, PA, 1983, July, pp. 488-512.
15. *Standard Practice for R-Curve Determination*, ASTM STP E 561-94, ASTM, Philadelphia, PA, 1994.
16. B.P. Bewlay, M.R. Jackson, W.J. Reeder, and H.A. Lipsitt: *High Temperature Ordered Intermetallic Alloys VI*, Materials Research Society Symposia Proceedings, Materials Research Society, Pittsburgh, PA, 1994, vol. 364, pp. 943-48.
17. P.R. Subramanian, M.G. Mendiratta, G.A. Henshall, and M.J. Strum: *High Temperature Ordered Intermetallic Alloys VI*, Materials Research Society Symposia Proceedings, Materials Research Society, Pittsburgh, PA, 1994, vol. 364, pp. 937-42.
18. P.R. Subramanian, T.A. Parthasarathy, M.G. Mendiratta, and D.M. Dimiduk: *Scripta Metall.*, 1995, vol. 32 (8), pp. 1227-32.

Ti-Modified Niobium-Silicide Based Directionally Solidified In-Situ Composites

B.P. Bewlay, M.R. Jackson and H.A. Lipsitt

MRS Proceedings on High Temperature Ordered Intermetallic Alloys VII, 1997

Ti-MODIFIED NIOBIUM-SILICIDE BASED DIRECTIONALLY SOLIDIFIED IN-SITU COMPOSITES

B.P. BEWLAY[1], M.R. JACKSON[1] and H.A. LIPSITT[2]
[1]General Electric Company, Corporate Research and Development Center, Schenectady, NY 12301, [2] Department of Mechanical and Materials Engineering, Wright State University, Dayton, OH 45435.

ABSTRACT

This paper examines microstructure-property relationships in high-temperature directionally solidified (DS) in-situ composites based on Nb silicides, such as Nb_3Si and Nb_5Si_3. These in-situ composites are based on the Nb_3Si-Nb binary eutectic, and are alloyed with Ti. They were prepared using cold crucible Czochralski crystal growth. Ternary Nb-Ti-Si alloys with Ti concentrations from 9 to 45%, and Si concentrations from 10 to 25%, were directionally solidified to generate aligned two- and three-phase composites containing a Nb solid solution with Nb_3Si and Nb_5Si_3 silicides. Fracture toughness values generally greater than 10 MPa$\sqrt{m}$ were measured in these composites. For a given Si concentration, the fracture toughness of the Ti-containing composites was increased ~ 6 MPa$\sqrt{m}$ over that of the binary alloy composites. The effects of Si concentration, and a range of Nb:Ti ratios, on microstructure, phase equilibria, and fracture toughness were examined.

INTRODUCTION

The present paper describes the microstructures and properties that have been generated in intermetallic-matrix composites based on niobium silicides, such as Nb_3Si and Nb_5Si_3. In this arena, Nb-Si in-situ composites that consist of a Nb-based solid solution, (Nb), with Nb_3Si and/or Nb_5Si_3 silicides have displayed an attractive balance of high and low temperature mechanical properties [1-4]. From model binary Nb-Si alloys, whole families of ternary, quaternary and higher order alloys have been generated and studied [1-2]. The present paper describes the improvements in room temperature fracture properties that can be effected by Ti additions.

Although monolithic Nb_3Si and Nb_5Si_3 have very poor room temperature fracture toughness [1], composites consisting of these silicides with a Nb-based solid-solution have recently been shown to possess sufficient toughness for component damage tolerance [1-4]. The basis for these niobium-silicide based composites is the Nb-rich side of the Nb-Si binary phase diagram where there is a eutectic between Nb_3Si and (Nb) [1, 2]. This eutectic occurs at 1880°C and 18.2Si. All compositions in the present paper are given in atom per cent. There is also a eutectoid of the form $Nb_3Si \rightarrow$ (Nb) + Nb_5Si_3, but this has little effect on the directionally solidified (DS) microstructures, because of slow decomposition kinetics.

The addition of Ti to binary Nb-Si based two-phase in-situ composites has been studied previously because it improves the composite oxidation behavior [1, 4]. The aim of the present paper is to describe the effects of Ti additions to DS Nb-Nb_3Si composites on the microstructure and fracture toughness. Nb-Ti-Si phase equilibria have also been studied recently and have been reported in more detail separately [5]. In the present study, ternary Nb-Ti-Si alloys with Ti concentrations from 9 to 45%, and Si concentrations from 10 to 25%, were directionally solidified to generate aligned two- and three-phase composites containing a Nb solid solution with Nb_3Si and Nb_5Si_3 silicides. The effect of Nb:Ti ratio (at constant Si concentration) on the room temperature fracture toughness is described. The effect of Si concentration at constant and equal Nb:Ti ratio is also discussed, since this has an important effect on the volume fraction of metallic phase in the composite. Fracture toughness measurements of Nb-Ti-Si ternary alloys are compared with data from binary Nb-Si alloys of similar Si concentrations and phase volume fractions.

A schematic diagram of the projection of the liquidus surface of the metal-rich end of the Nb-Ti-Si phase diagram is shown in Figure 1 [2, 5]. In the present paper the Nb_5Si_3 with Ti in solid solution is referred to as $Nb(Ti)_5Si_3$, the Nb_3Si with Ti in solid solution is referred to as $(Nb,Ti)_3Si$, and the Nb with Ti and Si in solution is referred to as Nb(Ti, Si). There are two important features of this projection. The first is the eutectic trough emanating from the Nb-Si binary at Nb-18.2Si and 1880 °C. This eutectic trough descends towards the Ti-Ti_5Si_3 eutectic with increasing Ti concentration. The second is the L + $Nb(Ti)_5Si_3$ → $(Nb,Ti)_3Si$ peritectic ridge on the hypereutectic side of the eutectic valley. Both of these features dominate the microstructures of the Nb-Ti-Si composites examined in this study. The compositions investigated are also shown in Figure 1.

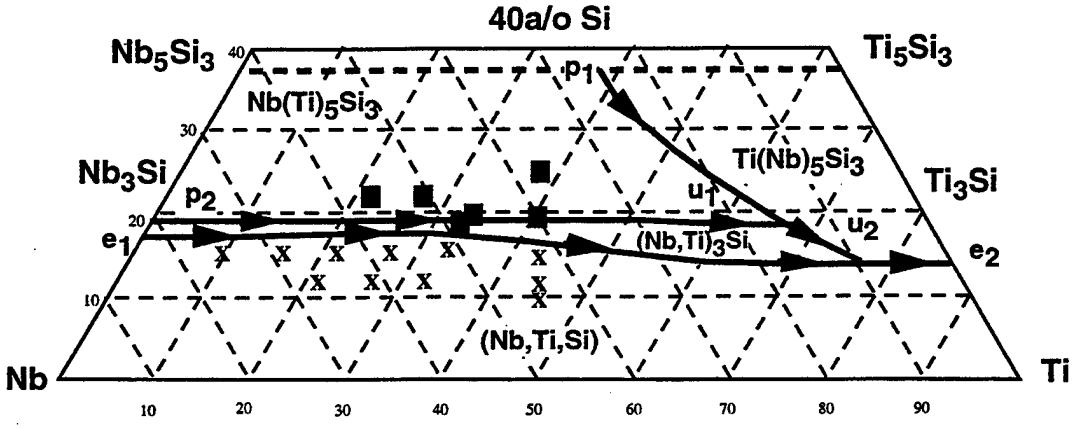


Figure 1. Schematic diagram of the projection of the liquidus surface of the Nb-Ti-Si ternary phase diagram (only the metal-rich end is shown). Compositions of the alloys that were directionally solidified are shown. Eutectic, peritectic and invariant reactions are described by **e**, **p** and **u** respectively.

EXPERIMENTAL

Directional Solidification

The starting Nb-Ti-Si alloys were prepared by triple melting high-purity elements (>99.9%) in a segmented water-cooled copper crucible [6]. Each alloy was triple melted in order to ensure homogeneity prior to directional solidification. This process has been described in further detail elsewhere [2, 6]. Samples with a diameter of ~10 mm and a length of ~75 mm were directionally solidified using this method. The melting and directional solidification operations were conducted sequentially in an atmosphere of ultra high-purity argon. Conventional microscopy and electron beam microprobe analysis were performed to characterize composite microstructures and phase chemistries. The compositions reported are those of the starting alloys, and they are listed in Table I.

Fracture Toughness Measurements

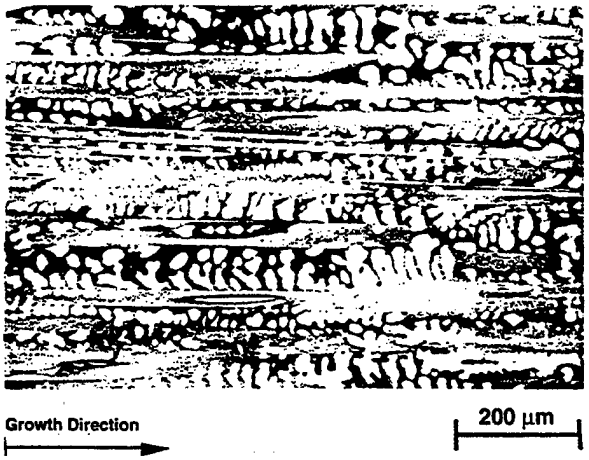
Single edge notched bending specimens (SENB) were prepared for room temperature fracture toughness measurements using electro-discharge machining (EDM). The SENB's were machined so that their longitudinal axis was parallel to the growth direction of the DS composite. Both monotonic loading experiments and R-curve measurements were performed using four point bending. Generally, two or three samples were tested for each composition. Toughness values which were determined from the monotonic loading experiments are reported as K_Q. K_{IC} values were obtained from R-curve measurements which were performed on separate samples using four point bending.

RESULTS AND DISCUSSION

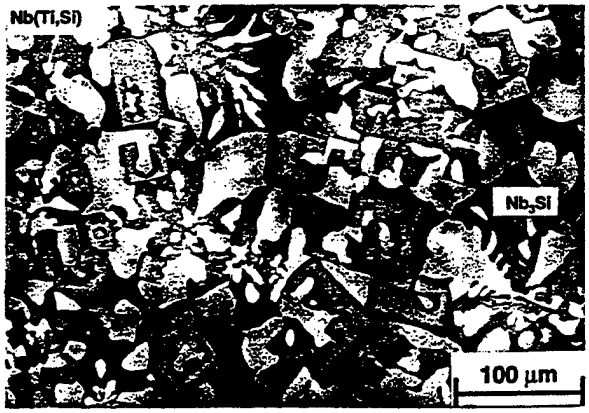
Microstructures of Nb-Ti-Si Alloys

Ternary Nb-Ti-Si alloys with Si concentrations of 10-16% and Ti concentrations of 9-45% were all on the metal-rich side of the eutectic valley. The microstructure consisted of Nb(Ti, Si) dendrites, together with large-scale, faceted $(Nb,Ti)_3Si$ dendrites. Typical microstructures (back scatter electron (BSE) images) of the longitudinal and transverse sections of the Nb-33Ti-16Si composition are shown in Figure 2 (a) and (b). The $(Nb,Ti)_3Si$ dendrites possessed the distinctive faceted morphology that has been reported previously in the hypereutectic binary Nb-Si alloys [5]. The Nb(Ti, Si) dendrites are the lighter phase in these BSE micrographs. Both the non-faceted metal dendrites and faceted $(Nb,Ti)_3Si$ dendrites were generally aligned with the growth direction. There was some variability in both the degree of alignment and the aspect ratios of the phases.

Bewley et al Sept 11



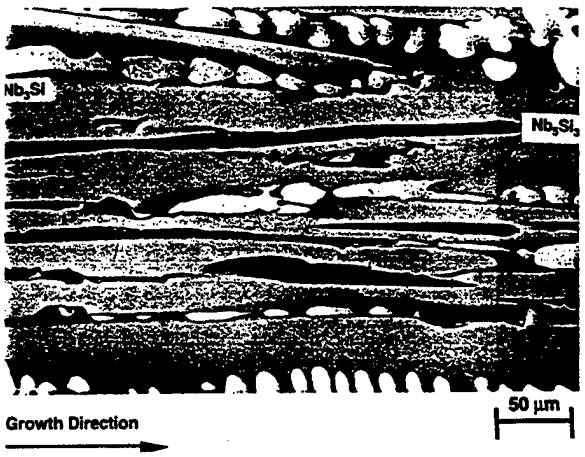
(a)



(b)

Figure 2. Microstructures (BSE images) of (a) the longitudinal section, and (b) the transverse section of a DS hypoeutectic Nb-33Ti-16Si Nb(Ti,Si)-$(Nb,Ti)_3Si$ composite.

Ternary alloys with Si compositions on the Si-rich side of the eutectic valley experienced the peritectic reaction, L + $Nb(Ti)_5Si_3 \rightarrow$ (Nb, $Ti)_3Si$. Composites from this alloy range possessed three phases; typical microstructures of the Nb-27Ti-22Si and Nb-21Ti-22Si composites are shown in Figures 3(a) and (b). First, there was a small volume fraction of primary $Nb(Ti)_5Si_3$ dendrites at the cores of the silicide dendrites; the $Nb(Ti)_5Si_3$ appeared as the dark phase in Figures 3. Second, there were faceted $(Nb,Ti)_3Si$ dendrites; these were the grey phase in Figures 3. Third, there were light Nb(Ti, Si) dendrites between the $(Nb,Ti)_3Si$ dendrites.



(a)



(b)

Figure 3. Microstructures (BSE images) of (a) the longitudinal section of a DS hypereutectic Nb-27Ti-22Si composite, and (b) the transverse section of a DS hypereutectic Nb-21Ti-22Si composite. These composites contain Nb(Ti,Si) (white phase), $(Nb,Ti)_3Si$ (grey phase) and a small volume fraction of $Nb(Ti)_5Si_3$ (dark phase).

Fracture Toughness : Effect of Nb:Ti Ratio

Room temperature fracture toughness measurements of the DS Nb-Ti-Si composites are shown in Table I and Figure 4. Fracture toughness data for binary Nb-Si composites with compositions in the range 10-22Si are also included in Table I. Typical errors in the fracture toughness measurements were ±1 MPa$\sqrt{m}$. Generally, Ti additions increased the composite toughness over that of the Nb-Si binary composites of the same Si concentration. For example, the toughness data of the Nb-33Ti-16Si, Nb-27Ti-16Si, and Nb-21Ti-16Si alloys were ~50% greater than that of the binary Nb-16Si composite. However, there was no systematic increase of fracture toughness with increasing Ti concentration; the toughness of the composite with 33Ti was essentially the same as that with 21Ti. This suggests that there may be a threshold Ti concentration above which the Ti additions have no further effect on the fracture toughness. The data for the Nb-9Ti-16Si suggests that the threshold may be close to that composition, but data from additional compositions are required. The toughness

improvement effected by Ti additions was also observed in the ternary alloys with 19, 20 and 22Si. However, for the 12Si compositions the composites from the ternary and binary alloys possessed similar fracture toughness values.

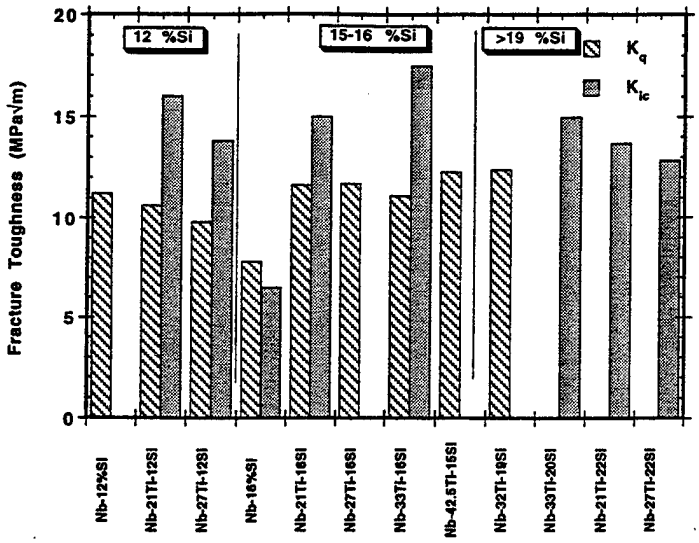


Figure 4. Room temperature fracture toughness of the ternary Nb-Ti-Si composites.

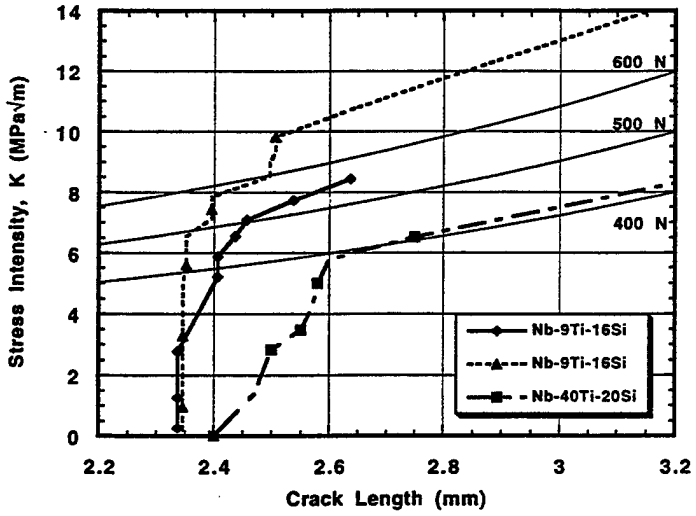


Figure 5. R-curve behavior of DS Nb-9Ti-16Si and Nb-40Ti-20Si composites, together with curves of stress intensity versus crack length at constant loads.

Table I : Room Temperature Fracture Toughness of DS Nb-Ti-Si and Nb-Si Composites (Nb(Ti,Si) is denoted M, $(Nb,Ti)_3Si$ is denoted M_3Si, and $Nb(Ti)_5Si_3$ is denoted M_5Si_3).

Composition (at%)	Constituent Phases	Fracture Toughness K_Q (MPa$\sqrt{m}$)	Fracture Toughness K_{IC} (MPa$\sqrt{m}$)
Nb-Ti-Si Alloys : Effect of Nb:Ti Ratio			
Nb-33Ti-20Si	M, M_3Si, M_5Si_3	10.8	15.0
Nb-32Ti-19Si	M, M_3Si, M_5Si_3	12.4	-
Nb-33Ti-16Si	M, M_3Si	11.1	17.5
Nb-27Ti-16Si	M, M_3Si	11.7	-
Nb-27Ti-12Si	M, M_3Si	9.8	13.8
Nb-27Ti-22Si	M, M_3Si, M_5Si_3	-	12.8
Nb-21Ti-16Si	M, M_3Si	11.6	15.0
Nb-21Ti-12Si	M, M_3Si	10.6	16.0
Nb-21Ti-22Si	M, M_3Si, M_5Si_3	12.1	12.9
Nb-15Ti-16Si	M, M_3Si	10.7	15.2
Nb-9Ti-16Si	M, M_3Si	-	9.6
Nb-Ti-Si Alloys : Effect of Si Concentration			
Nb-37.5Ti-25Si	M, M_3Si, M_5Si_3	--	10.4
Nb-40Ti-20Si	M, M_3Si, M_5Si_3	14.3	12.2
Nb-42.5Ti-15Si	M, M_3Si	12.3	-
Nb-45Ti-10Si	M, M_3Si	-	16.0
Nb-Si Alloys			
Nb-22Si	(Nb), Nb_3Si, Nb_5Si_3	8.5	-
Nb-20Si	(Nb), Nb_3Si, Nb_5Si_3	7.1	-
Nb-19Si	(Nb), Nb_3Si, Nb_5Si_3	6.7	9.0
Nb-18.2Si	(Nb), Nb_3Si	5.8	5.7
Nb-16Si	(Nb), Nb_3Si	7.8	6.5
Nb-14Si	(Nb), Nb_3Si	9.1	8.9
Nb-12Si	(Nb), Nb_3Si	11.2	7.0
Nb-10Si	(Nb), Nb_3Si	14.2	-

Figure 5 shows R-curves from the DS Nb-9Ti-16Si and DS Nb-40Ti-20Si composites. The form of these R-curves is similar to that reported previously in binary Nb-10Si in-situ composites, which displayed K_{IC} values of >20 MPa$\sqrt{m}$ in the extruded condition [3, 7]. All the DS Nb-Ti-Si composites exhibited R-curve behavior, that is they displayed stable crack growth characteristics. There appeared to be a lack of sensitivity of crack propagation behavior to the Si concentration. The K_{IC} values from R-curve measurements are included in Table I. Generally, the K_{IC} values from the R-curves are slightly higher than K_Q values from the monotonic loading experiments.

Bewlay et al 7 of 11

There are three possible reasons for the toughness increase generated by the addition of Ti to the binary Nb-Si composites. First, in the Nb-Ti-Si alloys the metallic phase exists only as large-scale Nb(Ti, Si) dendrites. However, in the binary alloy composites the metallic phase exists as a combination of fine-scale eutectic and large-scale dendritic morphologies. Thus, in the case of the Ti-modified composites the same volume fraction of metallic phase may provide more toughening. Second, fractography indicated that a larger volume fraction of the metal dendrites failed in a ductile manner in the Nb-Ti-Si composites (essentially 100%) than in the binary Nb-Si composites [1, 2]. Third, the Ti-modified metallic phase may have greater intrinsic ductility than the (Nb) in the binary composite. On this theme, fractography indicated that at test temperatures of –196 °C and above, the primary Nb(Ti,Si) dendrites failed by microvoid coalescence [2, 7, 8]. Microvoid coalescence has also been observed in binary (Nb) phases of Nb-Si composites, but only at higher temperatures [1, 7]. Typically at room temperature and below, the primary (Nb) dendrites of binary composites fail by a combination of cleavage in some areas and microvoid coalescence in other areas. However, in the case of the ternary alloy composites, the occurrence of microvoid coalescence and the fracture behavior are less sensitive to temperature. This suggests that the test temperature of –196 °C is above the ductile-brittle transition temperature (DBTT) of the Nb(Ti,Si) in the ternary composites, but below that of the (Nb) in the binary alloy composites. The implication is that Ti additions reduce the DBTT of the binary Nb solid solution. However, the DBTT of the Nb(Ti,Si) may still be above that of pure Nb, which is reported to be less than –200 °C [9].

Fracture Toughness : Effect of Si Concentration

The data in Table I indicate that increasing the Si concentration from 12 to 22 has little effect on the room temperature fracture toughness. For example, for the 21Ti compositions, the K_Q values were 10.6, 11.6, and 12.0 MPa$\sqrt{m}$ for the 12, 16, and 22Si compositions, respectively. Similarly, the K_{IC} values were 16.0, 15.0, and 12.6 MPa$\sqrt{m}$ for the 12, 16, and 22Si compositions, respectively. For the 27Ti, the K_Q and K_{IC} values are in the range 9.8-13.8 MPa$\sqrt{m}$ with no apparent trend with Si concentration. This apparent insensitivity of fracture toughness to Si concentration for the alloys discussed probably results from the inconsistent changes in the volume fraction of metallic phase with Si concentration [5]; for example, for the 21Ti-containing composite, increasing the Si concentration from 12 to 16% reduces the metal volume fraction from 54 to 35, but for the 27Ti-containing composite, the volume fraction of metal is only reduced from 49 to 41 for the same increase in Si concentration [2].

In the case of the binary Nb-Si in-situ composites, the toughness increased with decreasing Si concentration and increasing volume fraction of (Nb); decreasing the Si concentration from 18 to 10% increased the (Nb) volume fraction from ~0.35 to ~0.75 and the fracture toughness values from 6 to 14 MPa$\sqrt{m}$, respectively [2]. In the ternary alloys, the lower than expected reduction in volume fraction of metal with increasing Si concentration at high Ti concentrations is probably due to the form of the Nb(Ti, Si) solvus surface because the $(Nb,Ti)_3Si$ maintains the stoichiometric Si concentration, and the locus of the eutectic trough probably leads to only a small increase in the volume fraction of Nb(Ti,Si) with decreasing Si concentration. Thus, at constant Ti concentration (rather than constant and equal Nb:Ti ratio),

changing the Si concentration does not necessarily change the volume fraction of metal, as in the case of binary alloys, because the starting compositions do not necessarily move along a tie line between the phases.

In order to address this difficulty, the effect of Si concentration was examined at constant and equal Nb and Ti concentrations because these compositions are close to being on the same tie-line. Four compositions were selected at concentrations of 10, 15, 20, and 25 Si. The fracture toughness measurements of these composites are also shown in Table I, and indicate an increase of K_{IC} from 10.4 MPa$\sqrt{m}$ at Nb-37.5Ti-25Si to 16.0 MPa$\sqrt{m}$ at Nb-45Ti-10Si. This suggests similar sensitivities of K_{IC} to the volume fraction of metal for both the ternary and binary Nb-Si alloy composites. However, K_{IC} does not appear to reach a minimum at the eutectic trough (~15Si), as is the case for the binary Nb-18.2Si eutectic. A possible explanation for the absence of the toughness minimum is the microstructural scale of the metallic phases in the individual composites. In the Nb-Si binary eutectic, the majority of the toughening is provided only by the fine-scale eutectic (Nb), but in the ternary alloy that is close to the eutectic trough, there is a large volume fraction of the large-scale Nb(Ti,Si) to provide toughening. Thus, there are important differences in the toughening mechanisms that are active in the composites from the ternary and binary alloys.

Figure 6 shows the fracture surface of a Nb-27Ti-12Si composite. A large fraction of the Nb(Ti, Si) dendrites failed in a ductile manner, and the $(Nb,Ti)_3Si$ matrix failed by cleavage. Microvoid coalescence in the Nb(Ti, Si) dendrites was observed. Generally, Nb(Ti, Si) dendrite arms with dimensions as large as 50 μm failed in a ductile manner, and extensive microcracking of the $(Nb,Ti)_3Si$ silicide matrix was observed around the ruptured dendrites. The increase in the proportion of primary metallic dendrites that failed by microvoid coalescence in comparison with that observed in the binary alloys may be related to the higher ductility of the Nb(Ti, Si) dendrites, as compared to (Nb) dendrites. Ti may also modify the nature of the constraint of the metallic dendrites by the silicide. This could be related to both the scale of the metallic phase and the morphologies of both phases in the composite.

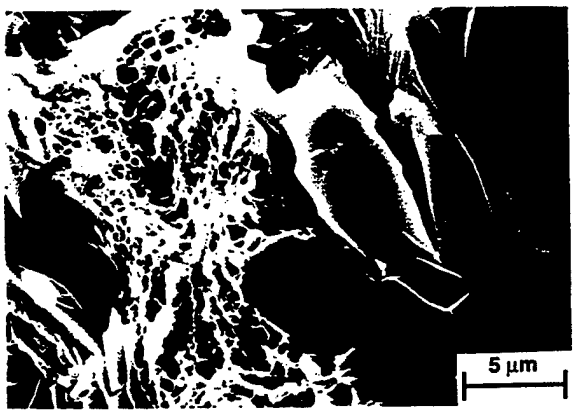
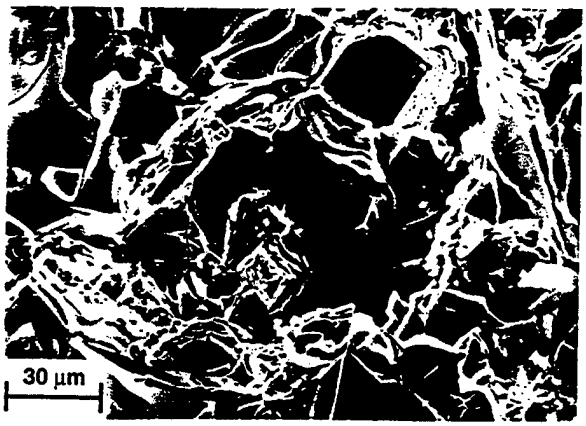
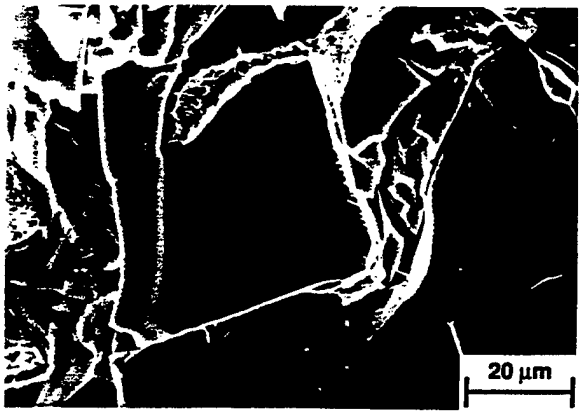


Figure 6. Fracture surface of a DS Nb-27Ti-12Si composite, showing microvoid coalescence in the metallic phase.

Fracture surfaces of a hypereutectic Nb-40Ti-20Si composite are shown at high and low magnifications in Figures 7(a) and (b). The fracture surfaces are similar to those of the hypoeutectic alloys. The fracture surfaces show extensive ductile failure of the metallic phase and cleavage of the faceted $(Nb,Ti)_3Si$ dendrites. Ductile failure of the fine-scale metallic phase between the $(Nb,Ti)_3Si$ dendrites is shown in Figure 7(b).



(a)



(b)

Figure 7. Fracture surfaces of the DS Nb-40Ti-20Si composite at (a) low and (b) high magnifications. Ductile failure of the Nb(Ti,Si) and cleavage of the $(Nb,Ti)_3Si$ were observed.

In several cases the crack paths were examined in samples that were unloaded mid-way through an R-curve experiment. These examinations revealed crack deflection and crack multiplication. The $(Nb,Ti)_3Si$ dendrites were observed to have caused crack deflection, and

this behavior probably provided additional toughening of the composite. Plastic deformation of the metallic dendrites which were intersected by the crack was also observed. Bridging events and crack blunting by metallic dendrites were also observed during the experiments.

CONCLUSIONS

The ternary Nb-Ti-Si composites investigated contained dendritic Nb(Ti,Si), $(Nb,Ti)_3Si$ and $Nb(Ti)_5Si_3$. Fracture toughness values greater than 10 MPa$\sqrt{m}$ were consistently measured using monotonic loading experiments. R-curve measurements provided K_{IC} values of >17 MPa$\sqrt{m}$. All the ternary Nb-Ti-Si alloy composites exhibited R-curve behavior at room temperature. Ti additions can increase composite fracture toughness values as much as 6 MPa$\sqrt{m}$ over composites from binary alloys with the same Si concentration. This is probably a result of a larger volume fraction of the metallic phase existing as large-scale dendrites, and also greater ductility of the metallic phase. Some sensitivity of the fracture toughness to the volume fraction of metallic phase was observed in the Nb-Ti-Si composites, but no toughness minimum of the form observed in binary Nb-Si eutectic composite was detected. In contrast with binary Nb-Si in-situ composites, a broad range of Nb-Ti-Si compositions can be accommodated without compromising fracture toughness.

ACKNOWLEDGMENTS

The authors would like to acknowledge W.J. Reeder for the fracture toughness measurements and D.J. Dalpe for the directional solidification experiments. This research was partially funded by AFOSR under contract #F49620-93-C-0007 with Capt. C.H. Ward as Program Manager.

REFERENCES

[1] P.R. Subramanian, M.G. Mendiratta, and D.M. Dimiduk, MRS Symp. Proc. **322**, 491-502 (1994).

[2] B.P. Bewlay, M.R. Jackson, W.J. Reeder, and H.A. Lipsitt, MRS Symp. Proc. **364**, 943-948 (1995).

[3] P.R. Subramanian, M.G. Mendiratta, and D.M. Dimiduk, JOM ***48*** **(1)**, 33-37 (1996).

[4] M.R. Jackson, B.P. Bewlay, R.G. Rowe, D.W. Skelly, and H.A. Lipsitt, JOM ***48*** **(1)**, 38 -46 (1996).

[5] B.P. Bewlay, M.R. Jackson and H.A. Lipsitt, Accepted for publication in the Journal of Phase Equilibria, October 1996.

[6] K-M. Chang, B.P. Bewlay, J. A. Sutliff and M.R. Jackson, JOM **44 (6)**, 59-65 (1992).

[7] J.D. Rigney, P.R. Singh, and J.J. Lewandowski, MRS Symp. Proc. **322**, 502-509 (1994).

[8] B.P. Bewlay, M.R. Jackson and H.A. Lipsitt, accepted for publication in Metall. and Mater. Trans., August 1996.

[9] A.G. Imgram, E.S. Bartlett and H.R Ogden, Trans. Met. Soc. AIME **227**, 131 (1963).

Bewlay et al 11 of 11

Refractory Metal-Intermetallic In-Situ Composites for Aircraft Engines

B.P. Bewlay, J.J. Lewandowski amd M.R. Jackson

J. of Metals 49, 1997

JOM
A publication of The Minerals, Metals & Materials Society

Refractory Metal-Intermetallic In-Situ Composites for Aircraft Engines

B.P. Bewlay, J.J. Lewandowksi, and M.R. Jackson

Reprinted from JOM, *Vol. 49, No. 8, August 1997, p. 44–45; p. 67.*

Refractory Metal-Intermetallic In-Situ Composites for Aircraft Engines

B.P. Bewlay, J.J. Lewandowksi, and M.R. Jackson

Author's Note: All compositions are presented in atomic percent.

There has been substantial progress in the development of properties in high-temperature in-situ composites during the last five years. For example, fracture-toughness values in excess of 20 MPa $\sqrt{m}$ have been reported in silicide-based composites toughened by niobium-based metallic solid solutions. These composites also have oxidation resistances and rupture lives comparable to those of single-crystal superalloys for temperatures up to 1,150°C. In this article, fracture toughness, oxidation characteristics, high-temperature mechanical behavior, and low-temperature fatigue properties of refractory metal-intermetallic composites (RMICs) are described and compared to aircraft-engine fundamental material property goals for the next millennium. Further avenues toward the pursuit of these goals are outlined.

INTRODUCTION

The use of refractory metals in the hottest parts of aircraft engines has been a recurring subject[1-3] in recent decades. Research efforts have focused on niobium and molybdenum as the bases for alloy families. However, there are two principal deficiencies of these systems at high temperature: inadequate mechanical behavior and catastrophic oxidation resistance.[3]

In the past ten years, the potential of intermetallic compounds with low densities, high elastic moduli, and high melting ranges[4-12] has been explored. The inherent poor toughness of monolithic intermetallics is such that aircraft-engine applications are not possible. However, a combination of intermetallic materials with metallic second phases can provide composites with promising toughness.[2,4-10]

The most promising composites rely on ductile metals to provide room-temperature toughening and on intermetallics to provide the high-temperature strength. In this arena, Nb-Si in-situ composites that consist of a niobium-based solid solution with Nb_5Si and/or Nb_5Si_3 silicides have great potential because of their attractive balance of high- and low-temperature mechanical properties.[4-9] Long-term chemical and morphological stability at temperatures up to 1,500°C are important characteristics of refractory metal-intermetallic composites (RMICs). Recent research has examined in further detail the toughening mechanisms in this family of composites.[13-18]

Several processing routes have been used to generate niobium-based RMICs, including extrusion,[6-9] directional solidification,[11,19,20,21] arc casting,[7,9] and physical vapor deposition.[22] Each process provides a characteristic microstructure with specific phase dimensions and different phase chemistries. For example, alternate layers of metal and intermetallic[22] can be generated with sputter-deposited composites; the laminate thickness and volume fraction of each phase can be controlled by time of exposure to the source and/or deposition rate. In addition, aligned microstructures have been generated using directional solidification. Directionally solidified (DS) ingots have been produced in a levitation melting facility at rates of 0.5–15 mm/min. for a broad range of niobium-based RMICs with melting points up to ~2,300°C.[19,20] The ingots can be machined into airfoil configurations, as is the practice for oxide-dispersion strengthened (ODS) nickel alloys.

High-pressure turbine blade temperatures have increased by 125°C in the past 30 years as a result of both controlled solidification to form single-crystal components and the use of substantial additions of Re, W, Ta, and Mo. The niobium-based RMICs[1,2,4,6,11] have a much higher potential application temperature because of their dramatically increased melting temperatures. The increased temperature capability is ~200°C compared to current single-crystal superalloys. The density goal for RMICs is less than 7 g/cm³ (25% lower than third-generation single-crystal superalloys—9.1 g/cm³);[2] a density of 7.35 g/cm³ has already been demonstrated for a niobium-based RMIC.[11]

FUNDAMENTAL PROPERTY REQUIREMENTS

Fracture Toughness

Minimum toughness is required to provide damage tolerance in order to make components that can survive the final engine assembly and tolerate impact loading in service from events such as foreign-object damage. Fracture toughness for a series of niobium-based RMICs is shown in Figure 1.[1,2,11] A more highly alloyed niobium-silicide RMIC has a toughness greater than 20 MPa $\sqrt{m}$.[11] This has also been demonstrated recently in a wider range of systems. R-curve measurements show that the resistance to crack growth increases with increasing crack length, an indication that crack growth occurs in a stable manner. More detailed explanations of toughness measurements and toughening mechanisms have been published elsewhere.[8,9,13-18]

For the further development of niobium-silicide-based composites, fracture toughness no longer appears to be a major barrier, provided that further alloying additions do not reduce the present toughness levels. Work is al-

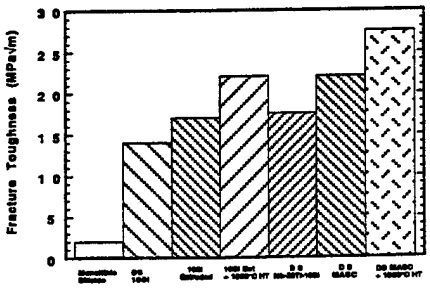


Figure 1. A comparison of room-temperature fracture toughness data for a range of RMICs, including those from binary Nb-10Si alloys in the DS, extruded, and extruded plus heat-treated condition. Heat treatment was performed for 100 hours at 1,500°C. Data from a more complex metal and silicide composite (MASC) that was directionally solidified from Nb-24.7Ti-16Si-8.2Hf-2.0Cr-1.9 Al are also shown.

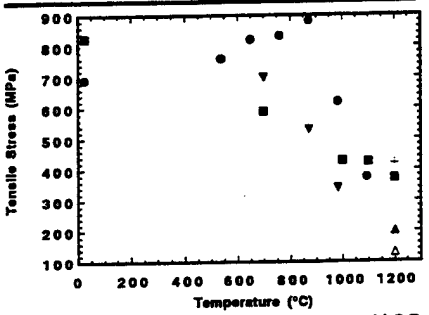


Figure 2. The tensile strength of the DS MASC as a function of temperature, showing the improvement of high-temperature strength over other intermetallic systems and NiTaC-13.[2] Literature data for the tensile strength of NiAl modified with hafnium[23] and bending strengths of monolithic $MoSi_2$ and $MoSi_2$-reinforced with 30% SiC[24] are also shown. ■—MASC; △—$Cr_2(Nb)$-60Nb; ●—NiTaC-13; ▲—$MoSi_2$; +—$MoSi_2$-30SiC; ▼—NiAl-Hf.

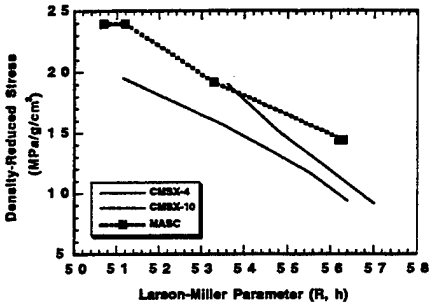


Figure 3. Density-normalized stress rupture behavior of a DS RMIC compared to that of second- and third-generation single-crystal nickel-based superalloys[2,11] in Larson-Miller plots (C = 20). Stress rupture testing was performed in argon.

ready in progress to address this issue. The levels of toughness measured, the crack-growth characteristics, and the ability to perform common cutting, grinding, and machining tasks with standard practices suggest that further gains in toughness are unnecessary at present.

High-Temperature Strength and Creep Behavior

Tensile stress is shown in Figure 2 as a function of temperature for a niobium-silicide-based DS RMIC and other intermetallic systems.[11] The DS RMIC displays excellent tensile strength at elevated temperatures in comparison with other intermetallic systems and NiTaC-13. In comparison with monolithic niobium-based alloys of compositions similar to the metallic phase within the DS RMIC, there is a substantial increase in the yield strength at 1,200°C[10] (55 MPa versus 350 MPa).[25,26]

The creep-rupture behavior of the DS RMIC is shown in the form of a Larson-Miller plot in Figure 3, where it is compared to a current generation single-crystal nickel-based superalloy (CMSX4) and an advanced generation single-crystal nickel-based superalloy (CMSX10).[2] The specific creep-rupture behavior indicates an increase of more than one Larson-Miller parameter in specific rupture performance that results from the substantial reduction in density of the DS RMIC compared to the third-generation single-crystal superalloy. However, the rupture performance required of the RMICs will be well beyond any behavior observed to date. Ultimately, a further increase of up to three Larson-Miller parameters is probably required. This goal may be reached through avenues such as increasing the silicide volume fraction and alloying both the metal and the silicide phases in the RMIC.

Fatigue Properties

There has been relatively little work on evaluating the performance of RMICs under cyclic loading conditions. Early work[27,28] on a variety of intermetallics toughened with niobium alloys revealed that while significant toughness improvements were obtained under monotonic loading conditions, such improvements were not necessarily realized when under cyclic loading conditions. In those cases, the fatigue-crack-growth resistance of the tough composite was often not substantially better than that of the brittle monolithic intermetallic, and the Paris law coefficients reported were similar to those of ceramics.

Initial results on Nb-Si in-situ composites are more encouraging.[29] Figure 4 shows fatigue-crack-growth data obtained for a range of RMICs, including the cast/extruded Nb-10Si composite,[6-9,29] a DS more complex metal and silicide composite (MASC),[11] and monolithic cast/extruded Nb-1Si.[29] The fatigue performance of monolithic Nb-1Si is significantly better than that of β-TiNb[28] and suggests that one source of the improved fatigue performance of such RMICs relates to the good fatigue characteristics of the metallic constituent in these systems. As a result, the threshold values are substantially higher than for other intermetallic systems,[27,28] and the Paris law coefficients are close to those of metallic systems.

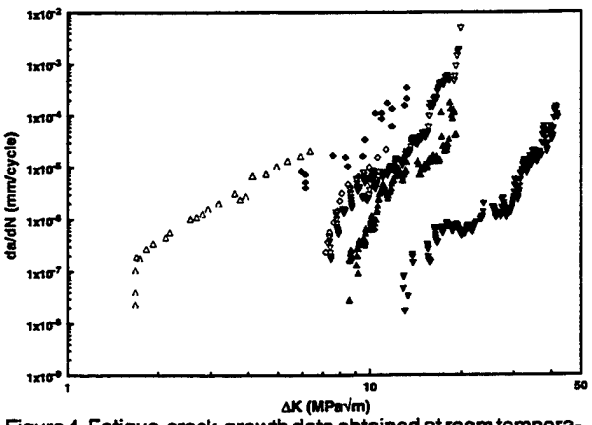


Figure 4. Fatigue-crack-growth data obtained at room temperature and a R ratio of 0.1 for a number of advanced monolithic and in-situ composites containing intermetallic materials. The threshold values are higher than for other intermetallic systems, and the Paris law coefficients are close to those of monolithic metallic systems. ▼—Nb-Si(ss) 135 μm grain size;[29] ▽—Nb-10Si arc cast/extruded/HT composite;[29] ▲—DS MASC;[29] △—β-TiNb;[28] ◆—Ti-47Al-2Nb-2Cr-0.2B;[30] ◇—Ti-48Al-2Nb-2Cr.[31]

Initial fatigue data have been obtained at room temperature to determine baseline properties; elevated temperature testing is also required, although earlier data on the toughness of RMICs did not show a significant change in toughness at temperatures up to 500°C. Also included for comparison in Figure 4 is recent fatigue-crack-growth data obtained for several titanium aluminides that are being considered for a variety of aerospace applications.[30,31] Although these materials are not being considered for the same applications as the RMICs, the preliminary fatigue-crack-growth data compare favorably.

Finally, the envisioned applications of RMICs will subject the structure to a variety of thermal-fatigue cycles. The thermal-expansion mismatch between the metal and the intermetallics over the envisioned application temperature range is relatively small.[2,4,11] Thus, it is expected that thermal ratcheting between the phases will be negligible, and the interface between composite phases will not suffer excess stress during thermal cycling.

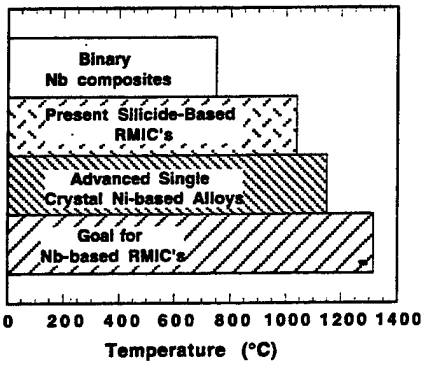


Figure 5. A comparison of the temperature capability for less than 25 μm of metal loss in 100 hours for initial and more recent niobium-silicide-based RMICs, together with the estimated goal. The temperature capability of an advanced single-crystal nickel-based superalloy is also presented in the figure for comparison.

Oxidation Resistance

Oxidation at 1,000°C and 1,200°C has been investigated for a number of niobium-based intermetallics and RMICs.[1,2,6,24] A comparison of the oxidation performances of a DS RMIC[11] and nickel-based superalloys is shown in Figure 5.[2] Many of the niobium-based silicide and Laves phase-based RMICs have oxidation resistances comparable to less-resistant superalloys such as IN738 at these temperatures. Subramanian et al.[1,6] have reported even better oxidation for some silicide RMICs. The DS RMIC[11] shows material losses at rates between the rapid losses of an older superalloy like IN 738 and the improved oxidation behavior of third-generation single-crystal superalloys.

Advanced superalloys can survive with surface temperatures of 1,150°C with metal losses of ~25 μm/100 h. Figure 5 indicates this same goal behavior for RMIC losses with surface temperatures of 1,315°C. Even if the goal

(Continued on page 67.)

Bewlay *(Continued from page 45.)*
of less than 25 μm loss/100 h at 1,315°C is achieved, the RMICs will need protective coatings, just like current superalloys. Considerable research has also been performed on molybdenum-based silicide coatings alloyed with tungsten, boron, and germanium,[32,33] which have shown promise of providing protection to 1,400°C. A likely coating goal for niobium-based RMICs is, therefore, ~10 μm loss/100 h in 1,315°C oxidation, extrapolating the behavior for coatings on superalloys at 1,150°C.

The use of niobium-based RMICs at surface temperatures much greater than 1,315°C will require further substantial increases in oxidation resistance for both the RMIC and the protective coatings into a temperature regime beyond the demonstrated protective capability of SiO_2-based scales. The oxidation resistance of both the RMIC and coating must be improved substantially from the levels of the presently coated RMIC system to be useful in turbine-blade applications. In this arena, further alloying studies of both the base composite and the coating are required.

CONCLUSIONS

High-temperature RMICs are attractive candidates for future aircraft engine components; a balance of the four fundamental properties examined in this article is required in these applications. Advanced airfoil designs probably require up to a 300°C improvement in the oxidation properties and an increase in the stress-rupture behavior of up to three Larson-Miller parameters from the present levels. Fracture toughness should not be a major barrier to the application of niobium-based RMICs. The achievement of the property goals will require adjusting phase chemistries to improve properties of both metallic and intermetallic phases, as well as optimizing architecture through advanced processing.

ACKNOWLEDGEMENTS

The authors thank D.J. Dalpe, W. Zinsser, and E.H. Hearn for their contributions to the experimental work. This research was partially sponsored by the Air Force Office of Scientific Research under contract number F49620-96-C-0022 (BPB and MRJ) and number F49620-96-1-0164 (JJL) with C.H. Ward as program manager. The authors are also grateful to M.G. Mendiratta and P.R. Subramanian, UES; D.M. Dimiduk, Wright Laboratory; and H.A. Lipsitt for very helpful discussions.

References

1. P.R. Subramanian, M.G. Mendiratta, and D.M. Dimiduk, *JOM*, 48 (1) (1996), p. 33.
2. M.R. Jackson et al, *JOM*, 48 (1) (1996), p. 39.
3. R.W. Buckman, Jr., "Alloying of Refractory Metals," *Alloying*, ed. J.L. Walter, M.R. Jackson, and C.T. Sims (Metals Park, OH: ASM, 1988), pp. 419–445.
4. D.M. Dimiduk, M.G. Mendiratta, and P.R. Subramanian, *Structural Intermetallics*, ed. R. Darolia et al. (Warrendale, PA: TMS, 1993), pp. 619–630.
5. D.M. Dimiduk, D.B. Miracle, and C.H. Ward, *Mat Sci & Tech*, 8 (1992), pp. 367–375.
6. P.R. Subramanian, M.G. Mendiratta, and D.M. Dimiduk, *Mat. Res. Soc. Symp. Proc.*, 322 (Pittsburgh, PA: MRS, 1994), pp. 491–502.
7. M.G. Mendiratta and D.M. Dimiduk, *Mat. Res. Soc. Symp. Proc.*, 133 (Pittsburgh, PA: MRS, 1989), p. 441.
8. M.G. Mendiratta, J.J. Lewandowski, and D.M. Dimiduk, *Metall. Trans.*, 22A (1991), pp. 1573–1581.
9. M.G. Mendiratta and D.M. Dimiduk, *Metall. Trans. A*, 24A (1993), pp. 501–504.
10. I. Weiss, M. Thirukkonda, and R. Srinivasan, in Ref. 6, pp. 377–386.
11. B.P. Bewlay, M.R. Jackson, and H.A. Lipsitt, *Metall. Trans.*, 27A (1996), pp. 3801–3808.
12. B.P. Bewlay et al., *Mat. Res. Soc. Symp. Proc.*, 364 (Pittsburgh, PA: MRS, 1995), pp. 943–948.
13. J.D. Rigney, P.M. Singh, and J.J. Lewandowski, *JOM*, 44 (8) (1992), pp. 36–41.
14. J.D. Rigney and J.J. Lewandowski, *Metall. Trans. A.*, 27A (1996), pp. 3292–3306.
15. A. Samant and J.J. Lewandowski, *Metall. Trans. A*, 28A (1997), pp. 389–399.
16. M.G. Mendiratta et al., *Metall. Trans. A*, 26A (1995), pp. 1767–1777.
17. J. Kajuch, J.W. Short, and J.J. Lewandowski, *Acta Metall. et Mater.*, 43 (1995), pp. 1955–1967.
18. J. Kajuch, J.D. Rigney, and J.J. Lewandowski, *Mat. Sci. & Engrg.*, A155 (1992), pp. 59–65.
19. B.P. Bewlay et al., *Processing and Fabrication of Advanced Materials for High Temperature Applications III*, ed. V.A. Ravi, T.S. Srivatsan, and J.J. Moore (Warrendale, PA: TMS, 1994), pp. 547–565.
20. K-M. Chang et al., *JOM*, 44 (6) (1992), p. 59.
21. G.A. Henshall et al., in Ref. 12, pp. 937–942.
22. R.G. Rowe et al., in Ref. 6, pp. 461–472.
23. R. Darolia, in Ref. 4, pp. 495–499.
24. R Aikin, in Ref. 4, pp. 665–798.
25. M.R. Jackson and K.D. Jones, *Refractory Metals Extraction, Processing and Applications*, ed. K.C. Liddell, D.R. Sadoway, and R.G. Bautista (Warrendale, PA: TMS, 1991), pp. 311–320.
26. M.R. Jackson, R.G. Rowe, and D.W. Skelly, in Ref. 12, pp. 1339–1344.
27. K.T. Rao, W.O. Soboyejo, and R.O. Ritchie, *Metall. Trans. A*, 23A (1993), pp. 95–104.
28. K.T. Rao, G.R. Odette, and R.O. Ritchie, *Acta Metall. et Mater.*, 42 (3) (1994), pp. 893–911.
29. W. Zinsser and J.J. Lewandowski, unpublished research, Case Western Reserve University (1997).
30. K.S. Chan and D.S. Shih, *Metall. Trans. A*, 28A (1997), pp. 79–90.
31. J.M. Larsen et al., *Gamma Titanium Aluminides*, ed. Y.W. Kim, R. Wagner, and M. Yamaguchi (Warrendale, PA: TMS, 1995), pp. 821–834.
32. B.V. Cockeram, Ph.D. thesis, Ohio State University (1994).
33. A. Mueller et al., *J. Electrochem. Soc.*, 139 (1992), pp. 1266–1275.

ABOUT THE AUTHORS

B.P. Bewlay earned his Ph.D. in metallurgy and materials science at Oxford University in 1987. He is currently a metallurgist at General Electric Corporate R&D. Dr. Bewlay is also a member of TMS.

J.J. Lewandowski earned his Ph.D. in metallurgical engineering and materials science at Carnegie Mellon University in 1983. He is currently director of the Mechanical Characterization Facility and professor of materials science and engineering at Case Western University. Dr. Lewandowski is also a member of TMS.

M.R. Jackson earned his Ph.D. in metallurgy and materials engineering at Lehigh University in 1971. He is currently a metallurgist at General Electric Corporate R&D. Dr. Jackson is also a member of TMS.

For more information, contact B.P. Bewlay, General Electric Corporate R&D, Schenectady, New York 12301; (518) 387-6121; fax (518) 387-5576.

Creep Mechanisms in High-Temperature In-Situ Composites

Annual Report: August 1996

Creep Mechanisms in High-Temperature In-Situ Composites

(Contract Number : FQ8671-96005872306/AS)

Research Contributors

Dr. Bernard P. Bewlay, GE-CRD, Staff Metallurgist
Dr. Melvin R. Jackson, GE-CRD, Staff Metallurgist
Prof. Harry A. Lipsitt, Wright State University
Dr. John A. Sutliff, GE-CRD, Staff Materials Scientist

1.0. Objectives

The primary objective of this research is to investigate high-temperature creep and low temperature toughening mechanisms in high-strength directionally solidified (DS) in-situ composites with melting temperatures above 1700°C. The composites under investigation consist of Nb-based silicides, such as Nb_3Si and Nb_5Si_3, and are toughened by a Nb-based solid solution. Composites investigated have been directionally solidified from model binary Nb-Si, ternary Nb-Ti-Si alloys, and higher order alloys. Significant toughening enhancements have already been demonstrated in these DS in-situ composites. The present study is focused upon investigating those mechanisms which can lead to enhancement of creep properties of these materials.

2.0 Approach

Five independent approaches are being adopted to investigate creep mechanisms in this family of composites. These include the effect of the metallic phase strength, the role of the volume fraction of intermetallic, the effect of increasing the creep performance of the intermetallic, the effect of texture, and the effect of dispersoids, such as carbides and nitrides, on the creep/interfacial behavior. These separate approaches are described in more detail below.

2.1 Solid Solution and Dispersoid Strengthening of the Metallic Phase

Solid solution strengthening is being performed by the addition of refractory and high modulus elements, such as W, Ta, or Mo, and dispersion strengthening is being affected by refractory MC carbides and/or nitrides (e.g. HfN, ZrN). The aim is to generate a dispersion of fine precipitates, rather than coarse particles. The phases may also be dispersed in the intermetallic.

2.2 *Volume Fraction of Intermetallic*

The volume fraction of metallic phase in the composite is critical for toughening, but the effect of the same on creep behavior is less well defined. As a parallel effort with the present study, parametric modeling is being developed. Previous modeling has indicated that the creep properties of these composites are insensitive to volume fraction of metallic phase. Thus, questions such as, "Do the properties of the silicide phase dominate the creep behavior of the composite?" and if so, "How sensitive is the creep rate/damage accumulation in the composite to the properties of the metallic phase?", will be addressed. The degree to which the volume fraction of intermetallic can be adjusted to balance creep behavior with room temperature fracture toughness will be studied.

2.3 *Intermetallic Creep Mechanisms*

Mechanisms of enhancing the creep behavior of intermetallics, such as alloying to produce higher order silicides, are also being explored. According to recent work by Subramanian et al, creep deformation in Nb_5Si_3 is controlled by diffusion in the Nb_5Si_3 phase. This suggests that the addition of elements with a large atomic size, such as Re, W, Mo, and Hf, to the intermetallic may be effective in improving the intrinsic creep performance of the composite.

2.4 *Control of Texture of the Composite Phases*

Texture measurements are being performed to fully interpret the fracture and other orientation-dependent mechanical behavior of these composites. Examination of creep data of binary Nb-16%Si composites indicates an order of magnitude difference in the creep rate for specific orientations.

2.5 *Effect of Dispersoids on Creep and Interfacial Behavior*

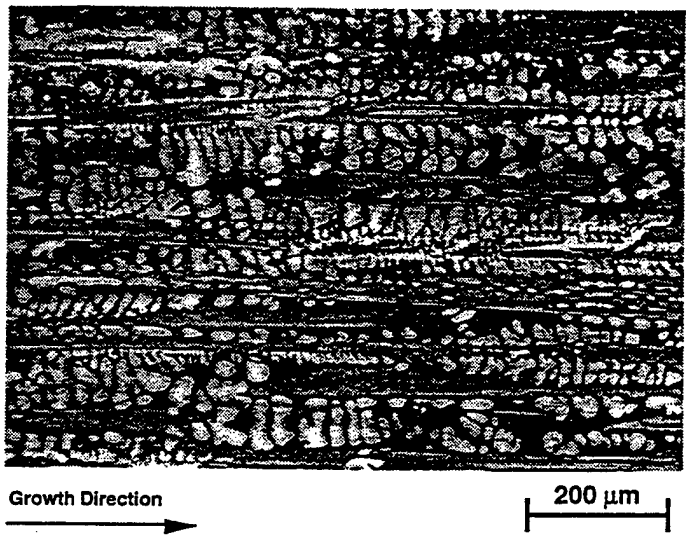
Microstructures of creep tested extruded composites suggest a relatively undeformed rotation of silicide phases within the surrounding metallic phase. This indicates that the interphase boundaries are not resistant to relative motion. Small amounts of refractory dispersoids, such as carbides or nitrides, will be added to reduce the mobility of the interphase boundaries in DS composites, and examine the effect on damage mechanisms and rupture life of the composite.

3.0 Progress and Status of Effort

The present program on creep mechanisms in high-temperature in-situ composites was initiated in June 96. The findings of the previous studies of toughening mechanisms in high-temperature DS composites have been reported in the annual, and final AFOSR

reports and published in refereed journals and conference proceedings. Only a brief summary is included in the present report.

DS composites have been prepared from binary Nb-Si, ternary Nb-Si-Ti alloys, and quaternary Nb-Hf-Si-Ti and Nb-Si-Ti-Al alloys. Preliminary studies of a more complex Nb-Ti-Si-Hf-Cr-Al in-situ composite have also been conducted. Toughening mechanisms have been investigated in all of these composites. These composites consist of high-strength, Nb-based M_3Si and $M_5(Si,Al)_3$ silicides together with a modest strength, high-toughness Nb-based metallic phase with volume fractions from 30 to 70%. Typical composite microstructures of a DS Nb(Ti,Si)-Nb composite are shown in Figures 1(a) and 1(b).



(a)

(b)

Figure 1. Typical scanning electron micrographs (BSE images) of (a) the longitudinal, and (b) the transverse sections of a DS Nb-33Ti-16Si composite. The structure consists of non-faceted Nb(Ti, Si) dendrites, together with faceted $(Nb,Ti)_3Si$ dendrites.

In the DS condition these composites can have room temperature fracture toughness values of >20 MPa$\sqrt{m}$, which is a substantial improvement over monolithic intermetallics. R-curve measurements have also been performed for a wide range of these composites. Typical R-curves are shown in Figure 2, and indicate stable crack propagation. A range of alloy compositions has been employed to determine the effect of the different silicide phases and their volume fractions on the fracture behavior of the DS in-situ composites.

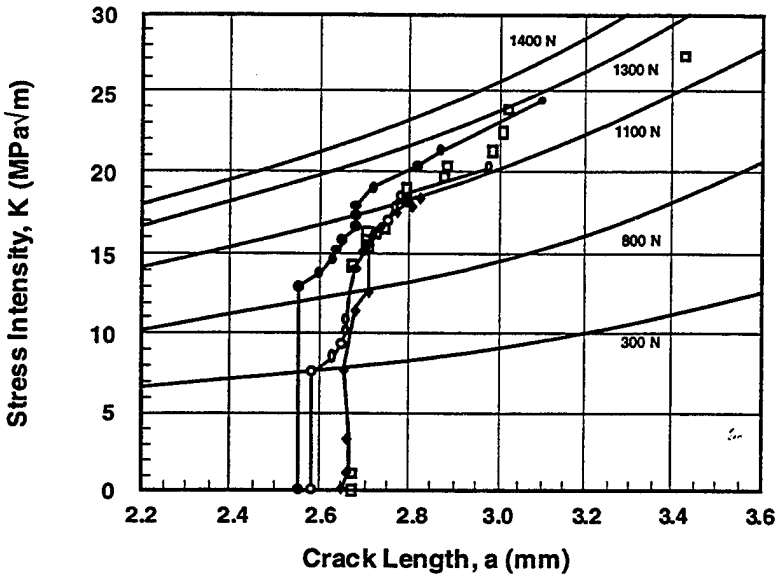


Figure 2. R-curves of DS composites which were generated from an alloy of composition Nb-24.7Ti-8.2Hf-2.0Cr-1.9Al-16.0Si. Data from four separate bending bars are shown.

The ternary Nb-Ti-Si composites that were investigated contained dendrites of Nb(Ti, Si) and $(Nb,Ti)_3Si$. Fracture toughness values greater than 10 MPa$\sqrt{m}$ were consistently measured in the DS in-situ composites. The Ti-containing composites showed slightly improved fracture toughness values (up to 6 MPa$\sqrt{m}$) over binary alloys with the same Si concentration. More significant toughness improvements were measured in the compositions from higher order alloys. The fracture toughness values of ternary alloys in the as-DS condition were similar to those in the arc-cast and thermo-mechanically processed (extruded) condition.

Elevated temperature properties of these composites are also critical. High-temperature tensile strength and creep behavior have also been examined in selected silicide-based composites; tensile strengths of >350 MPa at 1200 °C and creep rupture lives of >500 h at 1100 °C (100 MPa) have been measured. Creep rupture behavior of advanced Nb-Ti - Hf-Cr-Al-Si composites has been measured. Typically, the behavior is similar to an advanced generation single-crystal Ni-based superalloy, CMSX10. After accounting for the reduced density of these composites in comparison with CMSX10, the density-

reduced stress rupture behavior of these early silicide-based composites shows a significant improvement over current generation advanced Ni-based superalloys, as shown in Figure 3.

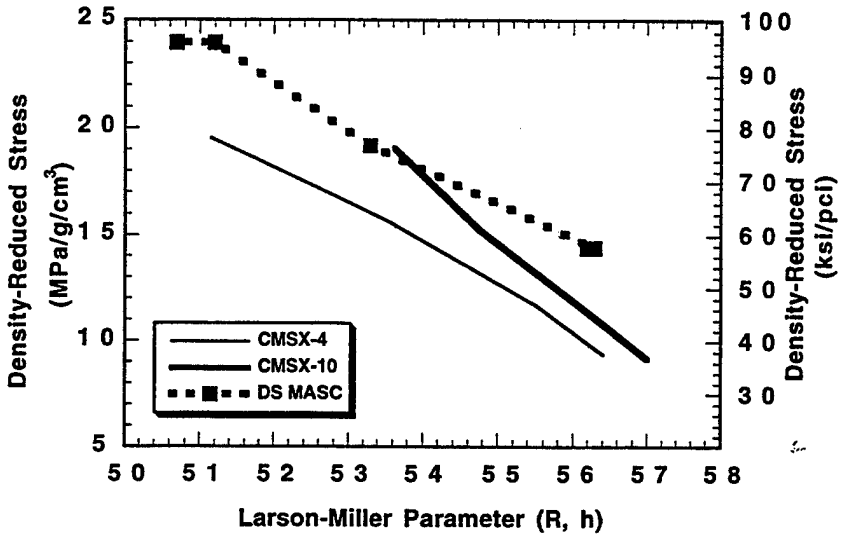


Figure 3. Stress rupture behavior of a DS in-situ composite generated from an alloy of composition Nb-24.7Ti-8.2Hf-2.0Cr-1.9Al-16.0Si. The stress rupture behavior is compared to that of second and third-generation single crystal Ni-based superalloys using a Larson-Miller plot (C=20), where the temperature-time parameter is plotted against the rupture stress/composite density. Stress rupture testing was performed in argon.

4.0 Publications

The following articles have been published during the last year of research in the area of the present contract :

1. B.P. Bewlay and M.R. Jackson, "The Effect of Hf and Ti Additions on Microstructure and Properties of Cr_2Nb-Nb In-Situ Composites", Journal of Materials Research, Vol 11(8), pp.1-6, 1996.

2. B.P. Bewlay, W.J. Reeder, H.A. Lipsitt, M.R. Jackson and J.A. Sutliff, "Toughness Enhancements In Intermetallic-Based Composites : Processing and Properties", to be published in *Processing and Fabrication of Advanced Materials for High Temperature Applications V*", Ed T.S. Srivatsan and J.J. Moore, TMS Publications, 1996.

3. M.R. Jackson, B.P. Bewlay, R.G. Rowe, D.W. Skelly and H.A. Lipsitt, Journal of Metals 46 (1), pp. 39-44, 1996.

4. G. A. Henshall, M. J. Strum, B. P. Bewlay and J. A. Sutliff, "Ductile-Phase Toughening in V-V_3Si In-Situ Composites", Submitted to Metall. Trans., August 1996.

5. J. A. Sutliff and B. P. Bewlay, "Orientation Imaging of a Nb-Ti-Si DS In-Situ Composite", to be published in the *Proceedings of the 54rd Annual Meeting of the Microscopy Society of America*," Editors : G.W. Bailey and A.J. Garret-Reed, San Francisco Press, 1995.

6. B.P. Bewlay, M.R. Jackson and H.A. Lipsitt, "The Balance of Mechanical and Environmental Properties of a Multi-Element Niobium-Niobium Silicide Based In-Situ Composite", accepted for publication in Metall. Trans., August 1996.

7. "The Nb-Ti-Si Ternary Phase Diagram : Evaluation of Liquid-Solid Phase Equilibria in Nb and Ti-Rich Alloys", B.P. Bewlay, M.R. Jackson and H.A. Lipsitt, Submitted to the Journal of Phase Equilibria, July 1996.

8. "Directionally Solidified High Temperature In-Situ Composites," B.P. Bewlay, H.A. Lipsitt, M.R. Jackson, Accepted for publication in the proceedings of the Engineering Foundation Conference on "Processing and Design Issues in High Temperature Materials", Davos, Switzerland, 1996.

Primary Contact :

Bernard P. Bewlay,
GE Corporate Research and Development
PO Box 8
Schenectady
NY12301

Tel : 518 387 6121

The Effect of Hf and Ti Additions on Microstructure and Properties of Cr_2Nb-Nb In-Situ Composites

B.P. Bewlay and M.R. Jackson

Journal of Materials Research, August 1996

The effect of Hf and Ti additions on microstructure and properties of Cr_2Nb–Nb *in situ* composites

B. P. Bewlay and M. R. Jackson
General Electric Company, Corporate Research and Development Center, P. O. Box 8, Schenectady, New York 12301

(Received 8 December 1995; accepted 15 March 1996)

The present paper describes the effect of Hf and Ti additions on the microstructures and mechanical properties of two-phase composites based on the Cr_2Nb–Nb eutectic. The microstructures of directionally solidified *in situ* composites containing 50–70% by volume of the Laves phase Cr_2Nb which was modified with Hf (7.5–9.2%) and Ti (16.5–26%) are described. Partitioning of Hf and Ti between the two phases is discussed using microprobe and EDS results. The tensile properties at 1100 and 1200 °C are described and compared with those of an analogous niobium silicide-based composite. The $Cr_2(Nb)$–(Nb) composite tensile yield strengths at 1200 °C were increased over that of monolithic Cr_2Nb to ~130 MPa. However, at 1200 °C the yield strengths of the silicide-based composites were approximately twice those of the $Cr_2(Nb)$–(Nb) composites.

I. INTRODUCTION

The Laves phase Cr_2Nb has been studied previously because of its potential for high temperature structural applications.[1–6] Cr_2Nb has a high melting temperature (1770 °C), a lower density (7.7 g/cc) than nickel (8.9 g/cc), promising oxidation resistance,[1–3] and a wide homogeneity range. Although Cr_2Nb has promising creep and tensile strengths,[1,2] it has very poor room temperature fracture toughness.[6] There have been previous attempts to improve the fracture toughness by generating two-phase composites with Nb and Cr,[6–8] but these have met with limited success.

In an attempt to improve the balance of high and low temperature properties of directionally solidified (DS) *in situ* composites based on the Cr_2Nb–Nb, eutectic alloys with Hf and Ti were prepared. Hf and Ti additions to the Cr_2Nb–Nb composites were considered for three reasons. First, Hf and Ti additions to both the Laves phase Cr_2Nb and the Nb-based solid solution, (Nb), improve the composite oxidation resistance.[9] Second, Ti additions to (Nb) improve the ductility,[9] and therefore in a composite there is the possibility of the (Nb) providing greater toughness. Third, Hf is a solid solution strengthener for the (Nb).[9] A silicide composite with ~50% of a Nb-based metallic phase was found to possess a room temperature fracture toughness of >20 MPa$\sqrt{m}$ and a strength of >350 MPa at 1200 °C.[10] By appropriate alloy selection, composites of $Cr_2(Nb)$ and (Nb) with metal volume fractions approaching 50% were designed to evaluate toughening and strengthening in Laves phase-based intermetallic composites.

In earlier studies of Laves phase based intermetallic composites,[11] alloys of Nb, Ti, and Cr with small additions of Hf and Al were evaluated; an alloy of 24% Nb, 20.4% Ti, 2.9% Al, 44.2% Cr, and 8.5% Hf was evaluated for phase chemistries. All compositions in the present paper are given in atom percent. Phase compositions are shown in Table I for the metallic and Laves phases of composites heat-treated at 1200 and 1400 °C. The concentration of Al in the metallic phase was approximately 2.5 times that in the Laves phase (~4.5% vs ~2%). Partitioning of Hf was approximately two times greater in the Laves phase than in the metal (~10% vs ~5%). The Cr concentration of the Laves phase was ~58% at 1200 °C and 57% at 1400 °C, while in the metal it was ~13% after heat treatment at 1200 °C, and ~18.7% at 1400 °C. Partitioning of Ti was stronger to the metal phase than to the Laves phase, and vice versa for Nb. Since the metallic phase strength and oxidation resistance is improved by Hf additions of 4–5%,[11] the overall composite alloy chemistry was chosen in order to provide ~5% Hf in the metallic phase and ~10% Hf in the Laves phase.

Four Laves phase-based alloys were selected in order to generate *in situ* composites by directional solidification; these compositions are shown in Table II. The first of these was the Cr_2Nb–Nb eutectic,[12–14] and the second of these was the same eutectic with Hf and Ti substituted for Nb by using a composition of Nb–16.5Ti–52.5Cr–9.5Hf. These chemistries were selected using the approximate phase chemistries shown in Table I and accounting for the absence of Al. The Cr_2Nb–Nb eutectic was preferred to the Cr_2Nb–Cr eutectic since it offers greater toughening potential.[1,6] The Hf-and Ti-modified Cr_2Nb–Nb eutectic was designed to possess ~70% by volume of the Laves phase, which is similar to the Cr_2Nb–Nb eutectic.[5] The Hf-and Ti-modified Laves phase is denoted by $Cr_2(Nb)$ in the

 © 1996 Materials Research Society

TABLE I. Phase compositions for the metallic and Laves phases in Cr_2Nb-based composites heat-treated at 1200 and 1400 °C for 50 h in vacuum.

Phase	Temperature (°C)	Nb	Ti	Cr	Hf	Al
$Cr_2(Nb)$	1200 °C	17.4	12.5	57.9	10.3	1.9
$Cr_2(Nb)$	1400 °C	18.2	12.8	56.6	10.4	2.0
(Nb)	1200 °C	38.9	38.7	13.0	4.6	4.8
(Nb)	1400 °C	36.6	35.6	18.7	5.1	4.0

present paper since Hf and Ti generally substitute for Nb on the Nb sublattice, although there may be some substitution on the Cr sublattice (the defect level is unknown). In addition there is some solid solubility of Cr, Hf, and Ti in the Nb-based metallic phase, and it is therefore described by (Nb) in the present paper. The third and fourth compositions investigated are also shown in Table II; they were selected in an attempt to generate total volume fractions of Laves phase of 60% and 50% in the composite; the compositions of these alloys are Nb–21.2Ti–44.5Cr–8.4 Hf and Nb–26Ti–36.5Cr–7.5Hf, respectively. These compositions with smaller volume fractions of the Laves phase were investigated because they were expected to possess greater room temperature fracture toughness than the eutectics.

The Cr–Nb phase diagram contains two eutectics between Cr_2Nb and the constituent individual refractory metals.[12–15] The temperature and composition of the Cr_2Nb–Nb eutectic are 1650 ± 50 °C and ~50% Nb, respectively. The eutectic contains a volume fraction of 30% Nb.[5] There are also two eutectics in the Cr–Hf phase diagram, Cr_2Hf–Hf and Cr_2Hf–Cr.[15] In this respect, there are similarities between the Cr–Nb and Cr–Hf phase equilibria. Cr_2Ti is also a Laves phase, but it forms from a bcc Cr–Ti solid solution rather than on solidification, as is the case for Cr_2Nb and Cr_2Hf. There has been little previous work on the Nb–Cr–Ti–Hf quaternary phase equilibria.

Cr_2Nb has the cubic C15 crystal structure at temperatures below 1585 °C and a hexagonal C14 structure at temperatures between 1625 and 1585 °C.[8,12–15] Cr_2Hf has a melting temperature of 1825 °C, and it also possesses low temperature, C15, and high temperature, C14, crystal structures. The low temperature C15 phase is stable from room temperature to 1335 °C, and C14 is stable from 1335 °C to the melting temperature. Thus, Cr_2Hf is very similar to Cr_2Nb, and they can be considered to be essentially isomorphous, leading to $Cr_2(Nb, Hf)$. However, in the Cr_2Nb case the C14–C15 transition is considered to be very fast,[5,8] and in Cr_2Hf the same transition has been reported to be very slow.[17] It would be expected, however, that Hf additions to Cr_2Nb would affect the C14–C15 transition temperature and the transformation kinetics. The effect of Ti is less clear.

There has been some recent work on the mechanical properties of Cr_2Nb–Nb composites. Anton and Shah[2] reported an order of magnitude increase in the creep resistance of the Cr_2Nb–Nb eutectic over the monolithic Cr_2Nb. Takeyama and Liu[7] also investigated toughening in Cr_2Nb-based composites. Davidson and Chan[16] have measured the room temperature fracture toughness of stoichiometric Cr_2Nb as 1.4 $MPa\sqrt{m}$.[16] There has also been some work on strength and toughness in binary Cr_2Hf–Hf composites.[17,18] However, there has been little previous work on composites from quaternary Nb–Cr–Hf–Ti alloys.

The aim of the present paper is to describe the microstructure and tensile properties of Hf and Ti-modified DS Cr_2Nb–Nb *in situ* composites. Phase volume fractions, morphologies, and chemistries are described using SEM and EDS results. The tensile properties are compared with those of a niobium silicide-based composite. The silicide-based composite displays a better balance of high and low temperature mechanical properties[10] than the Laves phase composites, as will be described.

II. EXPERIMENTAL

Cr–Nb–Hf–Ti alloys of the compositions shown in Table II were directionally solidified using Czochralski cold crucible crystal growth.[5,6] Each alloy was prepared from a 50 g charge of high purity (99.99%) elements using cold crucible induction levitation melting. Each alloy was triple melted in order to ensure homogeneity prior to directional solidification. The liquidus temperature of each alloy was estimated using a two wavelength optical pyrometer which was calibrated against the melting temperature of pure Ti. These temperatures are included in Table II. Directional solidification was performed by

TABLE II. Tensile properties of Ti and Hf modified $Cr_2(Nb)$–(Nb) composites.

Composition	Liquidus temperature (°C)	Phases	Volume fraction of Laves phases	Tensile stress (MPa) temperature: YS: UTS	Elongation (%)
Nb–50Cr	1650	Cr_2Nb, Nb	0.70	Test bars too brittle to machine	···
Nb–16.5Ti–52.5Cr–9.2Hf	1550	$Cr_2(Nb)$, (Nb)	0.76	Test bars too brittle to machine	···
Nb–21.2Ti–44.5Cr–8.4Hf	1563	$Cr_2(Nb)$, (Nb)	0.60	1200 °C: 132: ···	0
Nb–26Ti–36.5Cr–7.5Hf	1514	$Cr_2(Nb)$, (Nb)	0.53	1200 °C: 120: 153	56%
				1100 °C: 210: 265	2.2%

lowering a seed of the same alloy into the induction-levitated melt and withdrawing the seed at a constant preselected rate of 0.5–3 mm/min. The growth rate was adjusted to generate samples of sufficient diameter for tensile testing bars (~5 mm). Several samples were grown of each composition in order to generate enough bars for tensile testing.

Melting and directional solidification were performed under an atmosphere of ultrahigh purity argon in a chamber which had been evacuated to 10^{-5} Torr prior to backfilling. Atmosphere control during directional solidification of this class of materials is very important because the mechanical properties and phase equilibria are sensitive to interstitials, such as nitrogen, oxygen, and hydrogen. The compositions given in Table II are the selected alloy compositions. However, mass losses after directional solidification were measured in each case and were found to be <0.1%; therefore, the compositions given in Table II were assumed to be the actual compositions.

The tensile specimens were prepared by centerless grinding of the as-DS samples so that the growth direction was parallel to the axis of the tensile bar. Tensile testing was performed in a vacuum of $\sim 10^{-4}$ Torr using a 2 mm diameter gauge, 10.7 mm long uniform diameter button-head tensile specimen, and strain rate of 8×10^{-4} s^{-1}.

III. RESULTS AND DISCUSSION

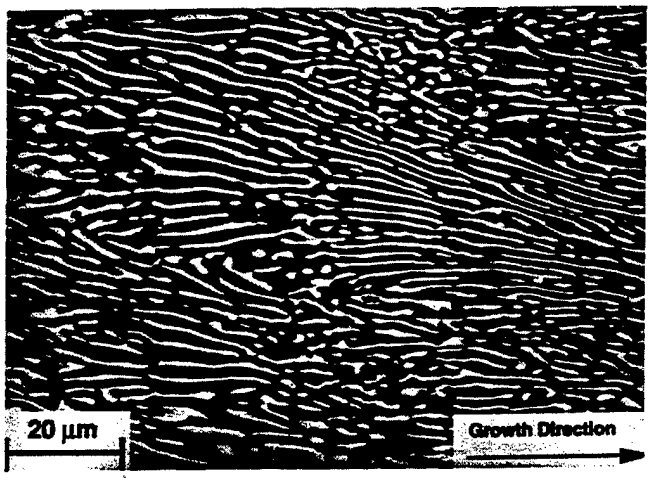
A. Composite microstructures

1. Cr_2Nb–30% Nb eutectic: Cr–50% Nb

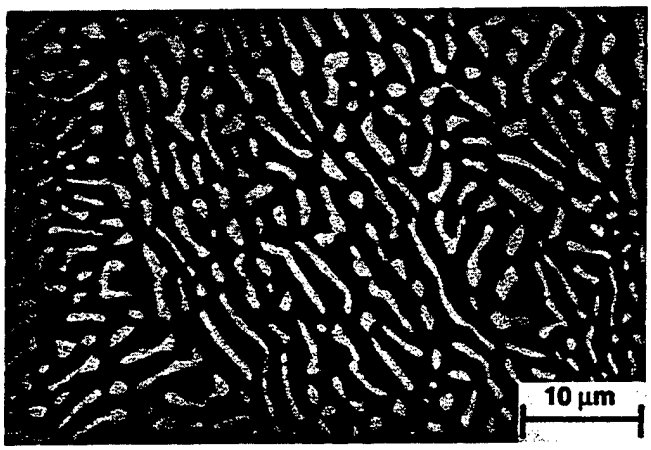
The microstructure of the DS Cr_2Nb–Nb eutectic grown at 1 mm/min is shown in Fig. 1. The micrographs shown in Fig. 1 and subsequent figures were obtained using back scatter electron imaging (BSE); the Nb is the light phase and the Cr_2Nb is the dark phase. The transverse and longitudinal sections show Nb rods and ribbons (0.5 ± 0.1 μm) aligned with the growth direction in a Cr_2Nb matrix. The aspect ratio of the Nb rods was typically ~10, and there was a degree of misalignment with the growth direction under these directional solidification conditions. The eutectic grew with a cellular rather than a planar front, as indicated by cell boundaries in the transverse and longitudinal sections. Interphase orientation relationships in this eutectic have been reported previously[5]; the Cr_2Nb has the C15 structure with the [110] parallel to the growth direction.

2. Cr_2(Nb)–30% (Nb): Nb–16.5Ti–52.5Cr–9.2Hf

Microstructures of the quaternary alloy based on the Cr_2(Nb)–(Nb) eutectic are shown in Fig. 2. BSE imaging and EDS showed the Cr_2(Nb) as the light phase and the (Nb) as the dark phase. The Laves phase Cr_2(Nb) contains more Hf and less Ti than the darker



(a)



(b)

FIG. 1. Longitudinal (a) and transverse (b) sections of the DS Cr_2Nb–Nb eutectic grown at 1 mm/min (BSE images).

metallic phase, and for this reason it gave brighter contrast than the (Nb), even though it contained more Cr and less Nb than the (Nb). Unlike the case of the binary composite, where partitioning between the phases is well specified and clear definition of the phases is possible using BSE in imaging, in the quaternary composites different partitioning of the elements occurs, and it is not possible to rely on BSE imaging alone. In addition, Hf is the heaviest element, and it partitions to both phases in the approximate ratio of 2:1 for the Laves phase versus the metal, and as a result it is more difficult to obtain BSE contrast between the two phases than for the case of the Cr_2Nb–Nb composite.

The transverse section shown in Fig. 2(b) indicates that the structure consisted of coarse laths which appeared to be arranged in grains with a width of ~300 μm. The width of the (Nb) laths was ~20 μm and the width of the Cr_2(Nb) laths was ~60 μm. There was some evidence of faceting of the individual phases, but it was not strong. The grains appeared to have

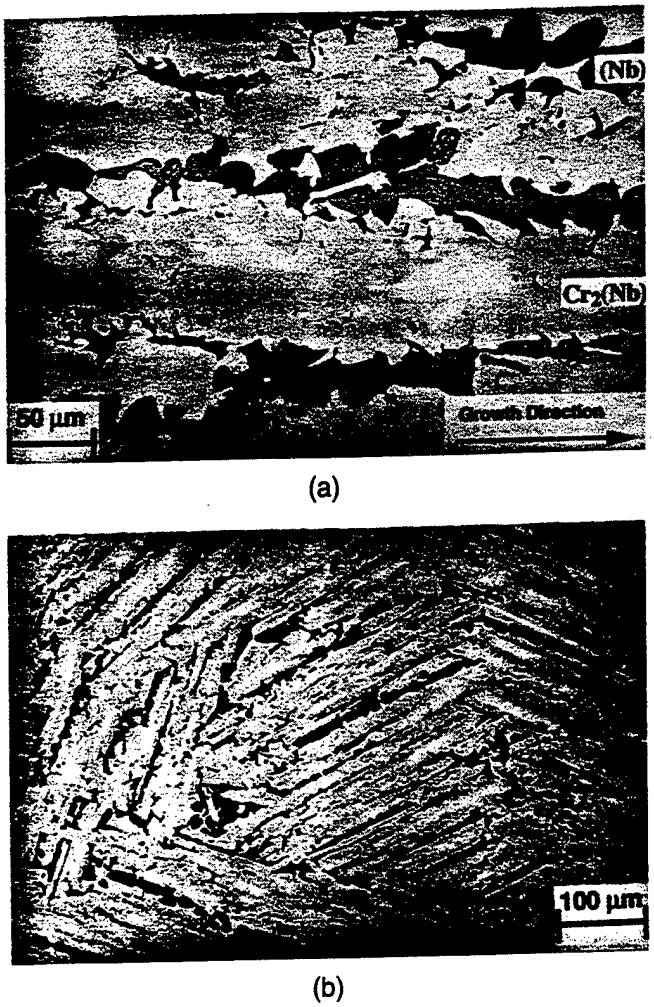


FIG. 2. Typical scanning electron micrographs (BSE images) of the longitudinal (a) and transverse (b) sections of DS $Cr_2(Nb)$–30%(Nb) (Nb–16.5Ti–52.5Cr–9.2Hf) composite.

an approximately hexagonal morphology; this may be related to the texture of the $Cr_2(Nb)$, but this type of grain morphology was not observed in the case of the binary eutectic. There may have been some precipitation within the (Nb) phase; this has been examined in more detail previously.[16] The measured volume fraction of (Nb) was 0.24, slightly smaller than that originally predicted for the selected alloy chemistry.

The longitudinal section shown in Fig. 2(a) showed some alignment of the $Cr_2(Nb)$ with the growth direction, but the (Nb) was not so well aligned, and it did not possess a high degree of continuity. The hexagonal lath-type nature of the microstructure which was visible in the transverse sections was not so evident in the longitudinal sections.

There was no evidence of any dendrites in the structure. The (Nb) did not exist as fibers, ribbons, or lamellae, as was the case for the binary eutectic. The microstructure of the $Cr_2(Nb)$–(Nb) eutectic was quite different from that of the Cr_2Nb–Nb binary eutectic, even though there were similar volume fractions of metallic phase in each case. The microstructure had a much coarser scale than that of the binary eutectic.

In both the longitudinal and transverse sections, lighter regions were observed at the centers of the $Cr_2(Nb)$ laths. This brighter contrast was probably due to the Hf enrichment and/or Ti depletion at the centers of the laths. Cr_2Hf is essentially isomorphous with Cr_2Nb, but it has higher melting temperature (1825 °C), which is probably consistent with it being observed at the cores of the laths. The crystal structure observed in DS Cr_2Nb was C15. An important question is how the substitution of Hf and Ti both individually and together effect the stability of the Laves phases. This question is not addressed in the present paper. However, since the C15 was observed in the binary DS Cr_2Nb, it was assumed that the $Cr_2(Nb)$ Laves phase also possessed the C15 structure. The melting temperatures of the three quaternary alloys investigated are shown in Table II; these temperatures are relatively low, being in the range 1514–1563 °C.

3. $Cr_2(Nb)$–40% (Nb): Nb–21.2Ti–44.5Cr–8.4Hf

The microstructure of the $Cr_2(Nb)$–40% (Nb) composite was similar to that of the $Cr_2(Nb)$–30% (Nb) composite in both its scale and morphology, but there was a smaller volume fraction of $Cr_2(Nb)$. EDS spectra of the $Cr_2(Nb)$ and (Nb) phases indicated that Hf and Ti partitioning between the phases was similar to that observed for the 30% (Nb) composite. The alignment of the structure with the growth direction was not strong and some precipitation within the (Nb) phase was observed.

4. $Cr_2(Nb)$–50% (Nb): Nb–26.0Ti–36.5Cr–7.5Hf

The microstructure of the transverse section of the $Cr_2(Nb)$–50% (Nb) composite is shown in Fig. 3. The microstructure had a similar morphology to that of the quaternary $Cr_2(Nb)$ eutectic-based composition, but it had a larger volume fraction of (Nb), and as a result the (Nb) "laths" had a greater degree of continuity. No primary (Nb) dendrites were observed. Again in this structure the (Nb) was the dark phase and the $Cr_2(Nb)$ was the light phase, as identified using EDS. The (Nb) was dark because it contained less Hf and more Ti than the $Cr_2(Nb)$, even though it contained more Nb and less Cr than the Laves phase. Some precipitation within the (Nb) was observed. The measured volume fraction of (Nb) was 0.47, very close to that originally predicted for the selected alloy chemistry. The EDS spectra for the individual (Nb) and $Cr_2(Nb)$ phases of the composites were similar for each of the three quaternary compositions, indicating that the change in

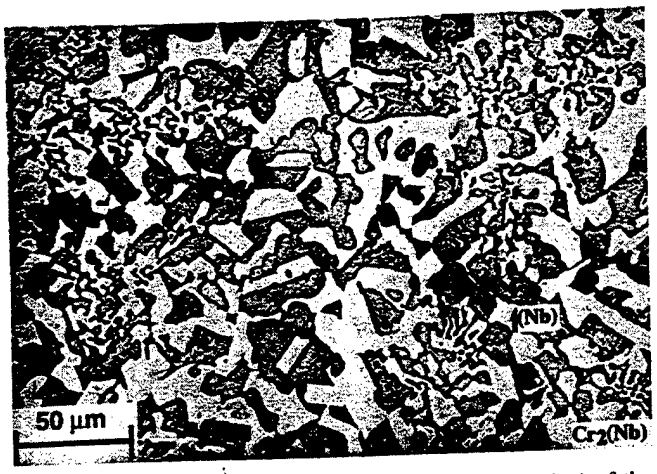


FIG. 3. Typical scanning electron micrograph (BSE imaging) of the transverse section of DS $Cr_2(Nb)$–50%(Nb) Nb–26.0Ti–36.5Cr–7.5Hf

composition adjusted the phase volume fractions and not the individual phase chemistries.

There are four important differences between the microstructure shown in Fig. 3 and those shown in Figs. 2(a) and 2(b) for the $Cr_2(Nb)$–(Nb) eutectic. First, the hexagonal-type grains observed in the $Cr_2(Nb)$–(Nb) eutectic were not observed in the 50% (Nb) composite. This could have been due to the lower volume fraction of $Cr_2(Nb)$, and the texture associated with it. Second, the volume fraction of metal is higher. Third, the widths of the (Nb) and $Cr_2(Nb)$ phases are 13 ± 4 μm and 12 ± 4 μm, the $Cr_2(Nb)$ being finer than in the $Cr_2(Nb)$–(Nb) eutectic. Fourth, the longitudinal section did not show particularly good alignment of either phase, and as a result the microstructure of the longitudinal section was quite similar to that of the transverse section, and is thus not shown.

At lower magnification than shown in Fig. 3, it was observed that solidification occurred with a cellular front, the scale of the (Nb) being coarser at the cell boundaries. In some cases the cell boundaries were 40–50 μm wide. The cells had a diameter of ~150 μm. In the longitudinal section these cell boundary regions were visible but not well aligned with the growth direction. Of the three quaternary alloys investigated, this was the only one that displayed evidence of cellular solidification.

B. Mechanical properties

1. Room temperature fracture toughness

Fracture toughness measurements of the composites from the quaternary alloys were not performed, but given the difficulty of preparing tensile specimens, as indicated in Table II, it can be assumed that the toughness is low, probably less that 10 MPa$\sqrt{m}$. The room temperature fracture toughness of the binary Laves phase, Cr_2Nb, has been reported as 1.4 MPa$\sqrt{m}$,[16] and fracture toughness values of the Cr_2Nb–Nb and Cr_2Nb–Cr binary eutectics have been reported as 3.1 MPa$\sqrt{m}$, and 3.6 MPa$\sqrt{m}$,[6] respectively. Kumar and Miracle[17] reported a room temperature fracture toughness of 7 MPa$\sqrt{m}$ for Cr–6.5% Hf (Cr_2Hf–Cr). Ravichandran *et al.*[18] also reported room temperature fracture toughness values of 5–7 MPa$\sqrt{m}$ for extruded hypoeutectic Cr–6.5% Hf and eutectic Cr_2Hf–composites.

It was not possible to grind tensile bars from the Cr_2Nb–Nb binary eutectics, or the $Cr_2(Nb)$–(Nb) eutectic modified with Hf and Ti. Thus, the room temperature fracture toughness of the $Cr_2(Nb)$–(Nb) eutectic was probably not much different from that of the binary eutectic, even though the (Nb) phase width in the quaternary alloy is larger than the Nb rod width in the binary eutectic; previously it has been shown that increasing the scale of the toughening phase can lead to an increase in the toughness.[6] However, it was possible to machine tensile bars from the 40% and 50% metal-containing composites, but the yield was low (<50%), so the fracture toughness values of these composites were probably also low (<10 MPa$\sqrt{m}$), and similar to binary Cr_2Nb and Cr_2Hf-based composites.

2. Elevated temperature strength

The tensile strength of the Laves phase-based composites are shown in Table II and Fig. 4. Given the flaw sensitivity of these composites, tensile testing at elevated temperatures was selected rather than room temperature. Also shown for comparison are compressive strengths at 1200 °C for monolithic Cr_2Nb, as reported by Fleischer,[4] and Anton and Shah.[2] No tensile data were obtained for the Cr_2Nb–30%Nb binary composite in the present study because it was too brittle to machine tensile bars from the DS samples. The $Cr_2(Nb)$–40%(Nb) composite had a fracture stress of 132 MPa at 1200 °C without any elongation. The yield strength of the $Cr_2(Nb)$–50%(Nb) composite at 1200 °C was 120 MPa, the slightly lower value being expected for the composite with the smaller volume fraction of Laves phase. At 1200 °C a UTS of 153 MPa and an elongation of 56% was measured for this composite. For comparison, a Nb-based alloy with a similar composition to that of the metallic phase in these composites (except for the addition of Al) had a yield strength of 70 MPa at 1200 °C. At 1100 °C, yield and ultimate tensile strengths of 210 and 265 MPa were measured for the same composite. Kumar and Miracle[17] reported a compressive yield strength of two phase as-forged Cr–6.5% Hf hypoeutectic Cr_2Hf–Cr composite of ~100 MPa at 1200 °C. This is somewhat less than that measured in tension for the $Cr_2(Nb)$–(Nb) composites investigated in the present study, and may be due in part to the lower volume fraction of Laves phase.

There are two important points regarding this data. First, the $Cr_2(Nb)$–(Nb) Laves phase composites which

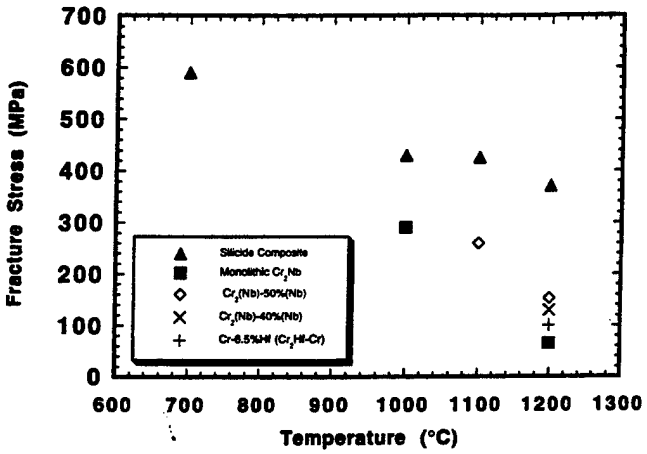


FIG. 4. The variation of tensile strength of $Cr_2(Nb)$–(Nb) composites as a function of temperature. Also shown are tensile strengths of a niobium silicide based composite.[10] Literature data for monolithic Cr_2Nb[2,4] and a Cr_2Hf–Cr[17] composite are included.

contained Hf and Ti had higher fracture strengths at 1200 °C than either the monolithic Cr_2Nb, or the binary Cr_2Hf-Cr composite.[17] The Hf and Ti additions increased the high temperature strength. Second, the fracture strengths of the $Cr_2(Nb)$–(Nb) with 50% and 40% metal were similar. Compressive strengths of ~600 MPa at 1200 °C have been reported for Cr_2Nb–Nb by Takasugi *et al.*[8] They also investigated the strain rate sensitivity of the compressive strength. However, strengths of this order at 1200 °C have yet to be demonstrated in tension.

The yield strengths of a silicide-based composite with a volume fraction of 50% (Nb) are also shown in Fig. 4. This composite contained ~50% in total of Nb_3Si and Nb_5Si_3 type silicides. The constituent phase chemistries have been described in more detail elsewhere.[10] It can clearly be seen that at temperatures up to 1200 °C the yield strengths of the silicide-based composites were approximately twice those of the Laves phase-based composites. The room temperature fracture toughness of the same silicide-based composite was ~22 MPa$\sqrt{m}$. Thus, for a given volume fraction of intermetallic, the silicide-based composites offer a more attractive balance of room temperature fracture toughness and high temperature strength.

IV. CONCLUSIONS

DS $Cr_2(Nb)$–(Nb) Laves phase composites with Hf and Ti additions have been prepared with $Cr_2(Nb)$ volume fractions in the range 70–50%. Hf and Ti additions in the ranges 7.5 to 9.2% and 16.5 to 26%, respectively, were investigated. The Hf and Ti additions provided a coarser two-phase structure than was observed in the binary Cr_2Nb–Nb composite. However, the room temperature fracture toughness values of all of these composites were low (<10 MPa$\sqrt{m}$). Tensile strengths for the Hf and Ti containing $Cr_2(Nb)$–(Nb) composites at 1200 °C of up to 132 MPa were measured. However, these strengths are lower than that of a niobium silicide-based composite with a similar volume fraction of metallic phase. In the silicide-based composite, the metallic phase provides more effective toughening, since toughness values of >20 MPa$\sqrt{m}$ have been measured. Thus, the niobium silicide-based composite possesses a better balance of room temperature and elevated temperature mechanical properties than the $Cr_2(Nb)$–(Nb) Laves phase based composites.

ACKNOWLEDGMENTS

The authors would like to thank D. J. Dalpe for the directional solidification, C. Canestraro for the tensile testing, and H. A. Lipsitt for helpful discussions.

REFERENCES

1. D. L. Anton and D. M. Shah, Mater. Sci. Eng. **A153**, 410–415 (1992).
2. D. L. Anton and D. M. Shah, in *High-Temperature Ordered Intermetallic Alloys IV*, edited by L. A. Johnson, D. A. Pope, and J. O. Stiegler (Mater. Res. Soc. Symp. Proc. **213**, Pittsburgh, PA, 1991), pp. 733–738.
3. H. J. Goldschmidt and J. A. Brand, J. Less-Comm. Met. **3**, 44–61 (1961).
4. R. L Fleischer, C. L. Briant, and R. D. Field, in *High-Temperature Ordered Intermetallic Alloys IV*, edited by L. A. Johnson, D. A. Pope, and J. O. Stiegler (Mater. Res. Soc. Symp. Proc. **213**, Pittsburgh, PA, 1991), pp. 463–474.
5. B. P. Bewlay, J. A. Sutliff, M. R. Jackson, and H. A. Lipsitt, Acta Metall. Mater. **42** (8), 2869–2878 (1994).
6. B. P. Bewlay, H. A. Lipsitt, M. R. Jackson, W. J. Reeder, and J. A. Sutliff, Mater. Sci. Eng. **A192/193**, 534–543 (1995).
7. M. Takeyama and C. T. Liu, Mater. Sci. Eng. **A132**, 61–66 (1991).
8. T. Takasugi, S. Hanada, and K. Miyamoto, J. Mater. Res. **8**, 3069–3077 (1993).
9. M. R. Jackson and K. D. Jones, in *Refractory Metals Extraction, Processing and Applications*, edited by K. C. Liddell, D. R. Sadoway, and R. G. Bautista (TMS Publications, Warrendale, PA, 1991), pp. 310–320.
10. B. P. Bewlay and M. R. Jackson unpublished.
11. M. R. Jackson, D. W. Skelly, and R. G. Rowe Annual Reports, WRDC Contract #F33615-91-C-5613 (1994, 1995).
12. M. Venkatraman and J. P. Neumann, Bull. Alloy Phase Diagrams **7** (5), 462–466 (1986).
13. D. J. Thoma and J. H. Perepezko, in *Intermetallic Matrix Composites*, edited by D. L. Anton, P. L. Martin, D. B. Miracle, and R. McMeeking (Mater. Res. Soc. Symp. Proc. **194**, Pittsburgh, PA, 1990), pp. 105–112.
14. D. J. Thoma and J. H. Perepezko, Mater. Sci. Eng. **A156**, 97–108 (1992).
15. T. B. Massalski, *Binary Alloy Phase Diagrams* (ASM INTERNATIONAL, Materials Park, OH, 1991).
16. D. L. Davidson and K. S. Chan, AFOSR Final Report (April 1995).
17. K. S. Kumar and D. B. Miracle, Intermetallics **2**, 257–274 (1994).
18. K. S. Ravichandran, D. B. Miracle, and M. G. Mendiratta, in *Intermetallic Matrix Composites III*, edited by J. A. Graves, R. R. Bowman, and J. J. Lewandowski (Mater. Res. Soc. Symp. Proc. **350**, Pittsburgh, PA, 1994), pp. 249–254.

Toughness Enhancements In Intermetallic-Based Composites: Processing and Properties

B.P. Bewlay, W.J. Reeder, H.A. Lipsitt, M.R. Jackson and J.A. Sutliff

Processing and Fabrication of Advanced Materials
for High Temperature Applications V, 1996

...EMPLATE (For final size o...

TOUGHNESS ENHANCEMENTS IN INTERMETALLIC-BASED COMPOSITES : PROCESSING AND PROPERTIES

B.P. Bewlay[1], W.J. Reeder[2] , H.A. Lipsitt[2] , M.R. Jackson[1] and J.A. Sutliff [1]

[1]General Electric Company, Corporate Research and Development Center,
Schenectady, New York 12301.
[2] Department of Mechanical and Materials Engineering,
Wright State University, Dayton, Ohio 45435.

Abstract

The present paper describes the room temperature fracture toughness of binary Nb-Si and also higher-order Nb alloy in-situ composites synthesized using cold crucible directional solidification. The composites consist of Nb_3Si and Nb_5Si_3 based silicides or both, and are toughened by a Nb-Si solid solution. Binary Nb-Si alloys with Si compositions in the range 10 to 25 were investigated in order to examine the effects of a range of volume fractions of Nb, Nb_3Si, and Nb_5Si_3 on fracture toughness. Higher order Nb-based alloys were also examined and the resulting composites consist of similar silicides alloyed with Ti and Hf. Room temperature fracture toughness measurements and R-curve experiments were performed using four point bending tests of pre-notched specimens, and fractography was performed to evaluate the toughening behavior of the composite.

Bewlay et al

Introduction

In-situ composites based on Nb-Si alloys have great potential for high temperature structural applications because of their combination of high temperature strength, creep resistance and room temperature fracture toughness [1-7]. Typically, these in-situ composites consist of Nb_5Si_3 and/or Nb_3Si and are toughened with a Nb-Si solid solution [8, 9], which throughout the present paper is abbreviated by (Nb). The present paper will describe the microstructures of binary Nb-Si alloy and higher order alloy directionally solidified (DS) in-situ composites together with fracture toughness measurements.

An extrinsic toughening approach has been adopted in the present study to generate a composite consisting of silicides and (Nb) [1-8]. Single phase Nb_5Si_3 has promising high temperature creep behavior and high temperature strength, but a room temperature fracture toughness of only ~3 MPa$\sqrt{m}$ [5]. However, fracture toughness values of greater than 20 MPa$\sqrt{m}$ have been reported separately in extruded and DS composites from Nb - Si alloys [4, 6].

The basis for the in-situ composites investigated in the present study is the binary Nb-Si phase diagram. The Nb-rich side of the Nb-Si phase diagram contains a eutectic between (Nb) and Nb_3Si, and a eutectoid between (Nb) and Nb_5Si_3 [10]. The assessed phase diagram indicates a eutectic point at 18.7%Si (all compositions in the present paper are in atom %) and 1883°C. Nb_5Si_3 melts congruently at 2484°C and there is a peritectic on the Si-rich side of the eutectic at 1980° C involving Nb_5Si_3 and Nb_3Si of near-stoichiometric compositions. Nb_3Si decomposes into (Nb) and Nb_5Si_3 at 1780° C. However, the decomposition kinetics are very slow [9], and in as-cast alloys with less than 19.5%Si (the liquid composition at the peritectic temperature), only Nb_3Si and no primary Nb_5Si_3 is observed.

In the present paper, the microstructures and room temperature fracture toughness of DS hypo and hypereutectic binary Nb-Si alloys with compositions between 10 and 25%Si will be described. DS hypoeutectic alloys possess (Nb) dendrites aligned perpendicular to the fracture plane, and allow measurement of their toughening contribution to the total toughness of the composite. In addition, the microstructure and room temperature fracture toughness of an advanced Nb-Si composite alloyed with Hf, Ti, Cr and Al are also described. This paper will describe how room temperature fracture toughness values of greater than 20 MPa$\sqrt{m}$ can be achieved in advanced intermetallic systems.

Experimental

Directional Solidification

DS samples were prepared from >99.99% purity elements by induction levitation melting in a segmented water-cooled copper crucible. The alloys were triple melted and then directionally solidified using the Czochralski method, as has been described in more detail elsewhere [8]. Samples were directionally solidified using rates of 1-5 mm/minute. Typical DS samples of a range of composites from binary Nb-Si alloys are shown in Figure 1.

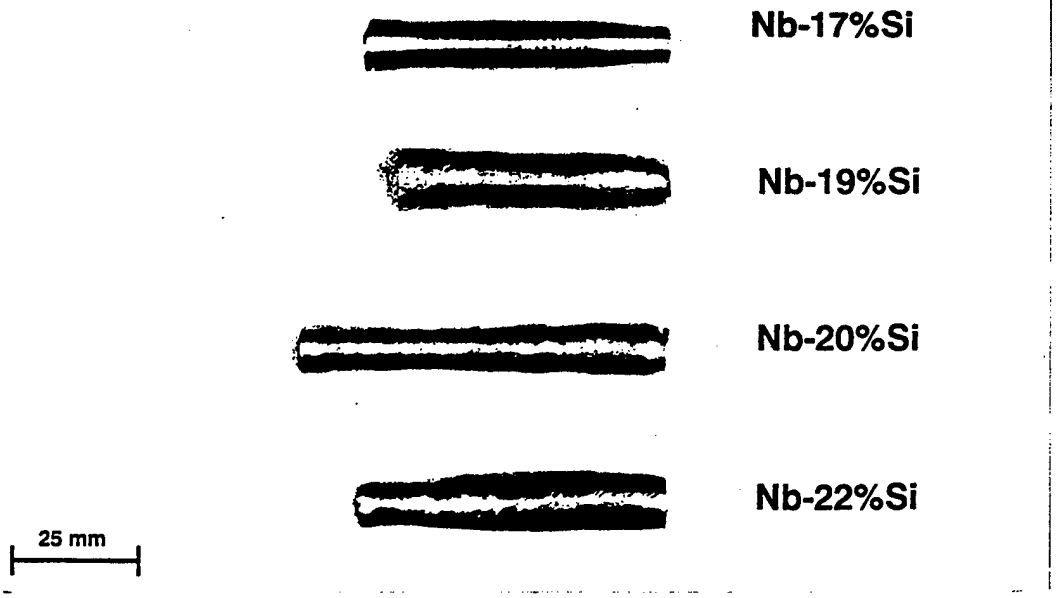


Figure 1: Photograph of DS Nb-Si in-situ composites with compositions of 17, 19, 20 and 22%Si.

Fracture Toughness Measurements

Fracture toughness measurements were performed using monotonic loading experiments and R-curve measurements. Single-edge notch beam (SENB) specimens were machined from DS samples by electro-discharge machining (EDM). These samples were oriented so that the longitudinal axes of the SENB's were parallel to the growth direction of the composites. The SENB's were surface ground to their finished dimensions to remove the EDM re-cast layer. The bars were notched at their mid-points using a 50μm EDM wire and machined to accept a crack opening displacement gage (COD). Fracture toughness was measured by four point bending at a cross-head speed of 7.2×10^{-5} mm/s. Generally, the crack propagated from the machined notch.

R-curve measurements were performed following the ASTM standard test procedure E-561-94. [12, 13]. These measurements were also performed in four point bending, but with a cross-head speed of 0.00025 mm/s in displacement control mode. The COD was monitored using an Instron double cantilever beam type COD gage. The specimen was loaded using ~25N increments and the COD was recorded as a function of load. After each loading increment, the crack length was measured using an optical microscope mounted on the cross-head when the crack was fully arrested. Fracture surfaces were examined subsequently using SEM.

Results and Discussion

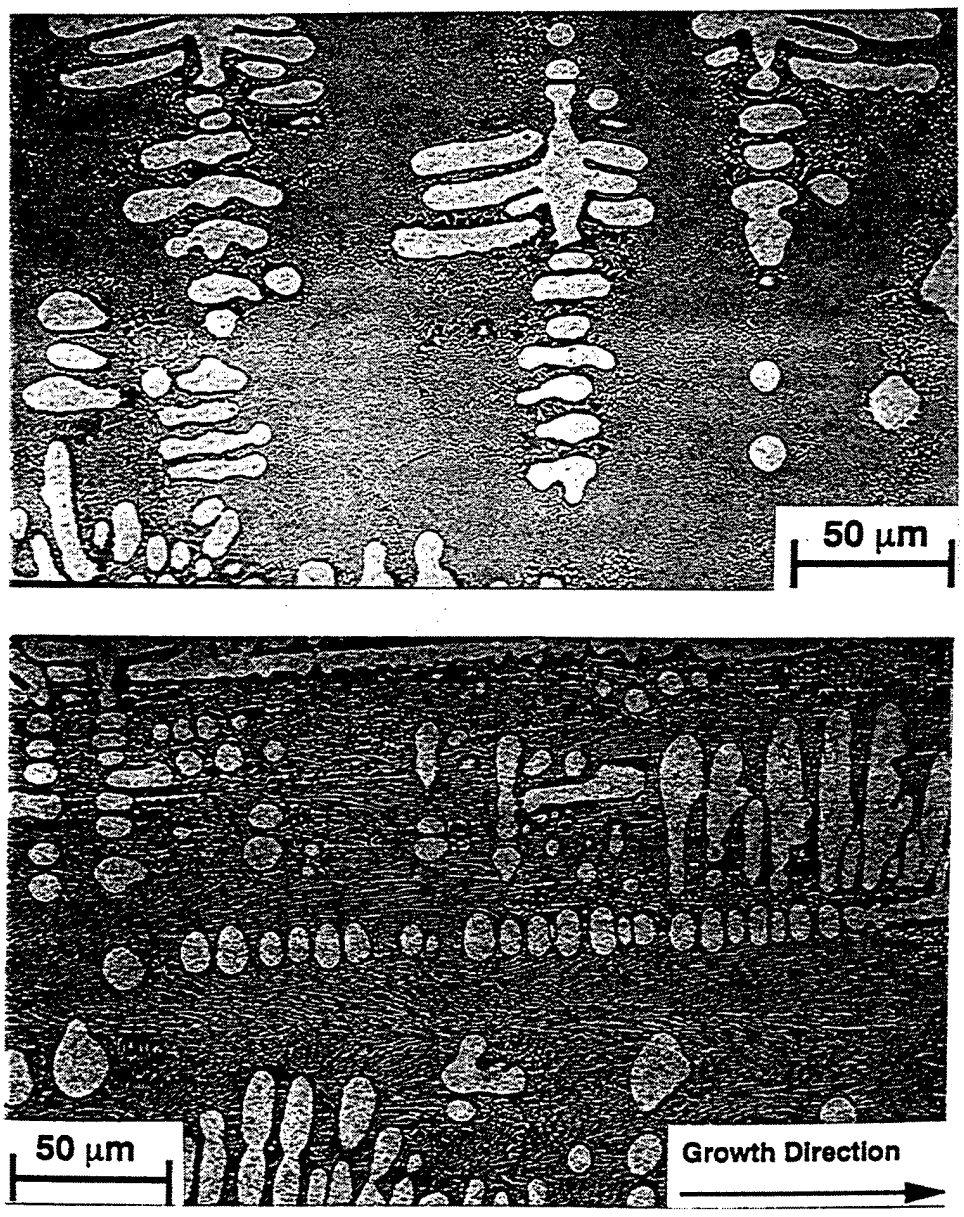
Microstructures

DS composites of Nb-Si alloys with compositions less than 18.2% Si contained primary (Nb) dendrites and a eutectic of (Nb) and Nb_3Si. Alloys with compositions greater than 18.7% Si and less than 20%Si were found to contain primary Nb_3Si dendrites with

Bewlay et al

interdendritic eutectic. The DS eutectic (18.2%Si) consisted of fine-scale (Nb) rods and ribbons aligned parallel to the growth direction in an Nb_3Si matrix. There was no decomposition of the Nb_3Si to Nb_5Si_3, on cooling, in any of the as-DS samples. The measured phase volume fractions were close to those expected from the binary phase diagram [9, 10].

Microstructures typical of all the hypoeutectic alloys are shown in Figures 2 (a) and 2(b) for the Nb-14%Si alloy. These micrographs are of polished sections and were taken using positive back scatter electron (BSE) imaging, which showed (Nb) as the light phase, and Nb_3Si as the dark phase. Transverse and longitudinal sections are shown. The Nb-10%Si alloy contained a volume fraction of 0.35 Nb_3Si, and the Nb-18.2%Si eutectic 0.64 Nb_3Si. The aspect ratios of the primary dendrites ranged from 200-300:1.



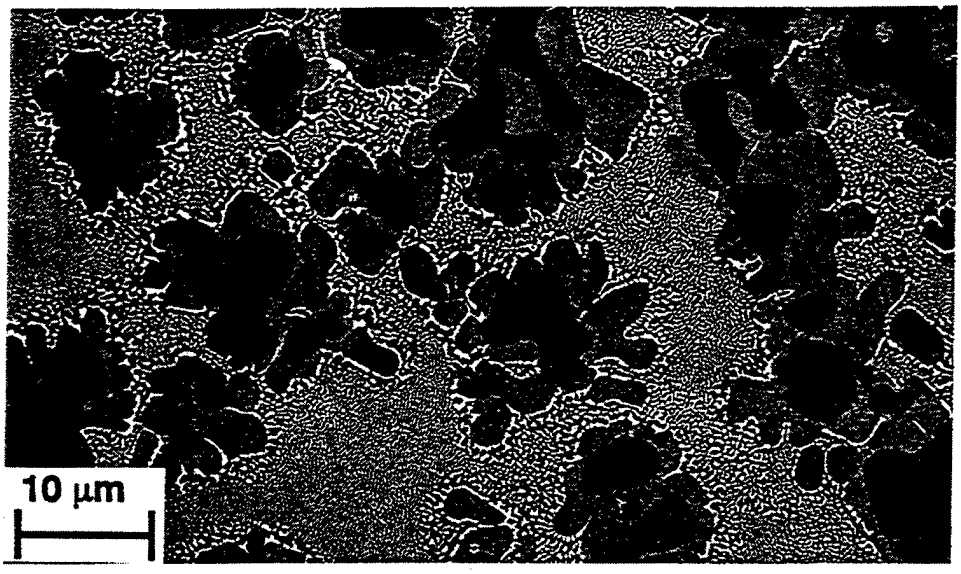
(a)

(b)

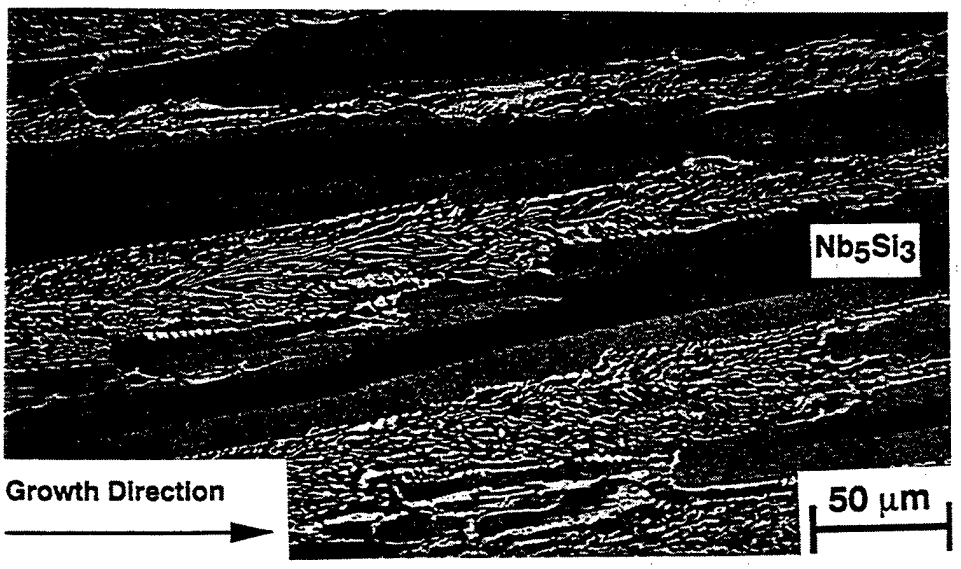
Figure 2: Scanning electron micrographs (positive BSE imaging) of (a) the transverse, and (b) the longitudinal sections of the Nb-14%Si alloy directionally solidified at 5mm/min.

Bewlay et al 4 13

Alloys with compositions between 20 and 25%Si contained primary Nb_5Si_3 dendrites with peritectic Nb_3Si, Nb_3Si dendrites, and the typical inter-dendritic eutectic of (Nb) and Nb_3Si. The peritectic Nb_3Si solidified on the primary Nb_5Si_3 dendrite cores and the dendritic Nb_3Si generally nucleated and grew on the peritectic Nb_3Si. Typical microstructures of transverse and longitudinal sections of the DS Nb-20%Si alloy are shown in Figures 3(a) and 3(b) respectively. The peritectic and dendritic Nb_3Si were indistinguishable. The Nb_5Si_3 was not strongly faceting, but the Nb_3Si on the Nb_5Si_3 had a faceted interface with the eutectic, generating the distinctively faceted Nb_3Si morphologies, similar to those observed for the primary Nb_3Si dendrites of the Nb-19%Si alloy. The faceted morphology of the Nb_3Si distinguishes it from the (Nb) and Nb_5Si_3.



(a)



(b)

Figure 3: Scanning electron micrographs (positive BSE imaging) of, (a) the transverse and, (b) the longitudinal sections of the Nb-20%Si alloy directionally solidified at 5mm/min.

A range of higher order Nb-Si based alloys were directionally solidified. These alloys contained additions of Hf, Ti, Cr and Al. The microstructure of a DS Nb-24.7Ti-8.2Hf-2.0Cr-1.9Al-16.0Si in-situ composite contained both metallic and M_3Si intermetallic dendrites, a small amount of a M_5Si_3 intermetallic, and an interdendritic eutectic of M_3Si intermetallic and metal; M designates a combination of Nb, Hf and Ti. The metallic dendrites were aligned with the growth direction. In this regard, this advanced composite was analogous to the binary hypoeutectic Nb-Si alloys with the exception of the primary M_3Si dendrites. The volume fraction of the metallic phase was 54%. Electron microprobe analysis showed that the metallic dendrites contained Nb, Ti, Hf, Si, Al and Cr. The M_3Si silicide phase contained 25%Si with 7.8 Hf, 18.2 Ti and the balance Nb. The $M_5(Si,Al)_3$ type phase contained 22.7 Ti and 12.7 Hf, with the Si and Al combining to 37.5%.

Composite Fracture Toughness

Fracture toughness measurements, K_q, from monotonic loading experiments are shown in Table 1 and Figure 4 for (Nb)-Nb_3Si composites with compositions from 10 to 25%Si. Toughness measurements on separate bending bars were reproducible to within 10%. For DS composites of hypoeutectic alloys, the fracture toughness increased with decreasing Si concentration and increasing (Nb) volume fraction, from 6 MPa$\sqrt{m}$ for the Nb-18.2%Si composition to 14.2 MPa$\sqrt{m}$ for the Nb-10%Si alloy. Figure 4 also shows previous fracture toughness measurements for arc-cast Nb-Si alloys in the arc-cast condition, and in the arc-cast, extruded and heat-treated condition [2, 3]. The fracture toughness of DS Nb-Si alloys is ~50% greater than that of arc-cast alloys, and ~20% less than that of extruded alloys of equivalent compositions [2, 3, 11].

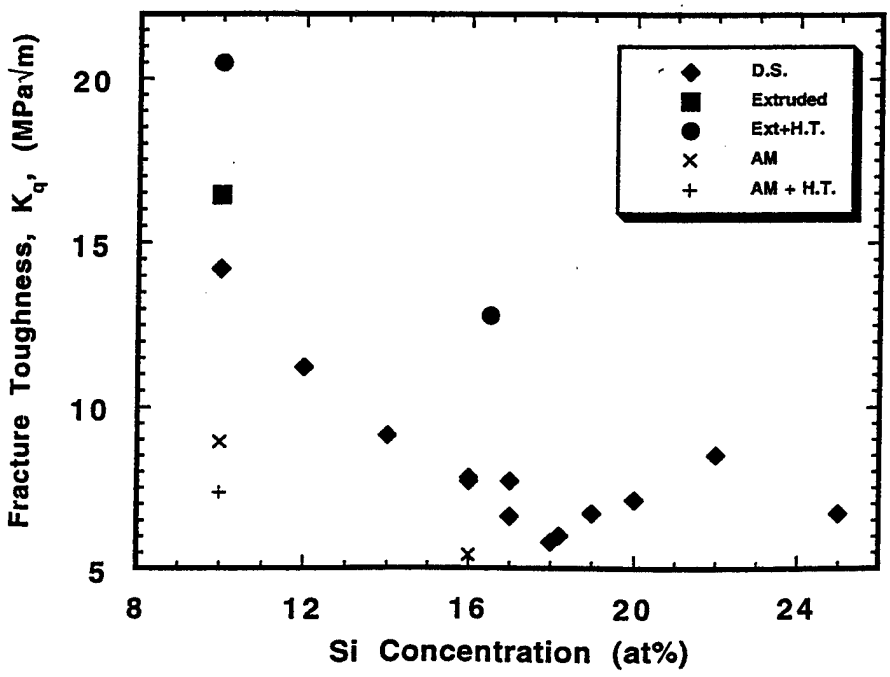


Figure 4: The effect of Si concentration on the fracture toughness of binary DS Nb-Si alloys with compositions from 10 to 25%Si.

Bewlay et al 6 13

Table I : Room Temperature Fracture Toughness of Nb-Si In-Situ Composites.

Composition	K_q (MPa√m)	K_{Ic} (MPa√m)
Nb-10 Si	14.2	-
Nb-12 Si	11.2	-
Nb-14 Si	9.1	8.5
Nb-16Si	7.8	6.5
Nb-17 Si	7.2	-
Nb-18.2 Si	5.8	6.5
Nb-19 Si	6.7	-
Nb-20 Si	7.1	-
Nb-22 Si	8.5	-
Nb-25 Si	6.7	-
Nb-24.7Ti-16Si-8.2Hf-2.0Cr-1.9Al	21	21

For hypereutectic alloys, the fracture toughness increased with increasing Si concentration and decreasing (Nb) volume fraction from that of the eutectic to 8.5 MPa√m for the Nb-22%Si composite, but then decreased to 6.7 MPa√m for the Nb - 25%Si composite. This trend was opposite to that observed in the hypoeutectic region, and suggests that toughening mechanisms other than ductile phase toughening also contributed to the work of fracture.

R-curves are shown in Figures 5(a) and (b) for the Nb-14, and 18.2%Si composites, respectively. Figures 5(a) and (b) indicate that in the binary Nb-Nb_3Si composites, the resistance to crack growth increased with increasing crack length, indicating that crack growth occurred in a stable manner. These R-curves are similar to those measured by Rigney for Nb-10 %Si composites [11]. The R-curves for the Nb-14%Si alloy reflect the effects of the dendritic and fine-scale eutectic (Nb) on crack propagation. Since the Nb-18.2%Si composite displayed rising R-curve behavior, this suggests that the eutectic (Nb) also had a substantial impact on the mechanism of crack propagation in the Nb_3Si matrix, probably due to crack bridging and crack blunting mechanisms. The rising R-curve behavior suggests, that in the region of the crack tip, there is a small process zone, and that the size of this process zone increases with increasing crack length; the state of stress in the region of the crack tip is intermediate between plane strain and plane stress.

R-curves are shown in Figures 6 for the Nb-24.7Ti-16Si-8.2Hf-2.0Cr-1.9Al composite and are similar for those of the binary Nb-Si composites. In the DS condition this composite had a room temperature fracture toughness of 18.9-22 MPa√m, as measured using either monotonic loading or R-curve measurements. Typically, the initiation toughness values were 7 to 13 MPa√m, and the K_{Ic} values were 19-22 MPa√m. These fracture toughness values represent ~50% improvement over the best DS binary Nb-Si composites.

Bewlay et al

7

13

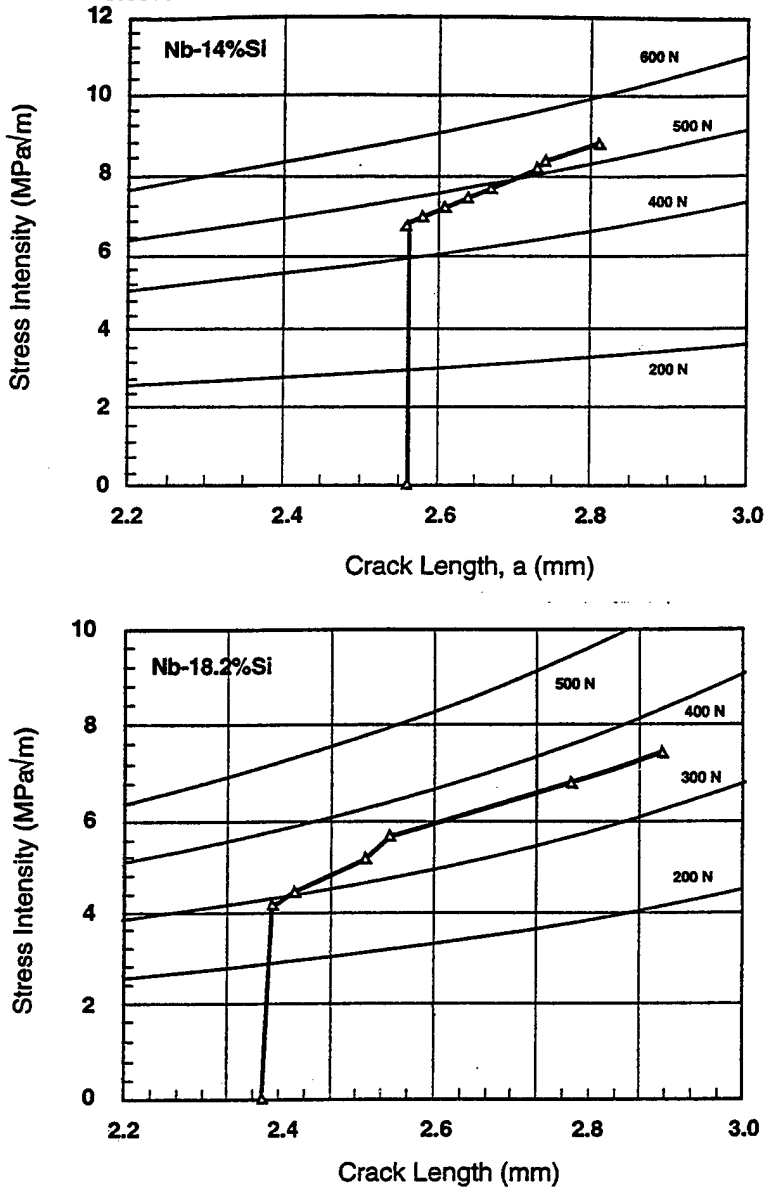


Figure 5: R-curve behavior of DS composites of (a) Nb-14%Si, and (b) Nb-18.2%Si.

The K_{Ic} measurements that were obtained from the R-curves are included in Table 1. There is reasonable agreement between the critical stress intensities derived from the monotonic loading and R-curve methods. The bending samples were not fatigue pre-cracked, but since the tangency point on the R-curve is not dependent upon the initiation event, the agreement between the two methods suggests that the deviations from the standard practice [12] in the monotonic loading experiments is relatively minor.

An important point to note about the measured R-curves shown in Figures 5 and 6 is that they extend beyond the instability point, K_{Ic}. This occurs because the R-curve tests were conducted using displacement control rather than load control [13]. Under load control conditions, the R-curve is only measured up to the point of instability, since beyond that point the constant driving force is greater than the resistance of the material to crack growth. However, in displacement control as the crack propagates, the unbroken cross-sectional area decreases and the compliance of the specimen increases; since the cross-

head is stationary and the specimen compliance is increasing, the applied load decreases thereby reducing the driving force for crack propagation and allowing the crack to arrest at a crack length that is greater than the critical crack length (the crack length at K_{Ic}). When the cross-head is stationary, the crack propagates under a continuously decreasing driving force.

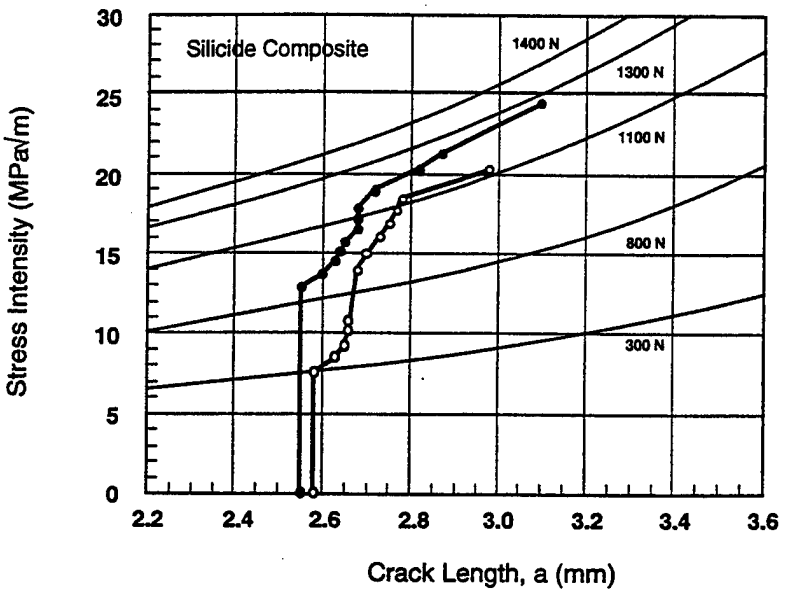


Figure 6: R-curve behavior of a DS Nb-24.7%Ti-16%Si-8.2%Hf-2.0%Cr-1.9%Al composite.

Composite Fractography

A typical fractograph of the DS Nb-16%Si composite is shown in Figures 7(a), indicating ductile failure of the dendrites with a high degree of pull-out from the matrix. In general, ~30% of the (Nb) dendrites failed in a ductile manner and the balance failed by cleavage. The mode of failure was related to the scale of the toughening phase; those dendrite arms which had a size between 5 and 10μm showed micro-voiding and ductile failure, while larger dendrites failed by cleavage. The inter-dendritic eutectic Nb_3Si matrix failed by cleavage, and the eutectic (Nb) generally was pulled out from the matrix to a chisel-point type failure. Micro-cracks were observed in the eutectic Nb_3Si around the (Nb). Figure 7(a) is typical of all the hypoeutectic DS alloys, except the Nb-10%Si composite. The DS Nb-10%Si composite contained coarser dendrites and generally all of the primary dendrites failed by cleavage. The cleavage faces of the primary (Nb) showed extensive river patterns. The cleavage failures suggest a high level of constraint of the dendrites. Crack bridging did not appear to be the dominant toughening mechanism in this composite. Other mechanisms were contributing, such as crack trapping by the (Nb) dendrites, crack blunting, and the work of fracture associated with complex cleavage in the primary (Nb).

The fracture surface of the DS eutectic alloy (Nb-18.2%Si) is shown in Figure 7(b). Almost all the eutectic (Nb) failed in a ductile manner and the Nb_3Si matrix failed by cleavage. The (Nb) exhibited plastic stretching, interface decohesion and necking to a chisel point. A small amount of micro-cracking of the Nb_3Si matrix was observed.

Bewlay et al 9 13

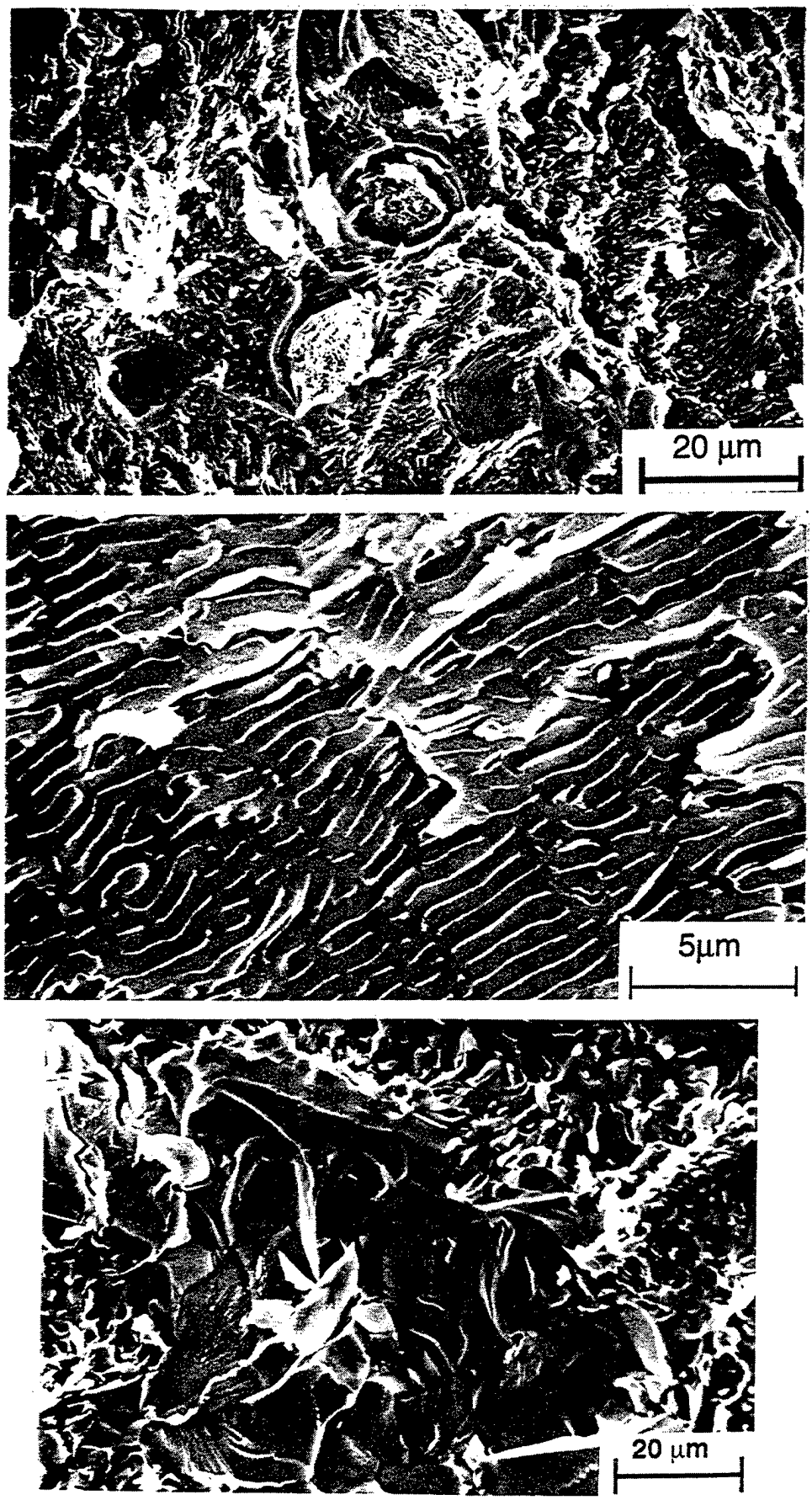


Figure 7: Fractographs of DS Nb-Si composites from alloys with compositions of (a) 16%Si, (b) 18.2%Si, and (c) 22%Si.

Bewlay et al 10 13

Multiple cleavage planes were observed in the Nb_3Si, but they were nearly parallel to each other. These observations suggest that the work of fracture of the eutectic is derived from ductile failure of the (Nb), micro-cracking and cleavage of the Nb_3Si matrix, as well as interface decohesion.

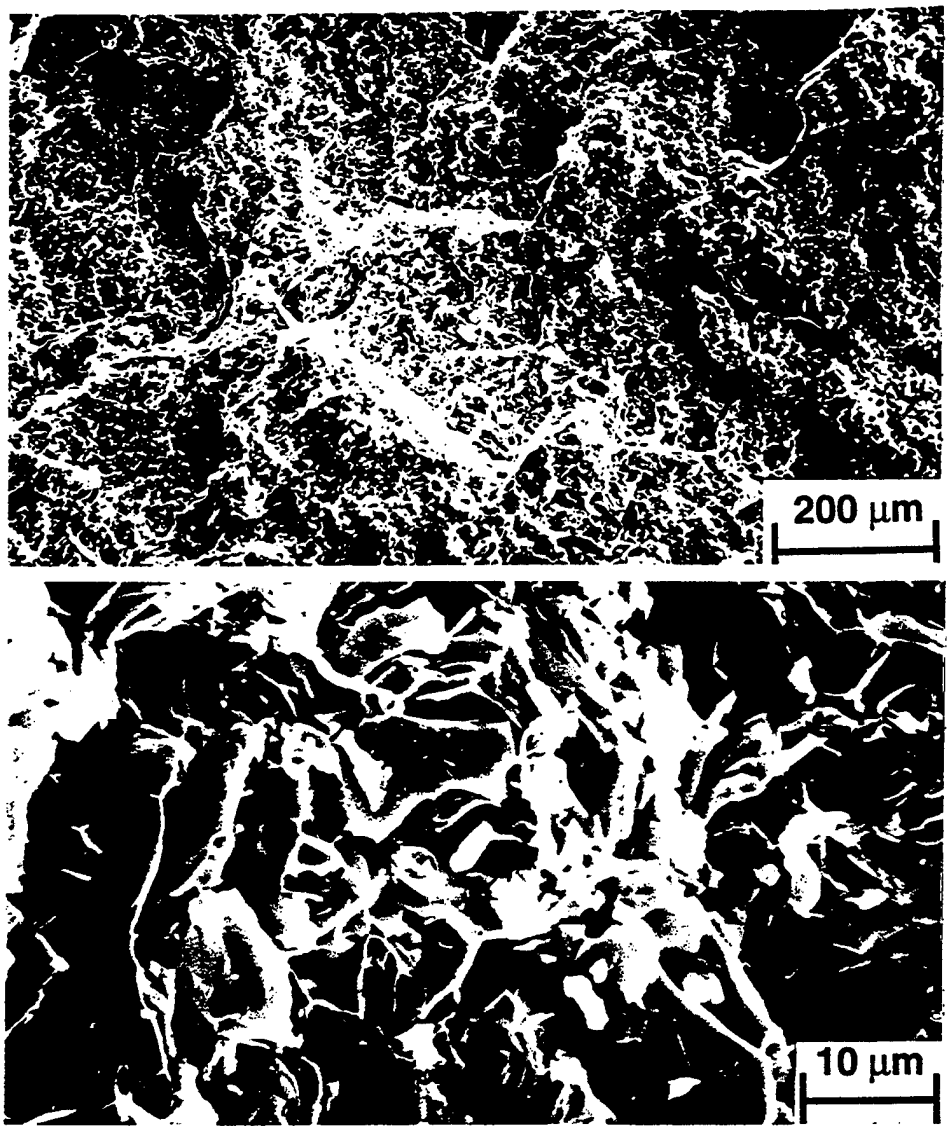
The fracture surface of a Nb-22%Si alloy is shown in Figure 7(c). This was typical of the binary Nb-Si composites with compositions in the range 20-25%Si. The primary Nb_5Si_3 dendrites and the Nb_3Si failed by cleavage, but the fracture path was highly convoluted. On a macroscopic scale, the fracture path deviated significantly from the transverse plane and was observed to make large steps, indicating deflection of the primary crack front. Fracture occurred on multiple planes with the propagation of many secondary cracks. Only the eutectic (Nb) failed in a ductile manner for these composites.

It is difficult to explain the increase in the toughness of the Nb-22%Si composite over the eutectic (8.5 vs 6 MPa$\sqrt{m}$). The toughening contribution provided by the eutectic (Nb) cannot explain the toughening increment, since there is a smaller volume fraction of (Nb) in the Nb-22%Si than the eutectic alloy and the toughness of the former is higher. Other than ductile failure of the eutectic (Nb) and the fine-scale (Nb) case around the peritectic Nb_3Si, the only other obvious work of fracture contributing to the toughening increment is multiple plane cleavage; this may have involved nucleation of new cracks, deflection of existing cracks, or branching of cracks during propagation. The higher Si concentration composite (25%Si) contained a larger volume fraction of Nb_5Si_3 which in the as-DS condition contained many transverse cracks and these may have provided a lower fracture stress for the composite.

Figure 8 shows fracture surfaces of the DS Nb-Ti-Hf-Cr-Al-Si composite. At low magnifications it can be seen that the fracture surface is highly convoluted, and at higher magnifications it can be seen that the metallic dendrites failed in a ductile manner, and were pulled out of the matrix. The metallic phase between the silicide dendrites was also pulled to a chisel point with microcracking of the silicide matrix. All of the M_3Si and M_5Si_3 intermetallic dendrites failed by cleavage.

Conclusions

The fracture toughness of as-DS composites of hypoeutectic Nb-Si alloys was found to increase with decreasing Si content (increasing volume fraction of the ductile Nb phase) from a minimum at the eutectic composition (18.2% Si) of 6 MPa$\sqrt{m}$ to 14 MPa$\sqrt{m}$ for the Nb-10%Si composite. In the hypereutectic regime, fracture toughness increased with increasing Si content to a maximum of 8.5 MPa$\sqrt{m}$ for the Nb-22%Si composite. Fractography revealed that toughening of these composites was derived from a complex mixture of mechanisms, including crack bridging, crack blunting, crack deflection and crack branching. Ductile phase toughening is observed in these Nb-Si-based composites. However, the fracture toughness increases approximately linearly with total (Nb) volume fraction, which suggests that ductile phase toughening is not the only operative toughening mechanism, because ductile phase toughening theories predict that the fracture toughness is dependent on the square root of the volume fraction of toughening



(a)

(b)

Figure 8: Fracture surfaces of the in-situ composite directionally solidified from the Nb-24.7%Ti-16%Si-8.2%Hf-2.0%Cr-1.9%Al alloy.

phase. The failure mode of the (Nb) was found to be related to the nature of the constraint imposed on it by the silicide matrix. R-curve measurements indicate that stable crack propagation can occur in these composites. The fracture toughness of DS Nb-Si alloys is ~50% greater than that of arc-cast alloys of equivalent compositions.

Room temperature fracture toughness values of >20 MPa$\sqrt{m}$ were measured in an advanced Nb-Ti-Si-Hf-Cr-Al composite. This composite combines high-strength low-toughness silicides with a lower-strength high toughness Nb-based metallic phase in order to generate a composite that has improved high temperature and low temperature mechanical properties.

Acknowledgments

The authors would like to thank D.J. Dalpe for the directional solidification and L. Peluso for the microprobe. This research was partially supported by AFOSR under contract #F49620-93-C-0007 with Capt. C.H. Ward as Program Manager.

References

[1] M.G. Mendiratta and D.M. Dimiduk, Mat. Res. Soc. Symp. Proc., 133 (1989), 441-447.

[2] M.G. Mendiratta, J.J. Lewandowski and D.M. Dimiduk, Metall. Trans. A, 22A (1991), 1573-1583.

[3] M.G. Mendiratta and D.M. Dimiduk. Metall. Trans. A, 24A (1993), 501-504.

[4] P.R. Subramanian, M.G. Mendiratta and D.M. Dimiduk, Mat. Res. Soc. Symp. Proc., 322 (1994), pp. 491-502.

[5] D.M. Dimiduk, M.G. Mendiratta and P.R. Subramanian, in Structural Intermetallics, Ed. R. Darolia, J.J. Lewandowski, C.T. Liu, P.L. Martin, D.B. Miracle, and M.V. Nathal, TMS Publications, Warrendale, Pa., (1993), pp. 619-630.

[6] B.P. Bewlay, M.R. Jackson, W.J. Reeder and H.A. Lipsitt, Mat. Res. Soc. Symp. Proc., 364 (1994), pp. 943-948.

[7] J.D. Rigney, P.M. Singh and J.J. Lewandowski, J. of Metals, 44 (8), pp. 36-41, 1992.

[8] K-M. Chang, B.P. Bewlay, J. A. Sutliff and M.R. Jackson, J. of Metals, 44 (6), 59, (1992).

[9] B.P. Bewlay, H.A. Lipsitt, W.J. Reeder, M.R. Jackson and J.A. Sutliff, Processing and Fabrication of Advanced Materials for High Temperature Applications III, Ed. V.A. Ravi, T.S. Srivatsan and J.J. Moore (TMS Publications, Warrendale, PA, 1993), pp. 547-565.

[10] T.B. Massalski, Binary Alloy Phase Diagrams, ASM Metals Park, Ohio (1991).

[11] J.D. Rigney, "Ductile-Phase Toughening of In-Situ Niobium Silicide-Niobium Composites," (Phd Thesis, Case Western Reserve University, 1993).

[12] "Standard Test Method for Plane-Strain Fracture Toughness of Metallic Materials", ASTM STP E-399, American Society for Testing and Materials, July 1983, pp. 488-512.

[13] "Standard Practice for R-Curve Determination," ASTM STP E 561-94, American Society for Testing and Materials, Philadelphia, 1994.

Bewlay et al

13

High-Temperature Refractory Metal-Intermetallic Composites

M.R. Jackson, B.P. Bewlay, R.G. Rowe, D.W. Skelly, and H.A. Lipsitt

Journal of Metals, January 1996

High-Temperature Refractory Metal-Intermetallic Composites

M.R. Jackson, B.P. Bewlay, R.G. Rowe, D.W. Skelly, and H.A. Lipsitt

In this article, toughness, oxidation, and rupture behaviors of present-generation refractory metal-intermetallic composites are compared to the performance requisites necessary to make these materials a competitive choice for the jet engine turbine environment of the future.

INTRODUCTION

A recent review of the development of single-crystal superalloys for gas turbine and jet engine applications discussed the significant gains in component operating temperatures.[1] In the past 30 years, high-pressure turbine blade temperatures have increased by 125°C as a result of controlled solidification to form single-crystal components as well as from the use of substantial additions of Re, W, Ta, and Mo. Total contents of these elements have been increased over levels of the first- and second-generation single crystals (alloys developed in the 1970s and 1980s) to levels of 20 wt.% in the third-generation alloys.

Surface temperatures at the hottest locations on state-of-the-art jet engine airfoils now approach 1,150°C, not only in hot-streak conditions but at the design condition. The most severe combination of stress and temperature in present engine designs corresponds to bulk average temperatures approaching 1,000°C (Figure 1). If the oxidation resistance of coated structures is sufficient, the third-generation single-crystal superalloys may make it possible to exceed the temperatures mentioned above by a further 25°C, and next-generation alloys (such as the blade alloy goal of the High-Speed Civil Transport program[2]) may achieve yet another 25°C increase in capability. However, further significant temperature gains are unlikely.

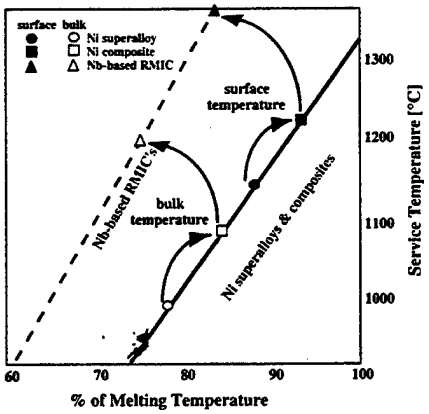


Figure 1. A comparision of service and melting temperatures for selected materials.

Improvements in performance over the single-crystal superalloys are anticipated for composites using a strong nickel superalloy as the toughening phase.[3] The strengthening phase may be a silicide intermetallic, a topologically close-packed phase such as σ, or a compound such as TiC. Such performance gains were demonstrated in past research on nickel-based, directionally solidified (DS), in-situ composites strengthened by monocarbides[4-6] or Ni_3Nb.[7] These composites had stress rupture resistance matching or exceeding that of third-generation single-crystal superalloys. In current efforts, the cost of low-rate, planar-front solidification is avoided by coupling a strong skin of composite material, possibly directly deposited, to a single-crystal spar material. This also avoids compositional restrictions implicit in the low-rate, planar-front solidification of nickel-based eutectic in-situ composites. An increase in the volume fraction of the strengthening phase above that in the nickel-based DS in-situ composite may result in as much as a 100°C performance improvement. As noted in Figure 1, however, increases that are much greater than this would result in surface temperatures nearly reaching the incipient melting temperature regime for interaction zones between coatings and superalloys.

For the systems currently under study, composite densities will be considerably less than densities for the advanced nickel-based single crystals. For example, the target for near-term nickel-based intermetallic composites is a density of less than 7.33 g/cm³, almost 20 percent less than third-generation single-crystal superalloys (9.05 g/cm³).[1] This target corresponds to a γ-γ′ composite containing either 35 vol.% TiC or 50 vol.% of a low-density σ phase.

Niobium-based refractory metal-intermetallic composites (RMICs)[8,9,10-12] have a much higher potential application temperature, based on their dramatically increased melting temperatures (T_m of 1,700°C for the example shown schematically in Figure 1). Potential increased temperature capability is estimated as nearly 200°C for both bulk average temperature and maximum surface temperature as compared to current single-crystal superalloys. The demonstrated rupture performance of the niobium-based RMICs compares well to second- and third-generation single-crystal superalloys; however, a 200°C improvement appears to be reasonable in terms of the limited alloy development attempted thus far for these systems[9,12-14] and the directions available to improve on their performance. The projected application temperatures represent a smaller fraction of the melting temperature for niobium-based RMICs than for single-crystal superalloys. Because of the ordered structure of the intermetallics, it may be

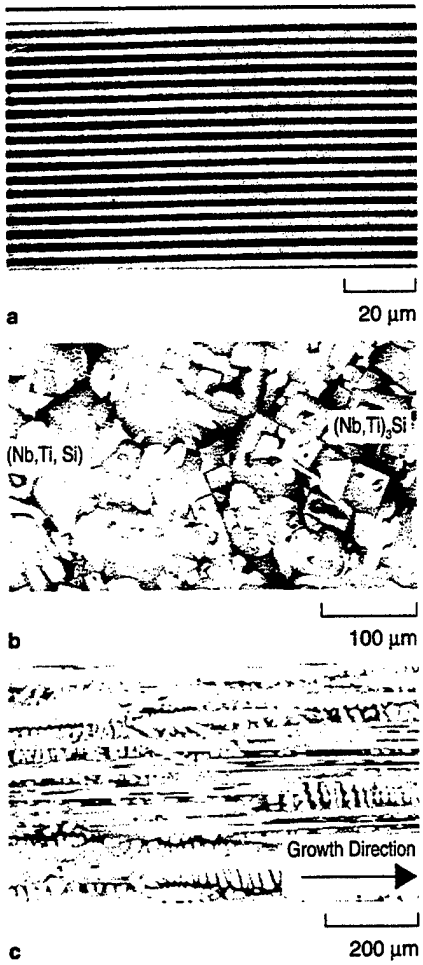


Figure 2. Examples of Nb-Ti toughened RMICs range from (a) the highly controlled microlaminate structures (Nb-$NbCr_2$) produced by PVD to the coarser, dendritic structures of a directionally solidified NbTi-M_3Si composite—(b) transverse to growth direction and (c) parallel to growth direction.

greater fractions of the melting temperature than is projected here. However, the use of niobium-based RMICs at surface temperatures much greater than 1,370°C will require further substantial increases in oxidation resistance for both the niobium-based RMIC and for protective coatings into a temperature regime beyond the demonstrated protective capability of SiO_2-based scales. The density target for the RMICs is <6.8 g/cm³, and a density of 7.2 g/cm³ has already been demonstrated for a tough, strong niobium-based RMIC.[8] This target is at least 25 percent lower than densities of third-generation single-crystal superalloys.

RMIC ARCHITECTURE

Processes and Microstructures

A number of processing routes have been explored for the production of niobium-based RMICs. They include multiple extrusion,[15,16] directional solidification,[17] arc casting, and physical vapor deposition (PVD).[13] Each process provides a different microstructure with a different scale to the phase dimensions and different phase chemistries. (Microstructures of arc castings are not described here because it is unlikely that airfoil structures will be made from such castings because of their high defect contents.)

Equiaxed mixtures of niobium solid solutions and silicide phases have been evaluated for extruded and heat-treated RMICs.[15] These have been extruded at ratios of ~4:1 at temperatures up to 1,600°C with subsequent heat treatments at 1,200–1,500°C. Depending on the silicon content, volume fractions of the silicide phase have been adjusted over an approximate range of 0.25–0.45. Extrusion of bar stock for eventual machining of turbine vanes and blades is an approach similar to that used for the oxide-dispersion-strengthened (ODS) nickel superalloy airfoils such as Inco alloys MA754 or MA6000.

Very different composite phase morphologies have been produced by sputter deposition of alternate layers of metal and intermetallic (Figure 2a).[13] With such processing, the laminate thickness and volume fraction of each phase can be exposure to the source and/or the deposition rate. The microstructure can also be graded or produced with specific architectures, again by controlling exposure time to the source. Sputtering is a very time-intensive deposition process, well suited to the study of a specific composite phase combination, but an impractical process for economic airfoil manufacture when wall thicknesses are in the range of 0.5–1.5 mm. However, electron-beam evaporation is a much more economically attractive route to producing such laminated structures, since rates of deposition of about 25 mm/min. have been achieved for nickel alloys,[18] and similar rates are anticipated for the refractory metals and intermetallics. Airfoil wall deposition times of less than an hour make this an economically attractive route to produce net-shape or near-net-shape outer walls.

Another microstructure that can be produced economically is the directionally solidified RMIC structure shown in Figures 2b and 2c.[17] Nonplanar-front DS ingots have been produced successfully in a levitation melting facility at rates of 0.5 mm/min. to 15 mm/min. for a broad range of niobium-based RMICs with melting points to about 2,300°C. These rates produce interpenetrating dendritic structures of the composite phases with dendrite cross sections on the order of 5–50 μm wide. These growth rates are consistent with economical low-defect ingot manufacture. The ingots could be machined into airfoil configurations, as is done for ODS nickel alloys.

These processes and their resulting microstructures appear to be capable of producing high-performance material. The economics of the processes and the optimization of properties will decide which is the best method for airfoil manufacture. It is possible that some of these processes can be combined to create more effective internal cooling geometries.

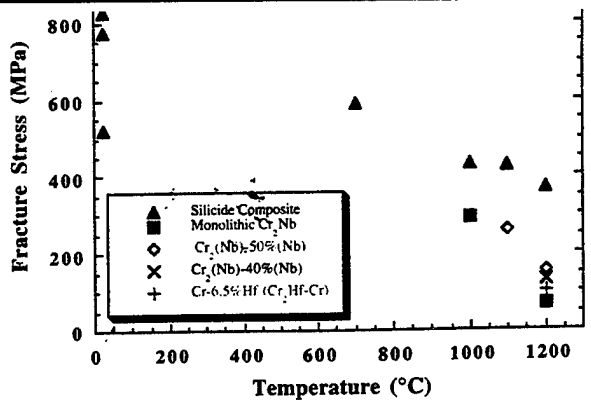


Figure 4. The tensile strength of a complex DS silicide-based RMIC shown as a function of temperature. There is a large improvement in high-temperature strength compared to monolithic Cr_2Nb and Laves-based composites.

Phase Chemistries

For most of the discussions that follow, binary Nb-Cr or Nb-Si phase equilibria are well established.[19,20] For ternary alloys, where titanium is substituted for some of the niobium, there have been few studies of the phase equilibria. A more complex RMIC composed of Nb, Ti, Hf, Cr, Al, and Si (referred to below as the complex DS RMIC) has been found to have attractive properties in toughness and strength.[8] For this composite, there has been some phase characterization. The complex DS RMIC contains a metal, an M_3Si phase, and smaller amounts of M_5Si_3. Measured phase compositions (in atomic percent) are as follows: metallic phase, approximately Nb-28.2Ti-5.1Hf-1.1Si-2.7Al-3.4Cr; M_3Si silicide phase, approximately Nb-18.2Ti-7.8Hf-25.0Si-0.1Al-0.2Cr; and $M_5(Si,Al)_3$ type phase, approximately Nb-22.7Ti-12.7Hf-36.5Si-1.2Al-0.4Cr. Ratios of Ti/Nb are 0.5 in the metal, 0.4 in the M_3Si, and 0.9 in the M_5Si_3. The partitioning of the hafnium is strongly into the silicides, with the greatest concentration being in the M_5Si_3 phase.

RMIC PROPERTIES

Fracture Toughness

Minimum toughness is required to make components and process them through heat treatments and other preparations, as well as to survive the final assembly into the engines and resist events in service such as foreign object damage. However, there is, at present, no defined design minimum for fracture toughness that makes a material suitable or unsuitable. Experience is being gained with materials such as NiAl, with a fracture toughness of 5–16 MPa $\sqrt{m}$,[21] and TiAl, with a fracture toughness of about 10–22 MPa $\sqrt{m}$.[22] A working hypothesis has been offered that once a material exceeds a threshold of ~20 MPa $\sqrt{m}$, toughness in the make-and-assemble stages is not a major issue.[23] This threshold may eventually be relaxed as further experience is gained.

Fracture toughness for a series of niobium-based RMICs is shown in Figure 3.[8,24] The addition of titanium has a marked beneficial effect on fracture toughness. A more highly alloyed RMIC, with 16 at.% silicon, has approached the threshold of ~20 MPa $\sqrt{m}$. The resistance

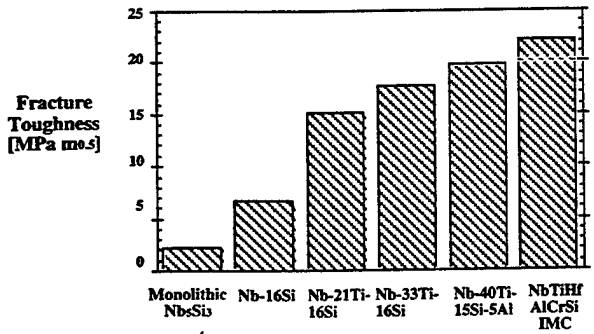


Figure 3. The fracture toughness of selected DS RMICs.

to crack growth also increases with increasing crack length, an indication that crack growth occurs in a stable manner. Crack initiation toughness values are 7–13 MPa $\sqrt{m}$, and K_{Ic} values are 19–22 MPa $\sqrt{m}$. Fracture surfaces of the complex DS RMIC are convoluted, consistent with a high work of fracture, and show the metallic phase fails in a ductile manner.

Similar fracture toughness behavior is seen for DS and extruded RMIC structures.[8,24,25] Other experiments suggest that double extrusion can produce further increases in fracture toughness in binary Nb-Si RMICs.[16] Tests of microlaminate structures of niobium and $NbCr_2$ have also shown fracture toughness of greater than 20 MPa $\sqrt{m}$.[13,26] The understanding of how microstructure and phase volume fraction influence fracture toughness has improved considerably in the past five years, and the influence of phase chemistry/strength on toughness is beginning to be understood.

For the further development of Nb-Ti silicides, fracture toughness no longer appears to be an insurmountable hurdle. The levels of toughness measured and the ability to perform common cutting, grinding, and machining tasks without inordinate care suggest that further gains in toughness are unnecessary for the present. However, as developments are made to improve RMIC oxidation resistance and high-temperature strength, any substantial loss in toughness must be avoided to insure these materials remain near the nominal minimum fracture toughness.

High-Temperature Strength

Tensile stress as a function of temperature is shown in Figure 4 for the complex (silicide) DS RMIC and Laves-phase RMICs.[8] Compared to high-temperature strengths of a number of Laves phases and Laves RMICs, the complex DS silicide RMIC has better strength at elevated temperatures. At 25°C, the tensile fracture stress was ~750 MPa (no elongation). The tensile yield stress of the composite at 1,200°C was 300 MPa, and an elongation of 19 percent was measured, indicating significant plastic deformation of both the metallic and silicide phases before failure at an ultimate strength of 370 MPa. Alloys of Nb-Ti bcc metals similar to compositions of the complex DS RMIC metallic phase have yield strengths of less than 55 MPa at 1,200°C.[27] Thus, the complex DS RMIC tensile properties are substantially improved compared to the metal phase. At room temperature, the metallic phase provides the composite with most of its toughness, whereas at elevated temperature (>1,000°C) the silicide phases provide the complex DS RMIC strength. The volume fraction of silicide in the composite can be increased to improve the high-temperature strength and oxidation resistance, but this may reduce room-temperature toughness below the threshold.

The tensile creep behavior for the complex DS RMIC is shown in Figures 5 and 6. At 1,100°C and 105 MPa, the rupture life was greater than 500 hours. Secondary tensile creep rates at 1,100°C and 105–140 MPa[15] are lower than those for PWA1480. The creep rate of the complex DS RMIC is lower than that of $MoSi_2$, but higher than that of the binary stoichiometric Nb_5Si_3. The tensile rupture behavior of the complex DS RMIC is shown in the Larson-Miller plots in Figure 6 and is compared to second- and third-generation single-crystal nickel-based superalloys.[1,8] The specific creep-rupture behavior (Figure 6b) illustrates the increase in specific rupture performance that results from the substantial reduction in density of the complex DS RMIC compared to the third-generation single-crystal superalloy. It should be noted that the single-crystal alloys are normally tested in the coated condition in air. Since coatings are not yet well-developed for protecting an RMIC under load, the comparison to single-crystal superalloys is made for the complex DS silicide RMIC tested in argon, and, thus, is probably optimistic.

The complex stress-rupture performance of DS RMIC is similar to that of advanced single-crystal nickel-based superalloys, and, therefore, is very promising considering the small number of niobium-based RMICs that have been evaluated in tensile creep rupture. However, designs using these RMICs will result in service at much higher bulk and surface temperatures than can be achieved with superalloys.[28]

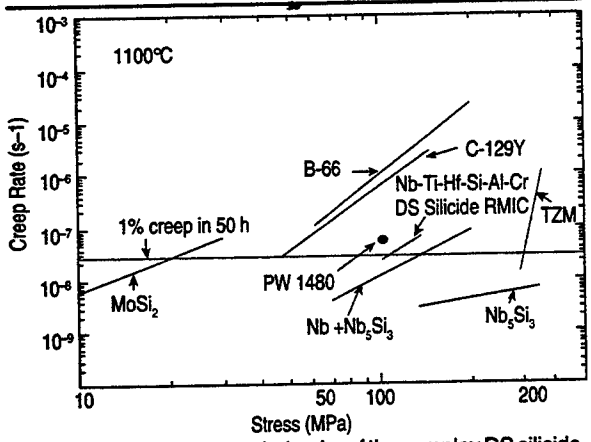


Figure 5. The tensile creep behavior of the complex DS silicide-based composite at 1,100°C compared with the compressive creep behavior of monolithic Nb_5Si_3 and Nb-Nb_5Si_3 binary composites (data courtesy of P.R. Subramanian and M.G. Mendiratta). Compressive creep behavior of several commercial alloys are included for comparison.

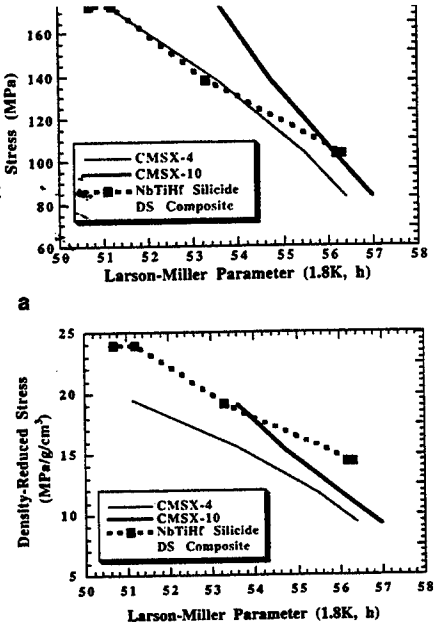


Figure 6. Stress rupture behavior of the complex DS RMIC compared to that of second- and third-generation, single-crystal nickel-based superalloys[1] in Larson-Miller plots (C = 20), where the temperature-time parameter is plotted against (a) rupture stress or (b) rupture stress/material density.

The rupture behavior that will be required of the niobium-based RMICs will be well beyond any behavior observed thus far. Current estimates predict that ultimately an 80-fold increase over current rupture lives may be required for successful application of the RMICs. This goal may be reached through increased silicide volume fraction, although modeling indicates this may not be successful.[29] The goal may be reached through alloying of both the metal phase and the silicide phase in the RMIC. For example, ductile (Nb-Ti)-based metals have been evaluated with about three times the high-temperature strength of the metal in the complex DS RMIC reported here.[30] It is not known what properties can be achieved for the silicide that would be in equilibrium with such a metal alloy or what properties the resulting RMIC would produce. Nevertheless, falling short of the goal of 80-fold improvement in rupture life would still offer substantially increased capability because of the strength/density and blade weight considerations, provided that oxidation goals can be approached.

Physical Properties

Thermal fatigue can occur for cyclic exposure of a structure when a thermal gradient is created within the material in transient and/or steady-state temperature fields. Stresses are generated by

differences in modulus (E), linear thermal expansion coefficient (α), and temperature (ΔT) between the hotter and cooler regions of the structure. Single-crystal nickel-based superalloys benefit in thermal fatigue from the low values of E that can be obtained for the <100> orientation of the crystal and from the absence of grain boundaries where fatigue can lead to cracking. The niobium-based RMICs must be able to withstand thermal stresses that will result from similar temperature gradients within airfoils.

Thermal expansion (25–1,250°C) and elastic modulus (25°C) have been reported for several arc-cast intermetallics homogenized at 1,200°C.[9,31] Metals with high-titanium or low-titanium concentrations, with compositions close to the equilibrium, with the high- and low-titanium Laves and silicide phases, have also been evaluated. The intermetallics included cubic Cr_2M and tetragonal M_5Si_3 (where M is Nb + Ti) with high-titanium (nearly equal niobium and titanium), low-titanium (about half as much titanium as niobium), or no titanium content. For all of the intermetallics, compositions were intended to be at the phase boundary with the niobium-based metallic phase. Measured densities were 6.6 g/cm³ and 7.2 g/cm³ for the metals, 6.7–7.4 g/cm³ for the Laves phases, and 5.7–6.8 g/cm³ for the silicides. Densities of arc-cast RMICs of nominally 30 vol.% metal were intermediate between metal and intermetallic values.

Dynamic elastic moduli were measured at room temperature, as shown in Figure 7.[9,31] For both Cr_2M and M_5Si_3, partial substitution of titanium for niobium does not affect the modulus significantly, and there is no apparent trend with titanium content. A substantial decrease of elastic modulus could be interpreted as indicating that the strength of the intermetallic phase might be degraded. No conclusions can be made about the effect of titanium substitution in intermetallics on high-temperature modulus or strength. The modulus measured for metals with compositions close to the equilibrium with the binary Laves and silicide phases is about 1.1 Mb, similar to pure niobium.

Thermal expansion behavior of the metals (Figure 7) is similar for both levels of titanium, with mean coefficients of thermal expansion of ~9.4 × 10⁻⁶/°C—close to pure niobium. The silicides had mean coefficients of ~9.0 × 10⁻⁶/°C.[9,31] The Laves phases showed a spread in total expansion, with mean coefficients of 8.7 × 10⁻⁶/°C to 11.8 × 10⁻⁶/°C. The expansion results suggest that Nb-Ti alloys are well matched to these intermetallics. Expansion mismatch over the expected airfoil temperature range is small, so that thermal ratcheting between the phases should be negligible.[6]

The generation of thermal stresses is driven by Eα ΔT considerations. Since ΔT will be greater for the RMICs because of the higher maximum temperatures expected as compared to superalloy airfoils, thermal stresses can represent a significant issue. However, Eα at 25°C for the niobium-based RMICs is about 10 percent less than for a single-crystal superalloy, even considering the high modulus of the strong intermetallics. Since modulus is not expected to fall rapidly with increasing temperature for the RMICs, the Eα difference between superalloy and RMIC will shrink with increasing temperature; however, projections of RMIC modulus at 1,250°C suggest that the Eα difference, relative to superalloys, will be near zero at that temperature. Thermal stresses in the niobium-based RMIC airfoils will be similar to the thermal stresses present in single-crystal superalloy airfoils. Differences in strength, toughness, and ductility between these two materials indicate that thermal fatigue must be evaluated for the RMIC systems.

Oxidation Resistance

Oxidation at 1,000°C and 1,200°C has been investigated for a number of niobium-based intermetallics and RMICs.[9,31] At 1,400°C and above, oxidation is catastrophic. The niobium-based aluminide intermetallics and RMICs are severely attacked in oxidation at both 1,000°C and 1,200°C. Many of the niobium-based silicide and Laves intermetallics and RMICs have oxidation resistance comparable to less-resistant superalloys, such as IN738, at these temperatures.

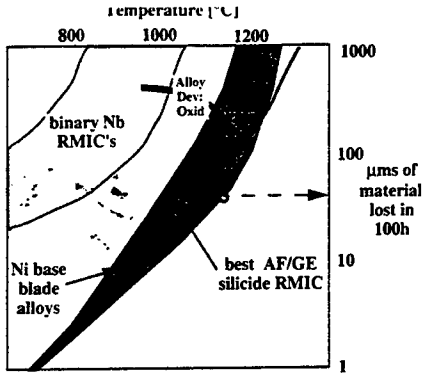


Figure 8. A comparison of oxidation performance of the DS RMIC and nickel-based superalloys.

The intermetallics and composites based on Laves Cr_2Nb generally possess greater oxidation resistance than the silicide alloys. Some tests of single-phase nonstoichiometric Cr_2Nb resulted in severe fracture during the 1,000°C and 1,200°C exposures and subsequent cooling to room temperature, so that only dust remained; in other tests, Cr_2Nb pins survived 150 hours at 1,200°C. This appears to be a pesting-type phenomenon (oxidation resistance dependent on stress and the defect content of the test sample). All titanium-modified Laves intermetallics and RMICs oxidized slowly through 200 hours at 1,000°C. Although spallation of oxide at 1,200°C occurred earlier for the titanium-containing Laves phases than for Cr_2Nb, the rates of consumption were less than for the Cr_2Nb pin, which was tested successfully. Adding nominally 30 vol.% niobium to produce a Cr_2Nb-Nb RMIC drastically increased the 1,200°C oxidation rate, with 100 µm of alloy lost after two hours. Adding titanium-modified metals at nominally 30 vol.% to the titanium-containing Laves phases increased oxidation-spallation rates slightly, as compared to the single-phase Laves phases, but attack was still less than 250 µm in 100 hours at 1,200°C.

Similar results were observed for the silicide alloys, although they were less oxidation resistant than the Laves alloys. At 1,000°C and 1,200°C, the titanium-free intermetallic crumbled after one hour of exposure in a pest-like behavior. The low-titanium $(Nb,Ti)_5Si_3$ phase spalled and reoxidized rapidly at 1,000°C, but the high-titanium intermetallic survived 100 hours before its appearance was poor enough to terminate the test. At 1,200°C, both single-phase Nb-Ti intermetallics oxidized rapidly and formed a very voluminous, thick scale. For the two-phase composites in 1,000°C oxidation, the titanium-free RMIC oxidized and spalled very rapidly. Both titanium-containing RMICs lost significant weight but visually appeared less degraded than their single-

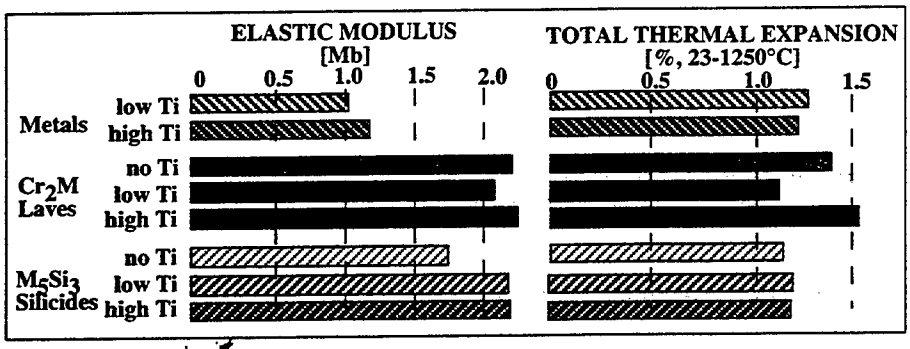


Figure 7. Measurements of room-temperature elastic modulus and linear thermal expansion from 23°C to 1,250°C for metals and intermetallic materials combined in RMICs[9,31]

phase intermetallic counterparts and were continued 50 hours longer in a 1,000°C test. Only the high-titanium RMIC showed oxidation at less than 250 μm in 100 hours at 1,000°C. Adding nominally 30 vol.% metal to the silicides resulted in a visual appearance of slower oxide growth at 1,200°C, so that the RMICs tests were continued longer even though erratic weight changes were noted. Compared to a desired oxidation rate of less than 250 μm in 100 hours at 1,200°C, the silicide alloys and RMICs were not adequate.

The oxidation resistance of niobium-containing silicide and Laves intermetallics and RMICs was improved by partial replacement of niobium with titanium. Oxidation resistance of Nb_5Si_3 was substantially improved by partial niobium replacement. Oxidation was erratic for Cr_2Nb; some binary samples failed almost immediately, while others were equivalent to the titanium-modified intermetallics. Addition of a metallic phase to these intermetallics to form RMICs produced the elimination of pesting, probably because of the improved fracture toughness and the resultant increased defect tolerance. For the RMICs, both binary Cr_2Nb-Nb and Nb_5Si_3-Nb composites were inferior to the higher order titanium-containing composites. The Laves-based RMICs had better oxidation resistance than the silicide-based RMICs at all temperatures evaluated.

A comparison of oxidation performance for the complex DS RMIC and nickel-based superalloys is shown in Figure 8. Subramanian et al.[32] have reported better oxidation for some silicide RMICs. The Laves RMICs were also better than the silicide RMIC shown. The complex DS RMIC shows material losses at rates intermediate between the rapid losses of an older superalloy like IN738 and the improved oxidation behavior of third-generation single-crystal superalloys. Goal behavior can be considered in terms of current superalloy capability. If superalloys can survive with surface temperatures of 1,150°C, then the rate of metal loss for the best superalloys at that temperature, ~25 μm in 100 hours, is a reasonable goal for the RMICs at their maximum surface temperature. The horizontal dashed arrow in Figure 8 indicates the goal behavior for RMICs with surface temperatures of 1,370°C.

Even if the goal of less than 25 μm loss in 100 hours at 1,370°C is met, the RMICs will need protective coatings. Considerable research has been performed on molybdenum-based silicide coatings alloyed with W, B, and Ge.[33,34] These coatings have shown promise of providing protection to 1,400°C. For thermal-spray-reaction silicide coatings on titanium-modified, niobium-based silicide RMICs, there was no coating failure observed in 1,200°C oxidation after 500 hours, and the measured weight gain was only 1.2 mg/cm^2.[35,36] Interaction of the coating and substrate is a desirable feature of fusion coatings,[37,38] since it insures full coverage of the surface with no pinholes through the coating that might leave the substrate vulnerable. Metallographic examination of the exposed sample showed oxidation of the outer coating, but very limited oxidation of the coating/substrate interaction layer (Figure 9). Coated RMIC performance at least equals the best current diffusion aluminide coatings on advanced superalloys (Figure 10). However, a realistic coating goal for niobium-based RMICs will need to be ~10 μm in 100 hours in 1,370°C oxidation, extrapolating the behavior for coatings on superalloys in the same manner as was noted above for the RMICs. Both RMICs and coating oxidation resistance must be improved substantially for the coated RMIC system to be useful in turbine blading applications.

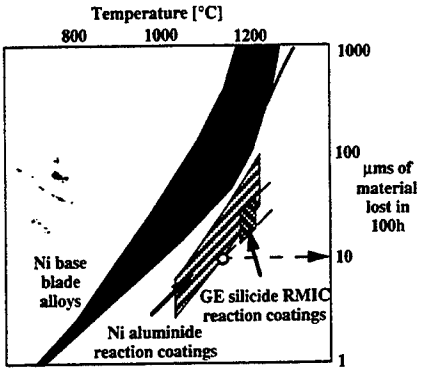


Figure 10. Coated RMIC performace as compared to aluminide-coated, nickel-based superalloys.

CONCLUSIONS

It is not clear which phase-strengthening mechanisms will be most beneficial to RMICs, but modeling and experimental efforts are now addressing this question. Microlaminate structures produced by PVD may allow greater volume fractions of silicide for strength while retaining toughness.

Although titanium additions to niobium-based RMICs have increased oxidation resistance substantially, considerable further improvement is needed. Even these improved RMICs will have to be coated to be useful in turbine components. Coating chemistries and processes must be compatible with those advanced-cooling turbine blade designs that are envisioned for the future engine performance goals. Coatings for niobium-based RMICs have matched the current performance of coatings on superalloys, but will have to operate at substantially higher temperatures. There is evidence that this oxidation resistance can be achieved with existing coating chemistries; however, these coatings may be difficult to produce on internal surfaces. Complex airfoil internal structures dictate the use of coating processes such as chemical vapor deposition or slurry reactions.

Concerns about fracture toughness are now less of an issue, in part because sufficient effort already has been expended in selecting airfoil materials. Provided that future chemistry and structure modifications do not decrease fracture toughness to substantially below 20 MPa $\sqrt{m}$, fracture toughness should not prove to be a major barrier to the use of niobium-based RMICs in jet engine turbine airfoils.

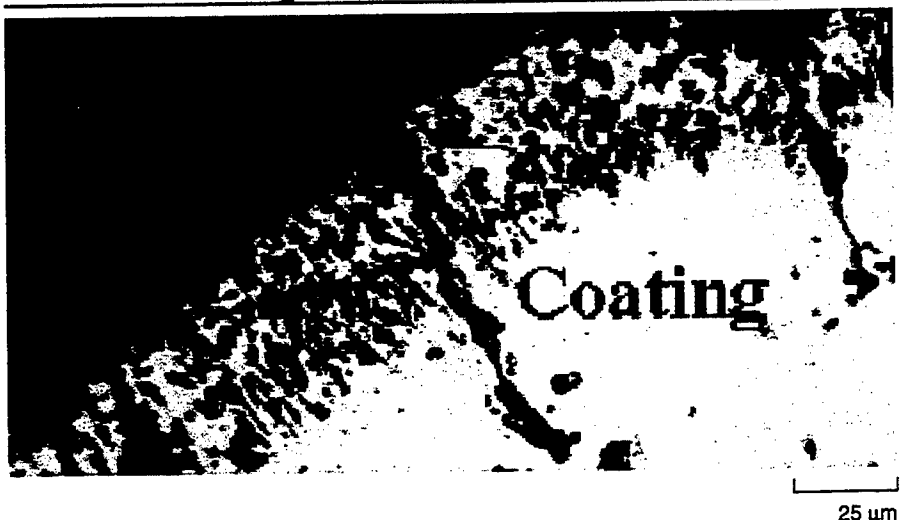


Figure 9. Microstructure of a fusion-silicide-coated silicide RMIC that has withstood 500 hours oxidation at 1,200°C. The coating is partially consumed by oxidation, but there is no internal oxidation of the underlying composite.

ACKNOWLEDGEMENTS

The authors thank W.J. Reeder, D.J. Dalpe, L.A. Peluso, and E.H. Hearn for their contributions to the experimental work presented. This research was partially sponsored by the U.S. Air Force Office of Scientific Research under contract number F49620-93-C-0007 with Dr. C.H. Ward as program manager; by Wright Research and Development Cen-

ter under contract number F33615-92-C-5977 with M.A. Stucke as program manager; and by Naval Air Warfare Center under contract number N68335-94-C-0207 with A.S. Culbertson as program manager. The authors are also grateful to Drs. M.G. Mendiratta and P.R. Subramanian, UES, Dayton, Ohio, and Dr. D.M. Dimiduk, U.S. Air Force Wright Laboratory, for their sustained focus on the refractory silicide composites and for helpful discussion of their results.

References

1. G.L. Erickson, *JOM*, 47 (1995), pp. 36–39.
2. T.A. Heppenheimer, *High Tech* (July 1986), pp. 46–51.
3. M.R. Jackson, D.W. Skelly, and R.G. Rowe, *Materials and Processes for Near-Term Intermetallic Matrix Composite Turbine Blades*, Annual Report (September 30, 1995) GE Corporate Research and Development, Schenectady, NY, NAWC contract N68335-94-C-0207.
4. C.A. Bruch et al., *Conf. on In Situ Composites-III*, ed. J.L. Walter et al. (Lexington, MA: Ginn Cust. Publ., 1979), pp. 258–267.
5. T. Khan, *Conf. on In Situ Composites-III*, ed. J.L. Walter et al. (Lexington, MA: Ginn Cust. Publ., 1979), pp. 378–388.
6. D.A. Woodford, *JOM*, 42 (1990), pp. 50–55.
7. A..D. Cetel, M. Gell, and J.W. Glatz, in Ref. 5, pp. 292–302.
8. B.P. Bewlay et al., *Investigation of High-Temperature Eutectic-Based Microcomposites*, Annual Reports (March 1994 and March 1995), GE Corporate Research and Development, Schenectady, NY, AFOSR contract F49620-93-C-0007.
9. M.R. Jackson, R.G. Rowe, and D.W. Skelly, *Alloy Development of In-Situ Intermetallic Composites*, General Electric Co Report 94CRD050, Annual Report #1 (September 20, 1993), WRDC contract F33615-91-C-5977.
10. D.M. Dimiduk, M.G. Mendiratta, and P.R. Subramanian, *Structural Intermetallics*, ed. R. Darolia et al. (Warrendale, PA: TMS, 1993), pp. 619–630.
11. M.G. Mendiratta and D.M. Dimiduk, *Metall. Trans. A*, 24A (1993), pp. 501–504.
12. B.P. Bewlay et al., *Mat. Res. Soc. Symp. Proc. 364* (Pittsburgh, PA: MRS, 1995), pp. 943–948.
13. R.G. Rowe and D. W. Skelly, *In-Situ Synthesis of Intermetallic Matrix Composites*, Semiannual reports #1 (September 1991 through March 1992), and #2 (April 1992 through September 1992), GE Corporate Research and Development, Schenectady, NY, WRDC contract F33615-91-C-5613.
14. B.P. Bewlay et al., *Processing and Fabrication of Advanced Materials for High Temperature Applications III*, ed. V.A. Ravi, T.S. Srivatsan, and J.J. Moore (Warrendale, PA: TMS, 1994), pp. 547–565.
15. P.R. Subramanian, M.G. Mendiratta, and D.M. Dimiduk, *JOM*, 48 (1) (1996). pp. 33–38.
16. I. Weiss, M. Thirukkonda and R. Srinivasan, *Mat. Res. Soc. Symp. Proc. 322* (Pittsburgh, PA: MRS, 1994), pp. 377–386.
17. K-M. Chang et al., *JOM*, 44 (1992), pp. 59–63.
18. D. W. Skelly, M.R. Jackson, and A.M. Ritter, *Evaporation Through Tungsten to Achieve High-Rate Vapor Phase Processing of Intermetallics*, Summary Report (June 1995), GE Corporate Research and Development, DOE contract De-FG02-94ER12142.
19. T.B. Massalski, *Binary Phase Diagrams* (Metals Park, OH: ASM, 1991).
20. B.P. Bewlay et al., *Acta Metall. Mater.*, 42 (1994), pp. 2869–2878.
21. S. Shrivastava and F. Ebrahimi, in Ref. 12, pp. 431–436.
22. R. Behr et al., in Ref. 12, pp. 781–786.
23. L.A. Johnson, GEAE, in panel discussion at Workshop on High Temperature Silicides, Wright State University, Dayton, OH (October 14, 1994).
24. B.P. Bewlay et al., "Toughness Enhancements in Intermetallic-Based Composites: Processing and Properties," (Warrendale, PA: TMS, to be published).
25. W.J. Reeder, M.Sc. thesis, Wright State University, February, 1995.
26. R.G. Rowe et al., *Mat. Res. Soc. Symp. Proc. 322* (1994), pp. 461–472.
27. M.R. Jackson and K.D. Jones, *Refractory Metals Extraction, Processing and Applications*, ed. K.C. Liddell, D.R. Sadoway, and R.G. Bautista (Warrendale, PA: TMS, 1991), pp. 311–320.
28. P.R. Viars, "The Impact of IHPTET on the Engine/Aircraft System," #AIAA-892137, Am. Inst. Aero., Astronaut., Sys., and Oper. Conf., Seattle, WA (1988).
29. G.A. Henshall et al., in Ref. 12, pp. 937–942.
30. M.R. Jackson, *Tungsten and Refractory Alloys 2*, ed. A. Bose and R.J. Dowding (Princeton, NJ: MPIF, 1995), pp. 665–672.
31. M.R. Jackson, R. G. Rowe, and D. W. Skelly, in Ref. 12, pp. 1339–1344.
32. P.R. Subramanian, M.G. Mendiratta, and D.M. Dimiduk, in Ref. 16, pp. 491–502.
33. B.V. Cockeram, Ph.D. thesis, Ohio State University, Columbus, OH (1994).
34. A. Mueller et al., *J. Electrochem. Soc.*, 139 (1992), pp. 1266–1275.
35. M.R. Jackson and A.M. Ritter, "Coatings Tailored for Nb-Ti Ductile Alloys" (Paper presented at Aeromat '92, 1992), p. 42.
36. A.M. Ritter and M.R. Jackson, "Silicide Coatings for Intermetallic Composites" (Paper presented at TMS Fall Meeting, Chicago, October 1994.)
37. S. Priceman and L. Sama, *Electrochem Tech*, 6 (1968), pp. 315–326.
38. K.D. Jones et al., in Ref. 27, pp. 299–310.

ABOUT THE AUTHORS

M.R. Jackson earned his Ph.D. in metallurgy and materials engineering at Lehigh University in 1971. He is currently a metallurgist at General Electric (G.E.) Corporate R&D. Dr. Jackson is also a member of TMS.

B.P. Bewlay earned his Ph.D. in metallurgy and materials science at Oxford University in 1987. He is currently a metallurgist at G.E. Corporate R&D. Dr. Bewlay is also a member of TMS.

R.G. Rowe earned his Ph.D. in metallurgical engineering at the University of Illinois. He is currently a metallurgist at G.E. Corporate R&D. Dr. Rowe is also a member of TMS.

D.W. Skelly earned his Ph.D. in physical chemistry at the University of Notre Dame in 1965. He is currently a physical chemist at G.E. Corporate R&D.

H.A. Lipsitt earned his Ph.D. in metallurgical engineering at the Carnegie Institute of Technology in 1956. He is currently a professor at Wright State University. Dr. Lipsitt is also a member of TMS.

For more information, contact M.R. Jackson, G.E. Corporate R&D, Schenectady, New York 12301; (518) 387-6362; fax (518) 387-7495; e-mail jackson@crd.ge.com.

MAKE PLANS NOW *for the*

TMS
Minerals • Metals • Materials

Second International Symposium on Microalloyed Bar & Forging Steel

July 8-10, 1996

To be held at the
Colorado School of Mines in Golden, Colorado

This conference will provide you with a review of recent worldwide developments and new innovations in microalloying, thermomechanical process design, property evaluation, and applications of bar and forging steels.

Organized and sponsored by the Ferrous Metallurgy Committee of the The Minerals, Metals & Materials Society's (TMS) Structural Materials Division

Co-Sponsors:
Advanced Steel Processing & Products Research Center (ASPRC)
ASM International (ASM)
Forging Industry Association (FIA)
Forging Industry Educational and Research Foundation (FIERF)
Iron & Steel Society (ISS)
Society of Manufacturing Engineers (SME)

TECHNICAL SESSIONS WILL BE ORGANIZED INTO THE FOLLOWING TOPICS:

- ➡ Alloy Development
- ➡ Process Design & Implementation
- ➡ Mechanical Properties
- ➡ Fracture Enhancement
- ➡ Machinability

FOR GENERAL AND ATTENDANCE INFORMATION, PLEASE CONTACT:
TMS • Customer Service Department • 420 Commonwealth Drive • Warrendale, PA 15086-7514
Telephone: (412) 776-9000, ext. 270 • Fax: (412) 776-3770 • E-mail: csc@tms.org

TMS OnLine **OR**

UP-TO-DATE MEETINGS INFORMATION AND REGISTRATION IS ALSO AVAILABLE THROUGH TMS ONLINE VIA THE WORLD WIDE WEB AT: http://www.tms.org.

Orientation Imaging of a Nb-Ti-Si DS In-Situ Composite

J.A. Sutliff and B.P. Bewlay

Proc. of the 54th Annual Meeting of the Microscopy Society of America

ORIENTATION IMAGING OF A Nb-Ti-Si DIRECTIONALLY SOLIDIFIED IN-SITU COMPOSITE

J. A. Sutliff and B. P. Bewlay

GE Corporate R&D, P.O. Box 8, Schenectady, NY 12301

In this paper we report on the microstructural characterization of a directionally solidified (DS) Nb-Ti-Si alloy. The solidified ingot had a nominal composition of Nb-33 at%Ti- 16 at% Si and was grown using the Czochralski technique with growth rate of 5 mm/min. The as-solidified ingot was approximately 50 mm long with a 10 mm diameter. The microstructure was examined using backscatter electron imaging and the microtexture of each of the phases was determined using the Electron BackScattering Pattern (EBSP) technique for electron diffraction in the scanning electron microscope.[1] The details of the experiments are similar to those we have reported previously.[2] Automated EBSP scans were acquired in order to map the local texture (microtexture) over most of a transverse cross-section through the ingot.

Figure 1 is a backscattered electron image (BEI) of a transverse section of the as-solidified microstructure. In this image, the bcc-Nb phase is the lighter gray phase and has a dendritic structure. The dark gray phase is $(Nb,Ti)_3Si$ having a Ti_3P crystal structure. The silicide phase appears as both multiply-faceted dendrites and irregularly bounded grains. A pattern of shading, due to Ti segregation, can be seen in figure 1 and suggests a cellular solidification structure. Figure 2 is a BEI taken at higher magnification to show a region that was analyzed by automated-EBSP. Figure 3 contains orientation images generated from the automated-EBSP data set. In Figure 3a, the color black signifies positions for which no Nb diffraction patterns could be indexed and other shades of gray signify specific Nb orientations, as described by a set of Euler angles. A similarly generated orientation image for the silicide phase is shown in Figure 3b. The greyscale image presented here is actually a rendering of a truecolor image based on a RGB triplet using the Euler angles.

From the automated-EBSP data, we draw two principle conclusions. First, the orientation images show distinct regions in which the silicide and metallic grains have a single orientation. These regions correspond to the solidification cells that were anticipated by the BEIs. Second, both phases in this composite exhibit strong texture. The silicide phase has a very strong alignment of [001] with the growth direction and significant orientation clustering in a radial direction, giving an appearance more like a single crystal than a fiber texture oriented polycrystal. This is true for additional measurements extending over many cells. The metallic phase has a less intense, broader alignment of [113] with the growth direction and has more evenly distributed fiber texture. Further analysis of the automated-EBSP data to determine additional information, such as intra- and inter-cellular misorientation distributions, will be made. These results are significant with respect to the anisotropic mehanical properties of this material.[3]

References

[1] J.A. Venables and C.J. Harland, *Philosophical Magazine*, **27** (1973) 1193

[2] J.A. Sutliff and B.P. Bewlay, Proc. 53rd Ann. MSA Meeting, (1995) 123.

[3] Funding form the Air Force Office of Scientific Research is gratefully acknowledged

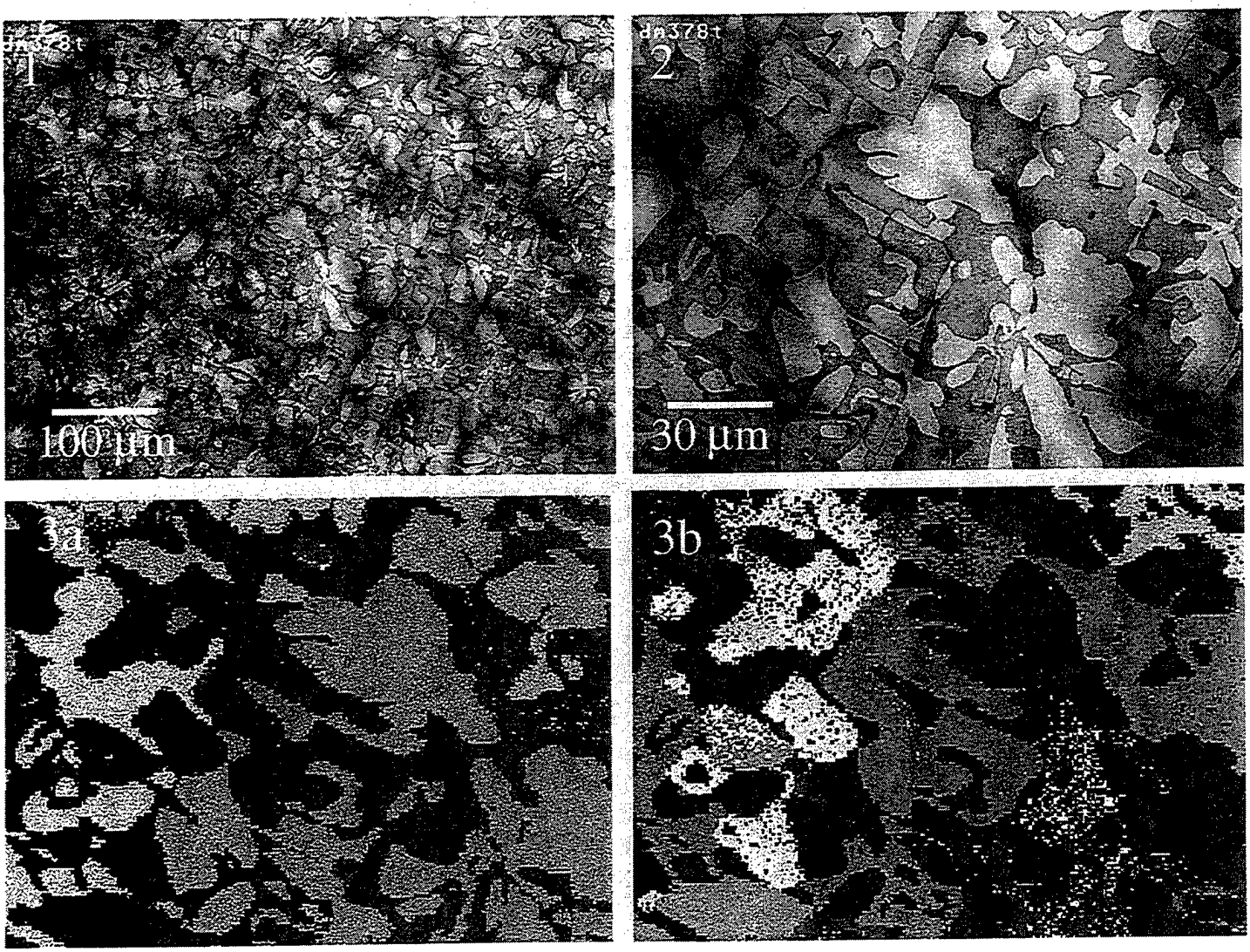


FIG. 1 - Backscattered electron image (BEI) of DS Nb-Ti-Si alloy.
FIG. 2 - A sub-region analyzed by automated-EBSP-(BEI).
FIG. 3 - Orientation images of sub-region for (a) the (Nb,Ti) phase and (b) the $(Nb,Ti)_3Si$ phase.